AGARD-CP-353

AD-A140 700

AGARD

ADVISORY GROUP FOR AEROSPACE RESEARCH & DEVELOPMENT

7 RUE ANCELLE 92200 NEUILLY SUR SEINE FRANCE

AGARD CONFERENCE PROCEEDINGS No.353

Combustion Problems in Turbine Engines

DTIC
ELECTE
APR 1 0 1984
S D
A

This document has been approved for public release and sale; its distribution is unlimited.



DTIC FILE COPY

DISTRIBUTION AND AVAILABILITY ON BACK COVER

84 04 06 030

COMPONENT PART NOTICE

THIS PAPER IS A COMPONENT PART OF THE FOLLOWING COMPILATION REPORT:

(TITLE): Combustion Problems in Turbine Engines Held at the Propulsion and Energetics Panel Symposium (62nd) Cesme (Turkey) on 3-6 October 1983.

(SOURCE): Advisory Group for Aerospace Research and Development Neuilly-sur-Seine (France)

TO ORDER THE COMPLETE COMPILATION REPORT USE AD-A140 700.

THE COMPONENT PART IS PROVIDED HERE TO ALLOW USERS ACCESS TO INDIVIDUALLY AUTHORED SECTIONS OF PROCEEDINGS, ANNALS, SYMPOSIA, ETC. HOWEVER, THE COMPONENT SHOULD BE CONSIDERED WITHIN THE CONTEXT OF THE OVERALL COMPILATION REPORT AND NOT AS A STAND-ALONE TECHNICAL REPORT.

THE FOLLOWING COMPONENT PART NUMBERS COMPRISE THE COMPILATION REPORT:

AD#:	TITLE:
P003 127	Aviation Fuel Specification Requirements - T... Significance and Future Trends.
AD-P003 128	Research on Aviation Fuel Instability.
AD-P003 129	Alternative Fuel Deposit Formation
AD-P003 130	Combustor Technology for Broadened-Properties Fuels.
AD-P003 131	Fuel Effects on Gas Turbine Combustion Systems,
AD-P003 132	Fuel Character Effects on Performance of Small Gas Turbine Combustion Systems.
AD-P003 133	U.S. Army Alternative Gas-Turbine Fuels Research; MERADCOM (Mobility Equipment Research and Development Command),
AD-P003 134	The Effects of Fuel Composition Upon Heat Transfer in Gas Turbine Combustors.
AD-P003 135	Alternate Fuels Use in a Vehicular Gas Turbine.
AD-P003 136	Recent Research on the Efflux of the Rolls-Royce Vaporiser Fuel Injector.
AD-P003 137	Effects of Airblast Atomizer Design Upon Spray Quality.
AD-P003 138	Optical Measurements of Droplet Size Distributions; Special Considerations in the Parameter Definition for Fuel Atomizers.
AD-P003 139	Liquid Fuel Atomization and Mixing nin a High Velocity Air Stream.
AD-P003 140	Detailed Fuel Spray Analysis Techniques.
AD-P003 141	Droplet Size Distribution and Liquid Volume Concentration in a Water Spray; Predictions and Measurements.
AD-P003 142	The Design and Performance of a Combustor with a Multiple Jet Primary Zone.
AD-P003 143	Soot Formation in Diffusion Flames.
AD-P003 144	Growth of Electrically Charged Soot Particles in Flames,
AD-P003 145	Formation and Destruction of Organic Pollutants in Thermal Systems and Flames
AD-P003 146	Optical Measurements of Soot Size and Number Density in a Complex Flow, Swirl-Stabilized Combustor.

COMPONENT PART NOTICE (CON'T)

AD#:	TITLE:
P003 147	The Design and Development of a Low Emissions Transply Combustor for the Civil Spey Engine.
AD-P003 148	Advanced Combustor Liner Cooling Concepts.
AD-P003 149	Development of Temperature-, Velocity- and Concentration-Profiles in a Curved Combustor.
AD-P003 150	An Investigation of the Interaction between Multiple Dilution Jets and Combustion Products.
AD-P003 151	Evaluation of Multi-Dimensional Flux Models for Radiative Transfer in Combustion Chambers : A Review.
AD-P003 152	A Droplet Evaporation Rate Controlled Combustion Model.
AD-P003 153	Predicted TF41 Performance with the AGARD Research Fuel.
AD-P003 154	Characterization of Heavy Oil Sprays in Isothermal and Burning Conditions with Laser Light Scattering Measurements in the Sideward Region.
AD-P003 155	Utilization of Laser Diagnostics to Evaluate Combustor Models.
AD-P003 156	Problem Independent Numerical Simulation of Two-Phase Flow in Combustors.

This document has been approved for public release and sale; its distribution is unlimited.

DTIC ELECTE MAY 1 1984 S D

Accession For
NTIS GRA&I
DTIC TAB
Unannounced
Justification
By
Distribution/
Availability Codes
Dist | Avail and/or Special
A-1

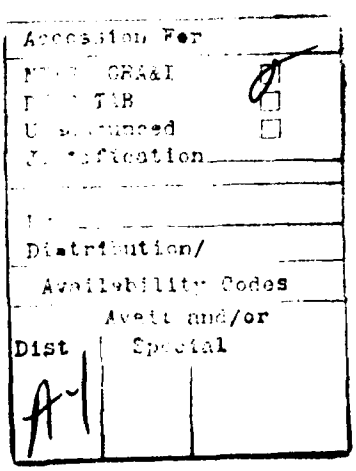
NORTH ATLANTIC TREATY ORGANIZATION

ADVISORY GROUP FOR AEROSPACE RESEARCH AND DEVELOPMENT

(ORGANISATION DU TRAITE DE L'ATLANTIQUE NORD)

AGARD Conference Proceedings No.353

COMBUSTION PROBLEMS IN TURBINE ENGINES





Papers presented at the Propulsion and Energetics Panel 62nd Symposium,
held in Çeşme, Turkey, 3–6 October 1983.

THE MISSION OF AGARD

The mission of AGARD is to bring together the leading personalities of the NATO nations in the fields of science and technology relating to aerospace for the following purposes:

- Exchanging of scientific and technical information;
- Continuously stimulating advances in the aerospace sciences relevant to strengthening the common defence posture;
- Improving the co-operation among member nations in aerospace research and development;
- Providing scientific and technical advice and assistance to the North Atlantic Military Committee in the field of aerospace research and development;
- Rendering scientific and technical assistance, as requested, to other NATO bodies and to member nations in connection with research and development problems in the aerospace field;
- Providing assistance to member nations for the purpose of increasing their scientific and technical potential;
- Recommending effective ways for the member nations to use their research and development capabilities for the common benefit of the NATO community.

The highest authority within AGARD is the National Delegates Board consisting of officially appointed senior representatives from each member nation. The mission of AGARD is carried out through the Panels which are composed of experts appointed by the National Delegates, the Consultant and Exchange Programme and the Aerospace Applications Studies Programme. The results of AGARD work are reported to the member nations and the NATO Authorities through the AGARD series of publications of which this is one.

Participation in AGARD activities is by invitation only and is normally limited to citizens of the NATO nations.

The content of this publication has been reproduced
directly from material supplied by AGARD or the authors.

Published January 1984

Copyright © AGARD 1984
All Rights Reserved

ISBN 92-835-0346-5



Printed by Specialised Printing Services Limited
40 Chigwell Lane, Loughton, Essex IG10 3TZ

THEME

In the Symposium, the following subjects were discussed: New problems and improvements in combustors and augmentors; combustion problems with alternative jet engine and industrial fuels; combustion of highly aromatic fuels; mixture preparation in low pollution and multi-fuel combustors; combustor modelling.

The Symposium was divided into 7 sessions: Fuel Research; Fuel Effects in Main Burners; Fuel Preparation; Kinetics and Soot Formation; Liner Cooling and Traverse Quality; Combustion Model Elements; and Modelling for Main Burners.

* * * *

Au cours de ce Symposium les sujets suivants ont été étudiés: nouveaux problèmes et perfectionnements dans le domaine des foyers et des augmenteurs; problèmes de combustion posés par les futurs carburants industriels et pour réacteurs; combustion des carburants à haute teneur aromatique; préparation de mélanges pour les foyers à faible taux de pollution et carburants multiples; modélisation des foyers.

Sept séances composèrent le Symposium à savoir: Recherches sur les carburants; Effets des carburants dans les brûleurs principaux; Préparation des carburants; Cinétique et formation de suie; Refroidissement de la chemise intérieure et étude des champs de température; Elements de modèle de combustion; et Modélisation des brûleurs principaux.

PROPULSION AND ENERGETICS PANEL

Chairman: Professor Ch.Hirsch
Vrije Universiteit Brussel
Dienst Stromingsmechanica
Pleinlaan 2
1050 Brussel, Belgium

Deputy Chairman: Professor Ir. H.Wittenberg
Delft University of Technology
Dept. of Aerospace Engineering
Kluyverweg 1
2629 HS Delft, Netherlands

PROGRAMME COMMITTEE

Professor A.M.Mellor (Chairman)
Drexel University
Dept. of Mechanical Engineering
and Mechanics
College of Engineering
Philadelphia, Pennsylvania 19104, US

Mr J.Acurio
Director, Propulsion Laboratory
US Army Research & Technology Labs.
(AVRADCOM)
21000 Brookpark Road
Cleveland, Ohio 44135, US

Professor R.S.Fletcher
Head of School of Mechanical Engineering
Cranfield Institute of Technology
Cranfield, Bedford MK43 0AL, UK

Professor R.Monti
Istituto di Aerodinamica
Università degli Studi
Piazzale Tecchio 80
80125 Napoli, Italy

M. l'Ingénieur en Chef M.Pianko
Coordinateur des Recherces en Turbomachines
ONERA
29 Avenue de la Division Leclerc
92320 Châtillon sous Bagneux, France

Professor Dr A.Üçer
Vice President
Middle East Technical University
ODTÜ
Makina Müh. Bölümü
Ankara, Turkey

Professor Dr-Int. G.Winterfeld
DFVLR
Institut für Antriebstecknik
Postfach 906058
5000 Köln 90, Germany

HOST NATION COORDINATOR

Professor Dr A.Üçer

PANEL EXECUTIVE

Dr-Ing. E.Riester
AGARD-NATO
7 rue Ancelle
92200 Neuilly sur Seine
France

ACKNOWLEDGEMENT

The Propulsion and Energetics Panel wishes to express its thanks to the Turkish National Delegates for the invitation to hold this meeting in Ceşme, and for the facilities and personnel made available for this meeting. The Panel wishes also to express its thanks to the Middle East Technical University in Ankara for its support in the preparation of the meeting.

CONTENTS

	Page
THEME	iii
PROPULSION AND ENERGETICS PANEL	iv
TECHNICAL EVALUATION REPORT by H.Mongia	ix
	Reference
SESSION I – FUEL RESEARCH	
AVIATION FUEL SPECIFICATION REQUIREMENTS – THEIR SIGNIFICANCE AND FUTURE TRENDS by L.Gardner and R.B.Whyte	1
RESEARCH ON AVIATION FUEL INSTABILITY by C.E.Baker, D.A.Bittker, S.M.Cohen and G.T.Seng	2
ALTERNATIVE FUEL DEPOSIT FORMATION by J.TeVelde, L.J.Spadaccini, E.J.Szetela and M.R.Glickstein	3
SESSION II – FUEL EFFECTS IN MAIN BURNERS	
COMBUSTOR TECHNOLOGY FOR BROADENED-PROPERTIES FUELS by W.J.Dodds	4
FUEL EFFECTS ON GAS TURBINE COMBUSTION SYSTEMS by S.A.Mosier	5
FUEL CHARACTER EFFECTS ON PERFORMANCE OF SMALL GAS TURBINE COMBUSTION SYSTEMS by P.Sampath and M.Gratton	6
US ARMY ALTERNATIVE GAS TURBINE FUELS RESEARCH: MERADCOM by C.A.Moses	7
THE EFFECTS OF FUEL COMPOSITION UPON HEAT TRANSFER IN GAS TURBINE COMBUSTORS by J.Odgers and D.Kretschmer	8
ALTERNATE FUELS USE IN A VEHICULAR GAS TURBINE by N.R.Marchionna	9
SESSION III – FUEL PREPARATION	
CONCEPTION D'UN FOYER A FLUX INVERSE POUR PETITES TURBOMACHINES par A.Mestre et G.Lagain	10
RECENT RESEARCH ON THE EFFLUX OF THE ROLLS-ROYCE VAPORISER FUEL INJECTOR by H.C.Low	11
EFFECTS OF AIRBLAST ATOMIZER DESIGN UPON SPRAY QUALITY by A.K.Jasuja	12
OPTICAL MEASUREMENTS OF DROPLET SIZE DISTRIBUTIONS: SPECIAL CONSIDERATION IN THE PARAMETER DEFINITION FOR FUEL ATOMIZERS by S.Wittig, M.Aigner, Kh.Sakbani and Th.Sattelmayer	13

Reference

LIQUID FUEL ATOMIZATION AND MIXING IN A HIGH VELOCITY AIR STREAM
by H.Eickhoff, D.Granser and W.Krockow 14

DETAILED FUEL SPRAY ANALYSIS TECHNIQUES
by E.J.Mularz, M.A.Bosque and F.M.Humenik 15

DROPLET SIZE DISTRIBUTION AND LIQUID VOLUME CONCENTRATION IN A WATER SPRAY. PREDICTIONS AND MEASUREMENTS
by G.P.Pita 16

THE DESIGN AND PERFORMANCE OF A COMBUSTOR WITH A MULTIPLE JET PRIMARY ZONE
by J.R.Tilston and J.P.D.Hakluytt 17

SESSION IV – KINETICS AND SOOT FORMATION

SOOT FORMATION IN DIFFUSION FLAMES
by J.H.Kent and H.G.Wagner 18

GROWTH OF ELECTRICALLY CHARGED SOOT PARTICLES IN FLAMES
by K.H.Homann, E.Ströfer and H.Wolf 19

FORMATION AND DESTRUCTION OF ORGANIC POLLUTANTS IN THERMAL SYSTEMS AND FLAMES
by J.Lahaye, G.Prado and A.Garo 20

OPTICAL MEASUREMENTS OF SOOT SIZE AND NUMBER DENSITY IN A COMPLEX FLOW, SWIRL-STABILIZED COMBUSTOR
by G.S.Samuelsen, C.P.Wood and T.A.Jackson 21

ETUDE EXPERIMENTALE ET MODELISATION DE LA CINETIQUE DE COMBUSTION DES HYDROCARBURES
par M.Cathonett, F.Gaillard, J.C.Boettner et H.James 22

SESSION V – LINER COOLING AND TRAVERSE QUALITY

THE DESIGN AND DEVELOPMENT OF A LOW EMISSIONS TRANSPLY COMBUSTOR FOR THE CIVIL SPEY ENGINE
by J.K.Banghu, D.M.Snape and B.R.Eardley 23

ADVANCE COMBUSTOR LINER COOLING CONCEPTS
by B.Simon, D.Schubert and U.Basler 24

DEVELOPMENT OF TEMPERATURE, VELOCITY, AND CONCENTRATION PROFILES IN A CURVED COMBUSTOR
by S.Wittig, R.Kutz, B.E.Noll and K-H.Platzer 25

AN INVESTIGATION OF THE INTERACTION BETWEEN MULTIPLE DILUTION JETS AND COMBUSTION PRODUCTS
by P.V.Chleboun, S.H.Nasser, F.B.Sebbowa and C.G.W.Sheppard 26

SESSION VI – COMBUSTION MODEL ELEMENTS

ETUDE DE PROBLEMES FONDAMENTAUX DE LA COMBUSTION DANS LES FOYERS DE TURBOREACTEURS AU MOYEN D'UN REACTEUR TUBULAIRE
par J.C.Bellet, P.Cambray, M.Champion et D.Karmed 27

EVALUATION OF MULTI-DIMENSIONAL FLUX MODELS FOR RADIATIVE TRANSFER IN COMBUSTION CHAMBERS: A REVIEW
by N.Selçuk 28

Paper 29 cancelled

Reference

A DROPLET EVAPORATION RATE CONTROLLED COMBUSTION MODEL
by A.D.Bayka 30

PREDICTION D'ECOULEMENTS TURBULENTS REACTIFS
par F.Dupoirieux 31

SESSION VII – MODELLING FOR MAIN BURNERS

PREDICTED TF-41 PERFORMANCE WITH THE AGARD RESEARCH FUEL
by J.E.Peters 32

ETUDE AERODYNAMIQUE DE LA COMBUSTION DANS LES FOYERS DE TURBO-MACHINES: APPROCHES EXPERIMENTALES ET THEORIQUES
par G.Frager, P.Hebrard, G.Lavergne et A.Mir 33

PREDICTION DES PERFORMANCES DE RENDEMENT ET DE STABILITE D'UNE CHAMBRE DE COMBUSTION
par Y.Chauveau, M.Desaulty et G.Bayle-Labouré 34

CHARACTERIZATION OF HEAVY OIL SPRAYS IN ISOTHERMAL AND BURNING CONDITIONS WITH LASER LIGHT SCATTERING MEASUREMENTS IN THE SIDEWARD REGION
by F.Beretta, A.Cavaliere and A.d'Alessio 35

UTILIZATION OF LASER DIAGNOSTICS TO EVALUATE COMBUSTOR MODELS
by W.M.Roquemore, R.P.Bradley, J.S.Stutrud, C.M.Reeves, C.A.Obringer and R.L.Britton 36

PROBLEM INDEPENDENT NUMERICAL SIMULATION OF TWO-PHASE FLOW IN COMBUSTORS
by W.H.Ayers, F.Boysan, B.C.R.Ewan and J.Swithenbank 37

TECHNICAL EVALUATION REPORT

by

Hukam C.Mongia

1. INTRODUCTION AND SUMMARY

With ever-increasing emphasis on improving gas turbine cycle efficiency, reducing engine development time/cost, reducing cost of ownership, minimizing pollutant emissions, and more recently the need to develop fuel-tolerant combustion systems, the combustion problems in gas turbine engines require special considerations. Consequently, the AGARD Propulsion and Energetics Panel (PEP) coordinated a 62nd Symposium that was held in Çeşme, Turkey on October 3–6, 1983.

A total of 36 papers was presented in this symposium entitled "Combustion Problems in Turbine Engines". The conference covered the following five subject areas:

- Alternative Fuels
- Fuel Preparation
- Kinetics and Soot
- Liner Cooling and Traverse Quality
- Combustion Modeling.

Each of these topics is covered in Paragraphs 2 through 6, respectively.

The meeting was well attended with delegates from various NATO countries. All of the sessions were lively with ample discussion time provided at the end of each paper. A number of interesting points were brought forward resulting in useful exchange of technical information.

It was the feeling of the delegates that the basic objectives of the meeting were achieved, and that intensive combustion research activities should continue for solving gas turbine combustion problems.

2. ALTERNATIVE FUELS

Nine papers were presented (1–9) covering the effects of alternative fuels on gas turbine combustion system performance with regard to soot emission, radiation heat loading, wall temperatures, ignition, relight altitude, nozzle performance, and fuel thermal stability. By combining presenters from universities, research laboratories and industry, it was possible to present a balanced view on the alternative fuels and their impact on gas turbine system design.

Gardner and Whyte (1) presented a summary of the work compiled by the AGARD Working Group 13 on Alternative Jet Fuels; the details are given in the AGARD Advisory Report No.181 (July, 1982). Normalized soot emission C* of a number of combustors was best fitted as a function of hydrogen content, i.e. a straight line on a semi-log scale. Here C* represents the ratio of the soot formed by any fuel to the soot formed by a fuel having hydrogen content of 12.5%.

An attempt was made to classify various combustion systems into the following four categories:

A. Conventional combustors
B. Semi-premix combustors
C. Stirred reactors
D. Pressure reactors.

For each of these categories, best-fit curves were presented of carbon emission index (C_{EI}) as a function of

$$\left(\frac{P}{O/C}\right)^{2.7}\left(\frac{H}{C}\right)^{-5.45}T_3^{-8.66}$$

The trends were predicted properly, although there was a significant scatter in the data base.

The NASA-sponsored and in-house work on jet fuel stability was presented by Baker (2) emphasizing the following major topics:

(1) Nature of fuel instability and its temperature dependence
(2) Methods of measuring the instability
(3) Chemical mechanisms involved in deposit formation
(4) Instrumental methods for characterizing fuel deposits.

Deposit formation investigation on four hydrocarbon fuels was presented in Reference 3; this NASA-funded work is being conducted at the United Technology Research Center and the Pratt and Whitney Aircraft West Palm Beach facilities.

How gas turbine industry views the special problems posed by alternative fuels was presented by Dodds of G.E. (4), Mosier of P&W (5), Sampath of P&W Canada (6) and Marchionna of Avco Lycoming (9). Moses summarized his work (7) at Southwest Research Institute, whereas Odgers and Kretschmer (8) covered the effect of fuel composition upon heat transfer in gas turbine combustors.

The following important observations can be made:

(1) Majority of the work reported concerns measurements of wall temperature (T_w), soot emission (C) and radiation flux (q_R).

(2) In recent work, emphasis has shifted to studying fuel thermal stability, ignition, relight altitude, and nozzle performance.

(3) Some effort continues on studying wall carbon, gaseous emissions, and burner outlet temperature quality.

(4) Hydrogen content seems to be the most popular parameter for correlating wall temperature, soot emission and radiation flux levels.

(5) Some investigators are pursuing other parameters, e.g. aromatic content, ring-carbon content, multiring aromatic content.

(6) How aromatic composition affects T_w, C and q_R has not been settled.

(7) Additional efforts are needed to improve the data base for the soot correlation performed by Odgers and Kretschmer (8).

A number of attempts have been made to develop universal curves for C^*, T_w^* and q_R^* for gas turbine combustors. Based on experience, it can be concluded that such an attempt has not been successful even for combustors burning conventional fuels, e.g. universal curves have not been developed for combustion efficiency, cooling airflow requirements, lean blowout and ignition fuel-air ratios. Therefore, normalized curves of C_{EI}, T_w and radiation intensity cannot be developed as a function of fuel properties. This is because combustor performance depends on many factors including the following:

(a) Combustor design philosophy
(b) Fuel injection system
(c) Dome/primary zone design
(d) Engine duty cycle
(e) Field-related environment.

We do not know enough about various fundamental processes leading to soot formation, including fuel preparation and turbulent spray combustion. It is therefore difficult to predict the effect of fuel properties on C, radiation emissions and hence wall temperature levels. Simple one-dimensional wall temperature calculation procedures (8) are useful for interpreting and correlating data. More complex calculation methods are needed for predicting wall temperatures as a function of fuel properties.

3. FUEL PREPARATION

Nine papers (10–17, 35) were presented covering the following areas:

(1) Performance of fuel injection systems, particularly vaporizers (11) and airblast nozzles (12, 14).
(2) Combustor/fuel injector interaction (10, 11, 17)
(3) Spray characterization and mixing (13, 14, 16)
(4) New optical measurement techniques (15, 35) for detailed spray analysis.

These papers were quite useful for further improving our understanding of the various complex processes involved in fuel preparation. This important field requires continuous funding support for the following reasons:

- Current injector/combustor system integration procedure is highly empirical
- Nozzle spray characterization is badly needed including mean droplet size; spray cone angle; droplet size; and velocity distribution
- Near-nozzle flow characteristics need to be known not only to better understand various processes but also to formulate a tractable simulation that can be incorporated in multi-dimensional calculation procedures
- The need for spray investigations with production type or near production type fuel injectors was stressed.

More work is needed in assessing effects of scale and other geometrical details on airblast nozzle performance. Many types of injector geometries have been investigated. There should be close collaboration between industry and academe.

A particular fuel injector design does not make it a good or a bad design. It is the combustion/injection system that makes a particular design more attractive than the other design. A number of research and development programs have supported the above statement. For example, Reference 6 and also Rosfjord and Briehl* have shown the vaporizer concept to be inferior, whereas the Rolls-Royce Bristol Division has achieved superior performance with vaporizing systems. The multiple jet combustor improved performance (17) may be partly due to the use of a vaporizing system.

Detailed spray/flow field mapping work is urgently needed; both mean and fluctuating components need to be quantified. The NASA-Lewis Research Center has made a good start (15) in this direction. The technique proposed in Reference 35 appears quite promising. Information is also needed for regions close to the fuel injector face to help solve shroud burning and carbon formation problems.

Wittig, like others, has again pointed out (13) the importance of spray characterization including droplet size distribution, various mean sizes, and how the airflow field changes these distributions.

4. KINETICS AND SOOT

Five papers were presented (18–22) covering kinetics and soot formation/oxidation. To improve our basic understanding of soot formation/oxidation processes, detailed studies should be conducted on turbulent diffusion flames. Kent and Wagner have made a good start in this direction. Basic studies like that of Homann and his associates (19) are needed to establish fundamental mechanisms of soot particle growth.

Prerequisites for predicting soot in practical gas turbine combustion systems are:

- Good hydrocarbon kinetic models
- Acceptable turbulence/chemistry models
- Acceptable spray/flow/chemistry models.

All these areas require further investigation.

In order to improve the understanding of the various processes, nonintrusive soot measurement techniques are needed for mapping "practical" flames. The work being performed (21) by Samuelsen and his associates is of immense interest to gas turbine industry.

5. LINER COOLING AND TRAVERSE QUALITY

The two most challenging problems in advanced technology combustors are:

- Liner cooling and structure durability
- Burner outlet temperature quality including pattern factor (PF).

Low combustion system pressure loss, high burner temperature rise, and high combustor heat release rate are some of the important factors that have contributed to the high PF problems of gas turbine combustors.

There are many solutions to reducing PF including:

- Minimize cooling air requirement
- Optimum dome/primary zone design
- Maximum utilization of the available dilution air.

---

* Rosfjord, R.J. Evaluation of Fuel Injection Configuration to Control
Briehl, D. Carbon and Soot Formation in Small GT Combustors, AIAA, Paper 82-1175, June 1982.

The cooling air requirement can be minimized by improving cooling effectiveness. Fundamental understanding of various cooling schemes should be enhanced by conducting tests under controlled test conditions, as being investigated by Simon, Schubert, and Basler (24). How a particular advanced cooling scheme performs in the field is being investigated by Rolls-Royce (23). Improvement in idle emissions and high-power temperature quality should be expected with a TRANSPLY combustor. Bhangu, Eardley, and Snape have given a good summary of the TRANSPLY combustor performance improvements over the conventional spray combustor.

The dilution air requirement can be minimized by making maximum utilization of the available air. In that respect, jet mixing in a can combustor should be investigated (as reported in Reference 26) to better understand dilution jet mixing processes.

Dilution jet mixing in transition liners of reverse flow combustors is of great interest to companies which make small gas turbine engines. In that direction, Wittig and his associates reported measurements in a 90-degree pipe bend (25). They also presented calculations for a plane geometry with a 90-degree turn. The measurements and calculations demonstrated the complex nature of the flow field involved. It should be noted that the flow field in annular transition liner geometries should be quite different from that of pipe bends.

6. COMBUSTION MODELING

A number of papers (27–34, 36 and 37) were presented covering a broad spectrum of combustion modeling including a fundamental investigation being conducted by Roquemore et al. (36). A number of comments are made regarding these papers in the following paragraphs.

Both simple and complex multidimensional models should be developed. These models include:

- Models based on characteristic time concept (32)
- Well-stirred and partially stirred reactors (34)
- Modular approach based on parabolic calculation procedures
- Multidimensional elliptic calculations.

There appears to be consensus among many researchers in regard to model validation efforts:

- "Benchmark" quality data should be collected
- Validation effort should proceed from simple to complex flows, first starting with nonreacting flows and then proceeding to reactive flows.

Current state-of-the-art models of turbulence, scalars, chemistry, radiation and spray transport/dispersion predict trends. Further improvements are needed to enhance their usefulness as combustor design tools. Concurrently, non-intrusive measurement techniques should be developed and "benchmark" quality data should be gathered to assess these models. Advanced numerical schemes should be developed to reduce false diffusion and computation times.

7. ACKNOWLEDGEMENT

The Propulsion and Energetics Panel (PEP) deserves commendation for having done such an excellent job in putting together the 62nd Symposium, on Combustion Problems in Turbine Engines. Special thanks go to Professor Mellor (Programme Committee Chairman) and the Host Nation Coordinator, Professor Uçer.

AVIATION FUEL SPECIFICATION REQUIREMENTS - THEIR SIGNIFICANCE AND FUTURE TRENDS

by
L. Gardner and R.B. Whyte
Fuels & Lubricants Laboratory
Division of Mechanical Engineering
National Research Council of Canada
Montreal Road
Ottawa, Canada K1A 0R6

AD-P003 127

Summary

During at least the next twenty years the only economically available fuels for aviation turbine engines will be hydrocarbons but the composition will change due to increased demand relative to other petroleum products, changes in available crudes, changes in refinery processing and the introduction of 'synthetic' crudes from heavy oils, tar sands, shale and coal. This paper attempts to predict some of the changes in fuel properties which are likely to occur and the problems these will cause in current turbine engines.

1. Introduction

It appears that the main transportation fuels and particularly those for aircraft will be hydrocarbons well into the next century(1). No other fuels have the high calorific value and ease of handling of liquid hydrocarbons and the present models of aircraft turbine engines have been designed and successfully used on these fuels. However the sources and properties of these liquid hydrocarbons will change over this time period. Refinery operation in most areas of the world is changing because of decreased relative demands for gasoline and heavy residual fuels coupled with increased relative requirements for middle distillates of which aviation kerosine is a small but important section. In many cases it will no longer be possible to produce the required quantities of aviation kerosine (and the competing low pour diesel fuels) using only simple distillation from the crude. The alternative streams available in the refinery generally tend to have higher aromatic contents (lower hydrogen contents) and require considerable upgrading to meet present requirements. Conventional crudes are becoming heavier and have higher aromatic contents and all the alternative sources have even higher carbon to hydrogen ratios. It is of course theoretically possible to produce fuels to present specifications from all the alternative sources - heavy crudes, tar sands, shale and coal - but the processing required, either elimination of carbon or addition of hydrogen or both are expensive both in capital investment and operating costs and use more refinery fuel for a lower yield. Therefore it is necessary to seek some compromise where the cost of the fuel will be held as low as possible without incurring severe penalties in increased engine maintenance and without compromising safety aspects.

At present throughout most of the world there are two general grades of aviation turbine fuel used, wide-cut and kerosine (Table 1). The wide-cut fuels were developed in the 50's to give the maximum fuel yield per barrel of crude and include straight run gasoline and kerosine fractions. The trend today is however towards the use of kerosine type fuels in civil aircraft because of a slightly increased margin of safety in handling and under survivable crash conditions, and in military aircraft because of lower vulnerability under combat conditions. The wide-cut fuels can nevertheless be made more readily available in larger quantity, are generally marginally cheaper and are also essential for operations in present engines in colder climates such as Alaska and Northern Canada.

Because of the relative scarcity and preferred use of the kerosine-type fuels most future forecasts and investigations of engine behaviour have been concentrated on this type of fuel.

The future changes in the properties of aviation turbine fuels which are expected to have the greatest influence on engine and aircraft operation and durability are:

Aromatic content (hydrogen content)
Viscosity
Volatility
Storage and thermal stabilities
Freezing point

These are discussed in the next sections below.

2. Aromatics (reviewed by J. Odgers (2))

(a) Smoke Formation: The generally accepted route of carbon formation in flames is shown in Fig 1.(2). This demonstrates the ease by which aromatic compounds give rise to soot compared with the aliphatic compounds. One of the difficulties in evaluating published smoke data is the large variety of techniques used to measure soot and some form of standard isokinetic sampling calibrated by means of a standard

gravimetric technique is badly required to enable comparisons to be made between different investigations. An approximate relationship between gravimetric exhaust carbon and that measured by various techniques is shown in Fig. 2 but, because variations occur with fuel type and geometry and operating conditions of the combustor, the accuracy is probably no better than ± 20% of carbon content.

The effect of the hydrogen content of the fuel on carbon formation has been widely studied. To overcome the problems caused by the variation in measuring techniques the term C*, the ratio of the carbon formed by any fuel to the carbon formed by a fuel having 12.5% hydrogen has been introduced. This gives the typical results shown in Fig. 3 from a wide variety of combustors both gas turbines and laboratory equipment including both premixed and diffusion flames. Whilst this correlation is useful the necessity of a reference point is inconvenient and it would be better if the actual carbon content could be predicted. Examination of the large amount of published work indicated that the factors of pressure, inlet temperature, hydrogen content and oxygen/carbon ratio are the major influences with temperature having a relatively small effect. Residence time must also play a large part but much of the data examined had a fairly constant residence time of 2-3 milliseconds in the reaction zone. Analysis of the results suggests

$$\text{Carbon Emission Index} = 1.08 \times 10^{-29} \left[\left(\frac{P}{O/C}\right)^{2.7} (H/C)^{-5.45}\right] T_3^{-8.66}$$

where all the variables refer to overall operating conditions. A plot of the data (Fig. 4) shows not only that from conventional pressure jet atomiser combustors but also so-called premixed combustor data and laboratory combustor figures. It can be seen that the general slope characteristics are quite similar except for the stirred reactor where carbon content was so low that there are no discernible trends. Since the variables in the gas turbine combustor data varied in pressure from 0.1 to 1.4 mPa, inlet temperature from 294 to 781°K, carbon/oxygen ratio 27 to 11 and hydrogen/carbon ratio 2.0 to 1.4 it would appear that it may be possible to predict the effects of different fuels and operating variables and also to predict high pressure results from low pressure tests. This correlation suggests a trend not yet sufficiently comprehensive nor accurate but provides a semi-quantitative estimation which might well be usefully modified as more precise information becomes available.

Combustor data for gaseous emissions and combustion efficiency generally show only small dependence on the various fuel properties although at some higher viscosity level, increase in droplet size and evaporation time will lead to increased unburned hydrocarbon and carbon monoxide emissions with a corresponding decrease in combustion efficiency.

(b) Flame Radiation: The other important effect of higher aromatic content fuels is the increased luminosity of the flame which increases radiation and hence combustion chamber liner temperature affecting the life of hot section components. Without the presence of film cooling the combustor wall receives heat by convection and radiation from the hot gases and loses heat by convection to the air in the combustor casing and by radiation from the combustor wall to the casing wall. Despite the complications of simultaneous heat and mass transfer it is possible to calculate combustor wall temperatures over a range of conditions. In real combustors the situation is further complicated by the use of air for film cooling of the combustor. Nevertheless empirical relationships have been worked out for a conventional combustor burning liquid fuel with conventional film cooling. In order to estimate the amount of radiation from the flame it is necessary to estimate its emissivity. A considerable amount of laboratory work has been done to establish the emissivity of transparent and non-transparent gases. However for gas turbine applications with luminous flames it is much more difficult and again empirical equations have been derived. Since the accuracy is only ±25% it is obvious that further work in this area is warranted. Figs. 5 and 6 show the effect on wall temperatures predicted by these equations at different engine compression ratios (π) with variable fuel hydrogen contents. The effect of hydrogen content is much more significant at low pressures and is greater within the secondary zone than the primary zone.

These predicted wall temperatures are compared with actual measurements in combustors in Figs. 7 and 8 (the predictions are the shaded bands). Agreement is reasonably good for the older engines in Fig. 7 but there is less effect of lower hydrogen content then predicted for the F101 engine in Fig. 8. This is reckoned to be due to the lean primary zone design of this particular engine which was not allowed for in the calculations.

Using conventional fuels with a premixed-prevapourized system should give blue non-luminous flames which would be insensitive to fuel composition. The results shown in Fig. 9 for two experimental combustors of this type are in good agreement with this supposition.

The effects of the increased liner temperature on combustor life has been investigated for three engines. For the J79 engine, combustor life predictions were based on measured metal peak temperature rise and crack propagation rates. In the F101 predictions the combustor was operated at scaled conditions and an attempt made to correct these to true operating pressure conditions. Near-to-air-entry-hole corrections were then applied and entered into a stress analysis program. The

resultant stresses were then used with the material low-cycle fatigue properties to predict cycle life to first crack initiation which has been shown from engine experience to be proportional to liner life. In each case the change in fuel hydrogen content from 14.5 to 13.0 reduced the predicted liner life to about 50%.

In an investigation (3) on the TF41 cannular type engine, rig results showed that the fuel composition had an effect on the combustion liner barrel temperature (Fig. 10). However in this engine combustor peak metal temperatures occur on the discharge nozzle inner wall. This peak metal temperature is dependent on liner pattern factor which had no correlation with fuel properties. Hence it was not surprising that peak liner temperature (and therefore combustor life) did not correlate with any fuel property change.

In actual use, one U.S. airline reported (4) that it has not found any deterioration in hot section life operating totally on Californian fuels (aromatic content in the reportable range of 22-25%) as compared to the average fuels with aromatic contents averaging 17%.

Thus the effects of fuel property changes can be seen to be dependent on particular engine design and can be modified by further developments in film cooling and/or wall insulation techniques to meet the challenge to combustor life.

3. Viscosity & Volatility (reviewed by G. Winterfeld (2)).

The influence of increasing the kinematic viscosity of the fuel is to increase the mean droplet diameter in the spray. The amount of the increase depends on the method of atomization. For instance a fuel with the maximum allowed by the AGARD Research Fuel of 12 cSt at -20°C would have a viscosity of about 3 cSt at +20°C. The atomization of this fuel in a pressure swirl atomizer would result in droplets which are roughly 15% larger than with Jet A-1 (Fig. 11). If the corresponding deterioration of combustion characteristics is to be avoided the viscosity effect can only be compensated for by an increase in the atomizer pressure difference of about 30%. Since the effect is greater at lower temperatures (Fig. 11) altitude relight problems would be seriously aggravated unless this higher pressure is available.

A similar effect of viscosity is observed with air blast atomizers but is markedly lower showing that they are better suited to atomize higher boiling more viscous fuels.

The volatility of the fuel also has an effect on combustion and ideally a fuel with a higher boiling range should have smaller droplet sizes to compensate for the lower volatility to keep combustion conditions constant. The increase in pressure drop across a pressure swirl atomizer to maintain constant evaporation times between Jet A and AGARD Research Fuel at average engine operating temperatures would be of the order of 90%. Because of the temperature dependence of kinematic viscosity, for a cold start at -10°C the pressure increase required to keep conditions constant would be about 150%. The increase in pressure drop across the nozzle at constant fuel flow means that the flow number of the nozzle must also be changed to a smaller size destroying the possibility of a multi-fuel engine. It appears that this requirement may be met by a spill-type nozzle although few data have been published on the quality of sprays from this type of nozzle.

Air-assist type of nozzles would be rather better than straight pressure types but the increase in pressure drop required under normal operating conditions would still be 40-45%. Calculations for air-blast nozzles are more complicated but an estimate can be made that pressure drop across the nozzle and hence across the combustor must be increased 25-30% to accommodate the highest viscosity and higher boiling range of the AGARD Research Fuel. There are various ways in which this might be overcome such as variable geometry in air flow around the nozzle (undesirable in a high temperature zone) or change in the fuel sheet thickness with a spill-type fuel supply to the pre-filming section.

This area requires further investigation to provide multi-fuel capabilities for future engines if they are to be capable of efficiently coping with higher viscosity lower volatility fuels. If such injectors can be developed to produce constant evaporation times then ignition and stability (blow-off) qualities will also be preserved since the chemical properties of the fuel are only of secondary importance.

4. Other Fuel Properties

The other fuel properties likely to change are storage and thermal stabilities and freezing point. Storage stability and freezing point are of importance in the handling of fuels prior to introduction into the engine and are therefore beyond the scope of the present Symposium.

Thermal stability (reviewed by A.E. Peat (2)) is, however, mainly an engine problem in that it is in the engine (heat exchangers and fuel lines in hot areas) that the fuel is subjected to high temperatures and the consequences of deposits in heat exchangers and in atomizers can seriously affect engine operation. Measurement of the thermal stability of a fuel presents problems since it is difficult in a short laboratory test with a small quantity of fuel to reproduce engine conditions with large volumes of fuel and differences of temperature levels and residence times at these levels. It is even more difficult to assess the possible thermal stabilities of future

fuels because of the dependency not only on the general chemical composition but also on small quantities of reactive components and traces of contaminants. Since future fuels will contain cracked components and larger quantities of heterocyclic compounds containing nitrogen and sulphur in particular, the trend will certainly be towards lower temperature break points and more rapid deposit build-up.

There are two possible approaches to alleviating these problems. On the engine manufacturer's side it may be possible to minimize both the temperatures to which the fuels are exposed and their residence time at these temperatures in spite of the general increases in engine environmental temperatures associated with more efficient higher pressure ratio engines. There may also be some scope for redesign of components to make them less vulnerable to malfunction due to deposits. On the fuel side it is important to investigate the use and efficiency of improved refining techniques and the use of additives to improve the thermal stability of the future fuels to attain a suitable compromise acceptable to the engine user.

5. Future Fuels

During the time allotted for AGARD/PEP Working Group 13 it was not possible to fully investigate the future supply/demand situation for aviation kerosine. As a result Working Group 16 was established to investigate this aspect. The situation is an incredibly complicated one made worse by the present reduction in petroleum product demand which is partly due to the economic recession and partly due to conservation inspired by increased cost of products. This is therefore probably the worst time during the whole petroleum era to attempt to forecast the future.

Nevertheless Working Group 16 is attempting to do this using a very flexible LP computer model for refineries of different complexities operating on the crude supplies generally believed to be available in the next twenty years. The model has been developed by the Exxon Corporation under NASA contract and is capable of being up-dated in the future as conditions change.

The study has been split into six geographical areas covering the NATO countries - East and West U.S., East and West Canada, and North and South Europe. There is a reasonable similarity between the crude supplies anticipated for Europe, the Eastern U.S. and Eastern Canada. The Western U.S. is considerably different because both Californian and Alaskan North Slope crude give a relatively high aromatic aviation kerosine. Western Canada is also different because of the two tar sands plants already operating (supplying about 10% of Canada's total crude requirements) and other developments planned. The aviation kerosine produced from the product of one of the plants is around 20% because of heavy hydrogenation of this stream but from the other, larger plant the aromatic content is much higher and the amount of this synthetic crude which can be blended into the refinery input stream is severely limited. The computer runs should be completed this year and the final report of Working Group 16 should be available late in 1984. Hopefully this will give some better indications of the ways and extent in which specifications may have to be relaxed to ensure adequate economical supply.

Predictions of future synthetic crudes from the various areas is also quite different because of the indigenous materials available. Canada will probably increase production from tar sands and other heavy oils, whilst the U.S. first choice would be shale and in Europe, coal. It is generally accepted that production from coal either by direct liquefaction which has not been tried on a commercial scale or via synthesis gas like the South African Sasol plants will not be a commercial proposition until well into the 21st century. Products from tar sands and shale are more expensive than crude oil because of the mining operations involved as well as the more severe upgrading to make commercially viable fuels. These sources are however much more economical than coal because they have a naturally higher hydrogen/carbon ratio and the economic penalty can be rationalized on the basis of security of supply and the effect on national balance of payments.

The ERBS fuel (Table 1) proposed by NASA (5) is, in the authors' view a very extreme case and would have such a severe effect on the whole system of fuel handling, combustion, engine durability, etc. that it would require redesign of the airframe to allow fuel heating and drastic changes to the engine to overcome problems caused by the high aromatic content and high viscosity. On the other hand the AGARD Research Fuel, allowing down to 13.0 per cent hydrogen corresponding to roughly 28-30% aromatics is still believed to be compatible with present elastomers used in fuel systems and to be acceptable in engines with some degree of increased maintenance of hot section components. The freeze point of AGARD Research Fuel was set at -30°C max. in order not to inhibit production of experimental blends for combustion studies but we believe that for practical fuels the freeze point should be maintained at -40°C (as in Jet A) and -47°C (as in Jet A-1) depending on location, length of flights etc. This would prevent the problems involved in retrofitting existing aircraft with fuel heaters and the weight and energy penalties associated with heaters even in new designs. This freeze point will also ensure that fuels can increase only marginally in viscosity and therefore that engines, particularly atomizers, will not require major changes. Any flight patterns, particular aircraft, etc. which preclude this fuel because of freeze point can use Jet B or make special arrangements for a low freeze point kerosine produced from selected crudes. These special arrangements are already made in some areas for long over-the-pole flights and are restricted to relatively small volumes of fuel.

A fixed value of flash point minimum throughout the free world has always appeared rather an anomaly since it is used as a measure of safety in handling the fuel. But the figure of 100°F or 38°C was chosen as giving a reasonable margin of safety (10-15°F) above the highest indoor normal living space temperatures in temperate climates and bears little relationship to fuelling temperatures in either tropical or arctic areas. Extensive measurements throughout Canada (6) have shown that fuel temperatures do not exceed 30°C even at our warmest airport (Windsor) under the most adverse conditions (refuelling vehicles standing in direct sunlight). By contrast there must be tropical airports where the fuel is continually being handled above its flash point. Only the strict airfield fuel handling rules where all fuels - kerosine, wide-cut and gasoline - are treated as flammable minimizes the dangers involved. Since aircraft are highly mobile moving rapidly from one climatic condition to another and the fuel flash point regulations are usually locally controlled and administered it would be a huge task to effect changes where only kerosine type fuel has previously been handled. But it does seem peculiar that one of the specification limits which obviously influences availability has so little relevancy in the real world.

6. Conclusions

It is not possible to improve on the conclusions of the Working Group 13 Report which said:-

Increasing shortages of suitable crude feedstocks and the threat of disruptions in supply due to world economic and potential international conflicts may require a broadening of current jet fuel specifications to improve availability and to allow, at minimum cost and maximum energy efficiency, the use of feedstocks from alternative sources including heavy petroleum crudes, tar sands, oil shale and coal. To prepare for an uncertain future in jet fuel quality and availability, research is needed to more fully understand the effects of varying fuel properties on engine and aircraft fuel system performance, reliability and durability and to build the technology base that would allow greater fuel flexibility in future aircraft. Since current production engines will still be in service at the turn of the century, research and advanced technology to accommodate possible future fuels must include cost-effectiveretrofit options for current production aircraft as well as new engine and aircraft fuel systems.

It is encouraging to survey the other 30 papers to be presented at this Symposium and see that all the problems outlined are the subject of a great deal of work throughout the NATO community with contributions from industry, government, and university covering theoretical, computer modelling and practical aspects. With this continuing effort we should at least have some of the answers - and few surprises - in fuel/engine interactions in future years.

References

NOTE: The present paper has relied heavily on the literature surveys and interpretations done by the authors of the various sections of the Working Group 13 Report (2). Readers are referred to this Report for fuller discussions and the references to original papers.

(1) K.H. Strauss, Future Jet Fuels - A Refiner's Viewpoint, J. Energy 7(3) 200 (May-June 83).

(2) R.B. Whyte (Editor) Report of Working Group 13 on Alternative Jet Fuels. AGARD Advisory Report No. 181 Vols I and II (July 1982).

(3) R.E. Vogel & D.L. Troth, Fuel Character Effects on the TF41 Engine Combustion System. J. Energy 7 (3) 218 (May-June 83).

(4) P.P. Campbell, Jet Fuel Properties, a 1978 Viewpoint Shell Aviation News 449 (1978) Updates at more recent IATA Aviation Fuels Sub-Committee Meetings.

(5) G.M. Prok & G.T. Seng, Initial Characterization of an Experimental Referee Broadened Specification (ERBS) Aviation Turbine Fuel NASA Tech Memo 81440 (Jan 80).

(6) T.A. Miller et al. CGSB Aviation Fuels & Lubricants Task Force Report on Canadian Turbine Fuels TEB 7612-3-GP (Oct 76).

Table 1: Relevant Fuel Specification Requirements

	Kerosine Fuels		Research Fuels		Wide-Cut Fuels	
	NATO* F-34	ASTMD1655 Jet A-1	ERBS	AGARD Research Fuel	NATO* F-40	ASTMD1655 Jet B
Aromatics, % Volume, max.	25.0	25.0**	Report	Report	25.0	25.0**
Hydrogen Content, % mass	(13.5min)***	-	12.8±2	13.2±2	(13.6min)***	-
Volatility						
Distillation Temperature °C						
Initital Boiling point	Report	-	Report	-	Report	-
10% recovered, °C max.	205	204.4	204	205	Report	-
20% recovered, °C max.	Report	-	-	-	145	143.3
50% recovered, °C max.	Report	Report	Report	-	190	187.8
90% recovered, °C max.	Report	Report	260	-	245	243.3
Final Boiling Point, max.	300	300	Report	-	-	-
Fluidity						
Freezing Point, °C, max.	-47	-47	-23	-30	-58	-50
Viscosity @ -20°C, cS max.	8.0	8.0	-	12.0	-	-
Viscosity @ -23°C, cS max.	-	-	12.0	-	-	-
Combustion						
Smoke Point, mm, min.	19	18**		Report	20.0	18**
Naphthalenes, % volume, max.	-	3	Report	Report	-	3
Thermal Stability (JFTOT)						
Maximum Tube Temperature, °C (ΔP = 25mmHg)	260	245	238	230	260	245

* NATO/MAS STANAG3747, Guide Specifications for Aviation Turbine Fuels.
** Reportable requirements.
*** US Military specification limits currently under consideration for inclusion in NATO specification.

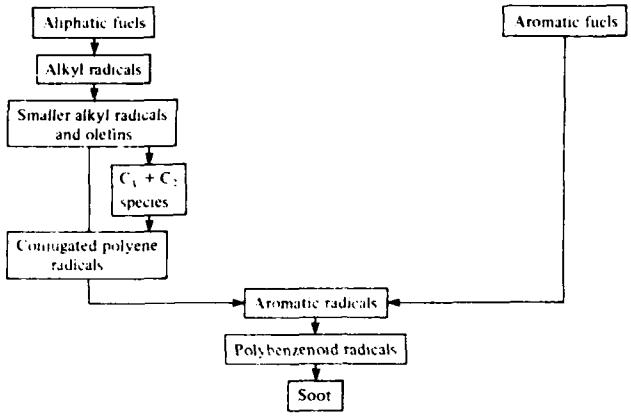
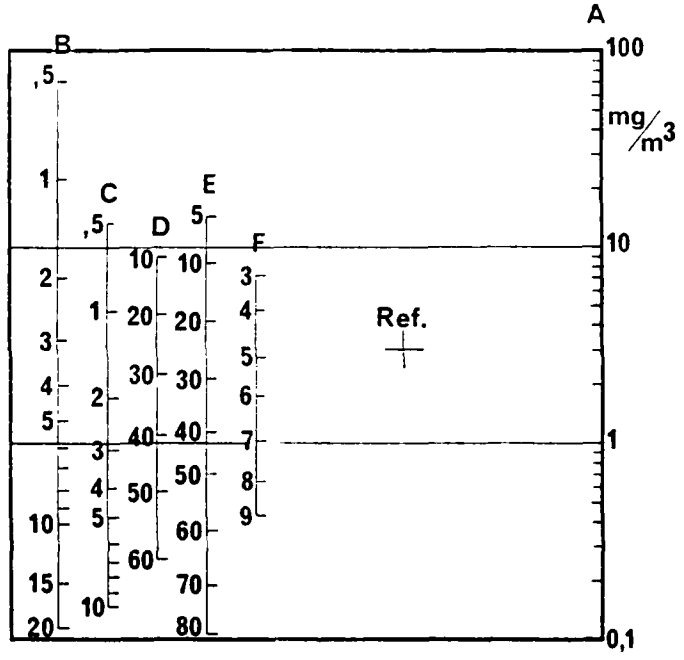


Fig. 1: Routes for Carbon Formation.



A. Particulate Smoke mg/m^3 (μ g/litre)
B. Rolls Royce Photo Smoke Units
C. Hartridge Smoke Units
D. Smoke Number, S.N.
E. SAE Smoke Number
F. Bacharach Units
Ref. Reference Point

Fig. 2: The Approximate Relationship between Gravimetric Exhaust Carbon and Several Instrument Techniques.

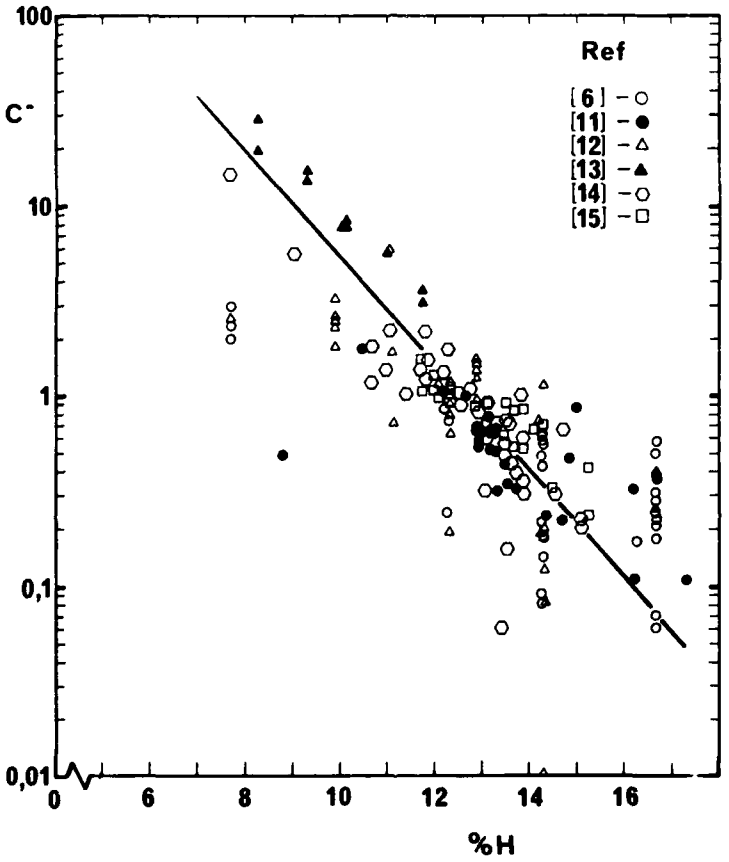
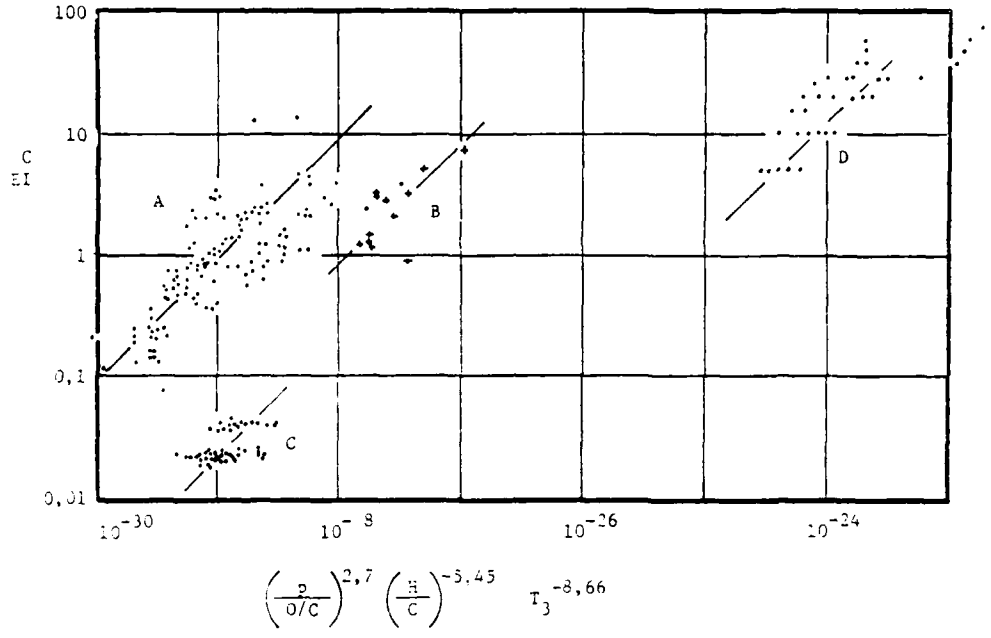


Fig. 3: Effect of Hydrogen Content on Carbon Formation in Various Combustors.



A Conventional Combustors
B Semi-premix Combustor
C Stirred Reactor
D Premixed Reactor

Fig. 4: Correlation for Carbon-Emission Index.

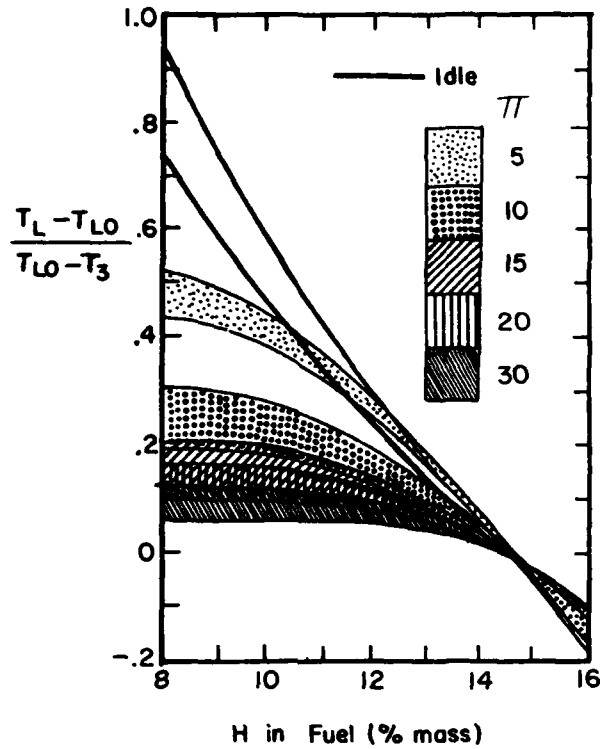


Fig. 5: Predicted Changes in Combustor Wall Temperatures (Recirculation Zone).

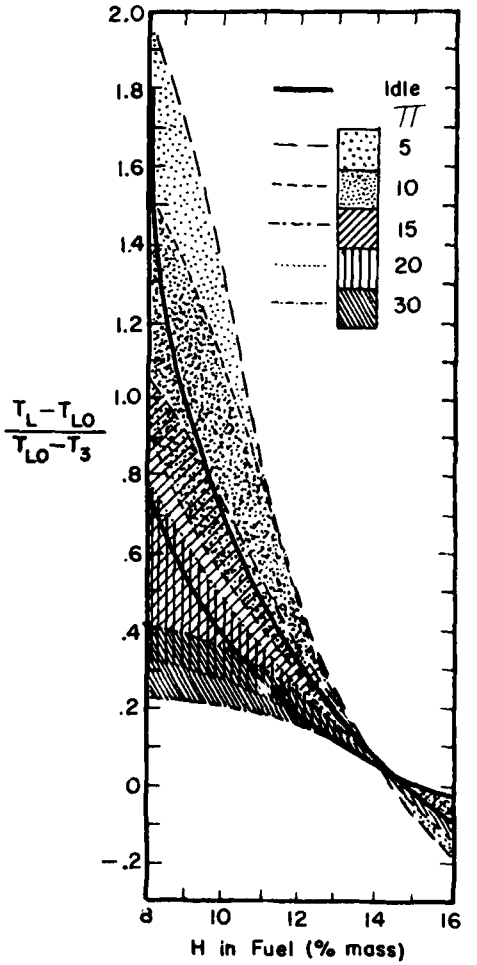


Fig. 6: Predicted Changes in Combustor Wall Temperatures (Secondary Zone).

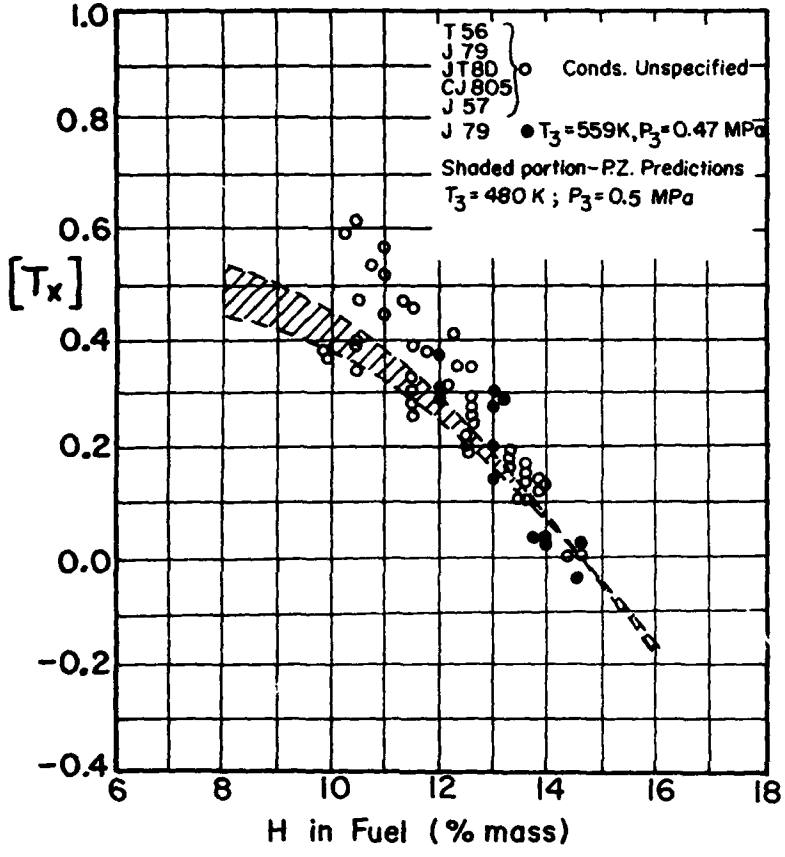


Fig. 7: Effect of Fuel Composition on Combustor Wall Temperatures.

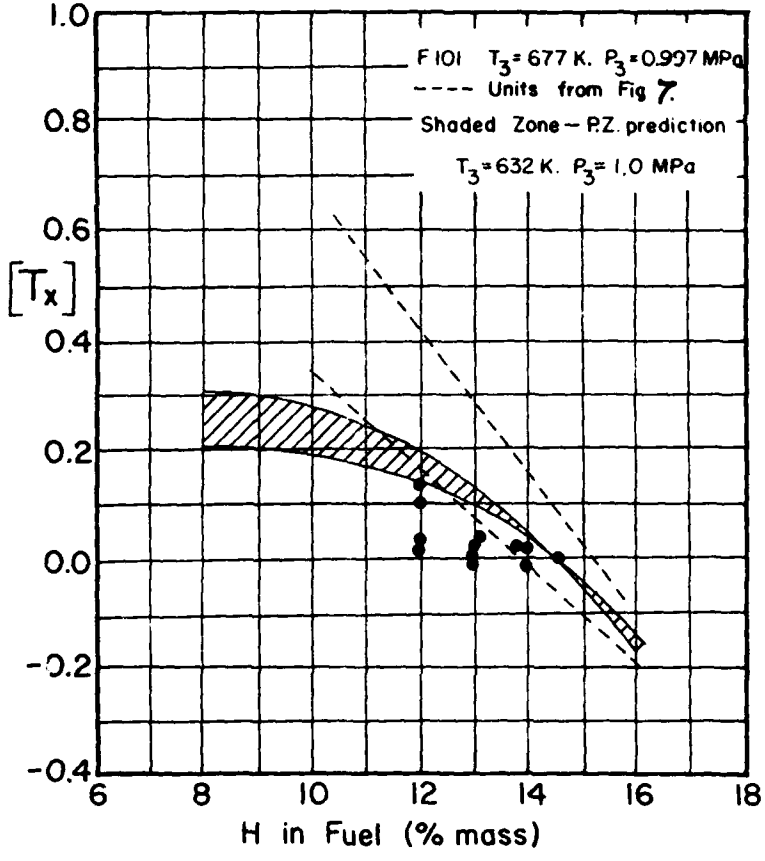


Fig. 8: Effect of Fuel Composition on Combustor Wall Temperatures.

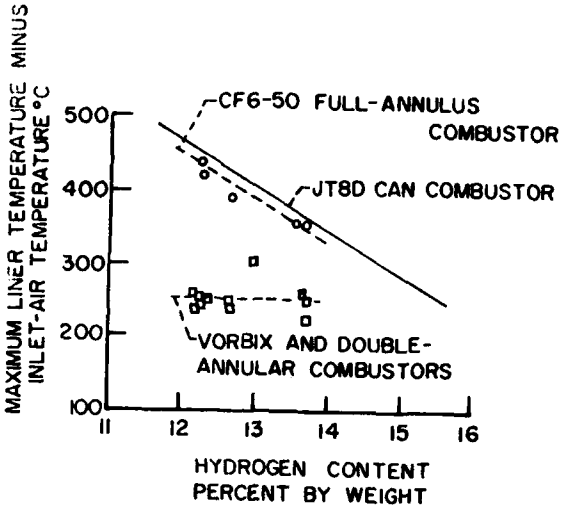


Fig. 9: Effect of Fuel Composition on Combustor Wall Temperatures.

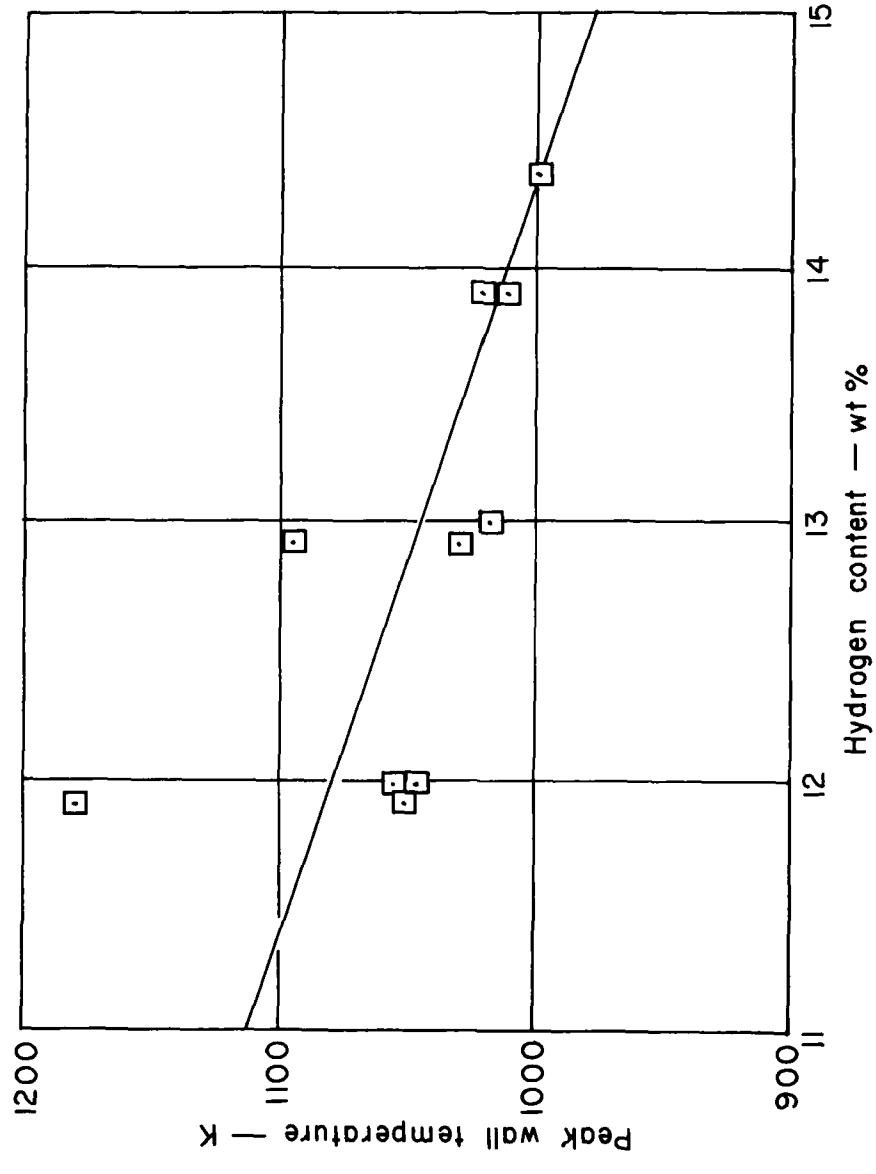


Fig. 10a: Effect of Fuel Composition on TF41 Combustor Wall Temperature.

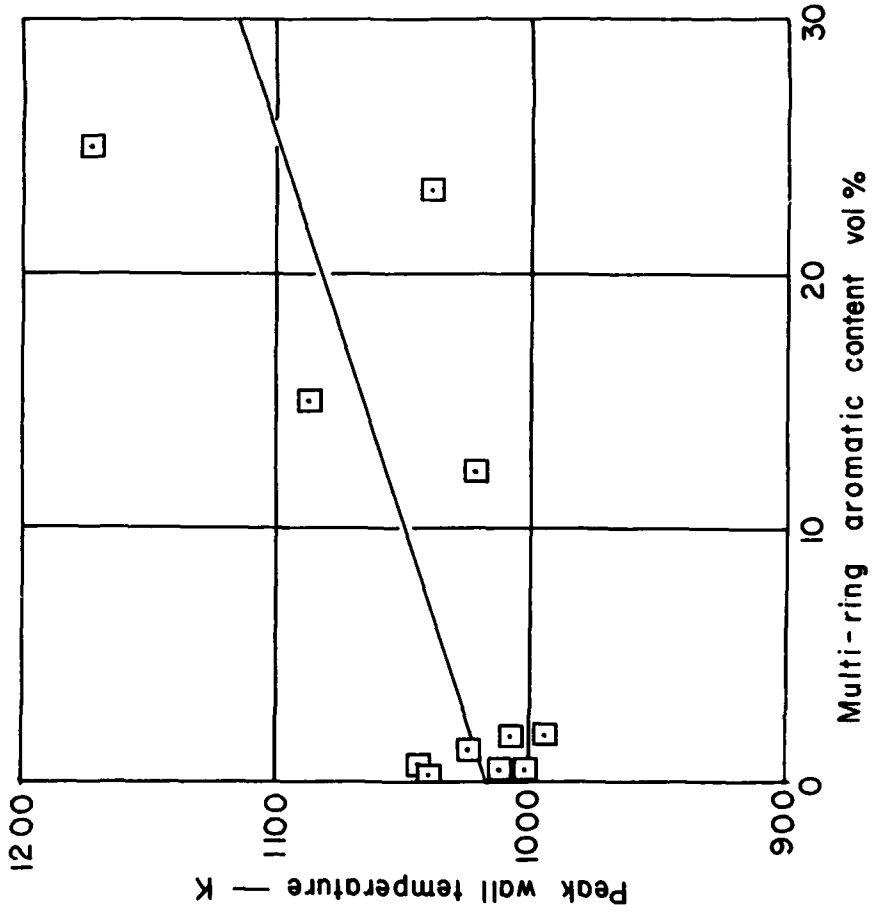


Fig. 10b: Effect of Fuel Composition on TF41 Combustor Wall Temperature.

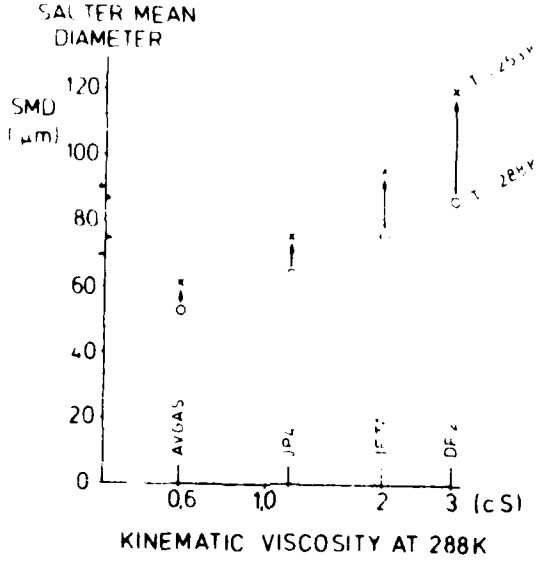


Fig. 11: Effect of Temperature and Viscosity on the Sauter Mean Diameter of Fuel Sprays from Pressure Swirl Atomizers.

RESEARCH ON AVIATION FUEL INSTABILITY

Charles E. Baker, David A. Bittker, Stephen M. Cohen, and Gary T. Seng
National Aeronautics and Space Administration
Lewis Research Center
21000 Brookpark Road
Cleveland, Ohio 44135 U.S.A.

AD-P003 128

SUMMARY

Current aircraft turbine fuels do not present a significant problem with fuel thermal stability. However, turbine fuels with broadened properties or nonpetroleum-derived fuels may have reduced thermal stability because of their higher content of olefins, heteroatoms, and trace metals. Moreover, advanced turbine engines will increase the thermal stress on fuels because of their higher pressure ratios and combustion temperature.

In recognition of the importance of this problem, NASA Lewis is currently engaged in a broadly-based research effort to better understand the underlying causes of fuel thermal degradation. The progress and status of our various activities in this area will be discussed in this paper. Topics ~~to be~~ covered include: nature of fuel instability and its temperature dependence; methods of measuring the instability; chemical mechanisms involved in deposit formation; and instrumental methods for characterizing fuel deposits. Finally, some preliminary thoughts on design approaches for minimizing the effects of lowered thermal stability ~~will be~~ briefly discussed.

INTRODUCTION

The purpose of this report is to define the problems associated with aircraft fuel instability, review what is currently known about the problem, describe the research program sponsored by NASA Lewis, and identify those areas where more research is needed. The term fuel instability generally refers to the gums, sediments, or deposits which can form as a result of a set of complex chemical reactions when a fuel is stored for a long period at ambient conditions or when the fuel is thermally stressed inside the fuel system of an aircraft.

Thermal instability was first identified as a problem in aviation turbine engines in the 1950's. During the 1960's, early studies in the United States on the supersonic transport (SST) gave considerable attention to the problem of fuel instability, because in this SST, the fuel was to be used as a heat sink for the wing surfaces which are heated aerodynamically. It is generally acknowledged that current aircraft turbine fuels do not present a significant problem with regard to fuel instability for current subsonic aircraft. However, turbine fuels with broadened properties or nonpetroleum-derived fuels (from shale, tar-sands, coal, etc.) may have reduced thermal stability because of their higher content of olefins, heteroatoms, and trace metals. (Heteroatoms include nitrogen, oxygen, and sulfur atoms contained in organic compounds.) Moreover, advanced turbine engines may increase the thermal stress on fuels because of their higher pressure ratios and combustion temperatures. Deposition of solids within the fuel systems of aircraft may lead to fouled heat exchangers, plugged fuel nozzles, and/or jammed fuel valves which may result in excessive oil temperatures and non-uniform fuel spray patterns which could cause distorted turbine inlet temperatures (hot spots).

During the past several years NASA Lewis has been engaged in a research and technology program to determine the effects of broadened-property fuels on engine and fuel system components and to evolve the technology needed to use these fuels. Broadening fuel properties may offer the potential for increasing the refinery yield of jet fuel. Moreover, additional energy intensive treatment of poorer quality crudes and syncrudes will be required if jet fuel with current properties is to be produced. One of the major problem areas that must be addressed is fuel instability because of the reasons given in the previous paragraph. In recognition of its importance, NASA Lewis has established a broadly-based research program to better understand the underlying causes of fuel thermal degradation. Our in-house research is supported by grants with universities and contracts with industry. The progress, status, and results for these various activities will be reviewed and discussed in the report, along with some preliminary thoughts on design approaches required to minimize the effects of lowered thermal stability. In order to place the NASA Lewis program on fuel instability in its proper perspective, we should point out that similar research programs are currently being sponsored by other U.S. Government agencies, particularly the Department of Defense. These programs have made significant contributions toward the understanding of fuel degradation processes and effects. However, it is beyond the scope of this report to discuss these programs in any detail, and they will only be mentioned in the course of providing background for the NASA-sponsored program.

NATURE OF INSTABILTY

The complex chemical and physical processes involved in the degradation of fuels have been studied extensively. The early work was covered by Nixon in a comprehensive review published in 1962 [1]. A thorough literature survey which included reports of investigations since 1962 was recently published [2] by the Coordinating Research Council (CRC), and Peat has summarized the major aspects of fuel thermal stability in a current AGARD advisory report [3]. NASA Lewis sponsored a workshop on jet fuel thermal stability in 1978 [4]. The consensus among the workshop participants concerning what is known about the chemistry and physics of fuel thermal oxidation stability included the following points:

- The initial process is the interaction of fuel and dissolved oxygen.
- The chemistry involves primarily free radical reactions, but polymerization, addition, and condensation reactions are also important.
- Deposit formation rate depends on temperature with the process starting at approximately 100° C.
- Deposit rate is affected by fuel flow parameters (velocity and Reynolds number, residence time).

- The amount of dissolved oxygen in the fuel is important; in general, removal of oxygen significantly improves fuel stability.
- Metals have a significant effect on deposit formation, with copper being the most deleterious metal. Both homogeneous effects (dissolved metals) and heterogeneous (surface) effects have been observed.
- Deposits can form both in the liquid and vapor phases with the presence of both phases causing the greatest amount of deposits.

Nature of Chemistry of Instability

The thermal decomposition of hydrocarbons can be approximately classified into three temperature regimes as follows:

1. Low temperature - below 300° C - decomposition by autoxidation
2. Intermediate temperature - between 300° and 500° C - decomposition by further reactions of autoxidation products and by some direct pyrolysis of the fuel molecules 3. High temperature - above 500° C - decomposition by direct pyrolysis of the fuel

The first two of these temperature regimes are operative in the fuel system of aircraft. It is desirable to understand the chemical mechanism or mechanisms involved in fuel degradation in order to facilitate coping with the problem of thermal instability. Because deposit formation is such a complex process, this can best be done by first obtaining both deposit formation and chemical kinetics information for less complicated systems, namely pure hydrocarbons and binary mixtures. This knowledge can then be applied to the more complex mixtures in practical fuels. One of the first studies of this kind was reported in 1977 by Hazlett at the Naval Research Laboratory [5]. He used a jet fuel thermal oxidation tester (JFTOT) connected to a gas chromatograph to study the thermal decomposition of pure n-dodecane in the presence of dissolved oxygen. (The JFTOT will be described in a later section of this report.) He measured dissolved O_2 consumption and formation of the stable intermediate hydroperoxide ROOH as a function of temperature. The mechanisms he proposed for the reactions occurring in the low and intermediate temperature regimes are presented in Fig. 1. Reaction 1 indicates the abstraction of a hydrogen atom from the fuel RH by a reactive molecule or free radical X to form the reactive alkyl radical R• which then reacts (reaction (2)) with O_2 to form the unstable RO_2• peroxide radical. The RO_2• reacts mainly by reaction (3) with the fuel to form the stable hydroperoxide ROOH and regenerate the alkyl radical. To a much smaller extent RO_2• undergoes unknown reactions to form ultimately the harmful solid deposit and sediment. Hazlett and other investigators have shown that the amount of deposit formation is not directly related to the rate of primary fuel oxidation at low temperatures, even though the oxidation must take place in order for any solid formation to occur. Reactions of intermediate oxidation products lead to solid formation, and these reactions are not understood at present.

At intermediate temperatures the secondary reactions involve the decomposition of ROOH (reaction (5)) to form ketones, alcohols and aldehydes (reactions (6) - (8)). In addition, direct pyrolysis of the fuel molecule, also a complicated chemical process, starts to occur as shown in reaction (9). Isomerization and decomposition of the radicals formed by pyrolysis leads to olefin formation. It is clear from the complexity of this partial mechanism for a pure hydrocarbon's decomposition that the elucidation of the degradation mechanism for a practical fuel will be a formidable task indeed.

Deposit Characteristics

The fuel deposits that form in aircraft fuel systems may occur as soft gums, as strongly adhering lacquers and varnishes, or as brittle cokes [3]. Studies of the morphologies of these deposits [6,7] indicate that they are generally an agglomeration of microspheres, although plate and rod forms have also been observed. Chemical analysis of fuel deposits has revealed these additional general characteristics: (1) The hydrogen/carbon ratio is lower in the deposits than in the original fuel, (2) oxygen concentration of the deposits is much greater than in the thermally unstressed fuel, and (3) other heteroatoms such as nitrogen and sulfur are highly concentrated in the deposits, with concentrations several orders of magnitude higher than in the fuel [3]. The high concentration of heteroatoms in the deposits relative to their concentrations in the fuel is strongly supportive of the importance of these trace organic impurities in the deposit formation process. The lower hydrogen/carbon ratio in the deposits suggests that aromatic compounds play an important role in deposit formation.

EVALUATION OF INSTABILITY

Attempts to measure the amount of deposit produced by a fuel under a given set of conditions have ranged from small-scale glass laboratory devices to full-scale fuel system simulators. These devices have been thoroughly reviewed in ref. 2, and this report will concentrate on the American Society for Testing and Materials (ASTM) test methods for evaluating fuel thermal stability and on the larger dynamic fuel stressing rigs commonly referred to as laboratory simulators.

ASTM Test Methods

The first standard specification test for fuel thermal stability was the CRC Fuel Coker Test (ASTM D-1660) which was designed to simulate the fuel manifold conditions that had led in the 1950's to the first operation problems caused by fuel instability [8]. The test device consists basically of a heated tube around which fuel flows at a rate of 4.5 liters/hr, followed by a heated 25 micron filter of sintered stainless steel. The former simulates the engine's hot fuel lines, and the latter the fuel nozzles and passages where fuel deposits and sediments could be trapped. The heated tube is maintained at 150° C and the filter at 204° C, with a system pressure of 1170 kPa (150 psig). Fuel is flowed through the system for 5 hours. A fuel is rated on the basis of color change on the heated tube and on pressure drop across the filter.

Because of some difficulties with the CRC Coker, primarily large sample size, low operating pressure, and long test duration, this device has been replaced by the JFTOT (ASTM D-3241), which is now used to determine if an aviation turbine fuel meets the current thermal stability requirement. A schematic of

the JFTOT is shown in Fig. 2. A small aluminum tube is heated electrically to the desired test temperature, and fuel from the reservoir is pumped through an annulus surrounding the tube, out through a test filter, and then back to the upper portion of the fuel reservoir. If the fuel is unstable, deposits will form on the heated tube, and any particulates formed will lead to an increase in pressure drop across the filter. The standard JFTOT procedure consists of flowing 0.18 liters/hr of an aerated fuel at 3447 kPa (500 psig) nitrogen gas pressure over the heated tube (260° C) for 2 1/2 hours. The amount of deposit on the tube can be rated either visually, on a scale of 0 (no deposit) to 4 (heavy deposit), or by using a tube deposit rater (TDR) that operates on a light reflectance principle. The visual rating is the method currently called for by ASTM D-3241, and a value of 3 or less is required to meet the current specification for thermal stability. However, the TDR is frequently used in fuels research, and its scale ranges from 0 to 50, with a value of 12 to 13 generally used as an equivalent criterion for passing the standard JFTOT test. In addition to the requirement on deposits, the Δp value across the filter must not exceed 3.3 kPa (25 torr) by the end of the 2 1/2-hour test if the fuel is to pass the test. By operating the JFTOT at temperatures other than 260° C, the temperature at which a fuel just fails either of the above tests may be determined. This is referred to as the "breakpoint temperature" and is used to compare the thermal stability of fuels.

Tests for storage stability usually involve placing the fuel in a small container and aging it at temperatures sufficient to accelerate the instability process, usually 80° to 100° C, so that measurable deposits are produced in a reasonable time. An ASTM procedure (D873) has been used to predict storage stability. Fuel was placed in an oxygen bomb for 16 hours at 100° C. However, experience showed that any fuel which passed the JFTOT test (breakpoint less than 260° C) always passed this storage test. Because of this, the specification for storage stability has been dropped [3].

Laboratory Simulators

There is a large gap between the operating conditions of a device such as a JFTOT and the conditions to which fuel is subjected in an actual aircraft fuel system. A laboratory simulator is an apparatus designed to bridge this gap. Important parameters such as inlet temperature, wall temperature, fuel flow rate, residence time, Reynolds number, pressure, etc. can be accurately controlled and are representative of actual engine conditions. A schematic of a laboratory simulator used in recent thermal stability studies at the United Technologies Research Center (UTRC) under NASA sponsorship [9] is shown in Fig. 3. Two closely fitted copper-beryllium alloy blocks formed the flow channel which had a cross-section 0.254 cm (0.10 in.) high by 2.84 cm (1.12 in.) wide. Because of the high thermal conductivity of this alloy, the wall temperature of the channel was very uniform. All surfaces were plated with nickel and then gold to minimize wall-material effects. Four specimen mounts were attached along the length of the test section. Each held a stainless-steel disc that was used to determine deposit formation rate by weighing the test disc on a microbalance before and after the experiment. Heating was accomplished by cartridge heaters in both the top and bottom plates. Pressure atomizing nozzles were used to control the flow rate and to observe any degradation in flow uniformity. Test temperatures ranged from 149° to 399° C (300° to 750° F), test pressures from 690 to 2070 kPa (100 to 300 psig), and fuel flow rates from 2.14 to 21.4 grams/sec.

A laboratory simulator of somewhat similar design has been built at NASA Lewis for in-house research and is currently being checked out. The entire test section and flow system were constructed of stainless steel to avoid any possibility of accelerated fuel degradation from copper materials. The NASA facility also has space for four test specimens for each experimental run, but it is capable of a wider range of operating conditions than the UTRC simulator. The flat specimens provided by both the NASA and UTRC simulators are significantly easier to characterize by most current analytical techniques than the tubular deposits produced by the JFTOT and Fuel Coker. Because of this advantage for a flat test specimen, NASA Lewis has modified one of its JFTOTs for use with a flat sample holder [10].

DESCRIPTION OF RESEARCH

Research on fuel instability can be classified into two general types: research designed to understand chemical mechanisms and research on the behavior of actual fuels. When the elucidation of chemical mechanisms is the main objective of the research, pure compounds or "model fuels" made up of a mixture of a few pure compounds are usually employed in order to simplify the chemistry. Compounds containing heteroatoms or trace metals are then added in small amounts to determine their effects on fuel stability. Other research efforts concentrate on the deposits produced by actual fuels when they are thermally stressed under controlled conditions. As has previously been discussed in this report, practical fuels are so complex and contain such a variety of trace impurities that mechanism studies using them would be extremely difficult. Common to both these types of research is the need to characterize the resulting fuel deposits. A variety of analytical techniques is required to provide information on both elemental and molecular composition. NASA Lewis' current work on fuel stability, both in-house and under grant or contract will be reviewed according to these three categories of research.

Chemical Mechanism Research

A modified JFTOT procedure was used in an in-house study to evaluate deposit and sediment formation for four aerated pure hydrocarbon fuels over the tube temperature range 150° to 450° C [11]. Stainless steel heated tubes rather than the usual aluminum tubes were used to permit higher test temperatures and to increase the deposition rate and thereby reduce test time. Four fuel types were studied: a normal alkane (n-decane), an alkene (1-hexene), a naphthene (cyclohexane), and an aromatic (benzene). Some results from this study are shown in Fig. 4, where tube deposit amounts, expressed as net TDR values, are plotted against tube position. TDR values are approximately proportional to deposition rate. At the lower temperatures of 150° and 250° C, all four fuels produced only small amounts of deposit during the 40 minute run, with TDR values less than 5. At 350° C the olefinic fuel, 1-hexene, formed the largest amount of deposit, cyclohexane the second largest, with the other two fuels forming much less deposit. The fact that 1-hexene formed the most deposit is consistent with its susceptibility to oxidation and polymerization. At the higher temperatures of 400° and 450° C all fuels except benzene formed large amounts of deposit, with TDR values of 40 to over 50. It is not surprising that benzene formed much less

deposit that the other three fuels. This can be attributed to the benzene aromatic structure, which is highly resistant to oxidation [12]. However, substituted benzenes and multi-ringed compounds are generally less resistant to oxidation. Sediment formation was also measured in these experiments and is shown in Fig. 4 as Δp in kilopascals (torr). For these fuels only benzene showed any significant Δp increase. Thus in these experiments, the aromatic benzene appears to form considerable sediment but very little deposit.

This research effort utilizing a modified JFTOT to thermally stress hydrocarbons is continuing. Effects of deoxygenation and pre-stressing of the fuel are currently under investigation. Liquid and gas chromatography as well as mass spectrometry will be used to determine reaction products, including chemical precursors that ultimately lead to deposits, in an effort to increase our understanding of the decomposition mechanisms involved in the fuel degradation process.

Effects of Fuel Nitrogen - We have already mentioned that heteroatoms such as nitrogen that are present in fuels seem to be concentrated in the fuel deposit. A number of experiments have been carried out in which a fuel is spiked with small amounts of nitrogen-containing compounds that are known to occur in actual fuels, in an effort to determine their effect on fuel deposit rates. Some results of this type experiment based on data from ref. 13 are shown in Fig. 5(a). Deposit rate for Jet-A and Jet-A spiked with 0.1 percent N from 2,5 dimethylpyrrole is plotted against temperature. It is clear from the figure that the deposit rate for the spiked Jet-A is dramatically higher at a given temperature, and that the increase in deposit rate with temperature is also considerably greater. In Fig. 5(b) the breakpoint temperature for Jet-A and Jet-A spiked with 0.01 to 0.1 percent nitrogen from pyrrole (a single-ringed N-containing compound) and indole (a double-ringed N-containing compound) are compared [14]. Since breakpoint depends on the rate of deposit formation, based on the results shown in Fig. 5(a), one would expect a reduced breakpoint for the spiked fuels. This is indeed what was observed. The Jet-A spiked with pyrrole and indole have breakpoint temperatures about 40° C and about 20° C less than the unspiked Jet-A, respectively.

Under a NASA grant with the Colorado School of Mines, Daniel has also studied the effect of various organic nitrogen compounds on deposit formation in both Jet-A and a simple model fuel [15]. He selected four classes of nitrogen compounds for study, each of which is found in petroleum and/or synthetic crudes: pyrroles, indoles, pyridines, and quinolines. The effect on deposition rate as a function of the amount of nitrogen added is shown in Fig. 6 for the four parent compounds. In this figure, the amount of deposit (expressed as micrograms) produced in 168 hours at 130° C is plotted against parts per million of nitrogen added to Jet-A. Pyridine and quinoline both show a large increase in deposition over unspiked Jet-A and this increase is strongly dependent on concentration. Conversely, indole and pyrrole exhibit only a small enhancement in the amount of deposit produced, and the increase is only slightly concentration dependent. Daniel pointed out that pyridine and quinoline each contain a nitrogen atom which contributes a single electron to the bonding in the ring, whereas in indole and pyrrole the nitrogen atom contains an unbonded electron pair which enters into the bonding of the ring. Based on these results, Daniel suggested that different mechanisms were operative in the two cases. The results of this figure may seem somewhat contradictory to those of Fig. 5(b) where pyrrole and indole produced a significant decrease in breakpoint temperature when used to spike Jet-A. It should be noted that the concentrations shown in Fig. 5(b) are 100 to 1000 ppm (0.01 to 0.1 percent) nitrogen versus a maximum of 30 ppm for Fig. 6. These large differences in nitrogen concentration plus the approximately 100° C difference in deposition temperature may have resulted in different mechanisms for the deposition process in the two sets of experiments. Nonetheless, because of the complexity of the degradation process and the presence of a great variety of trace impurities in fuels, seemingly contradictory results are not uncommon.

Oxidation Rates and Gum Formation - In an ongoing NASA-funded research contract with SRI-International, Mayo has been studying oxidation and deposit precursor formation in hydrocarbon fuels. His present approach involves measuring the rates of oxidation and rates of gum formation in an effort to relate fuel instability to the types of hydrocarbons and trace heteroatoms present in the fuels. He has found that the trace quantities of reactive components are depleted first and are concentrated in the resulting gums. The rate of oxidation may be either increased or decreased by these minor components. Some recent results [16] are presented in Fig. 7. Here, the oxygen absorbed by n-dodecane to which varying amounts of indene have been added is plotted against oxidation time. The amount of gum formed during each experiment is also shown. Indene is known to have a much faster oxidation rate than pure (or neat) n-dodecane. However, the figure shows that when a very small amount (0.009 molar) of the fast-oxidizing indene is added to the slow-oxidizing dodecane, the oxidation rate of dodecane is retarded rather than increased. From a simplistic point of view, one would expect the presence of indene to increase dodecane's oxidation rate. In fact, the oxidation rate for the indene-dodecane mixture does not exceed the oxidation rate of pure dodecane until the concentration of indene is increased to 1 molar. These results are consistent with results found by Russell many years ago for the cooxidation of cumene and tetralin [17]. It should be noted, however, that although the addition of 0.108 molar indene to dodecane slightly reduces the oxidation rate, the amount of gum formed is increased by more than a factor of 50. Since gums are believed to be precursors to solid deposits, these results illustrate that although oxygen plays a key role in deposit formation, the rate of oxidation does not directly correlate with the amount of deposit formed.

ESR Studies of Fuel Instability - An electron spin resonance (ESR) spectrometer responds to the presence of an unpaired electron in a chemical species. Such species are by definition free radicals, and we have already pointed out that the chemistry of fuel deposit formation involves primarily free radical reactions. Thus, an ESR spectrometer capable of operating at high temperatures and pressures can be used to directly monitor some of the important reactions occurring during deposit formation. We believe that the use of ESR to study fuel degradation offers the potential for significantly increasing our understanding of the reaction mechanisms and kinetics involved in this complex process. Accordingly, NASA Lewis has recently entered into an Interagency Agreement with the Oak Ridge National Laboratory (ORNL) to study free radical reactions in model compounds representative of constituents of jet fuel using ESR.

In previous research at ORNL involving coal liquids, Livingston and Zeldes developed a flow apparatus to use with an ESR spectrometer to study fluids at high temperatures and pressures [18]. Only minor modifications to this apparatus were required to enable work on fuel thermal stability to be undertaken. The

flow system used in conjunction with the ESR spectrometer is shown in Fig. 8. A liquid sample contained in a reservoir is purged with helium to remove dissolved oxygen. The liquid flows to a positive displacement high pressure pump, and pressures from 70 to 135 atm were used with a flow rate of 1 ml/min. There is provision for injecting a gas such as oxygen at high pressure. The liquid flows through a silica capillary that traverses the microwave cavity of the ESR spectrometer and then to a back pressure regulator where the system pressure is set. The liquid exiting the regulator is at atmospheric pressure and may be recirculated as shown in Fig. 8 or collected without recirculation for subsequent analysis. Thermal production of radicals is achieved by heating the silica capillary with air that has been heated electrically. The capillary is surrounded by a vacuum jacketed silica tube, and the air flows in the annular space. Radicals are also produced photolytically. This is done by focusing UV from a 500 W high pressure mercury arc onto the sample within the capillary. Photolysis is used at room temperature and up to temperatures where thermal production of radicals becomes fast enough to see signals. Typical steady-state concentrations of radicals from hydrocarbons are in the micromolar region with mean lifetimes ranging downwards from typical room temperature values near 1 millisecond.

A wide variety of model compounds is being examined that give observable spectra at temperatures up through the intermediate regime (through 300° C). Compounds include n-dodecane, aromatic hydrocarbons, unsaturated hydrocarbons, and spiking agents. Much of the work centers upon oxidizing effects and includes the use of peroxides and hydroperoxides as free radical initiators. The initial phase is a broadly based exploratory survey to search out major reaction pathways that will subsequently be examined in detail.

Deposit Formation in Practical Fuels

The deposit formation rate of actual fuels is usually determined in a flow device generally referred to as a laboratory simulator. Such devices are also capable of providing relatively heavy deposits on flat test specimens which are more easily analyzed and characterized than JFTOT tubes. The schematic of a laboratory simulator used by Vranos under contract to NASA Lewis was described previously in the discussion of Fig. 3. Vranos has used this apparatus to determine the thermal stability of four actual hydrocarbon fuels under conditions representing operation of an aircraft gas turbine engine [9, 19]. Surface temperature was varied from 149° to 399° C (300° to 750° F) for fuel flows of 0.64 to 12.8 grams per second (0.75 to 15 gal/hr) at pressures of 2040 kPa (300 psig). Test times varied from 1 to 8 hours. The rate of deposition was obtained by measurement of the weight gained by metal discs located along the channel wall.

Figure 9 shows representative results for the four fuels using stainless steel test discs: Jet A, home heating oil, a straight run diesel which has no cracked stock, and a normal diesel which has a large cracked fraction. Below 260° C (500° F), where there is an apparent change in mechanism, Jet A, straight run diesel, and the cracked diesel all had comparable deposition rates. Above 260° C, Jet A had the lowest rate, straight run diesel somewhat higher, and cracked diesel the highest. Up to 260° C the home heating oil had the highest rate while above 260° C it was lower than the cracked diesel.

The effect of wall material was determined by using stainless steel, aluminum, and brass test discs. Stainless steel and aluminum gave comparable results while the brass specimens gave a significant increase in deposition rate. Tests were also conducted in a static reactor at temperatures of 149° to 427° C (300° to 800° F) for times of 15 minutes to 2 hours. Much smaller deposition was found, indicating the importance of fluid transport in the deposition mechanism. As-received and stressed fuels were examined by liquid chromatography in an attempt to detect any changes in fuel composition caused by the heating. It is known that the changes being sought are very small and no differences were found, probably due to the limits of detection of the instrument.

The strong temperature dependence of deposition rate suggests that an Arrhenius plot, log of deposition rate versus reciprocal temperature, might correlate the data. Figure 10 is such a plot by Vranos [9] of his earlier data for Jet-A at two different flow rates. The overall activation energy, given by the slope of the lines, is in reasonable agreement with some previous results for Jet-A [20]. At higher flow rates, the deposit rate is lower at the same wall temperature, yet the temperature dependence, or activation energy, is approximately the same. The lower deposit rate at increased flow points out the importance of bulk-fluid heating and homogeneous reaction effects on the formation of deposits. In both cases, the magnitude of the activation energy, which is much less than that for typical homogeneous reactions, suggests a surface-catalyzed process.

Additional deposit-rate studies are planned for the NASA laboratory simulator previously described. In addition, this simulator along with the NASA JFTOT modified for flat test samples, will be used to generate deposits for detailed chemical and physical analysis.

Deposit Analysis

Due to the complex and intractable nature of the deposits, as well as the small quantities generally available for analysis, the detailed molecular structure of the deposits has remained largely unknown. Recent attempts to perform detailed characterization of the deposits have involved the use of a variety of modern analytical instrumental techniques which are listed in Table I along with a brief comment about the type of information each technique is capable of producing. Each technique has the potential to provide a portion of the structural information sought, but each has specific limitations as well. Through in-house research efforts and sponsored studies, each of the techniques listed is or will soon be employed to characterize deposits obtained from the JFTOT flat sample holder and the NASA thermal stability laboratory simulator under varied but carefully-controlled conditions. Both well-characterized commercial fuels and model fuels prepared from representative pure compounds are being used. To provide additional information, the deposit elemental composition will be determined, and studies to identify deposit precursors in the stressed fuels will be conducted. A combination of the deposit structural information provided by the techniques described, the deposit elemental analysis, the stressing conditions, the precursor studies and the fuel composition will yield the deposit formation mechanisms, an identification of the most active fuel components, and the sensitivity of the formation rates to fuel stressing conditions. These results

should ultimately lead to deposit prevention through the knowledgeable development of fuel additives, the types and levels of refinery fuel treatment required, and future fuel system designs.

DESIGN CONSIDERATIONS

We stated in the introduction that in the future, the thermal stability of fuels may be lower and the thermal stresses to which they are subjected, higher. One way to alleviate this problem is by additional processing at the refinery. Another is for the airlines to decrease the operating time between inspections or component removal and maintenance. Either of these approaches might be prohibitive in terms of increased costs to the airlines.

The most cost effective approach to utilizing fuels of reduced thermal stability in new, higher efficiency engines is to incorporate, in the design stage, components and designs tolerant to variations in this fuel property. It is beyond the scope of this report to discuss in any detail the types of design changes that might be required, but a few comments are appropriate.

In contracted analytical studies with NASA Lewis, General Electric and Lockheed California have been analyzing and assessing advanced fuel system concepts. Both contractors have identified thermal stability and freezing point as the two most important fuel properties affecting fuel system performance. They both have studied advanced fuel systems capable of using a fuel with a breakpoint temperature of about 205° C, considerably below the current specification for thermal stability (breakpoint of at least 260° C). Although the final results for these two studies are not yet available, the advanced concepts under consideration include the following approaches to reducing heat load on the fuel after it leaves the fuel tank: (1) relocate valves to lower temperature environment and use low Δp nozzles which permit larger injector ports, (2) use variable displacement pumps instead of the current gear type to reduce pump heat rejection to the fuel, (3) reject lubricating-oil heat to the bulk of the fuel in the fuel tanks rather than to the much smaller amount of fuel metered for the combustor, and (4) improve the thermal tolerance of fuel nozzles and fuel lines exposed to high heat load by using heat shields, insulation, and/or cooling air. While concepts such as these may potentially allow the use of fuels with reduced thermal stability, none of these concepts has been verified experimentally. Some additional words of caution are in order. At a workshop held at NASA Lewis [21], it was pointed out that heat shield and insulation devices designed to reduce heat soak-back to fuel nozzles might reduce the aerodynamic efficiency of air-blast nozzles. This would adversely affect the atomization quality of the fuel spray which is already an area of concern with alternative fuels. This example indicates that we must be wary of interaction effects when changing the design of fuel systems.

CONCLUDING REMARKS

Although fuel instability is not a serious problem for current fuels and aircraft, it could well be a major problem in the future because of the possible deterioration of the quality of petroleum crudes and the use of syncrudes. The problem could be exacerbated by the increased thermal stress that will probably be encountered in advanced turbine engines. We have tried to show in this paper that the instability of aircraft fuel is an extremely complex problem, with experimental investigations yielding results that sometimes appear to be contradictory. Although a great deal of work has been done to understand the mechanisms of deposit formation, deposit composition, the role of trace impurities, and the effects of fuel instability on airframe and engine fuel systems, much work remains to be done. It is anticipated that an increased understanding of fuel instability will lead to methods for minimizing deposit formation or of ameliorating its effects on fuel systems.

There is another potential benefit from an increased understanding of the fuel degradation process which is related to fuel processing. Petroleum refineries currently do not use any specific processing treatment to control the thermal stability of jet fuel, although selective chemical additives (anti-oxidants) are frequently used to improve storage stability. The desired level of thermal stability is a by-product of the other processing the fuel must undergo in order to meet other specifications. This practice will probably not be satisfactory for alternative fuels because of reasons already stated. However, a fundamental knowledge and understanding of the fuel degradation process will probably provide value insight as to what type or types of additional processing should be undertaken to improve the thermal stability of the resulting fuel.

Although there are many facets of the fuel instability problem that need to be explored, it is the authors' opinion that additional research with the following objectives will lead to significant benefits in understanding and dealing with fuel instability:

- Establish the roles and degree of importance of fuel hydrocarbon type and trace contaminants in determining fuel instability.
- Compare rates, morphologies, and compositions of deposits produced via simulators with actual deposits produced in an engine fuel system.
- Evolve a model which will predict fuel deposition rates in an actual engine fuel system based on input from laboratory simulators.
- Establish the relationship between storage deposits and thermal deposits. Are the mechanisms the same, precursors the same?
- Determine the effectiveness of additives (anti-oxidants, free-radical scavengers, dispersants) for improving fuel stability as well as their interactions with each other and fuel components.
- Experimentally evaluate conceptual fuel system components and fuel injectors that reduce exposure to thermal stress and are more tolerant to small amounts of deposition.

REFERENCES

1. Nixon, A. C.: Autoxidation and Antioxidants of Petroleum. Autoxidation and Antioxidants, Vol. II, W. O. Lundberg, Ed., Interscience Publishers, Inc., New York, 1962, pp. 695-856.

2. Anon., CRC Literature Survey on the Thermal Oxidation Stability of Jet Fuel. CRC Report No. 509, Apr. 1979.

3. Peat, A. E.: Fuel Thermal Stability. Propulsion and Energetics Panel, Working Group 13 on Alternative Jet Engine Fuels, Vol. 2, R. B. Whyte, Ed., AGARD-AR-181-Vol-2, July 1982, pp. 119-141.

4. Taylor, W. F.: Jet Fuel Thermal Stability. NASA TM-79231, 1979.

5. Hazlett, R. N., Hall, J. M. and Matson, M.: Reactions of Aerated n-Dodecane Liquid Flowing Over Heated Metal Tubes. Ind. Eng. Chem., Prod. Res. Dev., Vol. 16, No. 2, 1977, pp. 171-177.

6. Schirmer, R. M.: Morphology of Deposits in Aircraft Fuel Systems. REPT-5029-68R, Phillips Petroleum Co. Res. Div., Aug. 1968.

7. Schirmer, R. M.: Morphology of Deposits in Aircraft and Engine Fuel Systems. SAE Paper 700258, Apr. 1970.

8. Smith, M.: Aviation Fuels. G. T. Foulis & Co., Ltd., Cambridge, England, 1970, pp. 89-90.

9. Vranos, A., and Marteney, P. J.: Experimental Study of the Stability of Aircraft Fuels at Elevated Temperatures. (R80-954440-17, United Technologies; NASA Contract NAS3-21593.) NASA CR-165165, Dec. 1980.

10. Cohen, S. M.: Fuels Research - Fuel Thermal Stability Overview. Aircraft Research and Technology for Future Fuels, NASA CP-2146, July 1980, pp. 161-168.

11. Wong, E. L., and Bittker, D. A.: Effect of Hydrocarbon Fuel Type on Fuel Thermal Stability. NASA TM-82916, June 1982.

12. Bol'shakov, G. F., Bushueva, E. M., and Glebovskaya, E. A.: Effect of Some Naphthene-Aromatic Hydrocarbons on Solid-Phase Formation in Hydrocarbon Fuels. Khim.Tekhnol.Topl.Masel, Vol. 12, No. 4, Apr. 1967, pp. 40-43.

13. Taylor, W. F.: The Study of Hydrocarbon Fuel Vapor Deposits. Esso Research and Engineering Co., AFAPL-TR-69-77, Sept. 1969.

14. Antoine, A. C.: Effect of Some Nitrogen Compounds on Thermal Stability of Jet A. NASA TM-82908, June 1982.

15. Daniel, S. R.: Studies of the Mechanisms of Turbine Fuel Instability. NASA CR-167963, Jan. 1983.

16. Mayo, F. R., Lan, B., Cotts, D. B., Buttrill, Jr., S.E., and St. John, G. A.: Oxidation and Formation of Deposit Precursors in Hydrocarbon Fuels. SRI-2115, SRI International, NASA CR-168121, Mar. 1983.

17. Russell, G. A.: Oxidation of Unsaturated Compounds. J. Amer. Chem. Soc., Vol. 78, No. 5, Mar. 1956, pp. 1035-1044.

18. Livingston, R. and Zeldes, H.: Apparatus to Study the Electron Spin Resonance of Fluids under High Pressure Flowing at High Temperature. Rev. Sci. Instrum., Vol. 52, No. 9, Sept. 1981, pp. 1352-1357.

19. Marteney, P. J., Colket, M. B., and Vranos, A.: Experimental Study of the Thermal Stability of Hydrocarbon Fuels. (R82-955319-20, United Technologies Research Center; NASA Contract NAS3-22511.) NASA CR-168027, Dec. 1982.

20. Vranos, A., Marteney, P. J., and Knight, B. A.: Determination of Coking Rate in Jet A Fuel. Combust. Sci. Technol., Vol. 26, Aug. 1981, pp. 171-175.

21. Gerstein, M.: Fundamentals of Gas Turbine Combustion. NASA CP-2087, 1979.

TABLE I. - MODERN INSTRUMENTATION FOR DEPOSIT CHARACTERIZATION

INSTRUMENT	INFORMATION OBTAINED
SCANNING ELECTRON MICROSCOPE (SEM)	MORPHOLOGY OF DEPOSITS THROUGH HIGH MAGNIFICATION
ENERGY DISPERSIVE ANALYSIS OF X-RAYS (EDAX)	QUALITATIVE AND SEMI-QUANTITATIVE ANALYSIS OF μ-SIZE SAMPLE AREAS
ELECTRON SPECTROSCOPY FOR CHEMICAL ANALYSIS (ESCA)	QUALITATIVE AND SEMI-QUANTITATIVE ANALYSIS OF TOP 100 A OF SAMPLE SURFACE - PROVIDES BONDING INFORMATION
SECONDARY ION MASS SPECTROSCOPY (SIMS)	QUALITATIVE AND SEMI-QUANTITATIVE ANALYSIS OF 25 TO 2500 A LAYER OF SAMPLE PER MASS SCAN
FOURIER TRANSFORM INFRARED SPECTROSCOPY (FT-IR)	DETERMINATION OF FUNCTIONAL GROUPS - SUPERIOR SENSITIVITY TO CLASSICAL IR
RAMAN SPECTROSCOPY	DETERMINATION OF FUNCTIONAL GROUPS - COMPLEMENTS IR
PHOTOACOUSTIC SPECTROSCOPY (PAS)	CHROMOPHORE AND FUNCTIONAL GROUP DETERMINATIONS, AND THERMAL PROPERTIES CHARACTERIZATION
PYROLYSIS/GAS CHROMATOGRPAHY-MASS SPECTROMETRY	PYROLYZED FRAGMENTS FROM DEPOSIT IDENTIFIED - MOLECULAR COMPOSITION OF ORIGINAL DEPOSIT DETERMINED

LOW TEMPERATURE

(BELOW 300° C - AUTOXIDATION)

$$RH + X \longrightarrow R\cdot + HX, \text{ (INITIATION)} \quad (1)$$

$$R\cdot + O_2 \longrightarrow RO_2\cdot \quad (2)$$

$$RO_2\cdot + RH \longrightarrow ROOH + R\cdot \quad (3)$$

$$RO_2\cdot + ? \longrightarrow \text{DEPOSITS, GUMS, SEDIMENTS} \quad (4)$$

INTERMEDIATE TEMPERATURE

(300 - 500° C)

$$ROOH \longrightarrow RO\cdot + HO\cdot \quad (5)$$

$$RO\cdot + RH \longrightarrow ROH + R\cdot \quad (6)$$

$$HO\cdot + RH \longrightarrow H_2O + R\cdot \quad (7)$$

$$ROOH + X \longrightarrow \text{KETONE} + XH, \text{ (SECONDARY HYDROPEROXIDE)} \quad (8)$$

$$RH \longrightarrow R_1\cdot + R_2\cdot, \text{ (PYROLYSIS)} \quad (9)$$

ISOMERIZATION AND DECOMPOSITION OF $R_1\cdot$ AND $R_2\cdot$ TO FORM OLEFINS

Figure 1. - Proposed mechanisms for fuel degradation.

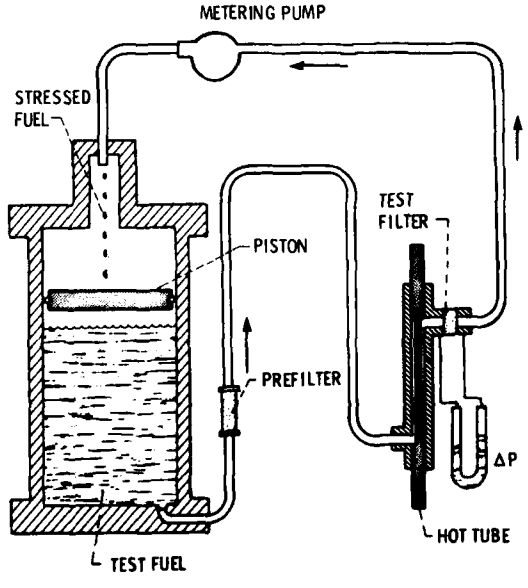


Figure 2. - Schematic of jet fuel thermal oxidation tester (JFTOT).

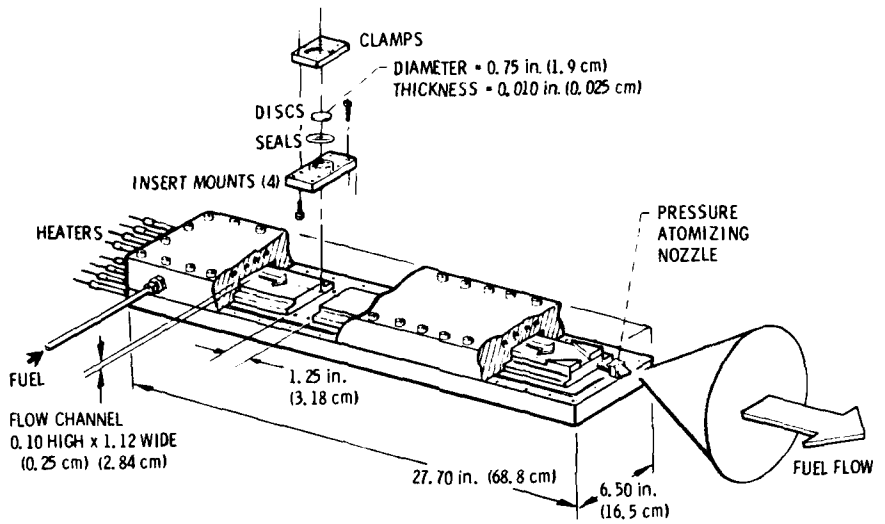


Figure 3. - UTRC thermal stability test section.

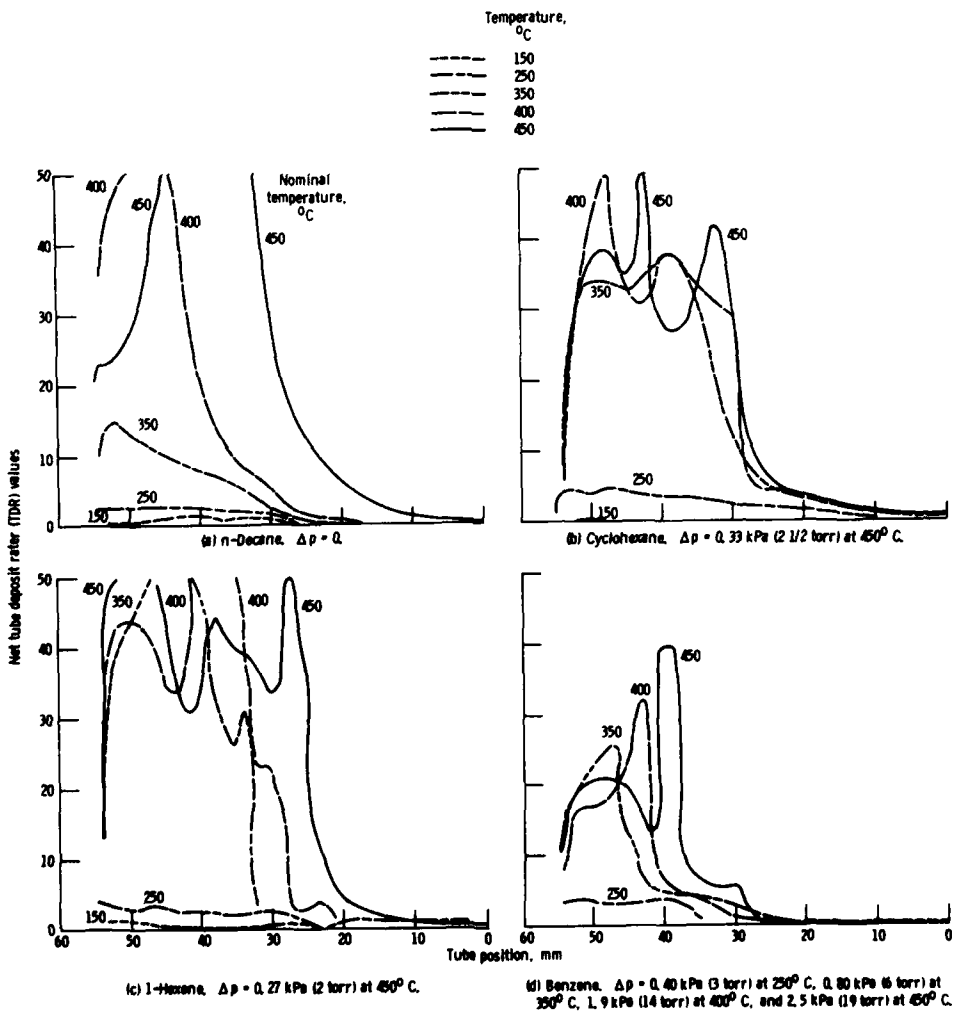
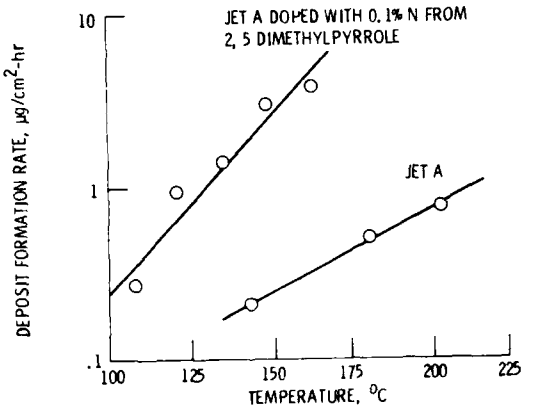
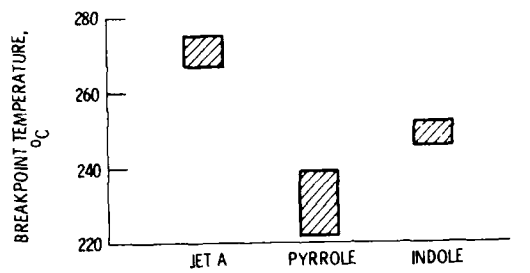


Figure 4. - Tube deposit and sediment formation for four hydrocarbon fuels.



(a) Effect of fuel nitrogen content on deposit formation rate.



(b) Breakpoint temeratures of Jet-A and solutions of nitrogen compounds in Jet-A ranging from 0.01 to 0.1 weight percent N.

Figure 5. - Effect of fuel nitrogen content on thermal stability.

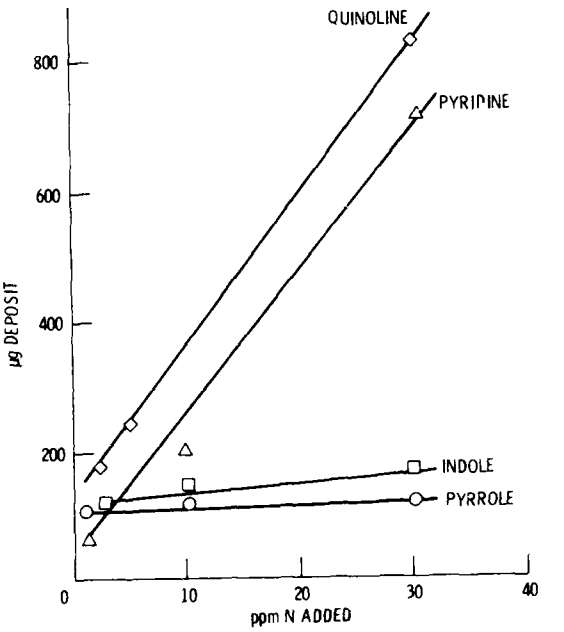


Figure 6. - Effect of added nitrogen concentration on deposit rate at 130° C.

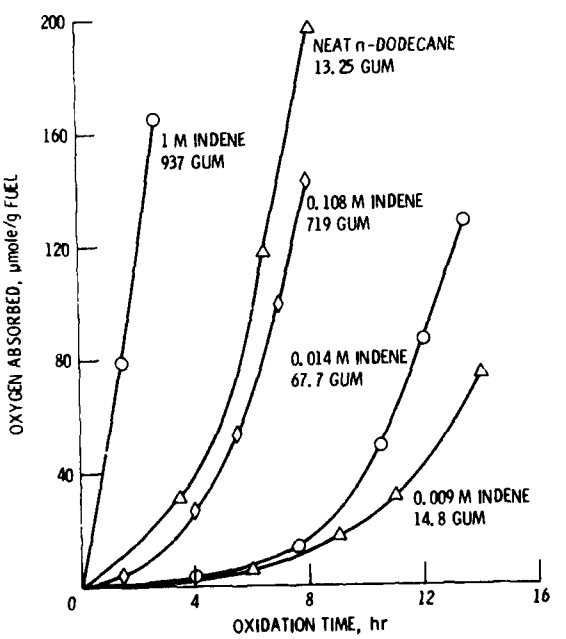


Figure 7. - Oxidations of n-dodecane with indene at 130° C (Gum is in mg/100 g fuel, determined at 100° C).

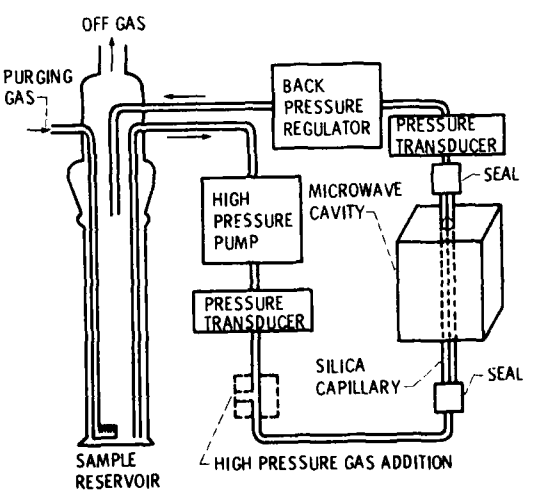


Figure 8. - Flow system for fuel thermal stability studies using electron spin resonance (ESR) spectrometer.

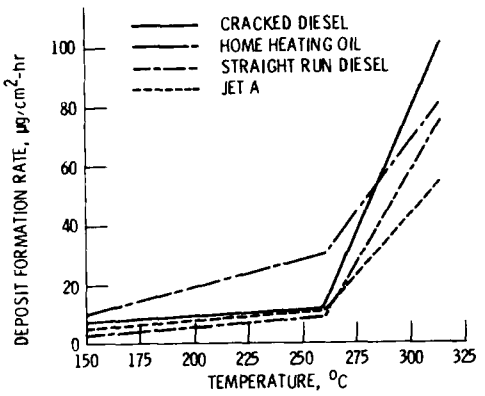


Figure 9. - Deposition rate of various fuels.

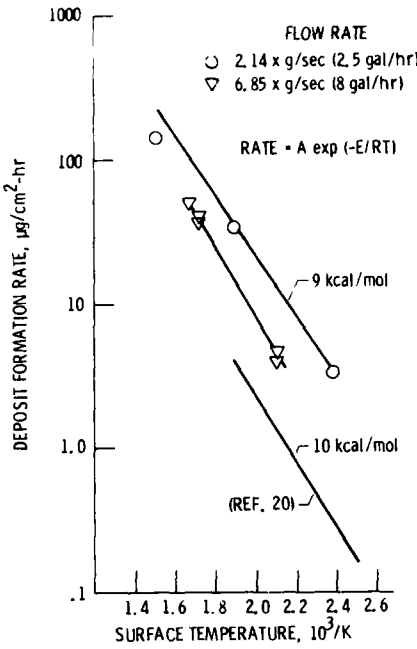


Figure 10. - Arrhenius plot of deposit rate in Jet A.

DISCUSSION

D.Snape, UK

Given a sample of a fuel deposit, what if any means are there of differentiating between the two principal deposition mechanisms, i.e. gas phase and liquid phase?

Author's Reply

I am not aware that any laboratory can predict, with any degree of confidence, the type of mechanism (i.e. liquid phase or vapour phase) involved in the formation of deposits based solely on the morphology of the deposit. I am quite certain that our laboratory at NASA-Lewis does not have this capability. Such a capability might well be useful in diagnosing deposition problems in actual aircraft fuel systems. However, one must keep in mind that a deposit may undergo marked morphological changes following its initial deposition due to exposure to subsequen thermal stressing.

ALTERNATIVE FUEL DEPOSIT FORMATION

J. TeVelde, L. J. Spadaccini and E. J. Szetela
United Technologies Research Center
East Hartford, Connecticut 06108
and
M. R. Glickstein
Pratt and Whitney Aircraft
West Palm Beach, Florida 33402

AD-P003 129

Abstract

A heated-tube apparatus was used to evaluate the deposit formation rates of four liquid hydrocarbon fuels and to determine the effect fuel deposits have on the heat transfer characteristics of aircraft gas turbine fuel systems. The fuels tested were: a low- aromatic JP-5, a blend of 80 percent JP-5 and 20 percent hydrocracked gas oil, a blend of 50 percent JP-5 and 50 percent No. 2 heating oil, and a shale derived JP-5. Deposit formation rates ranging from 10 $\mu g/cm^2$ hr to 3000 $\mu g/cm^2$ hr were obtained at tube wall temperatures ranging from 480 K to 800 K, with peak formation rates occurring at initial surface temperatures of 644 K to 672 K. Results indicate that deposit formation rate correlates very well with initial surface temperature and the thermal stability rankings derived from present experimental results agree very well with rankings based upon independent JFTOT analysis. The deposit thermal resistance, as calculated from heat transfer measurements, correlates well with measured deposit quantity and thickness. Heat transfer analyses indicate that the deposit thermal conductivity increases with increasing deposit thickness, and ranges from values approximating the thermal conductivity of the fuel to values approaching that of amorphous carbon.

Nomenclature

A	inner surface area of clean tube
A'	deposit inner surface area
D	tube inner diameter
D_o	tube outer diameter
D'	inner diameter of deposits
h	clean tube convective heat transfer coefficient
h'	convective heat transfer coefficient subsequent to start of test
k	fuel thermal conductivity
k_d	deposit thermal conductivity
k_w	tube wall thermal conductivity
L	tube length
Nu	Nusselt number
P	fuel pressure
ΔP	pressure drop across tube
Pr	Prandtl number
Q	heat flux
Q'	heat generation per unit volume
Re	Reynolds number
T_b	bulk fuel temperature
T_{w_i}	tube inner wall temperature
$T_{w_{o_i}}$	tube outer wall temperature at time = 0
t	deposit thickness
U	overall heat transfer coefficient
V	tube entrance velocity
τ	test duration

Introduction

In recent years, increased attention has been directed toward the effective utilization of alternative fuels in aircraft gas turbines. New fuel blends derived from crude oil, coal liquids, or shale oil require careful study prior to effective implementation, since significant deviations from conventional fuel specifications may occur. An important area of concern that is directly impacted by deviations in fuel specification is that of fuel thermal stability. Changes in fuel composition which may be detrimental to thermal stability are likely to include a higher fraction of aromatics and olefins as well as increased concentrations of minor species such as sulfur, nitrogen, and trace metal contaminants. Furthermore, higher pressure ratio engines and flight at supersonic speeds result in increased heat fluxes and higher thermal loadings on the fuel systems, and can lead to the production of insoluble deposits in the fuel. Thus, the potential for increased thermal loading and significant deviations in fuel specifications make fuel thermal stability a potentially serious problem.

Hydrocarbon fuel thermal stability has been investigated for many years by numerous authors[1-10]. The rate of deposit formation on heated surfaces has been found to vary with temperature in a unique

matter[2,3,7,9] characterized by a rapid increase with increasing surface temperature, up to approximately 670 K, followed by a rapid decrease and yet another more gradual increase as the reaction mechanism shifts from oxidation controlled to pyrolysis controlled. In addition to surface temperature, previous studies have shown that fuel deposition is a function of fuel composition, fuel temperature, fuel pressure, and velocity. While there is presently only a limited understanding of the mechanisms involved in deposit formation, it is generally believed that deposits are produced by free radical autoxidation of hydrocarbon molecules. Although questions regarding the mechanisms involved during deposit formation still remain, it is generally believed that deposit precursors produced by oxidation of the fuel are condensed out of the fuel in a stepwise manner[1]. Except for recent investigations[7,9] little effort has been directed toward evaluating the effects of fuel deposits on the fuel system heat transfer characteristics. Because of the number of factors influencing hydrocarbon decomposition, determination of the useful heat sink capacity (or temperature limits) for a specific fuel should be made at the conditions of planned application. While a standardized coker test yields a direct comparison with a fuel specification, it does not provide data for design of a new fuel application. Such data can only be obtained by evaluating decomposition-deposition characteristics at conditions simulating the desired application. Consequently, an experimental investigation was undertaken using a newly developed methodology for evaluating the thermal character of alternate fuels whose properties may be representative of changes in the properties of future fuels. Specifically, this characterization relates the evaluation of the fuel thermal stability to the deposit heat transfer characteristics at conditions representative of the engine application.

Fuel Selection and Characterization

The purpose of this study was to investigate the deposit formation of several fuels thought to have a relatively wide range of thermal stability and to relate how deposit formation impacts heat transfer characteristics and pressure losses within tubes. The detailed chemistry of the deposit formation mechanisms was considered beyond the scope of the present effort. Therefore, no attempt was made to systematically vary fuel composition. However, four fuels whose compositions were thought to span a wide range of thermal stability were selected for evaluation. These fuels were: a low-aromatic JP-5, a shale-derived JP-5 with nitrogen compounds partially replaced (NAPC-14), a mixture of 80 percent JP-5 and 20 percent hydrocracked gas oil (NAPC-7), and a mixture of 50 percent JP-5 and 50 percent No. 2 heating oil (NAPC-11). A tabulation of selected properties of the fuels tested is presented in Table 1. Note that the JFTOT thermal stability analyses performed subsequent to testing indicated that the JP-5 fuel sample failed the pressure drop criterion.

Table 1 Selected properties of test fuels

	JP-5	NAPC-7	NAPC-11	NAPC-14
Aromatics (vol. %)	14.99	32.57	21.6	24
Olefins (vol. %)	0.79	0.86	1.1	1.6
Sulfur (wt. %)	0.005	0.047	0.07	0.002
Nitrogen (ppm)	neg	57	33	2.6
API Gravity (at 288 K)	41.8	35.6	39.6	43.7
Distillation (K)				
IBP	454	466	460	457
10%	472	477	478	466
20%	476	482	486	469
50%	490	499	5-6	478
90%	516	545	567	504
EP, max	534	561	577	530
JFTOT Thermal Stability				
Breakpoint Temperature (K)	544	533	516	541
ΔP (25mmHg) Failure Temp (K)	522*	>533	>516	>541

*fails specification

Test Facility and Experimental Procedure

Deposit formation experiments were conducted under steady flow conditions in an apparatus containing a single resistance-heated tube which was insulated from the surroundings. The apparatus, shown schematically in Fig. 1, was capable of continuous unattended operation and consisted of the following major components: (1) a 275-gal fuel supply equipped with an air sparging system to ensure that the fuel was air saturated, (2) a fuel delivery system consisting of a fuel pump capable of supplying fuel at pressures up to 68 atm and associated filters to remove solid particulate contaminants larger than 2 μm, (3) a high-pressure-drop orifice to render the fuel supply insensitive to pressure changes in the test apparatus, (4) a turbine-type flow meter, (5) a resistance-heated tube connected electrically to a 64 kW d-c power supply, (6) a proportional temperature controller used to maintain a constant fuel exit temperature by regulating the input power, (7) a fuel cooler, (8) a back-pressure regulator, (9) another 275-gal reservoir for stressed fuel collection, and (10) a nitrogen purge system.

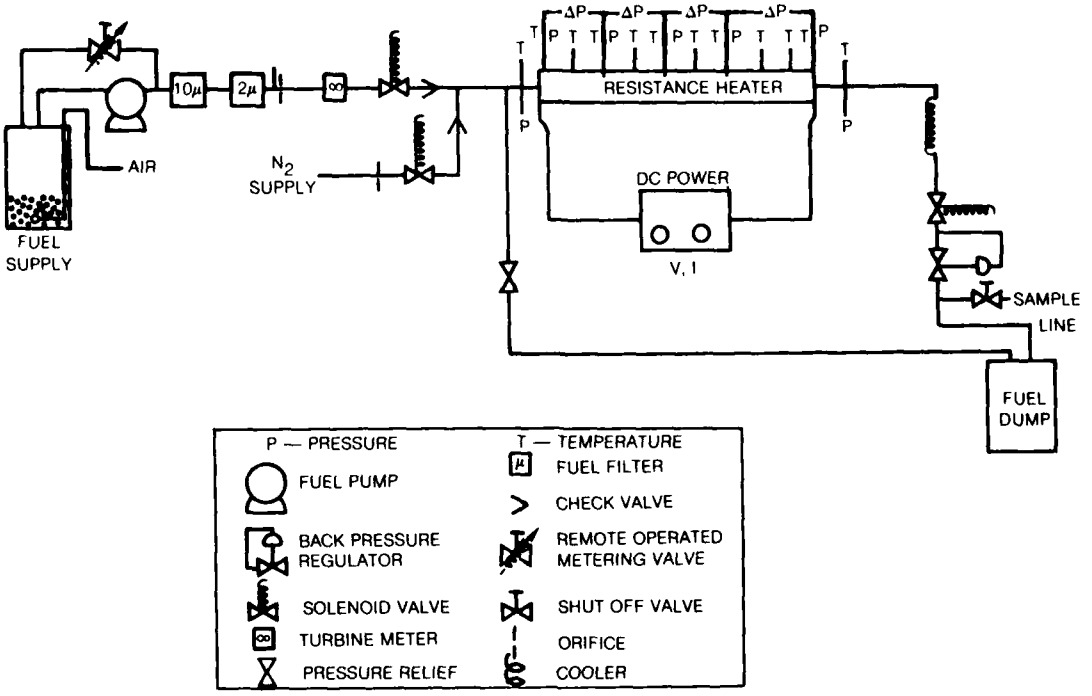


Figure 1. Deposit Test Apparatus

The standard heated test section is shown schematically in Fig. 2 and consisted of a 316 stainless steel tube having a length of 2.4 m, an ID of 0.22 m, and a wall thickness of 0.05 cm. A few tests were conducted with shorter 1.2 m tubes to investigate whether changes in the environmental history of the fuel had an effect on fuel deposition. Each 2.4 m test tube was instrumented with thirty-three thermocouples (spaced every 5 to 9 cm) to measure the outside wall temperature distribution; twenty-six thermocouples (spaced approximately every 4 cm) were used along the 1.2 m tube. Fuel pressures and temperatures were measured at the tube inlet, tube exit, and at three equally spaced intermediate locations along the 2.4 m tube, and at two equally spaced locations along the 1.2 m tube. In order to obtain an accurate measurement of wall temperature while using direct-current heating, each thermocouple was electrically isolated from the tube by a thin layer of ceramic paint. The thermocouple junction, whose size was no greater than 0.025 cm, was tightly pressed against the tube and secured with additional layers of ceramic cement. An automatic data acquisition system continuously monitored the data and recorded all data at regular preprogrammed intervals (15-min typical).

Prior to testing, the tube assembly was thoroughly cleaned in acetone and blown dry with nitrogen, and new fuel fitter elements were installed. To ensure a repeatable initial test condition, the fuel in the supply tanks was saturated by sparging with air for a minimum of twenty-four hours, and the dissolved oxygen content was measured. A test was initiated by first establishing the desired pressure and flow rate condition and then activating the electric power supply and adjusting the power level until the desired fuel exit temperature was achieved. The time necessary for attaining a steady fuel temperature was typically less than one minute. Interlocking switches for automatic shutdown were then activated, thereby permitting unattended operation, and the data acquisition system was activated. Any improper thermocouple attachments were readily identified from the initial wall temperature profile and data from such thermocouples were ignored in data analysis. At the conclusion of a test, the fuel flow and power were simultaneously terminated and a three minute nitrogen purge initiated. The test tube was then removed and sectioned for deposit analysis.

The quantity of deposit accumulated at various axial locations along the tube was determined by oxidizing individual 5.1-cm-long sections of tube in heated air with continuous analysis of the evolved gases. Approximately 12 sections were obtained by carefully subdividing the test tube using a thin-bladed saw and a special jig that was designed to minimize tube vibration and heating and, thereby, preserve the morphology of the deposit. Prior to analysis, each specimen was vacuum dried at 395 K for a minimum of 16 hr to remove any residual liquid fuel. The tube sections were then installed in a high-temperature laboratory furnace and the deposit was reacted with a metered flow of air, which was directed through the inside of the tube. The effluent gas stream was passed through a platinum/palladium catalytic converter to ensure complete oxidation of all carbonaceous species to CO_2 and was continuously analyzed for both the CO and CO_2 concentrations. The deposit (i.e., carbon) mass was determined from a knowledge of the air flow rate and the concentrations of CO and CO_2 in the reaction products. This procedure was validated by performing several calibration runs in which pre-weighed samples of spectrographic-grade carbon (ranging from 5 to 25 mg) were oxidized.

JP-5 Fuel Tests

A low-aromatic petroleum based JP-5 was chosen as the fuel with which to initiate testing and to identify the important physical parameters that affect deposit formation. The experiments were designed to evaluate the effects of key operating variables such as fuel pressure, fuel flowrate (velocity), test duration, and surface temperature. Tests were conducted at initial wall temperatures whose values ranged from 545 K to 800 K, fuel temperatures ranging from 450 K to 755 K, fuel discharge pressures ranging from 27.2 atm to 54.4 atm, and a tube entrance velocity of 2.6 m/sec. To achieve these variations, constant input heat fluxes ranging from 45 to 75 Watt/cm^2 were required.

An example of the progression of a typical wall temperature distribution throughout the duration of a test conducted at a baseline condition (tube entrance velocity of 2.6 m/sec, pressure of 27.2 atm and fuel discharge temperature of 755 K) is presented in Fig. 3. The initial rise and subsequent decrease in wall temperature at the tube entrance is believed to be due to an interaction between the developing temperature profile and the laminar-turbulent transition[11]. Therefore, because correlations of heat transfer are strongly dependent on the local Reynolds number and the state of the boundary layer all deposit formation data were obtained in the region of fully-developed turbulent flow downstream of the entrance. As fuel deposits form on the tube inner surface (downstream of the entrance), the outer wall temperature increases due to added thermal resistance of the deposit. The temperature data indicate that the increase in outer wall temperature realized at each time increment is greatest at axial locations which correspond to an initial wall temperature ranging from approximately 645 K to 672 K. The magnitude of the resulting increases in outer wall temperatures at locations corresponding to both lower and higher initial wall temperatures were considerably reduced.

The mass of carbon, determined from the oxidation analysis, was converted to a deposition rate for each of the 5.1-cm-long tube sections and correlated with the average local initial-wall-temperature. A composite plot of all the JP-5 deposit data is presented in Fig. 4 and clearly indicates that deposit formation exhibits a characteristic behavior that is strongly dependent on the initial wall temperature

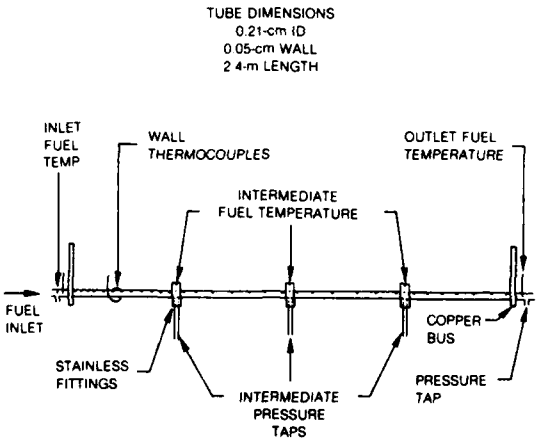


Fig. 2 Test Assembly Instrumentation

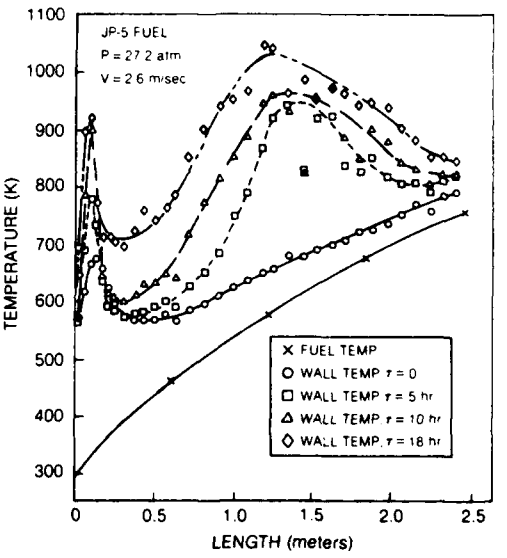


Figure 3. Tube Wall Temperature Distribution

of the tube. That is, the deposit formation rates peak at an initial wall temperature of approximately 645 K. At wall temperatures greater than and less than this value, the rates decrease very rapidly with temperature, as was suggested by the wall temperature increases shown previously in Fig. 3. Taylor[3] and Szetela and TeVelde[7] reported a similar effect of wall temperature on deposit formation.

The effect of pressure on fuel thermal stability was investigated by performing tests at fuel exit pressures of 27.2 atm and 54.4 atm. Results (shown in Fig. 4) indicate that, over the range investigated, fuel thermal stability was not affected by operating pressure. Furthermore, results of tests performed at identical conditions for durations of 1 to 14 hr indicate that deposit formation was relatively independent of time. In addition, a test was run to investigate whether intermittent fuel heating had an effect on deposit formation. A duty cycle consisting of two hours of hot fuel flow followed by one minute of cold fuel flow was repeated five times for a total test duration of ten hours. Results of the wall temperature and deposit burnoff measurements showed that intermittent operation had little or no effect on deposit formation or heat transfer. This was corroborated by the observation that, in almost all cases upon the resumption of fuel heating, the tube wall temperatures returned to their last previous values.

The histories of the pressure drop across a typical section of tube and the corresponding local wall temperatures obtained during a long-duration test are presented in Fig. 5. The pressure drop was measured across a 0.61-m-long tube section located near the midspan in an area of peak deposit formation, and the wall temperatures were measured at the entrance, midpoint and exit of the tube section. The pressure data indicate that deposits were continually being formed throughout the test; whereas, changes in the wall temperature gradients suggest that there may have been a decrease in the rate of deposit formation with increasing test time. It is hypothesized that rather than a decrease in formation rates, the structure of the deposits changes with time in a way which affects the heat transfer characteristics (e.g., thermal conductivity or roughness).

Alternative Fuel Tests

The alternative fuel test series were performed with a 20 percent hydrocracked gas oil/80 percent JP-5 fuel blend (NAPC-7), a 50 percent No. 2 heating oil/50 percent JP-5 blend (NAPC-11) and, by a shale-derived JP-5 fuel (NAPC-14). Test data were obtained at pressures of 27.2 and 54.4 atm, tube entrance velocities ranging from 2.6 m/sec to 5.2 m/sec, test durations ranging from 1 hr to 10 hr, surface temperatures ranging from 480 K to 800 K, and fuel temperatures ranging from approximately 425 K to 755 K.

A composite plot of the deposit formation rates obtained from the 20 percent hydrocracked gas oil/80 percent JP-5 fuel blend (NAPC-7) is shown in Fig. 6 and exhibits the same dependence on initial wall temperature as was described earlier for the JP-5 fuel. Also, test duration was again found to have no significant effect on fuel deposition rates. A few tests were conducted at an increased velocity (5.2 m/sec), and with a shorter tube (1.2-m long) in order to investigate the effect of reduced residence time and to determine whether the results were configuration-dependent. For the shorter

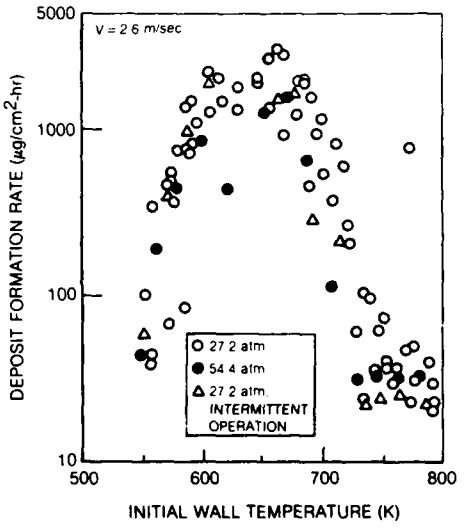


Figure 4. Rate of Carbon Deposition for JP-5 Fuel

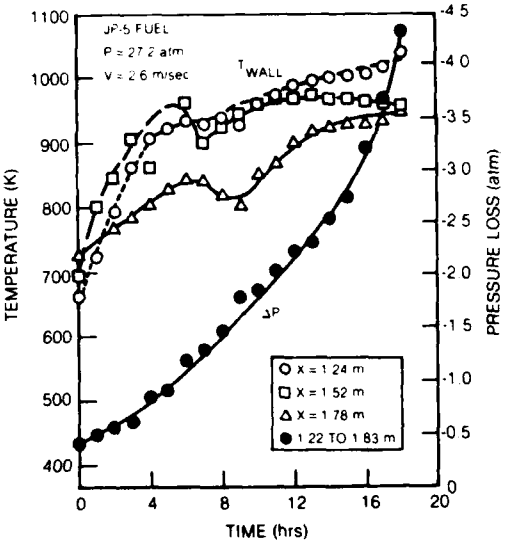


Figure 5. Wall Temperature and Pressure Drop Histories

tube, twice the input heat flux was required to attain the same fuel discharge temperature as was tested in the longer tube (i.e., 755 K) and, consequently, the corresponding tube wall-temperatures were significantly higher. As seen in the figure, the deposit formation rates obtained from the increased velocity and the short-tube tests were slightly higher than those obtained from the baseline test condition of 27.2 atm, 2.6 m/sec velocity, and a 2.4 m tube length, particularly over the range of initial wall temperature, 670 K to 770 K. Thus, it appears that there is a secondary dependence of deposit formation on residence time, possibly related to the rate of depletion of deposit precursor species from the fuel.

The deposit layer acts as a thermal barrier to heat transfer; therefore, to maintain a constant fuel discharge temperature, a constant heat flux is required and the wall temperatures must increase. The thermal resistance of the deposit (t/k) was determined according to the following relation:

$$\frac{1}{U} - \frac{1}{h} = t/k, \qquad (1)$$

where t is the deposit thickness, k is the deposit thermal conductivity, h is the clean tube convective ("film") heat transfer coefficient (determined at the start of the test), and U is the overall heat

transfer coefficient (determined for all subsequent times). The temperature differences across the thin-wall tubes were found to be small (generally less than 6 degrees K), consequently they were not included in the calculations. It is estimated that an error of five percent resulted from this approximation. Using a value of 0.21 Watt/m-K for the deposit thermal conductivity and 1 gm/cm^3 for the density of the deposit, the deposit rate was predicted based on the measured wall temperatures. A comparison of the measured and the calculated rates of carbon deposition for NAPC-7 fuel is also presented in Fig. 6 and there is relatively good agreement shown at wall temperatures below 700 K. However, at higher temperatures the calculated rates are greater than those measured, indicating that a lower value of deposit thermal conductivity and/or density would have resulted in better agreement.

The deposit formation and heat transfer data obtained for the 50 percent No. 2 heating oil/50 percent JP-5 fuel blend (NAPC-11), presented in Fig. 7, allow for a direct comparison between carbon loading per unit area and the deposit thermal resistance, both determined at the conclusion of the test. The straight line in the figure represents the predicted values, based on the assumption of a thermal conductivity of 0.21 Watt/m-K and a deposit density of 1 gm/cm^3. The results indicate that thermal resistance calculations can be correlated with deposit loading and that the constant values of thermal conductivity and density chosen for the calculations represent a good first approximation to the data. The data represented by solid symbols were obtained from a test whose duration was 1 hr, as compared to 5-hr durations used in the remaining NAPC-11 tests. It is obvious that a lower value of deposit thermal conductivity and/or density would better correlate the data for the 1-hr test. This result suggests that a formulation depicting the functional relationship of deposit thermal conductivity and density with surface temperature and thickness (time) is required to better predict deposit formation rates from heat transfer measurements. It is postulated that the thermal characteristics of thin deposit layers are better approximated by the thermal properties of the fuel and as deposits continue to build up and crystallize, the thermal characteristics begin to change and eventually approach those which might be expected from a graphitic type structure.

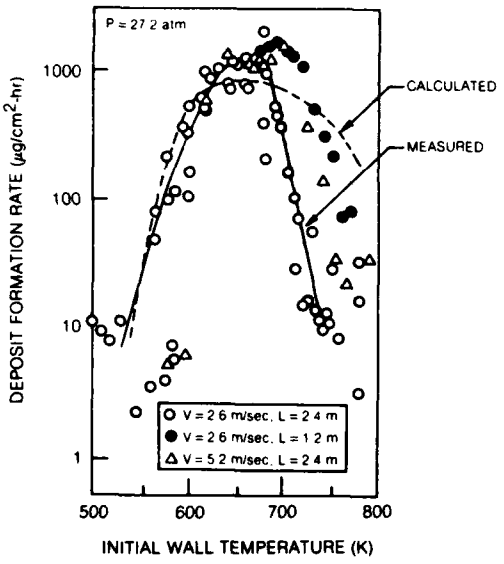


Figure 6. Rate of Carbon Deposition for NAPC-7 Fuel

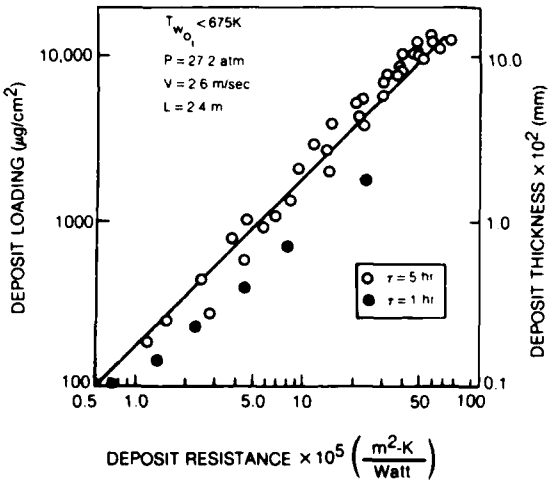


Figure 7. Deposit Loading vs Deposit Resistance for NAPC-11 Fuel

A comparison of the deposit formation rate correlations determined for each of the fuels tested is presented in Fig. 8. Although data scatter may have introduced a slight bias in the positions and slopes of the curves presented, it is believed that the curves accurately represent the trends and allow comparisons to be made. Because the thermal stability of the shale-derived fuel (NAPC-14) was unexpectedly high (due to stringent refining procedures) a 5-hr test duration resulted in relatively small amounts of deposit at wall temperatures below 600 K. Measurement of such small quantities of deposit (typically less than 150 μg) was beyond the accuracy of the analysis equipment and, therefore, these data are not included. The curves indicate that the deposit formation rates of all four fuels tested are strongly affected by the initial wall temperature. Corresponding JFTOT breakpoint temperatures for each of the three alternative fuels are also shown on the figure and indicate that the relative rankings of the fuels based on the results of the current study and on independent JFTOT measurements agree very well. A JFTOT breakpoint temperature is not reported for the JP-5 fuel because it failed the JFTOT pressure drop criterion. The agreement between the relative rankings suggests the possibility of correlating breakpoint temperatures with deposit formation rates and, therefore, deposit thickness and heat transfer effects.

Heat Transfer Correlations

The fuel-side convective heat transfer coefficient, h, is defined as the ratio between the heat flux and the temperature difference between the surface and the bulk fluid, as shown in the following relationship:

$$h = \frac{Q/A}{T_{w_i} - T_b} \tag{2}$$

The inner wall temperature, T_{w_i}, is determined from the outer wall temperature measurement by the following relationship:

$$T_{w_i} = T_{w_o} - (Q'/16k_w)[2D_o^2 \ln(D_o/D) - D_o^2 + D^2] \tag{3}$$

Assuming the convective heat transfer to generally behave in accordance with the Dittus-Boelter equation for turbulent flow in tubes, the relationship between the film coefficient, fluid properties, and flow conditions is described by:

$$Nu = 0.023(Re)^{.8}(Pr)^{.4} \tag{4}$$

The heat transfer data for all of the JP-5 tests are presented in dimensionless form in Fig. 9. All fuel properties used in the calculations were evaluated at the "film" temperature, defined as the arithmetic mean of the wall and bulk temperatures. The fuel thermophysical properties used in all data correlations were compiled from data obtained for JP-5 in the liquid state[12], from Maxwell's generalized data for hydrocarbons over a wide range of thermodynamic states[13], and correlated near-critical viscosity and thermal conductivity data for similar hydrocarbons[14,15]. As shown in Fig. 9, the test data are seen to be very consistent and, except in the inlet region, are well represented by an exponential relation similar to Eq. (4). As stated previously, the different behavior of the inlet region of the tube is apparently due to an interaction between the developing temperature profile and the laminar-turbulent transition.

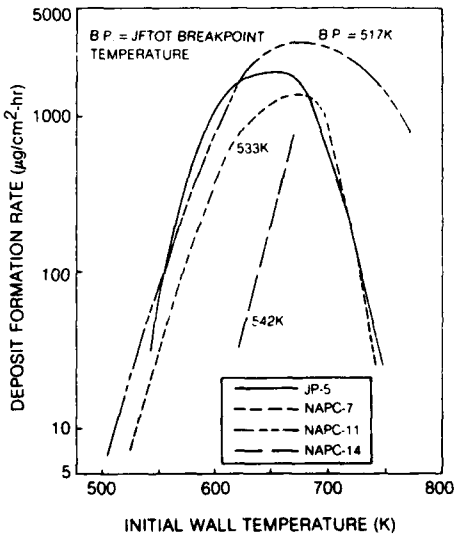


Figure 8. Comparison of Deposit Formation of Test Fuels

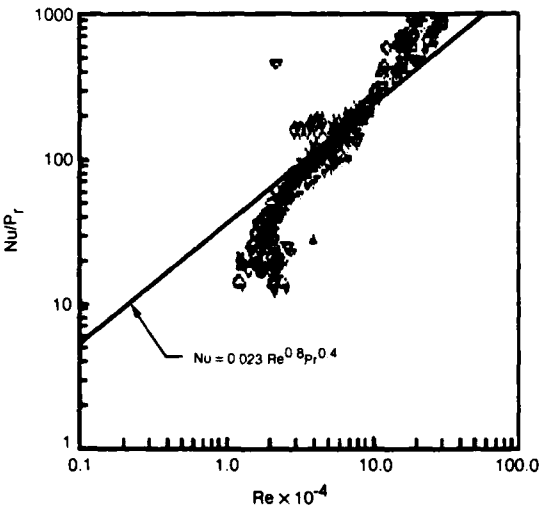


Figure 9. Convective Heat Transfer Data for JP-5

Because deposit accumulations cause a reduction in flow area and therefore an increase in fluid velocity, Eq. (4) should be modified to adjust the film coefficient at all times subsequent to the start of the test. The resulting modification is given by:

$$h' = h(D/D')^{1.8} \tag{5}$$

where D' = D-2t.

Similarly, because of the change in inner surface area, Eq. (1) is modified to:

$$1/UA = 1/h'A' + 2t/k_d(A+A') \qquad (6)$$

where A and A' are the inner surface areas of the clean tube and of the deposits, respectively, t is the deposit thickness, and k_d is the thermal conductivity of the deposited material. Combining Eqs. (5) and (6) yields:

$$k_d = \frac{2t\ D}{(D+D')} \quad \frac{1}{[1/U - (D'/D)\cdot^{.8}\ 1/h]} \qquad (7)$$

The deposit thickness can be obtained assuming a constant deposit density of 1 gm/cm^3 and a constant deposit formation rate. Therefore, Eq. (7) provides a relation for calculating the thermal conductivity of the deposits, based on the heat transfer and deposit rate data.

Results of the thermal conductivity calculations made using Eq. (7) indicated that the data do not fall naturally along a well-defined curve. Therefore, in an effort to develop a correlating parameter, the data have been compressed about a mean wall temperature (500 K) using an appropriate transformation function (see Fig. 10). As shown in the figure, the deposit thermal conductivity for JP-5 exhibited a minimum value approximating the conductivity of the fuel (i.e., .03 Watt/m-K) and increased with increased deposition to a value approaching that of amorphous carbon (i.e., 3 Watt/m-K). The observed relationship suggests a potential model for the deposition process, i.e., a very porous initial deposit layer, gradually being solidified by pyrolysis of fuel permeating the porous structure. As the deposit layer solidifies, the effective thermal conductivity increases from the value for the fuel toward a value for amorphous carbon.

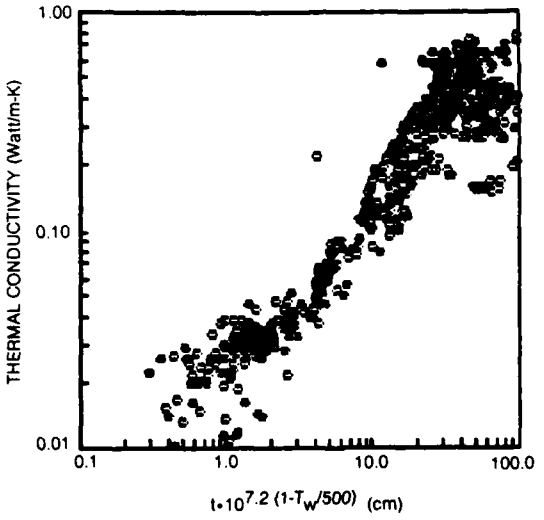


Figure 10. Deposit Thermal Conductivity Correlation for JP-5

Concluding Remarks

Thermal stability characteristics of four liquid hydrocarbon fuels have been evaluated using a heated-tube apparatus which permitted independent control of temperature, pressure and flow velocity. The results demonstrate the applicability of the apparatus for evaluating fuel thermal stability and deposit heat transfer characteristics over a broad range of test conditions. The deposit formation rate characteristics of all of the fuels tested were similar in that rates were very sensitive to the wall temperature, with peak formation rates occurring at initial surface temperatures of 644 K to 672 K. Comparisons of results indicated that, of the different fuels tested (i.e., JP-5, 50 percent hydrocracked gas oil/80 percent JP-5, 50 percent No. 2 heating oil/50 percent JP-5, and shale derived JP-5), the shale derived JP-5 fuel produced significantly less deposit than any of the other fuels at identical test conditions possibly due to the stringent refining process required to produce a low nitrogen content product. Heat transfer analyses indicate that the deposit thermal conductivity

increases with increasing deposit thickness, and ranges from values approximating the thermal conductivity of the fuel to values approaching that of amorphous carbon. Furthermore, over the range of conditions tested and to a first approximation, the effect of deposits on fuel system heat transfer can be predicted provided the variation of deposit thermal conductivity and density with temperature and deposit thickness (time) is known. Finally, fuel thermal stability rankings derived from the present experimental results agree very well with rankings based upon the standard JFTOT analysis.

Acknowledgement

This work was performed with the support of the Naval Air Propulsion Center, under Contract N00140-80-C-0097, Lot III, R. J. Delfosse, Project Manager. The valuable contributions of Mr. C. J. Nowack of the Naval Air Propulsion Center are also gratefully acknowledged.

References

1. Buttrill, S. E., Jr., F. R. Mayo, B. Lan, G. A. St. John, and D. Dulfin: Oxidation and Formation of Deposit Precursors in Hydrocarbon Fuels. SRI International Final Report No. PYU2115, October 1981.

2. Taylor, W. F.: Deposit Formation from Deoxygenated Hydrocarbons, Part I - General Features. Ind. Eng. Chem., Prod. Res. Devel., Vol. 13, No. 2, 1974.

3. Taylor, W. F.: Development of High Stability Fuel. Exxon Report GRU.13GAHF.75, January 1975.

4. Taylor, W. F.: Mechanisms of Deposit Formation in Wing Tanks. SAE Paper 680733, October 1968.

5. Wong, E. L. and D. A. Bittker: Effect of Hydrocarbon Fuel Type on Fuel Thermal Stability. NASA TM 82916, June 1982.

6. Antoine, A. C.: Effect of Some Nitrogen Compounds on Thermal Stability of Jet A. NASA TM 82908, June 1982.

7. Szetela, E. J. and J. A. TeVelde: Experimental Study of External Vaporization. ASME 82-GT-59, April 1982.

8. Vranos, A. and P. J. Marteney: Experimental Study of the Stability of Aircraft Fuels at Elevated Temperatures. NASA CR165165, December 1980.

9. Roback, R., E. J. Szetela, and L. J. Spadaccini: Deposit Formation in Hydrocarbon Fuels. Journal of Engineering for Power, Trans. ASME, Vol. 105, pp. 59-65, January 1983.

10. Smith, J. D.: Fuel for the Supersonic Transport. Ind. Eng. Chem., Process Des. and Devel., Vol. 8, No. 3. July 1969.

11. Szetela, E. J. and D. R. Sobel: Tube Entrance Heat Transfer with Deposit Formation. AIAA Paper 82-0918; AIAA/ASME 3rd Joint Thermophysics, Fluids, Plasma and Heat Transfer Conference, St. Louis, Missouri, June 1982.

12. Anon.: Coordinating Research Council Aviation Hand-book - Fuels and Fuel Systems. NAVAIR 06-5-504, Naval Air Systems Command, 1967.

13. Maxwell, J. B.: Data Book on Hydrocarbons. Oil Development Company, Van Nostrand Company, New York, 1950.

14. Stiel, L. I. and G. Thodos: The Prediction of the Transport Properties of Pure Gaseous and Liquid Substances. Prog. in International Research on Thermodynamic and Transport Properties, Am. Soc. of Mechanical Engineers, Academic Press, New York, 1962.

15. Kanitkar, D. and G. Thodos: Thermal Conductivities of Normal Liquids. Proc. of the Fourth Symp. on Thermophysical Properties, Am. Soc. of Mechanical Engineers, New York, April 1968.

DISCUSSION

G.Datschefski

I am very interested in the possible influences of chemical composition of the four very different fuels used in this research on deposit formation in the test apparatus. In Figure 8 you showed that there was quite a good correlation between deposit formation rate and JFTOT breakpoint temperature of the different fuels. Was any correlation found between deposit formation and concentrations of chemical components in the fuels, such as aromatics, olefins, hydrogen content? We have found that the bulk chemical corporation of a jet fuel has little effect on its deposit forming tendency, but that certain trace components can play a very significant role.

Author's Reply

In order to derive meaningful correlations regarding the influence of chemical composition on deposit formation it is necessary to selectively vary an individual fuel property over an adequate range while maintaining all other properties approximately constant. Because there were simultaneous variations of several fuel properties among the fuels tested in this study, it was not possible to isolate the effect of any one fuel property or chemical group. However, a comparison of the results indicates that sulphur content appears to correlate with deposit formation; that is, the fuels with the maximum and minimum sulphur concentrations also corresponded to the maximum and minimum fuel deposition rates.

S.Wittig

You indicated that the entrance region – almost 500 mm if I see it correctly – has been "neglected". However, in consulting Figure 3, the developing boundary layer may have some profound effects on the history of deposit formation rate and your results, as extremely strong temperature gradients are imposed. Did you analyze these phenomena in detail?

Author's Reply

An analysis of the entrance region effects and how deposit formation affects the heat transfer in the area has been made and is presented in a separate paper entitled "Tube Entrance Heat Transfer with Deposit Formation" authore by E.J.Szetela and D.R.Sobel (AIAA 82-0918). In addition, deposit quantities were measured in the entrance region and were found to be relatively high, considering that the corresponding fuel temperature was quite low (i.e. less than 375°F). However, as you have indicated, the temperature gradients are so severe that it was not possible to relate deposit quantity to a value of wall temperature in this region.

COMBUSTOR TECHNOLOGY FOR BROADENED-PROPERTIES FUELS

W. J. Dodds
General Electric Company
Aircraft Engine Business Group
1 Neuman Way
Cincinnati, Ohio 45215
U.S.A.

AD-P003 130

SUMMARY

In order to increase the availability and reduce the cost of future fuels for aircraft gas turbine engines, it may be necessary to broaden fuel specifications. Anticipated changes in fuel properties, and the effects of these changes on combustion system performance, operating characteristics, durability, and emissions are briefly reviewed, and results to date of a program being conducted to develop and demonstrate combustor technology required to utilize broadened-properties fuels in current and next-generation engines are described. Combustion system design considerations and tradeoffs for burning broadened-properties fuels are discussed, and test experience with several applicable combustor design modifications to the General Electric CF6-80A combustion system is reviewed. Modifications have been demonstrated to improve liner cooling and reduce smoke in the conventional annular combustor, thereby reducing effects of variations in fuel hydrogen content. Advanced staged and variable geometry combustor concepts for burning broadened-properties fuels have also been demonstrated.

1. INTRODUCTION

Long term use of fuels having a broader (wider) range of properties than current jet fuels is of interest as a means to reduce fuel cost and increase fuel availability in the future. Trends towards increased aromatics content (reduced hydrogen content) and increased freezing point have already been identified in commercial fuels used within the U.S., and use of syncrudes without extensive processing would result in further reductions in fuel hydrogen content. The U.S. Air Force has particular interest in changing from a volatile wide-cut fuel (JP-4) to a kerosine fuel (JP-8), motivated by NATO standardization and combat vulnerability considerations.

Several fuel effects programs have been or are being sponsored by the U.S. Air Force and the U.S. Navy to evaluate and quantify the effects of variations in fuel properties on combustion system and turbine performance, operating characteristics, durability, and emissions in current military aircraft gas turbine engines [1-8]. The U.S. National Aeronautics and Space Administration (NASA) and Federal Aviation Administration (FAA) have sponsored similar fuel effects programs for commercial engine combustors [9, 10]. NASA and the Navy have also sponsored programs specifically to evaluate and evolve combustor design technology to permit the use of broadened-properties fuels in future engines [11-14].

The objective of this paper is to describe the current technology status with regard to the design of combustion systems for burning broadened-properties fuels. This description will consist of a brief background discussion of the effects of burning broadened-properties fuels on combustor system operation, based on previous fuel effects studies, followed by a description of applicable combustor technology to reduce or offset these effects, based primarily on results of the NASA/General Electric Broad-Specification Fuels Combustion Technology Program [11].

2. DESIGN CONSIDERATIONS FOR BROADENED-PROPERTIES FUELS

Definition of appropriate combustion system features or design modifications to use broadened-properties fuels in a specific engine application requires a knowledge of (1) fuel properties, including the properties of the fuels currently in use in the engine as well as the expected range of future fuel properties; (2) the projected effect of the expected changes in fuel properties on combustor performance, operating characteristics, durability, and emissions; (3) the expected extent of engine operation, and any special operating requirements on broadened properties fuels; and (4) the operating and performance margins of the present, baseline combustion system when operated on current fuels.

Fuel Properties

Most currently used aviation turbine fuels can be classified as kerosines (F-34, F-35, Jet A, JP-5, JP-8, AVTUR) or more volatile wide-cut distillates (F-40, Jet B, JP-4, AVTAG). Future fuel specification limits, intended to cover the expected range of fuel properties required in future commercial aviation turbine fuels (except for fuels containing large proportions of coal liquids) were defined by the Jet Aircraft Hydrocarbon Fuel Technology Workshop conducted at the NASA-Lewis Research Center [15]. The resulting Experimental Referee Broad Specification (ERBS) Fuel specifications are similar to broadened-specifications for military jet fuels which have been proposed by the U.S. Air Force Aero Propulsion Laboratory [16], and to specifications for the AGARD Research Fuel (ARF) defined by the AGARD Propulsion and Energetics Panel Working Group 13 [17]. Key fuel specifications and typical test fuel properties for the JP-4, Jet A, and ERBS fuels being used in a current NASA/General Electric test program [11] are shown in Table I. Also shown for reference are AGARD Research Fuel specifications.

In terms of fuel composition, the ERBS fuel specification represents a sizable jump in aromatics content, and corresponding reduction in hydrogen content, relative to either of the current fuels. Thus, the use of an ERBS type fuel would represent a sizable change in fuel composition regardless of whether JP-4 or Jet A is currently in use. However, in terms of fuel volatility and fluidity, the difference between current JP-4 and Jet A is much larger than the difference between Jet A and ERBS. For example, the viscosity of the Jet A test fuel is nearly three times that of the JP-4, while the viscosity of ERBS is only 15 to 20 percent above that of Jet A. Thus, where JP-4 is currently in use (as in U.S. Air Force operations) volatility and viscosity effects of a transition to ERBS fuel would be substantial. On the

other hand, where Jet A is currently in use, effects of a transition to ERBS fuel should have less impact.

As with aromatics content, fuel thermal stability limits, as described by the Jet Fuel Thermal Oxidation Tester (JFTOT) breakpoint temperature, are the same for both of the current fuels, while the ERBS fuel can be less stable.

The similarity in ERBS and Jet A viscosity and volatility is largely a result of freezing point considerations. Any fuel having a freezing point low enough for general aviation use will almost inevitably have fluidity and volatility characteristics similar to current kerosines such as Jet A. However, a more severe change, particularly applicable to military applications, would be the short term use of non-aviation fuels in emergency conditions. In this case, consideration of operating limitations and short term effects of using heavier fuels is also applicable. Consideration of fuels having hydrogen content of about 12 percent is also applicable to the long term use of coal-derived fuels.

Fuel Effects

As indicated above, detailed fuel property effects have been determined for a wide range of different military and commercial engine combustion systems [1-9]. These studies indicate that, in general, fuel composition (hydrogen content) determines high power combustion characteristics; physical properties (volatility and fluidity) affect lightoff and low power characteristics; and thermal stability determines fuel injector life.

High power effects can be well characterized by fuel hydrogen content. As fuel hydrogen content is reduced, soot formation is increased, and peak flame temperature is also increased because the lower water content of the combustion products from the lower hydrogen content fuels reduces their specific heat. Increased soot formation leads to higher flame emissivity within the combustor and increased smoke emissions at the combustor exit. Higher flame emissivity leads to increased flame radiation, increased liner temperatures, and ultimately to reduced liner life. Increased soot formation tendency can also lead to carbon deposition on combustor surfaces. Increased flame temperature tends to further increase flame radiation, and also increases NO_x formation rates.

Table II indicates the extent to which fuel composition affected combustor emissions and performance in several recent fuel effects studies. In each case, the change resulting from a reduction from 14 to 13 percent fuel hydrogen content is shown. This is approximately equivalent to a change from Jet A to ERBS fuel. The strongest effect of fuel hydrogen content, in terms of percentage change, was on smoke emissions. Smoke levels were increased by up to 70 percent. An equally significant effect is the predicted life reduction brought about by increased liner temperatures. In the engines shown, predicted life was reduced by between 11 percent and 33 percent as a result of liner temperature rise increases of only 2 percent to 10 percent. NO_x emissions also increased consistently, though slightly, with reduced fuel hydrogen content. The NO_x increase averaged less than 5 percent, which is insignificant in terms of the current emissions regulations. Other potential effects of a reduction in fuel hydrogen content, including increased carbon deposition, increased turbine metal temperatures, and turbine erosion due to higher levels of carbon particulates were not found to be significant for systems tested.

As fuel fluidity is reduced (increased viscosity, surface tension, and density) the size of droplets produced by either a pressure atomizing or airblast type of fuel injector is increased. These larger droplets evaporate at a slower rate, and have different trajectories than smaller droplets, thereby changing the fuel distribution within the combustor. Reduced volatility, which is closely related to fluidity, also reduces the evaporation rate. Effects of variations in fluidity (expressed as relative drop size) on minimum ambient temperature for ground start are shown for several different combustors in Figure 1 (from Reference 5). Combustors having pressure atomizing nozzles which produce a fine spray at lightoff conditions were virtually unaffected, while the airblast injected F101 was strongly affected. Low power CO and HC emissions levels were also increased with decreased fluidity. CO levels were 10 percent to 35 percent higher with No. 2 Diesel than with JP-4. However, this translates to a reduction of only 0.5 percent in combustion efficiency at idle, and a much smaller reduction at higher power levels.

A reduction in fuel thermal stability increases the rate at which fuel nozzle control valves and fuel nozzle tips are affected by fuel fouling. As shown in Figure 2, fuel injector life is a strong function of the difference between the fuel temperature and JFTOT breakpoint temperature.

In summary, previous studies indicate that the truly significant problems arising from changes in fuel properties are limited to increased smoke emissions, reduced liner life, decreased ignition capability, and reduced fuel injector life. However, the extent to which these effects are actually significant depends on the anticipated change in fuel properties (as discussed above), and the performance margins of the specific combustion system being considered. For example, the F101 engine currently has a smoke level of less than 3 on JP-4. Even with a change to 12 percent fuel hydrogen content, resulting in a 45 percent increase in smoke number, smoke emissions would still be well below the visible level of 20. In this case, increased smoke might not be serious.

A final consideration affecting selection of design technology to be implemented is the design status of the engine under consideration. For an existing engine design, only the use of retrofittable modifications would be applicable, while more radical design changes, including advanced combustor concepts, would be applicable to a new engine in the design phase.

3. COMBUSTOR DESIGN TECHNOLOGY

Once the specific fuel property changes, expected effects, and current combustion system performance margins have been defined, the use of selected combustion system modifications can be evaluated. In the following discussion, combustion system modifications are considered as they relate to changes in fuel composition; fluidity and volatility; and thermal stability.

The following discussion deals specifically with the ongoing NASA/General Electric Broad-Specification

Fuels Combustor Technology Program [11]. This program involves the design and sector combustor component test evaluation of several different combustor configurations for operation on broadened-properties fuels. Combustor configurations are sized for the CF6-80A engine, which is a large (50,000 lb. Thrust Class), high pressure ratio turbofan. Combustor concepts evaluated in this program cover the range from retrofittable modifications to the standard CF6-80A combustor (Figure 3) to the use of the advanced double annular staged combustor and the ultra-short variable geometry combustor shown in Figure 4. Several different modifications to each of the three combustor concepts are being evaluated.

The double annular combustor is a parallel staged design. At lightoff and low power conditions, all of the fuel is burned in the pilot stage, which is designed to provide low-velocity, near-stoichiometric primary combustion for good ignition and low power performance. At high power, both stages are fueled. Most of the fuel is supplied to the main stage, which is designed to provide high-velocity, lean primary combustion for low smoke and NO_x formation.

The single stage, variable geometry combustor uses a variable area swirler to control primary combustion zone conditions. At low power, the variable swirler is closed to provide low velocities and near-stoichiometric fuel-air ratios as in the double annular combustor pilot stage. At high power, the swirler is opened to provide high-velocity, lean primary combustion as in the double annular combustor main stage.

Experimental evaluations of the combustors shown in Figures 3 and 4 are being conducted in a high pressure (4 MPa) 60° sector combustor test facility, which is capable of operation at the maximum combustor inlet pressures and temperatures encountered during actual engine operations. Instrumentation is provided to measure liner temperatures, flame radiation, exit temperature and fuel-air ratio profiles, smoke, and gaseous emissions over the full range of steady-state operating conditions. Additionally, lean blowout at idle operating conditions and altitude relight performance are being measured. A total of six test fuels are being used to span the wide range of chemical and physical properties indicated in Table III. Test fuels include JP-4, Jet A (which also meets JP-5 and Jet A-1 specifications), and No. 2 Diesel Fuel, which provide a range of viscosity and volatility. Three other specially blended Experimental Referee Broad-Specification (ERBS) fuels having physical properties similar to Jet A, but having different hydrogen contents, provide a range of chemical properties.

The NASA/General Electric program is aimed specifically at commercial engine applications. In these applications, the overriding concerns are combustion system life reduction and increased smoke emission, both of which are due to reduced hydrogen content. Since the current fuel for commercial applications is Jet A, and emergency use of heavier non-aviation fuels is unlikely to be required (as might be the case in a military application), fuel fluidity effects are of secondary importance in this specific application.

Fuel Composition

As described above, the most serious long term effect of a reduction in fuel hydrogen content is reduced liner life. One design approach to alleviate this problem is to change the liner material or mechanical design. For example, a change from a nickel based alloy to a cobalt based alloy can nearly triple predicted liner life. Mechanical design features, such as the use of a short film slot overhang, which reduces overhang closure and buckling, can also be used. Segmented liner designs providing extended life are also available, and transpiration cooled liners show promise. However, such mechanical changes all require combustor replacement, rather than retrofittable modification.

Aerothermal design modifications to reduce or offset the effects of changes in fuel hydrogen content are suggested by consideration of the physical phenomena which control combustor performance. For example, liner metal temperature under steady-state conditions is determined by energy transfer from the hot combustion gases to the liner by internal convection and radiation, and by energy transfer from the liner to the outer passage airflow and engine structure by external convection and radiation, respectively. Conduction within the liner also affects the liner temperature distribution, but conduction effects are small compared to convection and radiation, and can be neglected for consideration of fuel effects.

Internal radiation from the hot gases depends on the temperatures and emissivities of the hot combustion gases and of the inner surface of the combustor liner. The liner temperature increases observed with reduced fuel hydrogen content are almost totally attributed to increased internal radiation, primarily due to increased flame emissivity. Internal radiation heat transfer can be reduced by reducing the emissivity or temperature of the combustion gases, by increasing the liner surface temperature or by reducing the liner absorptivity.

Gas emissivity is due primarily to nonluminous CO_2 and H_2O, and luminous soot. Modern low smoke combustion systems are designed to provide an overall primary zone fuel-air ratio well below the level required for soot formation. Therefore, any soot formed is due to locally rich regions. Soot formation can be eliminated by providing a leaner or more uniform primary zone mixture. Improved uniformity and leaner mixtures also reduce peak gas temperature, thereby reducing flame radiation.

Improved primary zone uniformity can be obtained either by changing details of fuel injection for improved atomization and more uniform fuel distribution, or by modifying the primary zone airflow patterns for improved mixing. Figure 5 demonstrates the effect that a subtle change in fuel atomization can have. In this case, the only change was to increase the proportion of flow to the primary (pressure atomizing) orifice of the dual orifice fuel nozzle used in the CF6-80A combustor. This had the effect of improving atomization slightly, and increasing the fuel concentration towards the center of the spray cone. As indicated in Figure 5, liner temperatures and smoke were both reduced sufficiently to offset the effects of changing from Jet A to ERBS fuel.

A change in the air swirlers surrounding the fuel nozzle affects both fuel distribution and fuel-air mixing. The effect of a swirler modification is shown in Table IV. In this case, the standard swirler was replaced with a unit which had the same airflow rate, but produced a wider fuel spray and stronger recirculation. Smoke levels were substantially reduced, indicating reduced soot formation, but the wider spray angle increased the amount of fuel near the combustor walls, resulting in a significant increase in

liner temperature. This illustrates an important tradeoff between internal radiation, which was reduced, and conduction which was increased by the higher temperatures near the wall.

Changes in the size and location of primary dilution holes can be used to provide a lean and more uniform primary zone mixture. The marked improvement in smoke level and the slight reduction in average liner temperature shown in Table V were obtained by a relatively minor dilution modification in which about 5 percent of the combustor airflow was moved forward on the combustor liners by 3.5 cm.

One additional way to reduce gas emissivity is to reduce the mean radiation beam length across the gas stream, which is proportional to the annulus height. However, reducing the annulus height increases the flow velocity, which tends to increase convection and adversely affects ignition and low power performance.

The ultimate in uniform, lean mixtures with a short mean beam length (high velocity) is obtained in the advanced, lean burning variable geometry combustor and double annular combustor main stage. In tests conducted in the NASA/General Electric program, liner temperatures in the double annular combustor were virtually unaffected by fuel hydrogen content, as shown in Figure 6.

Another approach to reduce internal radiation heat transfer is to treat the inner surface of the liner to reduce emissivity and increase the temperature on the inner (hot side) surface of the liner wall. Both of these effects can be obtained by using ceramic thermal barrier coatings (TBC). TBC is more reflective than the base metal, so that less of the incident radiation is absorbed. A slight additional reduction in radiative heat transfer is also obtained because the hot side surface temperature of the insulating TBC is higher than that of an uncoated wall (although metal temperatures beneath the TBC are reduced). In the conventional annular combustor, TBC reduced the average liner metal temperature by 26 K, which more than offset a 13 K increase in temperature in going from Jet A to ERBS fuel in the uncoated combustor. Sensitivity to fuel hydrogen content was also reduced with the coating, presumably because of increased reflectivity. With TBC, the average liner temperature with ERBS fuel was only 6 K above that obtained with Jet A, compared to a 13 K increase in the uncoated combustor.

Heat transfer to the liners due to internal convection depends on the effective temperature adjacent to the combustor wall (the film temperature), the wall surface temperature, and the heat transfer coefficient at the wall.

As described in the previous discussion of internal radiation, the film temperature is influenced by the gas temperature profile across the combustor as well as the bulk, or average temperature of the combustion gases. The use of lean mixtures will reduce both radiation and conduction heat transfer. However, a center peaked profile with peak temperatures near the combustor pitch line is favorable for reducing convection, while a uniform temperature reduces smoke and radiation. Film temperature can also be reduced by increasing film cooling flows; however, this extra cooling airflow must be taken from either swirler or dilution airflow, and the net result will generally be an increase in peak temperature near the combustor pitch line.

Internal convection heat transfer can be reduced by increasing the hot side wall surface temperature. This can be implemented by using thermal barrier coatings, as discussed above. The heat transfer coefficient could also be reduced by reducing the velocity of the hot gases; however, reduced velocity would require either a primary zone airflow reduction (richer mixture) or increased annulus height (increased mean beam length and liner area) which would tend to increase flame radiation.

External heat transfer is dominated by convective heat transfer from the liner to the airflow in the passages surrounding the combustor. Radiative heat transfer from the liner to the engine structure is generally a small proportion of total heat flux, and there is little that can be done through design changes to increase external radiation. On the other hand, modifications to increase external convection have high potential for liner temperature reduction.

External convection heat transfer increases with increasing external surface temperature and heat transfer coefficient or decreasing cooling air temperature. Since the desired result is to reduce metal temperature, increasing external surface temperature is unacceptable. The cooling air temperature is identical to the combustor inlet temperature, which cannot be controlled. Thus, increasing the heat transfer coefficient is the only external convection variable which can be influenced by combustor design.

Two methods for increasing the external convection heat transfer coefficient are by increasing the airflow velocity adjacent to the liner, or by using impingement cooling. Both of these methods have been successfully demonstrated as means for reducing local liner temperatures in production combustors. The CF6-50 combustor uses liner-mounted baffles to increase local airflow velocities, while the J79-17C (smokeless) combustor uses combined cold-side impingement and hot side film cooling on the combustor dome. In the combustor shown in Figure 7, a liner temperature reduction of about 40 K was predicted for the panels using impingement cooling, assuming no change in internal flow patterns. However, no reduction was measured in component tests. This discrepancy has not yet been resolved, but it could be attributed either to changes in internal flow patterns due to reduced primary dilution jet strength (part of the normal dilution pressure drop was used for impingement cooling) or to better than predicted film cooling effectiveness, which could have dominated liner cooling. A potential drawback with design schemes to improve external convection is increased pressure drop in the cooling airflow, which affects dilution jet penetration and can reduce the pressure drop available for turbine cooling.

Increased smoke due to reduced fuel hydrogen content can be offset using the same types of modifications that are used to reduce flame emissivity by minimizing soot formation. Modifications which result in a leaner or more uniformly mixed primary zone will generally reduce smoke formation as demonstrated in Table IV and Figure 4. Conversely, fuel hydrogen effects on liner temperature were reduced in low smoke configurations of the conventional annular combustor, as shown in Figure 8.

Fluidity and Volatility

Reduced fuel fluidity and volatility affect ignition and low power operation by increasing the time required for fuel evaporation and changing fuel distribution due to droplet trajectory effects. These effects can be offset by implementing design changes to reduce droplet evaporation times, increase available time for evaporation, or otherwise improve combustion conditions by controlling combustor primary zone stoichiometry, effective volume, and mixing.

Fuel fluidity effects can be correlated using a calculated droplet size, which increases with fuel viscosity, surface tension, and density. Correlations to estimate drop sizes are available for pressure atomizing [18] and airblast [19, 20] injectors. Fluidity and volatility effects can be combined using a droplet lifetime (τ_{eb}) defined as

$$\tau_{eb} = \frac{SMD^2}{\beta}$$

where SMD is initial drop size. The evaporation coefficient, β, decreases (thereby increasing τ_{eb}) with increasing fuel boiling point, energy required for fuel evaporation, and fuel density. The evaporation coefficient also increases with increased local (primary zone) air temperature and relative velocity between the fuel droplets and the airflow. Details of droplet lifetime calculations are given in Reference 21.

Changes in droplet lifetime due to fuel effects can be offset by modifying the fuel injector design. Appropriate changes normally involve a reduction in nozzle scale, to increase fuel pressure drop for improved atomization and increased droplet velocities in pressure atomizing injectors, and to provide a thinner film or fuel jet in airblast injectors. However, drop size is not the only important fuel injector variable. Subtle changes in injector design can also have a strong (and not necessarily predictable) influence on low power operation, presumably by changing the initial fuel droplet trajectories. An improved understanding of these detailed spray effects is needed.

Recent tests have also been conducted in which droplet lifetime was varied by changing fuel type and temperature. Effects of variation in fuel type and temperature on minimum pressure for ignition at altitude relight conditions and on combustion efficiency at idle are shown in Figure 9. These same data are expressed in terms of droplet lifetime in Figure 10. In the case shown, the 50 percent recovery distillation temperature was used for fuel boiling point and a constant ambient temperature of 1000 K was assumed for droplet lifetime calculations.

Droplet evaporation times can also be reduced by maximizing the primary zone temperature. During tests of modifications of the selected test combustor, it has been observed that variations in fuel properties become less important as fuel flow is increased to the point where the primary zone is stoichiometric. This reflects more rapid vaporization due to both improved atomization as fuel flow is increased and to increased ambient temperatures.

In general, any modification which tends to improve ignition and low power performance will tend to reduce droplet (or fuel fluidity/volatility) effects. Swirl cup or dilution modifications to provide improved mixing, near stoichiometric fuel-air ratios, strengthened recirculation, or increased residence time within the combustor primary zone will all tend to improve ignition and low power performance.

In terms of fuel injector type, recent studies conducted at General Electric have generally indicated that sensitivity to fuel evaporation effects is lower with pressure atomizing fuel injectors than with airblast injectors [5, 14]. However, as shown in Figure 11, relative drop sizes (relative to JP-4) were virtually the same for the F101 airblast injector as for the J79-17A pressure atomizing injector using fuels that varied from JP-4 to No. 2 Diesel. Drop size data reported in the literature indicate that very fine atomization can be obtained with airblast injectors, even at altitude ignition conditions. Therefore, it is thought that either type of injector can be used successfully.

Fuel Thermal Stability

Fuel nozzle fouling normally occurs either at the fuel nozzle tip or at the flow metering valve. The flow metering valve, mounted at the injector inlet to provide the desired fuel flow/pressure drop characteristic, is normally the critical element with respect to fouling. The operating time before fuel nozzle fouling, as measured in accelerated fouling tests has been shown to correlate with a temperature parameter including the JFTOT fuel breakpoint temperature and the fuel temperature (as shown in Figure 2.)

Several different design techniques can be used to offset poorer fuel thermal stability [22]. An obvious method is to reduce the fuel temperature by the same amount as the fuel breakpoint temperature reduction, thereby maintaining the same temperature difference. In the case of ERBS fuel (Table I), the required fuel temperature reduction would be 22 K. Fuel is currently used as a heat sink to cool engine lube oil. Fuel temperature could be reduced by either using a fuel-air heat exchanger upstream of the fuel nozzle or using air to cool the lube oil. In either case, weight, complexity, and specific fuel consumption penalties would result. These methods would not be applicable for supersonic applications due to high air temperatures.

Another approach is to modify the fuel valve. Fuel metering valves are mounted on the injector in several current engines, where they are directly exposed or in close proximity to the hot combustor inlet airflow. Fouling tendency could be reduced by mounting the valves on the cooler fuel manifold, at the cost of increased fuel system fill time. Current fuel injectors use a sliding piston type valve. Increased fouling tolerance could be obtained by using a larger piston valve having a higher ratio of valve area (valve opening force due to fuel pressure) to wetted perimeter (resistance force due to fouling) at the cost of increased weight. The use of fluidic valves would also reduce fouling tendency.

Fuel nozzle tip fouling tendency could be reduced by using low pressure, airblast type fuel injectors having large fuel passages. Improved insulation of the fuel nozzle tubes where they penetrate the combustor inlet flowpath would also be beneficial to prevent fuel heating upstream of the injector tip.

Increased fuel fouling tendency also discourages the use of fuel staging, where some portion of the fuel nozzles are shut off at low fuel flows corresponding to lightoff and low power. This strategy is used to promote burning by providing a richer local mixture in the vicinity of the fueled injectors. When fuel flow is interrupted, there is no cooling of the injector. Under certain conditions, such as a rapid descent, the engine can be hot when the fuel flow is low enough to shut off some of the nozzles. Rapid heating and fouling of the nozzles can then occur.

4. CONCLUDING REMARKS

In summary, the use of broadened-properties fuels imposes several conflicting requirements on the combustor designer. In terms of combustor primary zone stoichiometry, reduced fluidity indicates the use of richer conditions for ignition, while reduced hydrogen content requires leaner conditions for reduced soot formation. This conflict could be resolved by using fuel staging, but fuel staging is discouraged by reduced fuel thermal stability. In terms of fuel injection, use of pressure atomizing nozzles and fuel heating will offset ignition and low power performance decrements due to reduced fluidity, while the use of fuel cooling and airblast injectors are preferred to prevent fuel nozzle fouling.

Common requirements to offset both fluidity and fuel hydrogen effects are improved fuel atomization, distribution, and mixing.

Much of the technology which has been developed in advanced high-temperature rise combustor development programs is directly applicable to design of fuel flexible combustors. The use of short, compact combustor flowpaths having low liner surface areas and advanced liner construction and materials, including thermal barrier coatings, are all beneficial. Also, many of the same problems encountered due to the high fuel-air turndown ratio (maximum fuel-air ratio divided by the minimum fuel-air ratio) in high temperature rise combustors are similar to the increased difficulty of operation both at high and low power with broadened-properties fuels.

For the specific case evaluated in the current NASA/General Electric program, involving a single annular combustor burning ERBS fuel, it has been concluded that satisfactory performance and operating characteristics could be obtained, with no life reduction relative to the baseline combustor operated on Jet A, by implementing retrofittable modifications to the baseline combustor design. Specific modifications to offset reduced fuel hydrogen content included installation of thermal barrier coatings on the combustor dome and liners and relocation of primary dilution holes to the first panel of the combustor liners. An additional, optional, modification to further improve performance would be the use of a revised fuel nozzle flow schedule in which a larger proportion of the fuel would be supplied to the primary orifice of the fuel nozzle at high power conditions. No modifications were recommended specifically for low power operation, since the ERBS fuel fluidity and volatility were only slightly poorer than the baseline Jet A. Fuel staging at lightoff and idle, as used in the baseline combustor, was retained. Fuel nozzle fouling would not be expected to be a problem in this application with a fuel meeting the ERBS specification.

Work is continuing to define more extensive combustor design modifications for improved fuel flexibility and applicable to more severe growth engine cycle operating conditions. Specific goals are to eliminate the requirement for fuel staging and to incorporate an improved airblast fuel injector/swirl cup assembly for fuels having poor thermal stability. The design strategy is to reduce primary zone airflow to provide lower velocities and richer mixtures for good ignition and low power performance. Smoke-free operation at high power levels will depend on improved fuel injector/swirl cup atomization and mixing performance. Evaluation of a quasi-transpiration cooled liner is also planned.

A key need, both for fuel flexibility and for high temperature rise combustors, is to develop improved fuel injector/swirl cup models and design procedures, and to obtain a more thorough understanding of the interaction between swirl cup and primary dilution flows. Current combustor development practice involves extensive development testing to obtain a satisfactory, but not necessarily optimum, definition of fuel injector/swirl cup system and liner dilution design features. With improved analytical design procedures, these combustor design features could be more nearly optimized, thereby providing increased performance margins to accommodate poorer fuels and more severe operating conditions without radical changes to current designs.

Ultimately, in order to satisfy increasing requirements for fuel flexibility and higher temperature rise, it will probably be necessary to use an advanced system, such as the double annular or variable geometry combustor concept. The variable geometry combustor has been selected as the preferred concept for continued development in the NASA/General Electric program. The double annular combustor was dropped from the current study, primarily because of potential fuel nozzle fouling due to the fuel staging requirement. However, the double annular concept was successful in that it was virtually unaffected by fuel hydrogen content at high power conditions. Variable geometry development is also being concentrated on development of an improved variable airflow fuel injector/swirl cup system configuration to provide good performance. Here again, availability of improved fuel injector/swirl cup system design procedures represents an important need.

5. REFERENCES

1. Gleason, C. C., Oller, T. L., Shayeson, M. W., and Bahr, D. W., "Evaluation of Fuel Character Effects on J79 Engine Combustion System," AFAPL-TR-79-2015, June 1979.

2. Gleason, C. C., Oller, T. L., Shayeson, M. W., and Bahr, D. W., "Evaluation of Fuel Character Effects on the F101 Engine Combustion System," AFAPL-TR-79-2018, June 1979.

3. Gleason, C. C., Oller, T. L., Shayeson, M. W., and Kenworthy, M. J., "Evaluation of Fuel Character Effects on J79 Smokeless Combustor," AFWAL-TR-80-2092, November 1980.

4. Vogel, R. E., Troth, D. L., and Verdouw, A. J., "Fuel Character Effects on Current, High Pressure Ratio, Can-Type Turbine Combustion Systems," AFAPL-TR-79-2072, April 1980.

5. Oller, T. L., Gleason, C. C., Kenworthy, M. J., Cohen, J. D., and Bahr, D. W., "Fuel Mainburner/ Turbine Effects," AFWAL-TR-81-2100, January 1982.

6. Russell, P. L., and Herrin, J. R., et al., "Fuel Mainburner/Turbine Effects," AFWAL-TR-81-2081, February 1982.

7. Vogel, R. F., Reider, S. B., and Karpovich, P. A., "Effect of Fuel Composition on Navy Aircraft Engine Hot Section Components," AIAA-83-1147, June 1983.

8. Anon., "Effects of Fuel Composition on Navy Aircraft Engine Hot Section Components," U.S. Navy Contract No. N00140-79-C-0483, Program in Progress.

9. Gleason, C. C., and Bahr, D. W., "Experimental Clean Combustor Program - Alternate Fuels Addendum Phase II Final Report," NASA CR-134972, January 1976.

10. Lyon, T. F., Dodds, W. J., and Bahr, D. W., "Determination of Pollutant Emissions Characteristics of General Electric CF6-6 and CF6-50 Model Engines," Report No. FAA-EE-80-27, March 1980.

11. Dodds, W. J., Ekstedt, E. E., Bahr, D. W.; and Fear, J. S., "NASA/General Electric Broad-Specification Fuels Combustion Technology Program - Phase I Results and Status," AIAA-82-1089, June 1982.

12. Lohmann, R. P., and Fear, J. S., "NASA Broad-Specification Fuels Combustion Technology Program - Pratt and Whitney Aircraft Phase I Results and Status," AIAA-82-1088, June 1982.

13. Kasper, J. M., Ekstedt, E. E., Dodds, W. J., and Shayeson, M. W., "Experimental Evaluation of Combustor Concepts for Burning Broad-Property Fuels," NASA CR-159855, September 1980.

14. Kenworthy, M. J., "Aircraft Turbine Engine Propulsion System Advanced Combustor Component Technology Development and Alternate Fuels Investigation Program - Phase I Interim Report," U.S. Navy Contractor Report, in Publication.

15. Longwell, J. P., ed., "Jet Aircraft Hydrocarbon Fuels Technology," NASA CP-2033, January 1978.

16. Churchill, A. V., Delaney, C. L., and Lander, H. R., "Future Aviation Turbine Fuels," AIAA-78-268, January 1978.

17. Whyte, R. B., ed., "Propulsion and Energetics Panel Working Group 13 on Alternative Jet Engine Fuels - Main Report," AGARD-AR-181, Vol. II, July 1982.

18. Lefebvre, A. H., Gas Turbine Combustion, McGraw Hill, New York, p. 400, 1983.

19. El-Shanawany, M. S., and Lefebvre, A. H., "Airblast Atomization: The Effect of Linear Scale on Mean Droplet Size," ASME Paper No. 80-GT-74, March 1980.

20. Jasuja, A. K., "Atomization of Crude and Residual Fuel Oils," ASME Paper No. 78-GT-83, April 1978.

21. Lefebvre, A. H., Mellor, A. M., and Peters, J. E., "Ignition/Stabilization/Atomization: Alternative Fuels in Gas Turbine Combustors," Progress in Astronautics and Aeronautics, Vol. 62, pp. 137-159, 1978.

22. Coffinberry, G. A., "Advanced Fuel System Concepts for Commercial Aircraft and Engines - Final Report," NASA Contractor Report, in Publication.

Table I. Test Fuel Specifications and Properties.

Properties	Fuel Type						
	Wide-Cut (JP-4)		Kerosine (Jet A)		ERBS		ARF
	Properties	Specifications	Properties	Specifications	Properties	Specifications	Specifications
Composition							
- Aromatics, Vol.	12	25 (Max)	18	25 (Max)	31	--	--
- Hydrogen Content, Wt.	14.4	--	14.0	--	12.9	12.8 + 0.2	13.2 + 0.2
Volatility							
- Distillation, K							
10%	366	--	467	478 (Max)	466	478 (Max)	478 (Max)
20%	381	418 (Max)	475	--	472	--	--
FBP	534	543 (Max)	539	573 (Max)	596	589 (Max)	--
Fluidity							
- Freezing Point, K	215	215 (Max)	231	233 (Max)	245	244 (Max)	243 (Max)
- Viscosity @ 250 K, cS	2.2	--	6.4	9 (Max)	7.5	12 (Max)	12 (Max)
Thermal Stability							
- JFTOT Breakpoint Temperature, K	--	533[a] (Min)	--	533[a] (Min)	--	511 (Min)	503 (Min)

[a] Commercial Specifications Allow Retest At 518 K

Table II. Fuel Hydrogen Content Effects.

- **Evaluation at Takeoff Operating Conditions**
- **Effect of Reduction from 14% to 13% Fuel Hydrogen Content**

Combustor	Percent Change In Value			
	Smoke Emission	Max Liner Temperature Rise*	Predicted Liner Life	NO_x Emission
CF6-80A (Baseline)	--	+10	-33	+5
J79-17A	+16	+5	-33	+3
J79-17C	+36	+2	-11	+3
J85-21	+70	+2	--	+1
TF39	+16	+9	-22	-4
F101	+17	+7	-28	+5

* Liner metal temperature minus combustor inlet air temperature

Table III. Range of Test Fuel Properties.

Properties	Minimum Value	Maximum Value
Composition		
- Aromatics, Vol. %	12.3 (JP-4)	59.7 (ERBS 11.8)
- Hydrogen Content, Wt. %	11.70 (ERBS 11.8)	14.35 (JP-4)
Volatility		
- Distillation, K		
10%	367 (JP-4)	494 (DF2)
50%	431 (JP-4)	573 (DF2)
90%	503 (JP-4)	593 (DF2)
Fluidity		
- Viscosity (310 K), cS	0.84 (JP-4)	2.73 (DF2)
- Freezing Point, K	216 (JP-4)	261 (DF2)

Table IV. Swirl Cup Configuration Effects.

	Baseline Swirl Cup	Airblast/Radial Swirl Cup
Swirl Strength	Low	High
Spray Angle	Narrow	Wide
Takeoff Smoke Number	13.6	6.7
Takeoff Liner Temperature, K		
- Maximum	1133	1224
- Average	1005	1092
Takeoff NO_x Emission, g/kg	31.7	30.4
Idle Combustion Efficiency, %	99.5	97.6
Idle Blowout Fuel-Air Ratio, g/kg	5.7	4.2

Table V. Primary Dilution Location Effects.

	Baseline	Lean Primary Zone
Primary Dilution Flow, %		
- Panel 1	0	4.9
- Panel 2	9.9	5.4
Takeoff Smoke	41.2	13.6
Takeoff Liner Temperature, K		
- Maximum	1119	1133
- Average	1017	1005
Takeoff NO_x Emission, g/kg	26.7	31.7
Idle Combustion Efficiency, %	98.6	99.5
Idle Blowout Fuel-Air Ratio, g/kg	4.2	5.7

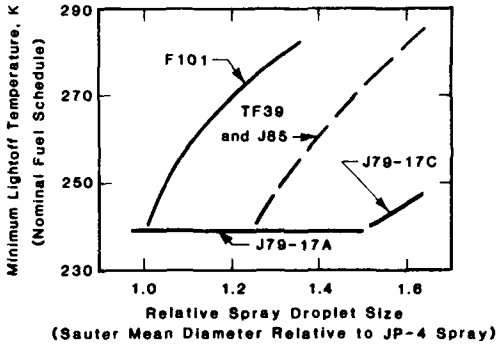


Figure 1. Fuel Effects on Minimum Ambient Temperature for Ground Start.

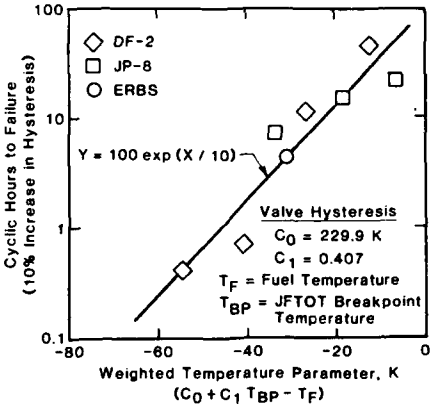


Figure 2. Effect of Fuel Thermal Stability on Fuel Nozzle Valve Life.

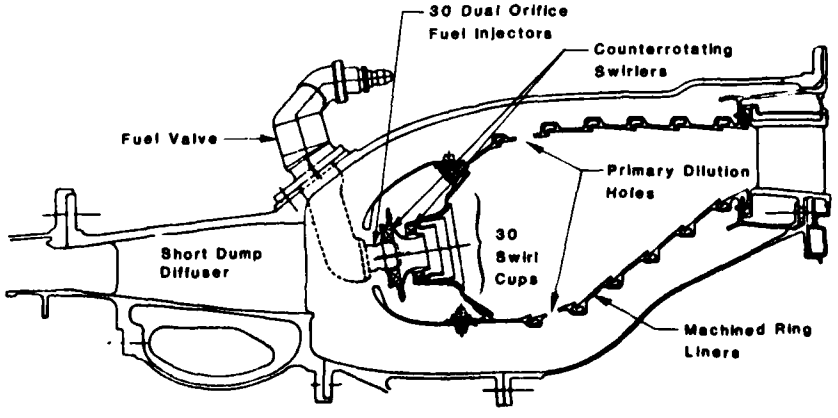
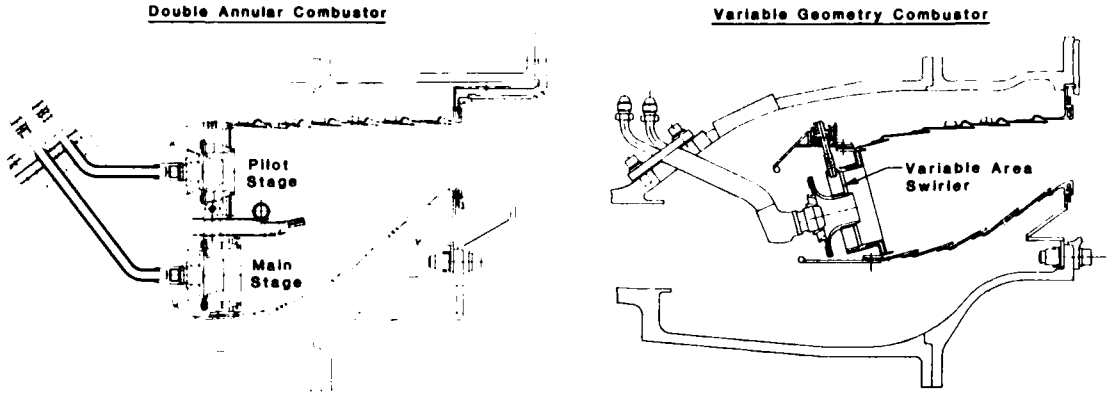


Figure 3. CF6-50A Annular Combustion System.



Short Double Annular Combustor Design

Low Velocity Pilot Stage
- Near Stoichiometric Primary Zone Combustion at Idle

High Velocity Main Stage
- Lean Primary Zone Combustion at High Power

Very Short Single Annular Design

Dome Swirler Closed For Low Power Operation
- Low Velocity
- Rich Primary Zone Combustion
- Increased Pressure Drop

Dome Swirler Open for High Power Operation
- High Velocity
- Lean Primary Zone Combustion
- Short Residence Time

Figure 4. Advanced Combustor Concepts.

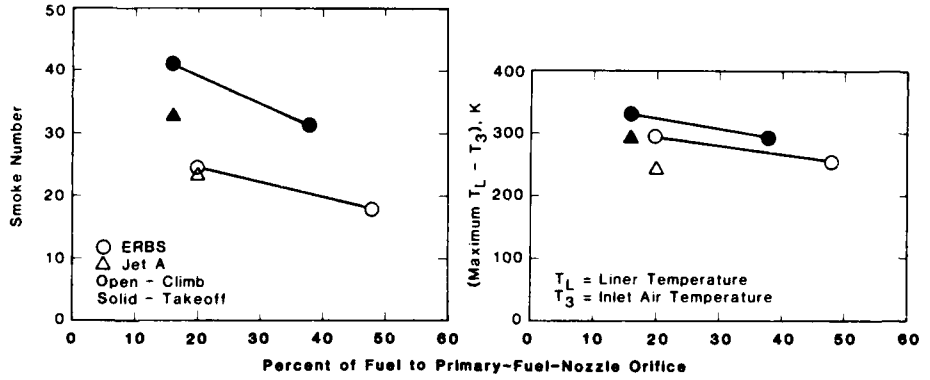


Figure 5. Fuel Atomization Effects on Smoke and Liner Temperature.

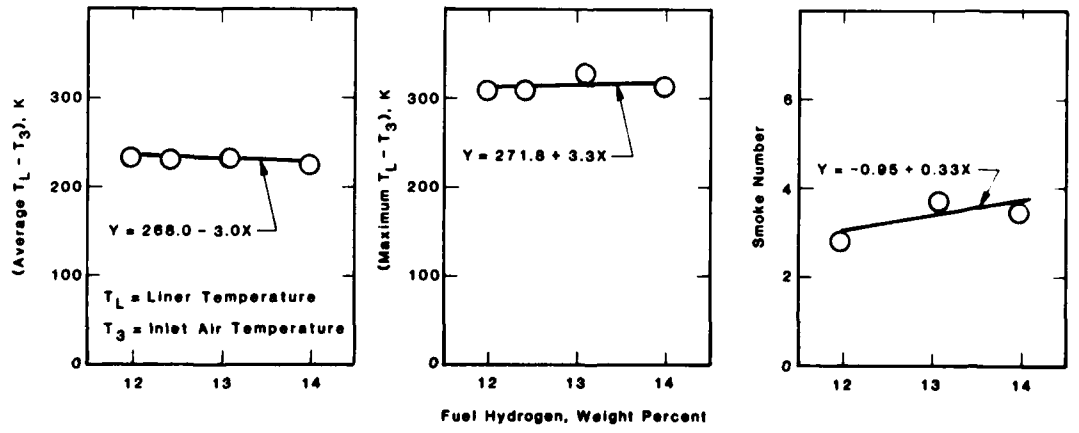


Figure 6. Lean Combustor Fuel Hydrogen Effects (Double Annular) at Takeoff Conditions.

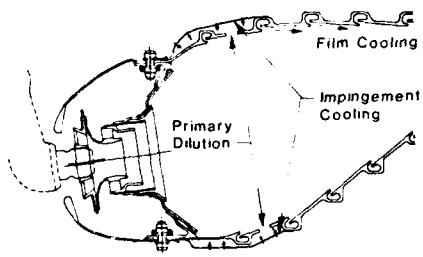


Figure 7. Inpingement/Film Cooling.

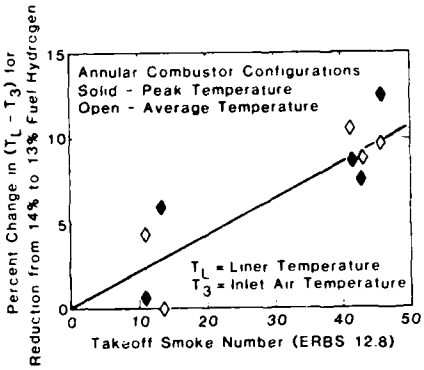


Figure 8. Correlation Between Smoke Level and Liner Temperature Sensitivity to Fuel Hydrogen Content (Takeoff Operating Conditions).

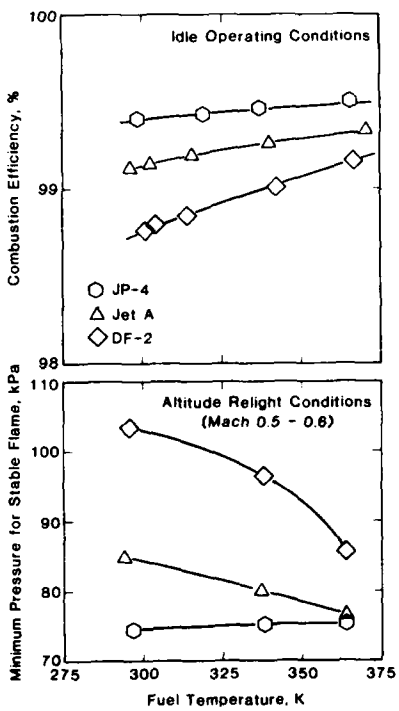


Figure 9. Effect of Fuel Type and Temperature on Idle Combustion Efficiency and Altitude Relight /Stability.

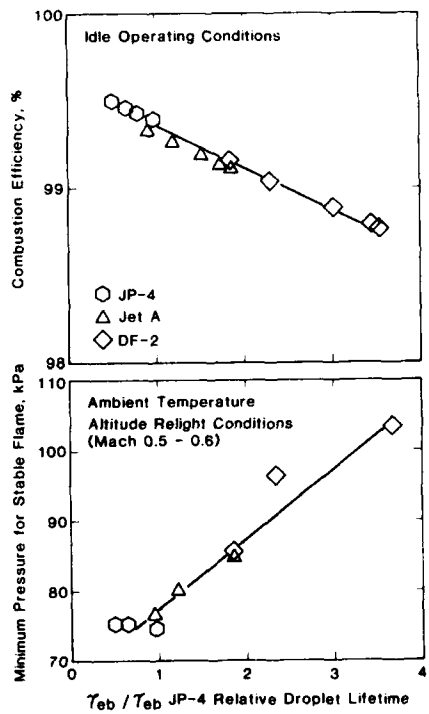


Figure 10. Effect of Droplet Lifetime on Idle Combustion Efficiency and Altitude Relight/Stability.

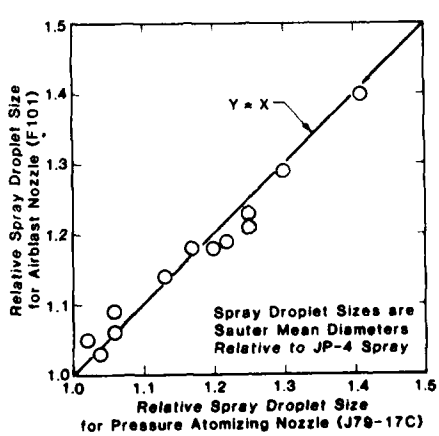


Figure 11. Comparison of Relative Droplet Sizes for Pressure Atomizing and Airblast Fuel Injectors.

DISCUSSION

S.Wittig, Ge

In calculating the droplet lifetime you used the SMD. The SMD, however, does not characterize the droplet size distribution which may vary with fuel composition. What, in your opinion, could be the effects of varying size distributions on your results?

Author's Reply

Droplet size distribution will certainly affect combustor performance and operating characteristics, probably in much the same way that volatility distributions (or distillation curves) do.

In this respect, for example, a 10 percent droplet size could be defined (representing the smaller droplets) which would be analogous to the 10 percent recovery point on the distillation curve. It would then be possible to evaluate ignition based on the 10 percent droplet size and 10 percent recovery temperature, while combustion efficiency could use the 90 percent droplet size and 90 percent recovery temperature.

I should point out that the SMD values used for this study were calculated from existing empirical correlations. They were not measured. Therefore, actual size distributions were not known. We are currently developing droplet size measurements for several of our fuel injector/swirl cup systems.

It is obvious from the correlations presented in the paper that SMD is very useful in correlating data where fuel type and temperature are varied, but the combustor hardware is not changed. However, for a hardware change such as using a different fuel injector, droplet size distribution, velocity distribution, and trajectory distribution could all be important.

G.Winterfeld, Ge

The dual-orifice injector displayed in the paper shows a very narrow spray angle which could give rise to higher fuel concentration in the center of the primary zone with detrimental effects on emissions, e.g. hydrocarbon emissions. Can you, please, comment on that problem?

Author's Reply

The figure showing the dual orifice atomizer is schematic. However, the actual atomizer does produce a rather narrow spray from the primary orifice. I believe that this narrow spray is actually important in reducing hydrocarbon emissions. As shown in the paper, a swirl cup modification which produced a wider spray actually increased hydrocarbon emissions (as evidenced by decreased combustion efficiency). With the wider spray, unburned or partially burned fuel can be quenched by the relatively cool film cooling air adjacent to the combustor walls.

FUEL EFFECTS ON GAS TURBINE COMBUSTION SYSTEMS

Stanley A. Mosier
Pratt & Whitney Aircraft
Engineering Division
West Palm Beach, FL 33402
USA

AD-P003 131

SUMMARY

The effects of variations in properties and characteristics of liquid hydrocarbon-base fuels in gas turbine engine combustors was investigated. Baseline fuels consisted of military-specification materials processed from petroleum and shale oil. Experimental fuels were comprised of liquid petroleum blends that were prepared specifically to exhibit desired physical and chemical properties. These fuels were assessed for their influence on ignition and performance characteristics in combustors of the F100, TF30, and J57 (TF33) engines at simulated operating conditions. In general, during relatively short duration tests, combustor ignition and performance became increasingly poorer as fuel quality deviated from specification or historical values.

NOMENCLATURE

B	Mass transfer number in equations (1) and (3)
COP	Combustor operating parameter in equation (2)
FCP	Fuel characterization parameter in equation (3)
FPR	Fuel characterization parameter ratio in equation (4)
LSP	Liner severity parameter in equation (7)
PF	Pattern factor in equation (5)
Pr_a	Prandtl number of air in equation (2)
RDS	Relative droplet size in equation (1)
ref	Reference, or referee
SG	Specific gravity in equation (3)
SMD	Sauter mean diameter in equations (1) and (3)
Spec	Specification
Tu	Percent turbulence intensity in equation (2)
U	Free-stream air velocity in equation (2)
VI	Vaporization index in equation (3)
ϕ	Equivalence ratio
ρ_a	Density of air in equation (2)
ρ_f	Density of fuel in equation (3)
μ_a	Dynamic viscosity of air equation (2)

1. INTRODUCTION

Gas turbine engines for military aircraft have been designed and developed historically to operate on high-quality, liquid hydrocarbon fuels produced to very exacting specifications. These specifications were formulated as a compromise between desired performance characteristics of the fuel and the concurrence of the processor to supply the quantities of fuel needed at an acceptable price using available technology. The specifications were composed at a time when crude oil was plentiful and cheap. Consequently, values of selected physical and chemical properties were chosen that were sufficiently conservative to fully accommodate the most extreme environmental conditions under which current and future turbine-powered military aircraft might operate. In 1973, before the oil embargo, refiners were supplying high-quality jet fuel to the military services for approximately eleven cents per gallon; the Air Force's bill at that time for 143 million barrels of turbine-engine fuel was less than 600 million dollars (Reference 1).

The specifications established in the pre-embargo era essentially committed operational aircraft engines and those both under development and on the drawing boards to use high-quality fuel during their lifetimes. Because of the ready availability of such fuel at that time, the specifications were not optimized using sensitivity tradeoffs relating the values of key fuel properties to the operation and

performance of engine components and systems. Few such tradeoff studies had either been conducted or documented. As a consequence, there is concern that in the light of today's economic and energy situations, the established fuel specifications might be too rigid: possibly limiting the availability of the jet-fuel supply and contributing to its high cost. In 1982, the price of a gallon of jet fuel supplied to the Air Force had been escalated to $1.30; the annual bill for the 95 million barrels used was over five-billion dollars (Reference 2). There is also concern that portions of the specification might be too loose and need to be made more restrictive; this type of change might again tend to limit fuel availability and increase its price.

Consequently, for several years the Department of Defense has been sponsoring fuel-accommodation investigations with gas turbine engine manufacturers and supporting organizations to quantify the effect of changes in fuel properties and characteristics on the operation and performance of military engine components and systems. Inasmuch as there are major differences in hardware, between the operational engines in the Air Force and Navy inventories, due to differences in design philosophy and requirements, efforts were initially expended to acquire fuel-effects data from rigs simulating the hot-sections of these different engines. Correlations were then sought using the data acquired to produce more general, generic relationships that could be applied to all military gas turbine engines regardless of their origin. Finally, models could be developed from these correlations that could predict the effect of fuel property changes on current and future engines.

This paper describes some of the work performed by Pratt & Whitney Aircraft under Defense Department-sponsored fuel-effects programs. The experimental work was conducted using hot-section components from the F100, TF30, and TF33 engines. The analytical effort incorporated data obtained from tests of these components as well as data obtained by other investigators from rig tests of their engine hot-section components. Reference has been made in the text to contractor reports in which the experimental results and data cited in this paper have been taken.

2. TEST PROGRAMS

Two test and evaluation programs were conducted to determine the impact of jet fuel property variations on the ignition and performance/durability characteristics of three combustion systems used in current operational military aircraf . One investigation addressed the F100 engine, which is used in the Air Force's F-15 and F-16 aircraft, and the TF33 engine, which is used in the Air Force's B-52H, C-135B, C-141 and E-3A aircraft. The other investigation addressed the TF30 engine that is used in the Navy's F-14 aircraft. Both programs were performed using test rigs comprised of engine combustion system hardware.

Tests were conducted at conditions that closely simulated those of the three engines under investigation using the experimental fuels that are described later. Ignition tests were conducted for both sea-level (groundstart) and altitude (airstart) operation over a range of fuel temperatures. For the airstart test program, simulated altitude conditions were selected from windmilling maps of each engine; these maps are shown in References 3-6. Performance tests were conducted at four simulated power settings. Rig test conditions are shown in Table 1. For the F100 and TF30 rigs these settings corresponded to idle, cruise, takeoff and dash. For the TF33 rig, the settings corresponded to idle, takeoff, and two cruise conditions; a second cruise condition was substituted for the high-altitude dash because the TF33 is not used in fighter applications.

Table 1. Nominal Operating Conditions for Performance/Durability Rig Tests

Rig	Condition	Inlet Air Temp, K	Inlet Air Press, kPa	Inlet Airflow Rate, kg/s
TF30	Idle	440	370	2
	Takeoff	750	1790	6
	Cruise	620	900	3
	Dash	790	1560	5
F100	Idle	490	450	4
	Takeoff	700	1160	8
	Cruise	810	1470	10
	Dash	900	1480	10
TF33	Idle	360	210	2
	Takeoff	550	430	4
	Cruise 1	600	530	4
	Cruise 2	660	1260	10

3. COMBUSTOR HARDWARE

Five mainburner test rigs were used in conducting the experimental programs. A 90-degree sector rig was used for determining both ignition and performance characteristics of the F100 combustor. Full sets of cans, in annular arrangements, were used for ignition testing of the TF33 and TF30 combustors; performance testing was accomplished using single cans.

The F100 burner rig consisted of a diffuser case, an instrumented combustor, and four, engine-quality airblast fuel injectors. The rig was fabricated by cutting the appropriate sector from an engine diffuser case and combustor and attaching louver-cooled sidewalls to both. The engine burner is shown schematically, in cross section, in Figure 1. The liner was instrumented with chromel-alumel thermocouples distributed axially and circumferentially to acquire temperature gradient data for estimating combustor liner life. A detailed description of the rig is provided in Reference 4.

Two rigs were used in the TF33 test program. The ignition rig was comprised of eight cans joined together with dome-located cross-over tubes in an annular arrangement within an engine case; each combustor was equipped with six pressure-atomizing fuel injectors. Engine igniters driven by engine exciter boxes supplied the energy and spark rate for ignition to two of the cans. The performance rig consisted of a single instrumented can, equipped with fuel injectors, mounted in a containment vessel that simulated a 45-degree segment of the engine case; and an inlet duct and transition duct constructed from actual engine hardware. The combustor can, shown in Figure 2, was instrumented with thermocouples and small-diameter tubes to obtain liner temperatures and static pressures, respectively. The combustor rigs are described in detail in Reference 4.

Two rigs were also used in the TF30 test program. The ignition rig was comprised of eight interconnected cans in an annular arrangement within an engine case; each combustor was equipped with four pressure-atomizing fuel injectors. Two of the cans were adapted with engine igniters driven by exciter boxes that simulated the energy and spark rate of the engine system. The performance rig, shown in Figure 3, consisted of a single instrumented can equipped with fuel injectors, mounted in a case, with inlet and transistion ducts, simulating one-eighth of the full-annular flowpath of the engine. The combustor liner and transition duct were instrumented with thermocouples to obtain information from which liner life could be estimated. In addition, the can and transition duct were fitted with small-diameter tubes for obtaining liner static pressure measurements. The combustor rigs are described in detail in References 3 and 5.

4. TEST FUELS

A total of 21 liquid hydrocarbon fuels in three categories were selected for use in the fuel-effects programs. The first category was comprised of jet fuels made to military specifications from both petroleum and shale oil. These served as referee fuels primarily to establish baseline values of combustor operating characteristics. The second category consisted of two sets of nonspecification fuels produced from petroleum. These fuels were blends of refinery streams that were proportioned to exhibit pronounced variations in values of selected properties. The properties addressed were those that were predicted to most significantly influence combustor ignition and performance. The third category included blended fuels that were prepared primarily to represent reduced-quality petroleum refinery products or emergency fuels. These were incorporated into the programs primarily for their holistic impact.

Six fuels were included in the first category. Two were produced to JP-4 specifications and four were made to JP-5 specifications. One of the JP-4 fuels and one of the JP-5 fuels were prepared from oil shale; the remainder were prepared from petroleum. Representative properties of the referee fuels are shown in Table 2 relative to JP-4 and JP-5 specification values; detailed property information is provided in References 3-6.

Table 2. Selected Properties of Referee Fuels

Fuel Reference No. Fuel Type	2-1 JP-4 (Spec.)	2-2 JP-4	2-3 JP-4 (Shale)	2-4 JP-5 (Spec.)	2-5 JP-5	2-6 JP-5	2-7 JP-5	2-8 JP-5 (Shale)
Hydrogen Content, % wt	13.6*	14.54	14.39	13.5*	13.93	13.79	13.81	13.85
Aromatics Content, % vol	25.0**	11.1	10.1	25.0**	15.9	15.8	22.6	24.0
Viscosity, mm^2/s	-	0.97(294K)	1.28(294K)	8.5(253K)**	2.29(289K)	1.58(311K)	2.04(289K)	2.00(289K)
Specific Gravity at 288K	0.751-0.802	0.760	0.781	0.788-0.845	0.815	0.817	0.809	0.807
Initial Boiling Point, K	-	293	273	-	431	454	450	459
10% Recovery Temp, K	-	358	400	478**	470	472	466	467
20% Recovery Temp, K	418**	374	421	-	474		471	469
50% Recovery Temp, K	463**	431	458	-	489		482	480
90% Recovery Temp, K	518**	495	500	-	516	516	509	505
End Point, K	543**	589	593	563**	535	534	529	527
Freezing Point, K	215**	214	214	227**	227	223	227	227
Flash Point, K	-			333*	338	335	339	339
Heat of Combustion, MJ/kg	42.8*	43.401	43.469	42.6*	43.260	43.041	43.100	43.144

* Minimum acceptable values
** Maximum acceptable values
\- No value specified

The second category consisted of eight fuel blends in two sets. The first set contained four fuels that were selected to exhibit parametric variations in those properties indicated to impact ignition characteristics most significantly. The properties of primary interest in the preparation of these ignition fuels were viscosity and volatility. Three of the fuel blends were produced to exhibit

specified variations in these two properties, including one blend for evaluating the significance of the shape of the front end of the distillation curve. The fourth fuel was selected for evaluating chemical effects, related to aromatic structure, on ignition characteristics. The second set of four fuels was produced to evaluate the sensitivity of combustor performance characteristics to variations in fuel properties. These characteristics included pattern factor, liner durability, exhaust gas objectionable emission concentrations, and combustion efficiency at low-power operation. Key properties operated on to produce the performance fuel blends were viscosity, aromatics content and type, hydrogen content, and volatility. Pertinent properties of the ignition and performance fuels are shown in Table 3. Properties of the seven blending stocks that were used in preparing the test fuels, as well as detailed characteristics of the test fuels, are provided in Reference 4.

Table 3. Selected Properties of Ignition and Performance Fuels

	Ignition Fuels				Performance Fuels			
Fuel Reference No.	3-1	3-2	3-3	3-4	3-5	3-6	3-7	3-8
Hydrogen Content, % wt	14.24	13.44	14.04	12.27	13.44	12.94	11.56	11.50
Aromatics Content, % vol	10.5	27.5	13.8	55.4	20.1	34.7	61.6	45.5
Naphthalene Content, % vol	2.1	0.7	0.7	0.4	2.8	3.8	4.0	14.9
Viscosity, mm^2/s								
239K	Solid	3.46	6.74	1.73	8.11	5.60	18.8	Solid
244K	5.56	3.03	5.68	1.50	6.56	4.25	12.6	Solid
273K	2.55	1.66	2.55	0.96	2.83	2.09	4.34	4.93
294K	1.71	1.17	1.71	0.74	1.87	1.46	2.65	2.85
311K	1.33	0.94	1.32	0.62	1.42	1.16	1.93	2.03
T (K) at % Recovered								
10	370	395	459	365	432	368	430	470
20	399	422	462	384	452	394	435	481
50	509	456	473	419	482	461	483	522
90	542	499	494	442	522	575	611	581
Specific Gravity at 288K	0.789	0.796	0.801	0.795	0.817	0.814	0.879	0.886
Freezing Point, K	244	216	225	204	226	239	235	253
Flash Point, K			315		319		313	336
Heat of Combustion, MJ/kg	43.287	43.001	43.232	42.560	42.818	42.537	41.212	41.451

The third category was comprised of seven petroleum-base blends. Four were prepared from refinery streams to be representative of production-type, relaxed-specification jet fuels. The remaining three were selected to be representative of emergency fuels. One of the emergency fuels was a No. 2 fuel oil; the other two were blends of nonaviation fuels and specification-grade JP-5. Some of the principal properties of these fuels are shown in Table 4. Detailed physical and chemical properties of these fuels are provided in Reference 5.

Table 4. Selected Properties of Relaxed-Specification/Emergency Fuels

	Relaxed-Specification Fuels				Emergency Fuels		
Fuel Reference No.	4-1	4-2	4-3	4-4	4-5*	4-6**	4-7***
Hydrogen Content, % wt	13.36	13.48	13.66	13.82	13.22	12.83	13.54
Aromatics Content, % vol	28.5	19.8	22.8	18.6	25.9	26.4	18.6
Viscosity, mm^2/s at 311K	1.78	2.27	1.62	1.74	2.60	1.77	2.06
Specific Gravity at 288K	0.830	0.836	0.819	0.817	0.839	0.847	0.830
Initial Boiling Point, K	436	441	444	453	426	466	453
10% Recovery Temp, K	463	500	465	475	491	477	477
90% Recovery Temp, K	549	545	534	537	590	545	570
End Point, K	570	554	549	555	606	561	596
Freezing Point, K	243	249	239	239	270	242	263
Heat of Combustion, MJ/kg	42.648	42.798	42.919	42.961	42.706	42.392	42.873
Flash Point, K	330	344	332	342	346	344	349

* No. 2 fuel oil
** 20% (vol) hydrocracked gas oil + 80% (vol) JP-5
*** 50% (vol) Diesel Fuel Marine + 50% (vol) JP-5

For ease of identifying the various test fuels throughout the test, all of the fuels in the three tables have been assigned two-digit reference numbers. The first digit refers to the table number and the second digit to the reference number of the fuel in the table. For example, the shale-base JP-5 referee fuel in Table 2 is Fuel 2-8, and the emergency fuel comprised of Diesel Fuel Marine and JP-5 is Fuel 4-7.

5. TEST RESULTS

A significant amount of experimental data was obtained during the conduct of the fuel-effects programs. No attempt will be made in this paper, however, to present all of the data acquired for the combustor rigs and 21 fuels investigated; this information is contained in contractor final reports (References 3-6). The objective of this paper is to provide a condensation of these reports, supplying representative results from the ignition and performance investigations. These results include both input - output information and correlations depicting fuel-property effects on combustor rig characteristics.

(a) GROUNDSTART IGNITION

Groundstart ignition testing was conducted over a range of airflow rates to determine the minimum fuel flow at which stable ignition could be achieved in a given combustor rig. For the can-annular arrangements, stable ignition was considered attained when all combustors lit within 30 seconds after fuel flow had been initiated. For the sector burner, stable ignition was considered achieved if burning was observed directly downstream of each of the four injectors within 30 seconds of fuel initiation. Prior to each ignition attempt, a common temperature was established for the inlet air, fuel, and test rig.

The data shown in Figure 4 are representative of those obtained during groundstart ignition testing. In this figure, results for the F100 sector burner rig are presented for a simulated cold day (244K) using the two baseline JP-4 fuels (Table 2) and the four ignition fuel blends characterized in Table 3. In general, petroleum-base JP-4 fuel lit at the lowest flowrates. The other fuel blends, and the shale-base JP-4 fuel, lit at higher flowrates. The increases were essentially proportional to the relative droplet size (RDS) of the fuel, i.e. the ratio of the Sauter mean diameter achieved for the fuel under investigation, using a given injector, to the Sauter mean diameter obtained for a baseline fuel when the same injector is used; and the fuel volatility, as represented by the 10% recovery temperature. As the relative droplet size of the test fuel increased, due to higher values of viscosity, surface tension, and density, and as the 10% recovery temperature increased, a higher fuel flowrate, indicative of a higher fuel-air ratio, was needed to effect groundstart ignition.

Figure 5 shows the results of a more general correlation that was developed for predicting groundstart ignition characteristics. In this case, the combustor was the TF30 and the fuels used were the referee low-aromatic content JP-5 fuel, identified in Table 2 as Fuel No. 2-6, and five of the fuels identified in Table 4. The fuel-air ratio required for full rig ignition at each of three airflow rates is presented as a function of a vaporization index, which is defined in equation (1).

$$VI = \frac{(RDS)^2(SG)}{\log\,(1 + B)} \qquad (1)$$

This equation,described in more detail in the Appendix, contains physical properties of the fuel both explicitely, as specific gravity (SG) and implicitely through relationships defining relative droplet size (RDS) and mass transfer number (B). As the index increases, there is less propensity for the fuel to ignite at any given value of airflow rate. Higher values of the index represent heavier, poorer-quality fuels having, inter alia, higher densities, surface tensions, and viscosities and lower volatility characteristics. In thi case, characteristics of heavier, poorer-quality fuels were also achieved by reducing the temperatures of three of the test fuels.

(b) AIRSTART IGNITION

Airstart ignition tests were conducted to determine the capability of each of the three combustor rigs to achieve stable ignition at simulated altitude conditions using a variety of test fuels. Stable ignition in these tests was defined as it was for groundstart ignition. Altitude conditions simulated for these tests were selected from standard-day windmilling maps. These maps represent known windmilling operating regions within the bounds of aircraft altitude and Mach number for the engine combustors under investigation. The aerodynamic variables involved include flowrate, total pressure, and temperature of the air entering the combustor rig; flight Mach number, and altitude. By specifying any two of these variables, the others can be obtained from the windmilling map for the engine.

The fuel-dependent variables include physical and chemical characteristics of the blends being introduced into the rig, and the fluid dynamical factors that determine the characteristics of the fuel-air mixture in the vicinity of the igniter. In general, as the quality of the test fuel deteriorated, as indicated by increased viscosity and surface tension, and decreased volatility, the capability of a combustor rig to ignite stably at simulated altitude conditions decreased. Figure 6 is representative of the impact of fuel properties on airstart ignition for the TF30 combustor rig at a temperature of 40 F (278K). The fuels used were a referee JP-5 that was described in Table 2 (Fuel No. 2-6), and five of the broadened-specification and emergency fuels described in Table 4. The referee JP-5 fuel and the emergency fuel blend (comprised of Diesel Fuel Marine and JP-5) clearly provided the best and worst airstart ignition characteristics, respectively. Performance of the other fuels lay essentially midway between the two extremes.

The capability of a combustor rig to ignite stably also decreased when the temperature of the fuel, inlet air, and rig were reduced. In a sense, the fuel viscosity, surface tension, and volatility were degraded artificially to simulate characteristics of poorer-quality fuels. Figure 7 shows the variation in airstart ignition capability with temperature for a TF30 mainburner rig fired with the

referee JP-5 fuel (No. 2-6) that was described in Table 2. The impact of increasing viscosity and surface tension, and lowering volatility on airstart ignition characteristics is as pronounced as if poorer quality fuels were used.

Airstart ignition results as presented in Figures 6 and 7 faithfully represent rig characteristics for the fuels investigated. However, fuel property influences are not in a form that would enable the degradation in altitude ignition capability with fuel properties to be readily ascertained. Consequently, a model was formulated and a correlation developed that did, indeed, allow this to be accomplished. The model is based on the work of Ballal and Lefebvre (Reference 7) and on the observation that over a wide range of combustor aerothermal operating parameters, the ignition process is evaporation-rate controlled. It is assumed that a spark creates a spherical volume of inflamed gas that, if it is to propagate through the gas mixture, must be of sufficient size that the rate of heat release within its volume exceeds the heat loss to the surroundings. The radius of the critical volume is termed the quenching distance and the energy required is the minimum ignition energy.

For a given combustor design the quenching distance and, hence, the required energy are functions of the aerodynamic conditions within the combustor, the fuel droplet diameter, and the fuel volatility. The internal combustor aerodynamics are directly related to flight conditions, viz. altitude and Mach number. The droplet size is determined by injector characteristics and by the fuel viscosity, density, and surface tension. The energy liberated by the igniter varies slightly with the aerothermal condition, but may be assumed to be constant over the range considered. Therefore, the quenching distance can be taken as a measure of ignition capability.

The relationship developed by Ballal and Lefebvre (Reference 7) for the quenching distance, was rewritten to isolate terms dependent on combustor aerodynamics from those dependent only on the fuel. The aerodynamic grouping, containing terms that vary with altitude and Mach number, is referred to as the combustor operating parameter, COP, and is defined as

$$COP = \frac{Pr_a}{10\phi}\left[\frac{Tu\ U}{\rho_a\ \mu_a}\right]^{0.5} \tag{2}$$

The fuel-dependent variables are collected in the fuel characterization, or correlation, parameter, FCP, which is defined as

$$FCP = \frac{\rho_f (SMD)^{1.5}}{\log\ (1 + B)} \tag{3}$$

The combustor operating parameter can be calculated from operating conditions defined on a windmilling map for the engine in question. Figure 8 shows the variation in altitude with combustor operating parameter for a TF30 combustor rig.

To the extent that the ignition scenario and model are valid, there is a fixed relationship between the values of the combustor operating parameter and the fuel characterization parameter that will result in ignition. Figure 9 shows such a relationship that was developed from airstart ignition data for the TF30 combustor rig using three of the referee fuels identified in Table 2. The fuels were a low-aromatic content JP-5 (Fuel No. 2-5), a high aromatic JP-5 (Fuel No. 2-7), and a shale-base JP-5 (Fuel No. 2-8). The data indicate a linear relationship between the two parameters for each of the four burner airflow rates investigated. For a particular airflow rate, any combination of the two parameters falling below the correlation line for a specific airflow rate would indicate a "no-light" situation; any combination falling on or above the line would indicate stable-ignition.

Figures 8 and 9 in combination form a basis for predicting the effect of fuel changes on airstart capability. For a given fuel, the fuel characterization parameter is first calculated from fuel properties and injector characteristics. For this value of the fuel characterization parameter, the ignition limit of the combustor operating parameter is then defined by Figure 9 at each airflow rate. Finally, the value of the combustor operating parameter is converted to altitude using Figure 8.

A refinement of the preceding model was formulated to provide a simplified airstart ignition correlation. Using Figure 8, with a referee JP-5 fuel as the baseline, the change in value of relight altitude between that resulting from the use of the referee fuel and that resulting from the use of the test fuel was determined as a function of the fuel characterization parameter for each of the four airflow rates. Each fuel characterization parameter was then normalized, using the fuel characterization parameter for the referee JP-5 fuel, to obtain a fuel characterization parameter ratio, FPR, which is defined in equation (4).

$$FPR = \frac{FCP}{(FCP)_{JP-5}} \tag{4}$$

The resulting plot is shown in Figure 10, where the difference in relight altitude for the TF30 combustor rig is presented as a function of fuel properties and airflow rates. Fuels having ignition qualities better than those of the referee military-specification fuel are identified by fuel parameter ratios less than unity, increases in relight altitude above that of the referee fuel are identified by fuel parameter ratios greater than unity.

The validity of the approach taken to produce Figure 10 was tested using data from airstart ignition tests in which a number of the fuels listed in Table 4 were evaluated. As discussed earlier, the fuels in Table 4 were prepared to be fully representative of relaxed-specification and emergency fuels. Figure 11 presents the results obtained for the specified test fuels relative to the 27,000 lb/hr (3.4 kg/s) airflow rate correlation line shown in Figure 10. The good correlatic achieved for this airflow rate line was also obtained for the remaining three airflow rate lines.

(c) **PATTERN FACTOR**

Pattern factor, PF, defined in equation (5), was determined from temperature measurements of the air entering the performance combustor rig and of the working fluid leaving the rig.

$$PF = \frac{T_{max,out} - T_{avg,out}}{T_{avg,out} - T_{avg,in}} \qquad (5)$$

where $T_{max,out}$ = maximum exhaust gas temperature measured in the plane of the turbine first-stage vane

$T_{avg,out}$ = average temperature of the exhaust gas in the same plane

$T_{avg,in}$ = average temperature of the combustor inlet air

This parameter provides a measure of the quality of the working fluid being supplied by the combustor to the turbine, which influences turbine durability and performance. The lower the pattern factor, the greater the durability of the turbine.

The best means of determining pattern factor for an engine is by using the engine itself as the test bed. In this way, the influences of combustor inlet air distribution, associated with a specific compression system, and internal aerodynamics, resulting from the interaction of the fuel and air injection systems, are measurable exactly. Unfortunately, this type of testing is not routinely possible because of the high costs of preparing for and conducting the tests. In the case of determining the effect of fuel properties on hot-section performance, engine hardware could be jeopardized because of the many unknowns involved. Therefore, although engine testing would provide the best data on fuel-dependent pattern factor effects, combustor rigs, with their inherent deficiencies, were used to develop relative trends. From these trends, however, the magnitude of fuel effects on engine hardware can be projected and then engine testing, incorporating automated recording temperature systems (ARTS) in the first turbine vanes, could be indicated to quantify the rig trends and refine the preliminary models and correlations.

The trends obtained in pattern factor variations with fuel properties were found to correlate, generally, with the vaporization index of the fuel, which was defined in equation (1). However, in the performance-test version of this index, the 90% recovery temperature of the fuel, was used in determining the relative droplet size and mass-transfer number. Processes within the combustor that would tend to influence droplet size, penetration, and evaporization and then impact pattern factor were considered to be more dependent upon the final stages of droplet life than upon the initial stages.

Figure 12 shows a correlation indicating the influence of fuel properties on pattern factor and, in turn, their impact on the predicted low-cycle fatigue life of a first-stage turbine vane for the TF30. The data have been normalized to emphasize trends rather than absolute values, which for this type of rig testing are of little value. As the pattern factor increases, the low-cycle fatigue life is predicted to decrease as would be expected. However, the impact of fuel properties on pattern factor, both explicitly in terms of hydrogen content of the fuel and implicitly through vaporization index, are well depicted. Although the magnitude of the trends observed are not especially pronounced, the potential impact on turbine life due to the fuel burned is significant. As fuel quality deteriorates in terms of viscosity and volatility, the resulting turbine performance, in terms of durability, is projected to deteriorate.

(d) **LINER DURABILITY**

The life of conventionally cooled combustor liners in operational aircraft engines is generally limited by cracks in specific louver seam welds caused by low-cycle fatigue. Low-cycle fatigue results from cyclic expansion and contraction of the combustor liner during engine operation. Crack initiation occurs at locations in the liner where high stresses exist due to severe thermal gradients. This location is usually at a seam weld between two adjacent louvers, as shown in Figure 13, where a relatively large temperature gradient exists between the louver wall and the knuckle. At high-power operating conditions the stress concentrations in the vicinity of the seam weld can be well above the yield strength of the material causing plastic deformation with each cycle.

For a specific engine operating condition at which a referee fuel is burned, a thermal gradient is established between the louver lip and the knuckle causing a bending stress in the seam weld. When a poorer quality fuel is substituted for the referee fuel and is burned, the flame luminosity increases, which increases the temperature of the louver lip, but not the colder knuckle. The knuckle temperature remains essentially constant because of the radiation shielding provided by the lip and the temperature invariance of the cooling air entering the vicinity of the knuckle. Consequently, the increased flame luminosity increases the lip-to-knuckle thermal gradient and causes higher stresses in the seam weld.

Estimates of relative liner life were made for the F100 and TF30 combustors using measured liner temperatures from tests in which both baseline and experimental fuels were burned. To ensure the achievement of maximum strain in the critical louvers of the liners, the Type I engine cycle (off to max to off) was used to estimate fuel effects on F100 combustor life, and the Type I and Type II engine cycles (off to max to off with Type II going to supersonic) for the TF30 estimates.

The technique used for the low-cycle fatigue analysis incorporated equation (6) for calculating thermal strains.

$$\frac{\Delta\epsilon_T}{\Delta\epsilon_{baseline}} = \frac{\Delta T_T}{\Delta T_{baseline}} \tag{6}$$

where $\Delta\epsilon_T$ = total strain from burning the test fuel

$\Delta\epsilon_{baseline}$ = total strain from burning the baseline fuel

ΔT_T = temperature differential between seam weld and knuckle when test fuel is burned

$\Delta T_{baseline}$ = temperature differential between seam weld and knuckle when baseline fuel is burned

A value of baseline strain was taken from a figure relating the dependence of total strain range on cycles to failure for the liner material over a range of metal temperatures. Field history provided information on cycles to failures for the engine combustors.

Figure 14 shows the variations in life for the F100 and TF30 combustors that were estimated using rig temperature data, equation (6), and the low-cycle fatigue properties of the liner materials as a function of the hydrogen content of the fuel burned. The abscissa has been normalized by the hydrogen contents of the baseline fuels used in the test programs for the two combustors. Also shown in figure 14 are variations in predicted combustor liner life with the fuel hydrogen content parameter for two models of the J79 engine (Reference 8) and for the F101 (Reference 9). All trends are generally the same; as the hydrogen content of the fuel is reduced, the predicted liner life is also reduced. The magnitude of the predicted reductions in life are dependent upon the strain model selected, the materials data used, and the baseline information from field experience.

During the conduct of the TF30 fuel-effects investigation, a porous-plug radiometer was installed in the liner to measure the radiative heat load from the burning of lower-quality fuels. Figure 15 shows the variation in measured radiative heat flux with the hydrogen content of the fuel being burned at a number of operating conditions. As expected, the thermal radiation contribution to the total heat transfer rate from the combustion process to the liner increased as the hydrogen content of the fuel decreased. The significance of the increased thermal radiation load on combustor liner life at sea-level takeoff conditions is shown in Figure 16. For a seven percent decrease in hydrogen content of the fuel, the radiant heat flux increased by 16 percent resulting in a predicted reduction in liner life of approximately ten percent.

Combustor liner metal temperatures measured in the test programs and used in the durability analyses were correlated using a liner severity parameter, LSP, which is defined in equation (7).

$$LSP = \frac{T_{metal,max} - T_{air,in}}{T_{gas,out} - T_{air,in}} \tag{7}$$

This parameter is similar in form to that for pattern factor, equation (5). When plotted against the hydrogen content of the fuel burned, the liner severity parameter indicates the sensitivity of liner hot-spot temperature to poorer quality fuels. As shown in Figure 17 for a variety of combustor rigs operating at sea-level takeoff conditions, as the hydrogen content of the fuel being burned was decreased, the liner severity parameter increased. Although the rate of change of this parameter to hydrogen content was relatively small for all of the combustors considered, the magnitude of the parameter differed significantly for each.

(e) COMBUSTION EFFICIENCY

The combustion efficiency for a gas turbine combustor is a measure of the effectiveness in which chemical reactions between fuel and air are completed within a given volume. This effectiveness is strongly dependent upon the preparation of the fuel-air mixture. Under high-power conditions, the fuel injectors operate in a range where atomization is optimum and rapid vaporization of the injected fuel is enhanced by high temperatures of the inlet air. At low-power operating conditions, atomization is generally poorer, resulting in larger droplets being injected; and inlet air temperatures are lower, resulting in less of the incoming fuel being vaporized.

Poorer preparation of the fuel-air mixture for reaction contributes to an observed lower combustion efficiency at idle: especially with those engines having low pressure ratios. Intrinsic in the variables affecting fuel preparation are the physical properties of the fuel. Higher values of viscosity and surface tension, and lower values of volatility can yield larger, less vaporization-prone droplets.

The effect of fuel properties on combustion efficiency at the idle power setting was examined using data acquired in the F100, TF33 and TF30 burner investigations (References 3-6). Data obtained from other sources were also examined to obtain fuel-dependency comparisons between different combustion systems (References 10-13). The correlating parameter selected for combustion efficiency at the idle power setting is the vaporization index, which was defined earlier in equation (1). It is conjectured that idle efficiency is controlled by the ability of the final portion of the fuel spray (the portion associated with the upper end of the distillation curve) to vaporize rapidly enough to react before leaving the combustor. For this reason the mass transfer number in the denominator of equation (1) was

evaluated at the 90% recovery temperature for each fuel investigated. As described in an earlier section, as the value of the vaporization index increases, the tendency for the fuel to vaporize decreases. The poorer preparation of the fuel-air mixture contributes to a lower value of combustion efficiency being obtained.

The vaporization index for each of the fuels tested in a given combustor was normalized by the value of the vaporization index for that combustor when a referee fuel was burned. Likewise, the value of combustion efficiency at idle power operation for each fuel was normalized using the efficiency measured for the combustor in question when the same referee fuel was burned. Consequently, the fuel effect trends, relative to conventional, military-specification fuels, can be more readily ascertained. In addition, this technique provided a means to compare the fuel-effects trends for all combustors on a common basis.

Figure 18 shows the resulting variation in idle efficiency ratio with vaporization index ratio for rigs representative of combustors in the F100, TF33 and J79 engines. These systems were selected as being typical of high pressure ratio modern powerplants and of more mature, lower pressure ratio systems. There is very little effect of fuel properties on the efficiency of the F100 sector burner at the idle operating condition. The combustor pressure and inlet air temperature as well as the air-blast fuel nozzles contribute to good fuel preparation and high combustion efficiencies at idle. Over the range of vaporization indexes for the fuels tested with this combustor (Tables 2 and 3), there is but a one-point decrease in idle efficiency attributed to fuel properties. However, for the lower pressure ratio TF33 combustor, there is a significant decrease in combustion efficiency at idle with fuel properties. Over the range of vaporization indexes corresponding to the fuels tested (Tables 2 and 3), the idle efficiency was observed to change by seven points. The effect of fuel property variations on preparation of the fuel air mixtures is significant. It is interesting to note that the correlation obtained for the J79 combustor can is essentially identical to that obtained for the TF33 can, even though the fuel blends evaluated in each were different. The fact that the results shown in Figure 18, for the J79 and TF33 were so similar indicates that the processes controlling mixture preparation and reaction in each were essentially identical and predictable through the use of the vaporization index.

(f) SMOKE

During the performance tests, the smoke number of the exhaust gas discharged from the combustor rigs was measured in accordance with the method described in Reference 14. Of the fuel properties and relationships examined for correlating the smoke numbers, the single variable hydrogen content of the fuel provided the best correlation.

The absolute values of smoke number that were measured in the performance rigs can be quite different from those that might be obtained during engine testing. Experience gained during engine development has shown this to be true. However, rig data is very valuable for providing information on relative changes and in indicating trends. Therefore, the smoke data obtained during the fuel-effects programs for the F100, TF33, and TF30 combustor rigs (References 3-6), as well as the data reported for the J79, F101, and TF41 combustor rigs (References 10-13), were operated on and are presented in Figure 19 in a form showing the tendencies of the different combustor rigs to produce smoke as fuel quality is reduced. In combination with actual engine smoke data, Figure 19 can also be used to estimate the increase in engine smoke number resulting from the use of poorer quality fuels.

To develop Figure 19, the smoke data for the different combustor rigs, operating at simulated sea-level takeoff conditions where smoke production is greatest, were first linearized against the hydrogen content of the fuel used. The smoke numbers measured when the various fuels were burned in a given rig were normalized with the smoke number that was obtained when a referee fuel was burned. The referee fuel selected for developing Figure 19, for all combustors except the TF30, was military-specification JP-4 fuel that contained 14.5 percent hydrogen. For the TF30 combustor, the procedure was somewhat modified because the referee fuel used was military-specification JP-5 that had a hydrogen content of only 13.79 percent. In this case, the linear relationship between smoke number and hydrogen content was extrapolated to a hydrogen content of 14.5 percent, and the smoke number corresponding to this value was used as the normalizing base for the TF30 rig results.

As shown in Figure 19, the rate of increase in smoke number with decreasing hydrogen content is essentially the same for the TF41, TF33, F100, and F101 rigs. However, the rates for the TF30 and J79 rigs are more than twice as great. These trends are the result of the different design features that have been incorporated into the combustors.

6. REFERENCES

1. Bryce Poe II, "Proceedings of the Air Force-Sponsored Industry-Military Energy Symposium", San Antonio, TX, 21-23 October 1980, p. 7

2. W.N. Thorp, "Air Force Fuel Savings," National Defense, December 1982, p. 41

3. J.R. Herrin, "Influence of Shale Oil Base JP-5 on a TF30 Combustor", NAPC-PE-59C, November 1981

4. P.L. Russell, "Fuel Mainburner/Turbine Effects", AFWAL-TR-81-2081, September 1982

5. G.W. Beal, "Effect of Fuel Composition on Navy Aircraft Engine Hot Section Components", NAPC-PE-74C, May 1983

6. J.R. Herrin, et al, "Alternate Test Procedures for Navy Aircraft Fuels-Phase I", NAPC-PE-63C, January 1982

7. D.R. Ballal and A.H. Lefebvre, "Ignition and Flame Quenching of Flowing Heterogeneous Fuel-Air Mixtures", Combustion and Flame 35, 1979, pp. 155-168

8. D.W. Bahr, "Comparison Effects on Broadened Property Jet Fuels on Older and Modern J79 Combustors", ASME Paper 83-6T-81, 1981

9. C.C. Gleason and D.W. Bahr, "Fuel Property Effects on Life Characteristics of Aircraft Turbine Engine Combustors", ASME Paper 80-GT-55, 1980

10. C.C. Gleason, et al,"Evaluation of Fuel Character Effects on J79 Engine Combustion System", AFAPL-TR-79-2015, April 1979

11. C.C. Gleason, et al, "Evaluation of Fuel Character Effects on F101 Combustion System", AFAPL-TR-79-2018, June 1979

12. C.C. Gleason, et al, "Evaluation of Fuel Character Effects on J79 Smokeless Combustor", AFWAL-TR-80-2092, November 1980

13. R.E. Vogel, et al, "Fuel Character Effects on Current High Pressure Ratio, Can Type Combustion Systems", AFAPL-TR-79-2072, April 1980

14. SAE Aerospace Recommended Practice 1179A, "Aircraft Gas Turbine Engine Exhaust Smoke Measurement", Society of Automotive Engineers, New York, N.Y., July 16, 1979

15. J. Emory, et al, "Effect of Gas Turbine Fuel Nozzle Design and Operation on Nozzle and Combustor Performance", P&WA Report PWA-3751 to the Naval Air Engineering Center, 1969

16. M.S.M.R. El Shanawany and A.H. Lefebvre, "Airblast Atomization", Prog. Energy Comb. Sci. 6, 1980, pp. 233-261

7. ACKNOWLEDGEMENT

The author wishes to acknowledge the support of the United States Air Force and Navy in sponsoring the alternative-fuel and fuel-effects programs from which this paper is derived. He would like to specifically thank Tom Jackson and Chuck Delaney of the Air Force's Wright Aeronautical Laboratories; and Buck Nowack and Pete Karpovich of the Navy's Air Propulsion Center for their technical and managerial contributions, and for their patience.

The author also wishes to acknowledge the valuable contributions of his collegues in fuel-effects technology at Pratt & Whitney Aircraft. These include John Herrin, Art Masters, Paul Russell, Rich Ernst, Tom Rolfe, George Beal and Dean Andreadis.

8. APPENDIX

Vaporization Index (VI)

The vaporization index (VI) is defined in equation (1') as

$$VI = \frac{(RDS)^2(SG)}{\log (1 + B)} \qquad (1')$$

and contains the three principal variables relative droplet size (RDS), specific gravity (SG), and mass-transfer number (B).

The relative droplet size, is defined in equation (2') as

$$RDS = \frac{SMD}{(SMD)_{reference}} \qquad (2')$$

and is the ratio of the Sauter mean diameter of a fuel obtained under a given set of operating conditions. For pressure-atomizing fuel injectors, for example, relative drop size has been estimated using relationships from Reference (16), which has been simplified to the expression shown in equation (3')

$$\left[\frac{\sigma}{\sigma_{ref}}\right]^{0.6} = \left[\frac{\nu}{\nu_{ref}}\right]^{0.2} \qquad (3')$$

where σ = surface tension
ν = kinematic viscosity
ref = reference

Similar relationships can be developed for air-blast fuel injectors (Reference 17).

The mass-transfer number (B) is defined in equation (4') as

$$B = \frac{(m_{o,g}\, H/r) + c\,(T_g - T_s)}{Q} \qquad (4')$$

where $m_{o,g}$ = mass fraction of oxygen

H = heat of combustion

r = stoichiometric ratio

c = specific heat at constant pressure

T_g = combustor inlet temperature

T_s = recovery temperature; 10% recovery point for ignition and 90% recovery point for combustor efficiency and pattern factor

Q = heat conducted from gas per unit mass crossing the phase boundary, as defined in equations (5') and (6') which is the sum of the latent heat of vaporization and the increase in enthalpy between the base temperature and the surface temperature

$$Q = L + c_l (T_s - T_o) \qquad (5')$$

$$Q = L_o + c_{vap} (T_s - T_o), \qquad (6')$$

where L = latent heat of vaporization at droplet surface

c_l = specific heat or liquid

T_s = surface temperature of liquid

c_{vap} = specific heat of vapor at constant pressure

L_o = latent heat of vaporization at T_o

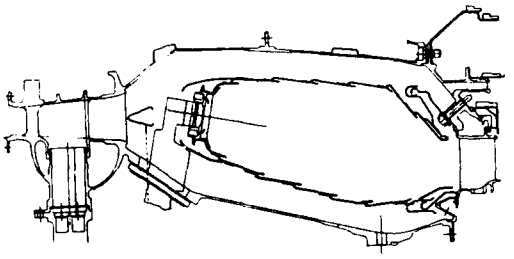


Figure 1. F100 Combustion Section Flow Path

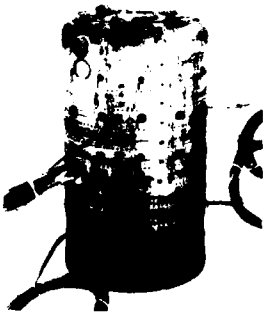


Figure 2. Instrumented TF33 Combustor Can

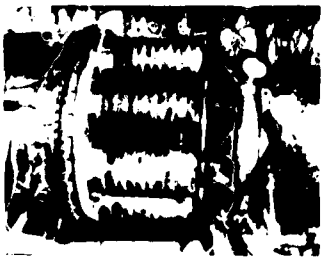


Figure 3. TF30 Can-Annular Ignition Rig

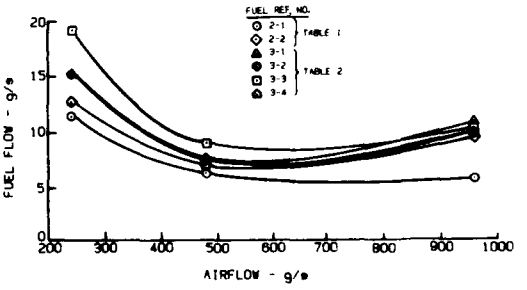


Figure 4. Cold Day (244K) Groundstart Ignition Characteristics for the F100 Sector Burner Rig

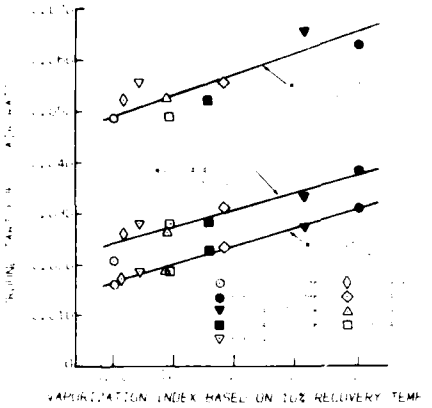


Figure 5. Groundstart Ignition Characteristics for the TF30 Combustor Rig

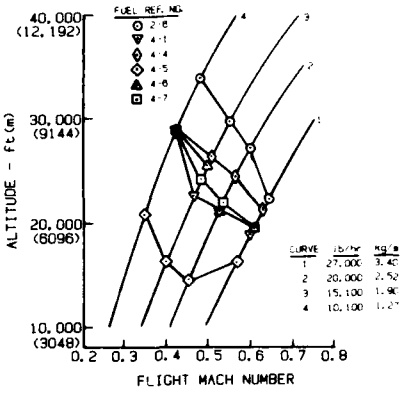


Figure 6. Fuel Effects on Airstart Ignition for Ignition Rig

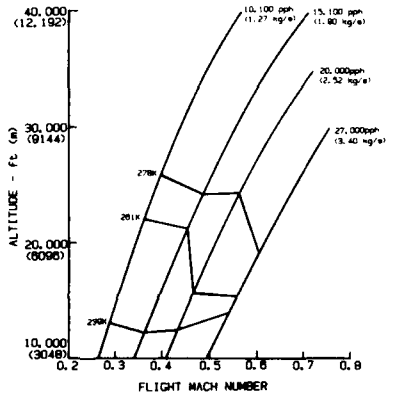


Figure 7. Temperature Effects on Airstart Ignition for TF30 Ignition Rig Using JP-5 Fuel (Fuel No. 2-5)

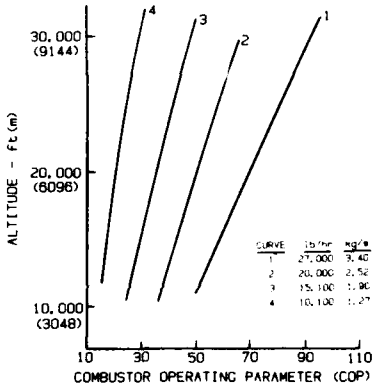


Figure 8. Effect of Altitude on Combustor Operating Parameter for TF30 Ignition Rig

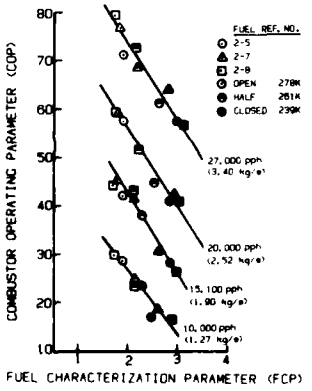


Figure 9. Variation in Combustor Operating Parameter with Fuel Characterization Parameter for TF30 Ignition Rig

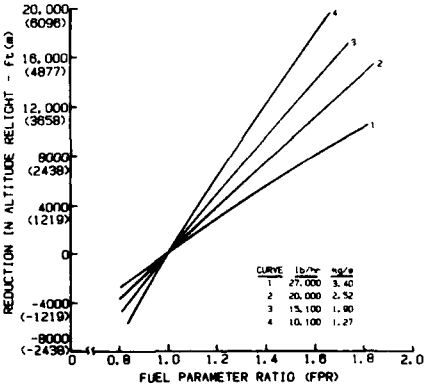


Figure 10. General Variation in Airstart Relight Altitude with Fuel Parameter Ratio for TF30 Ignition Rig

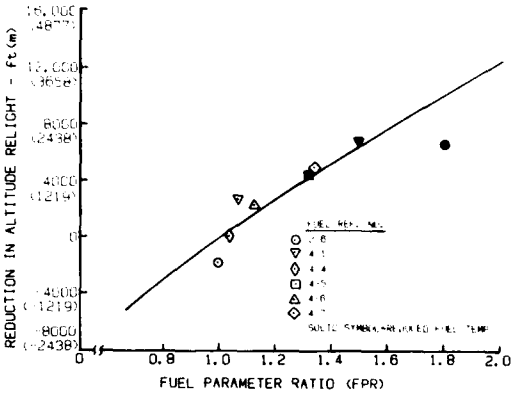


Figure 11. Specific Variation in Airstart Relight Altitude with Fuel Parameter Ratio for TF30 Ignition Rig

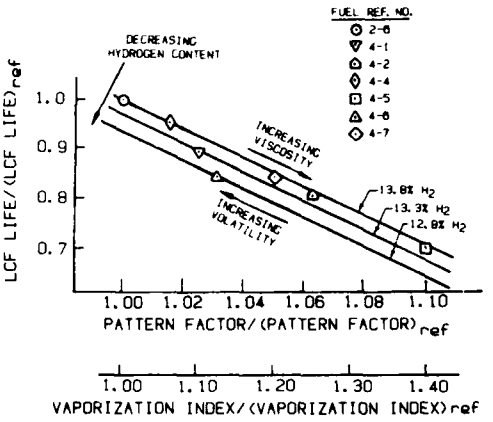


Figure 12. Predicted Fuel Effect On LCF Life for TF30 First Turbine Vane

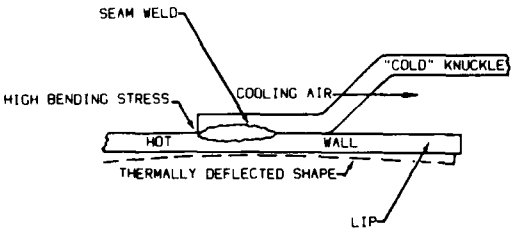


Figure 13. Thermal Stress Model

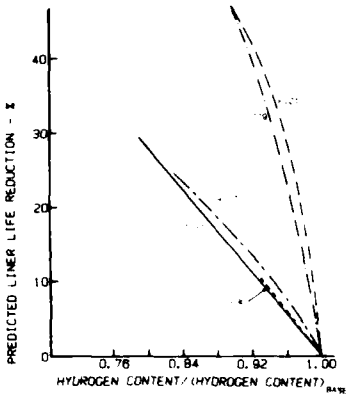


Figure 14. Predicted Liner Life Reduction

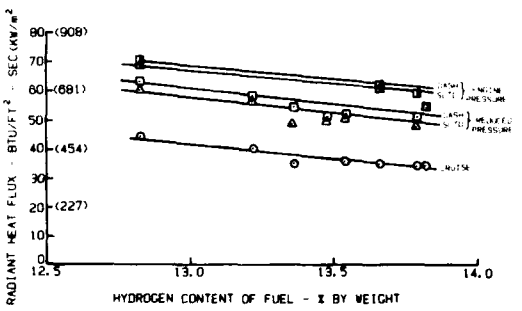


Figure 15. Measured Variation in The al Radiation Rate in TF30 Combustor Rig

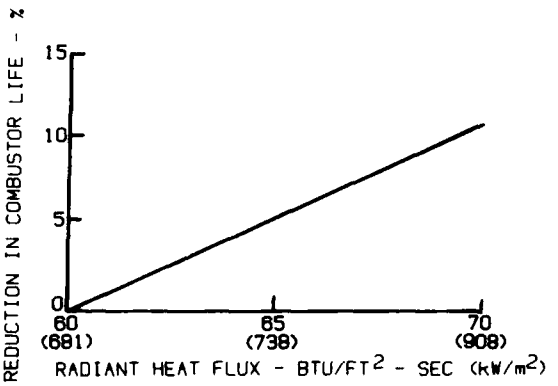


Figure 16. Reduction in Predicted Liner Life for TF30 Combustor Rig Due to Thermal Radiation

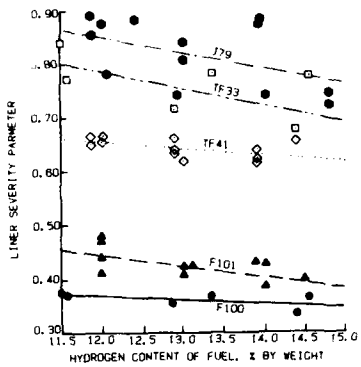


Figure 17. Variation in Liner Severity Parameter With Hydrogen Content of Fuel

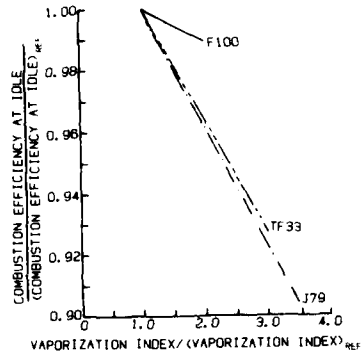


Figure 18. Variation in Combustor Efficiency at Idle With Vaporization Index

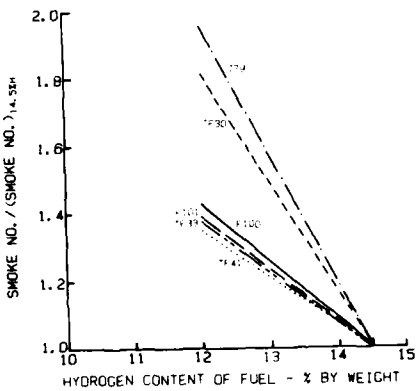


Figure 19. Variation in Smoke Number at Sea-Level Takeoff with Hydrogen Content

DISCUSSION

J.Vleghert

You mentioned effects of fuel temperature on several characteristics of combustion; is there also an influence on smoke production?

Author's Reply

An increase in the temperature of a fuel that is injected into a combustion chamber should, in general, serve to produce a lower level of smoke in the exhaust gas. The elevated temperature, in essence, increases the volatility of the fuel. Enhanced volatility has been demonstrated to assist in the suppression of smoke and carbon deposition.

C.Moses, US

You have had considerable success in developing a parameter for fuel properties for use in correlating engine performance characteristics. Have you done any work in trying to include engine design characteristics so that many engines can be correlated together into one model?

Author's Reply

We have been successful in correlating characteristics of specific engine burners using the parameters described in the paper. We have not yet developed a unified parameter that would apply to a wide range of gas turbine engine burners.

J.Peters, US

In regard to the question of extending your correlations (particularly for ignition) of fuel effects to include different engines, I believe it can be done by including air mass flow rates and geometry with reference velocity and fuel injector effects with drop size correlations. This is illustrated for ignition, lean blowoff and combustion efficiency in Paper No.32

G.Winterfeld, Ge

The two parameters used, vaporization index VI and fuel characterization parameter, FPC, look quite similar, with the exception of the exponent of drop size. Can you comment on that difference in the two parameters?

Author's Reply

The fuel characterization parameter FCP, defined in equation (3), was formulated for predicting altitude ignition characteristics from the quenching distance relationship of Lefebvre and Ballal (reference 7). The value of $(SMD)^{1.5}$, which appears in their basic equation, has been maintained per se. The vaporization index VI, as defined in equation (1), was developed for groundstart ignition, combustion efficiency, pattern factor and lean blowout from a relationship relating droplet lifetime to the square of the droplet diameter. In the derivation, the single droplet diameter term was replaced with SMD for a droplet array and was normalized using the value of SMD for a reference fuel. Therefore, the expression for VI includes an SMD ratio rather than an absolute value (as in the expression for FCP), and the exponent of the ratio has been maintained as a square term. The exponential difference between 1.5 and 2 is small; however, the terms being raised to the different powers are quite different.

FUEL CHARACTER EFFECTS ON PERFORMANCE OF SMALL GAS TURBINE COMBUSTION SYSTEMS

P.Sampath (Chief, Combustion Aerodynamics)
M. Gratton (Aerodynamicist)
Pratt & Whitney Canada
Box 4080,
Mississauga,
Ontario L5A 3Z4

AD-P003 132

SUMMARY

The effects of potential broadened specification and alternate source jet fuels on the performance of small gas turbine combustors are presented. The review is based primarily on the results of a AFWAL/CDND/DRIE/P&WC* sponsored research program to evaluate the performance of a small 'can' combustor and two reverse-flow-annular combustors with fifteen different fuels. The fuels represented variations in several key characteristics such as hydrogen content, aromatics, viscosity, boiling range, volatility and thermal stability. Alternate source fuels included oil shale and tar sand derived fuels. Results of property changes on performance parameters of the 'can' combustor, such as life, starting and stability characteristics, exhaust emissions and smoking tendencies, are discussed.

NOMENCLATURE

A_C	Cross-sectional area of combustion liner
FN	Fuel nozzled Flow Number = $W_f / \sqrt{\Delta P_f}$
K, K_1	Empirical constants
K_2, K_3	
M_C	Air velocity parameter
P_3	Combustor inlet pressure
T_3	Combustor inlet temperature
T_f	Fuel temperature
V_C	Combustor volume
W_C	Combustor air mass flow
W_f	Fuel flow rate, pph
ΔP_f	Fuel nozzle pressure drop, psi
σ_f	Fuel surface tension
γ_f	Fuel kinematic viscosity
Q_C	Air loading parameter
SMD	Sauter Mean Diameter

INTRODUCTION

Almost all projections during the past decade have forecasted reduced availability and increased cost of petroleum crudes. There have recently been some surpluses in oil supply and reductions in oil prices, but the long term scenarios (1,2,3) still appear valid. These forecast continued decline in the world supply of high quality petroleum crudes and increasing demand for middle distillate petroleum fuels. On the aviation fuels scene, broadened specification fuels are being considered to ensure increased jet fuel yield from conventional sources and, in the long term, permit the use of jet fuels derived from oil shale and tar sands.

Accommodation of lower quality jet fuels will necessitate investigation of effects of fuel property variations on operation of gas turbine combustion systems. There is now a significant data base on the impact of fuel property changes on the performance of large gas turbine engines. These are in commercial and military applications (4-6) which mainly have straight through, highly loaded annular combustion systems. However most small aviation turbine engines used for helicopters, business jets, general aviation and auxiliary power units employ can and reverse-flow annular combustion systems of moderate loadings and relatively high surface to volume ratios.

Investigations on small combustion systems have recently been conducted by Pratt & Whitney Canada under partial sponsorship by U.S. Air Force Wright Aeronautical Laboratories (AFWAL) and the Canadian Department of National Defence (CDND). These investigations have aimed at identifying and quantifying the impact of fuel properties on performance of a can combustor and two reverse-flow annular combustors (PT6 and JT15D). Investigations have included simulated operation of combustors for typical turboprop and turbofan cycles and use of several types of fuel injectors. This paper summarizes results of investigations on the can combustor system using fifteen different fuels and four different fuel systems.

BACKGROUND

Economics and supply will play a major role in determining the source mix of future jet fuels. While petroleum will continue to be the major source of jet fuels in the near future, non-petroleum sources are expected to become an increasing part of the source mix, and in some countries or regions assume the role of major source by the turn of the century. Alternative fuels will initially be broadened specification petroleum-based to increase the yield of high grade fuel per barrel of crude. Eventually, jet fuel specifications will likely be adapted to production from a combination of petroleum and non-petroleum sources, subject to constraints imposed by engine designs and environmental impact.

---

* - Air Force Wright Aeronautical Laboratories/Canadian Department of National Defence/Department of Regional Industrial Expansion/Pratt and Whitney Canada.

Table 1 shows comparison of current Jet A and JP4 fuel specifications. Also shown are specifications by NASA for ERBS (Experimental Reference Broadened Specification) fuel with relaxations in aromatics/hydrogen content, flash point and freeze point limits.

Table 1: Comparison of Jet Fuel Specifications

	Jet A-1	JP4	ERBS
Aromatic content (% vol.)	22 (reportable 25)	25 max.	35 typical
Hydrogen content (% wt.)	13.5 typical	14.2 typical	12.8 ± .2
Flash point (K)	311 min.	-	311/321
Freeze point (K)	233 max.	222 max.	244 max.

Investigations on large engine combustion systems (4-6) have examined effects of property changes of the type shown in Table 1 on performance, emissions, and durability. The major fuel effects were identified as follows:
- Lower hydrogen to carbon ratio and higher aromatics result in increased smoke, carbon and heat load to liner walls
- Higher fuel bound nitrogen leads to higher nitrogen oxide emissions
- Higher viscosity adversely affects atomization and starting
- Lower volatility can affect starting and low power combustion efficiency
- Reduced thermal stability may lead to contamination of fuel systems

To determine the magnitude of fuel effects on small combustion systems, the fuels listed in Table 2 were used. Fuel blends with reduced hydrogen contents were obtained by blending base fuels (Jet A-1 and JT4) with high aromatic 2040 solvent. Shale JP8 (AFWAL supplied) was prepared from oil shale and has properties similar to Jet A-1; JP-10, the high energy fuel was supplied by AFWAL, ERBS-3 by NASA, and the four tar sand blends by CDND. The initial L or H for the tar sand fuels signifies low, or high final boiling point; the final L, M or H signifies a (relatively) low, medium or high hydrogen content. L-H blend is from a tar sand stock called "kerocut" with boiling range of boiling range of 473-573K, while the H-M, L-M and L-L fuels were produced by blending kerocut with gas oil side stream having boiling range of 473-623K. The final blend was between JP4, diesel and 2040 producing fuel with 13.01% hydrogen content.

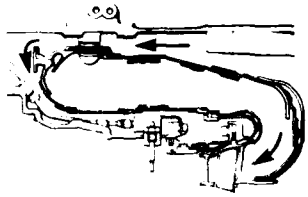
Table 2: Properties of Test Fuels

Fuel		Hydrogen wt. % (ASTM D3701)	Aromatics vol. % (ASTM D1319)	Naphthalene Content % vol. (ASTM D1840)	Kinematic Viscosity (cSt) @ 294K (ASTM D445)	Surface Tension (Dynes/cm) @ 298K (Capillary)	Distillation Range (K) (ASTM D86)	Net Heating Value (MJ/kg) (ASTM D1405)
Jet A-1	○	13.76	19.7	0.7	1.65	25.4	442-517	43.17
Jet A-1/B1	◑	12.88	30.2	9.2	1.62	26.2	446-539	42.80
Jet A-1/B2	◐	12.04	41.7	17.3	1.70	27.0	447-545	42.47
Shale JP8	●	13.82	21.1	0.6	1.70	25.1	448-521	43.20
JP4	□	14.2	14.5	0.3	1.00	22.5	334-492	43.46
JP4/B1	◨	12.86	30.2	11.0	1.07	24.1	337-536	42.85
JP4/B2	◧	11.93	42.5	17.6	1.18	23.9	331-541	42.47
JP4/2040/Diesel	■	13.01	28.3	10.7	1.60	23.4	341-602	42.94
ERBS-3	▽	12.95	29.1	12.5	2.55	27.2	460-602	43.07
Diesel	▽	13.05	31.9	7.8	4.53	26.3	464-619	43.21
JP10	▼	11.88	0	0	3.26	32.1	451-468	42.81
Tar Sands L-H	▲	13.38	29.1	1.0	2.55	26.4	444-556	42.93
Tar Sands L-M	▲	13.17	37.2	1.3	2.53	26.6	447-561	42.84
Tar Sands H-M	▲	13.21	33.4	1.7	2.77	26.8	445-584	42.80
Tar Sands L-L	△	13.03	41.8	1.6	2.67	26.2	455-558	42.70

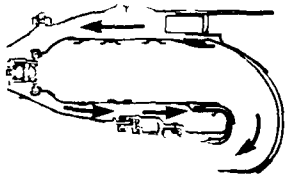
Over a thousand tests were conducted with a can combustion system using the above fifteen fuels. Detailed results of the test activity are contained in Reference 7; the paper gives a summary review of significant fuel effects on the performance of the can combustion system.

COMBUSTION SYSTEM

Bulk of published data on fuel property effects pertains to large engine combustion systems (4-6). Although some of the trends can be expected to be similar, there are significant geometric and aerodynamic differences which may cause small engine combustion systems to react differently to fuel property changes. Most small gas turbine engines are equipped with centrifugal compressor stages, to which reverse-flow (or folded) annular combustors are more suited, Figure 1. The relatively high surface to volume ratios encountered in reverse-flow configurations require larger amounts of liner cooling air than for axial-flow annular combustors common with large engines. Also, cost and weight constraints generally lead to simple fuel injection systems, which render high combustion efficiencies at low power more difficult to attain. The lower idle combustion efficiencies substantially increase the amounts of CO and THC emissions. Furthermore, fuel nozzle contamination and blockage may result due to the small orifices involved, especially when lower grades of fuel are being used, and these may affect the quality of exit temperature distribution. Also, the folded transition duct between the combustor and the turbine inlet vane further complicates the tailoring of combustor exit gas temperatures because of the sudden contraction of flow area.



PT6A-60/65-turboprop



JT15D turbofan

Fig. 1: Typical Small Engine Combustors

Three types of combustors were chosen for the study: can combustor, PT6 and JT15D. The first phase of the program involved tests with the can combustor which enabled a cost effective and relatively rapid investigation of performance over a wide range of operating parameters. The can combustor was approximately 8 cm in diameter and 15 cm long with four cooling louvres located one each in the primary and intermediate zones, and two in the dilution zone, Fig. 2. A single fuel nozzle was mounted axially at the combustor head where tangential entry holes provided swirling air to the primary zone. Four types of nozzles were tested with the can combustor to study the effects of fuel preparation (Figure 3); the simplex and duplex nozzles were pressure atomizers which use the fuel pressure drop to atomize the liquid into a fine spray. The airblast nozzle utilizes the energy of air flowing through the nozzle core to shear the relatively slow moving fuel into very small droplets. The vaporizing nozzle is a simple tube in the combustor, which allows transfer of thermal energy from the hot primary zone gases to the incoming fuel, thereby creating a rich vapor which enters the combustor through a small swirler and a mushroom shaped outlet.

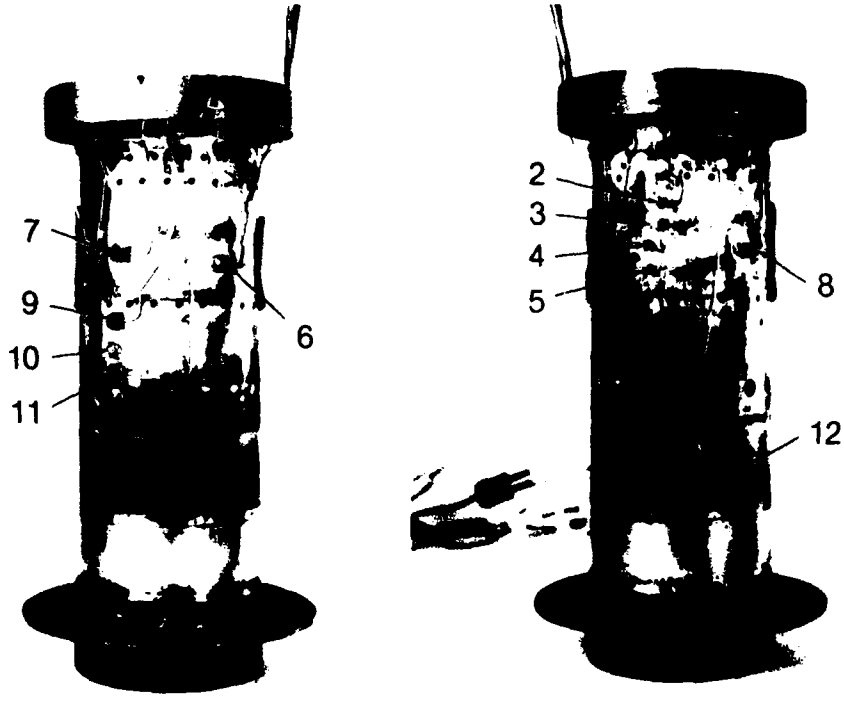


Fig. 2: Can Combustor System Showing Liner Thermocouple Locations

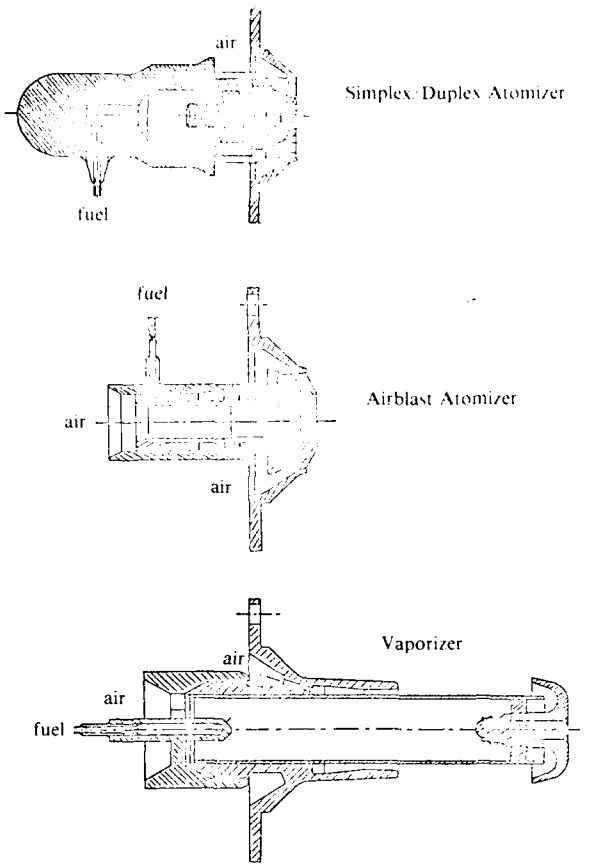


Fig. 3: Fuel Nozzles Used in Can Combustor Tests

The second phase of the test program evaluated PT6 and JT15D combustion systems. The PT6A-65 combustor, used in small turboprop engines (1020 KW), is designed for 10:1 pressure ratio and 1310K turbine inlet temperature (TIT). The JT15D-5 combustor, used in small turbofan engines (12.9 KN thrust), is rated at 12.1:1 pressure ratio and 1254K TIT. The geometrical characteristics of the three combustors are tabulated in Table 3. Table 4 summarizes the tests conducted on the three combustion systems.

Table 3: Geometrical Characteristics of Combustion Systems

	Can combustor	PT6A-65 combustor	JT15D-5 combustor
Surface-to-volume ratio (m^{-1})	67	57.2	39
Combustor loading (SLTO) ($W/m^3/Pa$)	573* 337**	584	445
Pressure drop (P/P) %	2.5	2.4	2.5
Number of nozzles	1	14	12

* 100% Thrust Simulation (JT15D)
** 100% Power Simulation (PT6)

Table 4: Types of Combustion Tests

	Pressure effect	Fuel nozzle effects	Stoichiometry changes	Liner temperatures	Gaseous emissions	Smoke emissions	Carbon deposition	Nozzle coking	Idle stability	Cold starts	Flame radiation	Exit temp. distribution	Fuels tested
Can combustor tests	X	X	X	X	X	X	X	X	X	X			15
JT15D-5 combustor tests		X	X	X	X	X		X			X		4
PT6A-65 combustor tests	X	X	X	X	X	X		X	X		X		10

Figure 4 shows a cross section of the can combustor rig. Combustion efficiency, gaseous emissions and smoke were monitored with a multi-point sampling probe in the exit plane of the combustor. The quartz window at the back end of the rig provided direct observation of flame behaviour both during steady state and transient performance tests. A transpiration radiometer probe was used to measure primary zone flame radiation (8). Combustor metal temperatures were measured with twelve thermocouples, locations of which were determined by thermal paint tests at the beginning of the test program.

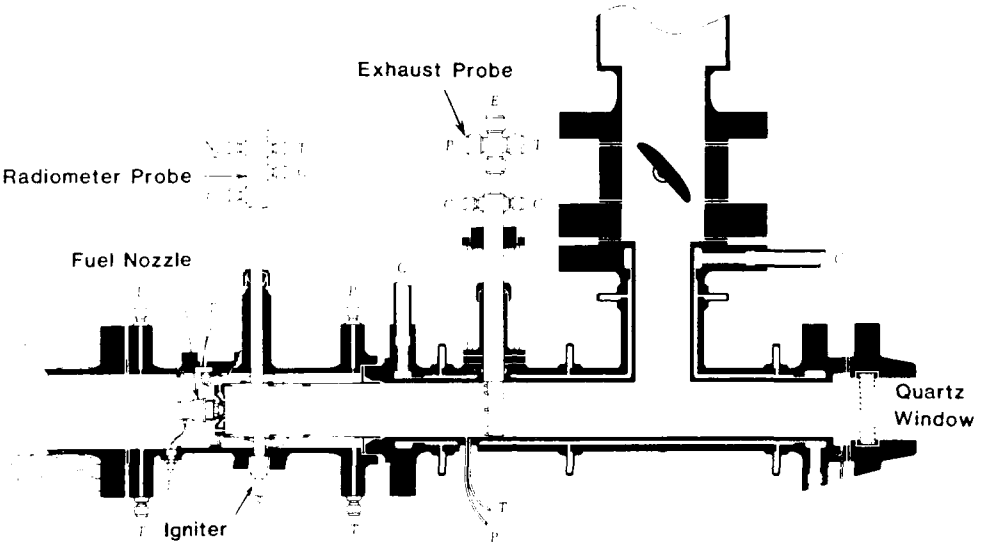


Fig. 4: Can Combustor Rig Test Section Assembly

To accommodate the geometrical differences between the can combustor and the reverse-flow (PT6 and JT15D) combustors, two modelling parameters were used to define the can combustor rig air flows which simulated actual conditions on the full engine. The "air loading parameter" simulated emissions at low power and the "air velocity parameter" simulated general performance at high power. These parameters are defined as follows:

"air loading parameter" $$\Omega_C = \frac{K_1 W_C}{P_3^{1.8} e^{T_3/K_2} V_C}$$

"air velocity parameter" $$M_C = \frac{K_3 W_C \sqrt{T_3}}{P_3 A_C}$$

Thus the air mass flow for the can combustor rig tests was determined from the modelling parameters, while inlet pressure, temperature, and overall fuel-air ratio were kept the same as in the engine. Fuel flows were adjusted according to the net heating value of the test fuel relative to that of Jet A-1.

Steady-state performance tests were performed simulating five conditions on the turbofan (JT15D) cycle and three conditions on the turboprop (PT6) cycle. At each condition gaseous emissions, smoke and liner skin temperatures were measured. Lean-limit tests were performed at four airflows bracketed around a (JT15D) ground idle condition, while ignition tests were performed at an airflow simulating engine cranking speed and temperatures (air and fuel) between 289 K (520° R) and 241 K (435° R). Additional parametric tests were performed with four types of nozzles to evaluate the effects of inlet pressure and fuel-air ratio on gaseous emissions, smoke, liner skin termperatures, and flame radiation.

IMPACTS OF FUEL PROPERTY CHANGES

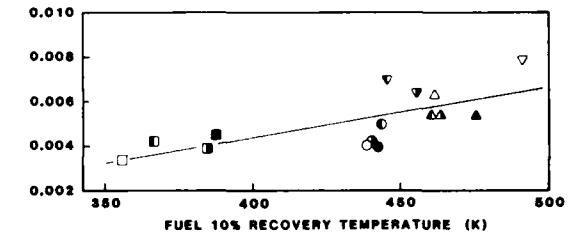
Liner stability: Figure 5 shows the impact of fuel properties on lean blow-off limits at air flows corresponding to idle condition. The test data have been presented under four groups: Jet A-1 (○), JP4 (□), Diesel (▽) and Tar Sands (△), Table 2. There is a fairly strong relationship between lean blow-off limits and volatility of the fuels, expressed as 10% recovery temperature (T10); this behaviour can be attributed to slower vaporization of higher boiling range fuels rendering them more unstable at equivalent fuel flows. However between Jet A-1, JP4 fuels and their blends, there are only small stability changes. The relationship of lean blow-off limit with hydrogen content shows a lot of scatter indicating other properties playing a role; by far the best correlation is with respect to relative droplet size of the atomizer, defined as SMD/SMD JP4 where,

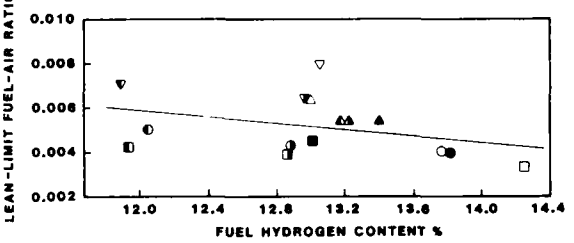
$$SMD = \frac{K\ \sigma_f^{.8} \vartheta_f^{.2} W_f^{.25}}{\Delta P_f^{.4}}$$

shows a strong correlating effect of fuel properties through their influence on fuel droplet size. Thus fuel viscosity, overall effect lean blow-off limits. Tests with an airblast injector showed similar trends with fuel properties, blow-off limits were considerably higher, i.e. the combustor was less stable. The lean blow-off limit is normally of excess heat from the combustion process to achieve adequate evaporation and initial pyrolysis of the residence time is not adequate for completion of the combustion process. Since both the fuel composition atomization and evaporation, variation in stability limits seen in these results in not surprising.

Ignition Performance: The ignition characteristics are critically influenced by evaporation of the fuel producing a local fuel-air mixture capable of immediate ignition and sustained combustion. The factors that can be expected to affect ignition include pressure and temperature of inlet air, fuel temperature which affects density and viscosity, and fuel properties influencing volatility, i.e. distillation temperature distribution. Ignition performance can be characterized by the minimum light-off temperature, minimum light-off fuel-air ratio and time to light.

Table 5 and Figures 6-7 describe light-off characteristics as a function of relative fuel properties, for two pressure atomizing nozzles. In the case of the fine (0.9 FN) injector, satisfactory ignition was demonstrated down to rig limited temperature of 242K (435°R); however both the minimum light-off fuel-air ratio and time to light were affected by fuel properties, Figure 6. The more significant effect appears to be with time-to-light. Table 5 and Figure 7 show light-off performance with the coarse (3.0 FN) fuel nozzle, strong dependence being apparent on volatility, relative droplet size and only poor correlation with hydrogen content. The data provides evidence of the significance of atomization characteristics and properties affecting vaporization of the fuel.





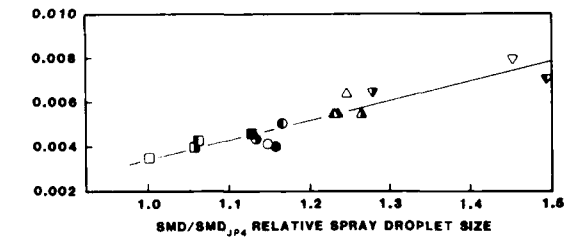
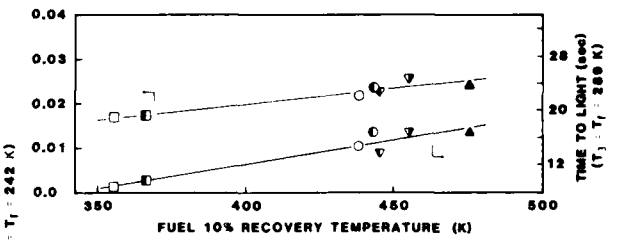
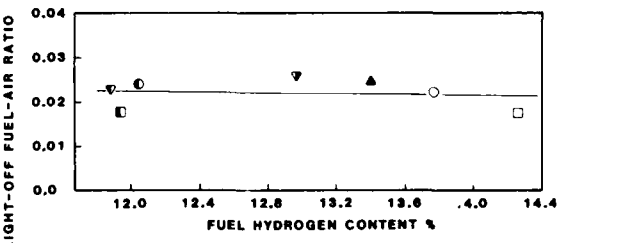


Fig. 5: Impact of Fuel Properties on Lean Stability Limits





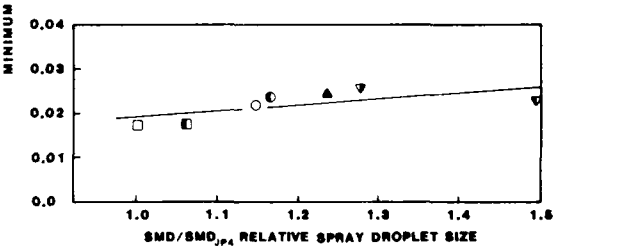


Fig. 6: Impact of Fuel Properties on Starting Characteristics (0.9 FN Nozzle)

Table 5: Minimum Light-Off Temperatures (W_a = 0.023 kg/sec; Max. W_f = 5.4 kg/hr.)

Fuel	Injector 1 0.9 FN pressure atomizing K (°R)	Injector 2 3.0 FN pressure atomizing K (°R)
Jet A-1	< 242 (435)	261 (470)
Jet A-1/B2	< 242 (435)	269 (485)
JP4	< 242 (435)	< 242 (435)
JP4/B2	< 242 (435)	261 (470)
Tar Sands (L-H)	< 242 (435)	276 (497)
ERBS-3	< 242 (435)	265 (477)
JP10	< 242 (435)	> 288 (520)

Combustion Efficiency and Gaseous Emissions: Steady state combustor performance was measured during operation simulating turboprop (PT6) and turbofan (JT15D) cycles and typical test data are shown in Figures 8-11. Both CO and THC emissions were affected by fuel changes, impact apparently of differences in atomization and evaporation of the fuel. Figure 8 shows impact of fuel properties on combustion efficiency while simulating idle condition on the turboprop cycle. In spite of considerable scatter, trends are toward lower combustion efficiency with reduced hydrogen content and volatility. However, there is a relatively strong correlation between combustion efficiency and relative droplet size of the pressure atomizer, indicating strong effect of fuel viscosity and surface tension.

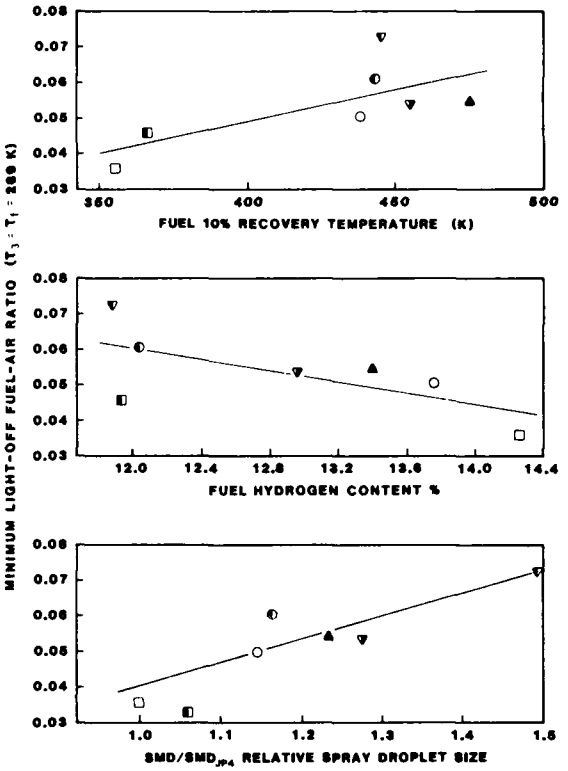


Fig. 7: Impact of Fuel Properties on Starting Characteristics (3.0 FN Nozzles)

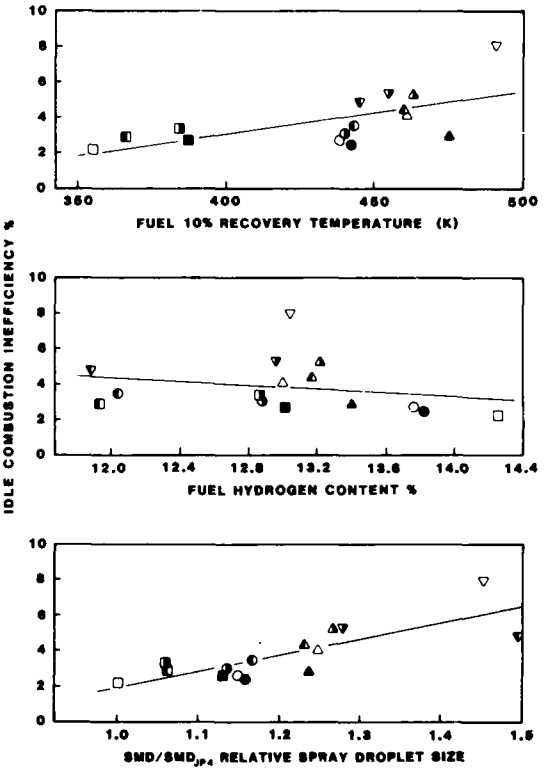


Fig. 8: Impact of Fuel Properties on Idle Combustion Ineffciency

In general, the emission index of THC at idle revealed poorest correlation with hydrogen content; however better correlations were observed at higher power simulations, Figure 9. This indicates a major role of atomization and mixing on THC and CO emissions. At higher operating pressures, such mixing is more easily achieved and changes in THC and CO emissions are then purely a function of fuel chemistry. Figure 9 also shows the impact of injector geometry, the poorly optimized vaporizer showing relatively high THC and CO emissions.

Figures 10 and 11 show impact of fuel properties on NO_X emissions at take-off and idle respectively. Published data reveal a sensitivity of NO_X emissions to the fuel composition, the emissions generally increasing with reduction in the hydrogen content of the fuel. This trend suggests that the increased flame temperature with reduced hydrogen content is the governing mechanism. Test data from the present program however indicate that take-off NO_X emissions with a pressure atomizer are largely insensitive to fuel properties, Figure 10. Idle NO_X emissions, Figure 11, decrease with reduction in hydrogen content, which is probably the impact of lower reaction zone temperatures resulting from decreased combustion efficiencies at idle. Comparison of fuel nozzles showed no consistent NO_X trends with hydrogen content. Data from other engines however indicates that the trends are influenced by combustor design; for example, J85 combustion systems with pressure atomizers appear to show only a poor dependence of NO_X emissions with hydrogen content, where as the F101 combustion system with airblast atomizers has a much stronger influence of hydrogen content (6).

Smoke Emissions: Most published literature on broadened specification fuels reports an increase in the smoke levels when fuel hydrogen content is decreased. However there are differences as to whether hydrogen content is an adequate parameter for correlating smoke forming tendency of a fuel (3).

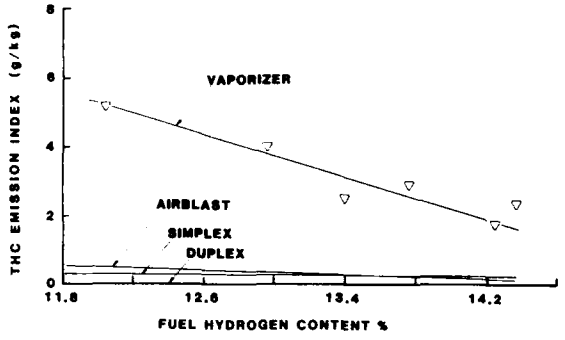


Fig. 9: Impact of Fuel Hydrogen Content and Injector Types on HC and CO Emissions (60% thrust simulation)

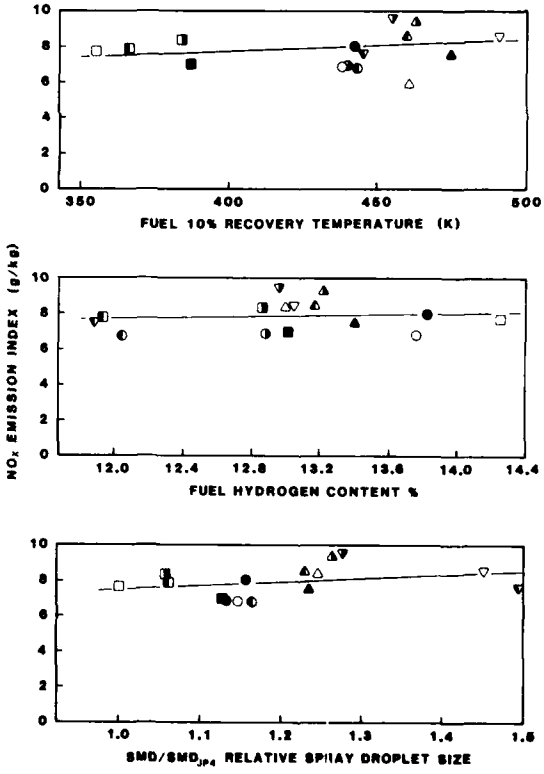


Fig. 10: Impact of Fuel Properties on NO_X Emissions at Simulated Take-off Condition

Figure 12 shows variation of measured smoke number at take-off using the pressure atomizer; while the general trend indicates increased smoke as hydrogen content is decreased and aromatic content is increased, there is considerable scatter in the data. Further analysis indicates possible impact of naphthalene content; with Jet A-1 and JP4 fuels,, the addition of 2040 solvent raises both aromatic and naphthalene contents (Table 2) and results in a strong increase in smoke level. However, fuels such as L-H, H-M and L-M tar sands have a relatively low naphthalene content accompanying moderately high aromatic content, and these fuels seem to result in smoke level increases less severe than with Jet A-1 and JP4 blends. Similarly ERBS-3 fuel with higher than average naphthalene content appears to result in higher smoke emissions. These results appear to indicate the types as well as overall levels of aromatics are significant, and that the presence of high concentrations of more complex multi-ring aromatic compounds may increase the propensity for smoke formation.

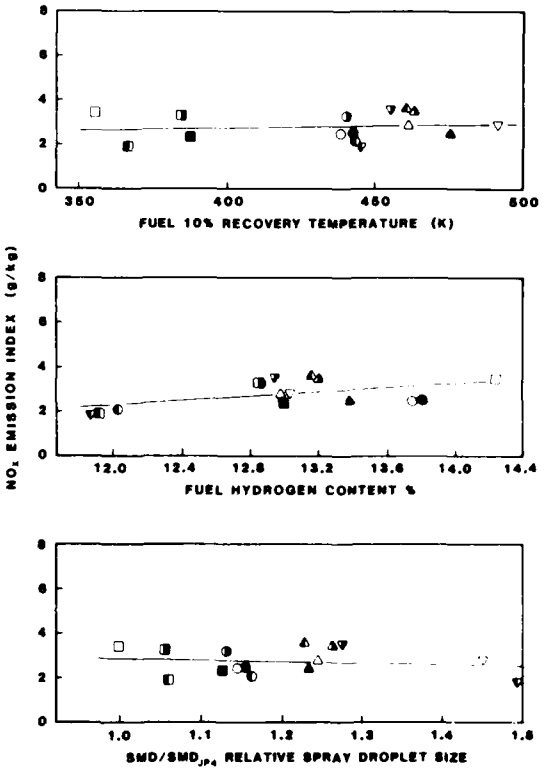


Fig. 11: Impact of Fuel Properties on NO_x Emissions at Simulated Idle Condition

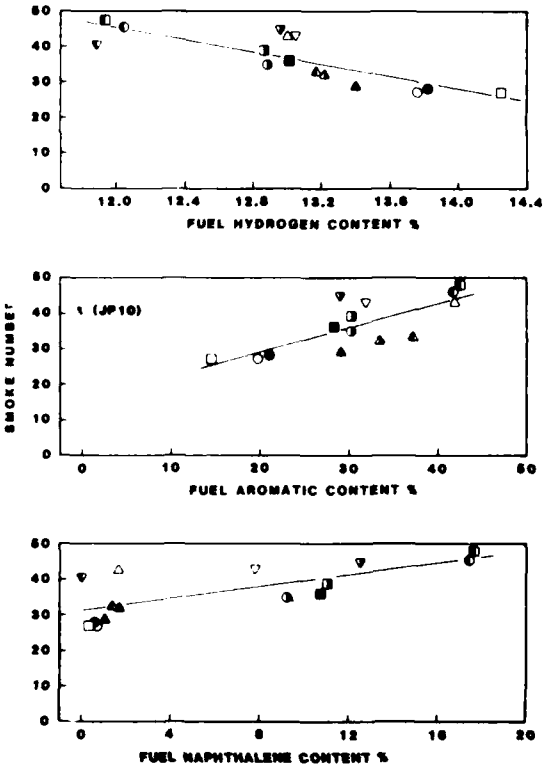


Fig. 12: Impact of Fuel Properties on Smoke Emissions at Simulated Take-off Condition

Figure 13 shows the effect of fuel injector type on smoke emissions. Airblast and vaporizer nozzles result not only in lower smoke emissions, but also appear to be less sensitive to hydrogen content. These trends are consistent with other published data comparing performance of airblast and pressure atomizing combustion systems (6).

Radiation and Liner Metal Temperatures: To evaluate the effect of fuel properties on radiation, measurements of radiation heat flux were made at two pressure levels using a transpiration radiometer. Figure 14 shows radiant heat flux as a function of fuel hydrogen content and relative droplet size of a pressure atomizer. Good correlations are apparent with hydrogen content and droplet ratios at high pressure, whereas at lower pressures relative droplet size has little effect on radiation levels.

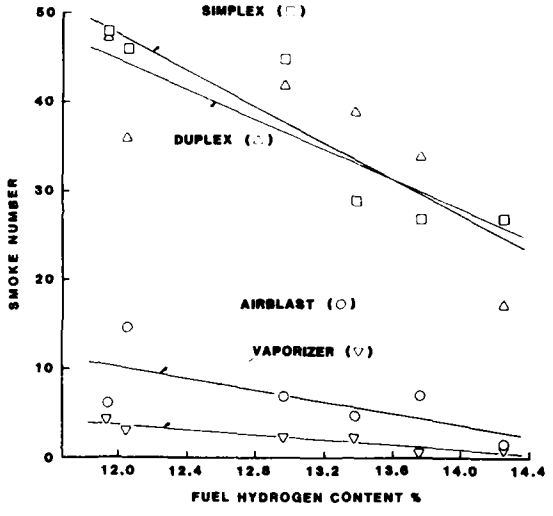


Fig. 13: Influence of Fuel Hydrogen Content and Injector Designs on Smoke Emissions

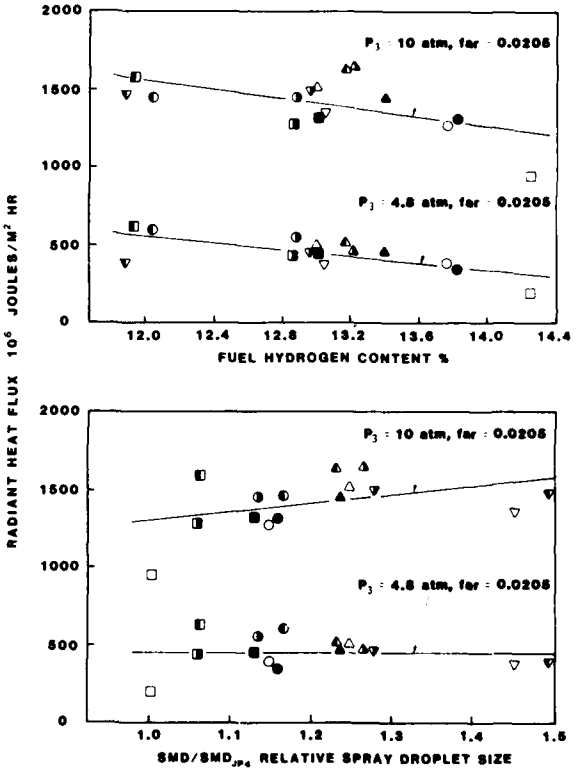


Fig. 14: Impact of Fuel Properties on Radiant Heat Loads

Liner temperature measurements were obtained with 12 thermocouples located on the cold side of the liner. The liner temperatures, in general, showed wide variations from test to test, apparently in a random manner. For example, while some liner temperatures appeared to increase with decreasing hydrogen content at some power settings, the reverse occurred at other power levels. These effects are thought to be the result of local fuel-air ratios and flame front locations being influenced by fuel properties and operating conditions. Figure 15 shows impact of fuel properties on average liner temperatures expressed as $\left(\frac{T_L - T_{LJP4}}{T_{LJP4} - T_3}\right)$. Although the data show considerable scatter, the general trends indicate substantial increase in metal termperatures as the fuel hydrogen content is reduced, due mainly to increases in radiation levels. Also shown for comparative purposes are the engine correlations by Blazowski (9), the dashed lines encompassing data from five combustors. It does appear from this comparison that there is good correlation between fuel hydrogen content and liner metal temperature. There is also reasonable correlation with fuel aromatic content, although the purely synthetic JP-10 fuel with no aromatics results in metal temperatures much higher than petroleum based fuels.

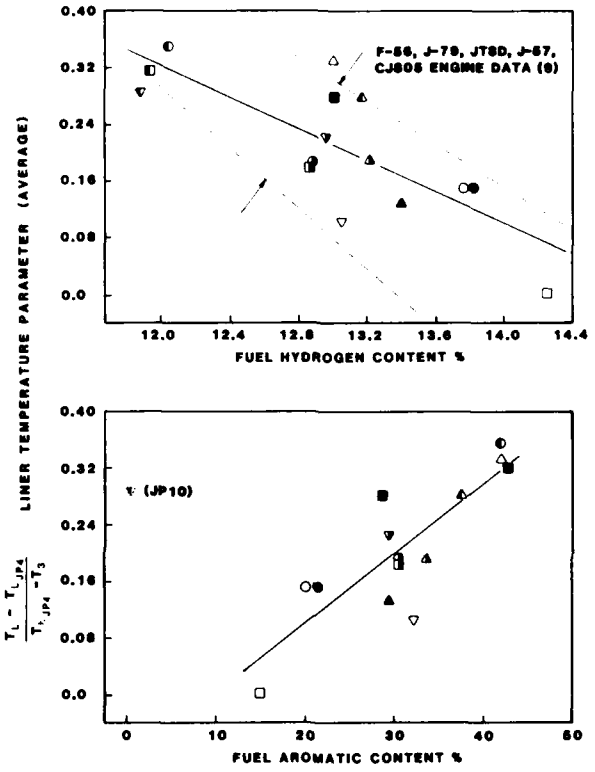


Fig. 15: Impact of Fuel Properties on Average Liner Temperatures

The following Table shows correlation coefficients describing impact of fuel properties on the above descussed parameters.

Table 6: Influence Coefficients Corresponding to Observed Fuel Property Effects

Combustion parameter (Y)	Fuel property parameter (X)	Linear regression equation	Reference figure
Lean limit fuel air ratio	10% distillation temp. (K)	$Y = 2.24 \times 10^{-5} X - .0046$	5
Lean limit fuel air ratio	Hydrogen content (%)	$Y = 0.0247 - .00148 X$	5
Lean limit fuel air ratio	Relative SMD	$Y = 0.00886 X - .0055$	
Minimum light-off fuel air ratio ($T_f = T_3 = 241K$)	10% distillation temp. (K)	$Y = 6.85 \times 10^{-5} X - .0073$	6
Minimum light-off fuel air ratio ($T_f = T_3 = 241K$)	Hydrogen content (%)	$Y = 0.0289 - .00055 X$	6
Minimum light-off fuel air ratio ($T_f = T_3 = 241K$)	Relative SMD	$Y = 0.0135 X - .0055$	6
Time to light (secs)	10% distillation temp. (K)	$Y = 0.0704 X - 15.8$	6
Idle inefficiency (%)	10% distillation temp. (K)	$Y = 0.0235 X - 6.4$	8
Idle inefficiency (%)	Hydrogen content (%)	$Y = 11.14 - 0.565 X$	8
Idle inefficiency (%)	Relative SMD	$Y = 9.10 X - 7.16$	8
EI - NO_x take-off (g/kg fuel)	10% distillation temp. (K)	$Y = 5.30 + 0.0060 X$	10
EI - NO_x take-off (g/kg fuel)	Hydrogen content (%)	$Y = 5.98 + 0.154 X$	10
EI - NO_x take-off (g/kg fuel)	Relative SMD	$Y = 5.55 + 1.96 X$	10
Smoke (SN)	Hydrogen content (%)	$Y = 14.6 - 8.33 X$	12
Liner temperature parameter	Hydrogen content (%)	$Y = 0.336 - 0.0189 X$	15

CONCLUSIONS

Fuel properties such as volatility, viscosity and hydrogen content have significant impact on the performance of the small gas turbine can combustor tested. The effects are also influenced by the type and performance of the fuel injection system. Investigations using fifteen different fuels and four different injector types showed the following effects.

- Lean blow out stability is strongly influenced by fuel hydrogen content and by spray quality. Volatility effects are mixed: for JP4 based fuels volatility appears to have little influence on lean blow out performance, whereas for other fuels volatility has a stronger effect. Airblast and vaporizer nozzles have worse lean blow out limits than pressure atomizing nozzles.

- Ignition performance expressed as minimum light off fuel-air ratio and minimum light up temperature is strongly influenced by volatility and by properties affecting fuel atomization. Fuel hydrogen content appears to have a weak influence on light-up characteristics.

- Steady state performance tests indicate that low end combustion efficiencies are significantly influenced by fuel properties; CO emissions are strongly influenced by fuel hydrogen content but do not correlate well with relative droplet size and volatility; THC emissions are strongly influenced by fuel hydrogen content and relative droplet size. Fuel effects on NO_x emissions at take-off are small and within range of repeatability; idle NO_x emissions appear to be influenced by combustion efficiency which affects reaction zone temperatures. Smoke levels are strongly influenced by fuel hydrogen content, aromatic content and atomizer design. The nature of the aromatics appears to influence smoke emissions as well.

- Radiation heat loads and liner temperatures are strongly influenced by fuel hydrogen content and by properties affecting fuel atomization characteristics.

ACKNOWLEDGEMENTS

The investigation benefitted from the valuable contributions of several people at P&WC, including Messrs. J.A. Saintsbury and F.J. Allan of the Combustion group. The authors also wish to acknowledge the support of Mr. R. Bradley, AFWAL and Dr. J. Coleman, CDND who were the project administrators.

REFERENCES

1. Grobman, J., Reck, G.M., "The Impact of Fuels on Aircraft Technology Through the Year 2000", AIAA-80-0896, May 1980.
2. Saintsbury, J.A., Sampath, P., "The Potential Impact of Future Fuels on Small Gas Turbine Engines". 82-GT-133, American Society of Mechanical Engineers, 1982.
3. Longwell, J.P., Grobman, J., "Alternative Aircraft Fuels". 78-FT-59, American Society of Mechanical Engineers, April 1978.
4. Jackson, T.A., "The Evaluation of Fuel Property Effects in Air Force Gas Turbine Engines - Program Genesis", ASME Gas Turbine Conference, March 1981.
5. Lohmann, R.P., Szetela, E.J. , Vranos, A., "Analytical Evaluation of the Impact of Broad Specification Fuels on High Bypass Turbofan Engine Combustors". NASA CR-159454, December 1978.
6. Bahr, D.W., "Impacts of Broadened Specification Fuels on Aircraft Turbine Engine Combustors", 81-GT-2, American Society of Mechanical Engineers, March 1981.
7. "Alternate Fuels Combustion Research - Phase II Interim Report", Pratt and Whitney Canada, AFWAL, CDND, 1983.
8. Moffat, R.J., Hunn, B.D., Ayers, J.F., "Development of a Transpiration Radiometer", Trans. Instrument Society of America, v. 9, 1971.
9. Blazowski, W.S., "Combustion Considerations for Future Jet Fuels", Proceedings of Sixteenth International Symposium on Combustion, August 1976.

DISCUSSION

K.A.Collin

Can you say what fuel pressure you need for the vaporizer?

Author's Reply

Since a vaporizer does not depend on atomization of fuel, the device can be operated with a relatively small pressure drop at the final orifice. The device used in the present programme had a characteristic resulting in a fuel flow (lb/hr) of approximately 4 times the fuel pressure drop in p.s.i., which was in the order of 0.5 psi.

AD-P003 133

U.S. ARMY ALTERNATIVE GAS-TURBINE FUELS RESEARCH: MERADCOM

Dr. C. A. Moses
Southwest Research Institute
San Antonio, Texas USA

ABSTRACT

The U.S. Army's alternate fuels program is the responsibility of the Mobility Equipment Research and Development Command (MERADCOM). The research program on the effects of alternative fuels on gas turbine engine combustion is reviewed. Experimental programs have primarily concentrated on two areas of changing fuel properties; one, the effects of volatility on combustor performance characteristics such as ignition and combustion efficiency; and, two, the effects of changing fuel chemistry on soot formation and flame radiation.

Introduction

Uncertainties about future production and supply of petroleum products have caused the U.S. Army, as well as other organizations responsible for fuel logistics and specifications, to study, in depth, the problems of combustion and engine performance and durability which are associated with fuel properties. The overall objectives of these studies are to develop the data and understanding necessary to consider the following options:

- o Relaxing fuel specifications to increase availability
- o Use of non-petroleum crude stocks to make "synthetic fuels"
- o Temporary use of non-specification fuels in emergency situations.

Further goals are the development of design guidelines for engines which are more fuel tolerant, and the development of prophetic reference fuels to be used in the specification and qualification of power plants. The Army has these concerns for all three major engine types: spark ignition, compression ignition, and gas turbine; only the gas turbine engine and fuels will be addressed here.

The Mobility Equipment Research and Development Command (MERADCOM) has the responsibility within the U.S. Army for fuel specifications and R&D support for fuel-related field problems. However, the only mobility fuels for which MERADCOM has responsibility are gasoline and diesel fuel; the primary fuel for Army aircraft is JP4 (NATO F-40) which is the responsibility of the U.S. Air Force. Recognizing that the Army has a large inventory of gas turbine engines in its helicopter fleet, and having encountered some fuel-related field problems in Vietnam, MERADCOM has established a turbine-fuels research combustor laboratory at its Army Fuels and Lubricants Research Laboratory (AFLRL) located at Southwest Research Institute (SwRI). This facility enables the Army to conduct in-house research on combustor performance and durability problems which are related to fuel properties and to assist in the development and testing of new fuel concepts. The laboratory became operational in 1974 and has been used in a continuous sequence of programs to study ignition, flame stabilization, combustion efficiency, flame radiation, exhaust smoke, and gaseous emissions. The scope of fuels has included specification, alternative, and emergency fuels including synthetic fuels, alcohols and emulsified fuels.

To attain maximum flexibility for fuels/combustion research, the facility was designed as an air-factory to provide appropriate inlet conditions for the combustor being used. Conceptually any combustor can be plugged in and operated within the air flow, pressure, and temperature capabilities of the system. The operating envelope is as follows:

Air flow	0 to 1.1 kg/sec	(0 to 2.5 lb/sec)
Air pressure	100 to 1600 kPa	(1 to 16 atm)
Air temperature (heated)	150° to 800°C	(300° to 1500°F)
Air temperature (cooled)	-54°C to Ambient	(-65°F to Ambient)

Three combustor rigs are currently available.

- o T63
- o 2-inch
- o Disc-in-duct

The T63 combustor is fabricated from T63 engine hardware. As illustrated in Figure 1, it is a single-can combustor with a dual-orifice pressure atomizer that is instrumented for flame radiation, liner temperatures, and exhaust emissions. Optical access is provided to view and photograph the combustion event. This combustor is especially useful in studying ignition, combustion efficiency, flame stabilization, and exhaust emissions; it also provides a means of verifying the results from the 2-inch research combustor on flame radiation and smoke. Turbine blade erosion and corrosion studies are also possible in this T63 combustor rig.

The 2-inch research combustor is a high-temperature, high-pressure combustor copied from the Phillips 2-inch combustor. Figure 2 shows the essential design features including the windows. It is capable of operating with burner inlet air temperatures up to 800°C at pressures up to 160 kPa and over a wide range of fuel/air ratio and reference velocity. This combustor is primarily used for flame radiation studies under high-pressure conditions. It can also be used for turbine blade erosion and corrosion studies.

The disc-in-duct combustor illustrated in Figure 3 is also a research combustor. Its main purpose is to simulate the primary zone of a real combustor and provide optical access to study ignition and atomization. Forward light-scattering techniques have been developed to measure drop-size distributions of evaporating fuel sprays.

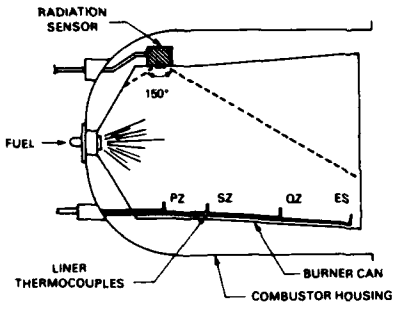


FIGURE 1. T63 ENGINE COMBUSTOR

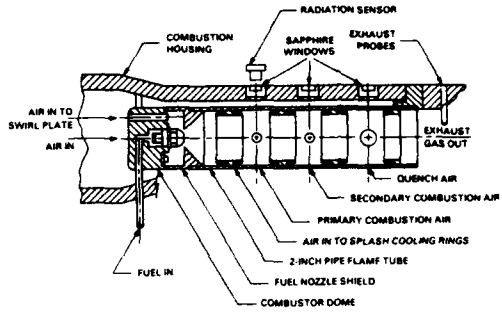


FIGURE 2. PHILLIPS 2-INCH COMBUSTOR

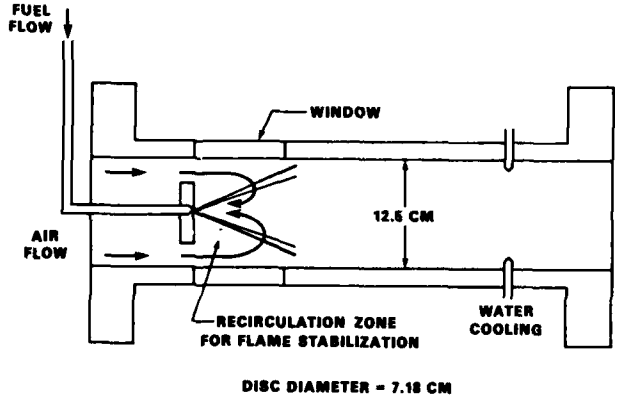


FIGURE 3. DISC-IN-DUCT COMBUSTOR

Future Fuels for Turbine Engines

Fuel properties of specification fuels can be expected to change for three reasons:

1. a relaxation of certain fuel property specifications which currently limit production in some producing regions
2. changes in refining procedures to upgrade lower-quality crude oils, generally higher in aromatics and sulfur, and to crack heavier crude stocks into light and middle distillate products
3. use of synfuels converted from shale oil and tar sands.

The use of non-specification fuels in emergencies as mentioned previously would most likely imply the use of diesel fuel or fuel oil either straight or as blending stock to extend jet-fuel supplies.

A number of studies have been reported in the literature on changing crude sources and refining trends and their impact on future gas turbine fuels (e.g., 1-3). Generally speaking, petroleum crudes will require more extensive use of mild hydrotreating to remove sulfur, and of hydrogenation to reduce aromatics and/or increase hydrogen content. Also there will be an increasing trend towards hydrocracking heavier fractions to increase the supply of middle and light distillate products. Hydrocracking and hydrogenation will also be used to make distillate from shale oil and tar sands.

The major impact of mild hydrotreating is fuel cost. More severe hydrotreating reduces the lubricity of the fuel as aromatics are saturated, and undefined contaminants, which also add to natural lubricity, are removed. Hydrocracked kerosene is distinguished by significant increases in naphthenes and in tetralin, decalin, and other multi-ring compounds as naphthalenes become saturated. Fuels from shale oil and tar sands appear to be similar to hydrocracked kerosene in that relatively large concentrations of tetralin and perhaps decalin are expected depending on the degree of hydrogenation. The presence of tetralin and decalin in the fuel leads to the formation of peroxides in the fuel, which can lower the stability of the fuel and cause problems with certain elastomers. Other contaminants found in shale oil, especially nitrogen, also reduce stability.

Emergency fuels, such as diesel fuel or blends of diesel fuel with aviation fuel, can be characterized primarily as having a higher end-point and viscosity, a higher freeze point, lower thermal stability, and lower volatility. Data are presented in Figure 4 for blends of JP5 and two different DFM's to illustrate the potential impact on thermal stability, viscosity, and final boiling point.[4] Other possibly significant degradations in the quality of emergency fuels are reduced hydrogen content, increased aromatics, and increased naphthalenes.

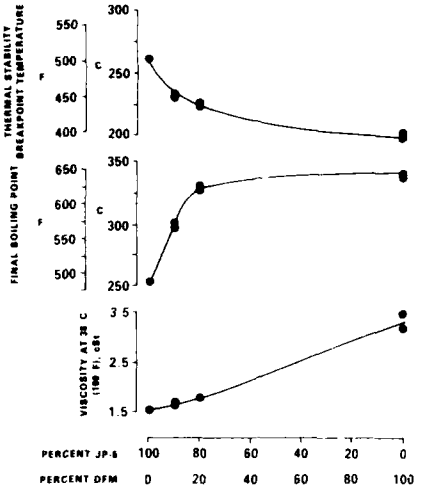


FIGURE 4. EFFECTS OF BLENDING DFM INTO JP-5

Impact of Future Fuels on Vehicle Systems

Table I summarizes the initial fuel properties identified above and identifies the area of impact in the performance and durability of vehicle fuel systems and engines. Only three of the properties, hydrogen content, viscosity, and boiling point distribution directly affect combustion and will be the subject of the remainder of this paper.

Table I. Summary of Critical Fuel Properties and Their Impact on Aircraft Systems

Fuel Property	Impact Area	Performance/Durability Problem
Reduced hydrogen content	Soot formation	Combustor liner durability Exhaust smoke
Hydrocarbon composition Contaminants	Materials compatibility	O rings, seals, and diaphragms in valves, fuel controls, etc.
Lubricity	Wear	Fuel pumps and controls
Thermal stability	Hot fuel deposits	Flow-divider valves Fuel atomizers
Viscosity and boiling-point distribution	Atomization and fuel/air mixing	Cold-day ignition Altitude relight Combustion efficiency Gaseous emissions

For convenience, the following technical discussion is organized according to problem areas rather than by fuel properties. The discussion is a summary of several studies conducted in the AFLRL combustor lab on fuel properties and their impact on turbine combustion; these studies were either conducted for MERADCOM or sponsored by the Navy, Air Force, or NASA with MERADCOM approval.

Soot Formation: Flame Radiation and Exhaust Smoke

Soot formation is important in gas turbine combustion for two reasons: increased flame radiation and exhaust smoke. An increase in flame radiation will increase the heat load to the liner, thus raising the liner temperatures and reducing the thermal fatigue-life of the liner. Exhaust smoke is that soot which is not oxidized in the secondary and quench zones; the major military concern is the increase in visible signature of the vehicle.

Soot formation in the primary zone is to a large part determined by combustor design, i.e., the stoichiometry and mixedness of the primary zone; however, fuel properties can play an important role. Currently, the soot-forming tendencies of jet fuels are controlled by the aromatic content and the so-called smoke point. Other distillate fuels, such as diesel fuel, are not controlled for this property. These controls have proved satisfactory for light-distillate jet fuels composed primarily of paraffins and single-ring aromatics (alkylbenzenes). The validity of these tests becomes suspect as fuel chemistry changes, e.g., more cycloparaffins, tetralins, and naphthalenes, and as viscosities increase; viscosity affects both the diffusion flame on the wick lamp used for the smoke point test and the FIA (ASTM D-1319) test used for measuring aromatic content.

One of the objectives of a series of combustor studies has therefore been to determine which fuel properties, physical and chemical, are important to soot formation in gas turbine combustors. Figure 5 reproduces data from an early program[5] using the 2-inch combustor to evaluate chemical properties. "Wt% ring carbon" is a measure of how much of the carbon is in aromatic ring structures as opposed to side-chains or saturated molecules; it differs from "aromatic content" in that the former procedure effectively counts only the aromatic rings while the latter counts aromatic molecules. If "aromatic content" were the fundamental fuel parameter, then the ring structure itself should be important. In Figure 5, hydrogen content and aromatic content appear to be of about equal value as correlating parameters, while ring-carbon is seen to be a relatively poor correlating parameter. This suggests that the aromatic ring structure itself is not important, and that aromatic content correlates the data well only because of the lower hydrogen content of the aromatic molecules.

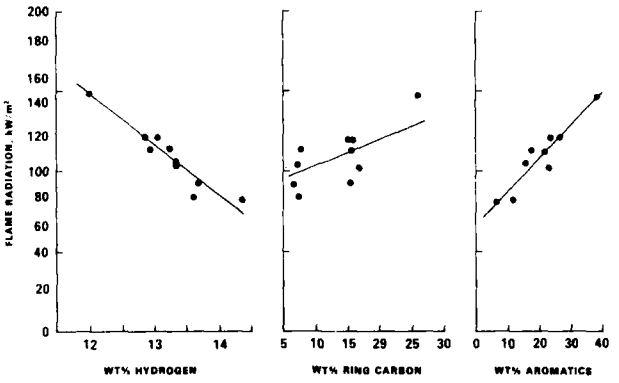


FIGURE 5. CORRELATIONS OF FLAME RADIATION WITH FUEL PROPERTIES

Subsequently, these same fuels along with 17 others were evaluated in the T63 combustor for their effects on flame radiation and smoke.[6] The additional fuels emphasized physical properties, such as viscosity and boiling-point distribution, as well as water/fuel emulsions and blends of methanol and aromatics. Figures 6 and 7 present the flame radiation data from these fuels as correlated against aromatic content and hydrogen content. Here the strength of the hydrogen correlation is more dramatic than in the previous example. The solid line in Figure 6 is drawn through the data for fuels which are simple blends of petroleum JP5 with aromatics. This illustrates that while the aromatic content correlates the soot-forming tendencies of petroleum-derived fuels, it is less acceptable for the synthetic hydrocarbon fuels and not at all adequate for the more unorthodox fuels. Contrast this with Figure 7 which shows that hydrogen-carbon ratio adequately correlates all of the data. These results indicate that soot formation is essentially independent of molecular structure. Note also that some of the jet fuels were blended with 10, 20, and 40 percent diesel fuel (DFM) and two of the fuels were DFM's. Since these increases in viscosity and end point did not affect their correlation, the combustion quality of such emergency fuels can be controlled by hydrogen content.

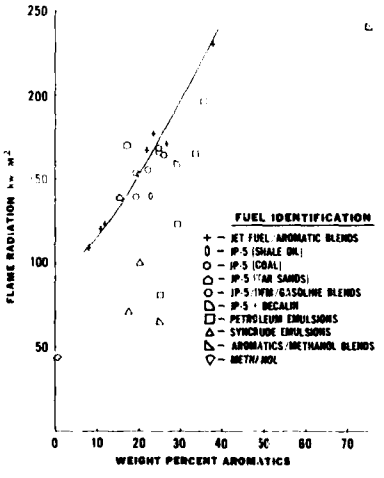


FIGURE 6. EFFECT OF AROMATIC CONTENT ON FLAME RADIATION

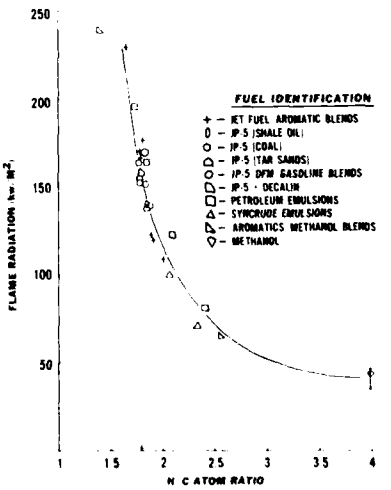


FIGURE 7. EFFECT OF HYDROGEN TO CARBON RATIO ON FLAME RADIATION

The fuels used in the above discussion did not contain significant amounts of such compounds. There have been some suggestions that polycyclic aromatics such as tetralins and naphthalenes might not follow the simple hydrogen correlation discussed above. For this reason, a study was conducted in the 2-inch combustor using 6 test fuels which all had a hydrogen content of 12.8 percent, but which stressed end point and polynuclear compounds, i.e. decalin, tetralin, naphthalene, and anthracene.[7] Again there was no effect of increased end point. The fuels with single-ring aromatics, single-ring cycloparaffins (naphthenes), and double-ring cycloparaffins (decalin) followed a simple hydrogen correlation; however, the fuels with the polynuclear aromatics produced more soot than their hydrogen content would suggest. Also this increase in radiation varied with combustor operating conditions. However, when these same fuels were burned in the T63 combustor, there was no difference in the measured flame radiation between the polycyclic aromatics fuels and the base fuels blended to the same hydrogen content. Thus the evidence indicates that fuels containing significant amounts of polynuclear aromatics (>5%) can produce more soot than their hydrogen content would predict, but that the increase is dependent on the combustor design and operating conditions.

A further study was then conducted with 14 test fuels containing alkyl-benzenes, methyl naphthalenes, tetralin, and indene blended into a Jet A fuel to produce hydrogen contents of 11.5, 12.5, and 13.5 percent.[8] These fuels were than burned in the 2-inch combustor over a wide range of operating conditions to determine the separate effects of temperature, pressure, fuel-air ratio, and reference velocity.

The sooting tendencies of the polycyclic aromatics themselves was determined by comparing the sensitivity to H/C ratio of fuels containing polycyclic aromatics to those with only single-ring aromatics. The difference was assumed attributable to the polycyclic aromatics. These trends are reproduced in Figure 8 showing the individual effects of temperature, fuel-air ratio, density, and reference velocity. The actual values are probably unique to this combustor, but the trends may apply to other combustors. If so, one would expect that engines would tend to be less sensitive to polycyclic aromatics at the full power condition where fuel-air ratios are greatest as are the burner inlet temperature and density. This is a desirable trend, since the full power condition is associated with the highest levels of soot formation and the highest liner temperatures, i.e., at the worst condition there is the least sensitivity to the polycyclic aromatics.

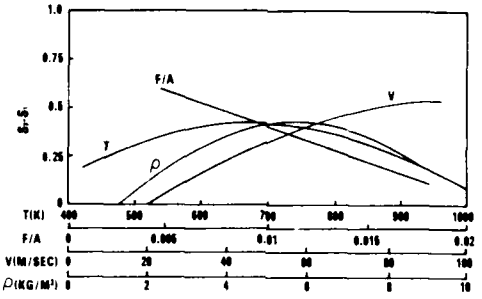


FIGURE 8. EFFECTS OF OPERATING PARAMETERS ON THE INCREASED SENSITIVITY OF THE SOOTING TENDENCY DUE TO POLYCYCLIC AROMATICS

In summary, this series of studies has shown that hydrogen content (or hydrogen-carbon ratio) is the essential fuel property for controlling soot formation in fuels which do not contain appreciable amounts of polycyclic aromatics. This is in agreement with other researchers, but the extension to include alcohols as well as emulsions of water or alcohol with hydrocarbon fuels strengthens this claim significantly. The presence of polycyclic aromatics in the fuel can lead to higher levels of soot formation depending upon the combustor operating conditions. Such compounds are not generally found in fuels in concentrations greater than a couple percent naphthalenes and a few percent tetralines/indenes; the impact of such concentrations is not significant.

Atomization and Fuel/Air Mixing

The ignition characteristics of an engine are highly dependent upon the design characteristics, e.g., ignitor energy and location, air flow pattern and velocity, and air-fuel ratio; however, fuel properties play an important role in determining how the air and fuel are mixed. Viscosity is the major fuel property that controls the size(s) of the droplets in the fuel spray; density and surface tension are also factors, but do not change as much as viscosity over the range of candidate fuels. A typical relationship for a simplex pressure atomizer as correlated by Jasuja[9] is given in equation (1):

$$SMD = \nu^{0.16}\ \sigma^{0.6}\ W_f^{0.22}\ \Delta P_f^{-0.43} \qquad (1)$$

where ν and σ are the viscosity and surface tension of the fuel and W_f and ΔP_f are the fuel flow rate and pressure drop across the nozzle. Higher viscosity fuels result in larger SMD's (Sauter mean diameter).

The boiling point distribution, i.e., volatility, governs the evaporation rate and hence the mixing of the fuel with the combustion air. Equation (2) shows the D^2-law for droplet evaporation in quiescent air (the modifications for convection are not necessary for this discussion):

$$\tau = \frac{D_o^2 \cdot \rho_f \cdot C_{pa}}{8\ K_a\ \ln(1+B)} \qquad (2)$$

where τ is evaporation time for a drop of initial diameter D_o and density ρ_f, C_{pa} and K_a are the heat capacity and thermal conductivity of the air. The important parameter here is the transfer number B; physically it represents the ratio of energy available for evaporation to the energy required, or

$$B = \frac{C_{p,a}\,(T_\infty - T_f)}{L + C_{p,f}\,(T_f - T_i)} \qquad (3)$$

Here T_∞ is the temperature of the surrounding medium and T_f is the boiling point of the liquid. For most fuels, T_f is not unique, but rather there is a boiling point distribution. Foster and Straight[10] and Peters and Mellor[11] have correlated ignition limits using the 10 percent evaporation point of the fuel. It is not clear, however, what should be used for T_∞ for an ignition problem. Peters and Mellor used the average of the ambient and the stoichiometric, adiabatic flame temperatures (approximately 1300K). Such argument is beyond the scope of this paper. It is sufficient to note that fuels with higher boiling ranges give a smaller value for B and hence a longer evaporation time.

Figure 9 reproduces some data from Ballal and Lefebvre[12] illustrating a combined effect of viscosity (drop size, SMD) and boiling range on the ignition energy. As would be expected, higher ignition energies are required for fuels of lower volatility and higher viscosity (larger SMD).

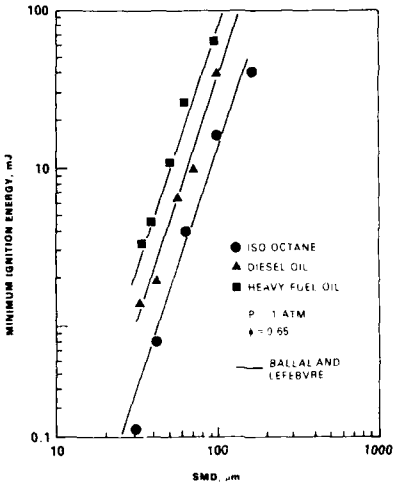


FIGURE 9. MINIMUM IGNITION ENERGY VERSUS SMD FOR QUIESCENT MIXTURES (Data from Ballal and Lefebvre[12])

In a gas turbine engine, these effects would be manifested in those performance areas which are mixing controlled rather than kinetic controlled, e.g.,

- o ignition and altitude relight
- o flame stabilization (lean blow-off)
- o combustion efficiency and gaseous emissions
- o exhaust temperature pattern factor.

Of these, ignition and altitude relight are the most significantly affected.

The first MERADCOM/AFLRL investigation into the fuel effects on ignition was conducted using JP4, Jet-A, and DF2 fuels.[13] Figure 10 shows the relative ignition characteristics of these fuels as the time required for ignition for a given fuel flow rate, all air-flow conditions and spark energy being held constant. For a given fuel, the characteristics are typical: at low flow rates, there is no ignition; then as the flow rate is increased, ignition becomes marginal; and finally, at sufficiently high flow rates, ignition is almost immediate. The more volatile and less viscous JP4 was ignitable at lower flow rates than the Jet-A which was easier to light than the DF2. Also included in Figure 10 are the ignition limits for blends of pentane with the DF2 to show that blending a more volatile material into the heavier diesel fuel will improve the ignition characteristics. About 8 percent pentane was required to match the vapor pressure of the JP4, but adding 10 percent to the Jet-A and 20 percent to the DF2 did not reduce their ignition limits to that of the JP4. Thus, adding more volatile components to increase the vapor pressure is helpful, but vapor pressure may not be a sufficient parameter to predict ignition limits with blends.

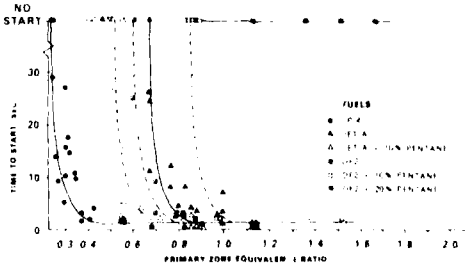


FIGURE 10. COMBUSTOR IGNITION CHARACTERISTICS FOR DIFFERENT FUELS

Subsequent ignition studies were oriented toward the potential use of DFM as a blending stock for aircraft.[5] Test fuels included 10, 20 and 40 percent DFM in JP5 along with gasoline, two DFM's, and [illegible]

blend. Figure 11 shows the thresholds for instantaneous ignition, but without the detailed data points of Figure 10. As would be expected, the gasoline had the leanest limit and the DFM's were the most difficult to ignite requiring much higher fuel flow rates. Adding 30 percent gasoline to the DFM made a significant improvement in the ignition limit. There is an inconsistency in the JP5/DFM blends; in some cases the limits appear to have been improved by the addition of DFM. Unfortunately the inlet air temperature was dictated by the ambient air and could not be controlled. During the tests the air temperatures varied by several degrees which accounts for the relative positioning of the ignition limits for these blends rather than according to their viscosity (increasing DFM). While this precludes a quantitative evaluation, it appears that blending DFM into JP5 would not seriously degrade the ignition requirements on warm days. Subsequent combustor studies by the Navy and Air Force have shown some degradation of cold-start and altitude relight limits.

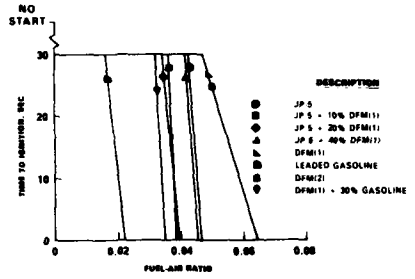


FIGURE 11. FUEL EFFECTS ON FUEL-AIR RATIO REQUIRED FOR IGNITION

The following is a brief look at the other, less critical performance areas listed above. Figure 12 compares the lean blow-off equivalence ratios for the nine fuels mentioned earlier ranging from gasoline through JP5 to diesel fuel (DFM) and blends thereof.[5] The data were taken at four different power conditions in the T63 combustor —10%, 40%, 50%, and 100%; engine power is represented by the air loading parameter, θ:

$$\theta = P^{1.75} A_{ref} D_{ref}^{0.75} \exp(T/300)$$

where P and T are the combustor inlet air pressure and temperature; A and D are reference area and dimension of the combustor. The fuel effects are more pronounced at the lower power conditions where the gasoline could be burned under much leaner conditions. There was very little difference among the jet/diesel fuel blends, however.

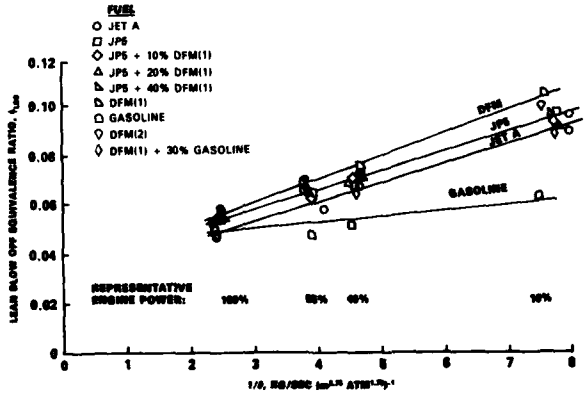


FIGURE 12. FUEL EFFECTS ON FLAME STABILIZATION

Combustion efficiency calculations were made for these same fuels burned in the T63 combustor from measurements of CO, CO_2, and HC as a ratio of energy actually released in the reaction to the energy that would have been released if the fuel had been totally oxidized to CO_2 and H_2O. Figure 13 shows that the range of the fuel effects is relatively minor except at the idle condition. Although the details are excluded, the jet fuels gave the highest efficiency, the diesel fuels the lowest, with the blends in between.

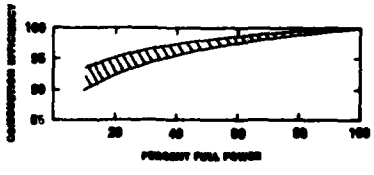


FIGURE 13. RANGE OF FUEL EFFECTS ON COMBUSTION EFFICIENCY

A similar result is seen in Figure 14 for the gaseous exhaust emissions, CO, HC, and NO_x. For the CO and hydrocarbons, the fuel effects are greatest at idle where the emissions are highest due to poorer mixing and lower temperatures which are aggravated by the poorer atomization and evaporation of the diesel fuels. The oxides of nitrogen exhibit the opposite trend with engine power since their formation is so highly temperature dependent. The fuel effects are fairly uniform across the power spectrum, and, while the more viscous fuels generally yielded higher concentrations of NO_x, the highest concentrations were obtained from the gasoline. This is presumably because of the high local stoichiometry in the primary zone caused by the rapid vaporization of the gasoline.

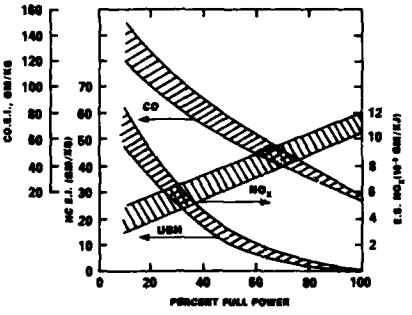


FIGURE 14. RANGE OF FUEL EFFECTS ON GASEOUS EMISSIONS

None of these fuel effects on emissions or combustion efficiency is considered critical. While the magnitude of such fuel effects are certain to be dependent on the combustor design, these conclusions have been confirmed in recent years in U.S. Air Force and Navy sponsored combustor programs on a variety of engine design and sizes.

Summary

Combustor test programs on alternative and emergency fuels have been conducted in the Army Fuels and Lubricants Research Laboratory over a period of years to identify which fuel properties appear to control certain problems in combustor performance. The types of fuels and the range of fuel properties have encompassed the fuels likely to be used in aircraft gas turbines over the next 20-30 years.

The most important problem areas would appear to be the following:

Performance Area	Controlling Fuel Property	Performance Problem
Ignition	Viscosity, Volatility	Degradation of cold-day ignition and altitude relight limits
Soot Formation	Hydrogen content	Reduced liner life increased exhaust smoke

Other non-combustion problems not addressed in this paper include thermal stability, materials compatibility, and lubricity.

Research on the influence of the physical and chemical properties of fuels on engine and aircraft performance and durability is very important right now as opposed to simply qualifying a system on a fuel specification. By identifying the critical fuel/hardware interfaces and developing quantitative models and impact statements, the impact of potential changes in fuel specifications, crude sources, and refining techniques can be minimized. More importantly, the high cost of requalifying every engine and aircraft to ensure their compatibility with new fuels can be reduced by concentrating on critical or representative systems and components.

REFERENCES

1. Sefer, N.R. and Moses, C.A., "Crude Sources and Refining Trends and Their Impact on Future Jet Fuel Properties," SAE Paper No. 811056, October 1981; SAE Transactions, Vol. 90, 1981.

2. Dickson, J.C. and Karvelas, L.P., "Impact of Fuel Properties on Jet Fuel Availability," AFAPL-TR-76-7, U.S. Air Force Air Propulsion Laboratory, Wright-Patterson AFB, OH, April 1976.

3. Liberman, M. and Taylor, W.F., "Effect of Refining Variables on the Properties and Composition of JP5," Final Report Contract No. N00140-78-C-1491. Naval Air Propulsion Center, Trenton, NJ, November 1980.

4. Speck, G.E., "Feasibility of Marine Diesel Fuel as an Emergency Aircraft Fuel, "Report No. NAPC-PE-44, Naval Air Propulsion Center, Trenton, NJ, February 1981.

5. Moses, C.A. and Naegeli, D.W., "Fuel Property Effects on Combustor Performance," ASME Paper No. 79-GT-178, March 1979.

6. Naegeli, D.W. and Moses, C.A., "Effects of Fuel Properties on Soot Formation in Turbine Combustion," SAE Paper No. 781026, November 1978.

7. Naegeli, D.W. and Moses, C.A., "Effect of Fuel Molecular Structure on Soot Formation in Gas Turbine Engines," ASME Paper No. 80-GT-62, March 1980.

8. Naegeli, D.W., Dodge, L.G. and Moses, C.A., "Sooting Tendencies of Fuels Containing Polycyclic Aromatics in a Research Combustor," AIAA Paper 82-0299, Journal of Energy, Vol. 7, No. 2, March-April 1983, p 168.

9. Jasuja, A.K., "Atomization of Crude and Residual Fuel Oils," ASME Paper No. 78-GT-83.

10. Foster, H.H. and Straight, D.M., "Effect of Fuel Volatility Characteristics on Ignition Energy Requirements in a Turbojet Combustor, NACA RME52J21, 1953.

11. Peters, J.E. and Mellor, A.M., "An Ignition Model for Quiescent Fuel Sprays," Combustion and Flame, Vol. 38, p 65, 1980.

12. Ballal, D.R. and Lefebvre, A.H., "Ignition and Flame Quenching of Quiescent Fuel Mists," Proc. R. Soc. Lond. A. 364, p 277, 1978.

13. Moses, C.A., "Studies of Fuel Volatility Effects on Turbine Combustor Performance," presented at the 1975 Joint Meeting of Western and Central States Sections of The Combustion Institute, San Antonio, Texas April 1975.

DISCUSSION

J.Tilston, UK

This paper contains references to differences in liner temperatures of the order of 11°C due to changes of fuel type. In our research we would expect very much higher differences than this, due entirely to day to day variations in rig operation or errors in establishing datum conditions after an in-run fuel change. Could Dr Moses please explain how these measurements are made?

Author's Reply

These data were not mine but taken at General Electric so if I may I will refer the question to Mr Willard Dodds of that company.

W.Dodds

We at General Electric have acquired much experience in alternative fuels testing, and often detect temperature changes of 11°C or less, using surface mounted thermocouples on the combustor liners. We have consistently seen this effect in dozens of combustor tests. Also, we see consistent changes in the output of a majority of the thermocouples mounted on the combustor liners (20 to 40 thermocouples are normally used for this type of test). In fact, we have repeatedly observed a larger change in liner temperature in the forward positions of the combustor (where flame radiation effects are strongest) than in the aft portions. There are three additional considerations. Firstly, we always report liner temperature relative to combustor inlet temperature. This corrects for small variations in inlet temperature. Secondly, we use exactly the same thermocouples for comparisons. Reinstrumentation of a combustor liner can make a significant difference in details of measured liner temperature. Finally, we measure temperatures at several different operating conditions with many different fuels, over a fairly wide range of properties (typically 12 to 14.5% hydrogen content), and use statistical analyses to establish fuel effects, so it is not merely a comparison of two test data.

J.Odgers, Ca

In your discourse you stated that a difference of 11°C in wall temperature could reduce the combustor life by some 25 percent. I find this very disturbing since when I was in industry two production combustors taken from the assembly line could show a temperature difference of 20°C, or even 40°C when measured at the same position. Since we can rarely measure wall temperatures better than ±20°C in regions of steep temperature gradients, the statement is even of greater concern. I would welcome your comments on this matter.

Author's Reply

I did not develop the data to which you refer myself and would again like to refer the question to Mr Willard Dodds from General Electric.

W.Dodds

When you say that you measured two different combustors in the same position, I would not be surprised if you observed 20°C difference in the temperature. In fact, if you ran a test with a thermocouple in a certain location and attempted to replace it with an identical thermocouple in the identical location, you would probably measure a different temperature in a subsequent test. However, if the combustor and instrumentation are not disturbed, very close agreement can be obtained. As for life analyses, these are described in two reports by Gleason et al. (references 2 and 3 in my paper). A simplified life estimation procedure from a paper by Foltz and Kenworthy (presented at the 1982 ASME International Gas Turbine Conference in London) would also be of interest.

THE EFFECTS OF FUEL COMPOSITION UPON HEAT TRANSFER IN GAS TURBINE COMBUSTORS

by

J. Odgers & D. Kretschmer
Dépt. de Génie mécanique
Université Laval
Québec, Canada
G1K 7P4

AD-P003 134

SUMMARY

The widening of fuel specifications will lead to fuels having a lower hydrogen content. This change will influence the heat transfer in combustion chambers, mainly through increased radiation from increased carbon in the flame. The influence of ring compounds is not very clear and - to date - the best correlation is with fuel hydrogen content. Due to this, the "Luminosity-Factor" is still the most convenient tool for the prediction of fuel effects upon heat transfer.

NOMENCLATURE

A/F	air to fuel mass ratio
C_A	aromaticity = $\frac{100 \times \text{Aromatic carbon atoms}}{\text{Aromatic carbon atoms + non-aromatic carbon atoms}}$, %
c/h	carbon-hydrogen mass ratio of the fuel
f	fuel-air mass ratio
h	hydrogen mass fraction in fuel
ℓ	effective radiation beam length, m
L	flame luminosity
p	pressure, Pa
p_O	air inlet pressure, Pa
R	heat transferred by radiation, W m^{-2}
T	temperature, K
T_O	air inlet temperature, K
T_L	combustor temperature for any fuel, K
T_{LO}	combustor temperature for a reference fuel (usually H = 14,5%), K
$[T_x]$	$\frac{T_L - T_{LO}}{T_{LO} - T_O}$
Z	non luminous emission parameter (Eqn. 2)
ε	emissivity
κ	effective soot emission parameter (Eqn. 5), m^{-1}
ϕ	equivalence ratio
Π	pressure ratio

Subscripts

g	hot gas
PZ	primary zone

1. INTRODUCTION

The introduction of new fuels-sources, to augment or replace existing ones, will result in fuels having increased boiling points, viscosity, freezing points, and aromatic contents. A major concern is that increasing aromatic contents will lead to increased carbon formation and, hence, to higher wall temperatures. This increase in wall temperatures could reduce the effective combustor life.

The following is an attempt to assess what effects fuels may have upon the heat transfer in gas turbine combustors.

2. GENERAL CONSIDERATIONS

Heat transfer in gas turbine combustors has been investigated extensively in the past. A bibliography [1], last updated in 1979, contains alone over 600 references. The models developed vary from quite simple to very complex, some giving mean temperatures for any axial location, others claiming to give detailed temperatures patterns. All the models, however, have one common weakness, the uncertainty in estimating flame radiation.

The uncertainty is two-fold. Firstly, so far, it has not been possible to predict local flame temperatures in the combustion zone. Reasonable estimates for mean flame temperatures can be made, however, the accuracy is necessarily limited. More difficult to estimate is the effective emissivity of the flame. A considerable amount of laboratory work has been done to measure the emissivity of both, transparent and opaque gases, but for gas turbine

applications, one has to resort to convenient semi-empirical equations which have been determined in combustion chambers.

A very useful set of equations for the non-luminous flame has been given in [2] -

$$\varepsilon = 1 - e^{Z} \quad (1)$$

$$z = -0{,}286\ p\ (f\ell)^{0,5}\ T_g^{-1,5} \quad (2)$$

Unfortunately, the flames in the combustion zone of liquid fueled combustors are highly luminous due to the presence of carbon particles. Since it is not (yet?) possible to predict the density and size distribution of carbon particles in the combustors, no theoretical prediction of the emissivity of luminous flames will be available in the near future - if ever. Consequently, resort is made to an empirical "fudge-factor", the so-called flame luminosity. Equation (3) gives the relationship developed for [2] using data from several sources [3 to 5], representing the best-fit line to the data available. It has proved to be satisfactory for most applications to date, but it has obvious limitations. It may be used for fuels having a molar mass of 44 g/mol or more, providing that

(a) they are saturated hydrocarbons, or

(b) they are commercial liquid fuels of a conventional character and ranging from gasoline to fuel oils.

Also it has to be noted that the relationship applied only in the recirculation zone of combustors working reasonably close to stoichiometric and being fed by a pressure atomizer.

If the mixture in the recirculation zone is very lean, the luminosity tends to decrease, also the use of air-blast atomizers decreases luminosity.

With these restrictions, the estimated accuracy of the equation is about ±25% (corresponding to about ±5% in terms of wall temperature). It is obvious that this is an area demanding further investigations.

$$L = 0{,}0691\ (c/h - 1{,}82)^{2,71} \quad (3)$$

Correction for luminosity is then made by inserting into Eqn. (2)

$$\varepsilon = 1 - \exp\ (L \times Z) \quad (4)$$

Theoretical considerations suggest a somewhat different type of luminosity correction to Eqn. (2) [6, 7]. In terms used here, the emissivity would have the form

$$\varepsilon = 1 - \exp\ (Z - \kappa\ell) \quad (5)$$

Values for κ given in [6] are plotted in Fig. 1. A direct translation is not possible, but, for example, the value quoted for propane implies a luminosity factor of the order of 4 to 5, much higher than usually experienced. It seems obvious that the values appropriate for jet diffusion flames do not apply in the highly stirred environment of a gas turbine combustor. This should not distract from the possibility that this type of correction might be better than the luminosity factor, however, it cannot be used unless more appropriate data become available.

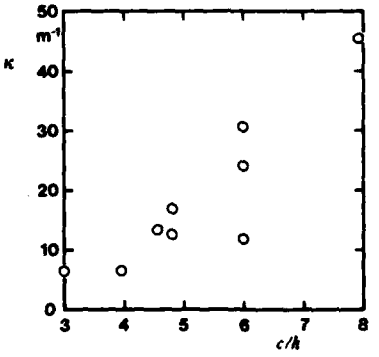


Fig. 1: Soot Emission Parameter [6]

3. PREDICTED CHANGES IN WALL TEMPERATURES DUE TO CHANGES IN FUEL COMPOSITION

The above mentioned model was applied to a hypothetical combustor having the following characteristics.

Combustor type - Pipe Chamber	-	
Combustor Diameter	-	230 mm
Primary zone equivalence ratio	-	1,0
Secondary zone equivalence ratio	-	0,5

The combustor exit combustion efficiency was assumed 100% at all of the following operating conditions.

Condition		A	B	C	D	E	F
Inlet temperature	K	300	480	630	723	800	925
Inlet pressure	MPa	0,1	0,5	1,0	1,5	2,0	3,0
Total mass flow (air)	kg/s	1,39	5,48	9,57	13,4	17,0	23,7
Total mass flow (fuel)	kg/s	0,028	0,112	0,193	0,270	0,342	0,477

For each of these conditions the wall temperatures were assessed for fuels having the specified hydrogen contents given below

Fuel	A	B	C	D	E
%H (mass)	16	14	12	11,11	8
Stoic A/F	15,11	14,65	14,19	13,73	13,28

In order to attain constant turbine inlet temperatures it was necessary to adjust the fuel flows so as to maintain a constant equivalence ratio in each section of the combustor. Thus at each condition , the fractional fuel flow was given by -

Fuel	A	B	C	D	E
Fractional fuel flow	1,03	1,00	0,969	0,937	0,906

This also ensured constant temperature conditions within the primary and secondary zones. The flame luminosities corresponding to the fuel were (eqn. 4)

Fuel	A	B	C	D	E
c/h (mass)	5,25	6,14	7,33	8,00	11,50
Flame luminosity (L)	1,95	3,65	7,06	14,44	32,45

The film cooling device was assumed to be a wigglestrip of gap width 2,5 mm, and the calculations were performed at 25 mm, 50 mm, and 75 mm downstream from the slot. The metal emissivity was assumed to be 0,8. Predictions were made for the film cooling slots in both primary and intermediate zones. For the present, only the primary zone will be considered; for more detailed information see Refs. [8 & 9].

No calculations were performed for the dilution zone, since in this region a constant luminosity factor of unity is assumed.

The results of the calculations are shown in Figs. 2 & 3.

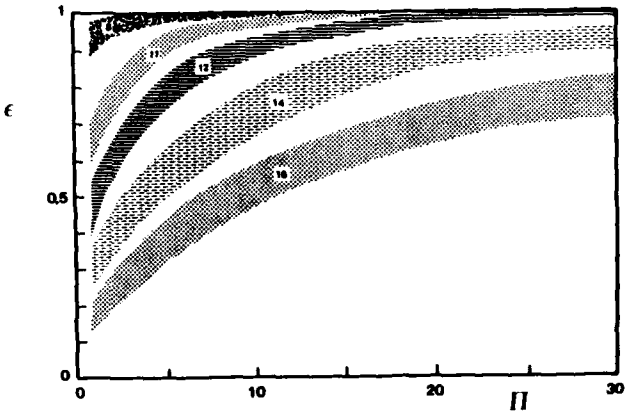


Fig. 2: Predicted Changes in Flame Emissivity in the Recirculation Zone

3.1 Flame Emissivity

Figure 2 shows the effect of flame emissivity for the recirculation zone. The band spread on the curves has no particular significance except that:

(a) it indicates the effect of position within the zone relative to the start of the film cooling;

(b) as the hydrogen content decreases, the width of zone decreases due to the higher "basic" emissivity.

3.2 Wall Temperature

Figure 3 shows the mean effects upon wall temperatures in the recirculation zone, expressed in the dimensionless form used by Blazowski [10], where T_{LO} is the wall temperature yielded by a fuel containing a standard amount of hydrogen (in this case, hypothetical JP5, h = 14,5%). The magnitude of the effects of hydrogen content is most significant when the emissivity is low, that is

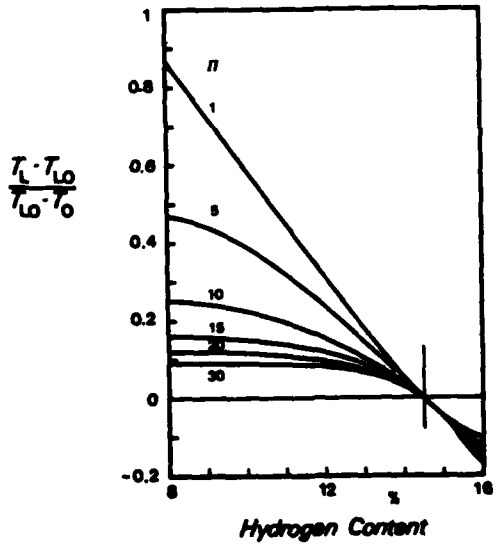


Fig. 3: Predicted Changes in Combustor Wall Temperatures in the Recirculation Zone due to Pressure Ratio and Fuel Composition.

(a) at low pressures and
(b) within the secondary zone more than in the primary zone.

3.3 Radiation from hot carbon particles

All the above phenomena have been based upon heat transfer from a flame having "mean" properties based upon empirical correlations. Such correlations were obtained from flames in practical combustion systems used in gas turbines, and generally using fuels containing not less than 11% hydrogen. In addition, it has been assumed that the behaviour of the fuel is completely defined by the hydrogen content, and that the type of compound has no effect upon the carbon formation and/or the heat transfer properties. Suppose that the latter supposition is untrue. Suppose also that the result is the formation of a large amount of relatively big particles of carbon which burn at their surfaces. Examination of the relevant thermodynamic data suggests that it is possible that the temperature at the surface of such particles could be considerably higher than the local hot gas temperature. Under such circumstances the total radiation might suffer a significant increase with a corresponding increase of wall temperature. However, it has to be kept in mind that the carbon particles burn in air vitiated by the combustion of the volatile fractions. Currently, there is no known technique for predicting this phenomenon, but with careful attention to experimental details, it might be possible to detect it, if it actually exists.

4. EXPERIMENTAL RESULTS

4.1 Flame emissivity

Very few experimental data are available with respect to flame emissivities for a range of fuels at various engine conditions. In general, the experimental work seems to be limited to the measurement of wall temperatures and flame radiation. The absence of measured hot gas temperatures renders it impossible to deduce the flame emissivities with any real accuracy.

Figure 4 indicates the range of flame luminosity reported by various authors [11]. It can be seen that there is a considerable spread of results, and if luminosity is to be retained for prediction purposes, it is desirable that further experimental work be done.

Figure 5 shows some experimental data obtained by Rolls-Royce [9]. Although insufficient information was available to make predictions, the results are typical, and similar to those of Fig. 2.

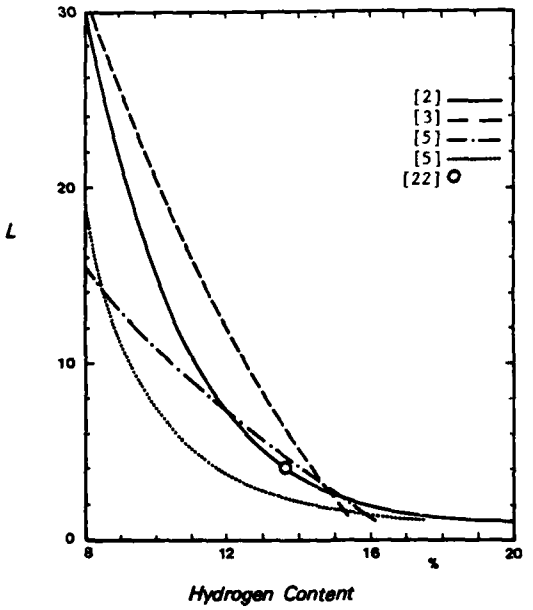


Fig. 4: Dependence of Luminosity Upon Fuel Composition

4.2 Wall temperature measurements

A fair amount of work has been published on the effects of fuel composition on wall temperature. All workers agree that diminishing the fuel hydrogen content increases the wall temperature of the combustor. Many of the data appear to correlate against a temperature parameter [8] defined by -

$$[T_x] = \frac{T_L - T_{LO}}{T_{LO} - T_O} \qquad (6)$$

where T_L is the actual liner temperature
T_{LO} is the temperature yielded by a "standard" fuel (usually 14,5% H)
T_O is the combustion inlet temperature

Examples of such data are given in Figs. 6 to 8 taken from references [12] to [14].

Figure 6 is based upon data from Gleason et al. [12] and plots the temperature parameter against the hydrogen content of the fuel for a number of

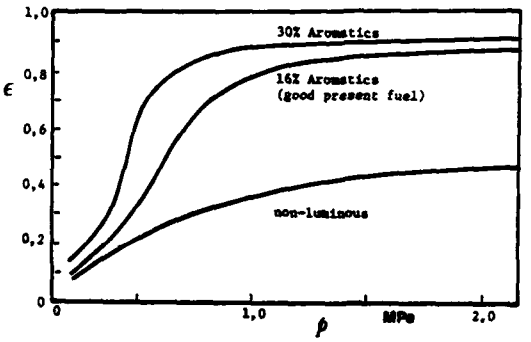


Fig. 5: Variation of Flame Emissivity with Fuel Composition and Pressure. (Rolls-Royce Spey Combustion Rig) [7]

aircraft combustors. The triangles are for the J79 data reported in [12], and they compare favourably with the primary zone predictions for similar inlet conditions. The predictions are those described in Paras 2 and 3. The remaining test units do not have their operating conditions specified, but presumably they are not too far removed from the J79 case. It is findings such as these that leads one, tentatively, to accept $[T_x]$ as a general parameter, at least for standard type combustors.

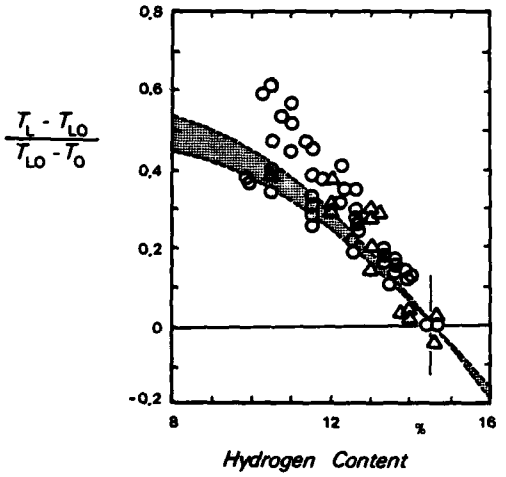


Fig. 6: Effect of Fuel Composition Upon Wall Temperature [12]

Triangles: J79 T_O = 559 K p_O = 470 kPa (Cruise)
Circles: T56, J79, JT8D, CJ805, J57 unspecified conditions
Shaded zone: Primary zone predictions T_O = 480 K p_O = 500 kPa

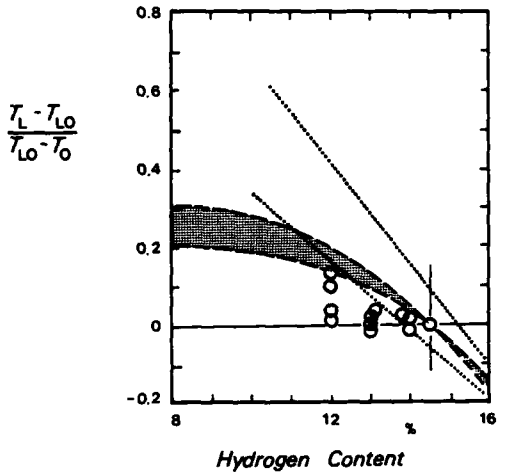


Fig. 7: Effect of Fuel Composition Upon Combustor Wall Temperatures [13]

F101 T_O = 677 K p_O = 997 kPa
Dotted lines are limits of units from Fig. 6
Shaded zone: Primary zone predictions T_O = 632 K p_O = 1 MPa

It will be remarked that the above mentioned units are all from engines which are fairly "old". In Fig. 7, data are plotted for a more recent combustor, the F101 [13]. The engine data points lie below the general scatter of the previous engines and also below the predicted values at similar conditions. This is generally accepted to be the result of a lean primary zone mixture compared with those of the older chambers. Since this "leanness" is not given in the reference it could not be "allowed-for" in the prediction technique (which in this case assumes ϕ_{PZ} - 1,0) and this may well explain the high prediction value.

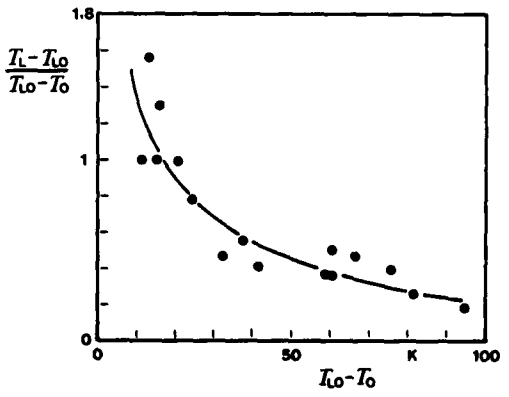


Fig. 8: Variation of Wall Temperature Correlation Group Inside a Combustor. Data from [15]

Change from JP4 to gasoline

The difference between the results for the J79 and the F101 makes it quite obvious that the correlation ($[T_x]$) used is far from general. Great caution has to be used when trying to generalize information from this type of correlation. Not only does the influence change somewhat from combustor to combustor - especially if the fuel injection system changes - it varies also within a given combustor. Much smaller changes will occur in regions where the emissivity is already close to unity. This effect is illustrated in Fig. 8 (after [15]) where the influence of a change from JP4 to gasoline is plotted as a function of the original wall temperature at various points throughout the combustor.

An example for the influence of changes in engine operating conditions is given in Fig. 9, where the data for the J79 from [12] are plotted for all 4 conditions. This figure shows also the type of scatter which seems rather typical.

The results of Bauserman et al. [16] also indicate the zonal influence upon the temperature parameter. Thus the primary-secondary zones show the largest influence, although not necessarily the highest temperature. This implies that the value of the parameter $[T_x]$ per se should not be used as an absolute measure of probable life. It is

obvious that at idling conditions a much larger range of $[T_x]$ may be tolerated than, say, at full-load take-off.

The dependence of $[T_x]$ upon the operating air/fuel ratio (combustor outlet temperature) was also noted by Singh et al. [17] using a 1/2-scale version of the W251. Their results are reproduced in Table I. The values of $[T_x]$ were obtained both as a function of the hydrogen content and the aromaticity. Aromaticity is negatively correlated with hydrogen content. The results indicate that the hydrogen content is a slightly better correlation parameter.

The concern with respect to the effect of the types of compounds present in the fuel is fairly general. Although a fair amount of experimental work has been carried c t, there is little positive evidence to answer this question. It is generally conceded that the worst effects will be given by pure ring structure compounds, whereas those hydrocarbons containing side chains will burn more akin to aliphatic compounds. What is not known, is the amounts of such multiple ring compounds which will actually occur in fuels. To-date, the correlation parameter giving overall least-scatter has been hydrogen. This bas been demonstrated above (Table I), and Fig. 10 [18] illustrates additional results. These latter indicate some of the difficulty of interpreting the experimental results.

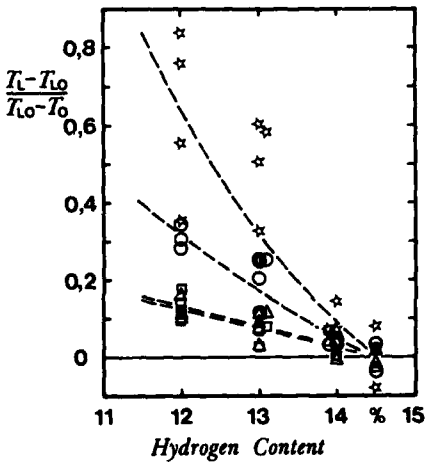


Fig. 9: Effect of Fuel Composition Upon Combustor Wall Temperatures [12] J79

Squares - Dash, Triangles - Take-off, Circles - Cruise, Stars - Idle.

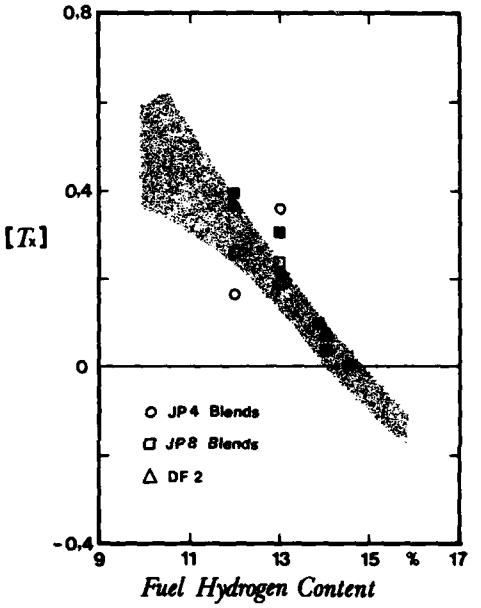


Fig. 10: Effect of Fuel Composition Upon Combustor Wall Temperatures [18]

Shaded portion indicates previous data (T56/J79/JT8D/CJ805/J57)
Solid symbols indicate monocyclic blends

TABLE I

INFLUENCE OF FUEL HYDROGEN AND AROMATICITY ON $[T_x]$

(after [17])

Burner Outlet Temperature K	Influence of Fuel Hydrogen *	Influence of Fuel Aromaticity
839	$[T_x] = -12,9\ (h) + 1,67$ $(\sigma = 0,19)$	$[T_x] = 0,012\ (\% C_A) - 0,22$ $(\sigma = 0,25)$
1172	$[T_x] = -9,2\ (h) + 1,19$ $(\sigma = 0,13)$	$[T_x] = 0,0087\ (\% C_A) - 0,16$ $(\sigma = 0,14)$
1311	$[T_x] = -7,9\ (h) + 1,02$ $(\sigma = 0,12)$	$[T_x] = 0,0074\ (\% C_A) - 0,14$ $(\sigma = 0,14)$
1422	$[T_x] = -7,8\ (h) + 1,00$ $(\sigma = 0,08)$	$[T_x] = 0,0074\ (\% C_A) - 0,14$ $(\sigma = 0,08)$

$^*h_A = 0,$ $C_{A_{Ref}} = 18,4\%$

Using conventional fuels, it is well known that the introduction of premix-prevaporized fuel gives rise to blue, non-luminous flames with fuels which, when burned as droplet diffusion flames, yield the strong yellow of sooting flames. Such premixing would argue insensitivity to fuel composition. Results reported by Rudy et al. [14] are in good agreement with this supposition (fig. 11).

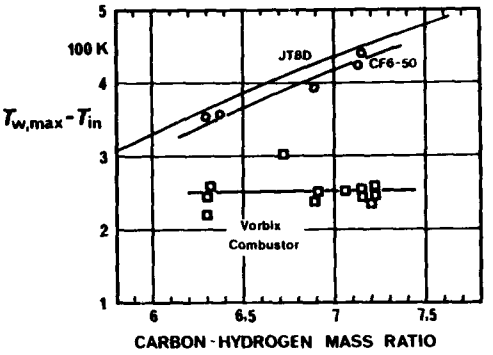


Fig. 11: Effect of Fuel Composition Upon Combustor Wall Temperatures [14]

4.3 Radiation measurements

Experimental investigation of the effects of fuel composition upon flame radiation has not been so extensive as that upon wall temperatures. However, sufficient information has accrued to enable broad conclusions to be drawn.

There is a small increase in peak flame temperatures as the fuel hydrogen content decreases. This gives rise to a small increase in radiation. From 15% H to 8% H, the theoretical increase will be considered negligible for the purpose of this report.

Schirmer et al. [19] reported the results illustrated in Fig. 12. The effect of both fuel composition and pressure (constant inlet temperature) are very significant. At a pressure of 1,5 MPa and an inlet temperature of 703 K the conditions approximate to those used for the example in Para 3 at 1,5 MPa (723 K). The different sizes and duties of the combustors make a direct comparison impossible, but if the radiation index is used, the two sets of data can be shown to agree [8].

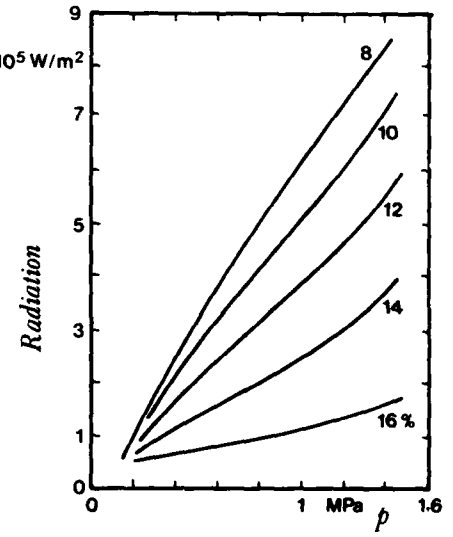


Fig. 12: Effect of Fuel Composition Upon Flame Radiation at Various Pressures [19]

Figures on curves denote fuel hydrogen content
T_O = 703 K

The radiation index is defined as the ratio of the radiation (R) at any hydrogen content divided by a radiation emitted by a fuel containing 14% hydrogen (R_{14}).

Using a similar combustor, Naegeli and Moses [20] examined the effect of fuel molecular structure on radiation. They used a reference fuel containing 14,22% hydrogen and attempted correlation against (a) smoke point, (b) total aromatics, (c) total aromatic ring carbon, (d) hydrogen content, and (e) hydrogen together with polycyclic aromatic ring carbon. The results indicated that, in addition to hydrogen, molecular structure played a significant role in effecting flame radiation. For example a 20% naphthalene content increased the radiation by about 20% over that indicated by a simple hydrogen correlation. A somewhat better parameter was the fuel smoke point, which seemed to include structure.

In other work [21] Moses et al. studied the flame radiation within a T-63 combustor. For these results, the hydrogen content was found to be the best correlation parameter, the detailed hydrocarbon structure apparently having only secondary effects. They also concluded that the Syncrude fuels (derived both from oil shales and coal) fell within the correlation scatter.

Radiation effects within the J79 combustor were investigated by Gleason et al. [12]. Their results indicate that there is some effect due to fuel structure, especially at the higher pressure conditions. Table II gives the effects of hydrogen content in terms of the radiation index. For comparison purposes, the theoretical data, calculated as per section 3, are given. The agreement is considered satisfactory.

5. CONCLUSIONS

5.1 The chemical composition of fuels has been shown to have considerable effect upon the heat transfer characteristics of gas turbine combustion chambers.

5.2 The effects are largely confined to increases in the flame radiation which, in turn, is due to the increased carbon formation within the combustion zone of the combustor.

TABLE II

EFFECT OF FUEL HYDROGEN CONTENT ON FLAME RADIATION INDEX, J79 ENGINE

(After 12)

	EXPERIMENTAL [12]				THEORY	
	Idle	Cruise	Take-off	Dash	———	———
T_O K	421	559	664	781	480	723
P_O MPa	0,25	0,47	1,36	1,59	0,50	1,50
R_{12}/R_{14}*	1,52	1,72	1,64	1,68	1,73+ 1,72 1,71	1,54+ 1,51 1,47
R_{13}/R_{14}*	1,26	1,39	1,33	1,37	———	———

* Radiation Index = $\frac{\text{Radiation at x\%H}}{\text{Radiation at 14\%H}}$

+ Depends upon position in combustor secondary zone

5.3 Despite the proven influence of hydrocarbon type (especially differences between 1-ring, 2-ring and 3-ring aromatics), the effects of fuels tested to date appear to correlate most satisfactorily with hydrogen content.

5.4 The assumption of the above conclusion is somewhat confirmed by the satisfactory prediction of radiation effects using the model described within this report.

5.5 The wall temperature correlation factor $[T_x] = (T_L - T_{LO})/(T_{LO} - T_O)$ should be used with caution since it is sensitive to inlet temperatures and pressures as well as position in the combustor. Generally, conditions most likely to lead to combustor failure, like take-off or dash, lie below the correlation. Also, the use of mean combustor temperatures can be very misleading. Nevertheless, it can be used as a guide for predicting the effects of combustors of similar design and/or operating conditions.

5.6 In view of the fact that hydrogen content still seems to be the most important factor, the simple model for the prediction of wall temperatures of [2] seems to be quite appropriate for the predictions of the effects of future fuels.

ACKNOWLEDGEMENTS

The authors would like to thank the National Sciences and Engineering Research Council Canada, for financial support of the above work. They also express their gratitude to the Canadian Department of National Defence who sponsored earlier work on the same topic which naturally progressed into the present work.

REFERENCES

[1] Odgers, J., "Heat Transfer in Combustors and Turbine Equipment with Special Reference to Film Cooling Processes. A Classified Bibliography", Report No. j.o. 73, Université Laval, Dept. de Génie mécanique, 1979.

[2] Kretschmer, D., & Odgers, J., "A Simple Method for the Prediction of Wall Temperatures in Gas Turbines", ASME Paper No. 78-GT-90, Gas Turbine Conference & Products Show, London, England, April 9-13, 1978.

[3] Lefebvre, A.H., Herbert, M.V., "Heat Transfer Processes in Gas Turbine Combustion Chambers", Proceedings of the Institute of Mechanical Engineers, Vol. 174, No. 12, 1960.

[4] Beer, J.M., and Siddal, R.G., "Radiative Heat Transfer in Furnaces and Combustors", ASME Paper No. 72-WA/HT-29, New York, N.Y., Nov. 26-30, 1972.

[5] Opdyke, G., Private Communication, AVCO Lycoming, Stratford, Conn., May 1976.

[6] Yuen, W.W., & Tien, C.L., "A Simple Calculation Scheme for the Luminous-Flame Emissivity", 16th Symposium (International) on Combustion, pp. 1481-1487, The Combustion Institute, Pittsburgh, 1977.

[7] Bueters, K.A., "Combustion Products Emissivity by F_E Operator", Combustion, March 1974, pp. 12-18.

[8] Odgers, J., "The Effects of Fuel Composition upon Heat Transfer within Gas Turbine Combustors", Report No. j.o. 94, Université Laval, Dept. de Génie mécanique, 1980.

[9] Odgers, J., "Combustor Heat Transfer and Exhaust Pollutants", Section A2.2 of "Alternative Jet Engine Fuels", Vol. 2, Ed. R.B. Whyte, AGARD Advisory Report No. 181, PEP Group 13, July 1982.

[10] Blazowski, W.S., "Combustion Considerations for Future Jet Fuels", 16th Symposium (International) on Combustion, p. 1631-1639, The Combustion Institute, Pittsburgh, 1977.

[11] Odgers, J., "Problems due to Multifuel Operation of Gas Turbine Combustion", p. 71-85, Gas Turbine Design Problem, Ed. A.H. Lefebvre, Hemisphere Publishing Co., 1980.

[12] Gleason, C.C., Oller, T.L., Shayerson, M.W., & Bahr, D.W., "Evaluation of Fuel Character Effects on J79 Combustion System", Report No. AFAPL-TR-79-2015 (CEEDO-TR-79-06), General Electric Company, Aircraft Engine Group, Cincinnati, Ohio, June 1979.

[13] Gleason, C.C., Oller, T.L., Shayerson, M.W., & Bahr, D.W., "Evaluation of Fuel Character Effects on the F101 Engine Combustion System", Report No. AFAPL-TR-79-2018 (CEEDO-TR-79-07) General Electric Co., Aircraft Engine Group, Cincinnati, Ohio, June 1979.

[14] Rudey, R.A., & Grobman, J.S., "Impact of Future Fuel Properties on Aircraft Engines and Fuel Systems", Paper No. 6, AGARD Lecture Series No. 96 - Aircraft Engine Future Fuels and Energy Conservation - AGARD LS-96, September 1978.

[15] Marchionna, N.R., "Turbine Fuel Tolerance Study: Multifuel Engines Tests", AVCO Lycoming Div., Stratford, TARADCOM Technical Report No. 12392.

[16] Bauserman, G.W., Spengler, C.J., and Cohn, A., "Combustion Effects of Coal Liquid and Other Synthetic Fuels in Gas Turbine Combustors - Part II: Full Scale Combustor and Corrosion Tests", ASME Paper No. 80-GT-68, Gas Turbine Conference & Products Show, New Orleans, La., March 10-13, 1979.

[17] Singh, P.P., Cohn, A., Pillsbury, P.W., Bauserman, G.W., Stein, T.R., Mulik, P.R., and Bazarian, E.R., "Combustion Effects of Coal Liquid and Other Synthetic Fuels in Gas Turbine Combustors - Part I: Fuels Used in Subscale Combustion Results", ASME Paper No. 80-GT-67, Gas Turbine Conference & Products Show, New Orleans, La., March 10-13, 1980.

[18] Jackson, T.A., "Fuel Character Effects on the J79 and F101 Engine Systems", Aircraft Research and Technology for Future Fuels - A Symposium held at Lewis Research Centre, Cleveland, Ohio, NASA Conference Publication 2146, April 16-17, 1965.

[19] Schirmer, R.M. & Quigg, H.T., "High Pressure Combustor Studies of Flame Radiation as Related to Hydrocarbon Structure", Phillips Petroleum Co., Bartlesville, Report 3952-65R, 1965.

[20] Naegeli, D.W., Moses, C.A., "Effect of Fuel Molecular Structure on Soot Formation in Gas Turbine Engines", ASME Paper No. 80-GT-62, Gas Turbine Conference & Products Show, New Orleans, La., March 10-13, 1980.

[21] Moses, C.A., and Naegeli, D.W., "Fuel Property Effects on Combustor Performance", ASME Paper No. 79-GT-178, Gas Turbine Conference & Exhibit & Solar Energy Conference, San Diego, Calif., March 12-15, 1979.

[22] Marsland, J., Odgers, J., and Winter, J., "The Effects of Flame Radiation on Flame-Tube Metal Temperatures", 12th Symposium (International) on Combustion, Combustion Institute, Pittsburgh, 1969, pp. 1265-1276.

DISCUSSION

C.Moses, US

You have given us a caveat in the use of the Blazowski parameter suggesting I believe that the changes are due not only to hydrogen content but also changes in operating conditions. I would like to point out that the parameter has been shown, by Kenworthy at the 1982 ASME Gas Turbine Conference, to be very useful in predicting the increases in metal stresses due to higher liner temperatures; this is then used to predict reduction in liner life due to low-cycle thermal fatigue.

Author's Reply

I would like to thank you for your information: I was not aware of Kenworthy's paper. However, I still think that the variation of the parameter, especially within a single chamber, still leaves me with some doubt unless very particular restrictions have been placed as to the definition of the parameter for the purpose you mention.

ALTERNATE FUELS USE IN A VEHICULAR GAS TURBINE

by

Nicholas R. Marchionna
Chief, Advanced Combustor Design
Avco, Lycoming Division
550 South Main Street
Stratford, Connecticut 06497

AD-P003 135

Practical aspects of combustor design for the use of alternate fuels in the AGT 1500 vehicular gas turbine engine are discussed. Engine performance test results are related to laboratory data and to combustor component performance over the range of engine operating conditions. Fuel effects on starting and low power efficiency are related to atomizer performance and to drop size distribution. Smoke emissions are correlated with fuel characteristics, engine operating conditions, and combustor primary zone design parameters. Results are presented for fuels ranging from gasoline to No. 6 oil.

INTRODUCTION

The ability of military vehicles to use alternative fuels can provide significant tactical advantages. The U.S. Army's new M-1 tank, powered by the AGT1500 gas turbine engine, was designed to operate on fuels ranging from gasoline to diesel fuel. A special feature of the design to assist operation on fuels of varying heating value is an electronic fuel control which senses engine speed and temperature and automatically adjusts fuel flow rate to make power. Figure 1 shows an illustration of the AGT1500 engine. This engine contains a two spool compressor/turbine with a free power turbine driving a reduction gearbox connected to the transmission. A recuperator on the exhaust of the engine heats up combustor inlet air to improve cycle efficiency. Another important feature of the engine for fuel economy is variable geometry power turbine inlet guide vanes which allow the gas producer to run at near peak efficiency over most of the engine cycle. An accessory gearbox is attached to the gas producer to provide a starting motor, hydraulic power, and fuel pumping capability.

The AGT1500 engine has a single can combustor, fuel nozzle and a scroll to distribute the hot combustor gas circumferentially to the turbine. Minimizing the number of fuel nozzles is an important consideration in the design of small gas turbines so that fuel passages can be made as large as possible. This is necessary in order to pass contaminated fuel and to keep the fuel nozzle as cool as possible, especially required with a recuperative operating cycle.

The recuperative cycle of the AGT 1500 assists in the achievement of two major design considerations for vehicular application: good flame stability and high combustion efficiency. Both are achieved in large measure by high combustor inlet air temperature which exceeds 600°F at idle and is close to 1000°F at full power. This cycle advantage, while assisting in the burning of alternative fuels, requires special consideration in the design of the liner wall cooling.

Figure 2 shows a cross section of the combustor up to the location where it discharges into the scroll. The liner wall

cooling design contains short louvers for high cooling effectiveness. The louver material is thoria dispersed nickel (TDNi) for high strength. In order to enhance multifuel capability by reducing flame radiation, the fuel injector is an air blast design. The injector receives its air directly from the compressor discharge which is at a slightly higher pressure and considerably cooler than the recuperator return air which goes to the rest of the combustor. A pressure atomizing pilot injector is used for starting. This injector is located directly in the center of the air blast fuel nozzle and operates continuously while the engine is running.

The combustor system design and development for the use of alternate fuels was strongly supported by the U.S. Army Tank and Automotive Command, ref 1-5.

STARTING

One of the most critical aspects of combustor design for highly viscous alternate fuels is getting the engine started. Problems can arise in both ignition and the acceleration region between ignition and idle. Starting can be affected because fuels can have up to two orders of magnitude variation in viscosity as shown in figure 3 for different fuels and different fuel temperatures. Viscosity has a significant effect on flow Reynolds number which, in turn, can affect the discharge coefficients of fuel system components such as the fuel metering valve and the fuel injector. Increasing viscosity can affect discharge coefficients in different ways.

Early experience with the AGT1500 operating on No. 4 oil indicated reduced flow from the fuel control to the combustor in the starting region due to low Reynolds numbers in the fuel control valving. The shape of the metering valve stem was changed to increase the Reynolds number and thereby reduce the sensitivity to viscosity. Figure 4 shows calibration data for the early design and for the modified design on viscosities ranging from 2 to 20 centistokes. In the starting fuel flow region where the objective was to supply 74 pph, the viscosity sensitive design provided only half the required flow with a fuel viscosity of 15 centistokes. A modified design provides a significant improvement by delivering 85 percent of the required value at a viscosity of 15 centistokes.

Fuel injector performance is also sensitive to viscosity. The discharge coefficient of a pressure atomizing injector usually increases with increasing fuel viscosity so that the same volumetric flow passes with less pressure drop. As a result of low pressure drop, atomization quality is sharply reduced. The deleterious effect of poor atomization on ignition has been shown to be very significant with everything else being equal, Ballal and Lefebvre, ref 6, have shown that the Minimum Spark Energy required for ignition varies with the 4.5 power on Sauter Mean Diameter (SMD), which is a measure of the spray's volume-to-surface ratio. If sufficient ignition energy is available, but the spray drops are so big that evaporation controls the growth of the spark kernel, then the minimum fuel flow required for ignition would be expected to vary with the total surface area of the drops. If the surface area alone were sufficient to define the fuel flow required for ignition at a given aero-dynamic condition, then, at the ignition limit, the required fuel flow (W_{fR}) would vary directly with the SMD.

$$\text{Surface Area} \sim W_f/\text{SMD} = \text{Constant}$$

then

$$W_{fR} \sim SMD \qquad \text{EQ 1}$$

For a pressure atomizing nozzle, SMD is most affected by three parameters: fuel viscosity (N), pressure drop (ΔP), and volumetric flow rate (W_f/ρ). A typically emperical equation for SMD is:

$$SMD \sim N^{.22}(W_f/\rho)^{.21}/\Delta p^{.5} \qquad \text{EQ 2}$$

Orifice discharge coefficients may be related to flow rate (W_f), density (ρ), and pressure drop by

$$C_D \sim W_f/(\rho\Delta p)^{.5} \qquad \text{EQ 3}$$

so that the SMD is found to be a function of viscosity, discharge coefficient and flow rate by combining equations 2 and 3.

$$SMD \sim N^{.22}C_D\rho^{.29}/W_f^{.79} \qquad \text{EQ 4}$$

The required fuel flow can then be related to SMD, EQ 1, as:

$$W_{fR} \sim SMD \sim N^{.22}C_D\rho^{.29}/\ W_f^{.79}$$

and at the ignition limit when $W_{fR} = W_f$

$$W_{fR} \sim N^{.123}C_D^{.56}\rho^{.162} \qquad \text{EQ 5}$$

For fuel nozzles which have no change in discharge coefficient with viscosity the effect of an order of magnitude change in viscosity (i.e. 1.5 to 15 centistokes) would require 33% more fuel for ignition:

$$W_{fR} \sim N^{.123} \text{ or } 10^{.123} = 1.33 \qquad \text{EQ 6}$$

However, if the discharge coefficient also increases with viscosity, considerably more fuel would be required. Figure 5 shows the viscosity sensitivity of the initial design of the pilot nozzle used for starting the AGT 1500. As originally designed the flow number (used as a measure of discharge coefficient) varies with viscosity to the .18 power over the range from 2 to 20 centistokes. As indicated by Equation 5, this would require still more fuel flow for ignition:

$$W_{fR} \sim N^{.123}(N^{.18})^{.56} = N^{.224} \qquad \text{EQ 7}$$

for an order of magnitude increase in viscosity, the requirement would be 67% more fuel flow for ignition. A redesign of the nozzle swirl chamber reduced its viscosity sensitivity to a very low value as shown in figure 5.

The minimum fuel flow required for ignition is shown in Figure 6 as a function of viscosity for a variety of fuels in a development AGT 1500 combustor. The operating condition is at a typical ignition air flow rate of 1200 pph and data are taken using the initial fuel nozzle design. The required fuel flow in the viscosity

range from 2 to 12 centistokes follows the trend expected from Equation 7. However, above 12 centistokes, considerably more fuel flow is required than expected from the above analysis.

It is hypothesized that the large increase in required fuel flow above 12 centistokes is related to evaporation effects because of the similarity of the curves to blowout data also obtained with these fuels. Figure 7 shows the lean blowout data expressed as fuel air ratio for different air flow rates, inlet air temperature and fuels. The same functions of viscosity which correlate the ignition data fit these blowout data as well. The results indicate that the assumptions and possibly the expressions for drop size calculation are not valid for viscosities over 12 centistokes. The assumption of equivalent surface area, for example, may not be as important as the number of drops per unit volume or the number of small drops. Laboratory investigations in the past have shown that the presence of small drops is crucial to the ignition process. Recently, an analytical investigation, by Zhou, ref 7, has come to the same conclusion.

EFFICIENCY

The combustor efficiency required for starting a gas turbine must be high and vary only slightly if starts are to be successful with both a cold and warm engine. Otherwise, the mass of fuel sufficient to start a cold engine would overheat a warm engine. In order to achieve high starting efficiency, the secondary portion of the nozzle must have a fine spray when fuel is introduced. This is achievable with high air to fuel ratios in an air blast fuel injector.

Lefebvre, ref 8, shows that drop size of the air blast injector can be described as

$$SMD = 3.33 \times 10^{-3}(\sigma_L \rho_L D_P/\rho_A^2 V_A^2)^{.5}(1 + W_L/W_A) + \ldots \quad \text{EQ 8}$$

$$+ 13.0 \times 10^{-3}(N_L^2/\sigma_L \rho_L)^{.425} Dp^{.575} (1 + W_L/W_A)^2$$

where
- σ is the surface tension
- N is the viscosity
- W is the mass flow rate
- Dp is a characteristic orifice dimension.
- V is the velocity
- and the subscripts A and L refer to the air and liquid fuel respectively

The first term of this equation accounts for surface tension effects when the viscosity is low. With high viscosities, the second term dominates the equation and the effect of the liquid to air ratio (to the second power) becomes an influential effect. In the starting region where only a little additional fuel is required to reach idle, the air blast type injector can provide a low SMD to obtain high efficiency. Figure 8 shows measured drop size distribution in the ignition and starting region using DF-2 with the current production injector. As the air density increases, as the engine approaches idle, the SMD decreases due to a reduction in the first term of the air blast equation above.

The efficiency of the AGT1500 combustor in the ignition and starting region.is plotted against the kinetic correlating theta parameter in figure 9 with DF-2 fuel. Efficiency is over 95% for most of the region. As the engine accelerates to idle, combustor operating conditions increase the value of theta since the pressure

and temperature terms increase more rapidly than the air flow rate. As a result, combustor efficiency continues to increase with increasing power.

Efficiency over the entire engine operating range from idle to full power is shown in figure 10 for fuels include gasoline, JP-4, DF-2, and No. 4 oil (unheated) which cover a range of viscosities from 0.5 to 42 centistokes and a wide range of boiling point temperatures. For most conditions, efficiency does not appear to be limited by drop size, droplet evaporation, or by reaction kinetics. Since combustion efficiency is normally classified as being limited by either evaporation, kinetics, or mixing, it is concluded that mixing remains the limiting parameter in this combustor system at operating conditions from idle to full power.

SMOKE

Exhaust smoke characteristics for the production AGT 1500 engine are shown in figure 11 for DF-2, the fuel usually burned in the M-1 tank. The smoke plume from the exhaust is invisible for all running conditions with an SAE smoke number of under 45. The engine specification limit of 30 ensures that there is adequate margin in meeting the requirement of an invisible exhaust smoke requirement.

The change in smoke number with power level is curiously different from many gas turbine engines because of the peak in smoke in the low power region where the engine is operating below its peak fuel-air ratio. It is hypothesized that this peak level is the result of the competition between soot production and soot oxidation, with oxidation predominating above the mid power range where flame temperatures are highest. Variability in the smoke data can occur with variations in the engine's variable power turbine geometry whose main effect on the combustor is to increase air flow and decrease inlet air and flame temperature when opened at constant power setting. Early work in the Full Scale Engine Development Phase showed that decreasing inlet air and flame temperature increased smoke considerably. That work also demonstrated that smoke can be controlled by the well known technique of adjusting stoichiometry and mixing in the combustor recirculation zone. Figure 12 shows a correlation of the Maximum Smoke Number (MSN) with primary jet hole diameter, D, and location from the fuel injector, L. The correlating parameter $D'^{.66}$ is based on jet penetration proposed by NREC, ref 9, for the primary zone. The correlation strongly implies that smoke is formed in the apex of the fuel nozzle spray where mixing is low and the fuel air ratio is high. This correlation was obtained with changes in both hole location, hole diameter, and number but without changes in combustor liner pressure drop. It suggests that similar results could be obtained by changes in liner design to increase pressure drop in order to achieve the same jet penetration.

The Maximum Smoke Number has been found ref, to correlate well with fuel aromatic content which has been suggested by Blazowski to be the result of fast condensation reactions of the aromatics, ref 10. Figure 13 shows the correlation with JP-4, DF-2, and unleaded gasoline. The analysis of the Amoco Supreme unleaded automotive gasoline was performed by Phoenix Labs. This type of gasoline was typical of blends used in the mid 1970's to achieve high octane without lead. As a result, the aeromatic content was increased with an accompanying decrease in hydrogen and heating value.

Once fuel evaporation or combustion kinetics begin to become influenced by fuel quality, the smoke number measurement can behave inconsistently. Figure 14 shows smoke measurement taken while burning No. 4 oil in the engine. Soot generated smoke has dropped

considerably and is more nearly constant with power level. Coke build up on primary zone liner wall surfaces increased because of delayed evaporation and fuel impingement on the liner walls. The reduced evaporation rate moves the combustion zone downstream where more air is available to reduce fuel rich pockets and thereby reduces smoke.

WALL TEMPERATURE

The effect of various fuels on wall temperature has been under serious investigation in several alternative fuel programs, ref 11. Since a change in flame radiation is the source of variation in wall temperature, it is reasonable to expect that flame temperature and fuel chemistry (as it effects flame emissivity) are the major variables. It is difficult however to separate these two variables since they have strong interactions with each other. Moreover, evaporation and kinetics can vary with stoichiometry which is determined by combustor geometry. The geometry effects make engineering correlations particularly difficult.

Despite the entanglement of variables that affect flame radiation, Oiler, ref 12, has correlated wall temperature against fuel hydrogen content, which works as well as other fuel characteristics in most cases. This variable is used in figure 15 in an attempt to correlate two combustor configurations with a variety of fuels. The development combustor configuration is the same one for which engine smoke data is presented in figure 13 and appears to correlate a reduction in wall temperature with increasing hydrogen content. However, the production configuration tests with two shale fuels do not follow the same trend. It is noteworthy that the problems encountered with this type of correlation normally occur with low hydrogen content fuels when the fuel chemistry changes from a simple paraffinic structure to a more complex multi-bonded (ie. aromatic) structure.

Figure 16 shows the same data using aromatic content as a correlating parameter. All the data now follow the trend of increasing wall temperature with increasing aromatics. This is similar to the trend found with the smoke data and strongly supports the hypothesis that the increased radiation is linked to an increase in gas phase soot production in this combustor. The differences in wall temperature level coincide with configuration changes in the combustor primary zone which gave lower wall temperature with less smoke.

CONCLUSIONS

The AGT1500 engine was designed to operate on a variety of fuels from gasoline to DF-2. Laboratory engine tests have shown satisfactory operation with these fuels without any fuel control compensating devices. This fuel tolerance has been achieved by a fuel system designed to minimize the viscosity effects in the fuel. The fuel is finely atomized and droplet evaporation does not limit combustion. In addition, the recuperative engine cycle provides sufficiently high temperature so that combustion is not limited by reaction rate. As a result, the combustor exhibits acceptably small change in efficiency, smoke, and wall temperature within the normal variation of these fuel types.

References

1. Marchionna, Nicholas, Watkins, Sidney, and Opdyke, George Jr., "Turbine Fuel Tolerance Study", TACOM Technical Report No. 12090, October 1975.

2. Marchionna, Nicholas, and Opdyke, George Jr., "Turbine Fuel Tolerance Study, Phase II", TACOM Technical Report No. 12191, August 1976.

3. Marchionna, Nicholas R., Opdyke, George Jr., Hudson, Rodney, and Hubbard, Arthur S., "Turbine Fuel Tolerance Study Initial Engine Tests: No. 4 Oil", TARADCOM Technical Report No. 12272, April 1977.

4. Marchionna, Nicholas, R., "Turbine Fuel Tolerance Study: Multi-fuel Engine Tests", TARADCOM Technical Report No. 12392, July 1978.

5. Cramer, Paul; Marchionna, Nicholas "AGT1500 Production Engine Alternate Fuels Capability", TACOM Technical Report No. 12671, in publication.

6. Ballal, D.R., and Lefebvre, A.H., "Ignition and Flame Quenching of Flowing Heterogeneous Fuel-Air Mixtures", Combustion and Flame 35:155-168 (1979).

7. Zhou, X-Q; Chiu, H; "Spray Group Combustion Processes in Air Breathing Propulsion Combustors", AIAA/SAE/ASME 19th Joint Propulsion Conference, AIAA 83-1323, June 1983.

8. Lefebvre, Arthur H. "Airblast Atomization", Prog Energy Combustion Science Vol 6 pp 233-261.

9. The Design and Performance Analysis of Gas Turbine Combustion Chambers by Northern Research and Engineering Corp, NREC Report No. 1082-1, 1964.

10. Blazowski, W.S., "Dependence of Soot Production on Fuel Blend Characteristics and Combustion Conditions", Journal of Engineering for Power, Vol 102, April 1980.

11. General Electric Co. Aircraft Engine Business Group "Evaluation of Fuel Character Effects on J79 Smokeless Combustor", AFWAL TR-80-2092, November 1980.

12. Oiler, T.L., Gleason, C.C., Kenworthy, M.J., Cohen, J.D., and Bahr, D.W. of General Electric Co, "Fuel Mainburner/Turbine Effects" AFWAL-TR-81-2100, May 1982.

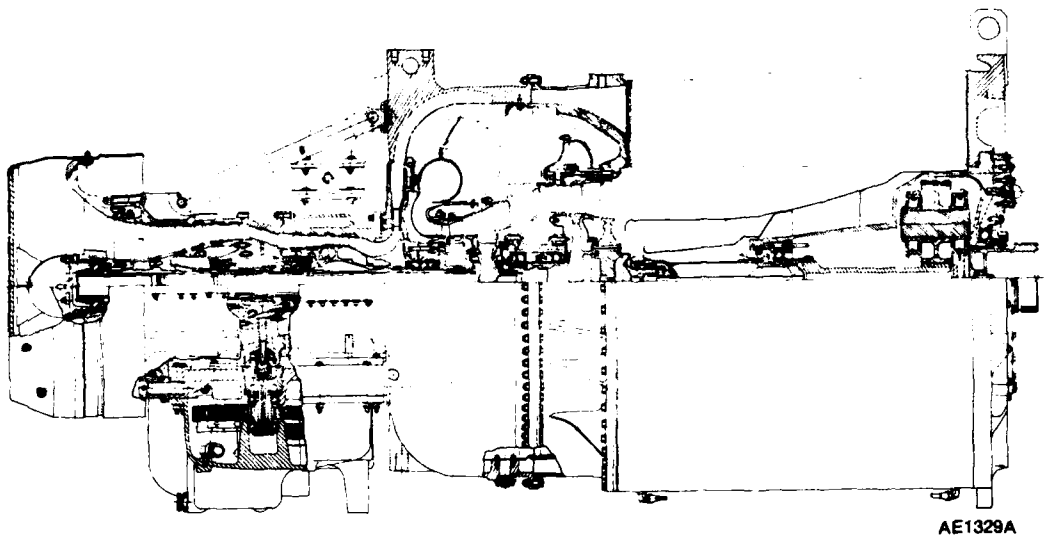


FIGURE 1 - AGT 1500 ENGINE

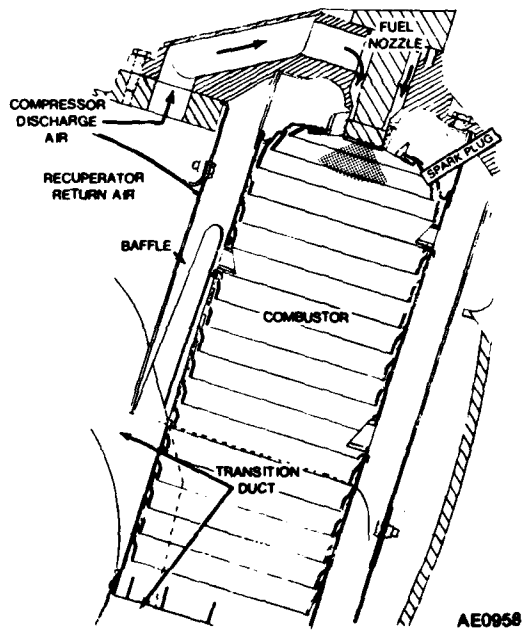


FIGURE 2 - MULTI-FUEL COMBUSTOR INSTALLATION IN AGT 1500

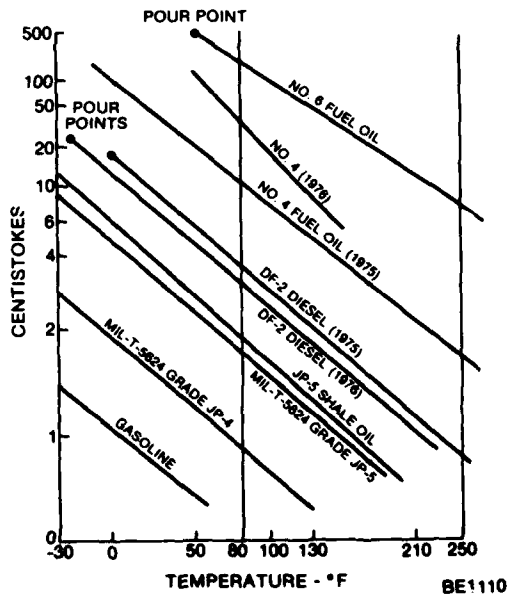


FIGURE 3 - VISCOSITY - TEMPERATURE CHARACTERISTICS OF FUELS

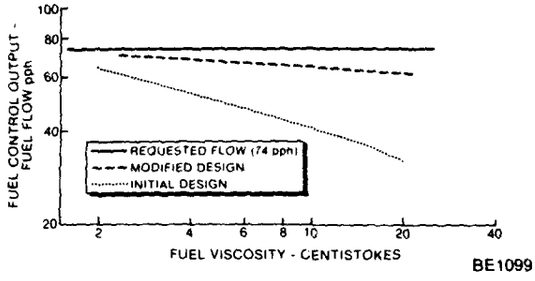


FIGURE 4 - FUEL CONTROL OUTPUT vs VISCOSITY

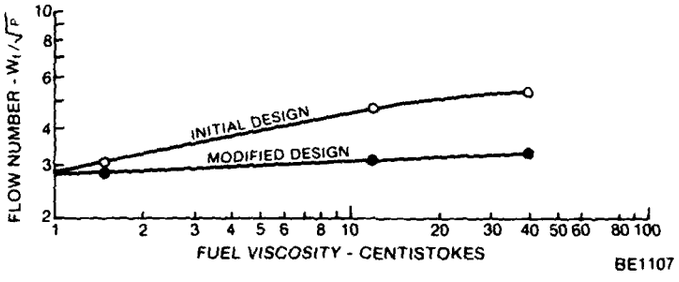


FIGURE 5 - EFFECT OF FUEL VISCOSITY ON PILOT FLOW NUMBER

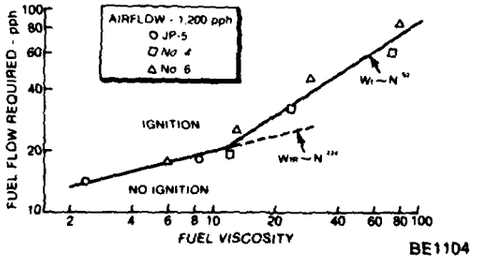


FIGURE 6 - FUEL FLOW REQUIRED FOR IGNITION

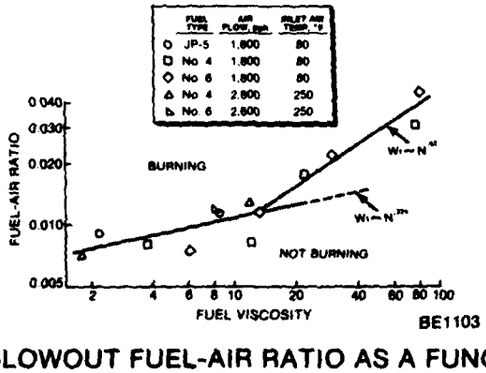


FIGURE 7 - BLOWOUT FUEL-AIR RATIO AS A FUNCTION OF FUEL VISCOSITY

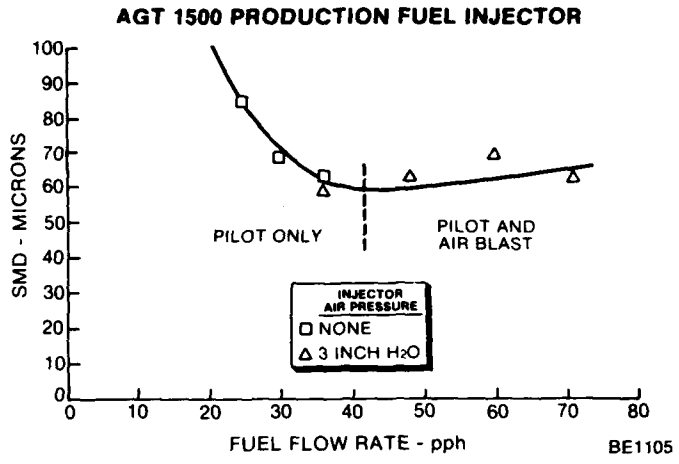


FIGURE 8 - MEASURD SMD vs FLOW RATE, DF-2 FUEL

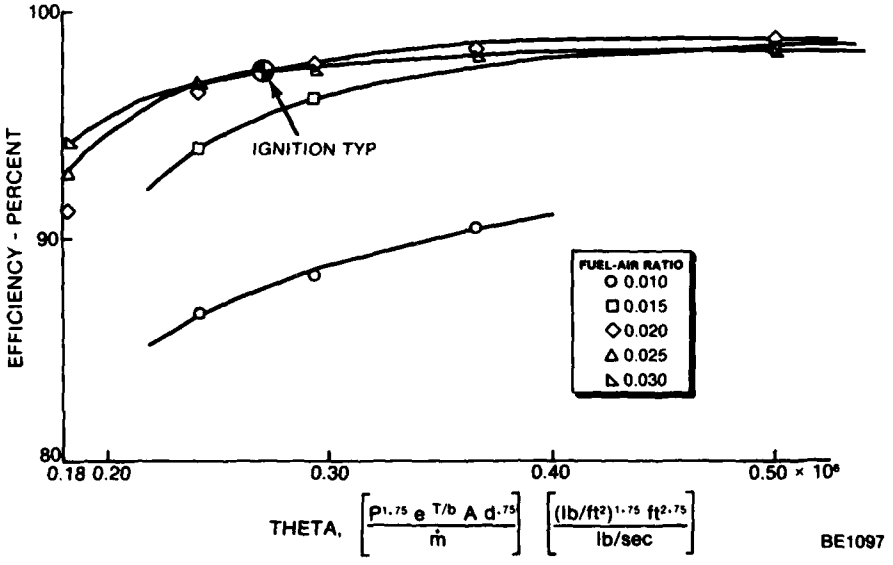


FIGURE 9 - COMBUSTION EFFICIENCY vs THETA PARAMETER

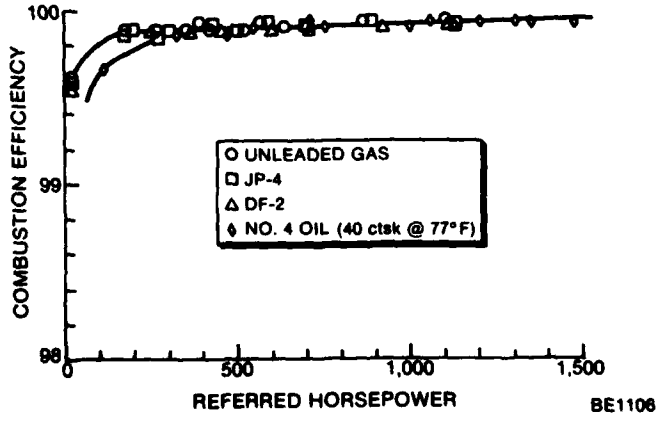


FIGURE 10 - MULTI-FUEL COMBUSTION EFFICIENCY

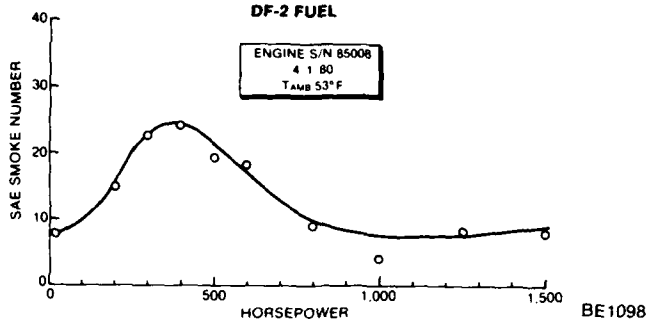


FIGURE 11 - AGT 1500 SMOKE NUMBER, DF-2 FUEL

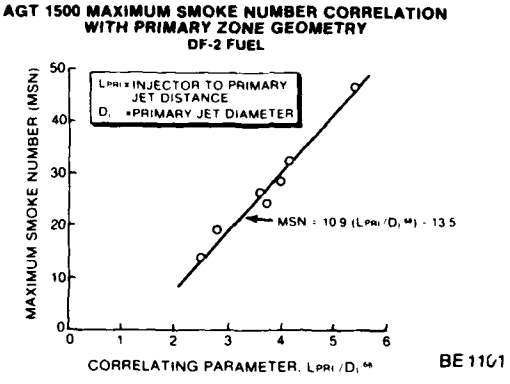


FIGURE 12 - EFFECT OF GEOMETRY ON MAXIMUM SMOKE NUMBER

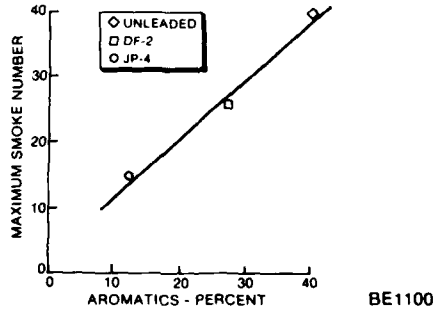


FIGURE 13 - EFFECT OF AROMATICS ON SMOKE NUMBER

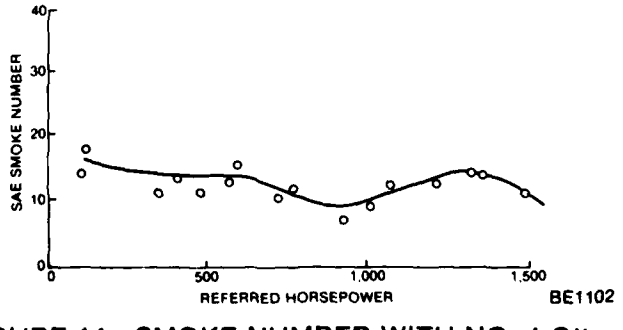


FIGURE 14 - SMOKE NUMBER WITH NO. 4 OIL

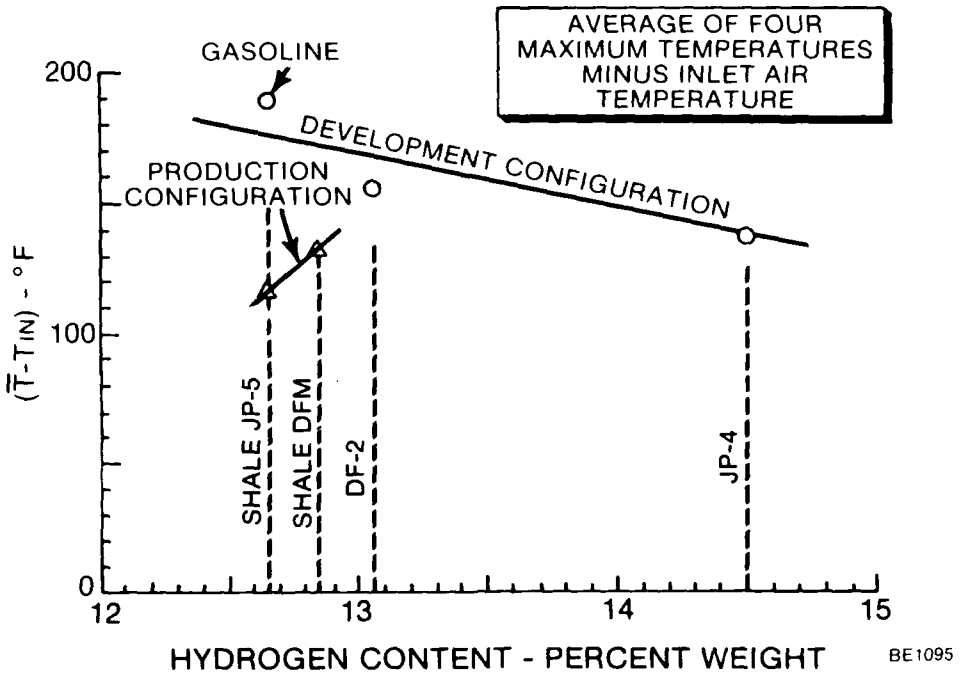


FIGURE 15 - EFFECT OF GEOMETRY ON MAXIMUM SMOKE NUMBER

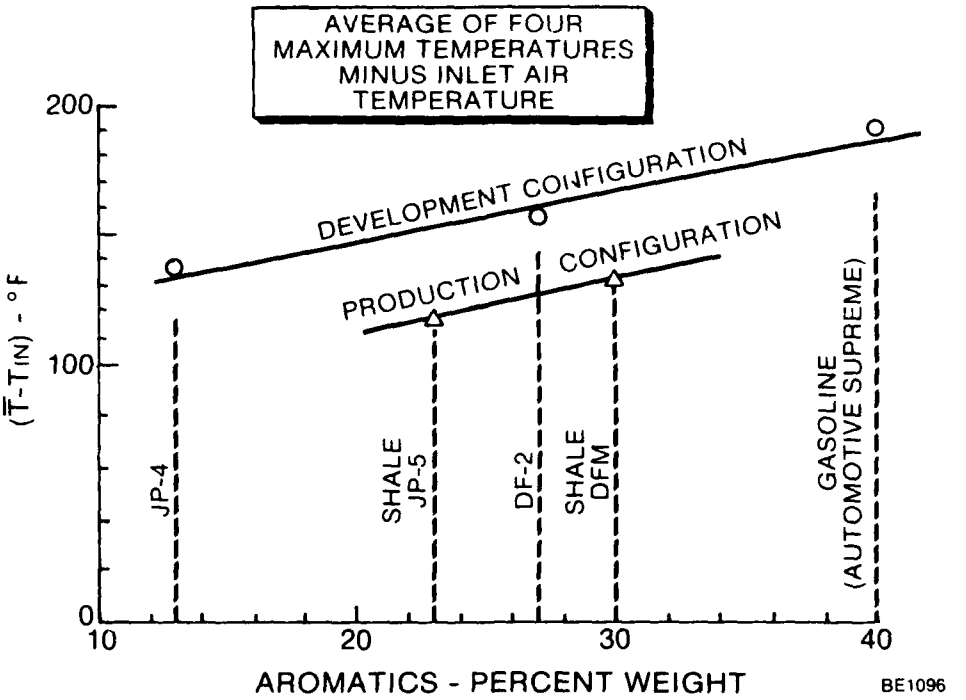


FIGURE 16 - AGT 1500 EFFECT OF AROMATICS ON SMOKE NUMBER

DISCUSSION

C.Moses, US

The anomaly shown in Figure 15 may not be real. For the shale oil JP5 and DFM you show liner temperature increasing with hydrogen content. The change in H is too small for the range of your graph and the change in temperature shown may just be due to normal scatter, not hydrogen content. If you had tested a fuel with 14.5 percent hydrogen content in that project as well, the temperature may well have been slightly lower giving you a correlation line very similar to the upper line in the figure rather than with an opposite slope.

Author's Reply

Regretfully, only the two fuels were tested with the combustor configuration before the test rig and combustor were disassembled. The data do emphasize the need for accurate measurements of temperature, hydrogen content, and aromatics.

H.Saravanamuttoo, Ca

The application of the gas turbine to tank propulsion introduces several new operational problems. These include extended low power operation, many power changes, and perhaps most importantly continuous operation under conditions of heavy vehicle vibration and shock. Have these factors had any effect on engine and combustor durability?

Author's Reply

The application of a gas turbine to a vehicular application does impose a greater number of operating cycles per hour than an aircraft application. Moreover, the duty cycle is completely arbitrary and can contain many hours of continuous low power operation as well as high frequency maneuvers. (But when compared to a diesel engine, the gas turbine has been shown to be extraordinarily well suited to this application). Obviously, LCF limitations require that the engine be overhauled at shorter operating intervals than in an aircraft application. Vibration and shock have not been a problem.

E.Mularz, US

Please elaborate more on your Figure 11 which shows a peak in smoke number at an intermediate engine power condition.

Author's Reply

This characteristic has been faithfully repeated in laboratory tests and has been observed since the engine conception, covering all combustor designs and fuel injection techniques used in development. The peak is evident with fuels from Gasoline to Diesel Fuel Marine. The peak does *not* occur close to the peak in combustor fuel air ratio (which occurs at approximately 1200 horsepower). Variations in the amplitude of the peak generally scale with the rest of the smoke data. The biggest change in smoke number has been found to occur with variations in combustor inlet air temperature, increasing temperature causing a decrease in smoke. It is presumed that the shape of the curve is different from aircraft gas turbine engine smoke characteristics because of the can-scroll design and the recuperative cycle which delivers high inlet air temperature at low power conditions. It is hypothesized that the effect is caused by high evaporation rates which cause locally rich burning and smoke production to occur in the primary zone with subsequent oxidation reactions to occur the turbine, the path length is fairly long and the time for oxidation to occur at high temperatures is considerably longer than would be present in annular combustor designs. It is inferred therefore that the soot oxidation rate is lower than the production rate at idle but higher at power levels beyond the peak in the curve.

CONCEPTION D'UN FOYER A FLUX INVERSE POUR PETITES TURBOMACHINES

par

André MESTRE et Guy LAGAIN*

OFFICE NATIONAL D'ETUDES ET DE RECHERCHES AEROSPATIALES
B.P. n° 72 - 92322 CHATILLON Cedex (FRANCE)

SOMMAIRE

En vue de la réalisation d'un foyer à flux inversé pour petites turbomachines une étude préliminaire a été entreprise à la pression atmosphérique en absence du convergent à retour, afin de permettre l'observation directe de la zone de combustion et d'améliorer la configuration initiale avant la mise en oeuvre des mesures appropriées.

L'emploi de cannes à prévaporisation a permis d'obtenir des performances intéressantes pour le constructeur du point de vue répartition de température à la sortie du foyer, émissions de polluants, rendement de combustion.

DESIGN OF A COMBUSTION CHAMBERS WITH REVERSE FLOW FOR SMALL GAS TURBINES

SUMMARY

Test bench experimentation of reverse flow combustion chambers for small gas turbines was first oriented towards atmospheric operation in order to allow direct observation of the flame and corresponding movie pictures.

Two different types of fuel injection were compared : mechanical pulverisation and prevaporisation. The latter technique gives higher performance : better temperature distribution, lower emission of pollutants, higher efficiency. On the other hand, cold start seemed easier with mechanical injection. Therefore auxiliary fuel injectors had to be used.

NOTATIONS

d : longueur de dilution

$\dot{m}$: débit massique

N : rapport de la vitesse de rotation à la vitesse maximale de rotation

p : pression

T : température

$\bar{T}$: température moyenne arithmétique

T_M : température maximale

T_{RM} : température maximale du profil radial moyen

V : volume du tube à flamme

X : fraction molaire

I_{CO} : indice d'émission de monoxyde de carbone

---

*Société TURBOMECA
Travail effectué sous contrat TURBOMECA.

IeCxHy: indice d'émission d'hydrocarbures imbrûlés

IeNO : 'ndice d'émission de monoxyde d'azote

IeNOx: indice d'émission des oxydes d'azote

α : rapport de mélange combustible-air

Δ : accroissement

ϕ : diamètre

η : rendement enthalpique de combustion

θ : repère angulaire de sonde

INDICES

a : air

k : combustible

1 : collecteur d'air

2 : entrée foyer sauf indication contraire

3 : sortie foyer

1 - INTRODUCTION

Les petites turbomachines utilisées notamment pour la propulsion d'hélicoptères comportent un compresseur centrifuge entraîné au moyen d'une turbine axiale. La sortie du compresseur, dont le diamètre est sensiblement deux fois plus grand que celui de la turbine, conditionne le maître couple de la machine, et le volume disponible à la périphérie de la turbine peut être utilisé pour loger la chambre de combustion. Afin de réduire le porte à faux entre les deux roues, l'écoulement moyen dans la chambre de combustion subit un changement de direction égal à 180°, d'où l'appellation "foyer à flux inversé". L'emploi d'un tel foyer permet d'utiliser au mieux le volume disponible entre compresseur et turbine, il permet en outre un démontage simple du carter et du tube à flamme sans qu'il soit nécessaire de désaccoupler la turbine du compresseur lors des révisions, c'est-à-dire une réalisation modulaire du moteur.

L'étude d'un foyer nouveau au banc d'essai comporte en général une phase initiale de mise au point au cours de laquelle l'observation directe ainsi que la cinématographie de la zone de combustion (couleur, localisation de la flamme...) fournissent au spécialiste des éléments d'appréciation qui servent de guide pour retoucher et améliorer la configuration initiale avant la mise en oeuvre des mesures appropriées. Dans le cas du foyer à flux inversé, l'observation de la flamme étant exclue par la présence du convergent à retour, il a paru souhaitable de retirer ce convergent au cours de la phase initiale afin de permettre une observation directe de la combustion suivant une direction parallèle à l'axe du foyer, et par suite de commencer l'étude de la combustion à la pression atmosphérique [1]. Les résultats ainsi obtenus permettent une amélioration de la chambre de combustion, tant en performance (rendement de combustion) qu'en tenue du tube à flamme.

2 - FOYER A FLUX INVERSE EXPERIMENTAL

Le dessin de ce foyer, dont une demi coupe est représentée sur la figure 1, a été effectué par la Société TURBOMECA. De type annulaire, il comporte deux éléments principaux et distincts emboîtés l'un dans l'autre :

- le tube à flamme,
- et le convergent (non utilisé lors des essais à la pression atmosphérique).

Le tube à flamme est constitué par l'assemblage de trois éléments distincts (virole externe, virole interne et fond) ; différents perçages assurent un partage conventionnel de l'air :

- air de combustion,
- air de dilution,
- air de refroidissement.

Les orifices d'air de combustion et d'air de dilution comportent des emboutis de rayons appropriés. Les multiperforations permettant le refroidissement de la virole externe et de la virole interne sont inclinées par rapport à la normale d'un angle égal à 60°.

La préparation du mélange combustible a été effectuée au moyen de la prévaporisation, mais des essais, non décrits ici, ont également été effectués avec des pulvérisateurs mécaniques. Un premier tube à flamme a été équipé de 8 cannes à prévaporisation en forme de T comportant chacune deux sorties dirigées vers la cime du foyer. La longueur des bras a été déterminée afin que les jets carburés rencontrent les jets d'air de combustion.

L'allumage a été obtenu à partir d'étincelles électriques à haute énergie ; dans le cas de la

prévaporisation l'allumage ne s'est révélé possible qu'en présence de pulvérisateurs auxiliaires alimentés en kérosène au moyen d'un circuit spécial. La durée d'utilisation des pulvérisateurs auxiliaires est généralement limitée à quelques secondes.

3 - BANC D'ESSAI POUR ETUDES DE FOYERS DE PETITES TURBOMACHINES

3.1 - Essais à la pression atmosphérique

Une demi coupe schématique du montage est représentée sur la figure 2 et comporte essentiellement un collecteur d'air de forme annulaire situé à l'extérieur de la chambre de combustion dont le volume est suffisant pour assurer la tranquillisation du flux. Ce collecteur est raccordé par l'intermédiaire d'un convergent à un distributeur d'air annulaire qui simule la sortie d'un compresseur centrifuge. Une chemise d'eau de forme annulaire permet d'éviter l'échauffement de la face interne du collecteur d'air au contact des produits de combustion. L'évidemment central du collecteur permet l'observation ainsi que la cinématographie de la zone de combustion suivant la direction axiale de l'écoulement.

3.2 - Instruments de mesure

Outre les mesures de débits (air, combustible), la qualification de l'écoulement issu du foyer est effectuée du point de vue pression, température, composition chimique, au moyen de sondes, mobiles autour de l'axe du foyer, et qui peuvent décrire des cercles concentriques équidistants. Ces sondes sont équipées, soit de 5 prises de pression d'arrêt, soit de 5 thermocouples à fil nu, soit encore de 5 prises de prélèvement d'échantillons de gaz ; elles sont disposées radialement sur des mâts profilés et refroidis par circulation d'eau.

Les échantillons de gaz sont transportés au moyen de lignes chauffées jusqu'aux analyseurs et dosés d'une façon continue :

- CO_2, CO par **absorption infrarouge**,
- CxHy par **ionisation de flamme**,
- NOx par **chemiluminescence**.

Au cours de chaque essai, la totalité de l'écoulement annulaire est exploré en pression d'arrêt, en température et en composition chimique. Les différentes mesures sont stockées dans les mémoires d'un ordinateur et un programme de calcul approprié assure les dépouillements en temps réel.

4 - RESULTATS D'ESSAIS

Les résultats détaillés concernent l'exploration de la section de sortie du foyer, soit en températures, soit en concentration d'échantillons de gaz suivant 32 rayons de référence régulièrement espacés.

4.1 - Observation et photographie de la flamme

L'observation directe de la flamme a notamment permis d'optimiser la position longitudinale des cannes afin que la flamme occupe entièrement le fond du foyer. Un excès ou un défaut de pénétration des cannes dans la zone de combustion s'accompagnait d'une localisation de la flamme, soit au voisinage de la virole interne, soit au voisinage de la virole externe. La figure 3 représente l'aspect de la flamme après optimisation de la position longitudinale des cannes et dans le cas du régime de ralenti au niveau du sol.

4.2 - Délai d'allumage

Le délai d'allumage a été déterminé en fonction du débit d'air ainsi qu'en fonction des débits de combustible injectés au moyen des pulvérisateurs auxiliaires et des cannes à prévaporisation. A débit d'air constant, l'augmentation du débit de combustible , soit au moyen des pulvérisateurs auxiliaires, soit au moyen des cannes à prévaporisation entraîne une réduction du délai d'allumage. Pour un couple de valeurs déterminées des débits de combustible, le délai d'allumage augmente relativement peu avec le débit d'air : il peut même diminuer lorsque la valeur du débit d'air est suffisante pour assurer la pulvérisation aérodynamique dans les cannes.

A la suite de l'expérimentation effectuée, pour les conditions normales de démarrage à la pression atmosphérique (allumage au sol), il est possible de choisir des valeurs de débits de combustible pour lesquelles le délai d'allumage n'excède pas 5 secondes, indépendamment de la valeur du débit d'air.

4.3 - Répartition des températures à la sortie du foyer

Les relevés de températures d'écoulement à la sortie du foyer ont été effectués dans un plan de mesure normal à l'axe du foyer. La figure 4 permet de situer la trace D de ce plan sur un plan de coupe méridien : cette trace est repérée par rapport à l'axe de l'orifice de dilution interne au moyen de la distance d. On distingue également sur la figure 5, les positions et les numéros (1 à 5) des thermocouples distants deux à deux de 8 millimètres.

En absence du convergent, les relevés de températures ont tout d'abord été effectués dans la section terminale du tube à flamme (d = 40 mm) ce qui correspond à une longueur de dilution relativement faible par rapport à la longueur réelle en présence du convergent. Afin d'apprécier l'effet de ce convergent, le tube à flamme a été prolongé par une virole annulaire de 32 mm de longueur, équivalente au convergent du point de vue temps de séjour, ce qui a permis d'augmenter la longueur de dilution de d = 40 mm à d = 72 mm.

Afin d'illustrer les principaux résultats, on a représenté sur les figures 5 et 6 deux évolutions circonférentielles des facteurs locaux de température FLT correspondant à des longueurs de dilution de d = 40 mm (fig. 5) et d = 72 mm (fig. 6) respectivement.

Ce facteur FLT défini par :

$$FLT = \frac{T_{3i} - \overline{T_3}}{\overline{T_3} - T_2}$$

a été déterminé aux cinq rayons Z_i indiqués sur les figures. Il caractérise l'écart local de la température T_{3i} par rapport à la température moyenne $\overline{T_3}$ rapporté à l'accroissement moyen de la température à la traversée du foyer, $\overline{T_3} - T_2$. Ce facteur a été déterminé dans le cas du niveau de température maximal, soit sensiblement $\overline{T_3}$ = 1250 K et pour une valeur de la température d'entrée foyer T_2 = 633 K.

Les courbes correspondant aux différents thermocouples peuvent être repérées par les différents traits précisés sur le schéma annexe.

Il ressort de la comparaison des deux figures que les facteurs locaux de température peuvent être réduits d'environ 50 pour cent par augmentation de la longueur de dilution (d = 40 mm à d = 72 mm), en particulier le FLTM (facteur local de température maximal) est réduit de 0,39 à 0,19.

L'effet de la longueur de dilution d sur les facteurs de température pour les différents régimes du moteur simulés peut être résumé au moyen du tableau numérique suivant :

d (mm)	N	T_2 K	T_3 K	FLTM	FGT	FRT
40	0,6	425	842	0,31	0,36	0,043
40	0,6	428	853	0,28	0,38	0,042
40	1	637	1233	0,37	0,38	0,052
40	1	637	1221	0,39	0,37	0,053
72	0,4	352	742	0,22	0,25	0,055
72	0,6	431	854	0,16	0,24	0,033
72	1	640	1195	0,17	0,20	0,031
72	1	632	1267	0,19	0,22	0,031

Les facteurs de températures correspondant aux trois dernières colonnes sont :

- FLTM : facteur local de température maximal

$$FLTM = \frac{T_M - \overline{T_3}}{\overline{T_3} - T_2}$$

- FGT : facteur global de température

$$FGT = \frac{\sqrt{\frac{2\Pi}{n} \sum_{i=1}^{i=n} (T_{3i} - \overline{T_3})^2}}{\overline{T_3} - T_2}$$

- FRT : facteur radial de température

$$FRT = \frac{T_{RM} - \overline{T_3}}{\overline{T_3} - T_2}$$

La réduction des facteurs de température résultant de l'augmentation de la longueur de dilution d est plus marquée dans le cas du régime maximal (N = 1) que dans le cas du régime de ralenti (N = 0,6), cette réduction est respectivement égale à :

- 53 pour cent pour le FLTM,
- 44 pour cent pour le FGT,
- 41 pour cent pour le FRT.

4.4 - Analyse des prélèvements d'échantillons de gaz à la sortie du foyer

L'analyse des échantillons de gaz prélevés à la sortie du foyer permet de connaître les fractions molaires CO_2, CO, CxHy (en équivalent de CH_4), NOx (en équivalent de NO_2). A partir de ces fractions molaires on détermine les valeurs locales du rapport de mélange combustible, des indices d'émission des polluants, du rendement enthalpique. Les relations utilisées pour effectuer les calculs sont rappelées en annexe.

a) Emissions de polluants

Les valeurs moyennes des fractions molaires X des polluants mesurées à la sortie du foyer ainsi que les indices d'émission Ie correspondants aux produits suivants :

- monoxyde de carbone,
- hydrocarbures imbrûlés, en équivalent de méthane,
- oxydes d'azote, en équivalent de bioxyde d'azote,

ont été représentées en fonction du rapport de mélange α sur les figures 7, 8 et 9.

Les courbes en trait discontinu ainsi que les points blancs correspondent aux fractions molaires X, les courbes en trait plein ainsi que les points noirs correspondent aux indices d'émission exprimés en gramme de polluant par kilogramme de combustible brûlé. Il ressort de l'examen de ces figures que :

- figure 7 : l'indice d'émission du monoxyde de carbone présente une valeur minimale qui correspond approximativement à la valeur nominale du rapport de mélange, soit α = 0,011 (IeCO = 50 g/kg), dans le cas du régime de ralenti (N = 0,6) et α = 0,022 (IeCO = 20 g/kg) dans le cas du régime maximal (N = 1) ;

- figure 8 : aucune trace d'hydrocarbures imbrûlés n'a pu être détectée à la sortie du foyer dans le cas du régime maximal (N = 1) ; dans le cas des régimes de ralenti (N = 0,6 - N = 0,4) les valeurs de l'indice d'émission restent toujours inférieures à 1 gramme d'hydrocarbure imbrûlé par kilogramme de combustible brûlé. (L'apparition locale d'hydrocarbures imbrûlés caractérise un injecteur partiellement bouché) ;

- figure 9 : la fraction molaire d'oxydes d'azote augmente régulièrement avec le rapport de mélange ainsi qu'avec la température de l'air à l'entrée du foyer : la valeur correspondant au régime maximal (N = 1) est égale à 60.10^{-6}.

Les valeurs de l'indice d'émission sont respectivement égales à 2,8 et 4,3 grammes de bioxyde d'azote par kilogramme de combustible dans le cas du régime de ralenti (N = 0,6) et dans le cas du régime maximal (N = 1).

b) Rendement de combustion

Les valeurs moyennes arithmétiques du rendement enthalpique déterminées à la sortie du foyer à partir des valeurs locales ont été reportées sur la figure 10 en fonction du rapport de mélange global α . Le tableau numérique situé à la partie supérieure de la figure permet de préciser les valeurs des paramètres :

- N , régime du moteur simulé,
- T_2 , température de l'air à l'entrée du foyer,
- Ω , facteur de charge aérodynamique.

Il ressort de l'examen de cette figure que les rendements correspondant au :

- régime maximal (N = 1) sont égaux à 0,994 et indépendants du rapport de mélange α dans le domaine d'expérimentation ;

- régime de ralenti (N = 0,6) présentent une valeur maximale η = 0,987 pour la valeur nominale du rapport de mélange, soit α = 0,011 ;

- régime de démarrage (N = 0,4) sont encore voisins de η = 0,980.

Il convient de noter que les bons rendements qui figurent ci-dessus ont été obtenus lors d'une expérimentation à la pression atmosphérique, c'est-à-dire dans le cas d'une charge aérodynamique relativement forte par rapport à celle du foyer réel.

5 - CONCLUSION

Dans le cadre de la conception d'un foyer à flux inversé pour petites turbomachines une première phase d'étude à la pression atmosphérique, sans convergent de retour, afin de visualiser aisément la zone de combustion et de supprimer les imperfections mises en évidence au cours des premiers essais, a été effectuée.

Cette étude a montré que l'emploi de cannes à prévaporisation permettait l'obtention de performances correctes dans un large domaine de variation des paramètres étudiés, tout particulièrement du point de vue :

- répartition des températures à la sortie du foyer,
- émission des polluants,
- rendement de combustion.

Les difficultés rencontrées lors de l'allumage en présence d'air froid ont pu être surmontées grâce à des pulvérisations auxiliaires.

Il faut cependant remarquer que l'étude effectuée à la pression atmosphérique n'a pas permis de juger de la résistance thermo-mécanique du foyer ainsi que l'efficacité du refroidissement par multi-perforations, aucun problème n'étant apparu à la pression ambiante.

REFERENCES

]1[- MESTRE A. et LACAIN G.
Foyer à flux inversé pour petites turbomachines. ATMA (Association Technique Maritime et Aéronautique), Paris 1983.

ANNEXE : Définition des paramètres caractérisant les performances des foyers.

La formulation suivante des résultats d'analyse de gaz est utilisée conjointement par les Sociétés TURBOMECA et SNECMA ainsi que par le CEPr (Centre d'Essais des Propulseurs de Saclay).

A partir des fractions molaires

XCO_2, XCO, XC_xH_y en équivalent de CH_4,

XNO, XNO_x en équivalent de NO_2,

on détermine successivement :

1 - Rapport de mélange

$$\alpha = \frac{XCO_2 + XCO + XC_xH_y - 29.10^{-5}}{2{,}078 + XCO_2 - 0{,}038\ XCO - XC_xH_y}$$

2 - Polluants : indice d'émission

$$IeCO = \frac{28}{29} XCO \frac{1+\alpha}{\alpha} 10^3$$

$$IeCxHy = \frac{16}{29} XCxHy \frac{1+\alpha}{\alpha} 10^3$$

$$IeNO = \frac{30}{29} XNO \frac{1+\alpha}{\alpha} 10^3$$

$$IeNOx = \frac{46}{29} XNOx \frac{1+\alpha}{\alpha} 10^3$$

3 - Rendement enthalpique

Avec :

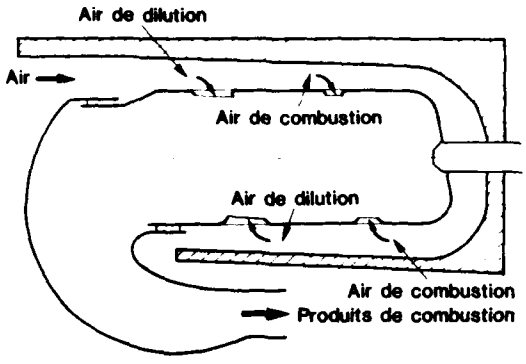
$$\eta = 1 - 10^{-2} (AI_eCO + BI_eC_xH_y + CI_eNO_x)$$

$$A = 0{,}0234 + 3.10^{-6} \frac{T2}{2}$$

$$B = 0{,}1148 + 7{,}5.10^{-6} \frac{T2}{2} + 1{,}5.10^{-8} \left(\frac{T2}{2}\right) 2$$

$$C = 0{,}00481 + 0{,}5.10^{-6} \frac{T2}{2}$$

T2 désignant la température en degrés Celsius de l'air à l'entrée du foyer.



Plan de coupe montrant les orifices d'air de combustion et de dilution

Fig. 1 - Foyer à flux inverse.

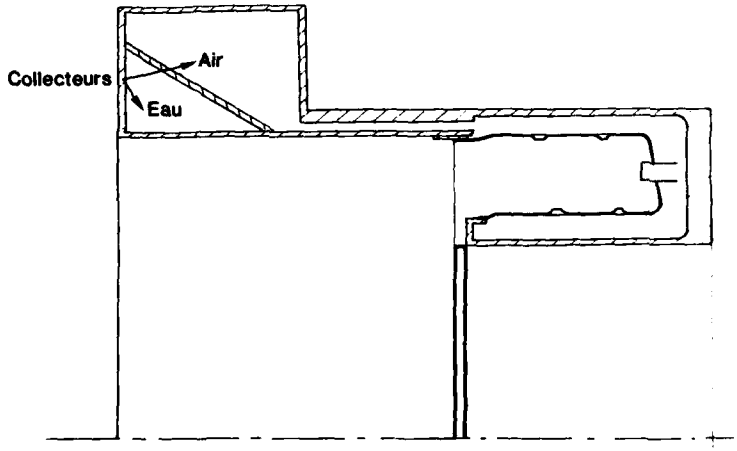


Fig. 2 - Montage pour essais à la pression atmosphérique.

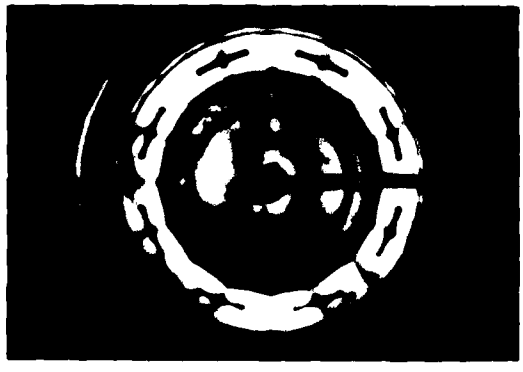
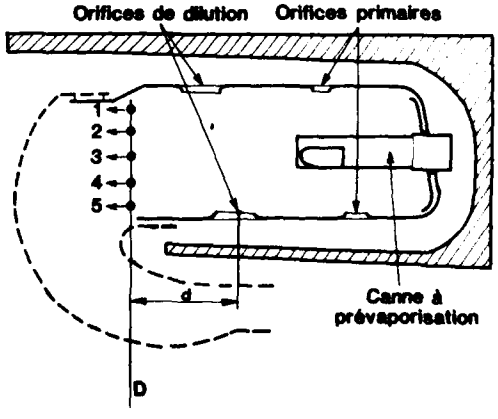


Fig. 3 - Régime de ralenti (régime moteur équivalent $N/N_M = 0,6$).



Convergent assurant le retour des gaz dans la direction axiale

Fig. 4 - Position des thermocouples à la sortie du foyer.

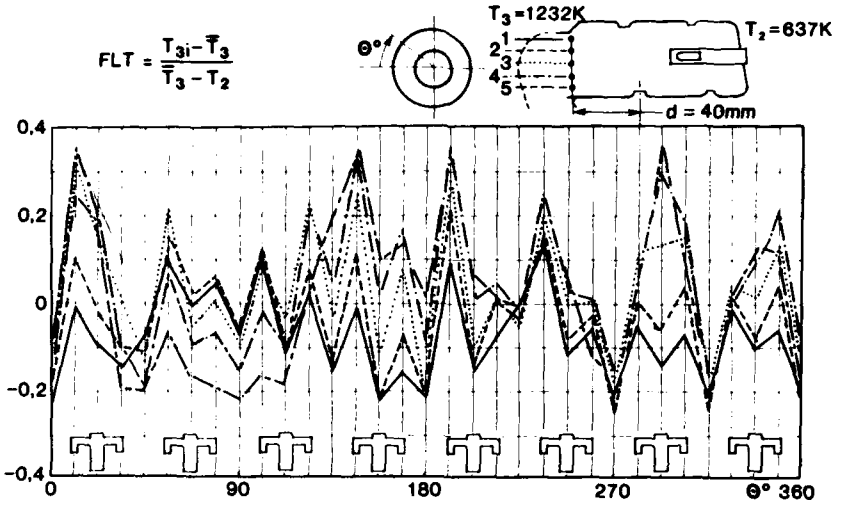


Fig. 5 - Répartition circonférentielle des facteurs locaux de température.

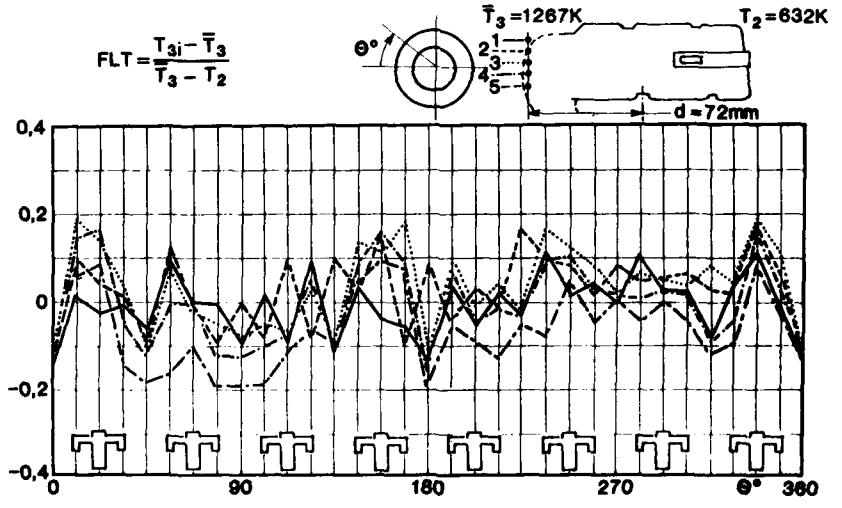


Fig. 6 - Répartition circonférentielle des facteurs locaux de température.

IeCO	XCO	N	T_2 K	Ω
♦	◊	1	630	7,5
▲	▲	0,6	430	20
●	○	0,4	350	28

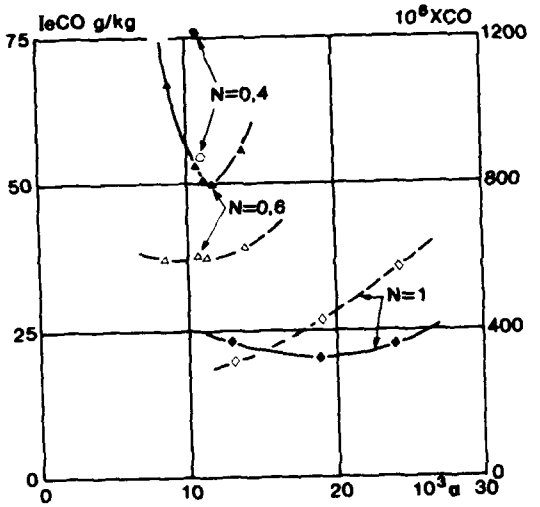


Fig. 7 - Emission de CO en fonction de la richesse.

IeC_XH_Y	XC_XH_Y	N	T_2 K	Ω
♦	◊	1	630	7,5
▲	▲	0,6	430	20
●	○	0,4	350	28

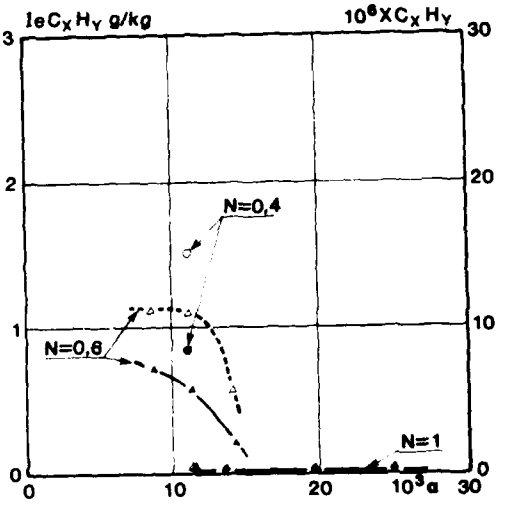


Fig. 8 - Emission de C_XH_Y (équivalent CH_4) en fonction de la richesse.

$Ie NO_X$	$X NO_X$	N	T_2 K	Ω
♦	◊	1	630	7,5
▲	▲	0,6	430	20
●	○	0,4	350	28

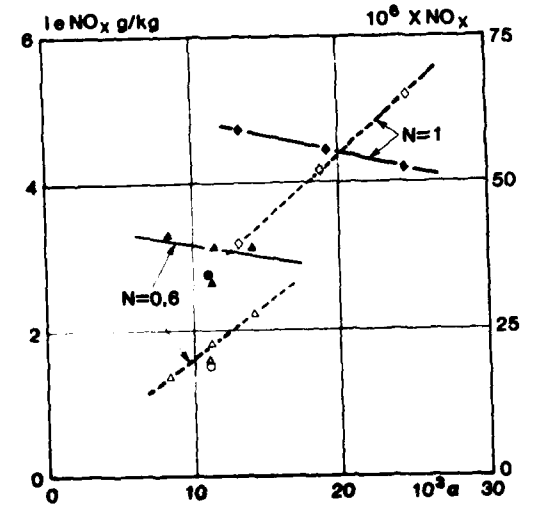


Fig. 9 - Emission de NO_X en fonction de la richesse.

η	N	T_2 K	Ω
♦	1	630	7,5
▲	0,6	430	20
●	0,4	350	28

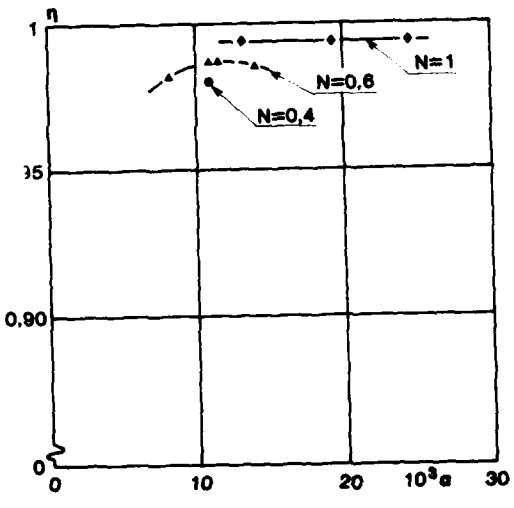


Fig. 10 - Rendement enthalpique en fonction de la richesse.

DISCUSSION

G.Winterfeld, Ge

The radial temperature distribution was measured without the elbow part of the reverse flow combustor. Can you comment on the influence of that bend on the radial temperature distribution at the entrance of the nozzle guide vanes?

Réponse d'Auteur

A la sortie du tube à flamme, le profil radial moyen de température est relativement plat. La nécessité de refroidir le convergent au moyen de films d'air permet d'obtenir à l'entrée du distributeur de turbine un profil radial moyen plus accentué, conforme à celui souhaité pour les aubes mobiles de la turbine.

B.Simon, Ge

For ignition, air temperature is very important. What was the air temperature during your ignition tests?

Reponse d'Auteur

Au cours des essais d'allumage, la température de l'air était voisine de 245 K; le kérosène était également injecté à la même température.

RECENT RESEARCH ON THE EFFLUX OF THE ROLLS-ROYCE VAPORISER FUEL INJECTOR

By

H C Low
Rolls-Royce Limited
PO Box 3, Filton
Bristol BS12 7QE
England

AD-P003 136

SUMMARY

The continuing effectiveness of the vaporiser fuel injection system is demonstrated in such engines as the Olympus 593 (in Concorde), the Pegasus (in Harrier) and the RB199 (in Tornado). Its potential is illustrated by its selection for the RB211-CE[3] advanced technology demonstration engine but, like other fuel injection systems, it is subject to increasingly severe demands and duties resulting from the imposition of emissions legislation, increasing engine pressure ratios, and reducing fuel quality. To meet these new challenges requires more detailed knowledge of the factors which determine how the device functions. The present paper describes a spark photographic study of a vaporiser efflux in combusting and non-combusting environments at pressures up to five atmospheres. At simulated engine idle conditions the two mechanisms of fuel heating within the vaporiser (wall and airstream) combine to produce a highly vaporised efflux.

INTRODUCTION

It is widely acknowledged that the condition of the fuel delivered to the burning zone is of crucial significance to the performance of a gas turbine combustor, in particular to the production of gaseous and particulate emissions. Consequently, numerous investigations of fuel injector systems have been carried out. However, with very few exceptions (Ref 1 and 2), these studies have been restricted to pressure jet and airblast atomisers operating, in the most, at ambient air conditions. The fact that the Rolls-Royce vaporiser has not been researched in any great depth reflects its relatively troublefree history (Ref 3 and 4), but like its competitors it is faced with trends towards more arduous operating conditions, deterioration in fuel quality and compliance with legislation restricting pollutant emissions. To meet these new challenges requires more detailed knowledge of the factors which determine how the device functions and the influence it has on the mechanical reliability of the adjacent flame-tube structure.

It is apparent from a simple analysis of the two-phase flow through the device that the airstream is the most likely source of heat to vaporise the fuel. An obvious effect, therefore, of higher compressor exit temperatures is a reduction in the quantity of fuel available for cooling the walls of the vaporiser and maintaining its mechanical integrity. This can be offset by reducing the fraction of combustor air which is fed through the vaporiser, but it is well established that high vaporiser air flows can contribute considerably to the control of pollutant emissions. It would appear favourable to achieve the situation where the last of the fuel vaporises as it leaves the vaporiser. To ensure the optimum choice of geometric and gas dynamic parameters, the current investigation to quantify the condition of the fuel at a vaporiser outlet in representative conditions was undertaken. The technique chosen to characterise the efflux was high-speed spark photography. At present this is one of the most accurate and least expensive methods of particle analysis allowing direct measurement of the size and shape of individual particles.

THE ANNULAR VAPORISING CHAMBER

The principal features of the modern annular vaporising chamber concept are depicted in Figure 1. The insensitivity of combustor performance to fuel injector location and the insensitivity of dump diffuser performance to combustor head position, sanction a one-piece, rear-mounted construction free from sliding joints. Compatibility with dump diffusion permits the use of a single skin combustor head which is adequately cooled by virtue of (a) exposure to compressor efflux and (b) a fuel-rich region in the combustor head resulting from upstream injection of the fuel by the vaporiser. In addition to delivering the fuel to the combustor, the vaporiser helps drive primary zone recirculations. T-vaporisers (Figure 2) have been chosen for recent combustors to double the fuel input points for a given number of injectors. Fuel is divided equally between both outlets of the vaporiser by the injector head (Figure 2). The absence of restrictions in these fuel feed arms render this injection system free from fuel gumming and blockage problems.

TEST HARDWARE

a) Test Unit

In order to meet the requirement of operation at all conditions between atmospheric pressure and full power, a sector was cut out from a typical combustor and fitted with a single vaporiser and transpiration cooled side walls. A film-cooled backplate was also fitted to achieve the required pressure drop across the combustor walls as shown in Figure 3. To provide realistic inlet flow to the vaporiser, a reasonable representation

of the prediffuser and dump geometry was necessary. To satisfy this requirement a curved sector with a bellmouth entry (to give uniform flow and provide a means of mass flow measurement) was manufactured.

A special feature of the model was the sight-tubes to provide optical access to the vaporiser efflux zone. Their size was determined by the space available between the combustor wall features. Their position was chosen to align with the efflux from one arm of the T-vaporiser, but at the same time to minimise obstruction to the wall features (in particular the primary ports) and disruption of the burning pattern within the unit. To this end they were angled to the flame tube walls as shown in Figure 4. To prevent soot entering the sight-tubes, holes were drilled in their leading edges to allow a purging flow of cool supply air through them into the combustion chamber.

Fuel was supplied to the model from a single, modified injector. The modification did not influence the fuel jet trajectory or the pressure drop. Ignition was achieved by a high-energy igniter which entered the unit via a transply side wall.

The unit was housed in high-pressure ducting with an outer casing simulation as shown in Figure 3. Suprasil quartz windows, aligned with the sight-tubes on the combustor, permitted optical access.

b) The Photographic System

The design procedure used in arriving at the optical arrangement employed in this study is summarised in Appendix 1 and a schematic representation of the system is shown in Figure 4. Illumination was provided by a Lunartron Argon Jet Light Source which produced a spark of approximately 300 ns duration. The internal optics of this device gave an in-focus image of the electrodes at a pinhole aperture in the end casing. A 100 mm focal length lens, used in conjunction with an aperture of 1.63 mm diameter, provided a parallel beam of light which passed through the sight-tubes of the model. The region illuminated is circled in Figure 5. The camera lens focussed images of droplets in the plane of the film, the droplets appearing as dark regions on a white background. The prints in this paper show a magnification of approximately four. To achieve best economy of running time, a Hasselblad camera equipped with a 150 mm lens and an automatic bellows extension was used. This permitted 24 frames to be taken remotely. The camera shutter and spark source were synchronised. At certain conditions, the luminosity of the flame was such that reaction was occurring between the film and the combustion flame. With the camera already operating at the maximum shutter speed of 1/500 s, the use of an optical filter was necessary to obviate this phenomenon. A Wratten filter, type 47B, was found most suitable.

The light source and camera were mounted on individual optical rails and enclosed in protective boxes, flameproofed by a regulated supply of clean, dry air. The boxes were extended as cylinders surrounding the window bosses on the model ducting, with a clearance to ensure that a large proportion of the purging air flowed around the windows and prevented contamination of optical surfaces by rig-generated moisture.

TEST PROCEDURES

Tests were carried out, with and without combustion, and a control experiment with airflows at different temperatures was also completed. Cold fuel (288K) was used throughout the investigation.

Photographs were taken before and after each test. These revealed that sooting of the windows was minimal and was having no deleterious effect upon the technique. However, the windows were cleaned with water and methylated spirits between tests to avoid accumulation of deposits.

RESULTS AND DISCUSSION

Phase 1 - Tests at 30 psia

Combusting - Effect of Air/Fuel Ratio (AFR)

The first test at this pressure revealed the effect of vaporiser AFR on the condition of the fuel in the efflux. At an AFR of 6:1 (Plate 1a) very few droplets are in evidence and the bulk of the fuel would appear vaporised. The cellular background in this photograph is attributed to inhomogeneities due to fuel vapour. Subsequent tests with high inlet air temperatures and no combustion (discussed below) support this claim. In addition similar effects have been observed at AERE Harwell in spark photographs of high temperature diesel sprays where high degrees of vaporisation have otherwise been shown.

It is important to stress that the fact that droplets can be seen in this efflux demonstrates that there is not an obscuration problem. The progressive decrease in the degree of vaporisation (increase in droplet density) observed as the fuel flow is increased (Plate 1b, c and d) is further evidence that, if droplets exist in the efflux, this technique is capable of exposing them. There is of course a limit to the size of droplets that can be detected by this technique in combusting environments. It would appear that different limits apply to different types of flames. Chigier claims detection of particles down to 5 μm in diameter in kerosene flames (Ref 5) whereas, in the highly luminous diesel spray flames studied at Harwell, a limit of 30 μm has been set. Analysis

of an enlargement of Plate 1d and similar photographs shows 20 μm diameter droplets clearly detectable.

One feature particularly evident in Plate 1b is the 'toe-in' of the vaporiser efflux towards the stem. This effect has been observed and quantified in a study of vaporiser flow patterns where an angle of approximately 20 degrees was measured at the outlet using a calibrated yawmeter probe.

As fuel passes through the vaporiser it is heated (a) by contact with the walls and (b) by mixing with the air. Although it is impossible to study each mechanism in isolation, tests were carried out to demonstrate that both are crucial to vaporiser performance.

Non-combusting - Effect of AFR

The airflow conditions were as in the previous test and the fuel flow was varied to cover the same range of AFRs. It is apparent from the comparisons made in Plate 2 that the convective and radiative fluxes from the hot primary-zone gases to the vaporiser walls are responsible for the vaporisation of a considerable proportion of the fuel.

Combusting - Effect of Inlet Air Temperature (T3)

In this test the inlet air temperature was varied in the range 453-723K. Rig pressure was increased in line with the temperature to give a constant AFR throughout the test. An AFR of 3:1 was considered suitable since this condition, already observed at 453K (Plate 1d), offered ample scope for improvements in vaporisation levels. The effect of inlet air temperature is demonstrated in Plate 3. A marked increase in the degree of vaporisation is observed as the temperature is raised to 523K and further increases in temperature are reflected in progressively improved vaporisation levels until no liquid fuel is detected in the efflux. This occurs at a temperature of 723K.

Although it is mentioned above that the two mechanisms of fuel heating cannot be separated (since increasing the inlet air temperature will increase primary-zone temperatures and hence vaporiser wall temperatures) the substantial improvement in vaporisation observed in going from 453-523K is far beyond that which would be brought about by a 70 degree increase in primary zone temperature. This implies intimate contact between fuel and air (high levels of premixing) within the vaporiser considering the short residence times involved (1 ms). In an attempt to quantify the efficiency of fuel heating by this mechanism a series of non-combusting tests were undertaken.

Non-combusting - Effect of Inlet Air Temperature over a Range of AFRs

These tests were carried out in the absence of combustion in order to minimise fuel heating due to contact with the vaporiser walls and show the effect of inlet air temperature over a range of AFRs. Air temperature was varied in the range 473-673K and, as in the previous series, the air pressure was increased in line with temperature to give a constant mass flow. At each setting fuel flow was varied to cover the range of AFRs (3-6). The trends observed, as exemplified in Plate 4, demonstrate the sensitivity of the degree of vaporisation to air temperature and provide further evidence of the significance of this mechanism of fuel heating.

Calorimetric calculations based upon these results show that to fully vaporise the fuel (delivered cold), the heat energy of the airstream must be of the order of 2.5 times that required to do so, ie this mechanism of fuel heating would appear 40-45 per cent efficient. At realistic engine running conditions this efficiency should increase due to higher fuel delivery temperatures (approximately 420K) and the lesser significance of latent heat effects.

It was concluded in an earlier section that vaporised fuel was giving rise to the inhomogeneities causing the cellular structure of some photographs. The fact that the same effect is present in these tests with no combustion is proof of this point.

Phase 2 - Tests at 55 psia

Combusting - Effect of AFR

Engine idle conditions were simulated with the exception of the fuel delivery temperature. At the representative AFR of 6:1 (Plate 5a) the fuel appears to be highly vaporised with no droplets observed in the efflux. This result, although somewhat unexpected, is accountable for in terms of the two mechanisms of fuel heating within the vaporiser.

Calculations show that approximately 20 per cent of the fuel will be evaporated by heat transfer from the vaporiser walls. To achieve complete evaporation would require approximately 45 per cent of the heat available in the airstream to be transferred to the fuel. In light of the efficiencies reported above for this mechanism, a high degree of vaporisation would be expected. At true engine idle conditions where the fuel delivery temperature is much higher, full vaporisation should easily be accomplished.

The technique is able to detect the very high frequency variations to which all fuel injectors and combustors are subjected; to obtain a good account of the average situation, up to 25 photographs were taken at each test condition. At idle no photograph showed unvaporised fuel.

As expected, the degree of vaporisation decreased as the fuel flow was increased. (Plate 5b, c and d). The fact that droplets are clearly detected at an AFR of 5:1 is encouraging in that the heat transfer calculations reported above showed the AFR 6:1 condition to be marginal regarding full vaporisation.

The photographs presented so far were taken with the focal plane in the centre of the efflux. A traverse of the vaporiser outlet in 2 mm steps demonstrated that the high degree of vaporisation applies to the entire efflux. Laboratory tests prior to rig running revealed that such intervals would give comprehensive coverage of the outlet.

Non-combusting

More evidence of the significance to vaporiser performance of heat removal from the walls by the fuel, was obtained in further tests comparing combusting and non-combusting effluxes.

A control experiment (in the absence of fuel) was carried out to determine whether inhomogeneities due to turbulence in the airstream were in any way responsible for the cellular structure of the efflux. Air temperature was varied in the range 373-673K. Results showed that no contribution to the appearance of the photographs is made by the airflow.

Phase 3 - Tests at 75 psia

Combusting - Effect of AFR

At a vaporiser AFR of 6:1, no droplets are detected in the efflux. This result is in line with the prediction based upon the empirical rules derived above as is the fact that unvaporised fuel is observed when fuel flow is increased to give an AFR of 4:1.

CONCLUSIONS

Spark photography has been applied successfully to the study of fuel condition at a vaporiser outlet in combusting and non-combusting conditions. The technique has been demonstrated to be capable of detecting droplets as small as 20 μm in diameter in combusting environments typical of annular vaporising flame-tubes. Although it is probable that smaller droplets exist in the vaporiser efflux at certain conditions, investigations have shown that they burn as would a completely vaporised mixture (Ref 6).

Contrary to international opinion, high degrees of prevaporisation are achieved within the vaporiser at realistic engine conditions. These observations are consistent, however, with the work of Vezhba (Ref 2). In a series of phase discrimination studies he measured degrees of vaporisation of the order of 90 per cent for both L-shaped and co-axial vaporising elements operating at conditions similar to those of the engine idle in the current investigation.

The efficient premixing of the fuel and air and the high fuel evaporation levels occurring within the vaporiser help to explain the low emission performance of the annular vaporising chamber.

If the empirical rules derived above apply to higher power conditions, fully vaporised effluxes will be typical of vaporiser performance.

REFERENCES

1) Rosfjord, R.J. and Briehl, D.
'Evaluation of Fuel Injection Configurations to Control Carbon and Soot Formation in Small GT Combustors'
AIAA Paper AIAA-82-1175
June 1982

2) Vezhba, I.
'Experimental Investigation of Fuel Evaporation in the Vaporising Elements of Combustion Chambers'
NASA TM-75383
February 1979

3) Sotheran, A.
'The Rolls-Royce Annular Vaporiser Combustor'
ASME Paper 83-GT-49
March 1983

4) Sotheran, A.
'Recent Advances in Vaporiser Fuel Injection Technology'
1983 Tokyo International Gas Turbine Congress

5) Chigier, N.A.
'Measurement in Multiphase Reacting Flows - A Review'
17th Aerospace Sciences Meeting, New Orleans
January 1979

6) Nicholls, J.A. et al.,
'The Effect of Fuel Sprays on Emissions from a Research Gas Turbine Combustor'
Combustion Science and Technology Vol.23, P.203
1980

APPENDIX 1

OPTICAL SYSTEM

The Lens

Using a 150 mm focal length lens and the standard lens formula

$$\frac{1}{F} = \frac{1}{u} + \frac{1}{v}$$

where F is the focal length, u is object distance and v the image distance

it was calculated that the distance between the camera lens and the plane of interest in the model should be 275 mm. The resulting image will be in focus on a plate 330 mm from the lens giving a magnification $\frac{v}{u}$ of 1.2.

In order to vary the position of the plane in the model to be photographed, both the lens and the camera back are moved together to maintain the same overall optical arrangement and produce consistent magnification.

The Aperture

The size of aperture together with the focal length of the lens in use defines the depth of field which is achieved, ie the depth which will produce images which are in focus on the film. In this study, where a small depth of field is desirable, the largest possible aperture - that provided by the sight-tubes of the model (23.4 mm) - was chosen.

The depth of field is defined as the difference between the lens Near Point and Far Point. These in turn are given by the following equation:

$$\text{Near Point} = \frac{Fu\ (F + cN)}{F^2 + ucN}$$

$$\text{Far Point} = \frac{Fu\ (F - cN)}{F^2 - ucN}$$

where F = focal length of overall lens system
u = object distance
N = relative aperture (F number)
c = diameter of circle of confusion

The circle of confusion of an image is the circle produced by a point object when nominally in focus. If it is assumed that the smallest droplet to be measured is 20 μm, then the image size for the 'Hasselblad' camera becomes 1.2 x 20 μm = 0.024 mm.

Now let the diameter of the circle of confusion be 10 per cent of this minimum droplet size,

ie $c = 0.0024$ mm

Thus for $F = 150$ mm
$u = 275$ mm

Aperture diameter = 23.4 mm giving $N = \frac{150}{23.4} = 6.41$

and $c = 0.0024$ mm

Near Point = 274.976
Far Point = 275.023
Depth of Field = 0.05 mm

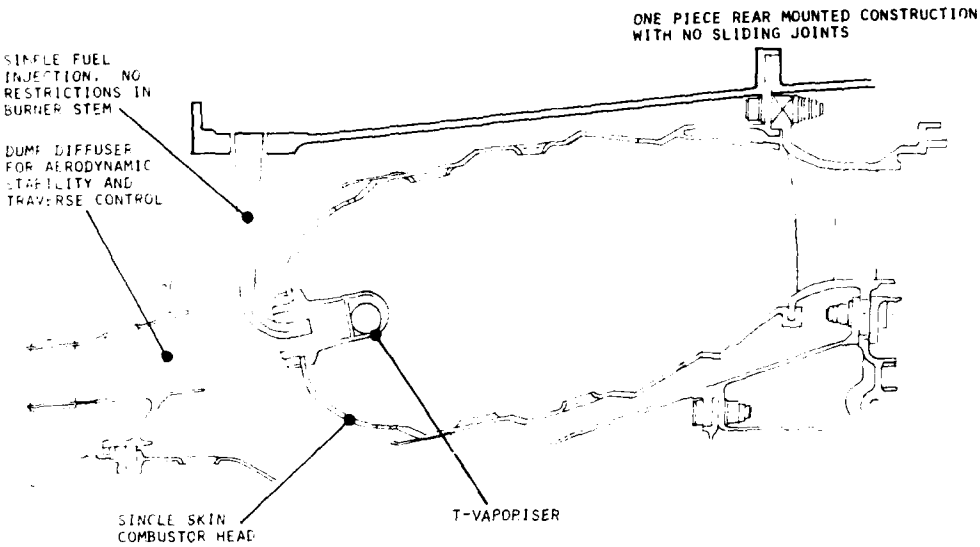


Figure 1 Annular vaporising chamber

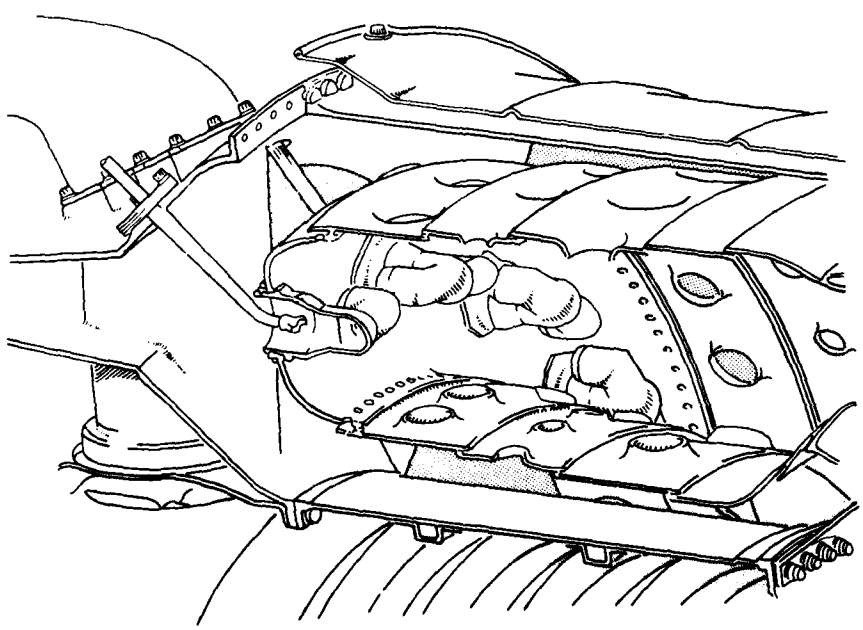


Figure 2 T-vaporiser

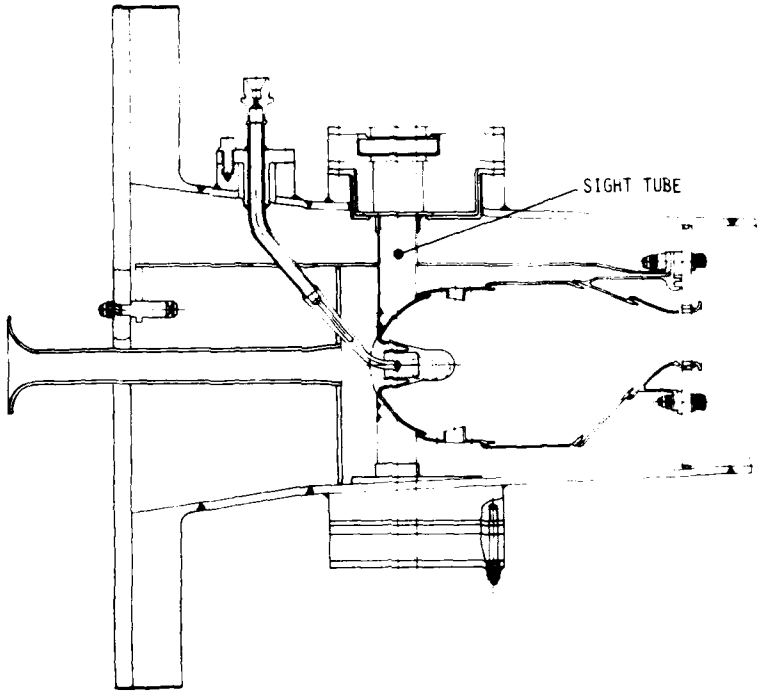


Figure 3 Test unit

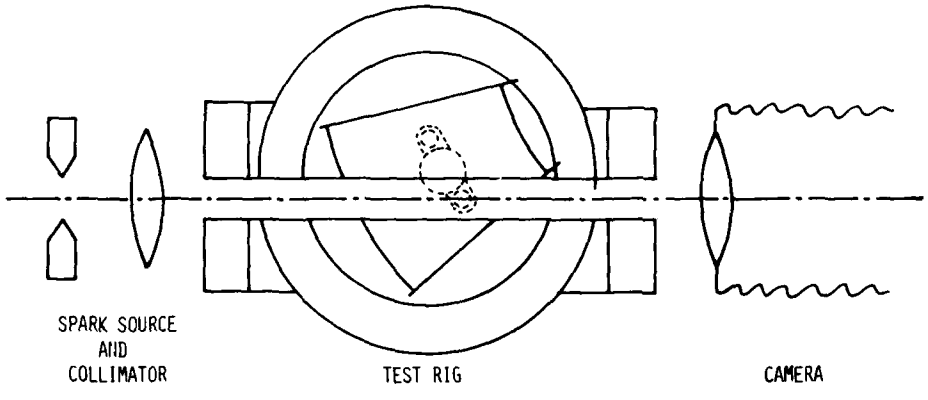


Figure 4 Schematic representation of rig layout

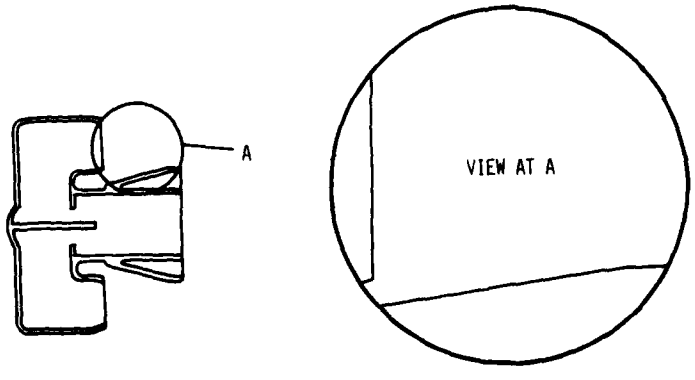
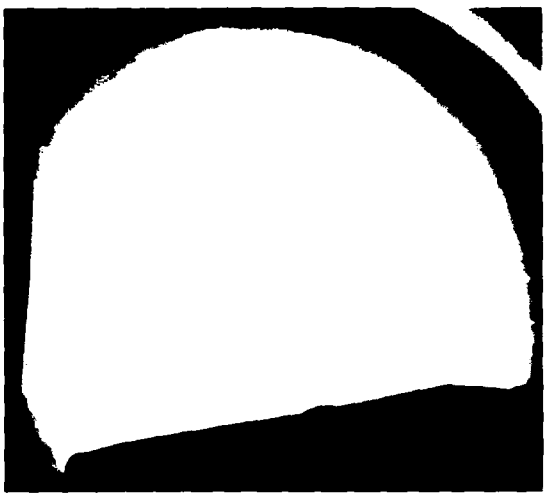
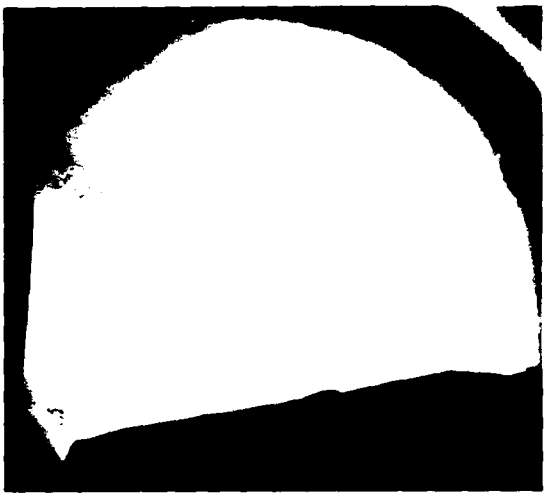


Figure 5 Zone illuminated by spark



(a) AFR = 6:1



(b) AFR = 5:1

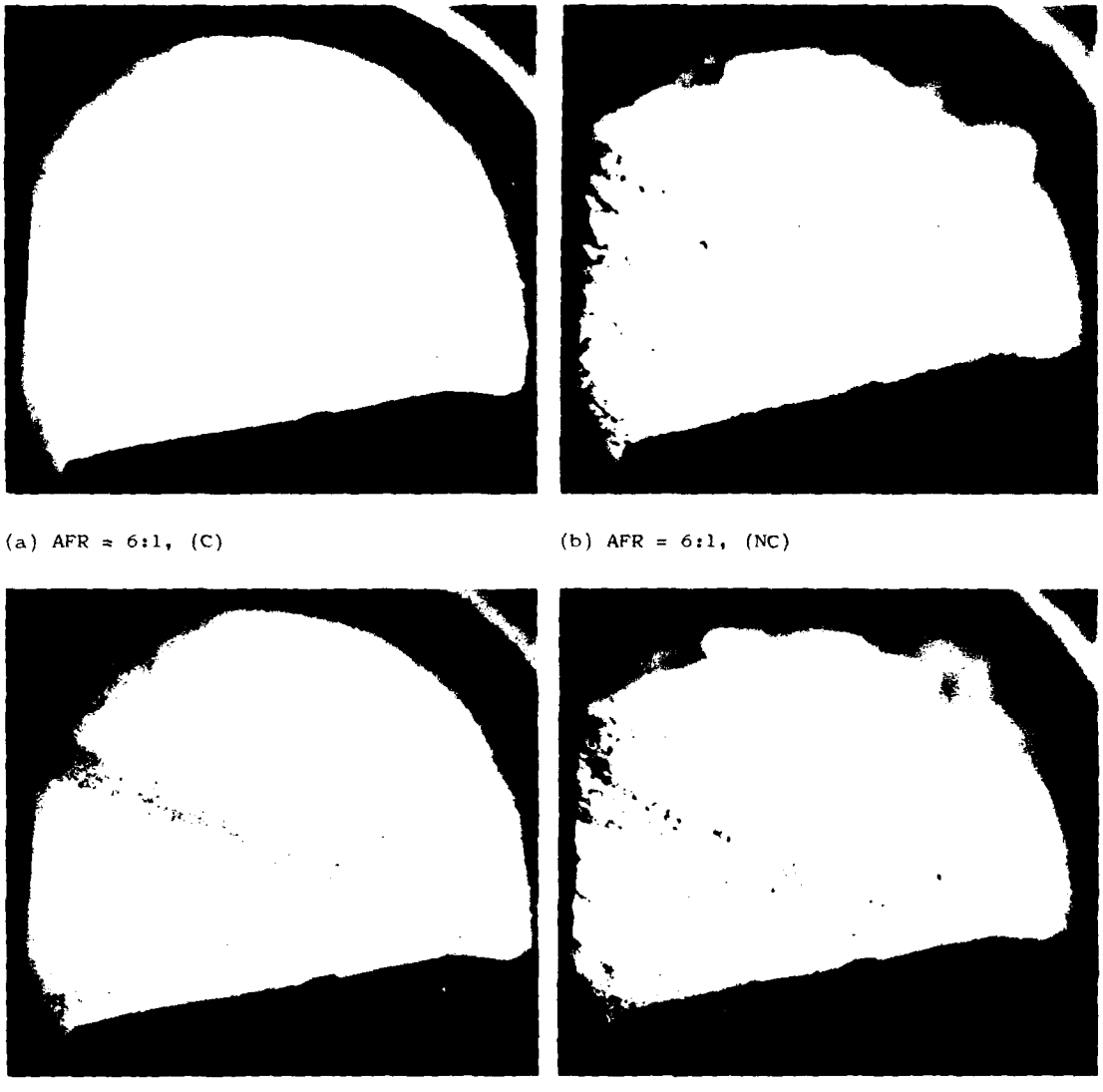


(c) AFR = 4:1



(d) AFR = 3:1

Plate 1 Combustion at 30 psia (T3 = 453K) - Effect of AFR



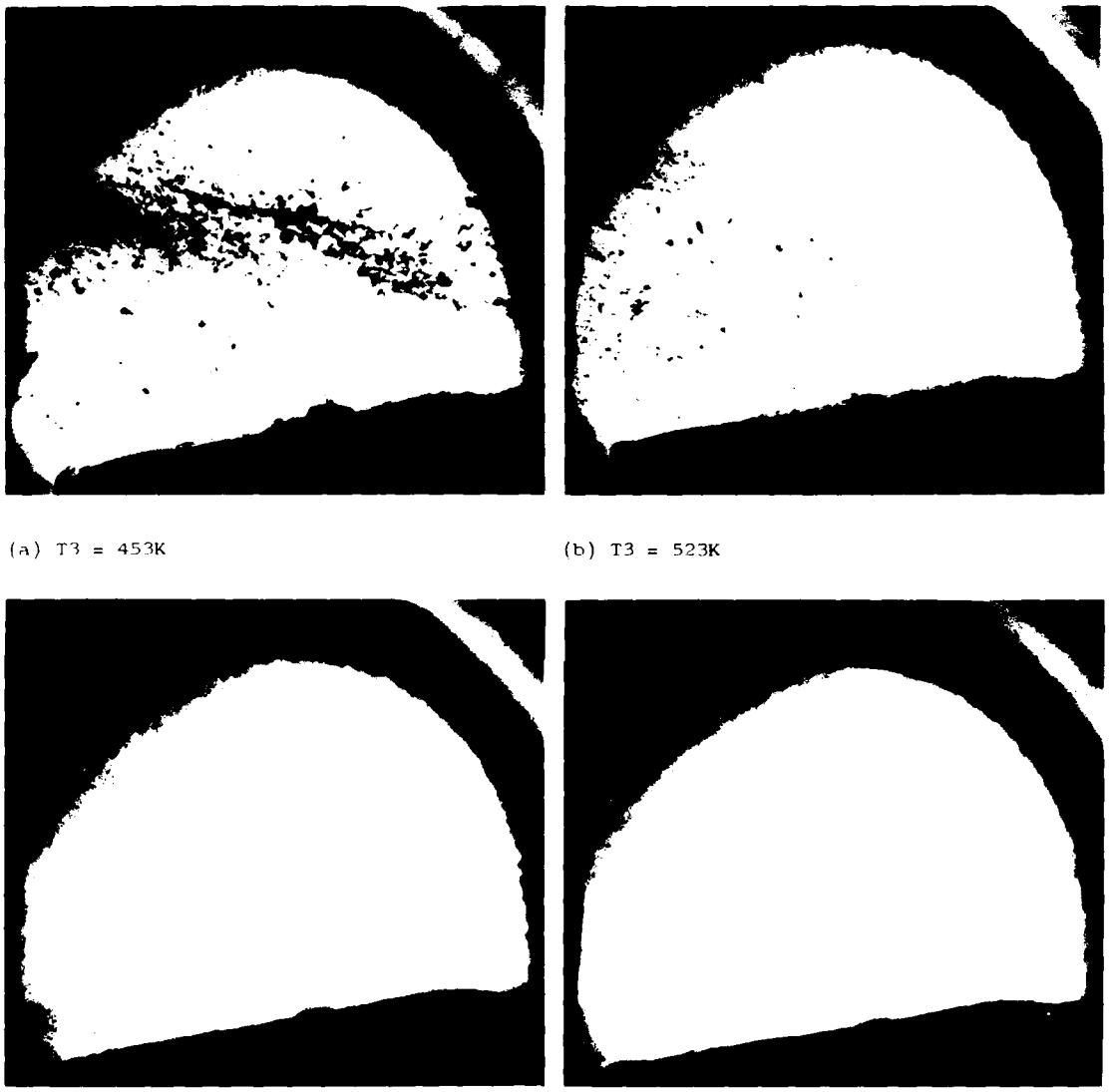
(a) AFR = 6:1, (C)

(b) AFR = 6:1, (NC)

(c) AFR = 5:1, (C)

(d) AFR = 5:1, (NC)

Plate 2 Combustion (C) versus non-combustion (NC) at 30 psia (T3 = 453K)



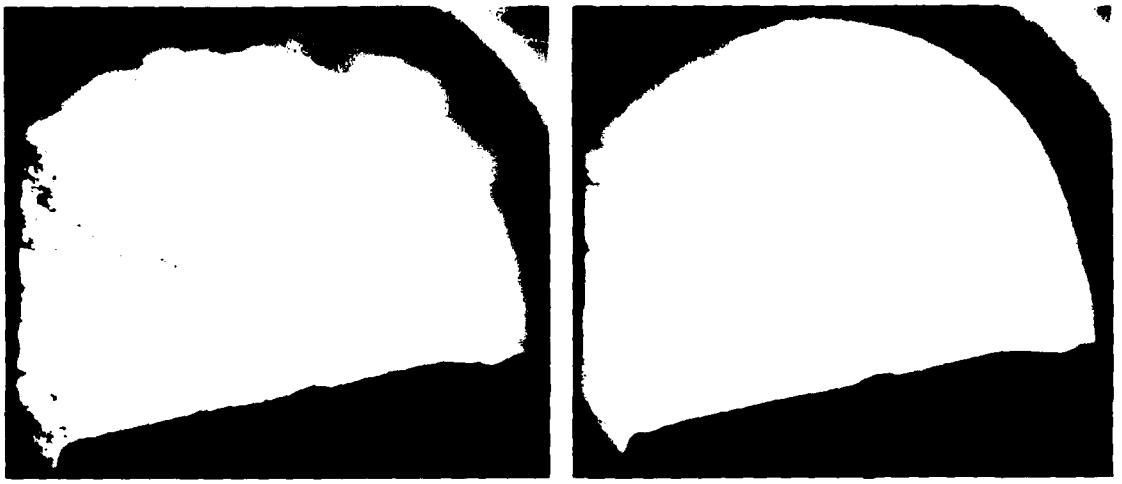
(a) T3 = 453K

(b) T3 = 523K

(c) T3 = 623K

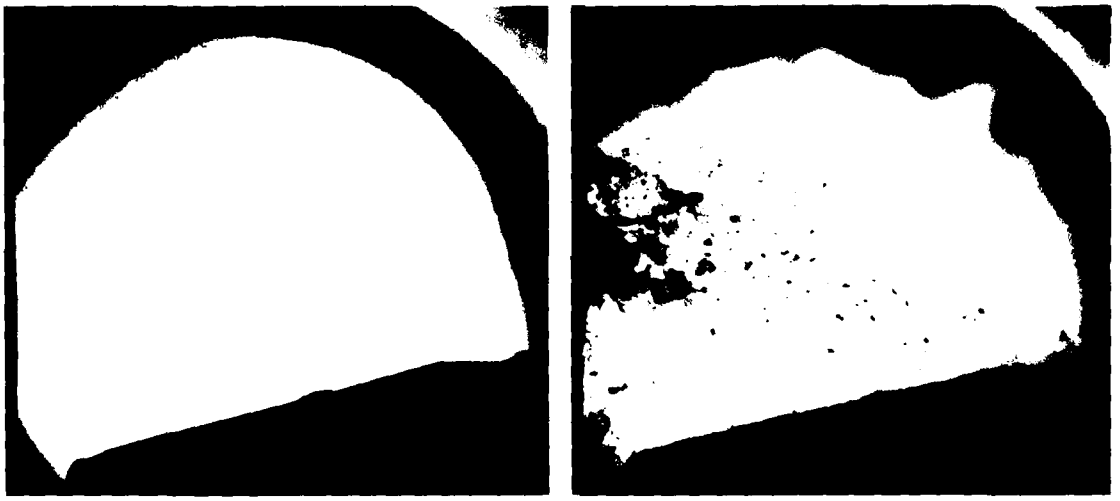
(d) T3 = 723K

Plate 3 Combustion at 30 psia (AFR = 3:1) - Effect of T3



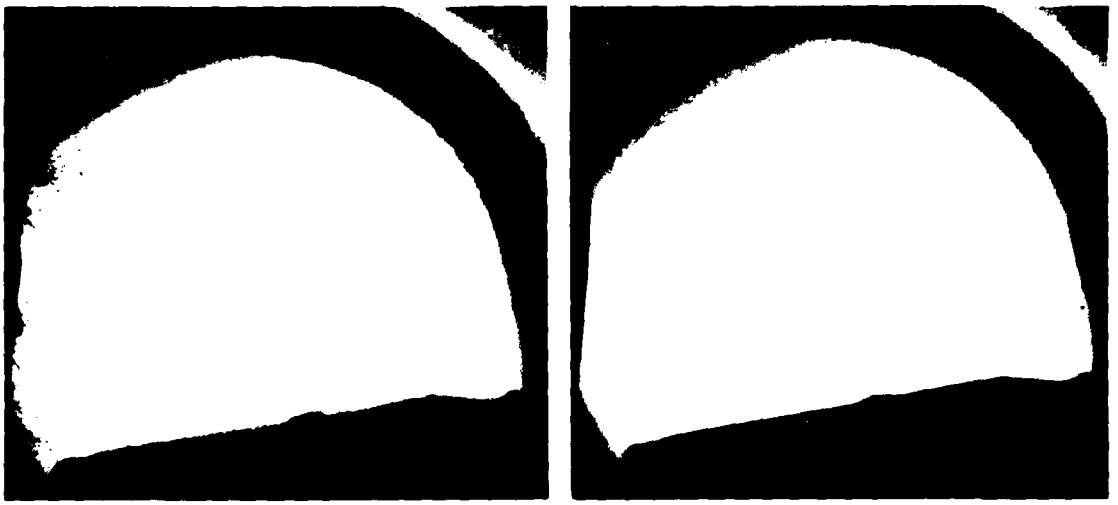
(a) AFR = 5:1, T3 = 473K

(b) AFR = 5:1, T3 = 573K



(c) AFR = 5:1, T3 = 673K

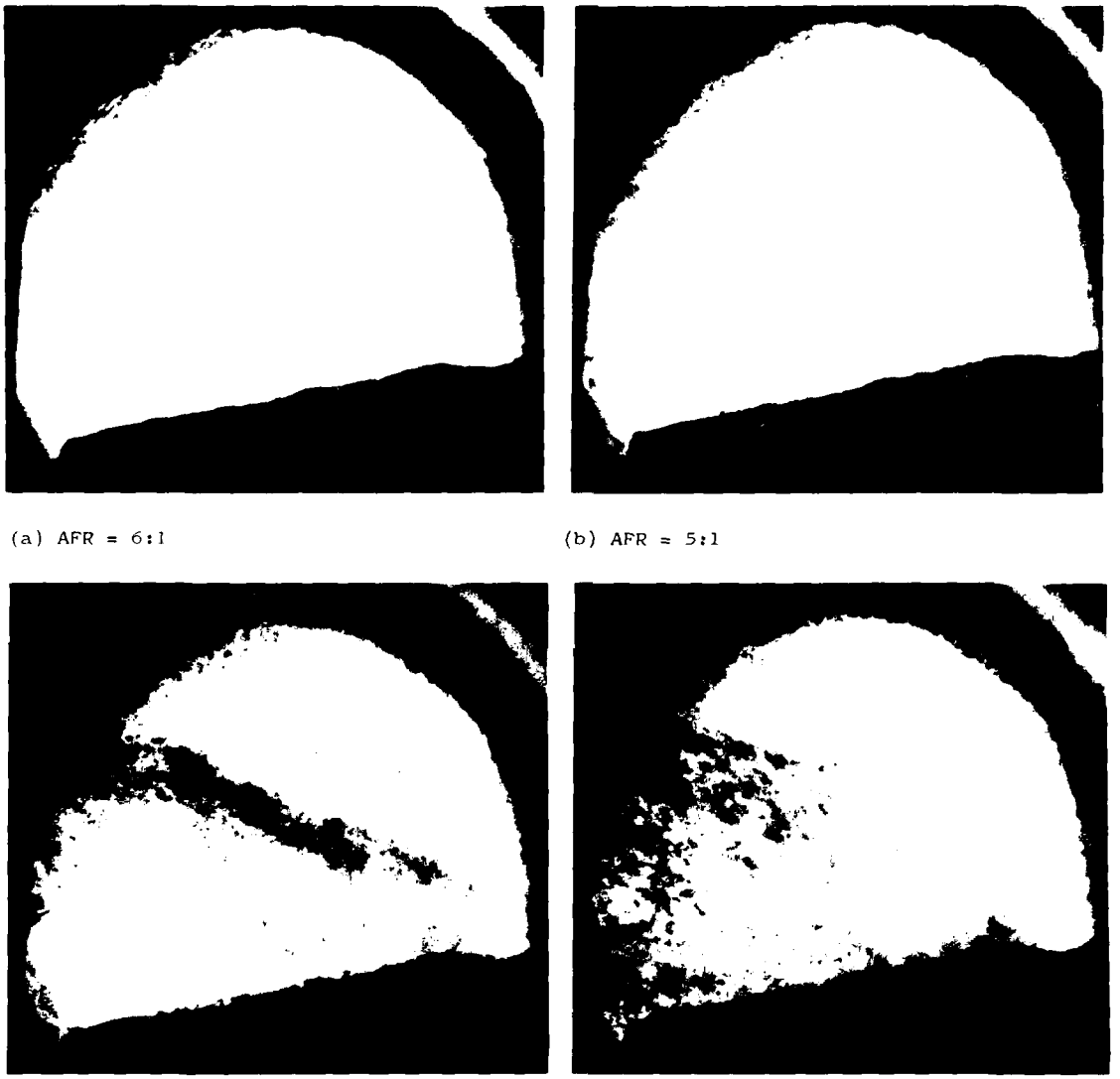
(d) AFR = 4:1, T3 = 473K



(e) AFR = 4:1, T3 = 573K

(f) AFR = 4:1, T3 = 673K

Plate 4 Non-combustion at 30 psia - Effect of AFR, T3



(a) AFR = 6:1 (b) AFR = 5:1

(c) AFR = 4:1 (d) AFR = 3:1

Plate 5 Combustion at 55 psia (T3 = 453K) - Effect of AFR

EFFECTS OF AIRBLAST ATOMIZER DESIGN UPON SPRAY QUALITY

AD-P003 137

By

A.K.Jasuja
School of Mechanical Engineering
Cranfield Institute of Technology
Cranfield, Bedford MK43 OAL
England

SUMMARY

This paper reviews the results of numerous investigations that have been conducted on airblast atomization as applied to gas turbine engines. The primary motivation for this is the need to identify the effect that various design features have upon the spray quality so that atomizers of optimum performance can be designed with a minimum of cost and complexity. Attention is focused upon such factors as the atomizer scale, configuration, the nature of fuel preparation before exposure to air, etc, for the most commonly used pre-filming and plain-jet airblast atomizers. The experimental mean drop size data included in this paper has been obtained through the use of well-established laser light-scattering techniques over a wide range of conditions. The general conclusion drawn from the data that is currently available is that the plain-jet airblast atomizers featuring multiple, transversely injected liquid jets into a swirling airstream yield spray quality comparable to that achieved by their pre-filming counterparts especially under high air pressure conditions.

LIST OF SYMBOLS

SMD	=	Sauter Mean Diameter, micron or m
V	=	Velocity, m/s
D, d	=	diameter, m, or mm or cm.
$\frac{\Delta P}{P}$	=	Atomizer air pressure drop, percent
P	=	Pressure, atmosphere
AFR	=	air-to-fuel mass ratio
ALR	=	air-to-liquid mass ratio
ρ	=	density, kg/m^3
σ	=	surface tension, N/m
η	=	absolute viscosity, Ns/m^2
α, β	=	liquid injection angle
γ	=	swirler vane outlet angle
t	=	film thickness (liquid), micron
T	=	temperature, ^0K

Subscripts

a	=	air
l	=	liquid
o	=	orifice (injection)
p	=	pre-filmer
j	=	jet (liquid)

INTRODUCTION

The quality of fuel preparation is now generally acknowledged to be of considerable importance in many key aspects of gas turbine combustor performance - notably for its influence upon such characteristics as ignition (sea level/altitude relight), efficiency and stability, temperature traverse quality, levels of smoke and other pollutants, levels of flame radiation and the inter-related issue of liner durability. Possible degradation in the quality of the gas turbine fuels is going to require a greater degree of fuel flexibility/multi-fuel capability from the combustors/fuel injectors of the future. Furthermore, the continuing trend towards gas turbines of higher compression ratio requires satisfactory fuel preparation over a far wider range of air pressures/temperatures as well as fuel flows than at present. In addition, there has been, for some time now, pressure to restrict the emission of gas turbine generated exhaust pollutants, and it seems unlikely that this pressure will be significantly relaxed in the near future. The attainment of effective fuel preparation has assumed added importance in order to achieve satisfactory combustion-pollution performance. In the light of this, the detailed performance characteristics of a variety of gas turbine fuel injection systems have been investigated over the years. The quality of atomization, as indicated by the sizes of the drops produced by a given injector following the fuel disintegration, has been the main feature under examination in most of these investigations in order to relate it to the injector design/operating conditions as well as fuel properties.

The superior combustion-pollution performance of the airblast atomizer relative to the conventional pressure atomizer is now well established (Ref.1) and this has led to its widespread adoption in the modern, high-pressure ratio gas turbine. The airblast atomizer spray is finer in character due to the intimate mixing of fuel and air achieved as an integral part of the atomization process. This yields a flame of low luminosity and soot, thus resulting in relatively cooler liner walls and a minimum of exhaust smoke. Furthermore, the placement of the fuel droplets in the burning zone is dictated mainly by the airflow pattern - being almost insensitive to the fuel flow variations. Consequently, airblast atomizers offer an important practical advantage from the viewpoint of nozzle guide vane/turbine blade

life development in that the outlet temperature profile of the combustor efflux gases is sensibly constant under all operating conditions and consequently may be predicted satisfactorily from experiments conducted at convenient operating conditions, such as lower levels of combustor pressure.

From amongst the many diverse geometrical configurations investigated by the different researchers over the years, two specific types of airblast atomizers appear to stand out clearly - namely the pre-filming and the plain-jet types. This is due to the extensive research that they have been subjected to, thus reflecting the interest in them from the gas turbine applications viewpoint. In common with all other forms of airblast atomizers, they utilise high velocity air for the purposes of disintegrating a relatively slow moving liquid stream. There are two main differences between the pre-filming and the plain-jet airblast atomizers. The first one relates to the extent of fuel preparation prior to its exposure to the shearing action of high velocity air, while the second one relates to the air flow passage arrangement/configuration and the intimacy of the resulting fuel and air contact. In the pre-filming arrangement, researched extensively by Lefebvre and his co-workers (2,3), the fuel is first spread into a thin, continuous annular sheet on a surface known as the pre-filming surface before exposure to two high velocity airstreams. Intimate fuel and air contact is achieved by arranging for the two airflows to 'sandwich' the thin fuel sheet. In the plain-jet arrangement, however, the fuel is not pre-filmed into a thin sheet but instead discharged in the form of one or more, discrete, circular jets. These jets of fuel undergo disintegration in-flight in a single airstream, usually provided by a conventional swirler (4). The intimacy of fuel and air contact achieved in this arrangement is related to the swirler/fuel orifice variables.

The purpose of this paper is to outline the present state of knowledge with regard to the fundamental design aspects of airblast atomization, as applied to gas turbines, by bringing together the findings of numerous research studies, especially those conducted during the last decade or so. The primary motivation for this is the need for a thorough understanding of the mechanics of airblast atomization so that atomizers of optimum performance can be designed with a minimum of cost and complexity. Clearly, in a situation of this kind where results have been brought together from a variety of diverse sources, there is the possibility of differences arising with regard to the actual details, for example the use of different drop size measuring techniques, the adoption of different mean drop size definitions, etc. Since this paper is addressing the design aspects of airblast atomizers, special care has been taken to ensure that the comparisons utilised herein are meaningful and valid.

ATOMIZER DETAILS

The conceptual details of the various airblast atomizers included in this study are illustrated in Figure 1. The evolution of the pre-filming type is covered by configurations of Figure 1(a) through to 1(e) with configuration 1(f) being a specially designed, two-dimensional flat sheet, research atomizer of the same family. The different plain-jet configurations that have been investigated are depicted in Figure 1(g) through to 1(i).

Configurations 1(a) and 1(b) show two of the early designs of pre-filming types of atomizers. In configuration 1(a), due to Bennet (5), fuel was given a swirl and made to flow over the face and edge of a disc located in a high velocity airstream. The resulting spray quality, assessed through the coated slide technique, was poor due to the problems of wall-wetting and non-uniform liquid film distribution. Of the four different configurations examined by Lefebvre and Miller (6), the one shown in Figure 1(b) was found to be the best. A swirl chamber, connected to the fuel feed tube through four radial spokes, was used for the purposes of pre-filming the fuel. The swirl chamber featured a shroud to enable the liquid sheet to develop without interference from the airflow. The problems of wall-wetting that had been experienced with the earlier designs had been eliminated by keeping the droplets airborne through the deployment of air on both sides of the fuel film. This 'sandwiching' of the fuel film was also conducive to the attainment of intimate physical contact between the fuel and airstreams, the importance of which from atomization performance viewpoint had previously been highlighted by Gretzinger and Marshall (7). Lefebvre and Miller also recognised the importance of minimising the liquid film thickness as well as that of exposing the liquid film to the shearing action of air on both sides at the point of maximum air velocity.

The configuration of Figure 1(c), featuring a diverging pre-filming arrangement culminating in a sharp lip combined with the somewhat more aerodynamically streamlined air passages (inner as well as outer), was found to yield the best atomization performance from amongst the various different designs studied in Reference 8. The sharp-lipped, diverging pre-filmer geometry was found to be more successful in achieving fuel detachment by centrifugal action. This resulted from the use of swirl slots, introduced in an attempt to obtain an even fuel film, in feeding the fuel on to the pre-filming surface.

This basic sharp edged, diverging pre-filmer geometry was retained in the configuration of Figure 1(d) (Refs.2,3). The main difference between this arrangement and its predecessor relates to the shape of the air passages - those of Figure 1(d) being somewhat more streamlined than of Figure 1(c). Another variant of this pre-filming atomizer family, shown in Figure 1(e), (Ref.9), uses a parallel pre-filming surface with a less sharp lip combined with the deployment of a swirler for the inner as well as the outer airstreams. A somewhat similar 'sandwiching' of the annular fuel sheet between two, swirling airstreams is also discussed in Reference 1. In the main Reference 1 and 9 differ with regard to the shape of the pre-filming surface - a diverging surface in Reference 1 (similar to that of Figure 1(d)) in contrast to the parallel surface of Reference 9.

The atomizer configuration shown in Figure 1(f) is a flat sheet, two-dimensional airblast atomizer that was specially designed by Rizk and Lefebvre (Ref.10) in an attempt to examine the effect of initial liquid film thickness upon atomization quality. The thickness of the liquid film generated by the pre-filming arrangement is, clearly, one of the fundamental features of this type of atomizer and consequently one that needs to be correlated adequately with the mean drop size.

Nukiyama and Tanasawa (ref.11) conducted the first major airblast atomization study using the plain-jet configuration of Figure 1(g). In this arrangement the liquid is injected in the form of a circular jet into a co-axial, co-flowing, high velocity airstream. This form of atomizer has been the subject of several further studies (Refs.12, 13, 14), because of its very simple design. Another simple form of plain-jet atomizer that has been examined in some detail (Refs. 11, 13, 15, 16) comprises the transverse injection of a circular, liquid jet into a high velocity, axial airstream as illustrated in Figure 1(h). The effect of injecting the liquid jet in a direction other than the transverse or co-axial had, up until recently, not been examined. By comparing the data from different atomizers, Rizk and Lefebvre (Ref.17) attempted to identify qualitatively the effect of liquid jet injection angle upon drop size. However, Hussein et al (Ref.18) conducted detailed experiments using the configuration shown in Figure 1(i). The injection angle (θ_{jo}) of the circular liquid jet was varied over the 30 to 90 degree range.

The plain-jet atomizer designs discussed so far have comprised the injection of single/multiple liquid jets into a non-swirling airstream. The configuration shown in Figure 1(j), comprising several radially-drilled holes for the injection of liquid in the form of discrete jets into a single high-velocity swirling airstream, was first investigated by Jasuja (Ref.4). This type of atomizer, due to its relatively simple nature (requiring only a swirler and some plain, circular holes), has since been studied in some depth (Refs. 13, 19, 20). The configuration illustrated in Figure 1(k) shows two of the key variables that influence the design and performance of this type of atomizer - notably the swirler geometry and the injection orifice orientation. Hussein (Ref.20) has recently examined in some detail the effect of swirler geometry, particularly the vane type (both straight and curved) and its outlet angle γ, upon the drop size performance. The influence of the liquid orifice orientation, α_o, upon drop size has been studied by Shaw (Ref.21). Clearly, the motivation for optimizing the design of this type of atomizer is the need to deploy the available air in the most effective manner, thus achieving the best possible level of atomization performance. In the arrangement depicted in Figure 1(l), the liquid is injected through several circular holes on to the concave surface of a splash cone located downstream of an air swirler. On emerging from the splash cone, the liquid is picked up by a single, high velocity, swirling airstream. The addition of a splash cone, to what is basically a configuration similar to that of Figure 1(j), has been observed to yield generally poor atomization performance (Refs. 15,22).

EXPERIMENTAL DETAILS

The pre-filming and the plain-jet airblast atomizers have been extensively studied under atmospheric as well as high air pressure conditions at the Cranfield laboratories. A schematic arrangement of the high pressure test facility is shown in Figure 2. The pressure chamber, inside which the atomizer is located, features windows for laser beam access to enable the measurement of the spray SMD. The drop size data, obtained largely at Cranfield, was collected through the use of well-established laser light-scattering techniques. The Cranfield technique, described in Reference 4, is an extension of that developed by Dobbins et al (Ref.23) and is shown schematically in Figure 3. Standard laboratory procedures were adopted for fuel and air mass flow measurements. The test fluids featured in this study are water ($\eta = 0.0010$, $\sigma = 0.0735$, $\rho = 1000$), kerosine ($\eta = 0.0013$, $\sigma = 0.027$, $\rho = 784$), gas oil ($\eta = 0.0053$, $\sigma = 0.0294$, $\rho = 846$) and a 55% residual fuel oil (RFO), 45% gas oil (GO) blend ($\eta = 0.036$ at 30°C working temperature, $\sigma = 0.0331$, $\rho = 913$).

RESULTS

This paper is devoted to a consideration of the effect that various design parameters have upon the airblast atomizer performance and consequently, the effect of operating variables such as the air pressure/temperature, the fuel viscosity, etc, will not be discussed directly. The pre-filming airblast atomizer is examined first, in view of its more widespread usage, followed by the plain-jet type.

Since airblast atomization relies upon the airstream momentum for fuel disintegration, the air-to-fuel (liquid) mass ratio would clearly seem to be an important variable influencing the spray quality. Deficiency of air would result in failure to overcome the viscous/surface tension forces that are resisting liquid disintegration where as an excess of air may result in some of the air not actually participating in the liquid break up due to its physical remoteness. Clearly the size of the air passages (and hence the atomizer bulk/weight) is related to the air mass flow requirement. It has been suggested in Reference 3 that to achieve optimum performance pre-filming atomizers should be designed to operate with an ALR in the 3 to 5 range. Figure 4, taken from Reference 24, shows the effect of atomizer AFR upon SMD for a range of ambient air pressures when using the pre-filming configuration of Figure 1(c). It is clear from this figure that the atomizer AFR effect is relatively weak for air pressures exceeding 3 atmospheres and atomizers designed with an AFR of 2 will give almost as good a drop size performance as atomizers designed with an AFR of 5. Over-sized atomizers are clearly undesirable from air requirement ,space, weight and cost considerations.

Engineers are continually faced with the demand to design gas turbine combustors that will operate effectively with a minimum of air pressure drop. This in turn requires careful attention to the detailed aerodynamics of the atomizer air flow passages in order to minimise pressure losses and hence obtain the best possible level of atomization quality. Figure 5 shows the influence that atomizer air pressure drop has upon the spray quality of the pre-filming configuration of Figure 1(a). Clearly, the higher the available air pressure drop, the superior the atomization performance although the degree of this superiority can be seen to diminish somewhat at higher ambient air pressures. The design philosophy behind the configurations (c) and (d) of Figure 1 has been to utilise, as much of the available air pressure drop as is practicable in obtaining the highest possible air velocity in the plane of the pre-filmer lip. An alternative approach (Ref.9) makes use of swirlers, see configuration of Figure 1(e), in the inner as well as the outer air flow passages. The use of swirlers is clearly going to impose additional air pressure drop, but to what extent this is effectively countered through greater intimacy of fuel and air contact and, therefore, better momentum interchange is not evident from the currently available drop size data on the pre-filming atomizer.

The physical scale of the pre-filmer/atomizer is clearly another key design parameter influencing the atomizer performance through its effect upon the thickness of the annular liquid sheet generated at the pre-filming surface. Using the basic configuration of Figure 1(d), El-Shanawany and Lefebvre (Ref.3)

examined the effect of atomizer scale upon mean drop size by conducting tests on three geometrically similar injectors with cross-sectional areas in the ratio of 1:4:16. The results obtained by them, see Figure 6, indicate that a simultaneous increase in the atomizer overall characteristic size as well as the pre-filmer lip diameter D_p has an adverse influence upon the spray quality in accordance with the relationship SMD $\propto D_p^{0.73}$. The influence upon drop size of a change in the pre-filmer lip diameter alone for a given overall characteristic size of atomizer is something which does not appear to have been examined so far. Intuitively, the bigger pre-filmer lip diameter should yield a thinner liquid annular sheet with a possible improvement in atomization performance.

Despite the extensive research on the pre-filming airblast atomizer over the last two decades, very little is known as regards the thickness/evenness of the annular liquid sheet generated by the pre-filming device. This is largely due to the difficulties associated with the measurement of very thin liquid sheets in a complex geometry. The importance of liquid sheet thickness has been recognised for some time now and this prompted Rizk and Lefebvre (Ref.10) to carry out experiments in an attempt to correlate it with the spray mean drop size. They used an atomizer specially designed to deliver two-dimensional, flat, liquid sheets through a discharge slot of known width (see Figure 1(f)). The results obtained by them, shown in Figure 7, confirmed that thin liquid sheets yield lower spray mean drop sizes in accordance with the relationship SMD $\propto t^n$ where n takes the values of 0.4 and 0.55 for low and high viscosity liquids respectively.

The main difference between the plain-jet configurations (g), (h) and (i) of Figure 1 is that relating to the angular orientation of the fuel injection orifice. This in turn is likely to influence the jet trajectory and its interaction with the surrounding air. Figure 8 provides a quantitative insight into the effect of liquid jet injection angle θ_{LO} (see Figure 1(i)) upon mean drop size for a range of airstream velocities. As can be seen clearly from this figure the transverse injection case (i.e. $\theta_{LO} = 90^0$) results in the smallest mean drop size. In Reference 18, θ_{LO} was varied in the 30 to 90 degree range out since the trend is well-established it can be confidently extrapolated to cover the $\theta_{LO} = 0$ case (i.e. the co-axial, co-flowing case). The marked superiority of the transverse liquid injection, relative to the co-axial, co-flowing case was observed by Ingebo (Ref.13) too, and is considered to be a reflection of the more intense air-to-fuel physical contact. This is borne out by the results of Figure 9 wherein the penetration/spatial spread characteristics of the liquid jet are plotted against the injection angle for a range of airstream velocities. In the co-axial, co-flowing case ($\theta_{LO} = 0$) the liquid jet and the airstream are moving parallel to each other and consequently the disintegrating liquid jet is likely to be in contact with the same air streamlines all the time - streamlines that are progressively being depleted of energy. The injection of liquid transverse to the air flow (i.e. $\theta_{LO} = 90^0$) gives maximum jet penetration and consequently allows a greater degree of air entrainment which in turn yields a more intimate fuel-to-air interaction. It should be pointed out here that the results shown in Figures 8 and 9 relate to the behaviour of a single jet in a square duct (Ref.18) supplied with a non-swirling airstream (i.e. configuration of Figure 1(i)).

The effect of liquid injection angle for a complete atomizer of the type shown in Figure 1(k) has recently been reported in Reference 21 and a typical set of results is shown in Figure 10. These results indicate that the transverse injection of liquid (i.e. $\alpha_0 = 0^0$, note $\alpha_0 = 90^0 - \theta_{LO}$) from an array of orifices would result in superior spray quality relative to the co-axial, co-flowing case (i.e. $\alpha_0 = 90^0$) even in a swirling airstream. Also investigated in this study was the effect of injecting liquid in an upstream direction (i.e. $\alpha_0 = -15^0$ and -30^0). It seems that the atomization performance can be improved further, especially at low airstream velocities, by utilising the upstream injection configuration.

Many plain-jet atomization research studies have used the size of the fuel injection orifice as the characteristic dimension for the purposes of developing mean drop size correlations. Figure 11 illustrates the adverse influence that an increase in injection orifice size has upon the spray quality for a high-viscosity liquid. Although not reported here, a somewhat similar trend has been established for low-viscosity liquids as well (Ref.16). The available evidence seems to suggest that SMD $\propto d_o^n$ where an average value of n is about 0.5. An additional factor whose influence is inter-related to the size of the liquid orifice, is the velocity at which the liquid is injected into the airstream - smaller orifice size requiring higher injection velocity and viceversa. It is well known that airblast systems operate with low fuel pressures/velocities and an examination of Figure 12 shows that the liquid injection velocity has very little effect upon the resulting mean drop size.

A key component of the atomizer configurations (j), (k) and (l) illustrated in Figure 1 is the air swirler. Although the swirlers have been in use for some time now, their usefulness in promoting more effective atomization quality has not been thoroughly investigated. Indeed it has been suggested that their use may in fact be detrimental to the attainment of good atomization performance. Ingebo (Ref.13) carried out a series of experiments using a 70^0 blade-angle air swirler and his results for the co-axial, co-flowing and the transverse liquid injection cases are shown in Figures 13 and 14 respectively. They clearly show that the use of an air swirler results in a marked improvement in the spray quality for both the configurations. Further experimental evidence regarding the influence of swirler geometry upon drop size has been recently obtained at Cranfield (Ref.20) as a part of an on-going research programme in plain-jet airblast atomization. The main swirler geometry variables that have been studied relate to the vane shape (straight or curved) and the vane outlet angle γ (see Figure 1(k)). Figure 15 shows a typical velocity profile at the outlet of a 45^0 curved-vane air swirler obtained with a standard cobra probe. Information of this kind is useful when attempting to optimize the atomizer geometry because it enables the liquid injection orifice to be oriented in a manner that encourages maximum physical contact between the liquid and air. Figure 16 illustrates the effect upon spray quality of an air swirler and its geometry for a transversely injected liquid jet. The mean drop size values are plotted against the experimentally measured axial velocities at the exit of four different air swirler configurations - namely the curved vane type with 30, 45 and 60^0 outlet angle and a 30^0 flat vane type. Also included is the non-swirling air configuration for the purposes of comparison. The use of air swirlers is clearly improving the spray quality - curved vane swirlers facilitating a greater degree of improvement relative to their flat vane counterpart. Furthermore, the 60^0 outlet angle curved vane configuration is yielding the best atomization performance. What is not evident from this figure is the level of air pressure

drop introduced by the different swirler configurations. From a combustor design viewpoint, clearly that is the constraint within which the use of a swirler for atomization purposes has got to be acceptable. Further examination of the data reveals that to achieve a given swirler exit axial velocity, the higher the curved vane outlet angle the higher the air pressure drop requirement. In other words the 60° curved vane swirler, whilst providing the best spray quality also, introduces the highest air pressure drop. It is also evident from the data that curved vanes introduce less pressure drop relative to the flat ones. It is clear from the foregoing discussion that although the use of a swirler is facilitating an improvement in the spray quality, through a more intimate fuel and air physical contact, its geometry needs to be carefully controlled to ensure its acceptability from the air pressure drop viewpoint.

It is perhaps worth pointing out here that the general trends as regards the effect of atomizer air pressure drop (and atomizer AFR) upon drop size are similar for the plain-jet and the pre-filming types of airblast atomizer.

Comparative Performance of the Two Types of Airblast Atomizers

It is possible to provide a comparative assessment of the pre-filming and the plain-jet airblast atomizers by bringing together the results of some comparable studies. Such a comparison is clearly of interest and value to the combustion engineer involved in atomizer design and performance but must be carried out carefully if variations specific to particular tests and techniques are not to inspire misleading conclusions.

Figure 17 facilitates a comparison under atmospheric pressure conditions between the co-axial, co-flowing plain-jet configuration (of Figure 1(g) investigated by Lorenzetto and Lefebvre (Ref.12) and the pre-filming configuration (of Figure 1(d)) studied by Rizkalla and Lefebvre (Ref.2). On the basis of this evidence the complex atomizer configuration of Figure 1(d) is significantly better than the simple configuration of Figure 1(g). A comparison under widely varying ambient air pressures and fuel viscosities for the pre-filming configuration of Figure 1(c) and the plain-jet configuration of Figure 1(j) was provided by Jasuja (Ref.19). An examination of Figures 18, 19 and 20 reveals that, under nominally comparable operating conditions, there is not a great deal of difference between the mean drop size performance of these two atomizer configurations, especially at higher air pressures for the low-viscosity kerosine/gas oil type of spray medium. A limited amount of comparative drop size data on atomizer configurations 1(d) and 1(j) is contained in References 17 and 25. The general conclusion that can be drawn from this is that the plain-jet configuration 1(j) gives spray quality that is comparable to that achieved from the pre-filming configuration 1 (c/d). The comparisons drawn from the work of Lorenzetto and Lefebvre and that of Jasuja are consistent in as much as the transverse injection of liquid in a swirling airstream will be significantly better than the co-axial,co-flowing liquid injection in a non-swirling airstream.

CONCLUSIONS

The two main conclusions to be drawn from the evidence that is currently available are as follows:

1. Despite the extensive research on both the pre-filming and the plain-jet atomizers, there still remain major design features that are worthy of further study. In particular the pre-filming device and the air swirler need to be examined in detail to optimize their geometry.

2. The drop size performance of the relatively simple plain-jet airblast atomizer featuring multiple, transversely injected liquid jets into a swirling airstream is comparable to that of its more widely used pre-filming counterpart especially when operating on low viscosity kerosine/gas oil type of media under high air pressure.

REFERENCES

1. NORSTER, E.R. and LEFEBVRE, A.H., "Effect of Fuel Injection Method on Gas Turbine Combustion", Emissions from Continuous Combustion Systems, ed. W. Cornelius and W.G. Agnew, Plenum Press, New York, pp 255-278, 1972.

2. RIZKALLA, A.A. and LEFEBVRE, A.H., "The Influence of Air and Liquid Properties on Airblast Atomization," ASME Journal of Fluids Engineering, Vol.97, No.3, Sept. 1975, pp.316-320.

3. EL-SHANAWANY, M.S. and LEFEBVRE, A.H., "Airblast Atomization: The Effect of Linear Scale on Mean Drop Size", March 1980, Gas Turbine Conference of the ASME - Paper No. 80 GT 74.

4. JASUJA, A.K., "Atomization of Crude and Residual Fuel Oils", ASME Journal of Engineering for Power, Vol.101, No.2, April 1979, pp 250 - 258.

5. BENNET , P.G., "Airblast Atomization", Cranfield College of Aeronautics Thesis, June 1962.

6. LEFEBVRE, A.H. and MILLER, D., "The Development of an Airblast Atomizer for Gas Turbine Application", Cranfield College of Aeronautics Report, Aero. No.193, (1966).

7. GRETZINGER, J. and MARSHALL, W.R., "Characteristics of Pneumatic Atomization", AI Ch E J. 7,(2) 312-318, 1961

8. BRYAN, R.H., "An Experimental Study of an Airblast Atomizer". Cranfield College of Aeronautics Thesis, 1967.

9. SIMMONS, H.C., "The Prediction of Sauter Mean Diameter for Gas Turbine Fuel Nozzles of Different Types", ASME Journal of Engineering for Power, Vol.102, July 1980, pp.646-652.

10. RIZK, N.K., and LEFEBVRE, A.H., "The Influence of Liquid Film Thickness on Airblast Atomization", ASME Journal of Engineering for Power, Vol.102, July 1980, pp 706-710.

11. NUKIYAMA, S. and TANASAWA, Y., "Experiments on the Atomization of Liquids", Transactions of the Society of Mechanical Engineers, Japan, 6 parts, 1938-40, English translation by the Dept. of National Defence, Canada, 1950.

12. LORENZETTO, G.E. and LEFEBVRE, A.H., "Measurements of Drop Size on a Plain Jet Airblast Atomizer", AIAA Journal, Vol.15, No.7, July 1977, pp.1005-1010.

13. INGEBO, R.D., "Atomization of Water Jets and Sheets in Axial and Swirling Airflows", ASME Paper No.79-GT-170.

14. RIZK, N.K. and LEFEBVRE, A.H., "Spray characteristics of Plain-jet Airblast Atomizers", ASME Paper No.83-GT-138.

15. INGEBO, R.D., "Effect of Airstream Velocity on Mean Drop Diameter of Water Sprays Produced by Pressure and Air Atomizing Nozzles". Paper presented at the Winter Annual Meeting of the ASME, Nov. - Dec. 1977.

16. HUSSEIN, G.A., JASUJA, A.K. and FLETCHER, R.S., "Effect of Air, Liquid and Injector Geometry Variables Upon the Performance of a Plain-jet Airblast Atomizer". Paper presented at the 6th International Symposium of Airbreathing Engines, Paris, June 1983.

17. RIZK, N.K., and LEFEBVRE, A.H., "Influence of Airblast Atomizer Design Features on Mean Drop Size", AIAA Paper No. 82-1073, June 1982.

18. HUSSEIN, G.A., JASUJA, A.K., and FLETCHER, R.S., "Penetration and Break-up Behaviour of a Discrete Liquid Jet in a Cross-flowing Airstream - A Further Study ", ASME Paper No. 83-GT-170.

19. JASUJA, A.K., "Plain-Jet Airblast Atomization of Alternative Liquid Petroleum Fuels Under High Ambient Air Pressure Conditions", ASME Paper No. 82-GT-32.

20. HUSSEIN, G.A., "Effect of Air, Liquid and Injector Geometry variables upon the Performance of a Plain-Jet Airblast Atomizer", Cranfield Institute of Technology Thesis, 1983.

21. SHAW, S., "The Optimisation of a Plain-Jet Airblast Atomizer", Cranfield Institute of Technology Thesis, 1983.

22. ROSFJORD, T.J. and BRIEHL, D., "Evaluation of Fuel Injection Configurations to Control Carbon and Soot Formation in Small GT Combustors ". AIAA Paper No.82-1175, June 1982

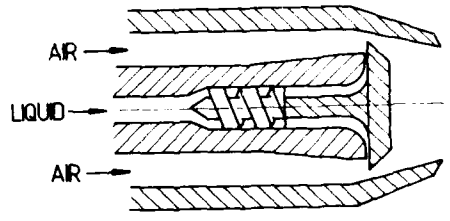
23. DOBBINS, R.A., CROCCO, L. and GLASSMAN, J., "Measurements of Mean Particle Sizes of Sprays from Diffractively Scattered Light", AIAA Journal, Vol.1, No.8, Aug.1963, pp.1882-1886.

24. JASUJA, A.K., "Airblast Atomization of Alternative Liquid Petroleum Fuels Under High Pressure Conditions", ASME Journal of Engineering for Power, Vol.103, July 1981, pp.514-518.

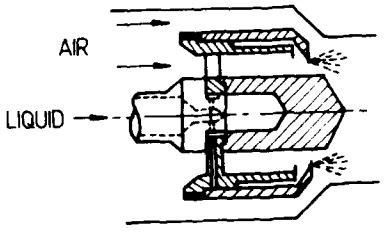
25. ANDERSSON, L., "The Rig Development of a High Performance Dual Fuel Combustor with an Air Swirl Atomiser". Stal Laval Turbin contribution to CIMAC Congress, Vienna, 1979.

ACKNOWLEDGEMENTS

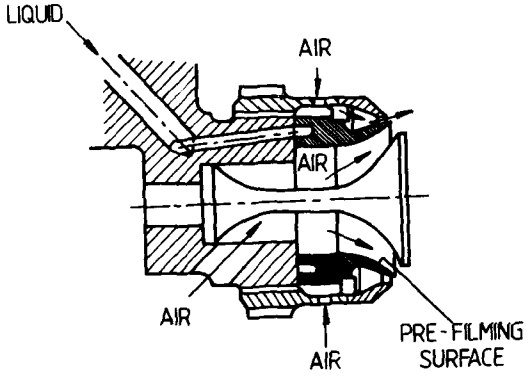
A large proportion of the work reported in this paper has been obtained at the laboratories of the School of Mechanical Engineering, Cranfield Institute of Technology. The author would like to gratefully acknowledge the continuing interest and support of the Head of School, Professor R.S.Fletcher. The author wishes to thank all his colleagues and students who have contributed in the preparation of this paper. The financial support of the Ministry of Defence, U.K. for the high air pressure atomization study is also gratefully acknowledged.



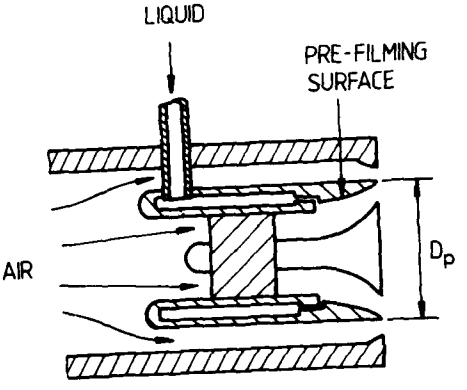
(a)



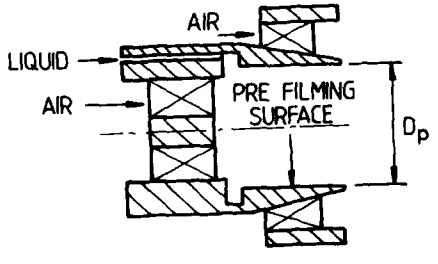
(b)



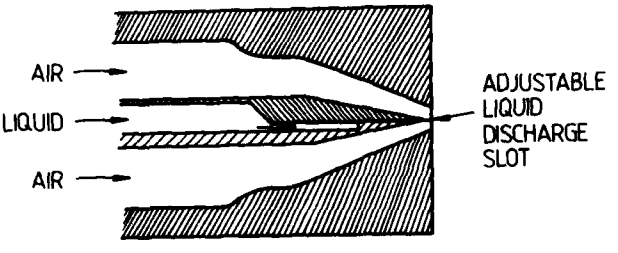
(c)



(d)

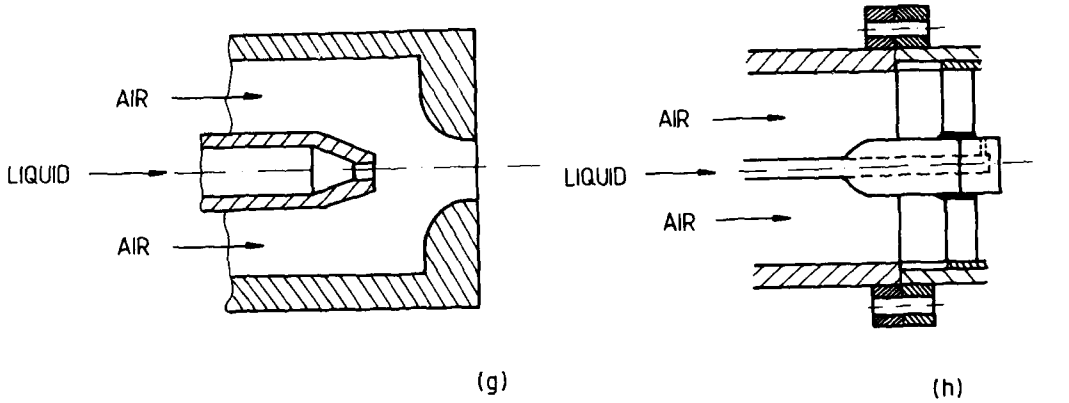


(e)

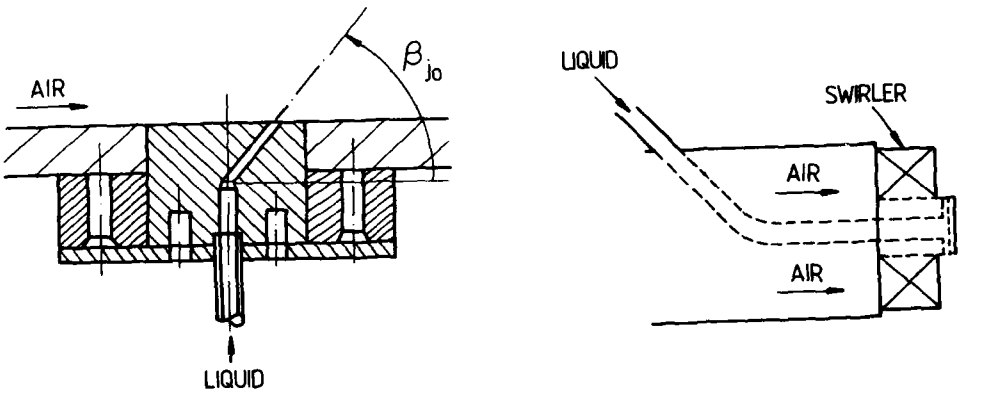


(f)

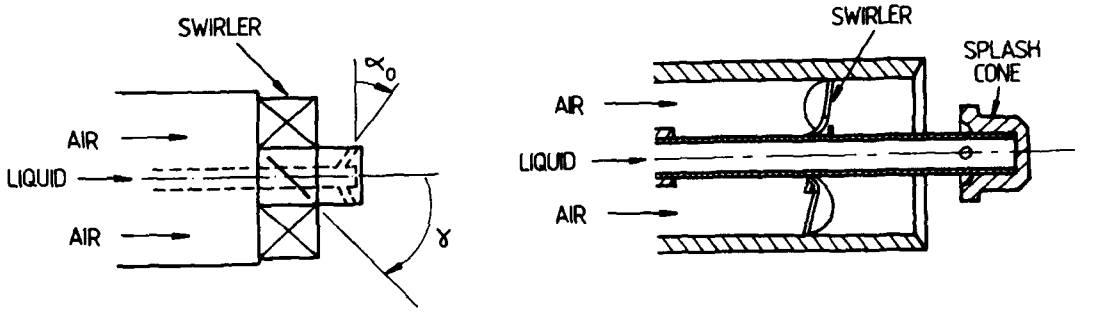
FIG. 1 ATOMIZER CONFIGURATIONS - PRE-FILMING TYPE (1a - 1f)



(g) (h)



(i) (j)



(k) (l)

FIG. 1. ATOMIZER CONFIGURATIONS - PLAIN JET (1g - 1l)

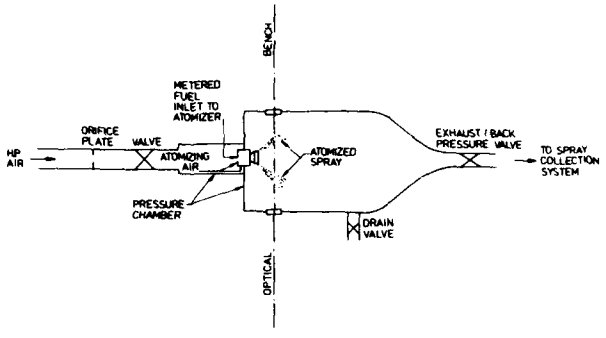


FIG 2 OUTLINE ARRANGEMENT OF THE TEST INSTALLATION

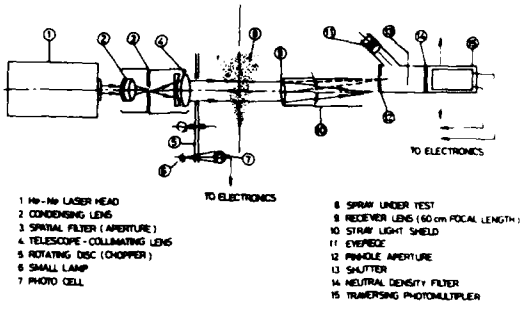


FIG 3 DIAGRAMMATIC FORM OF OPTICAL SYSTEM

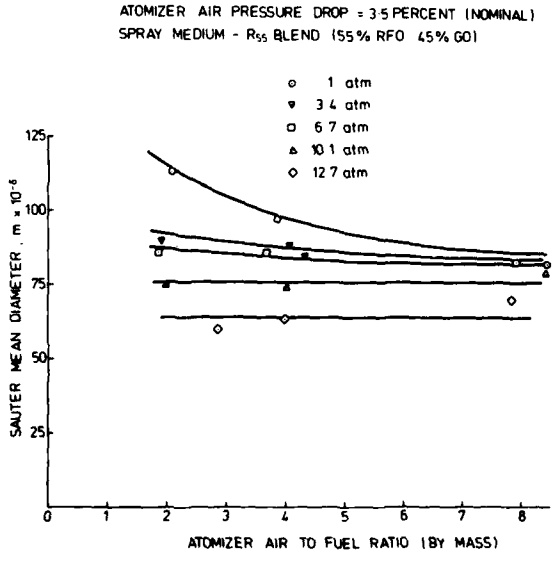


FIG 4 ATOMIZER MEAN DROPSIZE PERFORMANCE UNDER VARYING AMBIENT AIR UPSTREAM PRESSURE AND AIR TO FUEL RATIO (R_{55} BLEND)

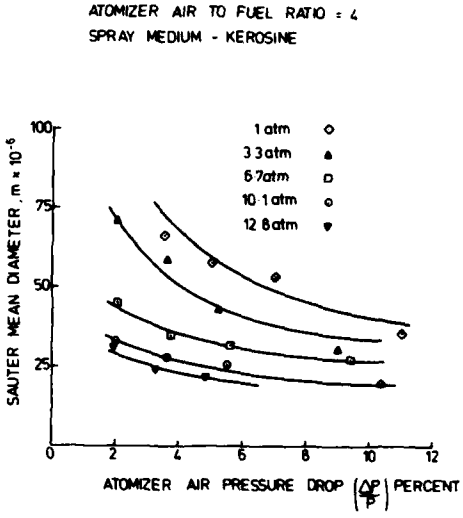


FIG 5 INFLUENCE OF VARYING ATOMIZER AIR PRESSURE DROP AND AMBIENT AIR UPSTREAM PRESSURE ON SPRAY MEAN DROPSIZE

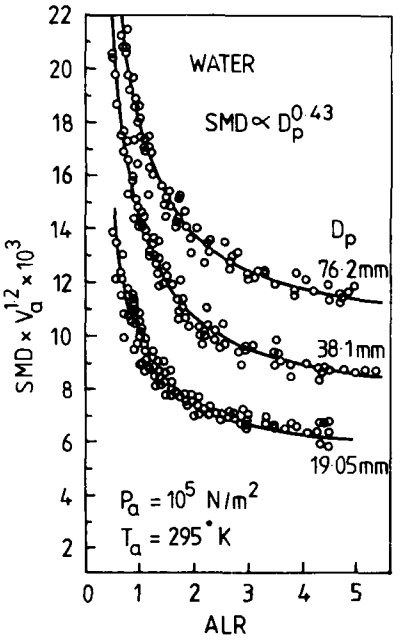


FIG.6 EFFECT OF ATOMIZER LINEAR SCALE ON MEAN DROP SIZE.[3]

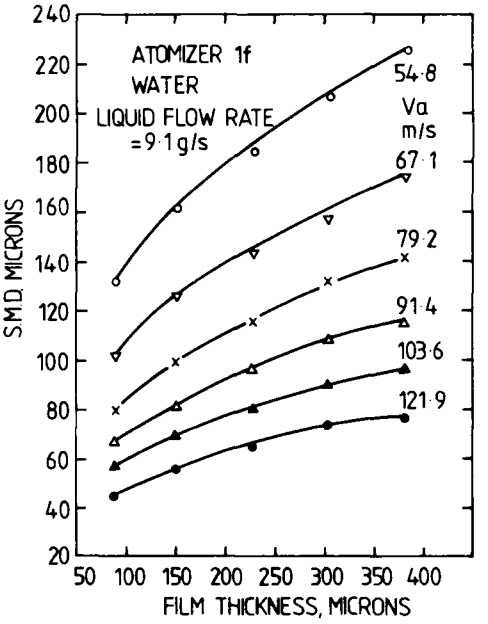


FIG.7. EFFECT OF FILM THICKNESS ON SMD FOR VARIOUS AIR VELOCITIES[10]

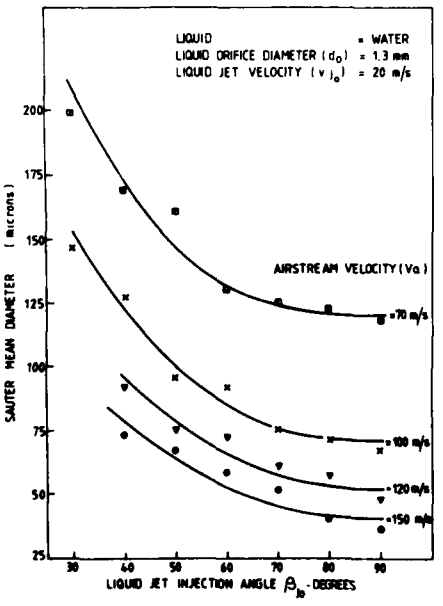


FIG. 8 VARIATION OF SMD WITH THE ANGLE OF INJECTION FOR VARIOUS AIRSTREAM VELOCITY LEVELS.

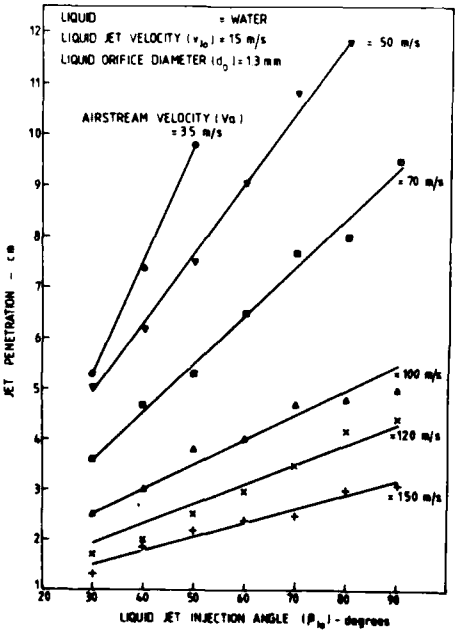


FIG 9 VARIATION OF PENETRATION WITH THE LIQUID JET INJECTION ANGLE FOR DIFFERENT AIRSTREAM VELOCITIES

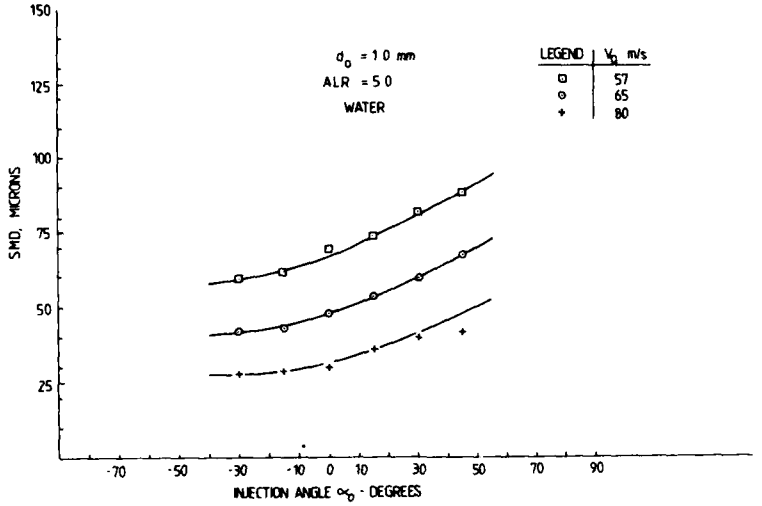


FIG 10 VARIATION OF SMD WITH LONGITUDINAL INJECTION ANGLE (α_o)-d_o = 1.00 mm

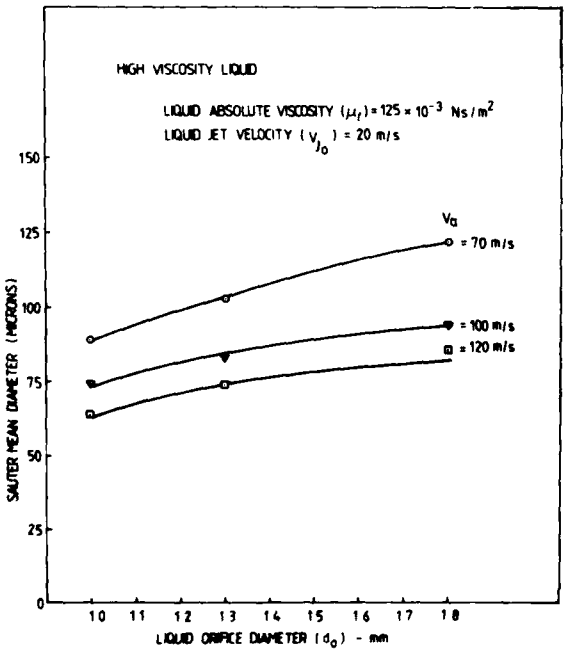


FIG 11 LIQUID ORIFICE SCALE EFFECT FOR A HIGH-VISCOSITY LIQUID

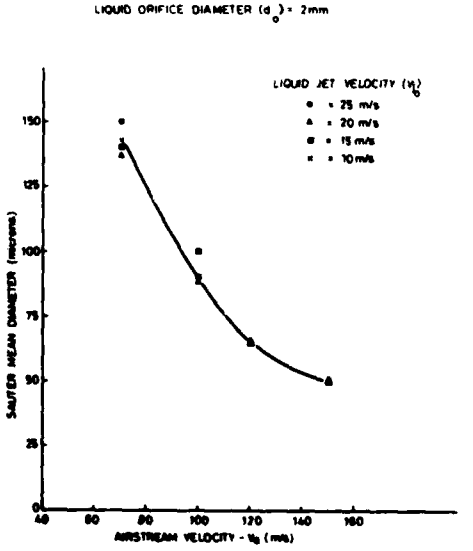


FIG.12 EFFECT OF AIRSTREAM AND LIQUID JET VELOCITY UPON SPRAY MEAN DROPSIZE

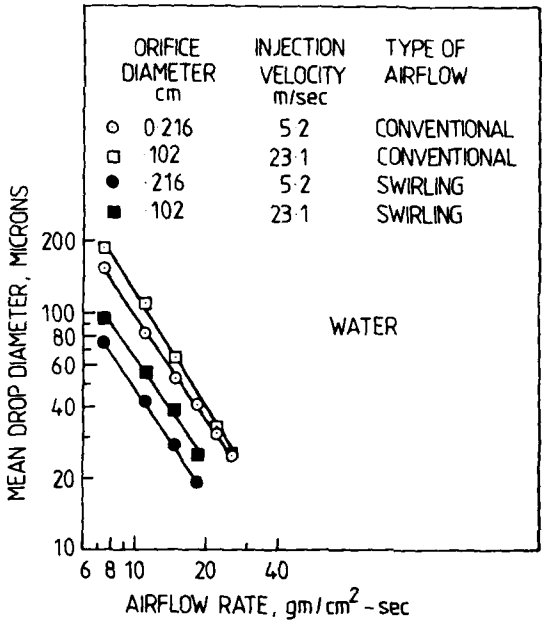


FIG. 13 VARIATION OF MEAN DROP DIAMETER WITH AIRSTREAM MOMENTUM FOR AXIAL DOWN-STREAM INJECTION WITH SINGLE TUBES[13]

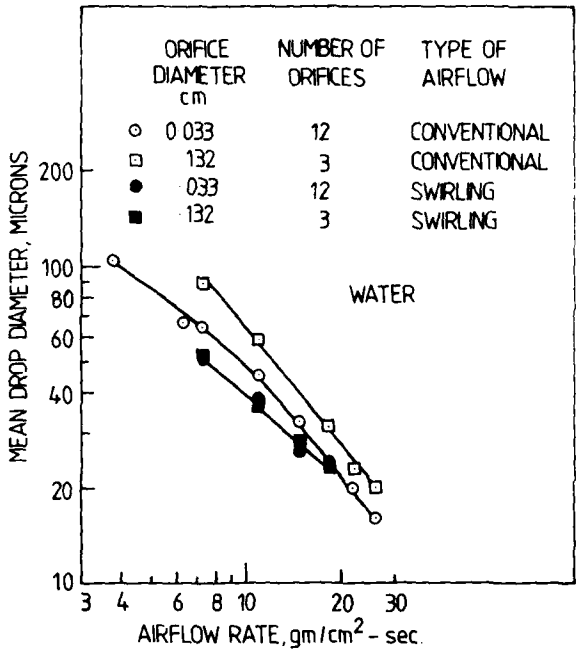


FIG. 14. VARIATION OF MEAN DROP DIAMETER WITH AIRSTREAM MOMENTUM FOR CROSS STREAM INJECTION WITH SPRAY BARS[13]

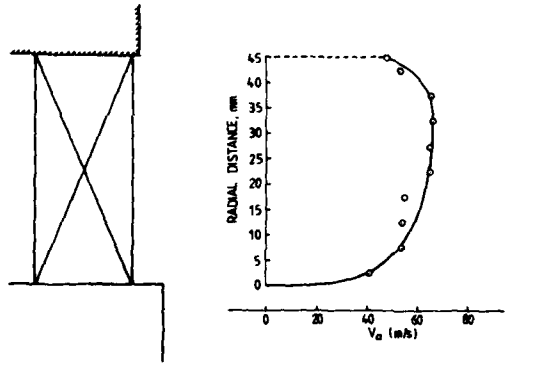


FIG 15 DISTRIBUTION OF AIR AXIAL VELOCITY AT THE EXIT OF 45° CURVED-VANE SWIRLER

$\frac{\Delta P}{P}$ = 1·5 PERCENT

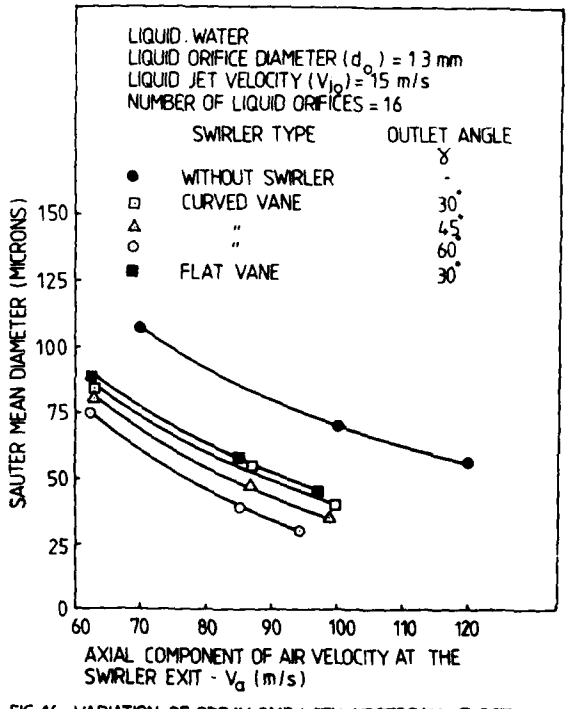


FIG 16. VARIATION OF SPRAY SMD WITH AIRSTREAM VELOCITY FOR DIFFERENT SWIRLERS

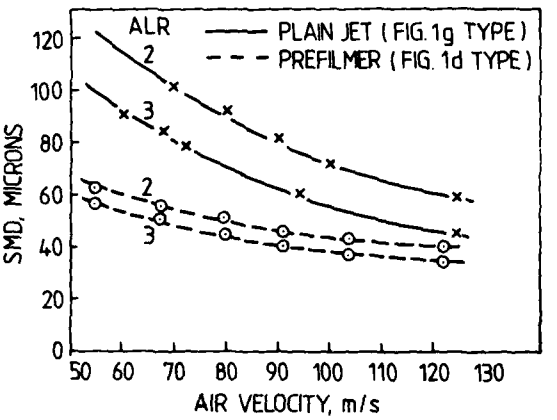


FIG. 17. COMPARISON OF ATOMIZING PERFORMANCE OF PLAIN-JET AND PREFILMING ATOMIZERS[12]

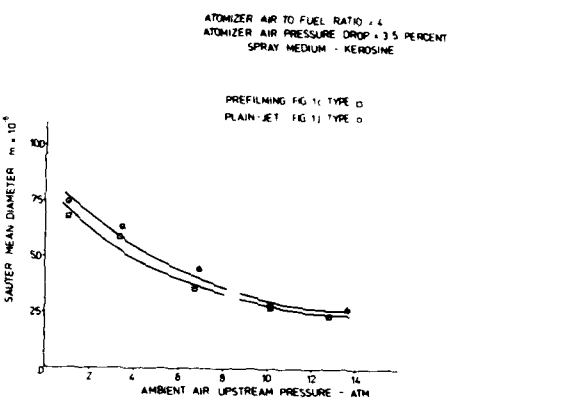


FIG 18 COMPARATIVE PERFORMANCE OF PREFILMING AND PLAIN-JET AIRBLAST ATOMIZERS UNDER VARYING AMBIENT AIR UPSTREAM PRESSURES - KEROSINE

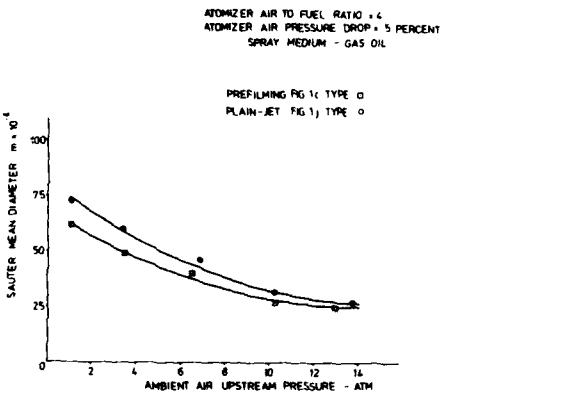


FIG 19 COMPARATIVE PERFORMANCE OF PREFILMING AND PLAIN-JET AIRBLAST ATOMIZERS UNDER VARYING AMBIENT AIR UPSTREAM PRESSURES - GAS OIL

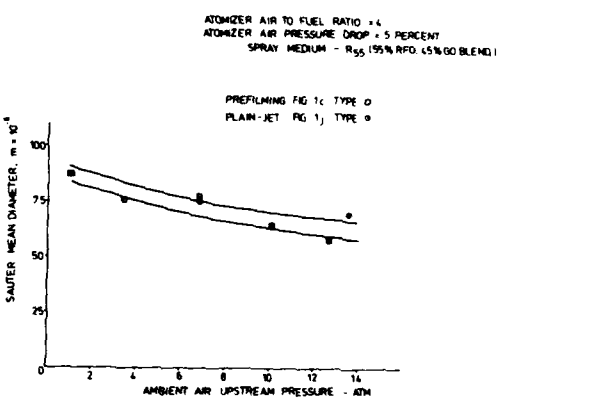


FIG 20 COMPARATIVE PERFORMANCE OF PREFILMING AND PLAIN-JET AIRBLAST ATOMIZERS UNDER VARYING AMBIENT AIR UPSTREAM PRESSURES - R55 FUEL

DISCUSSION

E.Mularz, US

With respect to Figure 15, indeed the air flow through the swirler is important in determining the fuel spray quality of the fuel injector. However, your measurement of the axial component of air velocity is not sufficient, since there is a substantial component of circumferential velocity as well. I recommend that further measurements be made, more completely mapping this airflow through the swirler.

Author's Reply

The author agrees with Dr Mularz as regards the importance of more detailed mapping of the velocity flow-field at the exit of the air swirler. Indeed the first conclusion emphasizes the need for further work on the air swirler. Figures 15 and 16 were included in the paper to highlight, from the atomization performance viewpoint, the importance of air swirler vane geometry as well as the detailed understanding of the swirler velocity flow-field as typified by the axial velocity measurements. It was neither implied nor suggested that the axial velocity component was the only one that mattered. Indeed there is a substantial swirl component, the value of which depends upon the vane outlet angle. For example, the swirl component is approximately 80 percent of the axial component for the 45° curved vane swirler case of Figure 15. Figure 16 could be replotted using the swirl velocity component as the basis, but the basic conclusions would remain unchanged.

OPTICAL MEASUREMENTS OF DROPLET SIZE DISTRIBUTIONS: SPECIAL CONSIDERATIONS IN THE PARAMETER DEFINITION FOR FUEL ATOMIZERS

by

S. Wittig, M. Aigner, Sh. Sanbani and Th. Sattelmayer
Lehrstuhl und Institut für Thermische Strömungsmaschinen
Universität Karlsruhe (T.H.), Kaiserstr. 12,
D-7500 Karlsruhe, W. Germany

AD-P003 138

SUMMARY

In evaluating fuel nozzle performance, the droplet size distribution - frequently characterized by the Sauter mean diameter - is found to be one of the dominant parameters. Using examples from ongoing experimental studies with pressurized and airblast atomizers, attention is directed towards the importance of flow parameters and size distribution in applying non-intrusive optical techniques.

In particular, an optical diffraction-type particle sizer has been used in analyzing fuel sprays from airblast and pressure atomizers. It is shown that the Sauter mean diameter alone is generally not suited for describing the nozzle performance. Emphasis is directed towards the influence of the flow field on the apparent droplet size distribution explaining a variety of observations reported in other studies.

LIST OF SYMBOLS

d_T	droplet diameter
D_{50}, $D_{15.9}$, $D_{84.1}$, $D_{63.2}$	mean diameters; indices indicating Vol% which has smaller diameter than $D_{63.2}$
f	focal length
N	Rosin-Rammler exponent
q_3	volume density distribution
R	normalized weight upper size d_T
RR	Rosin-Rammler distribution, $R = \exp(-d_T/D_{63.2})^N$
SMD	Sauter mean diameter
u_L	air-velocity
$u_{L,0}$	initial air velocity
u_T	droplet velocity
$\dot{V}_W$	water flow rate
x	distance to the atomizer lip
θ	diffraction angle
λ	wave length

INTRODUCTION

The droplet size distribution within a fuel-air mixture is one of the dominant parameters in determing the vaporization rate, ignition and the combustion including the pollutant formation. Dickinson and Marshall [1] report, for example, on the influence of the width of the droplet size distribution on the evaporation rate with the result, that wider distributions will yield higher rates than narrower ones with identical mean diameter.

In developing a new fuel nozzle it, therefore, is necessary to obtain fairly complete information on the dependency of the droplet size distribution on the determining parameters such as fuel flow rates, geometry and ambient pressures and, in particular for airblast nozzles, on the air-flow parameters. Up to now, a large number of parametric studies is required. Presently, we are concerned with the study of various fundamental effects such as film characteristics [2] concerning airblast as well as pressure atomizers.

As primarily optical diagnostic techniques are employed, high accuracy of the data and proper interpretation is a necessity. This has been emphasized by us at several occasions.

MEASUREMENT OF DROPLETS

Two different measurement techniques are available for analysis of the droplet spectra [4]:

First, there is the time-resolved particle analyzer, which counts the droplets passing through a small probe-volume during a predetermined time-span, resulting in a droplet-frequency at the location of the probe-volume. Typical examples are single-particle counting systems.

The second method determines at a particular instant all particles within a probe volume representing its droplet-concentration. Typical examples are photographic techniques and particle analyzers utilizing diffractive light analysis [5,6]. Both techniques are presently in use in our laboratory. However, the discussions of this paper are primarily concerned with the second method, as for our applications the so-called Malvern Particle-Sizer [7] allows generally for measurements of broader distributions. The typical experimental set-up is shown in Figure 1.

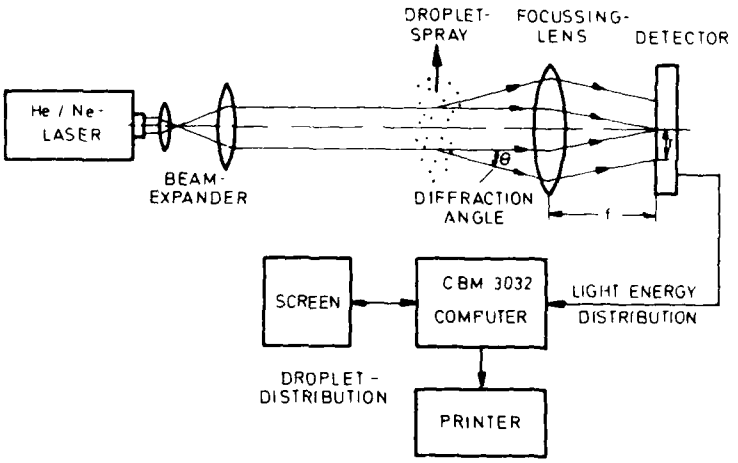


Fig. 1: Schematic of Malvern Particle-Sizer

The laser beam has been expanded to 9 mm diameter at a wave-length λ of 632,8 nm. As the droplet diameter d_m is considerably larger than λ, no dependency of the refractive index is to be considered and the scattered light intensity is a function of d_m/λ and the diffractive angle θ. A Fourier transform lens collects the scattered light, which is focused on the detector.

The light distribution recorded is compared with a theoretical light intensity distribution calculated for a specificly model-droplet size distribution such as "Rosin-Rammler"- or "Log-Normal"-distribution. Additionally, a "Model Independent" is available where 15 size classes are considered independently. For test and calibration purposes the results obtained with the Malvern Particle-Sizer were compared with those from various other Counters such as the Coulter-Counter, sedimentation technique [8] and photographic analysis using glass beads. Generally, the agreement was fairly good within 10 %, with the Malvern Particle-Sizer yielding slightly larger particle-sizes. In addition to the non-intrusive character of the analyzer, a major advantage is his short response time - conditions which allow for wide variations of the parameters determining the droplet size distribution in airblast as well as in pressure atomizers. The total measurement times,though, are determined by the capacity of the microcomputer, a problem which can easily be solved by using a minicomputer.

CHARACTERISTICS OF THE DROPLET-SIZE DISTRIBUTION

Frequently, the Sauter mean diameter (SMD) is applied in characterizing droplet-size distributions. The well-known definition of the SMD respresents the diameter of a sphere with an identical ratio of volume to surface area as the sum of all droplets. It, therefore, reflects the specific surface area and has been frequently used in describing the evaporation rates. However, as mentioned earlier, Dickinson and Marshall [1] observed that in addition of the SMD the width of the distribution is another important influence parameter.

Furthermore, in correlating fuel nozzle sprays, Simmons [9] states that in technical atomizers the ratio of the mean volumetric diameter D_{50} and the SMD is constant and is approximately 1.2. As we observed considerable deviations, a brief theoretical study was used to clarify the discrepancy. Using the Rosin-Rammler (RR) distribution, Figure 2 illustrates that the ratio D_{50}/SMD is strongly dependent on the width of the distribution. Specifically, this is important in technical applications where according to our experience the exponent N varies from N = 1.2 to 3. In comparing two different types of atomizers Figure 3 indicates that with an identical D_{50} the SMD is much smaller for broader droplet distributions. This is of primary importance in comparing pressure and airblast atomizers

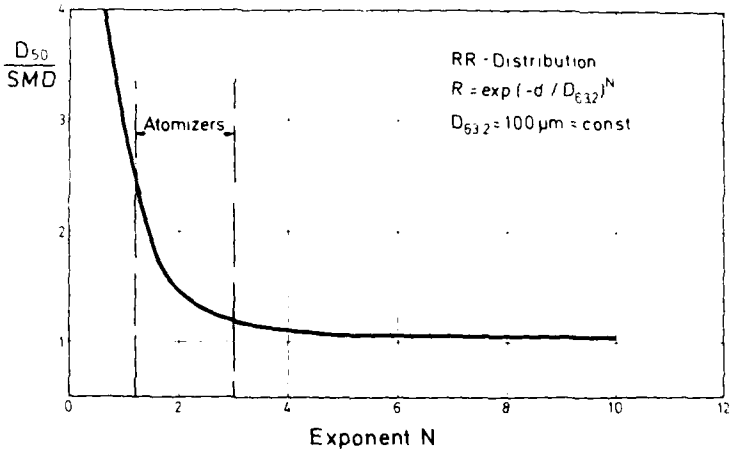


Fig. 2: SMD as a Function of the Distribution Width

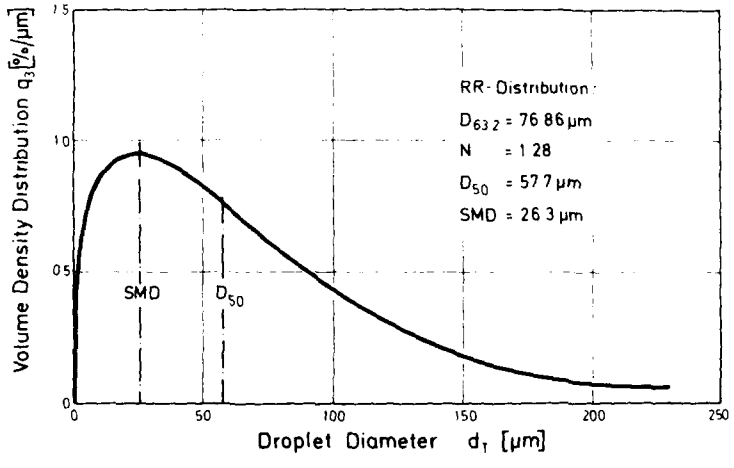


Fig. 3a: Airblast Atomizer: Droplet Distribution

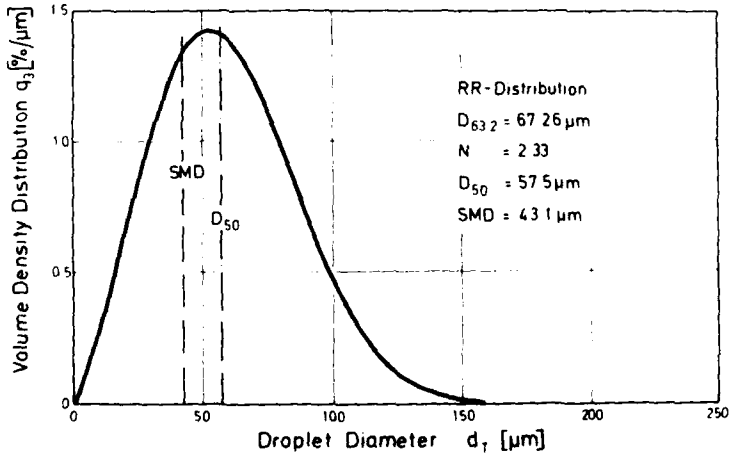


Fig. 3b: Pressure Atomizer: Droplet Distribution

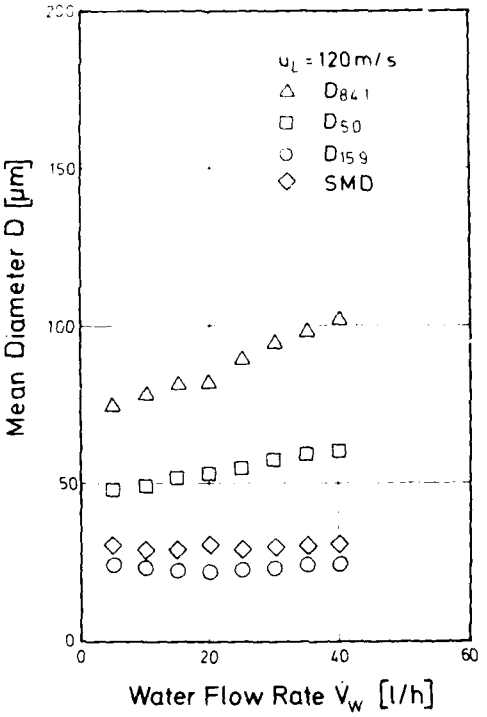


Fig. 4: Airblast Atomizer
Variation of the Mean Diameter

[illegible] shown in analyzing the [illegible] of a single jet [illegible] conditions, the [illegible] with [illegible] solutions.

Figure 4, for example, [illegible] that for a particular [illegible] with a constant air [illegible] the SMD remains constant [illegible] the liquid is varied whereas the parameters D_{84} and D_{159} increase [illegible]. It follows that the use of only [illegible] is insufficient to [illegible] the distribution. In order [illegible] and D_{159}, a simple approach will be chosen to achieve fairly unique and complete characterization without major complexities. In addition the three parameters are easily determined experimentally and the usual distribution functions can be fitted to them.

INFLUENCE OF FLOW PARAMETERS

In combustion processes, the local droplet-concentration is of major importance. In comparing different atomizers, however, the production frequency of the droplet classes should be considered. As the Malvern Particle-Sizer and similar techniques yield droplet concentrations only, it should be emphasized that for an evaluation of the droplet production rate the requirement of uniform velocities normal to the optical axis is introduced. For airblast and pressure atomizers, all droplets will have approximately the same velocity at the origin - i.e. close to the film flow speed - and in the far field of the nozzle, where they are approaching the air velocity, if no reaction occurs.

Figure 5 supports these statements. Here, assuming constant air velocities, available drag coefficients for spherical particles have been used with the Reynolds-number as the dominant influence parameter in solving the momentum equation for single droplets.

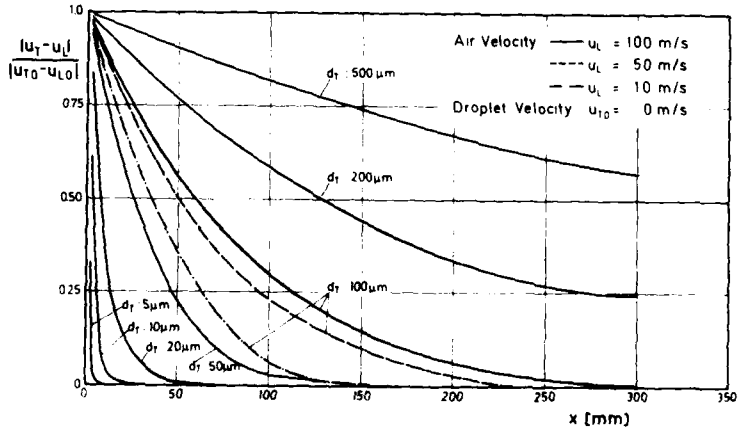


Fig. 5: Calculated Droplet Velocities

In corresponding to conditions found in airblast atomizers - i.e. small film velocities and high air speeds - Figure 5 indicates that small droplets will accelerate within an extremely short distance from the nozzle whereas larger particles will need in excess of one hundred mm to reach ambient air velocities. With reference to a standard droplet-size of 100 µm diameter, Figure 6 shows the relative velocity deviations defined as velocity-coefficients. The reference diameter seems to be appropriate as it is a typical droplet-size in various applications. It can be concluded that along the spray's axis small par-

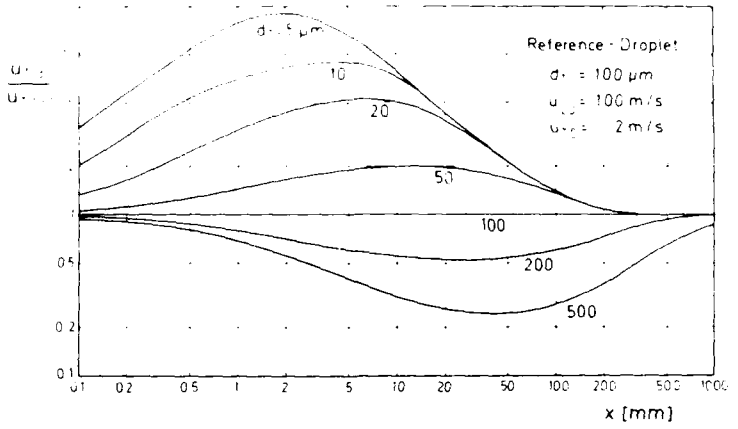


Fig. 6: Airblast Atomizer: Velocity-Coeffi[illegible]

The test of the principle validity of these conclusions was made [illegible] airblast atomizer with variable geometry. Two distinctly different [illegible] were [illegible]. In the first case, extremely high air ducts were employed thus yielding almost [illegible]. Here, the droplets will not enter the recirculation zone. The flow field behind the [illegible] was determined by Pitot-tube measurements indicating that the air speed is reduced at x = 200 mm to approximately 80 % of its initial value. The droplet speed was monitored [illegible] means of a Cranz-Hardin [illegible] double-exposure camera with flash frequencies between [illegible] and 10 Hz and flash duration of approximately 150 ns. Microscopic analysis yielded [illegible] velocities between 92 and 98 % of the initial air velocity with fairly large [illegible] the inaccuracy in evaluating the photographs.

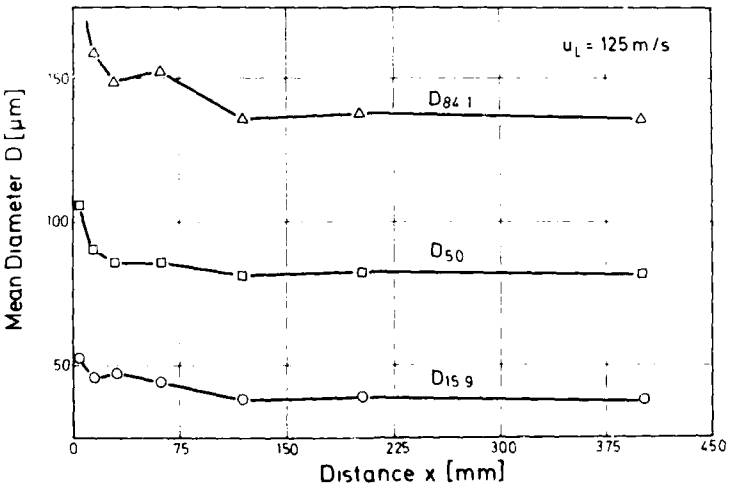


Fig. 7: Apparent [illegible] Size Distribution: Airblast Atomizer under Free Jet Condition

In supporting our earlier statement, [illegible] size distribution measurements along the spray's axis with the Malvern Particle-Sizer yielded a dependence of the changing droplet concentration up to about x = 150 mm as shown in Figure 7. The agreement with the conclusions derived from Figure 6 is evident. It can be seen that the high speed of the small particles leeds to their underprediction. A representative droplet-size distribution is obtained in the far field where the velocities of the liquid and the gas are the same for all droplet classes.

In changing the geometry to the conditions of an airblast nozzle with realistic channel height, the second condition is modeled. Here, the flow field is characterized by the recirculation zone as shown in Figure 8. The details of the flow field were obtained by numerical analysis using our finite difference scheme described elsewhere [11,12].

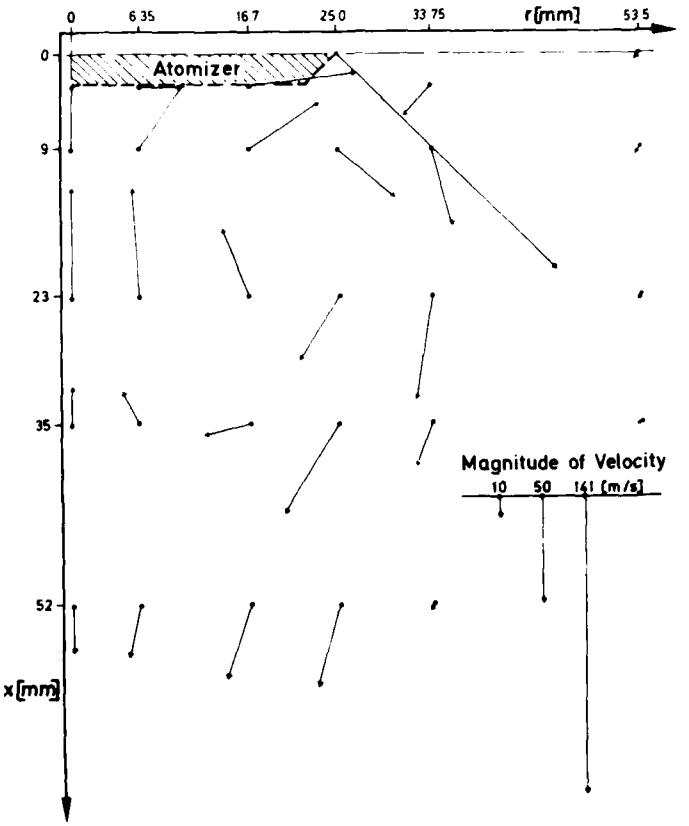


Fig. 8: Calculated Air Flow Field behind a Model Airblast Atomizer (Channel Height 1,5 mm)

The inner recirculation zone ends approximately 52 mm from the nozzle's lip with strong radial components between x = 35 and x = 52 mm. The small droplets, therefore, following the flow will have fairly large residence times in this zone leading to an over-representation of small particles whenever a Malvern type analyzer is used in this zone. These conclusions are supported by our measurements as shown in Figure 9.

Responsible for the minima of the diameter is the flow field and not physical processes during atomisation. In our opinion, therefore, explanations for the occurence of the minima such as late droplet formation and, possibly, droplet coalescence (see El-Shanawany and Lefebvre [13]) cannot be supported. Furthermore, effects due to geometry and, under certain conditions, air-liquid ratio must be carefully analysed with respect of variation of the flow field. Unfortunately, generalizations are extremely difficult to obtain as to transfer.

In addition to the study of airblast atomizers, interest arises whether pressure atomizers follow the above-mentioned charcteristics. Figure 10 represents typical measurements obtained using the Malvern Particle-Sizer. It is quite interesting to note that again a minimum mean-droplet diameter is found in the near field of the nozzle. However, the phyiscal phenomena actually are reversed from the previous observations. Here, due to their high velocity, the larger droplets are underrepresented in the near field of the nozzle as their deceleration is considerably smaller than for the smaller droplets. This is supported by the calculations shown in Figure 11. In comparing the velocity coefficients of Figure 6 and 11, the different character of the droplet flow is evident.

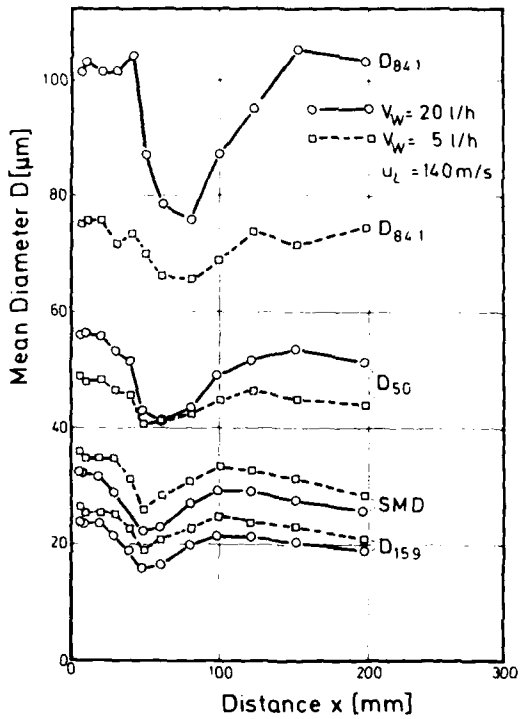


Fig. 9: Apparent Droplet Size Distribution: Model Airblast Atomizer

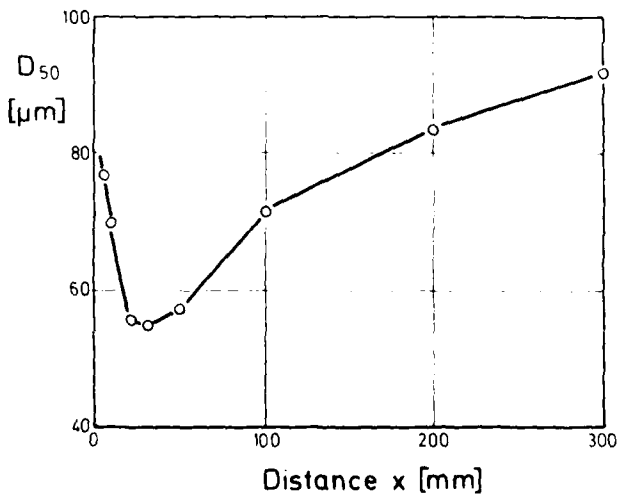


Fig. 10: Pressure Atomizer: D_{50} = f(x)

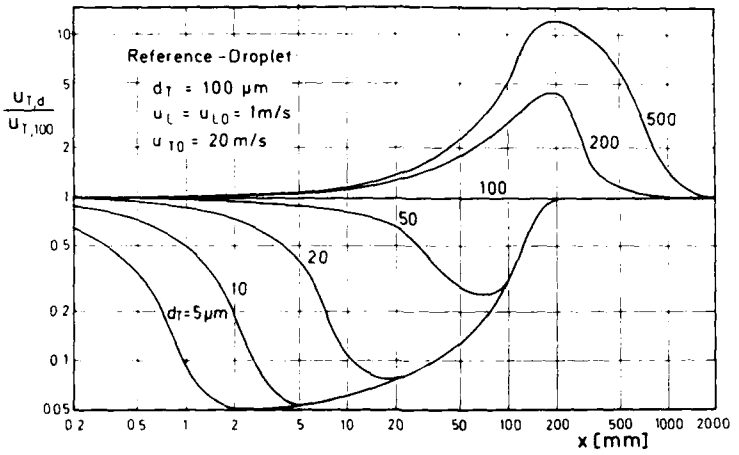


Fig. 11: Pressure Atomizer: Velocity-Coefficients

CONCLUSIONS

In evaluating fuel atomizers, special care should be directed in defining the characteristic parameters as well as the experimental conditions. The Sauter mean diameter is not sufficient in describing the spray. The droplet distribution should be defined at least by three independent moments. For simplicity, three characteristic diameters seem to be appropriate. This has been demonstrated by a large variety of measurements with atomizers of differing design using an optical diffraction-type analyzer. Furthermore, it should be recognized that in describing atomizer performance the utilization of various particle analyzers as well as the positioning of the probe volume requires careful analysis and is strongly dependent on the flow field surrounding the nozzle. Measurements indicate that the wrong choice of the measurement plane will lead to errors in excess of 50 % in the droplet size.

REFERENCES

[1] Dickinson, Dean R.; Marshall, W.R. Jr.: The Rates of Evaporation of Sprays, AIChE Journal, Vol. 14, Nr. 4, July 1968, pp. 541-552

[2] Wittig, S.; Sakbani, Kh.; Zahoransky, R.; Sill, K.H.: Einsatz optischer Meßmethoden zur Bestimmung von Tropfengrößen und Filmdicken in Zweiphasen-Strömungen. Die Industriefeuerung 21 (1981), pp. 39-45

[3] Raasch, J.; Umhauer, H.: Grundsätzliche Überlegungen zur Messung der Verteilungen von Partikelgröße und Partikelgeschwindigkeit disperser Phasen in Strömungen, Chem. Ing. Techn. 49 (1977), Nr. 12, S. 931-941

[4] Wittig, S.L.K.; Hirleman, E.D.; Christiansen, J.V.: Noninterfering Optical Single-Particle Counter Studies of Automobile Smoke Emissions in: Advances in Chemistry Series 166, (J.T.Zung, Ed.) , Washington, D.C. American Chemical Society, 1978, pp. 198-217

[5] Dobbins, R.A.; Crocco, L. and Glassmann, T.: Measurement of Mean Particle Sizes of Sprays from Diffractively Scattered Light, AIGG, 1(8), (1963), pp. 1882-1886

[6] Kayser, A.: Zur optischen Messung der Tropfengrößenverteilung bei der Zerstäubung von Brennstoff. Chemie-Ing.-Techn. MS 532/77, Synopse in: Chem.-Ing.-Techn. 49, Nr. 10 (1977), p. 845

[7] Swithenbank, J.; Beér, J.M.; Taylor, D.S.; Abbot, D.; Mc Greath, C.G.: A Laser Diagnostic Technique for the Measurement of Particle Size Distribution in: Progress in Astronautics and Aeronautics, Vol. 53, (B.T. Zinn, Ed.) 1977, pp. 421-447

[8] Batel, W.: Einführung in die Korngrößenmeßtechnik; Springer Verlag, Berlin, 1960

[9] Simmons, H.: The Correlation of Drop-Size Distributions in Fuel Nozzle Sprays. Trans. ASME, J. Enging. Power, (1977), pp. 309-319

[10] Häßler, G.: Untersuchung zur Verformung und Auflösung von Wassertropfen durch aerodynamische Kräfte im instationären Luft- und Wasserdampfstrom bei Unterschallgeschwindigkeit. Dissertation, Universität Karlsruhe, 1971

[11] Wittig, S.L.K.; Elbahar, O.M.F. and Noll, B.E.: Temperature Profile Development in Turbulent Mixing of Coolant Jets with a Confined Hot Cross-Flow. ASME Paper No. 83-GT-220 (1983)

[12] Wittig, S.L.K.; Noll, B.E.; Elbahar, O.M.F.; Willibald, U.: Einfluß von Mischluftstrahlen auf die Geschwindigkeits- und Temperaturentwicklung in einer Querströmung. VDI-Bericht Nr. 487, 1983

[13] El Shanawany, M.S.; Lefebvre, A.H.: Airblast Atomization: The Effect of Linear Scale on Mean Drop Size; Journal of Energy, Vol. 4, No. 4, pp. 184-189, 1980

ACKNOWLEDGEMENTS

Thanks are due to Dipl.-Ing. B.E. Noll for his help in performing the calculations and to Dr. J. Coulon for continuous discussions.

DISCUSSION

C.Moses, US

Was the air flow cold or were you allowing for droplet evaporation? We have made measurements in evaporating systems; the techniques are more difficult but it can be done. The distributions with axial distance are significantly changed as the small droplets immediately evaporate and the SMD increases rapidly with distance.

Author's Reply

The experiments were performed under cold-flow conditions. Our studies in this phase were directed towards the droplet production from the nozzle in order to characterize the nozzle. The next step will be measurements under pressure and with evaporation. We are convinced that a shift of the SMD with axial distance will occur. However, the SMD will also be affected by the evaporation of the larger droplets, which is probably more relevant in the latter stages of the evaporation process.

J.Peters, US

(1) Your results on SMD/D_{50} variations refute Simmons' work (SMD/D_{50} = constant). What do you think is the explanation for this?

(2) Was your work showing the difference in size distribution widths for different injectors performed on production injector hardware?

Author's Reply

Numerous measurements in our Institute indicate that the ratio $D_{50}/SMD = 1.2 \div 2.5$. In using the Rosin-Rammler distribution we find for the range of nozzles tested $N = 7.2 \div 3$. We even found an extreme case with $N = 4$. The pressure atomizers were production-type nozzles whereas the airblast atomizers were experimental and prototype designs. Simmons' data may not be in disagreement with our results as long as the nozzles in his study are of similar design. There is no question, though, that even for identical nozzles $D_{50}/SMD \neq$ constant with different flow rates as shown in Figure 4.

AD-P003 139

LIQUID FUEL ATOMIZATION AND MIXING IN A HIGH VELOCITY AIR STREAM

H. Eickhoff — DFVLR, Institut für Antriebstechnik
Linder Höhe, Postfach 90 60 50
D-5000 Köln 90
Germany

D. Granser
W. Krockow — Kraftwerk-Union
Wiesenstraße, Postfach 01 14 20
D-4330 Mülheim/Ruhr
Germany

SUMMARY

With respect to the reduction of emissions in combustion processes it is of recent interest to examine the atomization and mixing performance of different types of injection devices for liquid fuel. The present investigation concentrates on air blast atomizers of the plain jet and prefilming type. Measurements of the initial droplet size distribution and final mixing in a duct are presented and discussed.

INTRODUCTION

Liquid fuel injectors for gas turbine combustion chambers can be separated into three broad categories. These are pressure atomizers, air-assist atomizers, and air-blast atomizers. With respect to the reduction of emissions in combustion processes, for example carbon monoxide, nitrogen oxide, unburnt hydrocarbons and soot, the latter category of airblast atomizers is being used more and more. The best choice of fuel injection for the mixture preparation appears to be an airblast atomizing system, especially for premixed combustion. High velocity atomizing air is the primary factor in producing small droplets while simultaneously providing high initial relative droplet velocities.

A high degree of vaporization and fuel-air mixing is required for premixed combustion in order to reach the desired NOx-goals. It is therefore necessary to examine the basic atomization and mixing processes of the liquid fuel in a high velocity airstream.

There are two types of air-blast atomizers, plain-jet and prefilming ones. The plain-jet atomizers use discrete jets which are injected into a high velocity airstream. The prefilming atomizers produce a thin liquid film which is accelerated by a parallel high velocity air stream to a tip where the atomization process takes place. The characteristics of the two types of air blast atomizers were reviewed in Ref. 1. Further publications like Ref. 2 through 5 examined the droplet size distributions of the two different injection types. For the development of a premixing section the information on droplet sizes is not sufficient. As a high degree of homogeneity is one of the main requirements for this burner part, tests which also show the mixing performance are needed in order to determine whether the one or the other airblast system is more benefitial in connection with the premixing flow duct. It is apparent that there are differences in the dispersion characteristics of both systems. The present study, therefore, is an examination of both aspects, the atomization and the mixing.

2. Atomizer experiments

For the elementary atomizer investigations, a channel of constant restangular cross-section was used, as shown in Fig. 1. It is a blow-down wind tunnel originally designed for model investigations of the unsteady direct diesel injection process under varying engine conditions with respect to pressure and temperature. The height of the channel was reduced to 20 mm for the present study in order to obtain a flow velocity in the test section of 120 m/sec at a pressure of 20 bars. This relatively narrow channel limited the conditions for the plain jet experiments to those where the atomized fuel did not touch the wall. The fuel injection time was kept at 2 seconds in order to avoid a special treatment of the exhausting fuel-air mixture. The droplet size distribution was measured by the familiar laser light-scattering technique. The special system used for this investigation is described in Ref. [6].

In addition to droplet-size measurements, short-time shadowgraphs have been taken using a nanolight as the light source (spark time = 10^{-8} seconds). A schlieren system was used to identify more clearly the local distribution of droplets and the initial mixing process.

2.1 The plain-jet atomizer

The plain-jet atomizer, injecting transverse into the air flow, is located in the test section as can be seen on the shadowgraphs in Fig. 2. The measurements at atmos-

pheric conditions were performed in an open-ended test channel which was of a similar shape as that used for the measurements at elevated pressures. The injector orifices were designed with a length to diameter ratio l/d of about 5. Diesel fuel was used for all the present atomizer investigations, including the prefilmer.

The shadowgraphs in Fig. 2a-d show that with increasing dynamic head of the airflow the atomized jet becomes highly unsteady, indicating a vortical structure (Fig. 2d). Fig. 2b and c are for the same dynamic head of the air flow, but at different ambient air pressures of 5 and 20 bars, respectively. It is apparent that the liquid jets in this case break up and spread very similarly. Separation of droplets due to their different sizes, and contributing to the fuel distribution across the flow duct, occurs only at the lowest aerodynamic forces in this series of shadowgraphs, Fig. 2a. Hussein et al [4,5] determined the time-averaged penetration distance of plain jets of different diameter in a similar arrangement at atmospheric conditions. It becomes clear, however, from the shadowgraphs in Fig. 2, that the unsteady character can be essential for jet penetration.

Droplet sizes were measured at atmospheric conditions for orifices of d_o = 0.5 and 1 mm diameter and different fuel flow rates. Fig. 3 is a plot of the Sauter mean diameter SMD over the dynamic head of the airstream $\Delta p_a = \rho_a u^2_a/2$. The measured droplet sizes depend on the location of the laser beam within the spray. This is due to two reasons. The first concerns the measurement technique, i.e. all droplets have to have the same velocity because only concentrations are measured. The second is that the droplet size distribution can depend on the position across the jet, as it does,for example, for the conditions of Fig. 2a. Therefore, all the measurements have been made 50 mm downstream of the injection point [5] and in the middle of the atomized jet (determined by the observers eye). Of course this can provide only a rough characterisation of the atomization, because at low aerodynamic forces and relatively high fuel injection rates the width of the atomized jet is much larger than the diameter of the laser beam. The dependency of the droplet sizes across the jet is shown in Fig. 3 for $\dot{m}_L$ = 15 l/h, and p_a = 150 mbar at the upper (r_u) and lower (r_l) jet boundaries. The influence of increasing Δp_a on droplet diameter (SMD) can be seen. A significant influence from the fuel flow rate $\dot{m}_L$ and the orifice diameter d_o could not be observed within the relatively narrow variations. All the measurements at higher ambient air pressures (p_a = 5 and 20 bars, T_a = 100°C) are for an orifice diameter of 0.5 mm. These data are shown in Fig. 4. Although there is some scatter in the data, it can be concluded that the droplet sizes depend only on Δp_a, irrespective of the ambient air pressure level. Similar results have been obtained for a plain jet atomizer of a different design [3].

2.2 The prefilming atomizer

The plane prefilming atomizer investigated is shown in Fig. 5. The influence of Δp_a and the fuel flow rate $\dot{m}_L$ at atmospheric conditions is shown in Fig. 6. The droplet diameter (SMD) decreases with decreasing fuel flow rate, because at constant width of the prefilming surface the liquid film thickness decreases. The measurements at elevated pressures, shown in Fig. 7, indicate that the droplet diameters (SMD) at all ambient air pressures investigated depend only on Δp_a.

3. Mixing experiments

The experiments were performed in two different test facilities, one for atmospheric and one for high pressure tests. Both facilities were designed to measure the air-liquid flow distribution and the droplet size. The atmospheric test facility already described in Ref. 7 consists of a blower supplying air via a settling chamber to the model with atmospheric conditions at the exhaust.

The high pressure test facility shown in Fig. 8 consists of a closed pipe system with blower, cooler and liquid separators. A piston compressor together with a control system supplies high pressure air to maintain the system pressure at the desired level. The test section of the high pressure test facility is equipped with several windows for observation. Flanges at various axial and circumferential locations provide for probe traverses to measure the spatial distribution of the air-liquid flow. Water can be fed to either test facility through a pump. In addition it is possible to employ liquids other than water in the high pressure test facility.

The transparent model depicted in Fig. 9 was used in all experiments. It had an outer contour like a venturi tube. The inserted hub was kept in position by 8 struts. With the exception of the prefilmer tests, the struts were inclined to obtain swirl. The plain-jet elements and the prefilmer elements were mounted on the struts (see Fig. 9).

Additional plain-jet elements were fabricated by drilling holes into the hub perpendicular to the surface. Water was injected near the throat section of the model. The air and water temperatures in all experiments were kept near 30°C. The air and water mass-flow rates were measured with a venturi tube and a plate orifice, respectively, and according to DIN 1952. As a first step the velocity profiles were measured without water injection in a plane located 20 mm downstream of the exhaust. Afterwards the local water concentration of the air-water mixture was evaluated by isocinetic probing. The water was collected in a liquid separator, and mass and time were measured.

3.1 Atmospheric tests

In these experiments two plain-jet injection tubes on opposite struts were tested. The jets were injected tangentially ($\beta = 0°$) against the swirl of the air flow.

The idea behind these experiments was that the two jets would not merge and could easily be detected in the exhaust plane. (It should be possible to get a first approximation of the parameters which influence the development of the jet in this rather complex flow).

The test conditions are given below:

injection orifice diameter	d_o	= 0.5, 0.8 mm
air mass-flow	$\dot{m}_a$	= 0.9 kg/sec
water mass-flow	$\dot{m}_w$	= 11 g/sec

In order to analyse the jet and droplet propagation the velocity profiles and the local water concentration levels were measured in the entire plane.

Two typical results are shown in Fig. 10. The area which is covered by water has the shape of a crescent, the size of which increases with increasing injection orifice diameter and injection velocity to air velocity ratio. The jet mixing in this case is probably controlled by individual droplet motion according to Fig. 2a. A prediction of the paths of the droplets yields a distribution in the exhaust plane along a curved line which compares with the centre line of the crescent [8]. There exists a separation effect whereby the smallest and the largest droplets are located on opposite ends, the line extending with increasing injection velocity.

3.2 High pressure tests

The aim of the experiments described below was to test various injector systems with respect to their mixing behaviour. For carrying out experiments the question of appropriate test conditions arises.
According to Fig. 2a-d the jet mixing is governed by either individual droplet motion and/or by the unsteady vortical gas motion. It follows from Figs. 2-4, 6 and 7 that the dynamic air pressure head is an important influence on jet penetration and atomization. The conditions may be characterized in the most general way by the Reynolds number of the liquid and the gas phase, the Weber number, the density ratio, and the injection velocity to air velocity ratio. In addition the geometric similarity has to be considered. Without making any assumptions for the functional dependence of the model numbers, the conditions in the turbine have to be maintained. For simplicity reasons, water was employed in a first step instead of liquid fuel. The density and velocity of the air flow, the ratio of liquid to air mass flow, and the geometrical dimensions were kept constant at the values of the turbine. After optimizing the injector systems it is intended to adapt them to liquid fuels.

Plain-jet injector tests

In the first test series the model was equipped with a plain-jet injector device where the radial position of the injector tubes was kept constant. The first version had two orifices each with a diameter of 1 mm, one jet in the tangential direction ($\beta = 0°$) and the second with an inclination of $\beta = 30°$. The results are shown in Fig. 11. Probe traverses of the axial velocity, the water mass flow, and the calculated water-air ratio are presented.

The influence of the hub on the air flow is still present at the exit plane. The water mass flow, with a maximum at $r/R \sim 0.6$, is declining very rapidly towards the centre and the outer contour. For comparison purposes the standard deviation was calculated. It is quite clear that the mixing performance of this version does not meet the requirements for premixed combustion. Moving upstream or changing the direction (β) of the jets did not give any improvement. Calculations of the individual droplet motion revealed that droplets smaller than 30 µm, starting in different directions, are deposited at nearly the same radius in the exhaust plane. The best mixing in the test series was obtained with one jet in the tangential direction on each tube and 8 jets on the hub perpenticular to the surface. These results are shown in Fig. 12.

Prefilmer tests

Eight prefilmer elements designed for constant water mass flow per unit length were mounted on the struts. This resulted in a water mass flow rate per unit area proportional to 1/r in the injection plane. The mixing section was operated without swirl in this case. To check the circumferential mixing two traverses were made, one behind a strut and one in the middle between two struts. They gave about the same distribution.

The results, depicted in Fig. 13, show little water in the middle of the exhaust plane. In the range $0.3 \leq r/R \leq 0.7$ the water mass flow rate is approximately proportional to 1/r according to the distribution in the injection plane. This means that there is not much mixing in radial direction. The standard deviations for the best plain-jet version and the prefilmer are about the same.

CONCLUSION

The test results revealed the necessity of further refinement in order to get better mixing properties. This can be achieved by modifying the venturi contour to give a more plane radial velocity profile and by improving the fuel distribution in the injection plane. The latter is controllable by the number of plane jet elements, or alternatively by adjusting the prefilmer geometry (e.g. concentric rings) to yield a more uniform rate across the injection plane.

REFERENCES

[1] Lefebvre, A.H., "Airblast Atomization" Progr. Energy Comb. Sci., Vol. 6, 1980, pp 233-261

[2] Jasuja, A.K., "Airblast Atomization of Alternative Liquid Petroleum Fuels under High Pressure Conditions" Transactions of the ASME, Vol 103, 1981, pp 514-518

[3] Jasuja, A.K., "Plain-Jet Airblast Atomization of Alternative Liquid Petroleum Fuels under High Ambient Air Pressure Conditions" ASME-Paper 82-GT-32

[4] Hussein, G.A., Jasuja, A.K. and Fletcher, R.S. "Penetration and Break-up Behaviour of a Discrete Liquid Jet in a Cross Flowing Airstream - A Further Study" ASME-Paper-83-GT-170

[5] Hussein, G.A., Jasuja, A.K. and Fletcher, R.S. "Penetration and Break-up Studies of Discrete Liquid Jets in Cross Flowing Airstreams" ASME-Paper-82-GT-25

[6] Kayser, A. and Pita, G.P.A. "Messungen des Tröpfchenspektrums und der -konzentration und Untersuchung des Einflusses der Gemischaufbereitung auf die Schadstoffbildung in der Primärzone einer Gasturbinenbrennkammer" Die Industriefeuerung, Vulkan Verlag, Essen. Heft 21, 1981, pp 26-39

[7] Krockow, W. and Fiorentino, A.J. "Low Emission Silo Combustor" ASME Paper No 81-GT-46, 1981

[8] Pfost, H. and Mrugalla, J. "Berechnung von Tropfenflugbahnen in Luftströmungen" Interner Bericht der Arbeitsgruppe für Dampf- und Gasturbinen, Ruhruniversität Bochum, DGT 8301

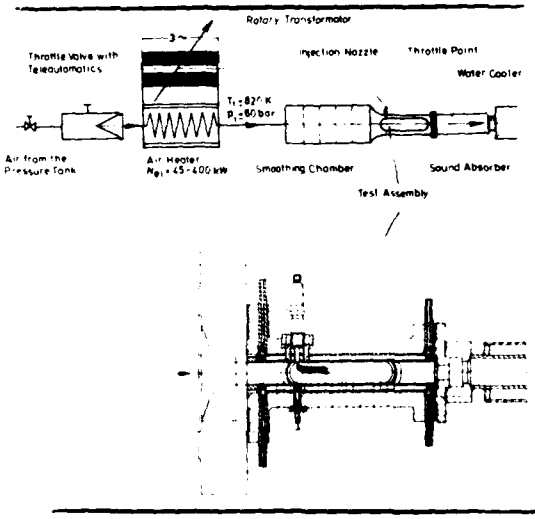


Fig. 1 High pressure test facility for jet penetration and atomization experiments

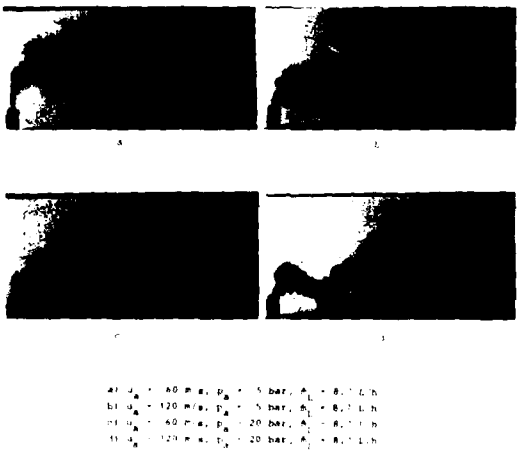


Fig. 2 Short time shadowgraphs ($1{,}8 \cdot 10^{-8}$ sec.)

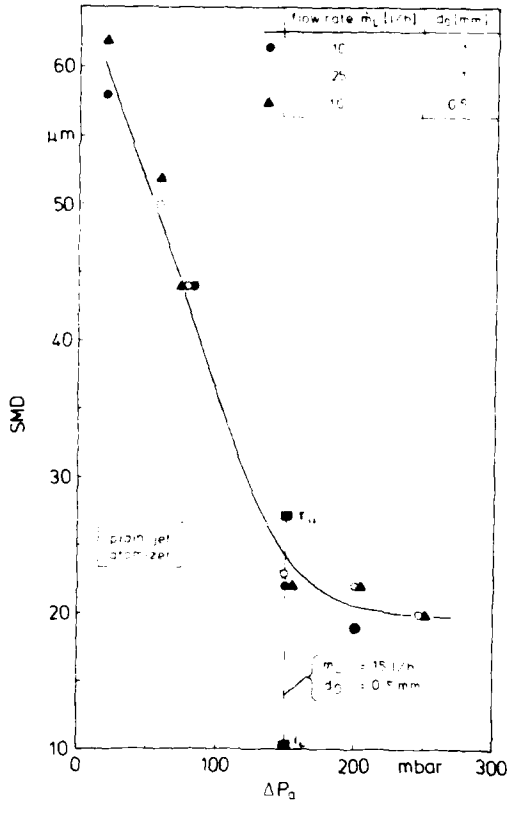


Fig. 3 Atmospheric tests; Sauter mean diameter (SMD) versus dynamic pressure head

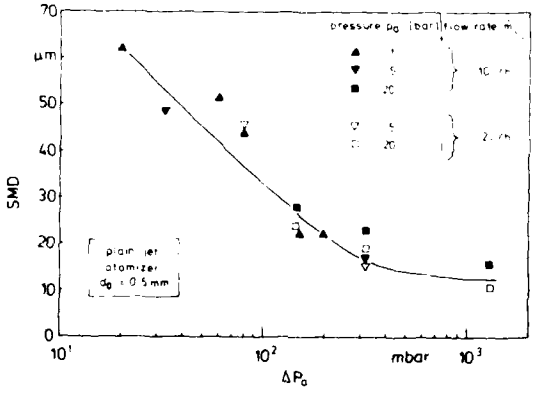


Fig. 4 High pressure tests; Sauter mean diameter (SMD) versus dynamic pressure head

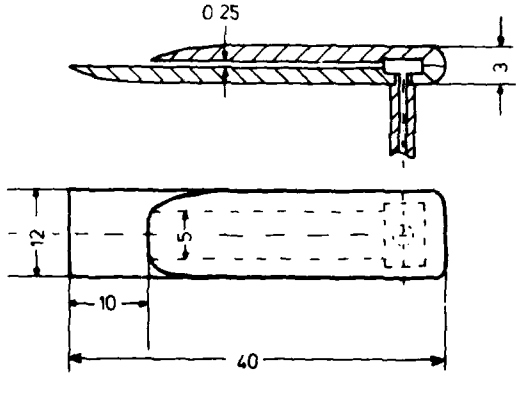


Fig. 5 Prefilming injector element

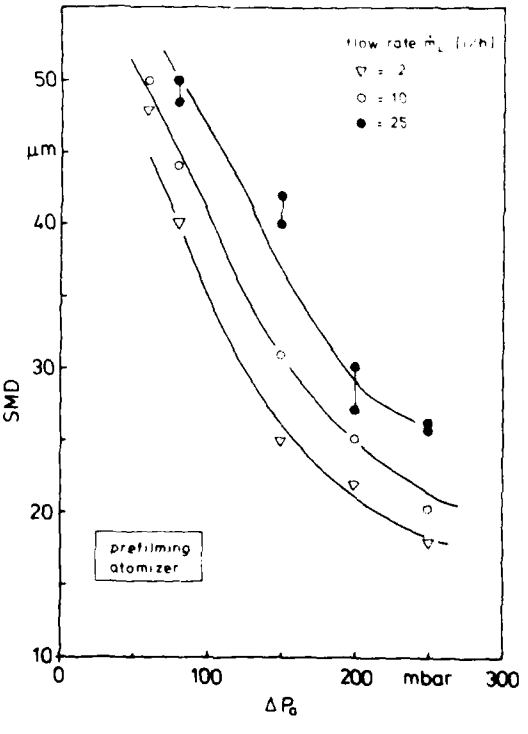


Fig. 6 Atmospheric tests; Sauter mean diameter (SMD) versus dynamic pressure head

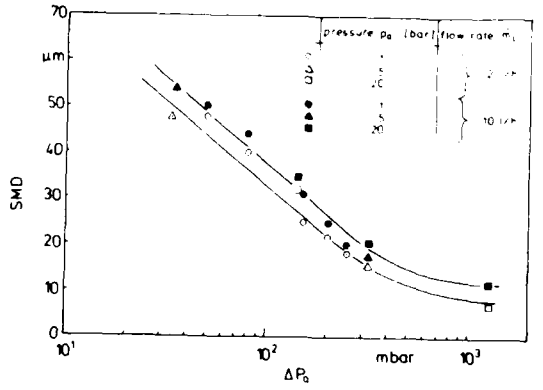


Fig. 7 High pressure tests; Sauter mean diameter (SMD) versus dynamic pressure head

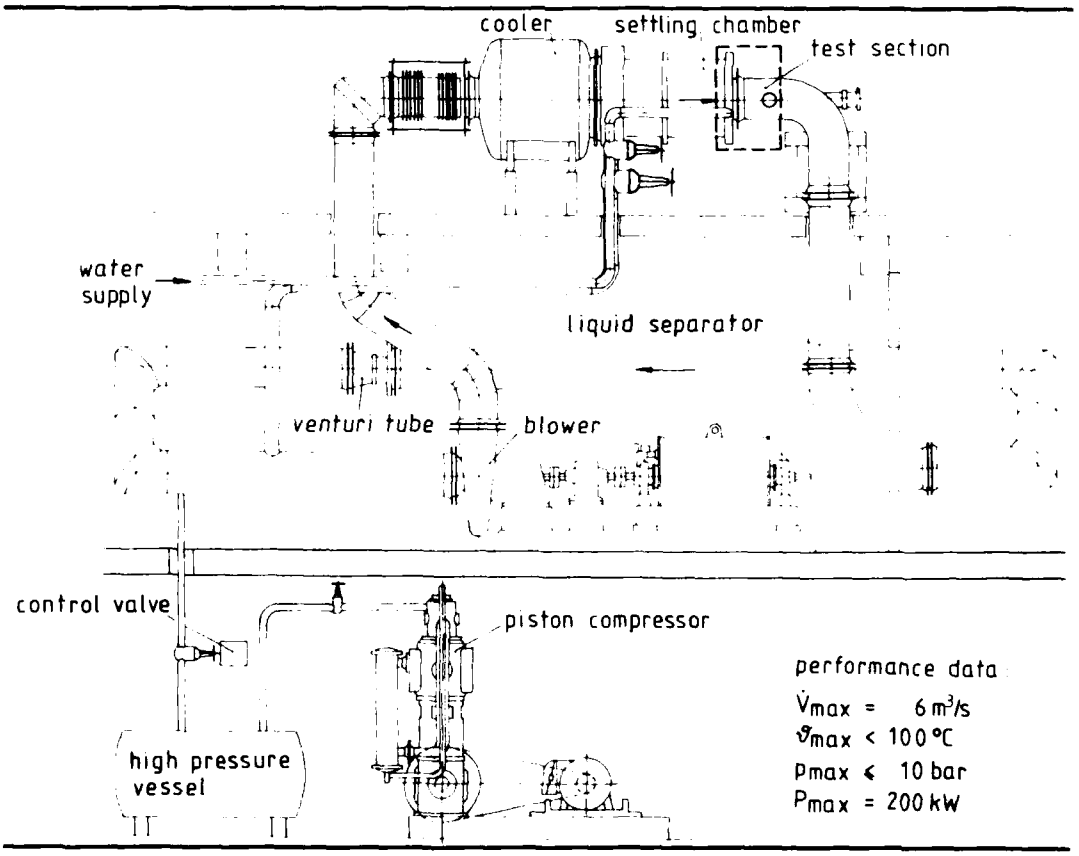


Fig. 8 High pressure test facility for mixing experiments

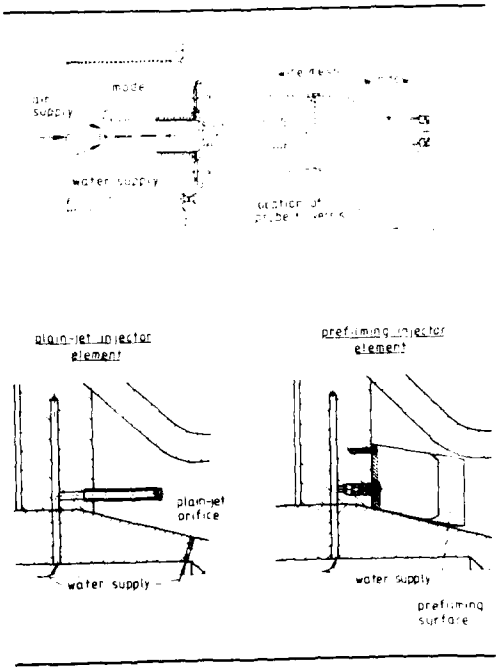


Fig. 9 Test section and injector elements

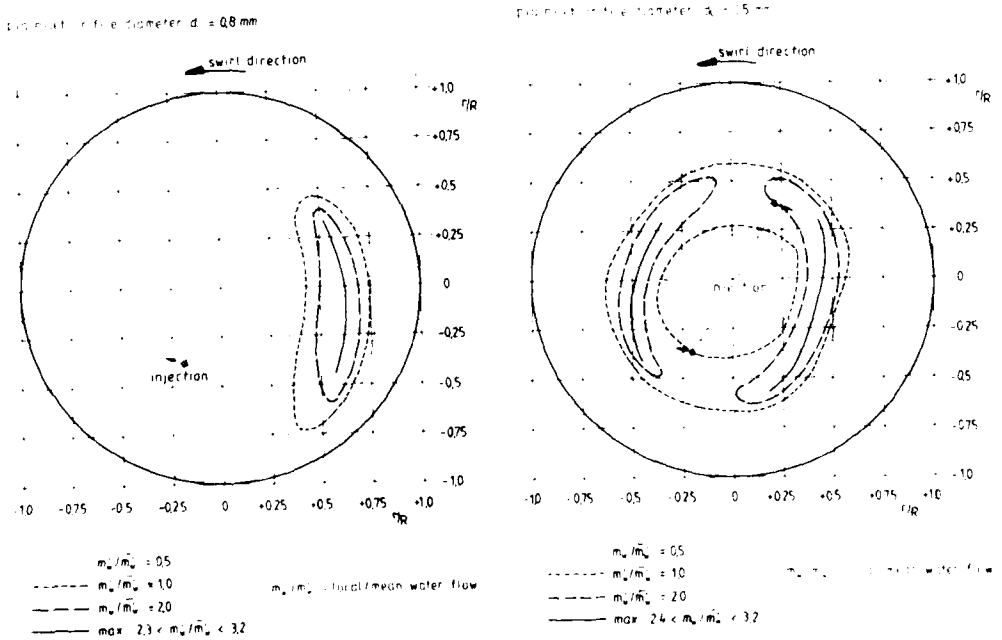


Fig. 10 Atmospheric mixing tests; water mass flow distribution in the exit plane

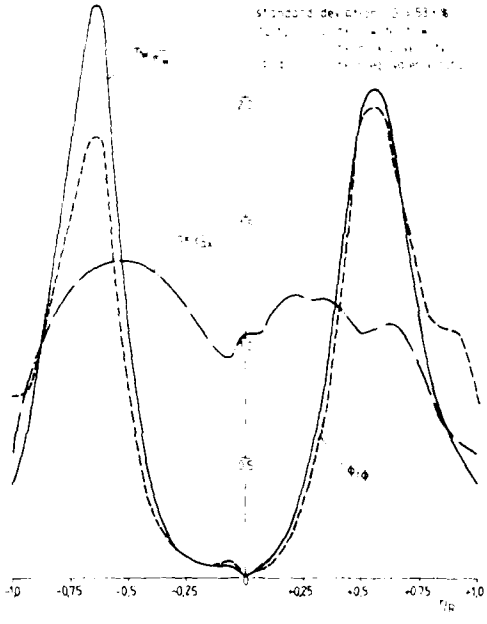


Fig. 11 High pressure mixing tests; 8 plain jet injector elements on the struts

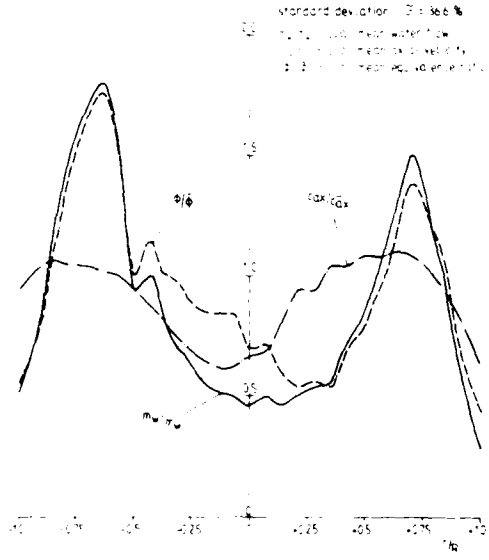


Fig. 12 High pressure mixing tests; 8 plain jet injector elements on the struts und 8 elements on the hub

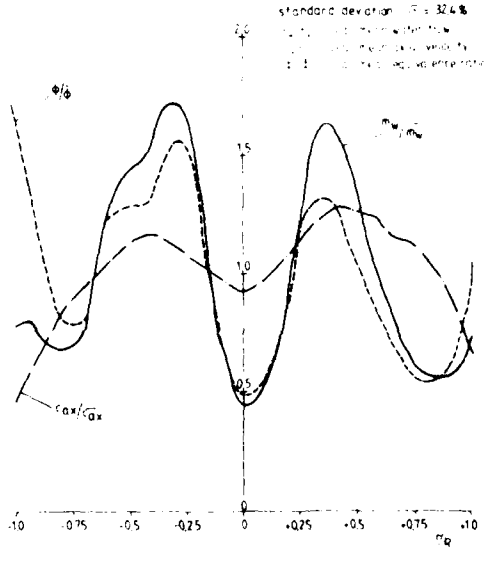


Fig. 13 High pressure tests of prefilming injector elements

DETAILED FUEL SPRAY ANALYSIS TECHNIQUES

Edward J. Mularz
Propulsion Laboratory
AVRADCOM Research and Technology Laboratory
Maria A. Bosque and Frank M. Humenik
National Aeronautics and Space Administration
Lewis Research Center
21000 Brookpark Road
Cleveland, Ohio 44135 U.S.A.

AD-P003 140

ABSTRACT

Detailed fuel spray analyses are a necessary input to the analytical modeling of the complex mixing and combustion processes which occur in advanced combustor systems. It is anticipated that by controlling fuel-air reaction conditions, combustor temperatures can be better controlled, leading to improved combustion system durability. Thus, a research program is underway to demonstrate the capability to measure liquid droplet size, velocity, and number density throughout a fuel spray and to utilize this measurement technique in laboratory benchmark experiments. The research activities from two contracts and one grant are described with results to date. The experiment to characterize fuel sprays is also described. These experiments and data should be useful for application to and validation of turbulent flow modeling to improve the design systems of future advanced technology engines.

INTRODUCTION

The economic pressures that face all of us today are also having a dramatic effect on the aircraft industry, commercial airlines, and the military. In the area of propulsion, the development costs to evolve a new engine for the next generation aircraft are becoming staggering. And in the interest of fuel economy new engines are operating at higher pressures and temperatures which can adversely affect the operating and maintenance costs of the hot section components. This situation is placing greater demands on the engine designer to produce a dependable and reliable system. This is especially true with the combustor, where fuel and air must be efficiently mixed and where combustion must take place in a minimum amount of space. It is perceived that a better understanding of the complex mixing and combustion processes which occur in a combustor could reduce the time required to design and develop new combustor concepts, and could also lead to more optimized designs resulting in improved component durability. It is for these benefits that the National Aeronautics and Space Administration's Lewis Research Center (LeRC) is engaged in combustion research. The objective of the research is to obtain a better understanding of these physical processes and to develop analytical models which can accurately describe these processes.

The current combustion program at LeRC is organized into two categories; combustion fundametals research and applied combustion research. Research activities under the combustion fundamentals category are classifed under the subject areas of fuel sprays, mixing, radiation/chemistry, and combustion dynamics, figure 1. Each of these subject areas have research activities to develop and improve analytical models and to perform experiments to better understand the physical processes and provide needed data for the modelers, references 1, 2. As shown in figure 2, the long range objective is to obtain predictive computer codes which the industry can utilize in their combustion design system. The remainder of this paper will focus on the experimental research activities in the subject area of fuel sprays.

A great deal of research, both experimental and analytical, had addressed itself to the problem of spray combustion. A liquid fuel spray undergoes vaporization and mixing with a turbulent airstream just prior to the combustion process. The relative velocities between the fuel's gas phase and liquid droplets affect the evaporation, burning rate, and the pollutant formation. In attempts to analytically model this two-phase flow, detailed information on the fuel spray and air boundary conditions are required, reference 3 and 4. Furthermore, assessments of the analytical models require detailed information of the fuel spray throughout the spray cone, reference 5. Thus, it is necessary to measure the size and velocity distribution of the spray droplets and the evolution of their distributions with the flow.

Several laser measurement methods can provide the required data in principle, references 6 and 7, and large strides in the area of laser velocimetry and signal processing have been made in recent years to improve these techniques. As part of the combustion research program, LeRC is conducting a program to demonstrate the capability to measure liquid droplet size, velocity, and number density throughout a fuel spray and to utilize this instrument in laboratory benchmark experiments to obtain the required data for the analytical models. This program is described below. In addition, two contracts are underway to further refine droplet sizing interferometer techniques. The Advanced Droplet Sizing System incorporates two similar but distinct techniques to use scattered laser light to determine particle size and velocity. The Phase Detection Droplet Sizing System also uses scattered laser light, but compares the phase differences at two points to determine particle size. These promising systems are highlighted with results to date presented. Finally, it is recognized that applying instruments such as these to reacting and non-reacting fuel sprays presents a formidable task of data processing and analysis. An effort is underway which focuses on further development of these analysis techniques. A co-axial free jet apparatus is being built to study the combustion parameters of a relatively simple liquid fuel spray combustion process. Modern diagnostic instruments will be utilized to establish data analysis procedures and provide experimental data for analytical model assessment. This research activity is described.

NASA LeRC FUEL SPRAY DIAGNOSTICS PROGRAM

The Fuel Spray Diagnostics Program is a part of the LeRC Combustion Fundamentals Research, references 1 and 2. The objective of this in-house program is to conduct de tailed investigations of fuel and air mixing downstream of fuel nozzles in order to su ply the analytical modeler with needed benchmark data for model assessment. Measure- ments of droplet size and velocity at conditions representing those of gas turbines ar required. A knowledge of the turbulent interactions between flowing air streams and simulated fuel sprays is also necessary; thus measurements of air velocity are made simultaneously with the droplet measurements to completely track the flow characteristics.

This experimental research is being conducted in the Fuel Spray Diagnostics Facil- ity. The major instrument used is a Droplet Sizing Interferometer (DSI). A photograp of the existing experimental configuration is presented in figure 3. The DSI is a two color, two-component system. Two independent, orthogonal measurements of droplet size and velocity components can be made simultaneously. The transmitter unit includes a . watt Argon ion laser. Two receivers, situated at different angles, measure the hori- zontal and vertical components. A water spray from a fuel nozzle is probed throughout with the DSI instrument to determine nozzle characteristics. The apparatus will be di cussed in more detail in the follcwing section.

The Fuel Spray Diagnostics Program consists of various experimental configurations presented in Table I. In the first part, water will be used to simulate fuel sprays. Several test conditions and probe volume positions for mapping typical fuel nozzle flo distribution will be selected. The second part will utilize a fuel nozzle/swirler com bination to study fuel/air mixing characteristics and flow seeding. Finally, measure- ments of more complex turbulent fuel spray chemical reaction flows are planned for ana lytical application to the combustion process.

Droplet Sizing Interferometer

The existing NASA LeRC Droplet Sizing Interferometer (DSI) is a laser based instru ment currently being developed for application to dense sprays. The instrument is use for measuring liquid droplets and solid particles in fluid flows. The measurement of droplet (or particle) size and velocity is based upon the observations of light scatte ed by small particles passing through the crossover region of two laser beams. The of axis light scatter detection method is used in the size and velocity measurements; droplets are treated as spheres that reflect or refract light, references 8, 9.

The DSI can operate in most spray and aerosol environments to provide size and vel city measurements to a high degree of accuracy. It is also capable of obtaining large quantities of spray data in a small time. There is an urgent need of such data to pro perly define the physical characteristics of two phase flows essential to many enginee ing applications in combustion systems.

The fundamental features of the instrument are: optics, signal processing, and da management system. The optical system contains two packages that are very critical in the accuracy of the measurements, the transmitter and the receiver. Figure 4 shows th basic configuration of the droplet sizing optical system for single component measure- ments. The transmitting optics define two parameters, the fringe spacing (determined the crossover angle of the laser beam) and the position of the probe volume. It is co posed of a 0.5 watt Argon Ion laser, beam expander, beam splitter and focusing lens. The laser is used to provide a coherent light source to non-intrusively measure small droplet size and velocity. A beam expander consists of two lenses placed focal point focal point where the diameter of the laser beam can be increased as necessary. The beam splitter produces two exit beams of approximately equal intensity and is used to adjust the separation between them. The beams are then intersected by focusing them with a lens. The probe volume or point of intersection of the laser beams forms an in terference pattern of fringes, figure 5(a). Droplets passing through these fringes pr ject scattered light with different patterns that are used in the measurement of size and velocity. The receiving optics collect the light scattered from droplets moving through the probe volume. It contains a collecting lens and a photomultiplier (PMT). The collecting lens is used to image the probe volume on the photomultiplier's apertur or pinhole, where the droplet signals are registered.

The signal processing components are enclosed in a Visibility Processor. It con- sists of Signal Filtering, Percentage of Error Setting, Doppler Integrators, Pedestal Integrators and also controls a programmable power supply that generates the high volt age for the photomultiplier tube. The Visibility Processor is mainly used to process doppler burst signals. The input signals to the processor are doppler signals superim posed on Gaussian pedestals, figure 5(b). The processor separates the doppler compone from the pedestal component. The droplet size is determined from the signal visibilit (that is the magnitude of the ratio between the Doppler and the pedestal components) a the velocity from the Doppler frequency.

The Data Management System (DMS) is a microprocessor that collects, stores and ana lyzes data. It acquires raw data from the Visibility Processor. The DMS contains dat display and acquisition programs with histograms of the visibility and period distribu tions. Floppy disks are used for software and data storage. A printer-plotter is in- cluded to provide hard copy records.

ADVANCED DROPLET SIZING SYSTEM

Two advanced techniques for the measurement of the size and velocity of particles will be incorporated in the original Droplet Sizing Interferometer to eliminate some c

the problems encountered in the real environment situations. This new instrument is the Advanced Droplet Sizing System (ADSS) and the referred techniques are: the Visibility Intensity Technique (V/I) and the Intensity Maximum technique (IMAX).

The Advanced Droplet Sizing System will be designed to be a modular type that includes the two combined measurement techniques. This design concept provides the system with capabilities for future expansions based on results of new developments in the research of light scattered methods. The research is being done under a NASA contract with Spectron Development Laboratories, Inc. and the principal investigator is Dr. Cecil F. Hess.

Limitations of Light Scatter Measuring Methods

Light scatter methods were developed with the intention of obtaining large quantities of significant particle measurements in a reasonable amount of time. Since the concept of visibility for particle sizing was introduced, many studies have been carried out in the development of this technology. However, limitations surface when these methods are applied to real environments.

The main limitation of the visibility technique, where the visibility of a doppler signal is used as a sizing parameter, is its incapability to measure particles in a dense field. In environments like dense sprays and turbulent media, particles appear to be larger due to the presence of multiple particles in the probe volume. Also, the fringe pattern at the probe volume is affected by particles intersecting the laser beams. An inaccurate visibility magnitude can result from various other causes, e.g. loss of fringe contrast due to imperfections in optical components, dependency on where the particle goes through probe volume, misalignment and increase in background noise due to small drops present in probe volume. Some of these limitations can be eliminated after they are recognized, but the most difficult ones are those due to the real environment situations.

The Visibility/Intensity (V/I) Technique

The V/I technique is based on the visibility and intensity of the scattered light signal to obtain the size and velocity of individual droplets. It is known that the relationship between visibility and size is not straight forward in real environments. The V/I technique, reference 10, eliminates some of the errors produced by measuring dense sprays. It uses the intensity of the pedestal of the scattered light in addition to the visibility. The signal from each particle produces both parameters and their cross-correlation can be used to select the right signals.

A correlation between the measured size of the droplet and the amount of scattered light (Mie theory) is used to eliminate signals that indicate the wrong size. This technique is based on the fact that droplets that produce certain visibility must have a given size, and consequently they must scatter light with a given intensity. In this manner, limits are fixed for every measured visibility.

Two of the main problems are solved by this technique. First, droplets with erroneous visibility (due to beam blockage that causes a disturbed probe volume) will scatter light with an intensity lower than the one pertaining to their apparent size. Second, droplets crossing the probe volume at the point of less intensity (the tail of the Gaussian intensity profile) will have the right visibility, but will scatter light with different intensity. The V/I technique sets limits for the probe volume and rejects invalid signals by establishing limits on the intensity of the pedestal, figure 6.

An advantage of the V/I technique is that it does not require calibration. However, it is currently limited to a size range of about 10:1 in low density sprays and about 5:1 in denser sprays for each optical setting.

Intensity/Maximum (IMAX) Technique

The second technique used by the Advanced Droplet Sizing System is the Intensity Maximum technique. This technique uses the peak intensity of the pedestal to estimate the size.

The intensity of the laser beam has a Gaussian distribution, therefore, the intensity of the pedestal depends on where the particle crosses the laser beam in the probe volume. This technique establishes limits within the probe volume where a particle can cross. It eliminates the uncertainty caused by the Gaussian beam intensity distribution and makes use of the direct relationship between intensity and droplet size.

In order to establish the limits within the probe volume, two laser beams of different diameter are crossed as illustrated in figure 7. An interference pattern of fringes is formed in the crossover where the intensity is almost uniform in the big beam. Size and velocity measurements are obtained from the peak intensity of the pedestal of the large beam and the doppler frequency for each signal.

The advantages associated with this method are: size measurements performed in a region of uniform intensity and capability of velocity measurement and size range possibilities up to 30:1 with appropriate electronic processing. One limitation is the beam blockage, caused by dense sprays, that results in a reduction of intensity. However, this limitation is not as serious as in other techniques with a non-uniform intensity distribution at the probe volume.

Measurements with the V/I and IMAX Techniques

Some experiments are underway to evaluate and compare the capabilities of the V/I and IMAX techniques. The up to date results for the experiments that will be presented here are explained in more detailed by Dr. C. F. Hess in reference 10.

The main limitation of the visibility technique, as was previously discussed, is its incapability to measure particles in a dense field. For this reason, experiments focused on the effect of beam blockage on size distribution. Figure 8 shows the effect of obstructing the laser beams with a dense spray before the crossing point. The first histogram (fig. 8(a)) pertains to a monodispersed string of droplets crossing through the middle of the probe volume. The second histogram (fig. 8(b)) presents the measurements obtained with the Visibility technique when a dense spray is placed before the probe volume. The fringe pattern is altered, resulting in a false extended size distribution. The third histogram (fig. 8(c)) corresponds to the V/I technique, under the same circumstances. The size distribution in this case is very similar to the one generated in the absence of spray blockage (fig. 8(a)).

The effect of beam blockage on size distribution was also investigated using the IMAX technique. Results are shown in figure 9. The first histogram (fig. 9(a)) presents the size distribution of monodispersed droplets going through the probe volume. The second histogram (fig. 9(b)) corresponds to the results obtained with the IMAX technique when a spray is obstructing the laser beams in front of the probe volume. This technique also shows very favorable results, with the average diameter nearly the same, even though some corrections were found to be needed. The V/I and IMAX techniques are still being developed and all the measurements taken are in a preliminary stage. A final report will be published with the results of this program.

PHASE DETECTION DROPLET SIZING SYSTEM

Laser light scatter interferometry techniques offer potential for non-intrusive real-time measurements in relatively dense sprays. A schematic of a generic optical system for droplet sizing is shown in figure 4 and is based on laser doppler velocimetry principles. This system features off-axis light scatter detection which was first analyzed theoretically by Bachalo (ref. 8). A schematic of an alternate system based on phase detection of scattered fringe patterns is shown in figure 10. This system is currently undergoing breadboard evaluation by a contractor for NASA LeRC, namely, Aerometics, Inc. The principal investigator is Dr. W. D. Bachalo who has authored several papers on droplet sizing techniques, e.g. references 8 and 9.

The approach utilizes the fact that light deflected by a sphere through the mechanisms described by refraction and reflection theory can be measured and analyzed to obtain the diameter of the sphere passing through the intersection region of two laser beams. Light scattered from one beam will be shifted in phase with respect to the other by an amount that depends upon the angle of observation and the optical paths through the sphere. The scattered light will have an associated phase difference which produces an interference fringe pattern surrounding the spherical droplet (see figure 10 inset). The spacing of the interference fringe pattern at some region in the space surrounding the droplet can be seen to be inversely proportional to the droplet diameter. Proper selection of a means for measuring the fringe spacing will result in a linear relationship between the measured quantity and the droplet size.

Using the proper configuration of two or more detectors will result in two or more identical Doppler burst signals that are shifted in phase (see figure 11). This phase difference which can be measured accurately is linearly proportional to the droplet size.

Furthermore, when a droplet moves through the intersection of the laser beams, light scattered from each beam undergoes a doppler frequency shift. The scattered fringe pattern appears to move at the doppler difference frequency between the scattered light from each beam. Using the known beam intersection angle and the laser wavelength, the measured signal frequency will produce an accurate meaurement of the droplet velocity. Thus, the same period information provides droplet velocity measurements as well as droplet size measurements. Both measurements are unaffected by beam attenuation provided that the signal-to-noise ratio is sufficient.

The relationships used to obtain the droplet size from the measured signal phase difference for the specified optical parameters are shown in figure 11. The significance of the result is that the instrument response is linear over the entire size range. The size range can be set easily by adjusting the beam intersection angle and the gain on the photodetectors.

Recent data samples from measurements of a monodisperse droplet stream produced by a Berglund-Liu generator are shown in figure 12. The size range corresponds to a phase difference range from 0 to 360 degrees divided into 72 bins of 5 degrees each. The data shown in figure 12(a) resulted in a measured mean droplet size of 125.9 μm compared to the calculated monodisperse stream size of 129.5 μm. The data shown in figure 12(b) were obtained while introducing an additional spray in the beam paths around the monodisperse droplet stream. These results are encouraging but further tests are planned to verify the technique with a variety of spray densities and a variety of spray droplet size distributions.

MEASUREMENT OF SPRAY COMBUSTION PARAMETERS

Historically, the precise measurement of spray combustion parameters has been precluded because of the lack of appropriate instrumentation techniques. However, with the recent development of the interferometric systems described above plus other laser-based diagnostics, fruitful experimental research on spray flames now appears possible. As a result LeRC has established a grant with the Gas Dynamics Research Division of the University of Tennessee Space Institute (UTSI) to utilize modern laser diagnostic techniques in making measurements of parameters in a relatively simple steady spray combustion process. The principal investigators for this project are Dr. Carroll Peters and Dr. Michael Farmer who have extensive experience in fluid mechanics and non-intrusive las instrumentation. This three year research effort has two objectives. First, to develop

well established procedures for making measurements in a typical spray combustion environment and for acquiring, processing, displaying and interpreting the voluminous data that are produced by the modern instrumentation systems. Second, to produce accurate experimental information that elucidates the fundamental mechanisms in spray combustion and that can be used to validate and refine analytical models of spray combustion. The techniques developed above, including specialized microcomputer hardware and software, will be applicable to the NASA LeRC Fuel Spray Diagnostics Program described above.

Experimental Apparatus

The experiments will be conducted with the specially designed coaxial free jet apparatus shown schematically in Figure 13. The central droplet-air jet will be the exhaust from a plain-jet atomizer of the type investigated by Lorenzetto and Lefebvre, reference 11. The diameter of the central nozzle will be about 1.3 cm, and the air-liquid massflow ratio will be about five. Therefore, for typical hydrocarbon fuel, the equivalence ratio of the central jet will be about three. For typical fuel properties, the central-jet atomizer will produce a Sauter mean diameter (SMD) of 60-70 μm at a nominal jet air velocity of 100 m/s.

The outer air flow will be varied, from velocities of zero to about 20 m/s. A recirculation zone will form at the blunt base of the center body (about 5 cm in diameter). For the combustion experiments, an igniter will be inserted into the recirculation region, which will be a flameholder for the spray flame.

The axisymmetric freejet apparatus was selected for two reasons. First, the apparatus provides the major features of typical spray combustion processes without the complexity of three-dimensional geometry. Second, the freejet configuration provides optical access to the entire flowfield.

Program Approach

After shakedown and calibration of the freejet apparatus, a series of droplet cloud experiments, without combustion, will be conducted. Measurements of the gas-phase velocity and turbulence field will be made with a two-component laser velocimetry system. Measurement of the droplet cloud parameters produced by the plain-jet atomizer will be made with the UTSI droplet sizing interferometer. Analytical studies of spray cloud dynamics will be carried out to aid in the interpretation of the results and to assess the dynamic interactions between the droplet cloud and the turbulent gaseous medium.

The freejet combustion apparatus will then be operated with an ignited spray of pure hydrocarbon fuel. Gas phase and droplet cloud parameters will be measured as above. Temperature and number density of major gaseous species in the hydrocarbon spray flame will be measured with a laser Raman system. A large number of measurements of the instantaneous properties will be made at each of many spatial stations in the spray flame in order to adequately define the statistical properties of the entire temperature and species field.

To date the coaxial freejet apparatus is being fabricated and the test facility built up. Initial experiments will be conducted in the fall of 1983. The initial and boundary conditions of the combustion experiments will be carefully defined so that the results can be used to evaluate systematically various aspects of the available numerical models of the spray combustion process.

Clearly, there is a need for careful experiments on the interaction between the dynamics of a cloud of droplets and the dynamics of the turbulent gaseous medium within the droplet cloud. Our goal is to produce a well-defined and well-controlled experiment that can be used for validation and refinement of numerical models of the entire spray combustion process.

CONCLUDING REMARKS

The advanced laser light scatter interferometry techniques described in this report show promise of providing improved capabilities for obtaining droplet size measurements and droplet velocity data in dense fuel sprays. Results to date have demonstrated that these techniques can be successfully applied to yield valuable data which are useful in modeling of combustion flow characteristics and dynamics. Fuel spray characterization, turbulence studies, and fuel-air reaction studies are highly important for predicting combustion performance. These research and development efforts are expected to provide a fundamental data base for turbulence model development and for an improved combustor design system.

REFERENCES

1. Combustion Fundamentals Research. NASA CP-2268, 1982.

2. Mularz, E. J.: New Trends in Combustion Research for Gas Turbine Engines. NASA TM 83338, 1983.

3. Gosman, A. D., Ioannides, E.: Aspects of Computer Simulation of Liquid-Fueled Combustors. AIAA Paper No. 81-0323, 1981.

4. Faeth, G. M.: Recent Advanced in Modeling Particle Transport Properties and Dispersion in Turbulent Flow. ASME JSME Thermal Engineering Joint Conference Proceedings. Vol. 2. ASME, 1983. pp. 517-534.

REFERENCES - Continued

5. Anderson, O. L.; Chiappetta, L. M.; Edwards, D. E.; and McVey, J. B.: Analytical Modeling of Operating Characteristics of Premixing-Prevaporizing Fuel-Air Mixing Passages. Vol. 1, Analysis and Results, NASA CR-167990-Vol-1, R82-915362-40-Vol-1, United Technologies Research Center, 1982; Vol. 2, User's Manual, NASA CR-167990-Vol-2, R 82-915362-40-Vol-2, 1982.

6. Laser Instrumentation for the Measurement of Aerosols. University of Tennessee Space Institute Short Course, April 19-23, 1982.

7. Chigier, N.: Group Combustion Models and Laser Diagnostic Methods in Spray: A Review. Combust. Flame , Vol. 51, No. 2, June 1983, pp. 127-129.

8. Bachalo, W. D.; Hess, C. F.; and Hartwell, C. A.: An Instrument for Spray Droplet Size and Velocity Meesurements. J. Eng. Power, Vol. 102, No. 4 Oct. 1980, pp. 798-806.

9. Bachalo, W. D.: Method for Measuring the Size and Velocity of Spheres by Dual-Beam Light-Scatter Interferometry. Appl. Opt., Vol. 19, No. 3, Feb. 1, 1980, pp. 371-381.

10. Hess, C. F.: "A Technique Combining the Visibility of a Doppler Signal with the Peak Intensity of the Pedestal to Measure.the Size and Velocity of Droplets in a Spray," (To be presented at the AIAA 22nd Aerospace Sciences Meeting, January 9-12, 1984 in Reno, Nevada).

11. Lorenzetto, G. E.; and A. H. Lefebvre: Measurements of Drop Size on a Plain-Jet Airblast Atomizer. AIAA J. Vol. 15. No. 7, July 1977, pp. 1006-1010.

TABLE I. - FUEL SPRAY DIAGNOSTICS PROGRAM

Experiment description
• Spray characterization-H_2O -Various nozzle types -Pressure differential effects Size and velocity distribution -Several sampling planes
• Turbulence studies - seeded -Various air swirler configurations -Vane angle effects -Airflow splits
• Fuel-air reaction studies -Various equivalence ratios -Fuel property effects -Measure turbulence intensity

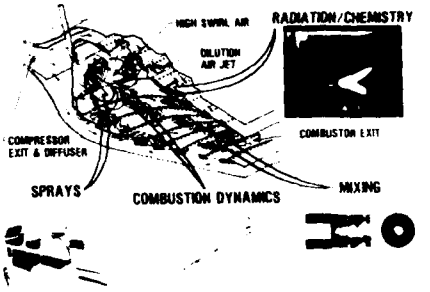


Figure 1. - Combustion fundamentals program at NASA Lewis Research Center is divided into four major subject areas: fuel sprays, mixing, radiation/chemistry, and combustion dynamics.

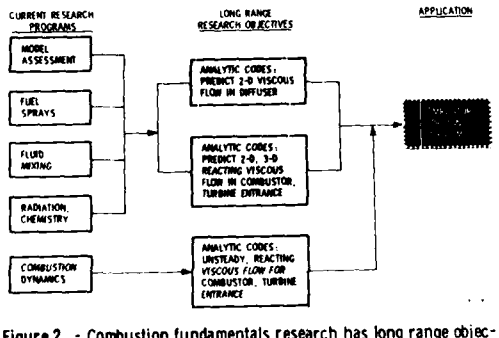


Figure 2. - Combustion fundamentals research has long range objectives to produce predictive analytic computer codes that have practical application in engine manufacturer's combustion design system.

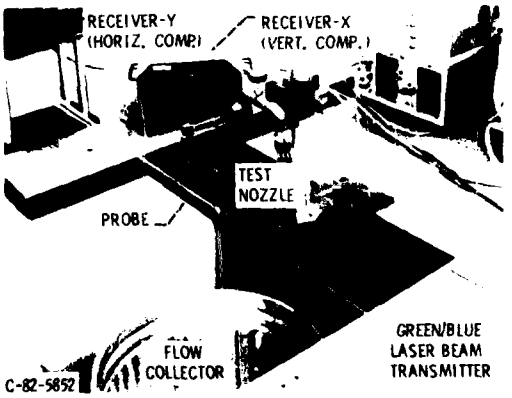


Figure 3. - Photograph of the existing two-component Droplet Sizing Interferometer (NASA LeRC).

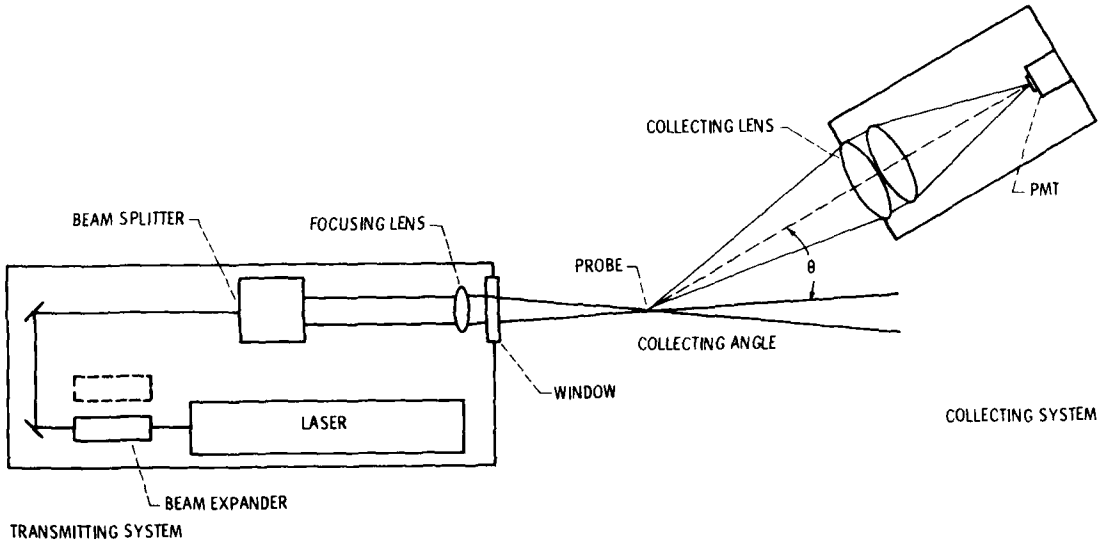
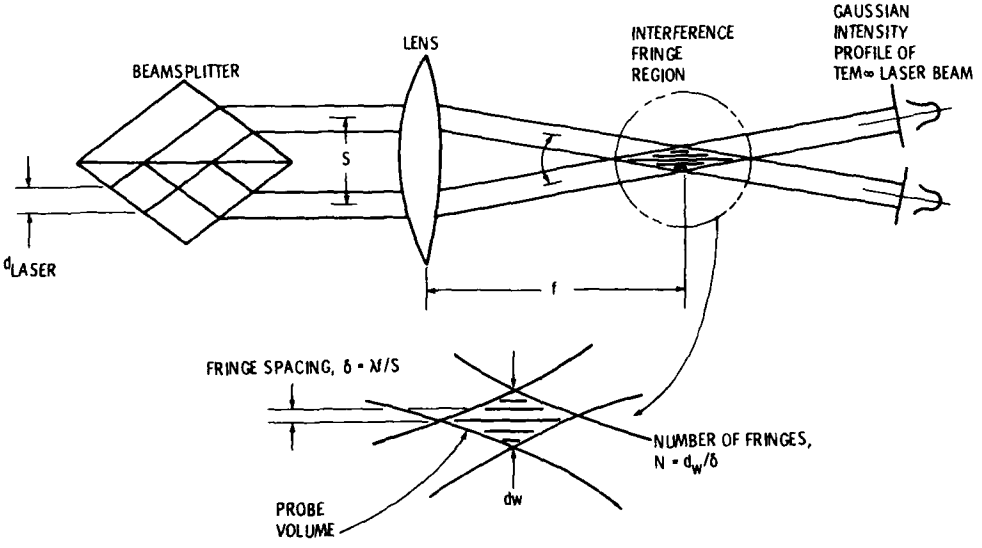
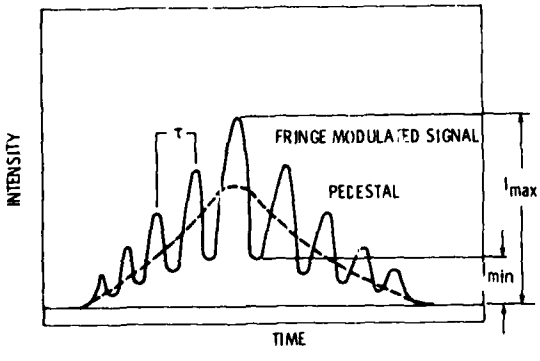


Figure 4. - System diagram of optical configuration for droplet sizing interferometer.



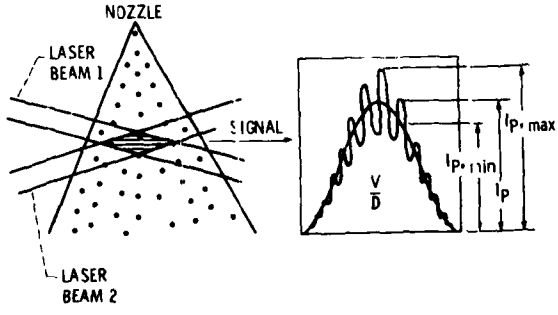
(a) Formation of fringes in the probe volume.

Figure 5. - Droplet sizing interferometer optics and signal processing.



(b) Doppler burst signal with the Doppler and pedestal components.

Figure 5. - Concluded.



(a) Spray going through the fringes produced at the crossing point of two laser beams.

(b) Doppler burst signal with the intensity limits.

Figure 6. - Schematic representation of the visibility/intensity technique.

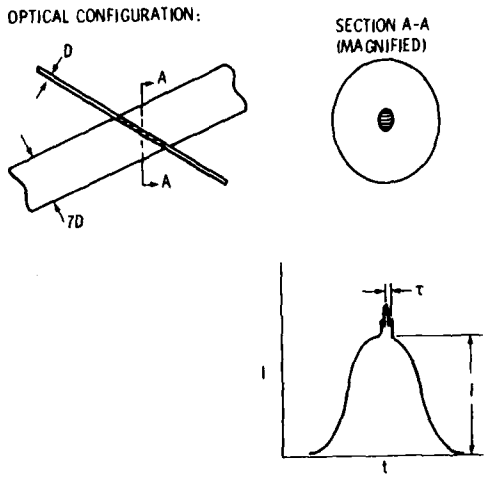
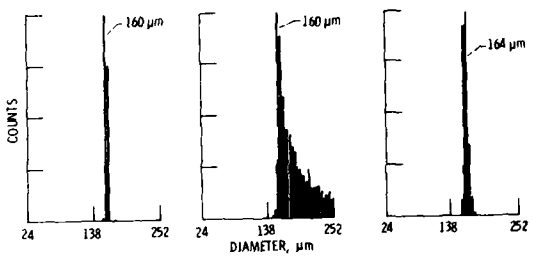


Figure 7. - Optical configuration, probe volume and Doppler burst signal as described by the intensity maximum technique.

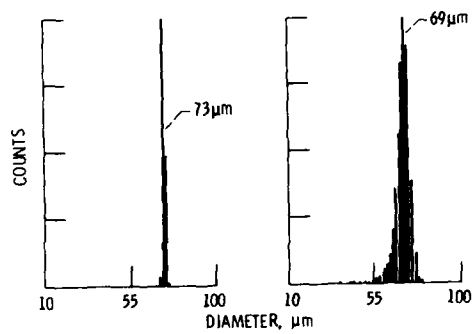


(a) Visibility or v/I measurements of monodispersed droplets with undisturbed laser beams.

(b) Visibility measurements of monodispersed droplets with dense spray blocking the laser beams before crossing.

(c) Visibility/intensity measurements of monodispersed droplets with dense spray blocking the laser beams before crossing.

Figure 8. - Size distribution of a monodispersed string of droplets using the visibility and visibility/intensity techniques.



(a) Intensity/maximum measurements of monodispersed droplets with undisturbed laser beams.

(b) Intensity/maximum measurements of monodispersed droplets with dense spray blocking the laser beams before crossing.

Figure 9. - Size distribution of a monodispersed string of droplets using the intensity/maximum technique.

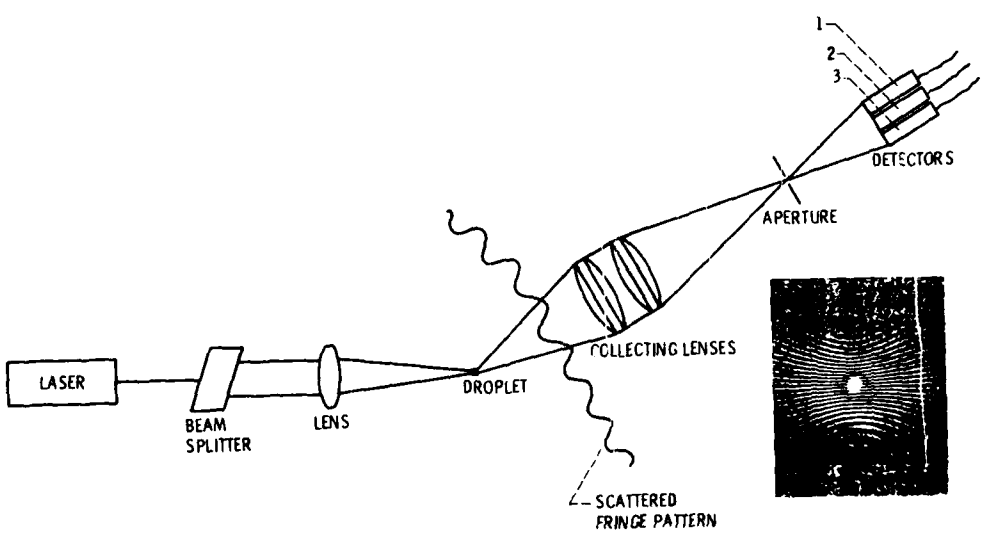


Figure 10. - Schematic representation of phase detection optical system with photograph of scattered interference fringes.

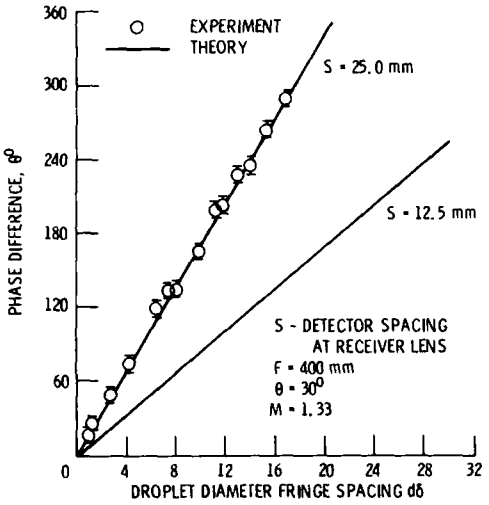
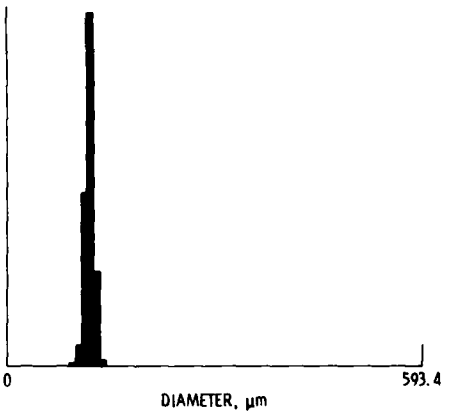


Figure 11. - Relationship of measured phase difference with nondimensional size ratio; experimental data compared to theoretical predictions.



B-L SIZE: 129.5 microns
MEAN SIZE: 125.9 microns
FRINGE SPACING = 26.02 microns
SAMPLES = 500

(a) Sample of data from measurements of a monodispersed droplet stream without beam interference.



B-L SIZE: 129.5 microns
MEAN SIZE: 122.3 microns
FRINGE SPACING = 26.02 microns
SAMPLES = 2092

(b) Sample of data from measurements of a monodispersed droplet stream with additional spray introduced in the beam paths.

Figure 12. - Size distribution of a monodispersed string of droplets using the phase detection technique.

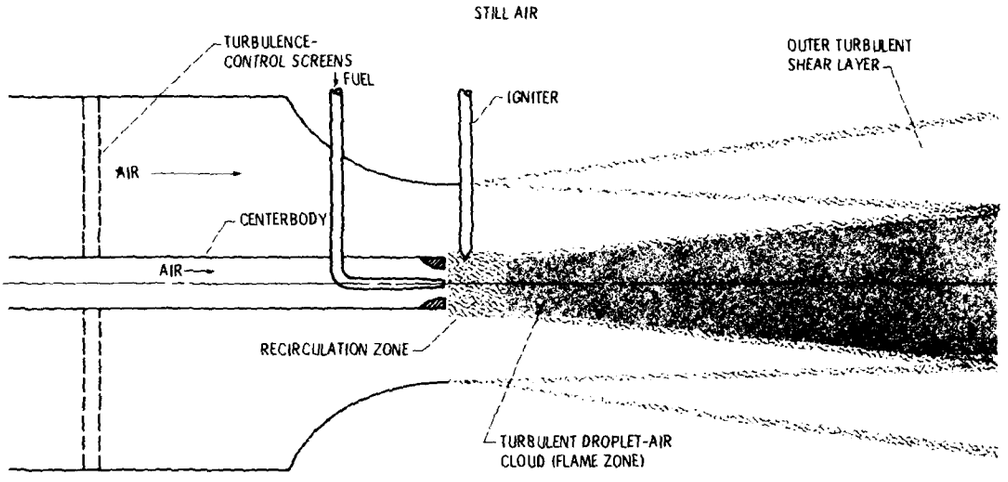


Figure 13. - Schematic of co-axial freejet apparatus which will be used to produce a benchmark spray combustion experiment for application of modern laser diagnostic techniques.

DISCUSSION

H.Low, UK

Have you any experience with the visibility technique in combusting environments?

Author's Reply

We have not done any visibility measurements in a reacting environment to date. Our in-house laboratory program will make measurements in a spray flame after we have acquired the experience and confidence with the techniques in more simple flowfields. Also, the grant with University of Tennessee Space Institute will also look at a reacting free-jet flow, but only after measurements at non-burning conditions.

DROPLET SIZE DISTRIBUTION AND LIQUID VOLUME CONCENTRATION IN A WATER SPRAY: PREDICTIONS AND MEASUREMENTS

Gabriel P. Pita
Instituto Superior Técnico
Dep. Engenharia Mecânica
1096 Lisbon
Portugal

AD-P003 141

SUMMARY

A water spray, from a twin-fluid atomizer, was studied at different air temperature and at atmospheric pressure.

The Sauter Mean Diameter, D_{32}, and the droplet volume distribution were measured at four different distances from the injector.

An optical method was used to measure droplet sizes.

Predictions of the Sauter Mean Diameter, liquid volume concentration and droplet size distribution were also evaluated. The influence of the air velocity, air temperature and of the water flow rate in the spray S.M.D. and in the liquid volume concentration at different distances from the injector have been measured. The predictions showed good agreement with experimental results.

NOMENCLATURE

- A - Droplet surface area
- C_p - Specific heat of droplet liquid
- C_v - Liquid volume concentration
- D_{32} - Spray Sauter Mean Diameter (S.M.D.)
- h - Heat transfer coefficient
- h_{fg} - Latent heat of vaporization
- M - Droplet mass
- P_r - Prandtl number
- R - Droplet radius
- R_e - Droplet Reynolds number, $Re = \frac{\rho u_{rel} D_d}{\mu}$
- T_∞ - Air temperature
- T_d - Droplet temperature
- u_{rel} - Relative velocity of the droplet to the mean stream
- ρ, μ - Gas properties evaluated a film temperature = $(\frac{T_\infty - T_d}{2})$
- ρ_ℓ - Liquid density

1. INTRODUCTION

Knowing the behavior of an evaporating liquid droplet is essential to the understanding and prediction of the performance of the spray.

The behavior of the liquid fuel spray plays an important role in the combustion efficiency and in the production of the pollutants in combustion chambers.

Theoretical studies of evaporating sprays have been carried out by several authors [1,2,3,4,5,9], however their validation with experimental data has not often been attempted, mainly due to the difficulty in getting experimental results.

The present work includes a theoretical analysis of the evolution of a water spray, given an initial measured droplet distribution, characterised by a modified Rink distribution function [8], and a comparison of the predicted values with the measured ones at three different downstream locations along the spray axis. The droplet distribution has been divided into a discrete number of size groups with single droplet equations applied to each one of them. The droplet size measurements were made using an optical technique, based on the diffraction pattern formed when the droplets are illuminated by a parallel beam of monochromatic, coherent light [7,9,11].

2. THEORY

The assumptions used where the following

1: Droplet with spherical symmetry

2: Large distance between droplets
3: Physical properties varying with temperature
4: Constant pressure
5: Uniform droplet temperature
6: No radiation heat transfer

2.1 Droplet heat balance

The heat balance of a droplet exposed to a hot environment is expressed by the equation:

$$h\,A\,(T_\infty - T_d) = M.C_p.\frac{dTd}{dt} + n_{fg}\frac{dM}{dt} \qquad (1)$$

The convected heat is equal to the increase of internal energy plus the latent heat of vaporization.

In the first period of the droplet life the vaporization rate dM/dt is small compared with the increase in internal energy, so it can be assumed that the convected heat is equal to the increase in internal energy of the droplet. When the droplet temperature reaches the equilibrium vaporization temperature, the temperature remains constant (dTd/dt = 0) and the rate of heat transmission determine the vaporization rate of the droplet. As the air temperature is much greater than the droplet boilling temperature, the equilibrium temperature is the boilling temperature at ambient pressure.

From equation (1), the droplet heating time is given by:

$$t = \ln\left(\frac{T_\infty - T_{do}}{T_\infty - T_{dt}}\right) \cdot \frac{M.C_p}{h.A} \qquad (2)$$

T_{do} - Droplet temperature at the beginning

T_{dt} - Droplet temperature at the instant t

and the evaporation rate is

$$\frac{dR^2}{dt} = -\frac{2K}{C_p \rho_\ell}\ln(1+B) \qquad (3)$$

Where B is Spalding mass transfer number defined as $\frac{C_p(T_\infty - T_d)}{h_{fg}}$

For the evaluation of the heat transmission coefficient h the empirical expression from Ranz and Marshall, which applies a convection correction, was used

$$Nu = \frac{hd}{k} = 2 + 0{,}6\ Re^{1/2}\ Pr^{2/3} \qquad (4)$$

The heat transmission, to the droplet, is a function of the Reynolds number, it increases with the velocity as well as with the droplet diameter, so a drag factor must be evaluated and used to calculate the change of the droplet Reynolds number with time.

2.2 Droplet equation of motion

The droplet motion equation is:

$$\frac{d(Mu)}{dt} = -\rho g\,\frac{u^2}{2}\,.\,\pi R^2.\,C_d + R_s \qquad (5)$$

R_s - source term, includes the gravity forces and others, neglected in this case

C_d - is the drag coefficient, evaluated from the empirical relation proposed by Mellor

$C_d = 28/Re^{0.85} + 0.48.$

To determine the relative velocity between the droplet and the gas the initial conditions must be known. The air velocity can be evaluated because the mass flow and the temperature are measured. The droplet velocity at the beginning is not measured, but the atomizer used in the experiments was a twin-fluid atomizer, described in [8], and the initial droplet velocity was assumed to be 15% of the mean stream velocity. As equation (5) shows, the droplet velocity in the control volume is a function of the droplet diameter, so in the measuring volume the droplet concentration is a function of the distance from the injector. Figure 1 shows the droplet volume distributions in a spray evaluated at four different axial stations. In figure 2 the evolution of the relative droplet velocity, for different droplet diameters, can be seen.

2.3 Diffracted Pattern

With the equations of motion and heat balance it is possible to evaluate the droplet size distribution in the control volume. Knowing this distribution the evaluation of the diffracted light pattern from a coherent light beam crossing the control volume, is made using the Fraunhofer theory [11]. The light diffracted by the smallest droplets (D<20 μm), for which this theory can not be used, is evaluated using the Mie-theory.

3. EXPERIMENTAL SET UP AND MEASUREMENTS

Figure 3 shows the experimental set up. In a rectangular channel (20 x 30 mm) an air stream flows at controlled temperature and velocity. In this flow a water film is injected and atomization occurs by the shearing action of the high velocity air stream against the low velocity liquid film. The length of the channel can be changed to allow the measurement of the droplet distribution and concentration at four different downstream distances, 10, 30, 70, 110 mm. The droplet distribution and concentration is measured with an optical method described in [7].

A parallel monochromatic light beam 10 mm diameter from a 5 mW He.Ne laser system, crosses the spray. Some of the light is diffracted due to the droplets, the diffraction pattern depending on the droplet size. A converging lens focuses the non scattered ligth in the centre of a receiving plane, where a photomultiplier measures the light intensity. Measuring this value with and without spray, enables the evaluation [11] of the liquid volume concentration Cv, based on the transmission law for polydispersed particles.

$$E/E0 = \exp(-3/2K\ Cv\ \ell/D_{32})$$

K - Mean scattering coefficient
ℓ - Spray dimension, crossed by the laser beam (see fig. 3)

Around the focus of the same converging lens a pattern of rings of the diffracted ligth is formed. Nine concentric circular sectors of photomultipliers measure the diffracted ligth intensity.

Ten sample-and-hold units were used to garantee that an instantaneous light profile from the photomultipliers was obtained. The signals were digitized with an A/D converter and the data was stored in paper tape for later processing in a BS 2000 (Siemens) digital computer.

With this system, the diffracted light, which has been shown to be a function of the droplet size distribution, and the transmitted light, which is related to the liquid concentration in the spray, were both measured.

3.2 Measurements

Three sets of measurements have been made, the first one at ambient temperature, one at 200°C and one at 400°C, all at atmospheric pressure.

The influence of the air velocity and water flow rate in the quality of the spray was first studied.

Figure 4 shows that increasing the air velocity, the spray Sauter Mean Diameter decreases, and increasing the water flow rate the Sauter Mean Diameter increases, but only for the smaller air velocities this parameter is important. With air velocity of 120 m/s the change in the water flow from 5 to 20 l/h has no influence in the S.M.D.

These results are in good agreement with the results of Mullinger and Chigier (10).

The air velocity is also important in the liquid volume concentration as figure 5 shows. Increasing the air velocity the liquid volume concentration, measured at the same distance (30 mm) from the injector, decreases. The liquid concentration is proportional to the water flow rate and inversely proportional to the air flow.

Figure 6 shows the influence of the distance in the Sauter Mean Diameter and in the liquid volume concentration for an air velocity of 120 m/s and ambient temperature. The S.M.D. remains constant and the liquid volume concentration decreases. The same can be observed in figures 7 and 8 for two other cases, air velocity 180 and 190 m/s and air temperature 400 and 200 C respectively and water flow rates of 10, 15, 20 l/h. In figure 8 the predicted change in liquid concentration with distance from the injector is also shown (solid lines). The predicted evolution is based on the first measurement of each curve.

The liquid concentration in the control volume changes with axial distance and with the air flow parameters. This is due to the different droplet velocities, the drag force changes with the air velocity and temperature and with the droplet diameter.

As figure 7 shows the droplet diameter does not change with axial distance, no evaporation or coalescense occurs. Predictions of the variation of the droplet diameter with distance from injector, are shown in figure 9, evaluated for case B.

We can see that although case B and C have almost the same velocity the S.M.D. in case C is smaller, this being due to the higher air temperature in case B that causes a worse atomization. For the same reason cases A and B have the same S.M.D. although the air velocities are quite different.

Figure 10 shows the measured and the predicted normalised light profiles for the three different experiments (A, B, C), at 30 mm from the injector.

Table 1
Experimental conditions

Case	A	B	C
Air vel. (m/s)	120	180	190
Air temp. (°C)	20	400	200
D_{32}	45	43	31

Table 1 defines the parameters of experiments A, B, C and the measured Sauter Mean Diameter.

Table 2 contains the measured and predicted values of liquid volume in the control volume.

Table 2
Liquid volume variation in the control volume (%)
Water flow rate 10 l/h

dist. (mm)	A	B	C
10	100	100	100
30	81	66(74)	72(72)
70	67	50(47)	53(54)
110	61	42(44)	44(42)

The experimental results, (in brackets) for a water flow of 10 l/h are in good agreement with the theoretical ones.

Case B is where the deviation from predictions is greater (see fig. 8) due to the higher temperature of the air stream that causes a shear layer of two different mediums to interfere with the light beam.

In some cases, interference of the oscillating shear layer between the hot and cold air was noticed.

3.3 Source of errors

As figure 10 shows, in the first inner ring the light intensity does not agree with the predictions. This is due to the small radius of the inner ring and the presence of some scattered light even during calibration, made without spray.

We have checked the influence of the oscilating interface between the hot and cold air, and it has been noticed that this influence principaly disturbs the first inner ring. It has also been noticed that this influence can be minimised with glass windows in the air channel.

In all the measurements, the first inner ring have not been taken into account.

4. CONCLUSIONS

Measurements of the Sauter Mean Diameter of a water spray from a twin-fluid atomizer have been made, for different air temperatures and velocities, using an optical method.

The influence of the air velocity and temperature and of the water flow rate in the spray S.M.D. and in the liquid volume concentration at different distances from the injector have been studied.

The results agree with the predicted ones and with previous measurements made in similar atomizers (10, 12).

Care must be taken when the light beam passes across regions of varying density, as in the case of heated air streams or flames.

5. REFERENCES

1 - Vicent, M.W., Fuel spray evaporation in gas turbine burners. Ph.d. Thesis, University of Sheffield, 1973.

2 - Chidananda, M.S., Eickhoff, H. and Kayser, A., An Analytical Method to Predict Spray Evaporation. DFVLR Internal Report IB 352/79/5.

3 - Elkotb, M.M., Fuel Atomization for Spray Modelling, Prog. Energy Combust. Sci. 1982, vol.8, p.61.

4 - Law, C.K., Prakash, S. and Sirignano, W.A., Theory of Convective, Transient, Multicomponent Droplet Vaporization, 16th Symposium (Int.) on Combustion, 1976.

5 - Yuen, M.C. and Chen, L.W., Heat Transfer Measurements of Evaporating Liquid Droplets. Int. J. Heat and Mass Transfer, vol. 21, p.537, 1978.

6 - Felton, P.G., Measurement of Particle Droplet Size Distributions by a Laser Diffraction Technique. Partikel Technologie Nurnberg, Partec 2. 1979, W. Germany.

7 - Kayser, A., Zur Optischen Messung der Tropfchengrossenverteilung be der Zerstaubung Von Brennstoff. Chemie Ingenieur Technik 49 (1977), nr. 10 sy 532/77.

8 - Kayser, A. and Pita, G., Messungen des Tropfchenspektrums und der Konzentration und Untersuchungen des einfluss der Gemischaufbereitung auf die Schadstoffbildung in der Primarzone einer Gasturbinenbrennkammer. Haus der Technik Vortragsveroffentlichungen Heft 437 "Verdamptung Von Brennstofftropfen und Brennstoffilmen, Vulkan-Verlag, Essen, July 1981.

9 - Styles, A.C. and Chigier, N.A., Combustion of Air Blast Atomized spray flames. 16th Symposium (Int.) on Combustion, pag.619, 1976.

10 - Mullinger, P.J. and Chigier, N.A., The Design and Performance of Internal Mixing Multijet Twin Fluid Atomizers. J. of Institute of Fuel 251, 1974.

11 - Dobbins, R.A., Crocco, L., Glassman, I. Measurement of Mean Particle Sizes of Sprays from Diffractively Scattered Light. AIAA Journal, vol.1, 1963.

12 - Wigg, L.D., Drop-Size Prediction for Twin-Fluid Atomizers. - J. Inst. Fuel (1964), 37, 500 - 505.

ACKNOWLEDGEMENTS

The author wishes to thank the D.F.V.L.R., Köln, Germany, and specially Prof. G. Winterfeld, Director from the Institut fur Antribsteknic, for allowing this work to be carried out and presented at this Symposium.

The colaboration received from Dr. Eickhoff and Eng. A. Kayser is acknowledged with pleasure.

AGARD provided the financial support throught the Propulsion and Energetics Panel-Program Support to Nations.

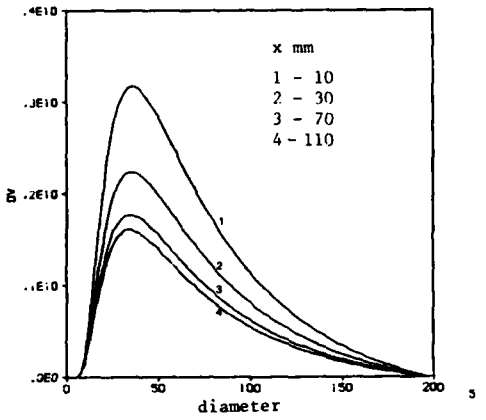


Figure 1. Droplet volume distribution evaluated at four axial stations.

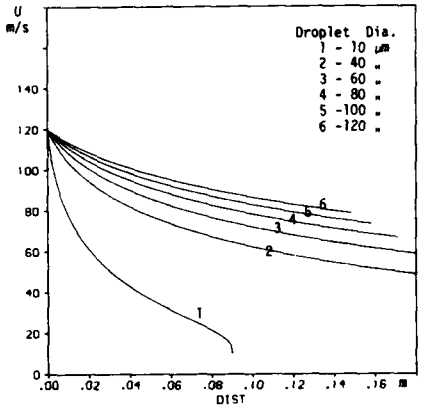


Figure 2. Relative droplet velocity.

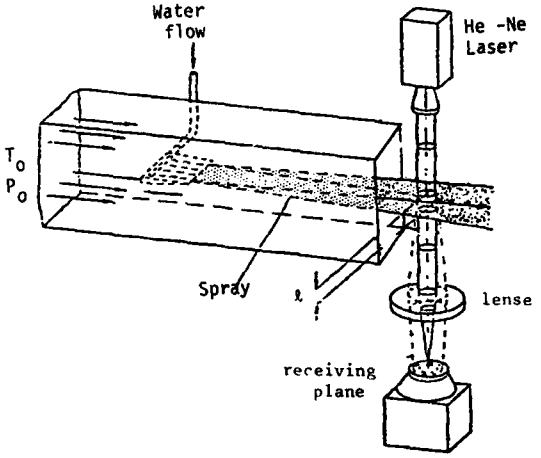


Figure 3. Experimental set up

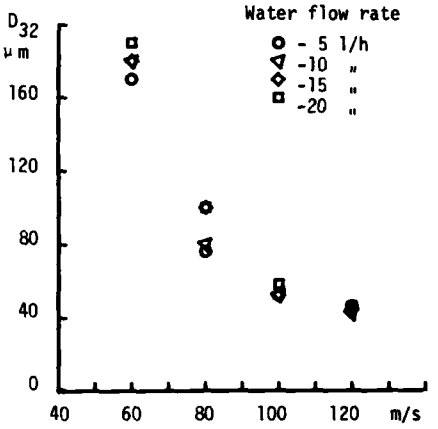


Figure 4. Variation of spray S.M.D. with the air velocity. Axial distance 30 mm.

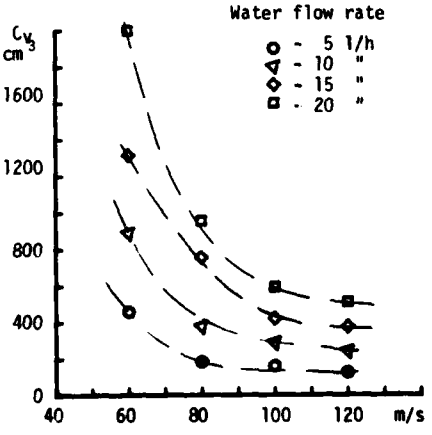


Figure 5. Variation of the liquid volume concentration with the air velocity and with the water flow rate.

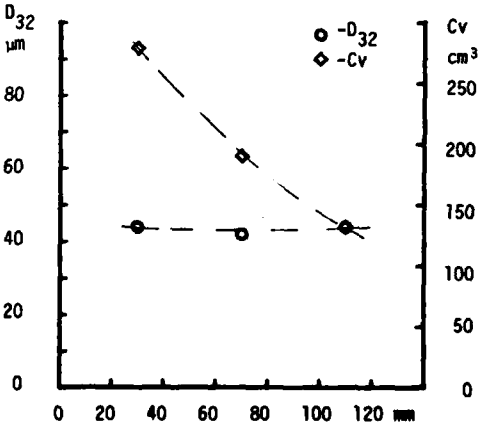


Figure 6. Variation of the S.M.D. and Cv with distance from the injector for case A (air temp. 209C, air vel. 120 m/s)

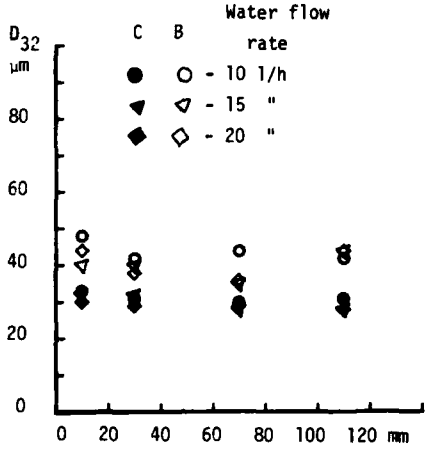


Figure 7. Variation of the S.M.D. with distance from the injector for case B (air temp. 400ºC, air vel. 180 m/s) and case C (air temp. 200ºC, air vel. 190 m/s)

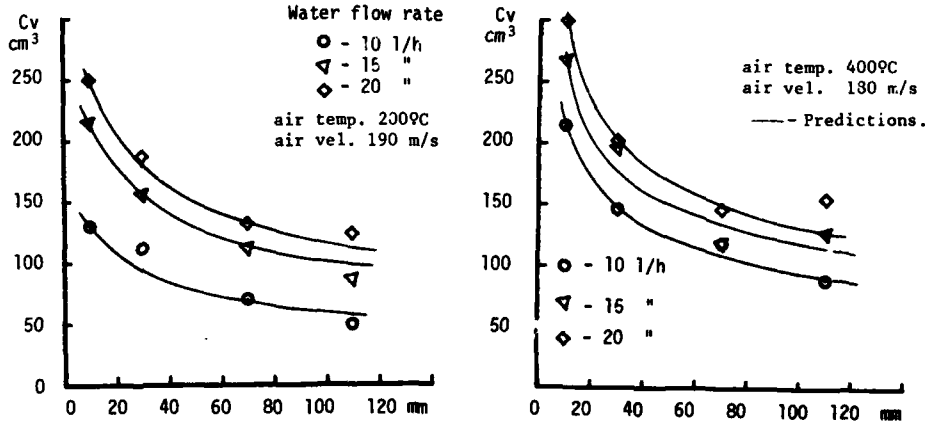


Figure 8. Variation of Cv with distance from injector, experiments C and B

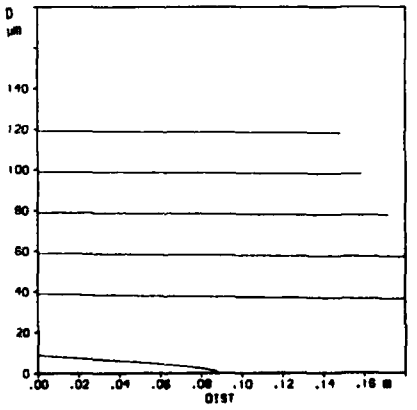


Figure 9. Variation of the droplet diameter with distance (case B).

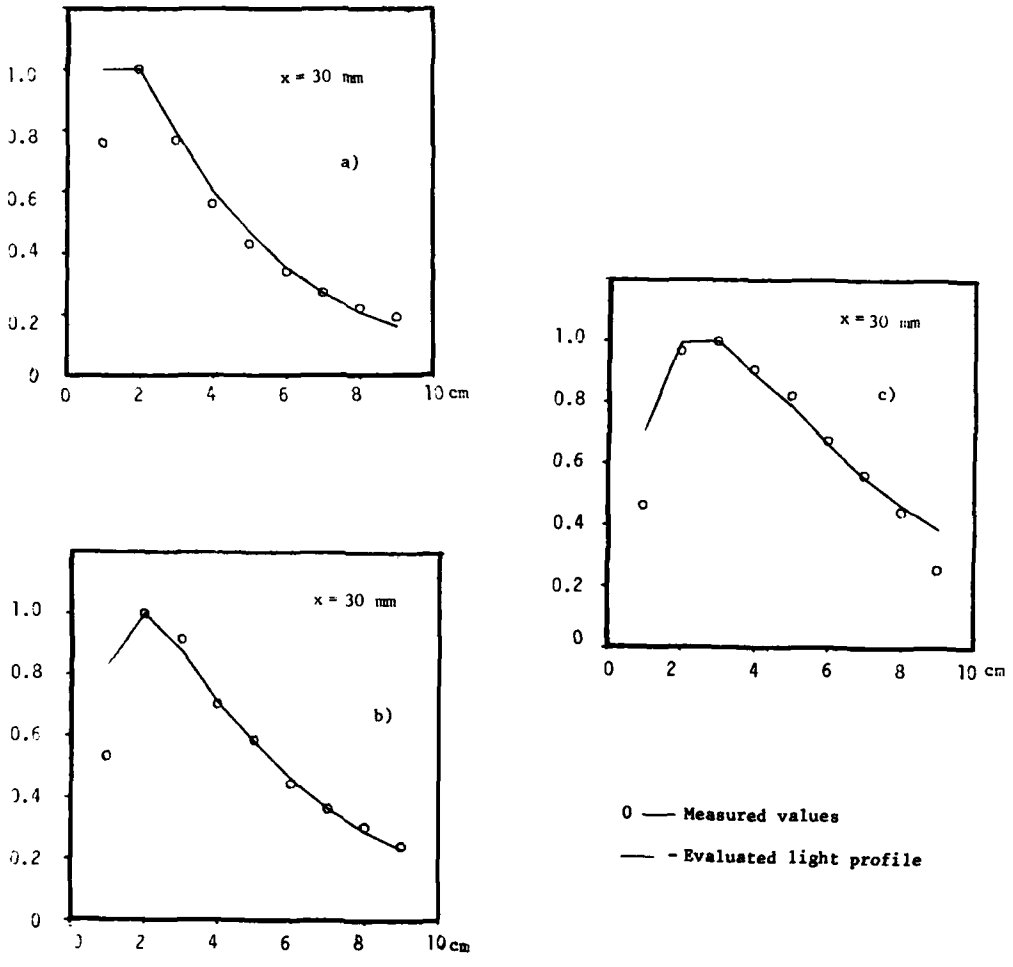


Figure 10. Normalized light profiles

DISCUSSION

P.Ramette, Fr

Vous avez présenté des corrélations en fonction de la vitesse de l'air et du débit du jet. Avez-vous essayé d'exprimer vos résultats en fonction de la vitesse relative du jet par rapport à l'air?

Réponse d'Auteur

Non. Nous avons choisi comme variables celles qui correspondent aux mesures directes.

THE DESIGN AND PERFORMANCE OF A COMBUSTOR WITH A MULTIPLE JET PRIMARY ZONE

by

J. R. Tilston
J. P. D. Hakluyt

Ministry of Defence (PE)
Royal Aircraft Establishment, Pyestock
Farnborough, Hants
GU14 OLS
UK

AD-P003 142

SUMMARY

Using large numbers of orifices in the head of the combustor to generate independent shear layers in a co-operative array, the so-called 'pepperpot' concept was evolved to secure efficient combustion in a weak primary zone. Specific targets were high efficiency and very low smoke at both low and high power levels when burning either kerosine or diesel fuels. Performance tests of a pepperpot demonstrator combustor at representative conditions of idle, intermediate and high power using both fuels are described.

An impressive combustion performance has been realised over the whole power range, together with excellent exit traverse quality and tolerance to fuel type.

1. INTRODUCTION

There has been mounting pressure over recent years to secure substantial improvements in gas turbine combustor performance, for which at least three reasons can be identified.

Firstly, impending civil legislation concerning emission levels require a dramatic improvement in combustion efficiency at idle conditions, from typical levels of 85-95 per cent to at least 99 per cent, together with reduction of smoke and control of oxides of nitrogen. For military applications the reduction of infra-red and visible signatures associated with black smoke emissions and the reduction of blue smoke, ie unburned fuel fumes, under idling conditions is increasingly important.

Secondly, fuel specifications are changing to response to international pressures on oil supplies. Such changes demand that combustors can not only operate on fuels of varying properties but can simultaneously contain emissions at a satisfactory level. The marinisation of aero engines, has generally required further combustor development in order to accommodate the change from kerosine (NATO Code F35) to distillate diesel fuel (F76). In order to minimise development and production costs the combustor should, ideally, have a dual fuel capability with no significant deterioration of performance.

Thirdly, the objectives of lower operating and maintenance costs have been accorded increased priority; as 'hot end' components make a major contribution to maintenance costs, the benefit to life extension of improved temperature traverse has acquired greater significance. Since blade erosion by carbon particles and 'coke' shedding may also be a life-limiting factor, cleaner combustion offers distinct advantages. Additionally, reduction in combustion chamber pressure loss, consistent with blade cooling requirements, leads directly to improvement of specific fuel consumption.

Several years of research addressing these objectives has culminated in the development of a tubo-annular demonstrator (References 1,2,3) which has become known as the pepperpot combustor. To date the combustor development and testing programme has fallen into three distinct phases:

i. Prototype development

Initially the combustor was developed for the most part at atmospheric pressure on an open-ended rig. Extensive use was made of high speed colour cine photography and lithium flame tracing as aids to discover the characteristics of combustion aerodynamics and fuel distribution.

ii. Prototype demonstration

In order to investigate the most important aspects of performance of this prototype combustor, rig tests over a typical range of engine operating conditions using both kerosine and diesel fuels were conducted.

iii. Pre-production combustor

As part of an engine demonstration programme, the prototype combustor was redesigned to an engine-worthy engineering standard and subjected to a comprehensive series of rig tests.

The key aspects of the work and some performance indicators form the subject of this Paper.

2. THE PEPPERPOT COMBUSTOR

The principal objective of the pepperpot concept is the achievement of a high degree of control over

the process of fuel/air mixing in the primary zone. Early work had clearly demonstrated the very large mixing energy potential available in the turbulent shear layers associated with jets of air entering the primary zone through the combustor head. Fuel placed in the appropriate regions of these jets would not only mix rapidly with this incoming air but would also stabilise and burn efficiently. Furthermore, it appeared that, within limits, the greater the number of such jets, each sustaining its own combustion locally, the more uniform became the combustion process within the primary zone as a whole and the sooner it was completed.

The chief feature of the pepperpot combustor is a cooled, conical, combustor head constructed of 'Transply' (ref 4) in which a large number of primary air entry orifices are cut to provide a well-controlled shear layer structure (see Figure 1). Fuel introduced into these shear zones, by means of a device described as a fuel-air nozzle, is entrained by the air jets in a progressive manner. The pepperpot holes are arranged in rings, indexed with respect to one another so that the holes also lie on slow spiral curves radiating from the centre. This spiral arrangement is intended to assist interception of fuel which would otherwise reach the wall cooling flow and leave the combustor as unburned hydrocarbon. The sizes of the holes increase progressively outwards in order to satisfy area-weighting and recirculation requirements. Measured upstream of the secondary holes, the pepperpot primary zone volume is about half of that of the nearly hemispherical head of the conventional Spey combustor which was used as the basic vehicle on which to test the concepts. The pepperpot head in fact, becomes a direct replacement of the standard head: the existing duple atomiser and turbine entry nozzle are however retained unchanged. The existing flame tube barrel was used unaltered in the prototype and with one minor modification in the final engineering standard design of the combustor.

The pepperpot primary zone is intended to operate at air/fuel ratios much weaker than stoichiometric and with shorter residence times than conventional combustors with the specific aim of smoke reduction coupled with high efficiency at idle power levels. Because of the great number of individual jet systems generated by the pepperpot and the consequential small-scale mixing of fuel and air, a highly uniform temperature profile is achieved upstream of the dilution zone. This has the effect that the combustor exit temperature pattern factor is largely a function of dilution zone aerodynamics and wall cooling performance.

3. PROTOTYPE COMBUSTOR TEST PROGRAMME

The principal objective of the prototype test programme was to establish the combustor performance in terms of combustion efficiency, emissions levels, combustor exit temperature distribution, weak combustion limits and mechanical integrity. These measurements were therefore taken at selected operating conditions of combustor inlet temperature and pressure. This encompassed the full range of marine and low altitude aero engine operating conditions typical of the Spey engine.

The tests were arranged to include direct comparisons of the performance of the combustor burning kerosine and diesel fuels.

Some additional testing was also conducted to examine the consequences of increasing combustor loading and further primary zone weakening by the expedient method of blanking off the dilution air holes, thus increasing primary zone air/fuel ratio by approximately 40 per cent.

The programme was planned to be conducted in two phases:-

i. The first using kerosine fuel only at idle and at simulated high power in order to allow a quick assessment of the potentialities of the combustor.

ii. The second phase, which was conditional upon the success of the first, entailed retesting at idle with both fuels and testing performance at the true pressures and temperatures which correspond to high power operation.

4. FURTHER DETAILS

Idle tests

The combustor was tested at aero idle conditions (7 per cent thrust) over a range of overall combustor air fuel ratios using kerosine fuel. Tests were also made at marine idle conditions at fixed air fuel ratios using both kerosine and diesel fuels.

Simulated high power tests

In these tests the combustor was operated at the correct air inlet temperature and air fuel ratio but at a reduced pressure of 820 kPa. Kerosine fuel only was used for both the simulated aero and marine high power conditions.

Actual high power tests

The combustor was run at marine high power conditions using both fuels. As an addition to the original programme, tests at a condition representing an uprating of the marine engine were also made using diesel fuel.

Finally, tests were conducted at the aero full-power condition using kerosine fuel.

5. TEST RESULTS

Presentation of the results

A summary of salient results for tests relating to the prototype pepperpot combustor is presented in Tables I and II. The first contains performance data obtained at idling conditions, the second gives results of the measurements at the high power conditions.

The following section (6) highlights the main aspects of the results and outlines some of the conclusions which have been drawn so far.

6. COMBUSTION PERFORMANCE

Combustion efficiency

Levels of efficiency at idle loading for both aero and marine conditions were above 99 per cent up to about 110 air fuel ratio, not falling below 98 per cent until 150 air fuel ratio was exceeded. Although measured values were marginally higher for diesel than for kerosine, it is probable that differences found are no more significant than rig-to-rig and run-to-run variations normally to be expected.

Figure 2 shows the behaviour of combustion efficiency with change of air fuel ratio at aero idle conditions.

At simulated and true high power for both aero and marine conditions, whether on kerosine or diesel, combustion efficiency exceeded 99.9 per cent.

Smoke

Both SAE (AIAA) and Bacharach smoke measurements were made for the high power tests, however only Bacharach measurements were made at low power. In view of the superior precision of the Bacharach technique at low smoke levels the Bacharach smoke readings have been converted to SAE smoke numbers via a standard correlation graph for each test.

The inferred SAE smoke data so obtained are, in all cases, somewhat higher than the actual SAE measurements. The scatter amongst results is however significantly reduced.

Using both kerosine and diesel fuels, measured levels at all operating conditions were exceptionally low (Tables I and II): at idling conditions, recorded values were too low to be determined satisfactorily.

Oxides of nitrogen

NO_x emissions results are displayed in Figure 3 in comparison with the mean correlation curve of Reference 5 for engine measurements. The data obtained at 825 kPa have been corrected by the ratio $(P_{true}/P_{simul})^{0.5}$. It is evident that there was considerable scatter of results which was not reduced significantly by humidity corrections. Within the limits of scatter it appears that the weaker primary zone tests, achieved by the blanking of the dilution holes showed useful reductions of NO_x whereas the standard combustor performance was comparable with that of conventional combustors. Additional data from tests on a preproduction combustor (see section 7), all at correct pressures, is also shown in Figure 3.

Temperature traverse quality

Although the pepperpot combustor consists of a new combustor head fitted to an existing standard flame tube barrel all results show substantial improvements in traverse quality arising from the use of the new primary zone.

Simulated and true marine high power tests gave almost identical pattern factors of 25.1 and 24.1 per cent OTDF[7], 9.3 and 8.3 per cent RTDF[7] respectively where these tests also include a change of fuel type. The uprated marine test gave 17.5 per cent OTDF and 10.1 per cent RTDF. Simulated aero and true aero high power gave pattern factors of 20.7 and 15.7 per cent OTDF, 8.4 and 10.9 per cent RTDF respectively.

Reduced data are given in Tables I and II.

Mechanical integrity

The main objectives of this work were essentially aimed at demonstrating the advantages of small-scale primary zone mixing. The relatively simple engineering modifications which were made to incorporate the pepperpot head into a standard combustor were not, therefore, intended as a definitive design change. In spite of this the mechanical integrity of the combustor suffered little from the substantial departure in primary zone aero/thermodynamic behaviour.

At the high power conditions the combustor head itself attained temperatures which are considered to be marginally high for long life. However the first and, to a lesser extent, the second rings of the combustor barrel reached excessive temperatures, in well-defined areas, and showed signs of thermal distress at the conclusion of the programme. The inner rims of the secondary air chutes also showed evident signs of thermal damage. (Subsequent development testing however has shown the route to control these

---

[7] OTDF is given by $(T_{max,\ exit} - T_{average,\ exit})/(T_{average,\ exit} - T_{average,\ inlet}) \times 100$.
RTDF is given by (average, circumferential $T_{max,\ exit} - T_{average,\ exit}$)/
$(T_{average,\ exit} - T_{average\ inlet}) \times 100$.

high metal temperatures. This is outlined in section 7 dealing with the further development of the prototype.)

No significant signs of accumulating carbon deposit were found at any condition. However, there was some slight staining of the fuelling tube and several small stains on the pepperpot surface.

Influence of fuel type

Tests were performed at marine idle and true high power to compare directly performance obtained on kerosine and diesel. Tables I and II show that there was no significant difference of performance between them. The limited scatter of results is no greater than might be expected to be generated by rig-to-rig and run-to-run variations. There was no detectable effect of fuel type on liner temperature.

Effects of closing the dilution holes

The results of these tests, which are not tabulated, are as follows:

Blanking off the dilution jets eliminated the downstream mixing mechanisms entirely and simultaneously weakened the primary zone by 40 per cent to 50 per cent thereby increasing its air loading in proportion. At 825 kPa, this modification improved combustion efficiency whilst reducing the NO_x emissions levels significantly for simulated aero high power conditions, but incurred a marked (3 per cent to 4 per cent) fall-off in efficiency at idle air loading level.

At the simulated high power condition, there was a considerable deterioration of temperature traverse quality, with increase in OTDF from 21 per cent to 53 per cent and in RTDF from 8.4 per cent to 27.5 per cent. This retrogression can be attributed for the most part to persistence, as far as the plane of measurement, of wall cooling (about 40 per cent of total airflow) surrounding the hot central flow.

Combustor metal temperatures were significantly lower for this version of pepperpot compared with the standard model.

Whilst noting potential gains to be achieved by re-scheduling wall cooling and dilution flows, which would be essential in order to counter the adverse effects on efficiency and traverse quality, it was decided to select only the standard combustor with the normal dilution system for further testing.

7. PRE-PRODUCTION COMBUSTOR EVALUATION

Modifications to prototype combustor

As a pre-requisite to an engine demonstration of pepperpot combustors in a Marine Spey engine, to be conducted by Rolls-Royce, it was considered to be essential that the local overheating problems be solved along with various mechanical improvements and an improved ignition system be developed.

Considerations of the overheating patterns adjacent to the secondary air chutes suggested the existence of horseshoe vortices generated by the interaction of high velocity wall cooling air with the chutes. Indeed subsequent water analogy simulation demonstrated dynamics compatible with this theory. These vortices, attached to the secondary air chutes and lying along the combustor wall, offer both stable aerodynamics for flame stabilisation and regimes of enhanced heat transfer. This evaluation was supported by test results in which it was found that the overheating was in fact reduced by a local reduction of wall cooling flow in line with the secondary air chutes and also by the removal of the chutes themselves. It appeared that the influence of the chutes was dominant and, since they were subject to overheating and since their removal produced no detectable change in performance, the local wall cooling was restored and the chutes deleted. After these modifications re-testing has demonstrated that combustor metal temperatures, including those of the pepperpot head, are acceptable.

Ignition

Under MOD contract Lucas Aerospace have developed a combined spray/igniter torch. This unit has secured an excellent combustor ignition loop (Figure 4) distributed around the weakest practicable engine fuel air ratio characteristic. The torch/igniter is required in two of the ten combustors that make up an engine set.

Combustion weak limit

The actual weak limit air fuel ratio of the combustor has not been measured on a routine basis. However tests have demonstrated stable idling combustion at air/fuel ratios in excess of 200/1 at which conditions combustion efficiencies in the region of 96 per cent were still being achieved.

Other Combustion Parameters

Subsequent rig tests of the pre-production standard of pepperpot combustor have demonstrated that the performance of the prototype as described has been maintained in all respects and that wall temperatures are now acceptable.

8. CONCLUSIONS

i. The work, so far, has shown that the new pepperpot concept, in which fuel and air mixing is achieved at a much finer scale than in conventional combustors, offers substantial all-round improvements in combustion performance.

ii. The combustor has shown a remarkable tolerance to fuel type in the range of kerosine to, the more difficult to burn, distillate diesel fuel and no noticeable change in the measured performance parameters has been recorded throughout the development programme.

iii. Whilst showing substantial improvements in smoke and efficiency the combustor in its present form does not offer any significant reductions in NO_x, however tests have shown a line of research which might fruitfully be pursued. Such an approach would however require a radical rebalance of primary, dilution and cooling flows within the combustor.

iv. In a programme of work designed to transform the prototype combustor to a unit whose engineering standard is matched to the requirements for engine testing no major difficulties have been encountered: experience so far leads to an impression that, in relation to conventional, large scale recirculation systems, the concept is fundamentally less sensitive to small engineering modifications which are so much a part of combustion development programmes.

9. REFERENCES

1. Hakluytt J P D and Tilston J R, Patent Specification No 1575641, February 1977

2. Hakluytt J P D and Tilston J R, Patent Specification No 1532636, October 1975

3. Hakluytt J P D and Tilston J R, 'On the Prospects for close control of combustion by shear layer mechanics'. Paper No C87/83. International Conference on Combustion in Engineering, Oxford, April 1983.

4. Wassell A B and Bhangu J K, 'The development and application of improved combustor wall cooling techniques; ASME Paper No 80-GT-66, March 1980

5. Lipfert F W, 'Correlation of gas turbine emissions data', ASME Paper No 72-GT-60 1972

10. ACKNOWLEDGEMENTS

The authors wish to gratefully acknowledge the invaluable contributions made by Rolls-Royce Ltd and Lucas Aerospace to the work described in this Paper.

This Paper is British Crown Copyright.

TABLE I

		Aero conditions			Marine conditions	
		7% idle			Idle	
Fuel type		Kero	Kero	Kero	Kero	Diesel
Air inlet pressure	kPa	275	275	275	293	293
Air inlet temp	K	421	420	421	408	408
Air mass flow	kg/s	0.88	0.89	0.89	1.06	1.06
Air/fuel ratio		60.1	80.3	120.3	97.1	96.9
Combustion efficiency	%	99.45	99.44	98.44	99.0	99.3
Carbon monoxide	ppm	361	266	423	320	280
	EI	22.6	21.3	50.2	30.4	26.6
Unburnt hydrocarbons	ppm	5	14	21	79	28
	EI	0.2	0.6	0.9	4.3	1.5
Nitrogen oxides	ppm	27	19	11	17	19
	EI	2.7	2.6	2.2	2.7	3.0
SAE smoke number		0.5	0.5	1.1	0.0	1.3
OTDF	%	-	-	-	29.0	-
RTDF	%	-	-	-	11.0	-
Weak extinction afr		-	327	-	-	286

TABLE II

		Aero conditions		Marine conditions			
		Pressure simulated high power	True high power	Pressure simulated high power	High power		Uprated high power
Fuel type		Kero	Kero	Kero	Kero	Diesel	Diesel
Air inlet pressure	kPa	825	2171	829	1762	1765	1971
Air inlet temp	K	785	788	743	705	705	736
Air mass flow	kg/s	1.87	4.9	2.03	4.77	4.77	5.1
Air/fuel ratio		51.6	50.9	63.5	63.0	63.7	54.1
Combustion efficiency	%	99.98	99.9	99.98	99.9	99.9	99.9
Carbon monoxide	ppm	3.8	80	2.40	9.0	14.0	14.0
	EI	0.2	4.0	0.2	0.6	0.9	0.9
Unburnt hydrocarbons	ppm	0	8.0	0	28	14	3.0
	EI	0	0.2	0	1.0	0.5	0.1
Nitrogen oxides	ppm	275	480	168	293	289	349
	EI	23.8	40.3	17.6	29.9	29.8	35.9
SAE smoke number		2.8	11.5	6.3	3.5	4.0	9.0
OTDF	%	20.7	15.7	25.1	-	24.1	17.5
RTDF	%	8.4	10.9	9.3	-	8.3	10.1

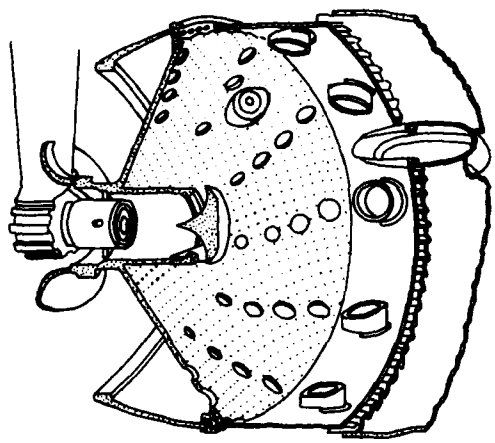


Figure 1 PEPPERPOT COMBUSTOR PRIMARY ZONE

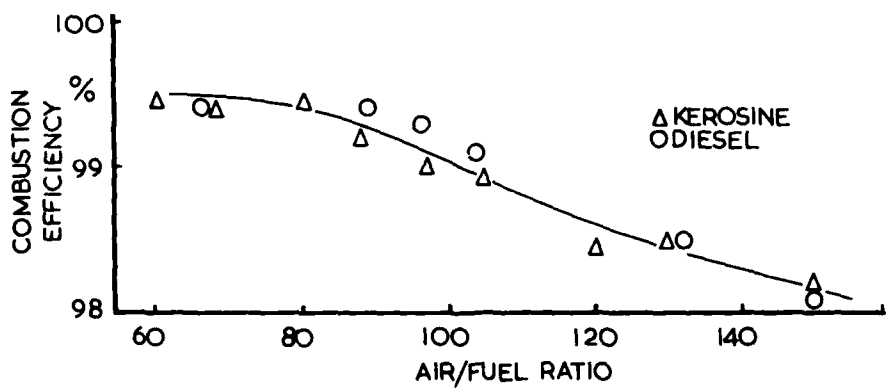


Figure 2 AERO IDLE COMBUSTION EFFICIENCY

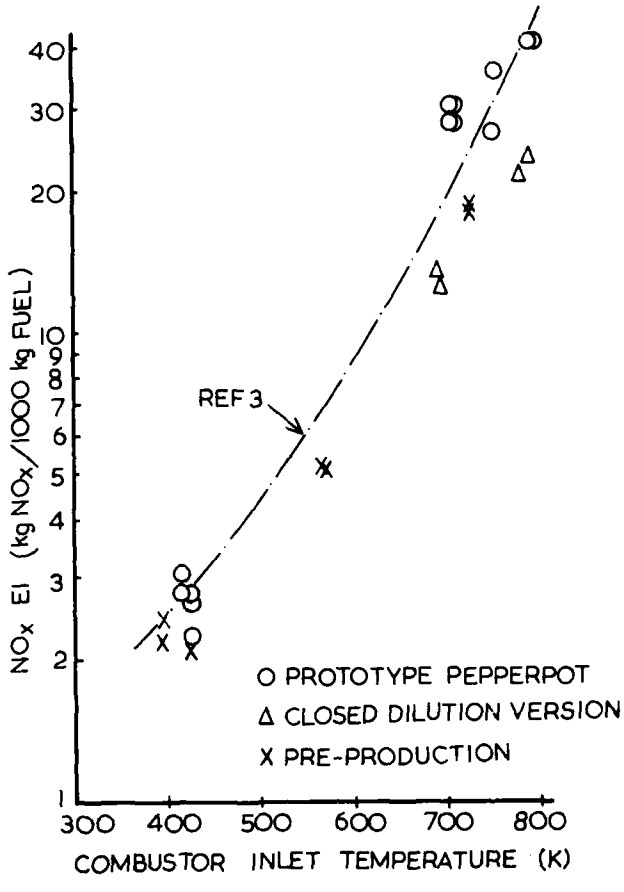


Figure 3 NO_x EMISSIONS

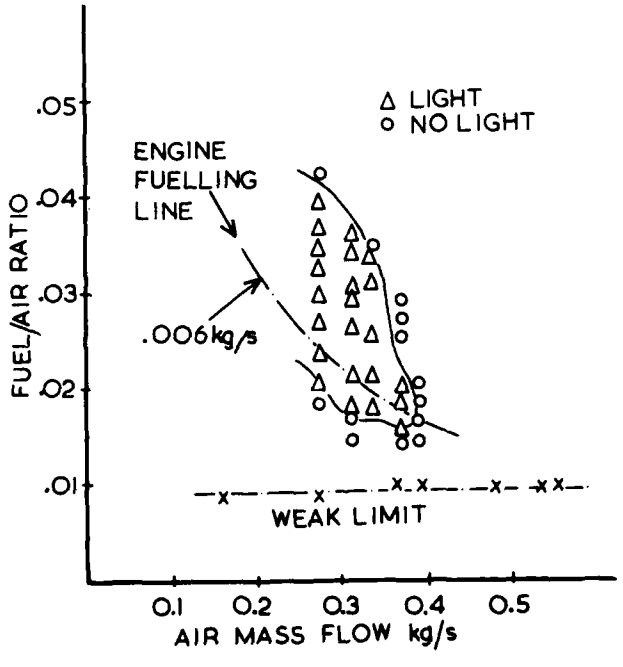


Figure 4 IGNITION LOOP WITH TORCH IGNITER

DISCUSSION

R.Wood

Has this combustor been run on gaseous fuel? If not, do you see any problems?

Author's Reply

This combustor has not been run using gaseous fuels. However, I see no reason why the combustor should not be operated using a gaseous fuel. It is possible that staged injection may be necessary if the combustor is very large.

P.Sampath, Ca

Was there a difference in liner metal temperature between kerosene and diesel (with the new combustor)?

Author's Reply

Within the fairly coarse temperature intervals given by thermal paints there was not. Certainly however the extent, gradients and exact areas of hot spots/cool areas can change somewhat with change of fuel.

P.Ramette, Fr

Pour des conditions d'utilisation maritime, au ralenti avec du kérosène, vous avez obtenu un nombre de fumée de O,O. Ce nombre peut-il vraiment être si faible?

Author's Reply

The measurement technique is having a great deal of trouble for small smoke number. When smoke is very low, the difference for the filter with a clean paper is unreadable.

B.Simon, Ge

I have a question concerning the lean stability limit. In Figure 4 you gave a value of AFR = 100, while in your last table the value is 250.

Author's Reply

The weak limit in Figure 4 relates to combustor operation at atmospheric pressure and with air and fuel temperatures between 10–20°C. The weak limit which we measure for specification purposes is measured at idling conditions, i.e. pressure ratio of approximately 2.7 and air temperature of approximately 410°K.

D.Kretschmer

(1) Did you do any flow visualization?

(2) It seems to me that you broke up the primary zone into a multitude of mini-primary zones. You had very good success with what seems to me a mismatch between fuel-supply and these many burning zones. Have you considered a fuel supply system better fitted to the flow pattern?

Author's Reply

(1) Yes, we had water analogy work done for us by Lucas Aerospace. We also used a lithium flame tracer in the operating combustor.

(2) The mushroom vaporizer has served us well; however I have commented on its deficiencies for some purposes such as in the areas of ignition and NO_x production. It is certainly our intention to experiment with air blast atomizers. I would not say that there is a mismatch between the fuel supply and the mode of operation of the combustor. Each jet in the cooperative array entrains a quantity of vaporized fuel proportional to its designed capability and this fuel then burns in the shear layer of the jet. The jet is simultaneously entraining hot burned products from slightly further downstream which provides the recirculation flow necessary to stabilize combustion. This entrainment is again proportional to its designed capacity. The mini-primary zones are therefore the jet shear layers themselves.

SOOT FORMATION IN DIFFUSION FLAMES

AD-P003 143

by

J.H. Kent
Department of Mechanical Engineering
University of Sydney
NSW 2006 Australia

and

H.Gg. Wagner
Institut für Physikalische Chemie
Universität Göttingen
Tammannstr. 6, 3400 Göttingen, FRG

SUMMARY

Soot measurements in laminar and turbulent diffusion flames are reviewed. In laminar flames, soot particles have high formation rates near the reaction zone and growth takes place in the fuel rich interior. Optical methods have revealed the regions of these separate processes with good spatial resolution.

Sampling and optical techniques have been applied to turbulent flames to determine parametric influences upon soot formation and burnout rates. Recent experimental evidence indicates that formation rates can be mixing or chemically controlled. Burnout rates are additionally very influenced by temperature. Under simple conditions the smoking propensity of a flame may be determined only by the temperature near the tip.

INTRODUCTION

The objectives of this article is to review the understanding of soot formation and burnout processes in laminar and turbulent diffusion flames. We shall generally concentrate on the more simple and well defined laboratory configurations which have given insight into the separate regions of sooting processes and which seek to determine soot volume, particle sizes and formation and burnout rates. It is not an aim here to discuss soot formation chemical mechanisms or the precursors thereof. More general comprehensive reviews are to be found in (1), (2) and (3).

LAMINAR FLAMES

Laminar flames provide a good means of studying the structure of diffusion flames without the complications of turbulence. From the practical viewpoint the aim is to fully understand the detailed sooting regions and rates and then introduce this knowledge into models for turbulent flame combustion.

Early work on the structure of sooting diffusion flames was carried out by Wolfhard and Parker (4,5) who identified the sooting zone on the fuel side of the reaction zone some millimetres from the region of maximum temperature in a sandwich burner. More detailed sampling measurements of soot in axisymmetric flames were made by Spengler and Kern (6) and Tesner et al. (7). Spengler and Kern measured soot flow rate profiles (g/min) in a hexane diffusion flame. Tesner found for C_2H_2-H_2 flames that the particle formation rate had a peak of about 10^{15} particles/cm³-s very early (10^{-3} s) in the flame and then decayed rapidly. The measured flow rate of soot (g/min) however continued to increase with height above the burner. A subsequent study by Tesner et al. (8) investigated a number of different hydrocarbon (1-4%) in H_2 mixtures. Their measurements show the increase of soot in the formation region and the subsequent decline further up in the burnout region. The fuel gas temperature was raised and generally showed an increase in formation rates (earlier peak) and earlier burnout. Again peak particle formation rates occurred much earlier than the region of large soot yield. The "activation energy" for the formation rate taken from the temperature dependence was 140 - 180 kcal/mole.

Lee, Thring and Beer (9) measured soot particle oxidation rates by sampling and temperature measurements above a hydrocarbon flame. They obtained an expression for the oxidation rate in terms of oxygen partial pressure and with an activation energy of 39.3 kcal/mole.

Detailed measurements of the soot structure in laminar diffusion flames including profiles of soot volume fraction, particle size and number density have required optical techniques. The fine position resolution, lack of flame disturbance and faster data collection rates have made these methods popular. An early work by Kunugi and Jinno (10) presents contours of soot volume fraction (f_v) and number density (N) for an axisymmetric LPG flame. They used the ratio of vertical to horizontal scattered light intensities to obtain particle sizes of 100 - 200 nm but these were large compared with their sampled size measurements. Kuhn and Tankin (11) used spectral absorptivity to obtain particle sizes of 20 - 30 nm in a propane flame.

Recently a number of investigations (12-20) have appeared which fundamentally all use the same technique on a range of different diffusion flame configurations. Laser light extinction is used to determine soot volume fraction and the ratio between the soot scattered light intensity and extinction coefficient leads to particle size and number density . For an axisymmetric configuration the path extinction measurements first need to be inverted to obtain radial profiles of soot volume fraction.

A fairly consistent picture emerges of the sooting structure, which we will describe from our measurements on a Wolfhard-Parker (sandwich) burner using ethylene fuel and air (14-15). Figure 1 shows the optically derived measurements of soot volume fraction, particle diameter and number density in a nearly two dimensional diffusion flame. Soot volume fraction f_v increases with height above the burner and the peak is located well on the fuel side of the flame. At a given height f_v decreases towards the flame (peak temperature zone) and towards the centreline of the burner. Particle diameter contours (20-120 nm) are very similar showing a general correlation with soot volume fraction as is also found in premixed flames. Number density, however, shows a steep decline of one to two orders of magnitude (general range 10^{16} - 10^{18} m^{-3}) with distance from the flame.

The measurements indicate (13-15) that particles are formed in the high temperature zone near the flame and are transported to the fuel rich interior where real soot mass growth subsequently takes place as the particles are convected upwards. If the flame is overventilated - closes in upon the centreline - then partial or complete burnout of the soot particles will follow as they then pass through the high temperature oxidizing region. Temperature and velocity measurements in our flames (14,15) confirm these views. Figure 2 shows temperature contours and gas flow streamlines obtained from Laser-Doppler measurements. Particles are transported from the flame to the interior by convection and thermophoretic effects will drive them further from the high temperature region. During this period number densities fall rapidly by coagulation, but soot volume fraction does not increase greatly until the interior is reached.

The temperature and velocity measurements allowed soot volume and particle number production rates to be deduced from the conservation equations and a realistic coagulation rate model. Figure 2 shows how particle production rates increase towards the flame whereas soot volume production rates are highest closer to the centreline. The peak number production rates here correspond with the sampled peak rates of 10^{21} $m^{-3}s^{-1}$ of Tesner et al. (7). Soot volume production rates df_v/dt were generally found to be around (100-300) x 10^{-6} s^{-1} in a temperature region of 1200 - 1400°C and in the lower half of the flame.

We can follow a hypothetical particle along a streamline as it progresses through the flame field as shown in Fig. 3. (This is a longer flame than shown in Figs 1 & 2.) Time is calculated from the reaction zone. The particle begins its trajectory where soot production rate, temperature and number density are high. Soot volume fraction and particle diameter increase rapidly but number density drops because coagulation rates exceed generation rates. As the particle continues up the flame, temperature drops, soot production rate decreases. f_v levels out and diameter increases slowly due to continued coagulation. Measurements at other conditions (16) show that in the burnout region particle diameter decreases with soot volume fraction. The highest values of peak soot volume fraction and particle diameter are found to occur in those flames where the particle trajectory was parallel to the flame zone and particles spent a relatively long time in the high soot production contours. Number densities in the highly sooting regions did not correlate with soot quantity and are therefore propably not a soot production rate determining quantity. In large diffusion flames new particles may possibly be formed along the centreline.

Jagoda et al. (12) measured soot in axisymmetric polystyrene and polypropylene flames. Generally characteristics were similar to ours although their maximum soot volume fractions occur quite low in the flame. Soot particle sizes measured by sampling were about 40 nm at all heights in the smoking polystyrene flame. This compared with the light scattered measurements which gave a range or 50 - 100 nm. The authors concluded that in the lower parts of the flame individual particles are found whereas higher up the optical measurements give an indication of aggregate sizes.

Kennedy et al. (16,17) investigated propane and ethylene stagnation point diffusion flames stabilized around a porous cylinder, through which the fuel is ejected. This is essentially a one dimensional configuration with the flow perpendicular to the flame from the air to the fuel side and with no possibility of air leakage around burner lips. The structure of the sooting zone is again the same as shown in the Wolfhard-Parker burner. An increase in the air velocity reduced f_v and particle diameter but did not significantly affect the number density profiles. An increase in O_2 in the air increased temperature, soot volume fraction and diameter and slightly increase number density.

Santoro et al. (19) investigated the effect of increasing port velocity in an axisymmetric ethylene flame. As the port velocity is increased the flame length increases proportionally and at a certain flow rate the flame begins to smoke - i.e. soot is emitted as a plume. Santoro showed that when the axial co-ordinate is non-dimensionalized by the fuel flow rate (Burke and Schumann (21) scaling) then the axial profiles of soot volume in the formation region are very similar for all flame conditions. Particle size and number density in the formation region are also very close for the smoking and non-smoking flames. In the burnout region large differences become evident with the non-smoking flames showing a rapid decrease in f_v. Particle size and number density also decrease. The soot volume fraction for the smoking flame, however, remains almost constant with increasing height.

The similarity of the normalized soot profiles is to be expected on theoretical reasoning. At any flow rate, particles have the same species concentration-time histories as they pass through the flame. The question is why does burnout cease for the higher flow rate flames? In the case of turbulent flames, to be discussed in the next section, similar behaviour is attributed solely to the temperature in the oxidizing region. This cause is not clear here because the flame size is proportional to flow rate (Roper et al. 22) and so the temperature loss due to radiation is expected to be invariant with flow

rate. In reality the temperature may drop with increasing flow (for example the flame becomes narrower with height and so the surface to volume ratio is increasing). because of the exponential temperature dependence (9), a small difference may significantly reduce the oxidation rate. This in turn means there is more soot left to reduce the temperature further by radiation losses.

Other detailed studies on the effects of changed conditions or differing fuels are scarce. The experimental work of Roper and Smith (20) shows that as air supply is reduced soot formation rates can decrease, the onset of burnout is delayed and burnout rates decrease. The work of Glassman and Yaccarino (23,24) and Schug et al. (25) determine the net effects of temperature, oxygen, inerts and other additives on the smoking propensity of different fuels, but the relative effects upon the formation and burnout fields have yet to be measured.

To conclude this section, a summary of experimentally determined soot quantities in laminar flames is presented in Table 1. This is to provide a perspective rather than a direct comparison since conditions vary quite widely.

Table 1: Soot Particle Measurements in Laminar Diffusion Flames

Author	Flame configuration	Fuel	Method	$f_{v,max} \times 10^6$	$N(m^{-3})$	d(nm)
Lee et al. (9)	axisymmetric	C_3H_8 mix	sampled			◂40
Kunugi and Jinno (10)	axisymmetric	LPG	optical	1	10^{12}-10^{15}	100-200
" "	"	"	sampled			40-50
Kuhn and Tankin (11)	axisymmetric	C_3H_8	optical			20-30
Tesner et al. (7)	axisymmetric	H_2-C_2H_2	sampled		10^{18}	
Roper and Smith (20)	axisymmetric	CH_4	optical	0.4		
" "	"	C_3H_8	optical	2		
Jagoda et al. (12)	axisymmetric	polystyrene	optical	10-30	10^{16}-10^{17}	50-100
" "	"	"	sampled			40
Haynes and Wagner (13)	sandwich	C_2H_4	optical	2	10^{16}-10^{18}	5-70
Kent et al. (14,15)	sandwich	C_2H_4	optical	7	10^{16}-10^{18}	10-120
Kennedy et al. (16,17)	stagnation	C_3H_8	optical	1	10^{17}-10^{18}	5-25
" "	"	C_2H_4	optical	0.3-2	10^{16}-10^{17}	15-70
Nakamura et al. (18)	axisymmetric	methanol/ benzene	optical	4		
" "	"	C_3H_8	optical	3		
Santoro et al. (19)	axisymmetric	C_2H_4	optical	10	10^{16}-10^{18}	10-100

TURBULENT FLAMES

Turbulent flames which are the more interesting from the practical viewpoint have not been researched as extensively as laminar flames by optical means. Soot concentration measurements by sampling are in the majority.

Hein (26) presented soot and other species concentrations measurements by sampling in a large industrial furnace burning either heavy fuel oil or propane. The axial profiles show the initial soot formation region in the fuel rich region of the flame followed by the decline in the burnout region. The peak in soot concentration is considerably closer to the burner than the CO_2 peak and is in fact similar to the CO concentration profile.

Hein found that increasing the percentage of primary air increased both the soot formation and burnout rates. Increased velocities decreased soot formation and increased burnout rates. The author concluded that combustion of soot is controlled by the entrainment rate of secondary air into the flame. By assuming a first order reaction he obtained an activation energy of 21-22 kcal/mole for the soot formation process.

A probe-sampling investigation by Maravel (27) in an industrial furnace burning heavy oil or natural gas gave similar results. The axial soot profiles were again spatially similar to the CO distributions. The fraction of carbon in the fuel converted to soot was 5% for natural gas and 20% for the heavy fuel oil. Particle sizes were measured to be 20-30 nm along the axis of the furnace. Chemical analysis of the soot particles showed atomic ratios H/C = 0.18 for natural gas and H/C = 0.72 - 0.19 for the fuel oil.

Sjögren (28) carried out experiments with an oil burner to determine the effects of excess air, droplet size and recirculation on soot emission. He separated the effects of excess air into two components. The conclusions were that increased air velocity relative to droplet velocity extinguishes droplet diffusion flames and reduces soot. Decreased O_2 concentration (such as occurs in recirculation) generally reduces soot formation by lowering the required extinction velocity. Extinction velocity increases with droplet size and so small droplets produce less soot.

Dalzell, Williams and Hottel (29) investigated a turbulent free acetylene flame by optical means and their method agreed with sampled concentration within a factor of two. Soot particle diameters of around 205 nm were obtained from polar scattering distributions and they presented radial profiles of soot mass concentration through the flame.

Magnussen et al. (30.31) investigated free turbulent acetylene flames by light scattering and some sampling. The statistics of the fluctuating light scattering signal indicated a very intermittent soot structure in the flame. The length scale of the indicated structure increased with distance from the fuel nozzle up to the location of the peak in the scattered signal intensity. The authors concluded that soot is formed in eddies separated by regions with very little soot. Large soot agglomerates are indicated by the disymmetry of the scattered signal in downstream regions. The probability density functions of the signal also change from a Gaussian-plus-delta function near the nozzle to a continuous skewed distribution further downstream. Inert additives to the fuel and increased fuel jet velocity were found to decrease the amount of soot in the flame.

Some theoretical modelling based upon particle formation and burnout rates in laminar flames applied to the turbulent field were also presented and were favourably compared with experiment.

Prado et al. (32) sampled soot (and polycyclic aromatic hydrocarbons) in furnace flames of kerosene and benzene. PCAH profile peaks always preceded soot profile peaks as in laminar diffusion flames (6). They found that at low velocity, a slight decrease in atomizing air pressure resulted in a 20 fold increase in soot concentration and a large increase in smoke emitted. At higher velocity this sensitivity was not evident. They explained the effect as being due to larger fuel droplets at low pressure whose flame envelopes are sensitive to extinction by the relative air velocities. Particle sizes were measured and ranged from 14 - 30 nm and they were agglomerated in larger units or chains. Atomizing air pressure did not affect particle size. Average particle size tended to increase slightly in the burnout region. This was attributed to smaller particles burning out first and possible internal oxidation and collapse of other particles.

Pagni and Bard (33) and Schönbucher (43) measured soot in solid and liquid fuel fires. These flames would probably be considered more as flickering laminar flames rather than turbulent in the present context. Pagni and Bard used multi-wavelength laser light extinction to determine soot volume fraction and particle size. For purposes of analysis the flames were considered as homogeneous sooting bodies. Isooctane, one of the liquid fuels, had a soot volume fraction 0.62×10^{-6}, particle size 46 nm and number density $2.7 \times 10^{15} m^{-3}$.

Becker and Yamazaki (34) investigated buoyant free turbulent propane and acetylene flames by scattered light intensity. This was related to sampled soot concentrations. They found that similarity of profiles could be achieved when plotted against Richardson number. Their measurements also imply constant particle size in the burnout region. In further work Becker and Liang (35) sampled soot from the exhaust of turbulent flames from a variety of fuels. They established a soot yield order $C_2H_2 \gg C_2H_4 > C_3H_8 > CH_4, C_2H_6$. The soot yield was again found to correlate well with Richardson number but the authors point out that Richardson number is in turn correlated with the flame residence time and so the determining factor cannot be established.

Beretta et al. (36-39) investigated the flame yield of a free diesel oil spray flame under laboratory conditions. Light scattering and extinction techniques were used to determine droplet and soot particle quantities. The polarization ratio of the scattered light was used to distinguish between soot particles (small polarization) and fuel droplets (larger polarization). Scatter to extinction ratios were used to determine soot particle volume fraction and size. Volume fraction in the downstream region was up to 10^{-6} and particle sizes ranged from 20 nm initially to 120 nm further downstream. In the region near the nozzle they found the soot production zone to be located in a compact high temperature annulus surrounding the fuel jet. Further downstream the profiles are more uniform and believed to be determined more by mixing and recirculation than by local production processes. PAH, indicated by fluorescence, preceded the region of soot formation which occurred in higher temperature zones.

Further work by sampling on the same burner was carried by Ciajolo et al. (40). They showed that in the fuel vapourization region ethylene, light PAH and other pyrolysis products are formed followed by heavier PAH and soot in subsequent zones at higher temperature.

Nishida and Mukōhara (41) measured soot and other species concentration profiles in a turbulent C_3H_8 diffusion flame. They varied the inlet air temperature and inlet velocity to determine the effect upon sooting. Axial and radial soot profiles peaked just on the fuel side of the temperature peak. The radial profiles showed a very steep drop indicating rapid burnout at the peak in the radial temperature profile. For the high velocity flame an increase in inlet air temperature led to an increased soot formation rate but also an increased burnout rate so that smoke emission ceased. In the case of the low velocity flame,

the increase in air temperature again increased the soot formation rate but this time because of the lower velocity, temperature losses by radiation meant that the burnout rate remained the same and more smoke was emitted. This clearly demonstrated the importance of temperature on the burnout as well as formation rates and on the subsequent smoking propensity of the flame.

The picture which emerges from these studies is that soot is formed on the fuel side of the peak temperature contour after the initial light pyrolysis products, but before the main products CO_2 and H_2O. In several of the studies the peak in the soot concentration profile is close to that of CO. The soot formation rate is sensitive to initial conditions - air velocity, fuel droplet size, fuel type initial temperature. Soot burnout begins to occur very close to the peak in temperature where O_2 starts to penetrate. The burnout rate is sensitive to mixing rates (amount of air present) and particularly to temperature.

Individual particle sizes are probably around 20 - 40 nm but may appear (particularly by light scattering measurements) as large agglomerates of 200 nm or more in the downstream flame regions. The structure of the soot burning zones is highly intermittent (as is that of other products and temperature) in the turbulent flame field.

A comparison of the maximum measured soot concentrations from the reviewed studies is presented in Table 2. Apart from the data for the heavy fuel oil and for acetylene there is not a great deal of variation.

Table 2: Maximum Measured Soot Concentrations

Author		Flame type	Fuel	Soot (g/N m³)
Hein	(26)	Furnace	Heavy fuel oil	30 - 50
Beretta et al.	(34-39)	Free	Light diesel oil	5
Ciajolo et al.	(40)	Free	" " "	5
Prado et al.	(32)	Furnace	Benzene	10
" "		"	Kerosene	4
Pagni and Bard	(33)	Fire	Isooctane	3*
Dalzell et al.	(29)	Free	C_2H_2	5*
Magnussen et al.	(31)	Free	C_2H_2	10 - 15*
Becker and Yamazaki	(34)	Free	C_3H_8	0.8
Hein	(26)	Furnace	C_3H_8	6 - 7
Nishida and Mukōhara	(41)	Enclosed	C_3H_8	5
Kent and Bastin	(42)	Free	C_2H_2	100*

* Published light scatter measurements - have been multiplied by 5 here to approximate standard volume conditions.

Overall it is still not possible to reliably predict soot formation and burnout rates for a particular system. In some cases (Becker et al. 34,35) the rates may be entirely mixing rate controlled although more generally this is not true. Some recent work by Kent and Bastin (42) is aimed at determining soot formation and burnout rate influences in turbulent acetylene flames. Free turbulent flames were investigated over a range of nozzle sizes and jet velocities to ascertain the effects of initial conditions upon the soot field. Test conditions ranged from 20 - 200 m/s nozzle velocity with nozzle sizes of 1.5 - 5 mm.

These flames were generally not affected by buoyancy as evidenced by near constant soot profile peak positions over all conditions. Richardson numbers gD/U_o^2 (D is nozzle diameter, U_o is nozzle fuel velocity) ranged from $(0.5 - 20) \times 10^{-6}$. The flame time constant, $\tau = D/U_o$, was found to determine the sooting behaviour of the flame. Laser light extinction measurements were made transversely across the flame axis and were converted by way of Mie extinction theory to equivalent soot volume fraction. This is the soot volume fraction which has the same extinction over a path length equal to the nozzle diameter.

Figure 4 shows six test conditions with varying nozzle diameters and velocities but with only two time constants, 0.1 and 0.33 ms. The axial profiles agree very well at their respective time constants and the differences between the two series is quite marked. The agreement is perfect on the soot formation side with some divergence appearing in the

burnout region.

Soot cross-section average temperature measurements made by the Kurlbaum method are also shown. They show a drop in temperature with distance from the nozzle due to radiation losses. The temperature is therefore also a function of the amount of soot present and the profiles also fall into two groups according to the flame time constant.

The effect of increasing fuel jet velocity upon the equivalent soot volume axial profiles for the 3 mm nozzle are shown in Fig. 5. Velocity varied from 30 - 150 m/s. Conditions 1-3 were heavy smoke emitters as can be seen from the high values of the profiles in the downstream regions. However, for conditions 1-5 (velocities 30-69 m/s) the profiles are almost identical in the formation region at the peak and in the burnout region up to X/D = 100. That is,at the point where the curves begin to diverge,soot conditions in all these flames appear to be the same. The reason why the burnout rates quite suddenly drop for conditions 1-3 is apparently due to the lower temperatures in the slower flames as shown. Temperatures are lower in the slower flames as residence time is longer for similar radiation loss rates. The smoking propensity of the flame therefore appears to be entirely due to temperature in the downstream region and is independent of the peak amount of soot formed.

As jet velocity is further increased (conditions 6-8, velocities 91-150 m/s) the soot formation regions and peak values also show significant reductions in soot quantity. Relative soot formation rates were obtained from the slopes of the profiles at X/D = 50 for all conditions and nozzle sizes. In order to get a nominal time-based formation rate, the gradients are multiplied by nozzle velocities,as local velocities at X/D = 50 were not measured. These are shown in Fig. 6 against $1/\tau$ which is termed the flame mixing rate. The soot formation rate is linearly proportional to the mixing rate with very little scatter up to $1/\tau = 20\ ms^{-1}$. Thereafter soot formation rates level out and show more scatter. These data therefore indicate that at low mixing rates,soot chemistry is faster than mixing rates and the rate of soot formation is controlled by mixing rates. At higher mixing rates, chemistry is the controlling rate and it may in turn depend on other factors such as temperature and minor species concentrations in the flame.

In the burnout region the situation is a little more complicated. Figure 7 shows nominal burnout rates against mixing rates at X/D = 125 and 175. The dependence on mixing rate is again clearly evident but it is no longer linear. A threshold in $1/\tau$ below which burnout rates are zero has developed and this threshold increases with X/D. Falling temperature is evidently the important factor since O_2 concentration increases with downstream distance. At higher mixing rates, burnout rates level out and are therefore dependent upon other factors too such as species concentrations.

The dependence of burnout rates on temperature is shown in Fig. 8 for all $X/D \geq 100$. The well defined upper bound shows the limiting influence of temperature. Burnout effectively ceases below 1000 - 1100°C.

The conclusions from this study regarding burnout rates were that mixing rate, temperature or species concentration can place a limit on burnout rates. Near the peak in the soot profile it is likely to be species concentration (since burnout rates fall to zero here). Further downstream it can depend upon mixing rates and towards the end where oxygen concentration is high, low temperature can be the dominant factor.

CONCLUSIONS

The experimental investigations of laminar diffusion flames particularly by optical means have yielded a good understanding of the separate regions of soot particle formation, particle growth and soot burnout. What is still not clear, however, is the dependence of the rates of these processes upon the local species concentrations and temperatures. Experimental data where fuels, temperatures and concentrations are varied and where optical soot measurements are combined with gas analysis would be invaluable but very laborious. Glassman's data show that neither fuel type nor temperature alone determine sooting behaviour and so simple relationship may not be easy to find.

Ultimately modellers of practical combustors would like to insert local soot reaction rates, gleaned from laminar flame data, into turbulent flame models and thus be able to predict the sooting field. This fundamental approach may be the most difficult. The alternative is to try to obtain experimental data in turbulent flames to directly establish the controlling parameters. Some headway has been made here. The regions of soot formation and burnout have been recognized and some effects of changed initial conditions upon these rates have been discovered. The importance of fuel, temperature, flame time constant and the addition of active or inert additives upon the separate processes has been noted. What remains now is to measure absolute formation and burnout rates in terms of these recognized parameters in order to obtain useful correlations for the combustion engineer.

ACKNOWLEDGEMENTS

The support of the Alexander von Humboldt Foundation for granting J.H. Kent a fellowship is gratefully acknowledged.

REFERENCES

1. Palmer, H.B. and Cullis, C.F., The Formation of Carbon from Gases, Chemistry and Physics of Carbon, (editor Walker, P.L.), Vol. 1, pp. 265-325, Marcel Dekker, New York (1965).

2. Wagner, H.Gg., Soot Formation in Combustion, Seventeenth Symposium (International) on Combustion, pp. 3-19, The Combustion Institute (1979).

3. Haynes, B.S. and Wagner, H.Gg., Soot Formation, Prog. Energy Combust. Sci. 1, 229-273 (1981).

4. Wolfhard, H.G. and Parker, W.G., A new technique for the spectroscopic examination of flames at normal pressures, Proc. Phys. Soc. A, 62, 722-730 (1950).

5. Wolhard, H.G. and Parker, W.G., A spectroscopic investigation into the structure of diffusion flames, Proc. Phys. Soc. A, 65, 2-19 (1952).

6. Spengler, G. and Kern, J., Untersuchungen an Diffusionsflammen - Konzentrationsverteilung in einer Hexan-Diffusionflamme, Brennst. Chemie 50, 321-324 (1969).

7. Tesner, P.A., Snegiriova, T.D. and Knorre, V.G., Kinetics of dispersed carbon formation, Comb. Flame 17, 253-260 (1971).

8. Tesner, P.A., Tsygankova, E.I., Guilazetdinov, L.P. Zuyev, V.P. and Loshakova, G.V., The formation of soot from aromatic hydrocarbons in diffusion flames of hydrocarbon-hydrogen mixtures, Comb. Flame 17, 279-285 (1971).

9. Lee, K.B., Thring, M.W. and Beer, J.M., On the rate of combustion of soot in a laminar soot flame, Comb. Flame 6, 137-145 (1962).

10. Kunugi, M. and Jinno, H., Determination of size and concentration of soot particles in diffusion flames by a light scattering technique, Eleventh Symposium (International) on Combustion, pp. 257-266, The Combustion Institute, Pittsburgh (1967).

11. Kuhn, G. and Tankin, R.S., Spectroscopic measurements to determine temperature and carbon particle size in an absorbing propane diffusion flame, J. Quant. Spectrosc. Radiat. Transfer 8, 1281-1292 (1968).

12. Jagoda, I.J., Prado, G. and Lahaye, J., An experimental investigation into soot formation and distribution in polymer diffusion flames, Comb. Flame 37, 261-274 (1980).

13. Haynes, B.S. and Wagner, H.Gg., Sooting structure in a laminar diffusion flame, Ber. Bunsenges. Phys. Chem. 84, 499-506 (1980).

14. Kent, J.H., Jander, H. and Wagner, H.Gg., Soot formation in a laminar diffusion flame, Eighteenth Symposium (International) on Combustion, pp. 1117-1126, The Combustion Institute, Pittsburgh (1981).

15. Kent, J.H. and Wagner, H.Gg., Soot measurements in laminar ethylene diffusion flames, Comb. Flame 47, 53-65 (1982).

16. Kennedy, I.M., Vandsburger, U., Dryer, F.L. and Glassman, I., Soot formation in the forward stagnation region of a porous cylinder, Western States Section, Combustion Institute Meeting, Paper 82-39, April 1982.

17. Vandsburger, U., Kennedy, I., Glassman, I. and Dryer, F.L., The effect of oxygen index on the sooting structure of a diffusion flame, Eastern Section, Combustion Institute Meeting, December 1982.

18. Nakamura, M., Koda, S. and Akita, K., Sooting behaviour and radiation in Methanol/Benzene/Air diffusion flames, Nineteenth Symposium (International) on Combustion, pp. 1395-1401, The Combustion Institute, Pittsburgh (1982).

19. Santoro, R.J., Semerjian, H.G. and Dobbins, R.A., Soot particle measurements in diffusion flames, Comb. Flame 51, 203-218 (1983).

20. Roper, F.G. and Smith, C., Soot escape from laminar air-starved hydrocarbon flames, Comb. Flame 36, 125-138 (1979).

21. Burke, S.P. and Schumann, T.E.W., Diffusion Flames, Ind. Eng. Chem. 20, 998-1006 (1928).

22. Roper, F.G., Smith, C. and Cunningham, A.C., The prediction of laminar jet diffusion flame sizes: part II, Experiment verification, Comb. Flame 29, 227-234 (1977).

23. Glassman, I. and Yaccarino, P., The effect of oxygen concentration on sooting diffusion flames, Combust. Sci. Tech. 24, 107-114 (1980).

24. Glassman, I. and Yaccarino, P., The temperature effect in sooting diffusion flames, Eighteenth Symposium (International) on Combustion, pp. 1175-1183, The Combustion Institute, Pittsburgh (1981).

25. Schug, K.P., Manheimer-Timnat, Y., Yaccarino, P. and Glassman, I., Sooting behaviour of gaseous hydrocarbon diffusion flames and the influence of additives, Combust. Sci. Tech. 22, 235-250 (1980).

26. Hein, K., Recent results on the formation and combustion of soot in turbulent fuel oil and gas flames, Combust. Sci. Tech. 5, 195-206 (1972).

27. Maraval, L., Characteristics of soot collected in industrial diffusion flames, Combust. Sci. Tech. 5, 207-212 (1972).

28. Sjörgren, A., Soot formation by combustion of an atomized liquid fuel, Fourteenth Symposium (International) on Combustion, pp. 919-927, The Combustion Institute, Pittsburgh (1973).

29. Dalzell, W.H., Williams, G.C. and Hottel, H.C., A light-scattering method for soot concentration measurements, Comb. Flame 14, 161-170 (1970).

30. Magnussen, B.F., An investigation into the behaviour of soot in a turbulent free jet C_2H_2-flame, Fifteenth Symposium (International) on Combustion, pp. 1415-1425, The Combustion Institute, Pittsburgh (1974).

31. Magnussen, B.F., Hjertager, B.H., Olsen, J.G. and Bhaduri, D., Effects of turbulent structure and local concentrations on soot formation and combustion in C_2H_2 flames, Seventeenth Symposium (International) on Combustion, pp. 1383-1393, The Combustion Institute (1978).

32. Prado, G.P., Lee, M.L., Hites, R.A., Hoult, D.P. and Howard, J.B., Soot and Hydrocarbon formation in a turbulent diffusion flame, Sixteenth Symposium (International) on Combustion, pp. 649-661, The Combustion Institute, Pittsburgh (1976).

33. Pagni, P.J. and Bard, S., Particulate volume fractions in diffusion flames, Seventeenth Symposium (International) on Combustion, pp. 1017-1028, The Combustion Institute, Pittsburgh (1979).

34. Becker, H.A. and Yamazaki, S., Soot concentration field of turbulent propane/air diffusion flames, Sixteenth Symposium (International) on Combustion, pp. 681-691, The Combustion Institute, Pittsburgh (1976).

35. Becker, H.A. and Liang, D., Total emission of soot and thermal radiation by free turbulent diffusion flames, Comb. Flame 44, 305-318 (1982).

36. Beretta, F., Cavaliere, A., D'Alessio, A. and Noviello, C., Visible and UV spectral emission and extinction measurements in oil spray flame, Combust. Sci. Tech. 22, 1-15 (1980).

37. Beretta, F., Cavaliere, A. and D'Alessio, A., Laser excited fluorescence measurements in spray oil flames for the detection of polycyclic aromatic hydrocarbons and soot, Combust. Sci. Tech. 27, 113-122 (1982).

38. Beretta, F., Cavaliere, A., Ciajolo, A., D'Alessio, A., Langella, C., Di Lorenzo, A. and Noviello, C., Laser light scattering, emission/extinction spectroscopy and thermogravimetric analysis in the study of soot behaviour in oil spray flames, Eighteenth Symposium (International) on Combustion, pp. 1091-1096, The Combustion Institute, Pittsburgh (1981).

39. Beretta, F., Cavaliere, A. and D'Alessio, A., Soot and PAH distribution in oil spray flames, inferred by elastic and inelastic laser light scattering, Nineteenth Symposium (International) on Combustion, pp. 1359-1367, The Combustion Institute, Pittsburgh (1982).

40. Ciajolo, A., Barbella, R., Mattiello, M. and D'Alessio, A., Axial and radial measurements of soot and PAH in a light oil flame, Nineteenth Symposium (International) on Combustion, pp. 1369-1377, The Combustion Institute, Pittsburgh (1982).

41. Nishida, O. and Mukōhara, S., Characteristics of soot formation and decomposition in turbulent diffusion flames, Comb. Flame 47, 269-279 (1982).

42. Kent, J.H. and Bastin, S.J., Parametric effects on sooting in turbulent acetylene diffusion flames, Comb. Flame (to appear).

43. Schönbucher, A., Wärme-, Stoff- und Impulstransportvorgänge unter Berücksichtigung kohärenter Strukturen in Tankflammen organischer Flüssigkeiten, Brennstoff-Wärme-Kraft 33, 371-373 (1981).

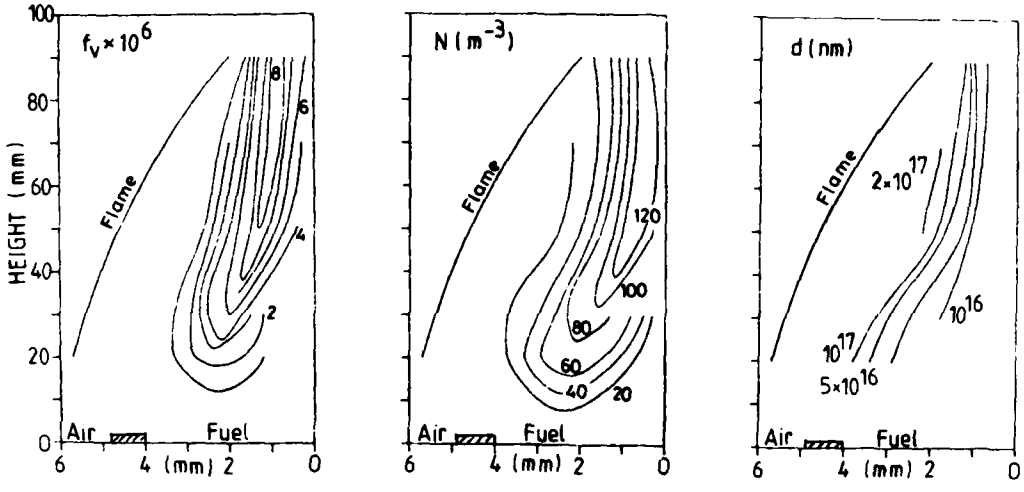


Fig. 1: Soot volume fraction (f_v), number density (N) and particle diameter (d) contours in a laminar ethylene diffusion flame (15).

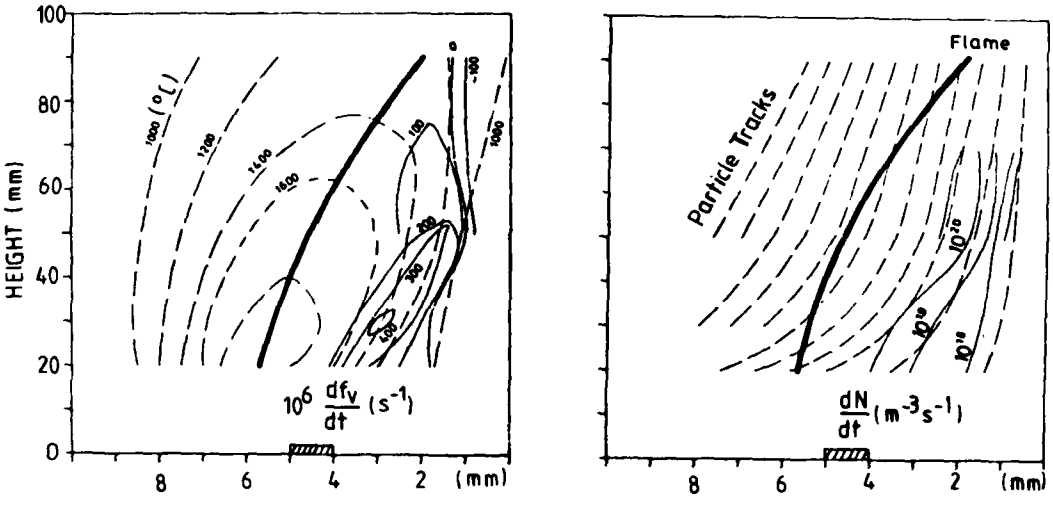


Fig. 2: Soot volume and number production rate contours in a laminar ethylene diffusion flame (15). Temperature contours and particle trajectories also shown.

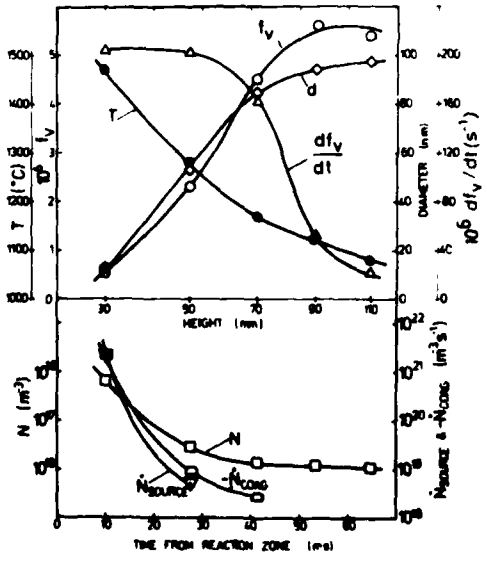


Fig. 3: Lagrangian view of conditions along particle trajectory through diffusion flame. Particle enters near base of flame and travels up into fuel side (14).

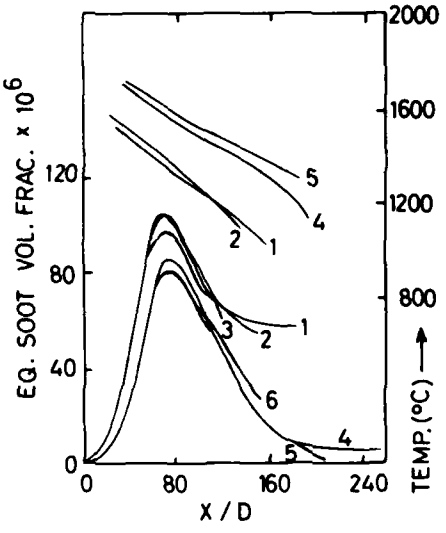


Fig. 4: Equivalent soot volume fraction and temperature axial profiles in turbulent acetylene diffusion flames as a function of time constant τ. 1,2,3 - τ = 0.33 ms; 4,5,6 - τ = 0.1 ms (42).

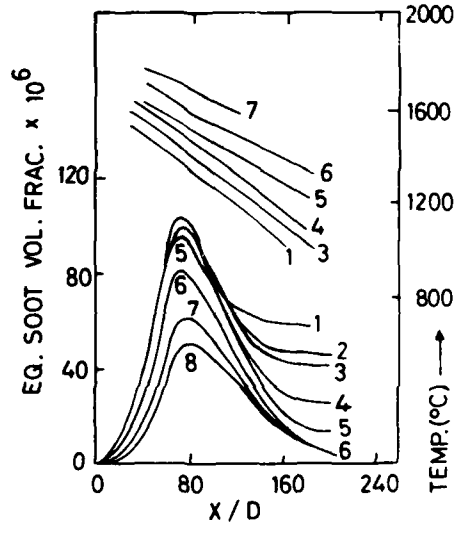
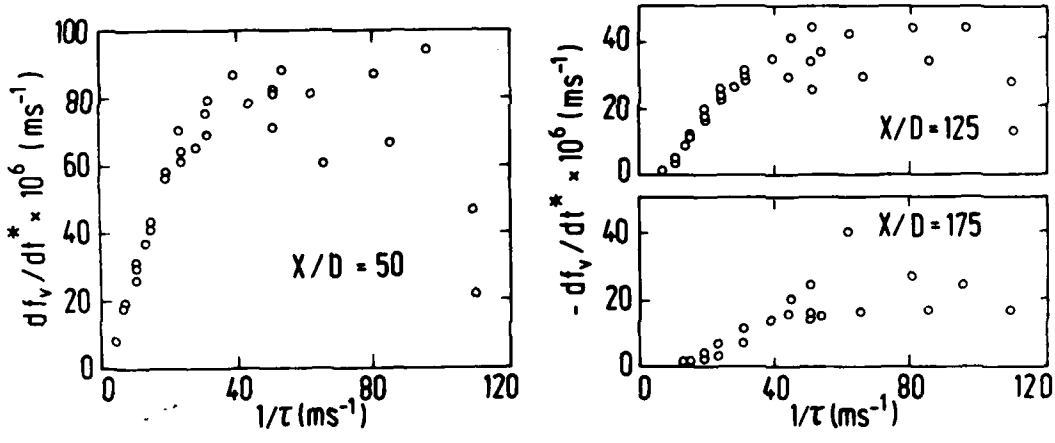


Fig. 5: Same as Fig. 4 but for fixed nozzle size and varying nozzle velocity. Conditions 1-6 velocity increases from 30-150 m/s. Conditions 1-3 heavy smoke emitters (42).



Figs. 6 and 7: Equivalent soot volume formation (Fig. 6) and burnout (Fig. 7) nominal rates in turbulent acetylene diffusion flames against mixing rate $1/\tau = U_o/D$. (42)

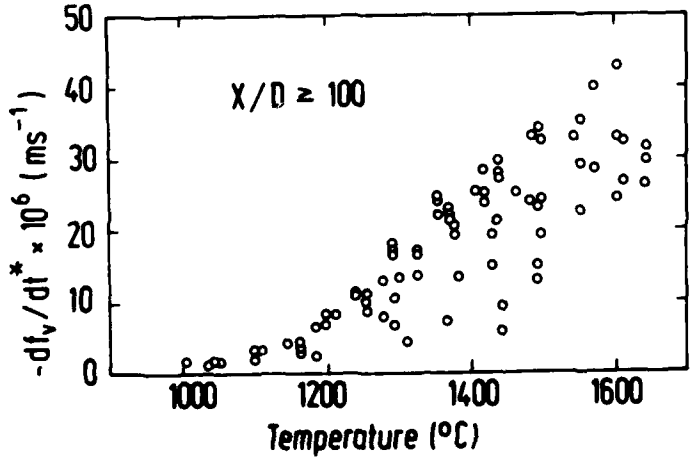


Fig. 8: Nominal soot burnout rates as a function of local temperature in turbulent acetylene diffusion flames. (42)

DISCUSSION

K.Homann, Ge

What was the limitation for the temperature measurements at low X/D values in Figures 4 and 5?

Author's Reply

The Kurlbaum temperature method compares the intensity of radiation from the reference lamp viewed directly with that when viewed through the flame. We found that discrimination became difficult when soot absorption (of the laser beam) dropped below about 10 percent. This limited the range of temperature measurements.

Growth of Electrically Charged Soot Particles in Flames

K.H. Homann, E. Ströfer and H. Wolf
Institut für Physikalische Chemie, Technische Hochschule Darmstadt
Petersenstraße 20, 6100 Darmstadt, Fed. Rep. of Germany

AD-P003 144

SUMMARY

A part of the soot particles in fuel-rich hydrocarbon flames carry an electric charge. Charges of both signs occur on soot particles in the same flame. Through a molecular beam sampling system, charged soot particles and smaller ions have been drawn from low pressure flames of acetylene and benzene and analyzed in an electrostatic mass filter and a deflection system. The development of particle mass, number density and the volume fraction of charged and neutral soot is reported for these flames under different burning conditions. The volume fraction of charged soot in acetylene flames increases with temperature while there are no large charged soot particles at all in benzene flames. The role of charged species in the mechanism of soot formation and the process of charging is discussed in terms of a chemiionization mechanism.

INTRODUCTION

Soot particles can acquire a positive or negative electrical charge when they are formed in the flame. The degree and the sign of ionization depends on the fuel and on the burning condition. This fact has been used to influence carbon formation through external electric fields with special laboratory flames by drawing the particles to the electrodes or into oxygen-rich parts of the flame where they are burned [1,2].

On the other hand, the role of electrically charged soot particles and their precursors in the mechanism of carbon formation has been and still is studied and discussed [3,4]. With some fuels thermal equilibrium of soot ionization seems to be established fairly soon, for others this is not true [5]. The degree of soot ionization can be strongly increased by the addition of alkali or alkaline earth salts to the flame [5,6]. Thereby, a large fraction of particles is charged negatively so that their agglomeration to larger aggregates is impeded and very small particles leave the flames which may be burned faster with additional oxygen. Conversely, the presence of solid soot particles in the flame has a strongly promoting influence on the rate of metal ionization as compared to this process in non-sooting flames [7]. These short introductory remarks on the ionization in sooting flames and the means to influence it show that this subject is of considerable interest both from a practical point of view and for the understanding of the physico-chemical processes leading to carbon formation in flames.

The subject of this paper is the investigation of the degree of positive and negative ionization of soot in premixed flames of acetylene and benzene under different burning conditions and of the mass distribution of charged soot particles.

EXPERIMENTAL

Burner and Flames

The flames studied were premixed acetylene-oxygen and benzene-oxygen low pressure flat flames burning on a 7.5 cm diameter water-cooled sintered disk burner. The burner could be moved vertically in the burner housing to make possible sampling from different heights in the flame. The sampling nozzle was always held at ground potential. The flow of acetylene and oxygen was controlled in the usual way with capillary flow meters and needle valves. For benzene flames pure oxygen was saturated with benzene vapor and then mixed with further oxygen to get the desired ratio. Temperatures in the burned gas of these flames had been measured in a precedent work using the sodium line reversal method [8].

The Sampling Nozzle and the Detection Systems for Charged Particles (Fig. 1)

The flames were sampled through an orifice on top of a conical quartz probe of 60 mm height and 50 mm base diameter. A supersonic nozzle beam from the soot-loaden flame gases was formed inside this probe and expanded at a background pressure of about 0.1 Pa generated by a 1000 l s^{-1} diffusion pump. Since charged particles were to be sampled platinum paint was burned onto the inner and outer surface of the probe which was kept at ground potential, so that no uncontrollable surface charges could form on the probe. For the detection of positively and negatively charged species two different techniques were applied. The first, an electrostatic energy filter, was used for smaller particles with masses up to about $2 \cdot 10^4$ atomic mass units (u). It has been described previously [9,5]. In short, it consists of an array of three parallel grids made of fine copper mesh which were placed inside the sampling cone near the sampling nozzle, perpendicular to the axis of the beam. The first grid at ground potential together with the inside wall of the probe provided a field-free space for the nozzle beam to expand to free molecular flow condition. An energy separation of the charged particles was obtained by applying a repelling voltage ΔU to the second grid. This let through only those particles for which $1/2\ mv^2 \geq Q\Delta U$, where m, v and Q are mass, velocity and charge of the particle, respectively.

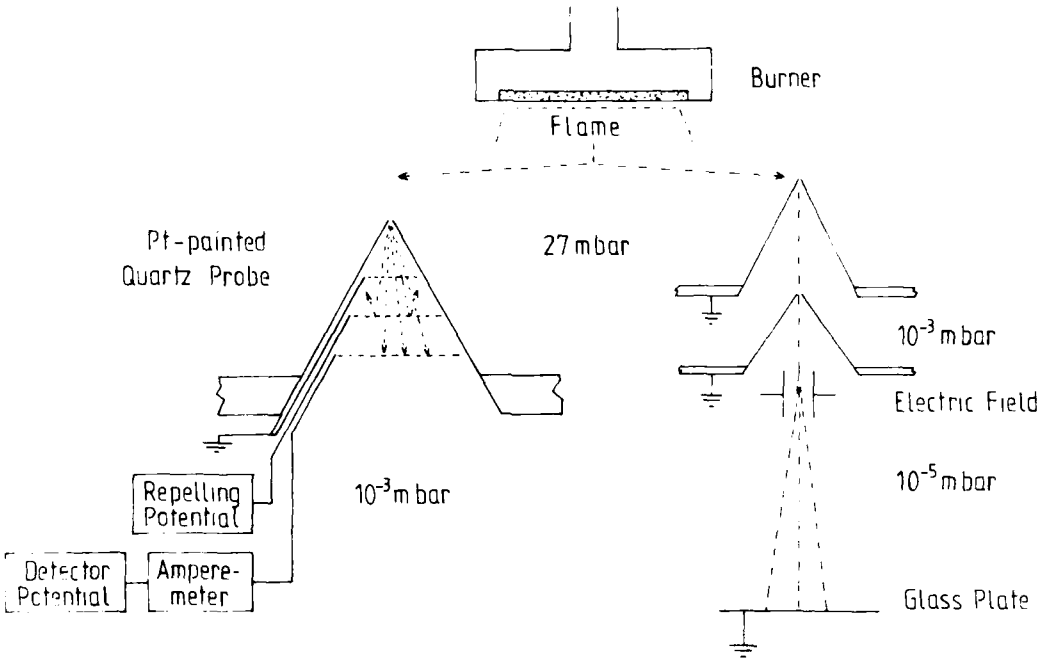


Fig. 1. Two different experimental set-ups for the detection and mass analysis of charged soot particles

ΔU was positive for positive and negative for negative ions. The third grid served as the detector. For positive ions it was biassed negatively and vice versa for negative charge carriers. An integral kinetic energy spectrum was obtained when the detector current was monitored as a function of the repelling voltage ΔU. The spectrum is then differentiated. To convert it into a mass spectrum the velocity and the charge of the particles must be known. This mass separator can be used for ions with masses between about 20 and $2 \cdot 10^4$ u. Higher repelling voltages were not used because of corona discharges. Total ion currents could be measured with zero repeller voltage or using the first grid as detector. Fig. 2 shows typical mass spectra of charged particles obtained with this mass separator.

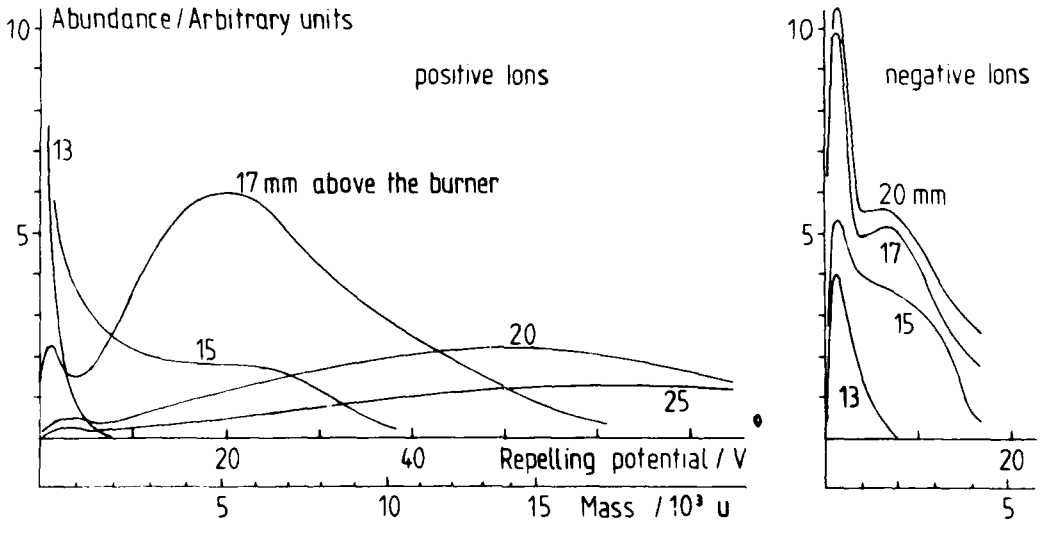


Fig. 2. Mass distributions of positive and negative soot ions in a flat C_2H_2-O_2-flame. C/O = 1.12, p = 27 mbar, v_o = 42 cm s^{-1}

The mass scale is only approximate since the velocities of the particles in the beam are not known exactly. Measurements on flames seeded with Cs^+ ions (m = 133 u) and new results on the mass of large negatively and positively charged particles made necessary a correction of the mass scale published previously [5,9].

The other detector was used for larger soot particles, both neutral and charged ,see Fig. 1. The center part of the beam entered a second high vacuum chamber ($p \approx 10^{-3}$ Pa) through another circular orifice (0.8 mm diameter). The charged particles were deflected in the transverse electric field of a plate capacitor. They impacted on a glass plate in some distance from the field where the soot particles were deposited.The pattern of deposition from neutral, positively and negatively charged soot particles was then measured undera microphotometer. The absorption of light was taken as a measure for the amount of soot deposited. It proved necessary to use glass plates covered with a uniformly transparent conducting layer in order to hold them at ground potential. Otherwise, surface charges of the deposited soot generated local electric fields preventing the following particles from being captured on the glass.

Fig. 3 shows an absorption curve of the deposits on the glass plate. The absorption due to neutrals is of circular symmetry so that its shape can be determined by a photometric scan at a right angle through its center. The shoulder on the peak of the positive soot ions is most probably due to doubly charged particles since its position is just at double distance from the center of the neutrals (beam axis) compared to the maximum of the singly charged soot particles. Doubly charged particles were only found in acetylene flames of higher temperature. The figure shows experimental absorption curves and the contributions of the neutral and the charged soot particles from a sooting acetylene-oxygen flame. The area under the individual curves is a measure for the respective amount of differently charged soot in the flame.

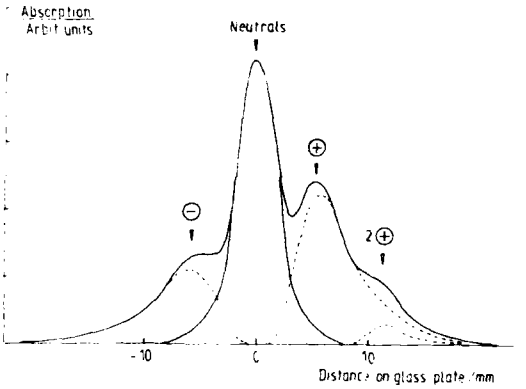


Fig. 3. Absorption curves (solid lines) for deposits of neutral, negatively and positively charged soot particles on the glass plate from a C_2H_2-flame. The dashed lines show the separate contributions of the charged particles.

Although the main purpose of the separate detection of larger neutral and charged particles was the determination of their relative amount in flames of different fuels and burning conditions the deflection by the electric field could also serve as a rough mass discriminator. Carrying the same charge light particles are deflected more than heavy ones. The reason is the same as for the mass separator described above. The soot particles in the beam are accelerated to velocities much higher than their thermal velocities in the flame. The gain in kinetic energy in this expanding gas beam seeded with the soot particles is the larger the heavier the particles are.

Burning and Measuring Conditions

The flames burned under a pressure of 27 mbar (20 Torr). Flat flames of this size and pressure have been extensively studied as concerns concentration profiles, temperature and absolute concentration of soot and size distribution of comparatively large soot particles so that these results can be discussed and compared within a larger frame [10,11,12,13]. Initial flow velocities of the unburned mixture covered the range between 30 and 60 cm s^{-1}. An increase in the flow velocity or the throughput, respectively, results in a higher temperature at the maximum and in the soot forming zone of the burned gas. The Table gives the burning conditions of the different flames.

For each flame, samples were taken from different heights in the soot forming zone. The measurements with the electrostatic mass filter were also extended into the oxidation zone. Sampling times for evaluable deposits on the glass plates varied from 20 s for a strongly sooting benzene flame at a height of fully developed soot concentration to about $12 \cdot 10^3$ s at a height near the oxidation zone of an acetylene flame where soot formation just began. Care was taken that the orifice did not clog during the sampling time.

Table: Burning conditions of C_2H_2 and C_6H_6-flames

Flame No. and Fuel	C/O	v_o / cm s^{-1}	p / mbar
1, C_2H_2	1.12	50	27
2, C_2H_2	1.12	37	27
3, C_2H_2	1.12	30	27
4, C_2H_2	1.3	60	27
5, C_2H_2	1.3	50	27
6, C_2H_2	1.3	42	27
7, C_6H_6	0.82	44	27

RESULTS

Relative Volume Fractions of Neutral and Charged Soot

Fig. 4 shows the relative volume fractions of neutral and charged soot in two slightly sooting C_2H_2-O_2-flames of a C/O ratio of 1.12 (same as that of Fig. 2) but with different flame temperatures caused by different flow velocities of the unburned gas. The respective temperature profiles are also given in the figure. Positive soot ionization becomes first measurable at a height between 14 and 15 mm above the burner. (The term "above the burner" is used traditionally although in this set-up the flame burned under the burner which does not influence its shape.) This compares well with the mass distribution functions obtained with the electrostatic mass filter (Fig. 2) at this height of the flame. Positively charged particles of some thousand mass units are being formed at this height. From a comparison of these two methods and the fact that with the mass filter negative soot ions of masses ≤2500 u can be found at this height but do not yet appear on the glass plate, it is estimated that only particles with masses larger than about 6000 u can be detected by the glass plate method.

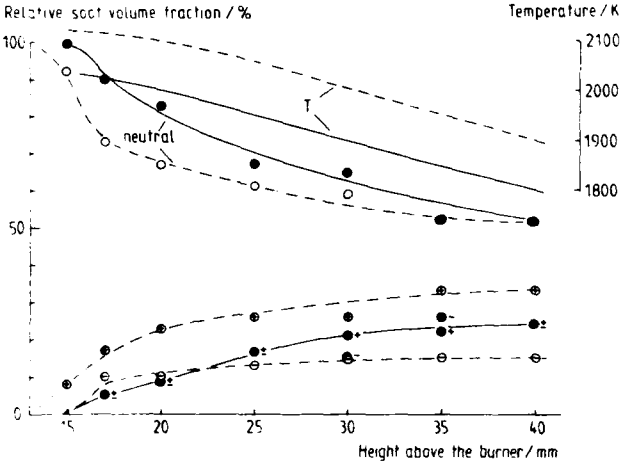


Fig. 4. Profiles of relative soot volume fractions of neutral and charged soot and of the temperature in flames No. 1 (dashed lines) and 2 (solid lines)

In the hotter flame the fraction of positively charged soot increases steadily reaching about 33 percent while the profile of negatively charged carbon particles shows a similar shape but is lower by a factor of about 0.5. In the flame with lower temperature the fraction of the positively ionized amount of soot is smaller. But in this case it is equal within the limits of experimental error to that of the negatively charged soot. The lower flame temperature does not only influence its electrical state but also leads to a larger yield of soot. The latter effect has been studied before without separation of neutral and charged soot [9,10].

The same is true for a more strongly sooting C_2H_2-O_2-flame with a C/O ratio of 1.3 as shown in Fig. 5. Again the ionized fraction increases from the beginning of soot formation and levels off at height of 30-40 mm. In flames of higher temperature there is relatively more positively than negatively charged soot while these fractions are again almost equal in the lower temperature flames.

Fig.6 gives relative total soot volume fractions in flames No.'s 1-6 showing the influence of C/O ratio and flow velocity on the yield of soot. At the beginning of the curves at low heights the real amount of soot might be somewhat higher since the sampling efficiency for very small soot particles on the glass plate is not 100%.

Flames No. 2 and 6 have almost the same temperature profiles between 20 and 40 mm above the burner. Their fractions of charged soot are also very similar, while the total soot concentration is larger by a factor of 3 to 4 in the flame with the higher C/O ratio. Flames No.2 and 5 do not differ very much in their total soot concentration. However, the temperature in flame No. 5 is higher and so is the fraction of positively charged soot. Thus, the fraction of charged soot in different flames is more strongly correlated to the temperature than to the total soot concentration. That in one and the same flame there seems to be quite a different correlation (increasing fraction of charged soot with increasing soot concentration and decreasing temperature) is not true.

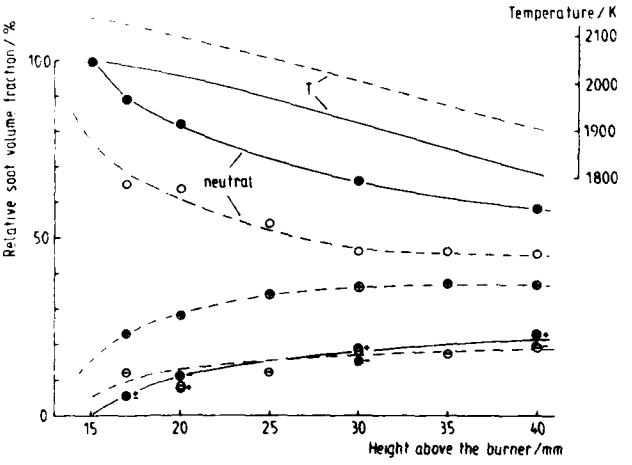


Fig. 5. Same as in Fig.4 for flames No. 4 (dashed lines) and 6 (solid lines)

To explain it the change of number density, size of the soot particles, and the number density of all ionized species in a flame has to be taken into consideration.

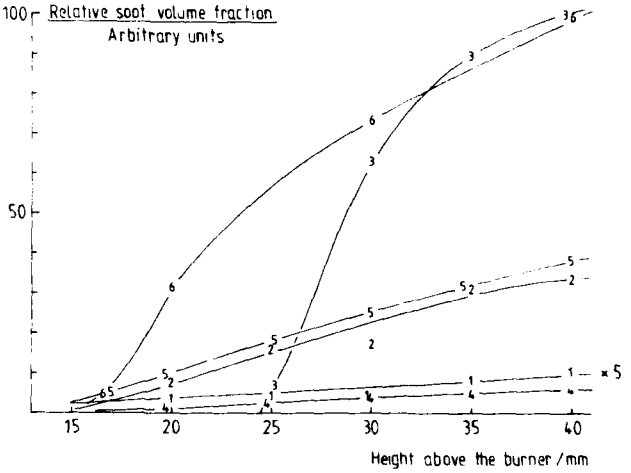


Fig. 6. Profiles of relative total soot volume fractions from the deposits on the glass plate for flames No.'s 1-6 (see table).

Approximate Mass Distribution Curves for Large Charged Soot Particles

From the absorption pattern of the deposits on the glass plate a rough mass distribution of the heavy charged particles can be obtained.

For the deflection of a beam of charged particles of mass m and charge Q in the homogeneous field between two plate electrodes the following equation holds for the distance r (from the center of the beam of neutral particles) where the charged particles hit the glass plate

$$r = \frac{U\ Q\ l\ L}{m\ v^2\ d}$$

Herein is U the voltage, d the distance between the electrodes, l the length of the capacitor and L the distance between the middle of the capacitor and the glass plate. An exact evaluation of m according to this formula is difficult since the velocity distribution of the large particles in the beam is not known with sufficient accuracy. v(m) has been estimated from the measured mean velocity of Cs^+ in the beam [5] and the results of the seeded beam theory for large particles [14,15]. In Figure 7 a mass distribution for charged soot from the glass plate deposits is shown. Because of the uncertainties in v and the neglect of the beam width this distributions are not exact. The real distributions should be somewhat narrower. However, the curves show that there is no appreciable difference in mass of positively and negatively charged soot particles. The average diameters calculated for a density of 2 g cm^{-3} are also about the same as those obtained from optical measurements on soot at this height of the flame. In an earlier work an overestimation of the particle velocity in the beam lead to the conclusion that charged soot particles in C_2H_2 - O_2-flames are smaller than neutral ones. It is believed now that if there is any difference in size it must be much smaller than assumed previously.Thus, one may conclude that for the comparatively low degree of ionization in flames not seeded with alkali salts the charge has no influence on the growth of the soot particles.

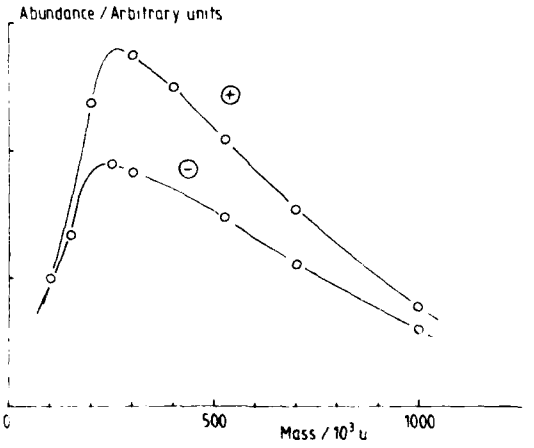


Fig. 7. Approximate mass distribution for large charged soot particles from a height of 40 mm above the burner in flame No. 6

Mass Distribution in the First Stage of Soot Formation

The development of the mass distribution of charged particles in the very first stage of soot formation can be seen from the results obtained with the electrostatic mass filter (Fig. 2). This stage corresponds to a flame zone between about 13 and 17 mm above the burner in most of these flames (except flame No. 3). Here, most of the charged particles have masses of a few thousand mass units and only a small fraction of them has already gained more mass to be detected by the glass plate method. In this stage the positive soot ions have a distinctly larger mass on the average than the negative ions. An appreciable part of the negative ions even has masses below 10^3 mass units. Another part of the negative charge carriers consists of free electrons. The reason for this lies in the mechanism of soot charging which takes place in this early stage of soot formation. From these results is can also be seen that the difference between the volume fraction of positively and negatively charged soot in the high temperature flames must be due to the presence of small negative soot ions and free electrons which do not deposit on the glass.

Benzene Flames

When benzene-oxygen flames were sampled no deposits due to charged soot particles could be detected on the glass plate, even with flames in which the soot concentration was higher than in the strongly sooting C_2H_2-O_2 -flames. This astonishing fact, however, was not quite unexpected since measurements with the electrostatic mass filter had shown that there are practically no soot ions with masses larger than about 5000 u in a benzene flame.

There is a strong increase in ionization between 10 and 15 mm above the burner of particles having masses between some hundred and about $4 \cdot 10^3$ mass units [5,7]. But these charged particles do not grow (see Fig. 8).

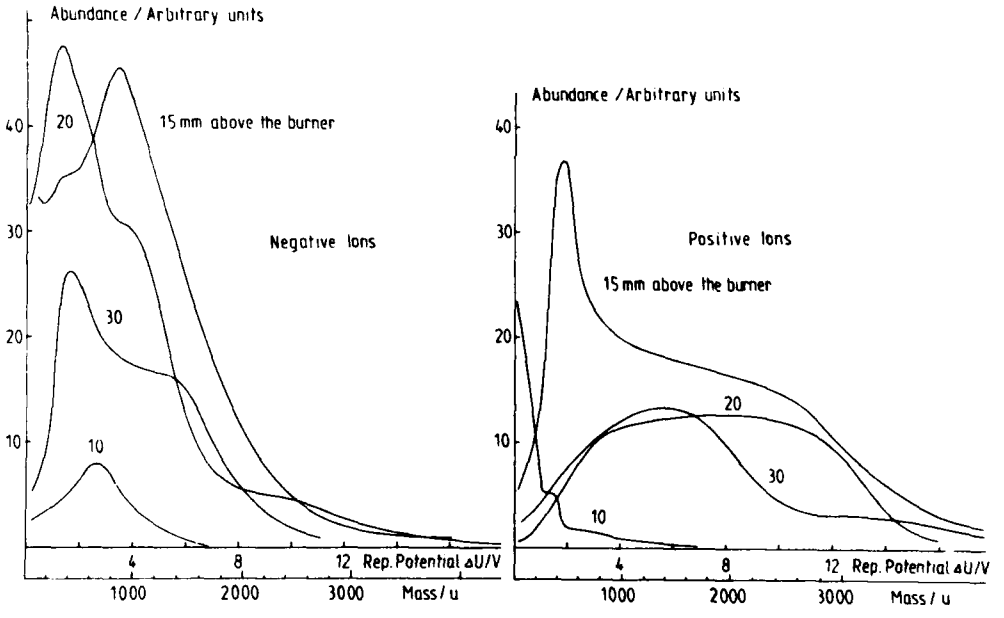


Fig. 8. Mass distributions of positive and negative soot ions in a flat C_6H_6 -O_2 -flame. C/O = 0.82, p = 27 mbar, v_o = 44 cm s^{-1} .

In fact, the average mass of these positive soot ions decreases with the height above the burner in contrast to the growth of charged particles in acetylene flames. In other respects there are similarities in the mass distribution of small soot ions in acetylene and benzene flames. At least two groups of positive and negative ions differing in mass can be distinguished. The mass spectra of positive ions in benzene flames look more complicated and suggest that there might be three different groups of ions

1) small molecular and radical ions from the oxidation zone
2) ions in the range 300 - 500 u and
3) ions covering a broader mass range from 500 - 4000 u.

The absence of charged particles of larger mass is surprising since in flames of acetylene and benzene that have the same concentration of soot in the burned gas the temperature of the benzene flame is higher. The diffuseness of the neutral soot deposit on the glass plate is an indication that in benzene flames soot formation starts with a relatively high number density of very small particles which coagulate. Conversely, in acetylene flames the initial

number density is smaller, but the rate of particle growth by surface reaction is larger, leading finally to the same amount of soot for the respective initial C/O-ratios.

DISCUSSION

From the existence of charged soot particles in hydrocarbon flames and their growth or disappearance, respectively, more can be learned about the complicated process of carbon formation in flames. On the other hand, the additional facilities to manipulate charged particles and to influence their state and degree of charging can be profitably used for analytical purposes and to control the amount and the state of carbon formed in flames.

General Mechanism of Soot Formation

The behaviour of charged soot particles shall be discussed within the more general frame of processes occuring in a premixed sooting flame. Through pyrolytic and oxidative reactions in the main reaction zone of the flame a number density of particles of hydrocarbon-type in the mass range between some hundred and about one thousand mass units is formed at the end of the oxidation zone. These are sometimes called nuclei for soot particles or primary particles. These primary particles grow by surface reactions with reactive, mainly unsaturated hydrocarbons and their radicals from the gas phase and simultaneously coagulate. Through the former process the total amount of soot increases with increasing height in the flame or reaction time, respectively. The latter process causes a rapid decrease in particle number density and an increase in the size of the particles without influencing the total amount of soot. The random coagulation of the particles causes a certain distribution in particle size which has often been described as a log-normal distribution. In low pressure flames, such as these, the process of soot formation ends with the formation of quasi-spherical particles having diameters between about 10 and 20 nm. In normal flames at atmospheric pressure the single particles can grow larger and they stick together in chain-like or grape-like irregular clusters.

Whereas the coagulation law which governs the decrease in number density is well understood the largest uncertainties in interpreting or predicting the amount of soot formed in the flame lies in the number density of the primary particles and in the individual rates with which different gas phase species undergo surface reactions on the growing soot particles. The number density curve must necessarily go through an early maximum. The position and the height of this maximum, however, depends on how exact number densities of small particles can be determined.The beginning of this curve is also dependent on how primary particles are defined or in other words where one sees the transition between a large molecule and a primary soot particle on a mass or diameter scale.

Mass spectrometry in combination with gaschromatography has been used to analyze hydrocarbons with masses of some hundred mass units and to determine their concentration. This is difficult for molecules with m > 300 u. Moreover, not all large hydrocarbon molecules can be considered as primary soot particles or their direct predecessors. There is evidence that mainly hydrocarbon radicals in the mass range 10^2 u < m < 10^3 u should be considered as potential primary particles. Mass analysis of electrically charged soot particles together with measurements of their volume fraction and number density can give additional information on the number density of primary soot particles and on the character of the surface reactions. Through these experiments the smallest soot particles are defined as those that have gained a mass of a few thousand atomic mass units and whose ionization potential has become as low as about 4.8 to 5 eV so that they can be ionized much easier than large hydrocarbon molecules [5]. Total soot volume fractions calculated from those of charged particles and their mass should be compared to volume fractions obtained with other methods.

Calculation of Total Number Density and Soot Volume Fraction

For the total soot volume fraction ϕ_s the relation

$$\phi_s = \frac{C_s \langle m_s \rangle}{\rho_s}$$

holds where C_s is the total number density of soot particles, $\langle m_s \rangle$ the number average mass and ρ_s the density of the single soot particle. Since ρ_s is certainly the same for charged and neutral particles the ratio of the volume fraction of positively charged particles, ϕ_+, to the total volume fraction is

$$\frac{\phi_+}{\phi_s} = \frac{C_+ \langle m_+ \rangle}{C_s \langle m_s \rangle}$$

where C_+ is the number density of positive soot ions and $\langle m_+ \rangle$ their average mass. If $\langle m_+ \rangle = \langle m_s \rangle$ (see above) then C_s can be determined from a measurement of C_+ and ϕ_+/ϕ_s.Fig. 9 gives a profile of C_s along the height in the flame obtained from a previous measurement of C_+ [5,7] and the reported relative soot volume fraction of positively charged particles

for flame No. 6. It shows that C_s is about $2 \cdot 10^{11} cm^{-3}$ at a height where soot formation begins in this flame. The total number density of hydrocarbon molecules in the mass range from about 200 to 600 u is of the order of 10^{12} cm^{-3} at this height in the flame [16,17]. In view of the fact that not all of these hydrocarbon molecules are transformed into soot but form the comparatively stable aromatic hydrocarbons such as pyrene, chrysene or coronene etc. a number density of $2 \cdot 10^{11}$ is a reasonable figure for nuclei of soot particles in this acetylene-oxygen-flame.

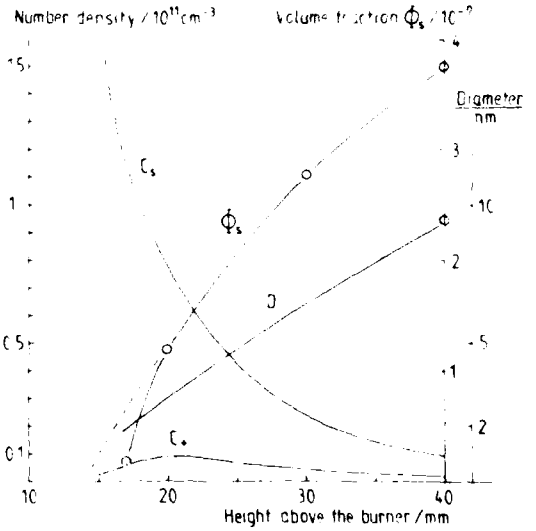


Fig. 9. Number densities of positively charged soot particles C_+, total number density C_s, total soot volume fraction Φ_s and average particle diameters D in flame No. 6.

The mass analysis of charged particles gives an average mass of about $5 \cdot 10^5$ u for soot particles at a height of 40 mm in this flame. This corresponds to a total soot volume fraction Φ_s of $3.8 \cdot 10^{-9}$ if a density of 2 g cm^{-3} is adopted for the soot. For comparison , from optical measurements by Bonne et al. a value of $4.5 \cdot 10^{-9}$ for Φ_s can be interpolated for an C_2H_2-O_2-flame burning under these conditions [10]. Taking this figure as a benchmark a profile of Φ_s can be obtained from the total deposits on the glass plate. As very small soot particles are not collected with 100% efficiency on the glass this curve must be extrapolated to a height of 13 to 14 mm where soot formation begins according to optical measurements. From the Φ_s and C_s-curves the growth of the average mass of the soot particles can be calculated. It starts from $5 \cdot 10^3$ u (17 mm) over $17 \cdot 10^3$ u (20 mm) , $145 \cdot 10^3$ u (30 mm) to about $500 \cdot 10^3$ u at 40 mm above the burner. For the lower heights this result is confirmed through a mass determination with the electrostatic mass filter. A smoothed curve for the diameters corresponding to these average masses of spherical particles is also shown in Fig. 9. This result is in line with earlier optical and electron microscopic measurements on low pressure C_2H_2-O_2-flames [10,11,18].

When the cold gas velocity of the flame is lowered keeping the C/O ratio constant there is a strong increase in the amount of soot formed while the flame temperature decreases. It has been shown in a previous work that there is an increase by a factor of 5 in the maximum number density of positively charged particles when the cold gas velocity is lowered from 50 to 30 cm s^{-1}[9]. Since the volume fraction of the positively charged soot decreases in the flames with lower flow velocity and temperature this means that the larger amount of soot is largely due to an increased number density of primary soot particles.

In a benzene-oxygen flame that forms the same amount of soot in the burned gas the situation is different. Since at a height of e.g. 40 mm above the burner $\langle m_+ \rangle$ is very much smaller than $\langle m_s \rangle$ and Φ_+/Φ_s is too small to be measured the profile of C_s cannot be determined from that of C_+. However, the maximum C_+ at a height of 15 mm is about two times larger than that in the corresponding C_2H_2-O_2-flame [5,7]. In this zone of the benzene flame $\langle m_s \rangle$ cannot be so much larger than $\langle m_+ \rangle$, as it is at larger heights. That Φ_+/Φ_s is not measurable means that it is smaller at least by a factor of five than that at the beginning of soot formation in C_2H_2-flames. Taking together these results leads to the conclusion that the number density of primary soot particles in the benzene flame is larger at least by a factor of ten than in the acetylene flame that forms the same amount of soot. This is in line with the much higher concentration of large cyclic hydrocarbons in benzene flames [17,19]. Thus, a larger amount of the finally formed soot is already present in the primary particles and less is formed through surface reactions from the gas phase hydrocarbons.

Ionization of Particles and its Role in the Mechanism of Soot Formation

It has been argued that molecular or radical hydrocarbon ions are the nuclei for soot particles [3,4]. The profile of the total number density and that of the positively charged soot particles in Fig. 9 shows that this cannot be true. In the zone of incipient soot formation the number density of neutral soot particles byfar outweighs that of the charged ones. In fact, the production of charged particles starts when the surface growth and the coagulation of the neutrals has already begun. Its maximum rate is reached when the particles have grown to an average mass of about $6 \cdot 10^3$ u in acetylene flames and between $5 \cdot 10^2$ and $1.5 \cdot 10^3$ in benzene flames. The mass distributions also show that this ionization takes place independently from the chemiionization of small molecules and radicals that can be traced back into the oxidation zone. Soot ions are directly formed from neutral primary soot particles and do not come from small molecular ions such as $C_3H_3^+$ by addition of unsaturated hydrocarbons as it has been postulated [4].

The mechanism of charging is still an unsolved question. The shape of the C_+-profile in C_2H_2-flames above a height of 20 mm when compared to that of the C_s-profile, suggests

that there is equilibrium ionization. In fact, this part of the C_+-profile can well be simulated by use of the Saha equation, assuming a work function for soot of 5 eV and an estimated free electron number density that is about 1/10 of C_+ [5] . If this is really a state of equilibrated ionization that is maintained while the particles grow and coagulate, it can only be reached and maintained fast enough from a state of non-equilibrium over-ionization by recombination with negative charge carriers. A purely thermal ionization process from neutral particles by collisions is by far too slow [20]. This explains the absence of charged soot particles in the even hotter benzene flame. The equilibrium calculations on C_2H_2-flames, however, cannot explain the rate of formation and the high number density of soot ions below a height of 20 mm in the flame. Therefore, the question remains how these soot ions and the ones with still smaller mass in benzene flames are formed and why the charge is no longer found on larger soot particles in benzene flames.

The charging takes place in a flame zone where there is a rapid growth of the primary soot particles through reactions with gas phase species. Moreover, this flame zone is directly behind the oxidation zone in the case of C_2H_2 flames and even partly overlaps with it in benzene flames. In C_2H_2 -flames this zone is somewhat thicker including particles up to more than $2 \cdot 10^4$ mass units whereas in benzene flames it is quite narrow producing a greater number density of primary soot particles that are smaller on the average. Here they reach masses of several hundred to a few thousand mass units before a more effective growth through coagulation is the dominant process. The thickness of the zone of strong ionization corresponds to this flame zone in both flames. It is close enough to the main reaction zone so that there are still relatively high concentrations of free hydrocarbon radicals. There also is a rapid decrease of the concentrations of polyacetylenes in the acetylene flame and an even stronger decrease of polyacetylenes and many polycyclic hydrocarbons in the benzene flame. Since the reactions of these gas phase species with the primary soot particles and their predecessors are highly exothermic, it must be assumed that the primary soot particles have a higher temperature than the surrounding gas phase. Estimations of the energy balance of small soot particles show that their main energy loss is through radiation. However, since these small particles have an emission coefficient that is much smaller than that of a black body [10], they can easily reach temperatures a few hundred degrees in excess of the surrounding gas temperature if it is assumed that polyacetylenes and large free radicals are the reactants. It is not possible to make more exact energy balance calculations since it is not yet known which gas phase species mainly contribute to the mass growth of the primary soot particles and what the individual reaction rates and their energies of activation are. In benzene flames this process takes place with very small soot particles that still have a higher ionization potential than the larger ones formed later. Accordingly, there is a rapid decrease, after a steep maximum in the concentration of these small soot ions, through recombination of positive and negative charge carriers when the process of growth through gas phase species slows down. This rapid decrease in ionization has been measured [5,7] and takes place where the concentration of some gas phase species has fallen to very low values [17]. Since the ext phase of particle growth is dominated by coagulation which also causes recombination of charges, no large charged soot particles can be formed. The addition of the remaining very small soot ions to larger soot particles is a very slow process because of the low number densities of both kinds of species.

In acetylene flames the process of surface growth is not completed when the soot particles have reached some thousand mass units. Since the number density of primary soot particles is not as high as in benzene flames the gas phase is not swept empty of those hydrocarbons and radicals in such a short time as in benzene flames. Thus, the process of surface growth and therefore ionization continues to larger mass particles and the charged particles themselves can also grow larger by surface reactions. Since the ionization potential of these larger particles is lower, growth of particles can take up with charge recombination. This is the reason why large charged particles of about the same mass as neutral are found in acetylene flames but not in benzene flames. The formation of negatively charged particles is difficult to discuss without knowing the profile of free electron concentration in the flame. In the region of primary soot particle ionization negative ions are smaller than positive soot ions. They are probably formed through the addition of free electrons to the neutral gas phase species. However, a simultaneous formation of a positive soot ion and a smaller negative ion may also be possible. The presence of large negatively charged soot particles in acetylene flames was revealed by the glass plate method. From previous measurements with the electrostatic mass filter alone it was concluded that negative soot ions do not grow. This could only be confirmed for benzene flames but they grow in almost the same way as positive soot ions in acetylene flames.

REFERENCES

1. F.J. Weinberg; Electrical aspects of aerosol formation and control, Proc.Roy.Soc.A307, 137 (1968)
2. J. Otterbeck and K.H. Homann: Zum Einfluß elektrischer Felder auf die Rußbildung, Kurznachr.Akad.Wiss.Göttingen, Nr. 18, Vandenhoeck und Ruprecht, Göttingen 1966
3. B.L. Wersborg, A.C. Yeung, and J.B. Howard: Concentration and mass distribution of charged species in sooting flames, 15th Symp.(Internat.) on Combustion, The Combustion Institute, Pittsburgh 1975
4. H.F. Calcote: Mechanism of soot nucleation in flames, Combust.Flame, 42, 215 (1981)

5. K.H. Homann and E. Ströfer; Charged soot particles in unseeded and seeded flames, in "Soot in combustion systems and its toxic properties", ed.J. Lahaye, p. 219, Plenum Publ.Corp. New York 1983
6. B.S. Haynes, H. Jander, and H.Gg. Wagner: The effect of metal additives on the formation of soot in premixed flames, 17th Symp.(Internat.) on Combustion, p. 1365, The Combustion Institute, Pittsburgh 1979
7. E. Ströfer: Über elektrisch geladene Teilchen in rußenden Kohlenwasserstoff-Sauerstoff-Flammen, Dissertation, Technische Hochschule Darmstadt 1981
8. U.v. Pidoll; Optische Temperaturmessungen und Berechnung der Thermoionisationsprofile rußender Ethin-Sauerstoff-Flammen, Diplomarbeit, Technische Hochschule Darmstadt 1981
9. K.H. Homann: Charged particles in sooting flames, Ber.Bunsenges.Phys.Chem. 83, 738 (1979)
10. U. Bonne and H.Gg. Wagner: Untersuchung des Reaktionsablaufes in fetten Kohlenwasserstoff-Sauerstoff-Flammen, III. Optische Untersuchungen an rußenden Flammen, Ber. Bunsenges.Phys.Chem. 69, 35 (1965)
11. K.H. Homann and H.Gg. Wagner: Untersuchung des Reaktionsablaufes in fetten Kohlenwasserstoff-Sauerstoff-Flammen, II. Versuche an rußenden Acetylen-Sauerstoff-Flammen bei niedrigem Druck, Ber.Bunsenges.Phys.Chem. 69, 20 (1965)
12. K.H. Homann, W. Morgeneyer and H.Gg. Wagner; Optical measurements on carbon forming benzene-oxygen flames, Combustion Institute Europ.Symp., p. 394, Academic Press, London 1973
13. B.L. Wersborg, L.K. Fox, and J.B. Howard: Soot concentration and absorption coefficient in a low-pressure flame, Combust.Flame 24, 1 (1975)
14. N. Abuaf, J.B. Anderson, R.P. Andres, J.B. Fenn and D.R. Miller: Studies of low density supersonic jets, Rarefied Gas Dynamics, Adv.Appl.Mech.,Suppl.4, Vol. II (ed. C.L. Brundin), p.1317, Academic Press, New York 1967
15. M.H. Schwartz and R.P. Andres; Theoretical and experimental study of heavy species velocity in low density supersonic free-jets, Rarefied Gas Dynamics, 10th Symp., p. 135, ed. J.L. Potter, Progr.Astronaut.Aeronaut., Vol 51, Part I, Academic Press, New York 1977
16. K.H. Homann and H.Gg. Wagner: Some new aspects of the mechanism of carbon formation in premixed flames, 11th Symp.(Internat.) on Combustion, The Combustion Institute, Pittsburgh 1967
17. H.W. Wenz; Untersuchungen zur Bildung von höhermolekularen Kohlenwasserstoffen in brennerstabilisierten Flammen unterschiedlicher Brennstoffe und Gemischzusammensetzungen, Dissertation, Technische Hochschule Darmstadt 1983
18. B.L. Wersborg, J.B. Howard and G.C. Williams: Physical mechanisms in carbon formation in flames, 14th Symp. (Internat.) on Combustion, The Combustion Institute, Pittsburgh 1973,p. 929
19. J.D. Bittner and J.B. Howard: Pre-particle Chemistry in soot formation, in "Particulate carbon, formation during combustion" ed. D.C. Siegla and G.W. Smith, p.109, Plenum Press, New York 1981
20. D.R. Hardesty and F.J. Weinberg; Electrical control of particulate pollutants from flames, 14th Symp.(Internat.) on Combustion, p.907, The Combustion Institute, Pittsburgh 1973

ACKNOWLEDGEMENTS

We are indebted to the Deutsche Forschungsgemeinschaft and the Fonds der Chemischen Industrie for financial support of this work. This is gratefully appreciated.

AD-P003 145

FORMATION AND DESTRUCTION OF ORGANIC POLLUTANTS IN THERMAL SYSTEMS AND FLAMES

J. LAHAYE, G. PRADO and A. GARO

Centre de Recherches sur la Physico-Chimie des Surfaces Solides - C.N.R.S.
24, Avenue du Président Kennedy 68200 MULHOUSE France
and
Université de Haute-Alsace
2, rue des Frères Lumière 68093 MULHOUSE Cedex France

SUMMARY

The main pollutants formed in thermal systems are soot, cenospheres, polyaromatic hydrocarbons and cyclic molecules including heteroelements such as oxygen and nitrogen. PAH are produced through reactions between aromatic and unsaturated aliphatic structures. PAH are intermediate species in soot formation. Some PAH, however, remain in flames and can be adsorbed on soot particles. In flames, hydroxyl radicals are responsible for soot post-combustion. Some practical results on soot production in turbines are reviewed.

Burning hydrocarbons give off organic particles consisting of complex mixtures. They can be described as solid particles, on which polyaromatic molecules (hydrocarbons and molecules containing heteroelements) are adsorbed. These particles may be classified under 2 heads :
- the cenospheres : particles of a few tens of µm, mostly hollow and resulting from processes of liquid phase carbonization.
- soot, occuring as spherule aggregates of a few tens of µm, resulting from gas phase carbonization. The present lecture is only concerned with soot.

In a flame soot results from extremely rapid processes, typically in the 5-10 ms range. Its appearance is always preceded by the formation of polyaromatic hydrocarbons. In a first part, it will put forth arguments supporting the view that polyaromatic hydrocarbons are precursors of soot, and not polyacetylene.

Although no direct experimental evidence for this role of PAH in flames was ever found, many observations bear out this statement in all systems investigated, in order of increasing complexity :
- thermal systems
- laminar premixed flames
- diffusion flames.

In all these systems a PAH peak precedes soot formation. Let us review a few examples.

I. The role of polyaromatic hydrocarbons in soot formation

- Pyrolysis in the absence of oxygen

Soot particles can be formed by inert atmosphere pyrolysis of hydrocarbons, a process used in the manufacture of certain carbon blacks (thermal blacks). It, probably, also takes place inside diffusion flames, where the quantity of oxygen-containing compounds is very low. Figure 1 shows the results in the case of benzene (1).

In this system, we were able to make an accurate balance, and to prove clearly that tars (PAH_s for the most part), or at least most of them, are soot formation intermediates.

- Premixed flames

In the case of toluene flame (2), the intermediates were taken with a quartz microprobe ; a very prominent peak, corresponding to products which were extracted with methylene-chloride, appears at about 2 mm above the burner (Figure 2).

The concentration peak coincides with the appearance of a yellow brilliance, pointing to soot formation. It should be observed that, later on, the PAH concentration increases slightly with the height above the burner.

Similar peaks have been reported by others (3,4) for aliphatic and aromatic flames.

It is worthy of note, however, that in the case of aliphatic hydrocarbons the maximum is less pronounced than for aromatic hydrocarbons. In some cases no peak has been recorded (5).

- Laminar diffusion flames

Another example, demonstrating the fastness of the process and the role of PAH'S is provided by diffusion flames. In this case, because of the small size of the flame front, the characterization requires the use of optical methods, such as : laser diffusion (soot) and laser fluorescence (PAH_s).

It is, thus, possible to determine accurately the areas where these compounds are formed and destroyed. PAH_s are formed very rapidly, in an area where the temperature is only around 500°C.

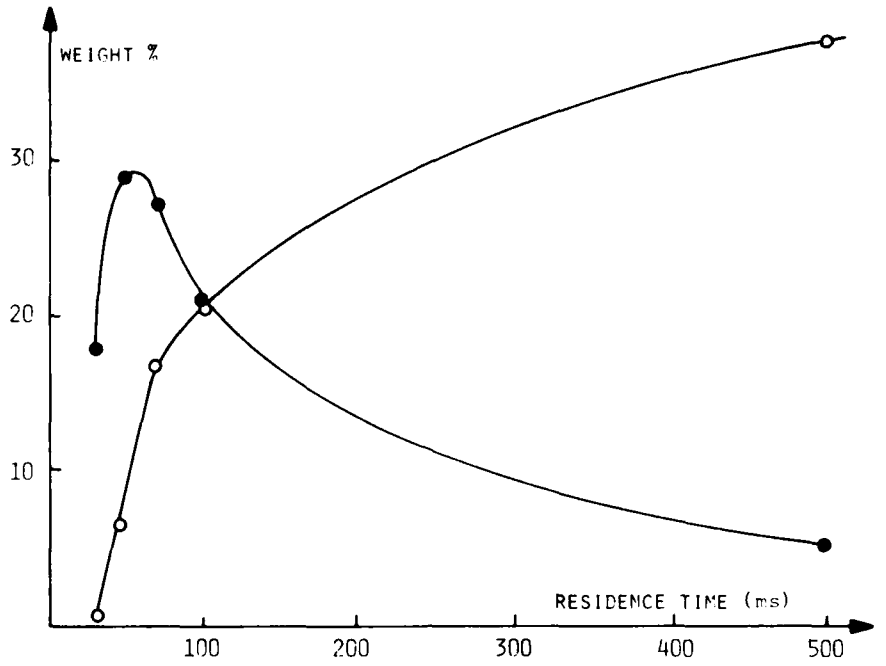


Fig. 1 - Yields of carbonaceous residue (o) and tars (●) as function of residence time. 2 % benzene in nitrogen T = 1383 (ref. 1)

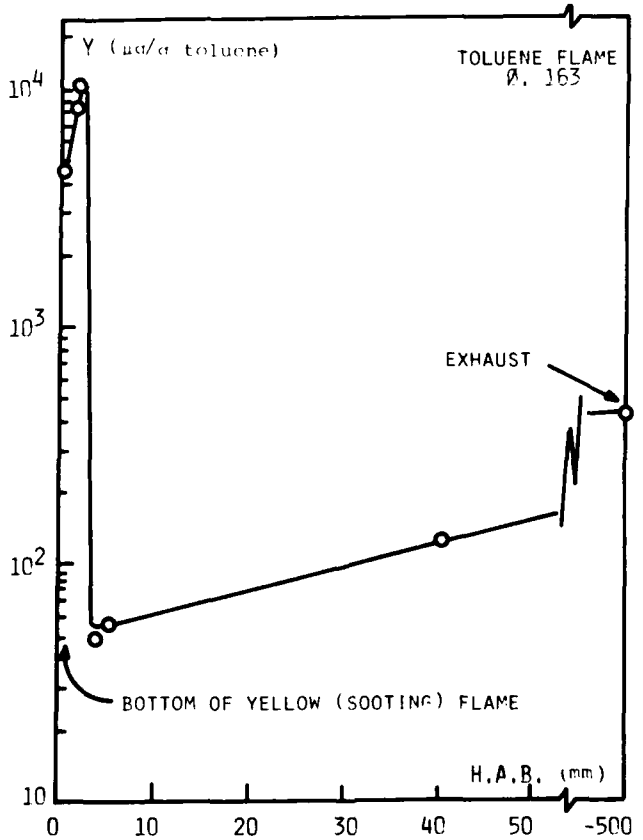


Fig. 2 - Effect of height above burner (H.A.B.) upon yield of methylene chloride soluble compounds Y (ref. 2)

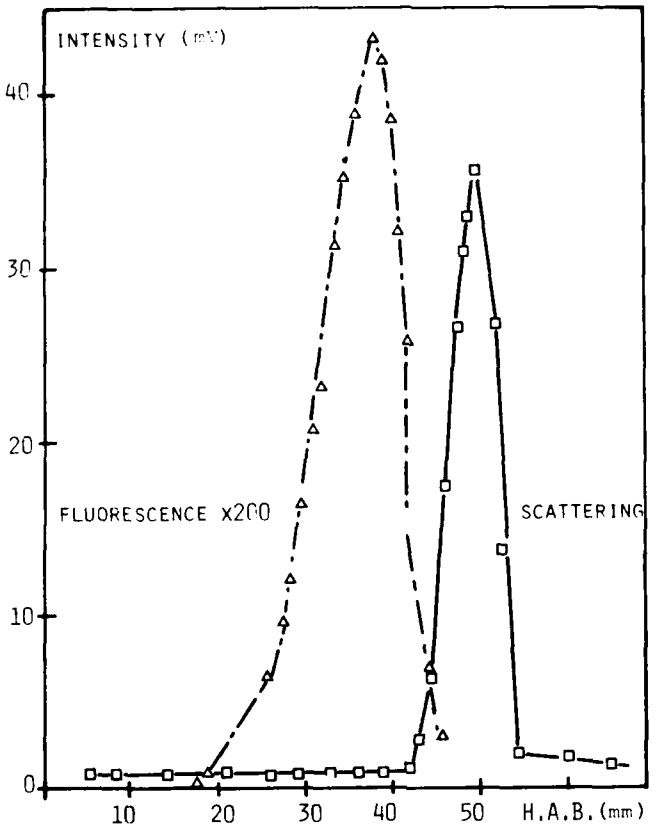


Fig. 3 - Axial profiles of scattering (6) and fluorescence (6) intensities

The PAH_s decrease is accompanied by soot formation. Similar results were reported by d'Alessio et al. (7)

It is worth mentioning turbulent diffusion flames, for which quite similar results were recorded. (8)

Clearly, in all these examples PAH_s formation takes place before soot formation, and the local PAH concentration is in process of decrease when soot formation begins.

If PAH_s are the intermediates of soot, one can understand soot formation and set up a model for its kinetics only if one understands the formation of PAH_s. Accordingly, it is worth while to sum up our knowledge of PAH_s formation, as it will permit to draw certain inferences on soot formation.

II. The mechanism of polyaromatic hydrocarbons formation

We have mentioned that PAH_s are formed in flames within a few ms. Various mechanisms have been suggested in the literature, notably :
- the cyclization of polyacetylenes.
- the direct addition of cycles in the case of aromatic hydrocarbons.
- the possible role of ions.

The state of the art will be given, the main attention being focussed on recent work by J.D. Bittner and J.B Howard (9).

1) The case of polyaromatic hydrocarbons

Data recorded by Bittner provide a clearer insight into the role of aromatic rings when soot formation takes place. The purpose of the study was to clear up the mechanism of disruption of aromatic rings, and also to investigate the role of these rings on soot and PAH_s formation in a premixed flame at low-pressure. The flame investigated was a benzene-oxygen-argon flame ; fuel equivalence ratio : 1.8 ; pressure : 20 torr.

The primary products of aromatic ring disruption are C_6H_6O and C_5H_6. The following mechanism, which, basically involves an attack of benzene by oxygen atoms, agrees with the experimental data :

$$C_6H_6 \xrightarrow{+O} C_6H_6O \xrightarrow[(CO)]{} C_5H_6 \xrightarrow[+ OH]{+H} C_5H_5 \xrightarrow[(H_2O)]{(H_2)} \cdots$$

Disruption of the aromatic ring has far-reaching implications, as it provides a means for reducing soot formation when burning aromatic fuel. Indeed, it was observed that the aromatic ring itself, and not its break-down products, accounts for the strong tendency of aromatic fuels to produce soot.

In figure 4 the relative concentration of species with a molecular weight higher than 700 amu are plotted for 2 fuel equivalence ratios : 1.8 and 2.0.

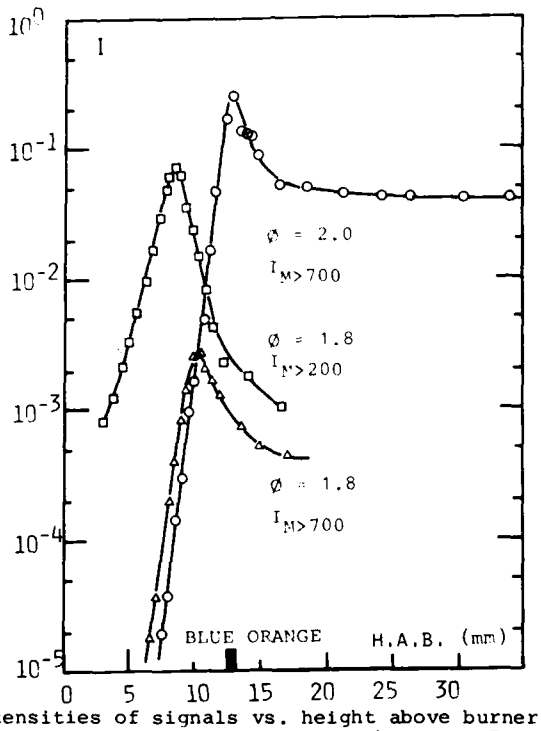


Fig. 4 Relative intensities of signals vs. height above burner (□) species larger than mass 200, $I_{M>200}$; and (Δ) species larger than mass 700, $I_{M>700}$, in near sooting (Ø = 1.8) benzene (13.5 m%) - oxygen (56.5 m%) - argon (30.0 m%) flame. (o) benzene (14.7 m%) - oxygen (55.3 m%) - argon (30.0 m%) flame. Pressure = 2.67 kPa (20 torr), cold gas velocity = 0.5 m/s for both Ø = 2.0 flames. Shaded region at 13 mm designates blue-orange boundary in sooting (Ø = 2.0) flames. (Ref. 9)

The orange brilliance, which is characteristic of soots, appears for Ø = 1.9 under these conditions. It was observed that the number of molecules with a high molecular weight increases rapidly and decreases as rapidly when soot is formed (≃ 13 mm). The maximum is 100 times larger than for a flame with no soot formation.

All the results recorded by J.D. Bittner and J.B. Howard (9) show that the role of the aromatic ring is to provide a structure making the stabilization of non-aromatic addition products more rapid than the reverse decomposition to the starting reagents.

Mass addition to the system is probably due, for the most part, to non-aromatic species, such as acetylene or vinyl acetylene (polyacetylenes are incapable of cyclizing without preliminary hydrogenation).

Of course, flame reactions are controlled by a chemistry of free radicals and soot has, furthermore, a radical character directly after being formed. It follows, therefrom, that radical mechanisms have frequently been suggested for soot and PAH_s formation.

Three conditions are required if a radical mechanism is to explain the rapid growth of the species :
- the product resulting from the addition reaction should be rapidly stabilized, to prevent the reverse decomposition.
- the radical character should either be retained or rapidly regenerated.
- the reactions should involve species at comparatively high concentrations.

Thermodynamic and kinetic facts, together with the previous criteria, make it possible to suggest a consistent mechanism (Table I and Table II).

The process starts with vinylacetylene addition to the phenyl radical, which yields naphtalene. The added vinylacetylene can cyclize through a sequence of very rapid unimolecular reactions.

The cis-trans isomerization is the slow step of this sequence. Subsequent reactions may include the formation of a benzyl-type radical by substitution of a methyl radical at the α position of the naphtalene and abstraction of one hydrogen. C_2H_2 addition to this radical leads to cyclization through a reaction of internal substitution. The process

proceeds further by substitution of a methyl, loss of hydrogen, C_2H_2 addition and unimolecular loss of hydrogen, thus yielding pyrene. As both the reactivity during the substitution by a methyl, and the number of possible reactive sites increase with the size of the molecule, one arrives at an autocatalytic process leading to soot formation. (9)

In this mechanism, the growth kinetics depends on the concentrations of $CH_3^{\cdot}$, C_2H_2, H and OH. This accounts for the marked tendency of alkylated aromatics to soot formation. For example :
- toluene produces soot at a lower fuel equivalence ratio than benzene in a premixed flame. (19)
- toluene produces soot at a lower flow-rate than benzene in a laminar diffusion flame (11,12)
- during acetylene pyrolysis, the efficiencies of the following molecules in soot formation increase in the sequence :
Benzene < naphtalene < toluene < α-methyl-naphtalene < anthracene << methylanthracene.(13)
- the limits of soot emission in a perfectly stirred combustor are as follows :
toluene (1.39) > xylenes (1.3) > α-methylnaphtalene (1.21).(14)

2) The case of aliphatic hydrocarbons

If one compares the structures of a benzene flame (Ø 1.8, limit of soot formation) and an acetylene flame (Ø = 3.0, soot formation), it is apparent that (Figure 5) in both flames, PAH_s with comparative low masses ($C_{14}H_{10}$ for benzene, $C_{14}H_8$ for acetylene) exhibit a maximum in the presence of benzene, near the maximum of C_4H_4 and before the maximum of higher masses.

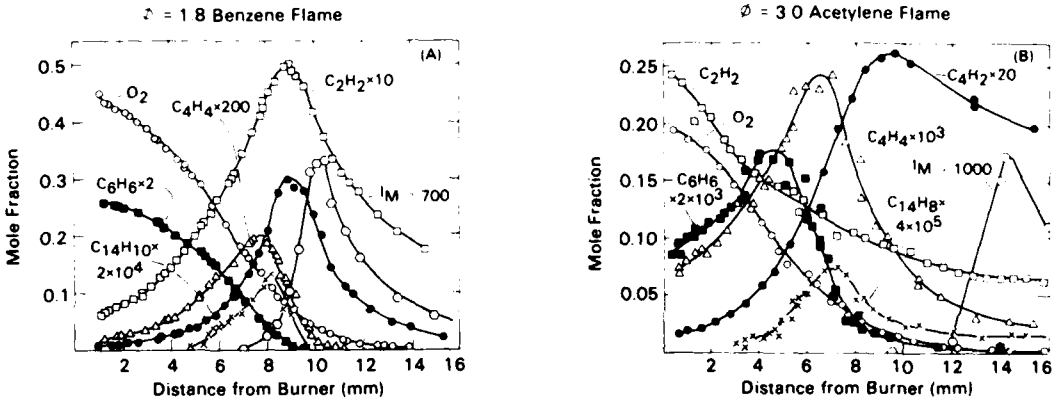


Fig. 5 - Mole fractions of several species and high mass signals ($I_{M>m}$, scale arbitrary) vs. distance from the burner in (A) a near-sooting (Ø = 1.8) benzene (13.5 mol%) oxygen (56.5 mol%) - argon (30.0 mol%) flame and (B) a sooting (Ø = 3.0) acetylene (52.9 mol%) - oxygen (44.1 mol%) - argon (3.0 mol%) flame. Pressure = 2.67 kPa (20 torr), cold gas velocity = 0.5 m/s for both flames (Ref. 9)

This fact suggests that the mechanisms occuring in aliphatic flames bear a close relationship to those in aromatic flames.

The preceding mechanisms provide information on the first stages of the mechanism of soot formation, which produce comparatively large amounts of bulky PAH molecules. The transition from these molecules to spherical soot particles and then to aggregates, can be explained by thermodynamical reasonings of collisions between these species.

III. Physical mechanisms of soot growth (15)

Taken as a whole, we are in the presence of a carbonaceous "aerosol" placed in a hot and reactive surrounding. We will characterize this aerosol by the number of particles N, their diameter d and their volume fraction f_v. On the assumption that the particles are spherical, $f_v = \pi/6\ N\ d^3$

Two stages of aerosol formation are taken into account :
- the appearance of the first small particles (nucleation)
- their subsequent growth, which is the result of two separate processes :
  * the coagulation
  * the surface growth.

The growth of the particles can, therefore, be described as follows :

$$d\ Ln\ N = \frac{1}{3}\ d\ Ln\ f_v - \frac{1}{3}\ d\ Ln\ N$$

The nucleation-growth transition does not take place abruptly and, even, is not easily defined. In actual practice, however, it is apparent that the formation of new particles takes place in a restricted region, close to the reaction zone, where the temperature and ionic and radical concentrations are highest.

In other words, the nucleation and growth zones are spatially separate.

Many particles are formed when nucleation takes place ($N \simeq 10^{18}$ m^{-3}, $\dot{N} = 10^{21}$ m^{-3} sec^{-1}), but they are very small ($\simeq$ 1.5 nm) and make only a very minor contribution to the total amount of soot formed ($f_v = 10^{-9}$). In most cases this f_v is negligible in comparison with the mass formed, and surface growth determined for the most part the amount of soot formed.

From a phenomenological view-point, the process can be summarized as follows :

	N	f_v
source sink	nucleation coagulation	surface growth oxidation

Let us take a quantitative survey of these processes.

1) The coagulation

The time-dependence of the number of particles, N, is expressed by the classical coagulation theory :

$$\frac{dN}{dt} = \dot{N}_w - \dot{N}_c$$

$\dot{N}_w$: nucleation kinetics $\quad - \quad \dot{N}_c$: coagulation kinetics.

Very rapidly, the process is controlled only by $\dot{N}_c$ and : $\frac{dN}{dt} = - K (D) N^2$

For neutral particles :

$$\frac{dN}{dt} = - \frac{6}{5} k_{th} f_v^{1/6} N^{11/6}$$

where : $k_{th} = \frac{5}{12} (\frac{3}{4\pi})^{1/6} (\frac{6 KT}{\rho})^{1/2} G.\alpha$

f_v : particulate volume fraction
ρ : density of the particles
G : a factor which takes into account the inter-particle dispersion forces (can be expected to have a value of about 2 for spherical particles).
α : a function of the particle size distribution.

Upon integration at constant volume fraction and temperature

$$N = N_o \left[1 + 9.03 \times 10^{-13} N_o^{5/6} T^{1/2} f_v^{1/6} t\right]^{-6/5}$$

where N_o : the initial particle number density
N^o : the particle number density at time t

for large enough values of N_o ($>10^8/m^3$) the equation can be reduced to :

$$N = 2.84 \times 10^{14} \left[T^{1/2} f_v^{1/6} t\right]^{-6/5}$$

In these computations, the aggregate is treated as a sphere of equal volume.

This relation predicts that N is independent of N_o and weakly dependent on T and f_v. This has been verified on premixed flames by different investigators, burning different fuels : methane, ethylene, benzene ... (5, 16, 17)

These results will be merely illustrate by a single system : a propane-oxygen premixed flame, burning at atmospheric pressure.(18)

The quantities measured include the soot volume fraction, the size and the number of aggregates and spherules. These quantities were measured by laser scattering and electron microscopy.

These curves are representative of practically all the systems investigated : N, the number of agglomerates, reaches a maximum at the very beginning of the process, while f_v is comparatively low. The number of spherules is little affected.

A comparison of the results with the theoretical predictions is provided by the figure 7.

A good agreement is obtained, except at the end of the process, probably because the sticking coefficient for the collisions is smaller than one and/or the aggregates become too large and asymetrical.

As predicted by the theory, N is significantly affected neither by the fuel equivalence ratio nor by the temperature.

It should be clearly understood that these parameters affect the amount of soot formed, f_v and, therefore, the size of the aggregates.

In a premixed flame :

- f_v and D increase with increasing ϕ
- f_v and D decrease with increasing temperature.

The problem which claims the attention of the practical man is the amount of soot given off by an actual combustor. We have just mentioned that this amount is controlled by the surface growth of the particles and, therefore, it is most important to understand this growth and find its equation.

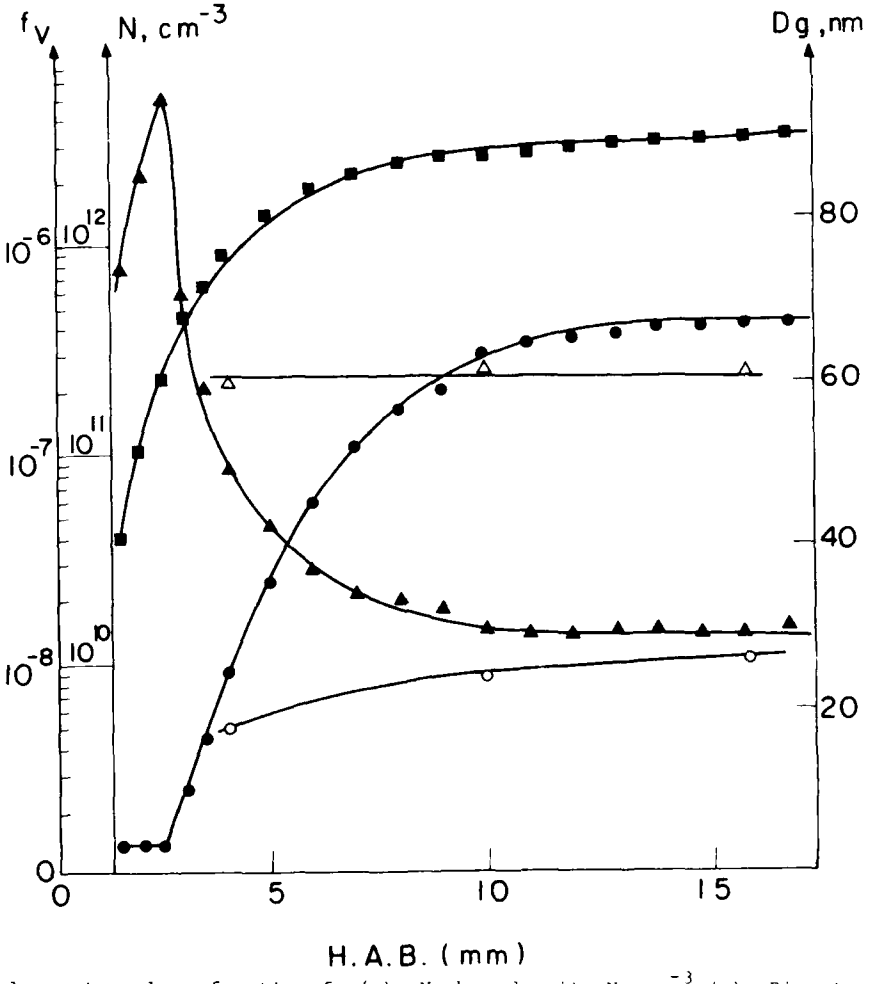


Fig. 6 - Agglomerate volume fraction f_v (■). Number density N, cm^{-3} (▲). Diameter D_g, nm (●). Spherical units number density, N, cm^{-3} (△). Diameter D, nm (○), as function of height above burner (H.A.B., nm). Propane/oxygen flame. Fuel equivalence ratio 2.9 cold gas velocity = 5.5 cm/s (Ref. 18)

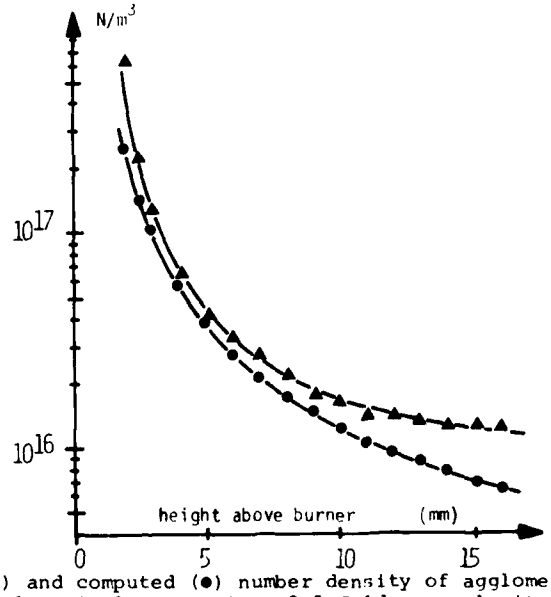


Fig. 7 - Experimental (▲) and computed (●) number density of agglomerates (N, cm^{-3}). Propane/oxygen flame. Fuel equivalence ratio = 2.5 Cold gas velocity = 5.5 cm/s (Ref. 18)

2) Surface growth of the particles

This phenomenon is, at present, not adequately understood. The nature of the species responsible for carbon deposition on prime soot particles remains a much debated question : polyacetylenes, PAH_s, acetylene, methane ... ?

A valuable review of the present state of knowledge has been provided by Wagner in in a recent paper (19).
The quantities of soot formed in a welltuned combustor (diesel engine, burner ...) are of the order of 10^{-7} g of soot/cm^3, contained in about 10^9 particles. The reaction times are of the order of 10 ms.

Hence, a surface growth rate of $\sim 10^{-5}$ g s^{-1} cm^{-3} or 10^{-6} mole cm^{-3} s^{-1}. Tesner, Howard and others determined the kinetics of soot growth on surfaces and proposed kinetic relations, for example :

$7.86 \times 10^2 \exp -65/RT$ g cm^{-2} s^{-1} bar^{-1} for CH_4 (970-1280 K)

$3.3 \times 10^2 \exp -55/RT$ g cm^{-2} s^{-1} bar^{-1} for C_6H_6 (1000-1250 K).

It should be observed that the times are smaller than those recorded with flames.

The great bulk of the data were measured on flat flames by optical methods. Wagner correlated these data by plotting $\frac{df_v}{dt} = f(f_v)$

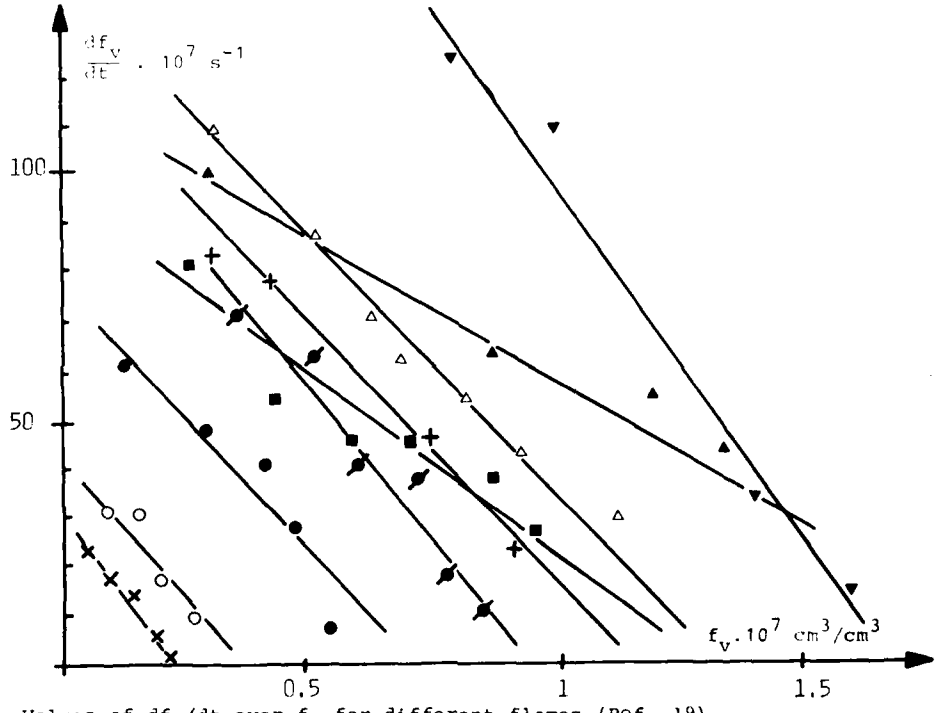


Fig. 8 - Values of df_v/dt over f_v for different flames (Ref. 19)

- △ C_2H_4-air C/O = 0.76 Haynes
- ○ C_6H_6-air C/O = 0.71 Haynes
- + C_6H_6-air C/O = 0.73 Haynes
- × C_6H_6-air [1] C/O = 0.75 Haynes
- ■ C_3H_8-O_2 C/O = 0.63 Prado
- ▲ C_3H_8-O_2 [1] C/O = 0.71 Prado
- ● C_3H_8-O_2 [2] C/O = 0.83 Prado
- ◪ C_6H_6-air C/O = 0.74 Baumgartner, T_o = 475 K
- ▼ C_2H_4-air C/O = 0.76 Baumgartner with 0.24 % $C_{10}H_8$

1) axis reduced 10 times
2) axis reduced 100 times

One obtains linear relations of the form :

$$\frac{df_v}{dt} = K f_M (1 - f_v/f_M) \qquad f_M = \int (\frac{df_v}{dt}) dt \text{ maximum value function}$$

K : apparent rate constant

$K = - \Delta (\frac{df}{dt}) / \Delta f_v \simeq 100\ s^{-1}$

An extrapolation towards zero values of df/dt gives f_M.

The value of K is little affected by additives. Only naphtalene-air flames seem to have a larger K, of the order of 150 s^{-1}.

In the same way, K is little affected by T (slight increase). In other words, the

knowledge of f_M makes it possible to set up a model of the surface growth, as a first approximation.

All the research work we thus surveyed leads to a satisfactory, though approximate description of soot formation. It should be noted, however, that part of the soot produced undergoes post-oxidation and, therefore, it is important to get an insight into the mechanisms of this oxidation.

V. Oxidation of carbon black particles

The oxidation or post-oxidation of soot [20] in flames has only been dealt with in a restricted number of rigorous investigations.

Let us go back, first, to fundamental features of the crystalline structure of soot, in keeping with their reactivity. The structure of soot is closely related to that of graphite. The latter consists of parallel planes. To a first approximation, there are two types of carbon atoms : the basal and the outer boundary atoms.

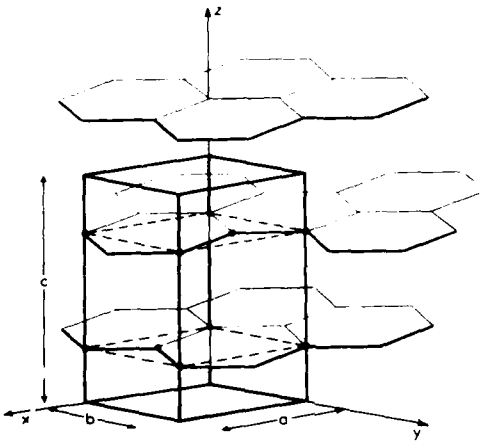


Fig. 9 - Crystalline structure of graphite.

In soots, the graphitic structure has become degenerate ; their stackings are disordered by random rotation in their planes. The planes are of small size, and there are many imperfections so that, in comparison with the case of graphite the outer boundary atoms are numerous with respect to the atoms of the basal planes. It is generally accepted that, precluding reagents becoming intercalated between the graphitic layers, the higher the ratio $\frac{\text{boundary atoms}}{\text{basal plane atoms}}$, the easier a carbonaceous material is oxided. Thus, Laine et al. [21] showed that at 300°C, in 0.5 torr oxygen, the oxidation of boundary atoms is 2000 times higher than for basal plane atoms.

This kinetic information, together with the phenomenon of imperfection annealing under the influence of the temperature, and resulting in the transformation of boundary atoms into basal plane atoms, make it possible to explain the following curve, which was proposed more thar 20 years ago.

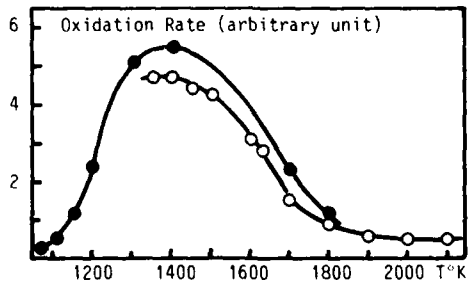


Fig. 10 - Reaction rate R (arbitrary unit) of $C+O_2$ as function of temperature (two curves corresponding to different pressures of filaments) (Ref. 22)

At low oxygen pressure, the oxidation rate of a non graphitized carbon filament passes through a maximum : a competition takes place between the increase in oxidation rate of the carbon sites and the growth of the number of boundary atoms, due to the healing process. The maximum oxidation rate is situated arour 1400 K ; of course, it depends on the type of material.

A last general remark is that the differenc in reactivity of the carbon atoms may give rise to a phenomenon of holl wing out of the carbon materials during the oxidation.

Let us consider two important cases of carbon oxidation :

1) oxidation by oxygen (in the absence of flame) of carbonaceous material.
2) soot oxidation in a methane/oxygen flame.

1) Oxidation of carbonaceous material

Nagle and Strickland-Constable (23) investigated the oxidation of artificial carbon, graphite and pyrographite by oxygen at a pressure of about 20 kPa. Above 2000 K, the oxidation rate becomes reasonably constant.

The investigators explained their results by assuming the existence of two reaction sites A and B, giving rise to the following reactions :

$$A + O_2 \rightarrow A + 2\ CO$$

$$B + O_2 \rightarrow B + 2\ CO$$

$$A \rightarrow B$$

Taking into account the data obtained later on by Laine et al, and which we mentioned in the foregoing, it would seem that A corresponds to the boundary atoms and B to those of the basal planes. The quantitative kinetic explanation of Nagle would fit with our qualitative explanation of research work done by Boulangier, Duval and Letort.

The investigation by Nagle and Strickland-Constable, which is an outstanding one because of its methodology and its conclusions, seems to have impeded for nearly 10 years the development of factual research-work on the carbon oxidation in flames.

2) Soot oxidation in flames

Nagle et al. have been so prominent in their day that almost all research work dealing with oxidation in flames was conducted and processed with the a priori conception that the oxygen molecule was the main oxidizing agent. Studying the burning of soot obtained by partial combustion of a C_2H_2, O_2 and Ar mixture, Fenimore and Jones (24) found out in 1967 that the rate of soot oxidation is little dependent on the concentration of molecular oxygen. It seems that they were first to consider the OH radical as the main oxidizing agent of soot in flames.

It is not until 1980 that significant headway was made, with the remarkable results achieved by Neoh, Howard and Sarofim (25,26), who demonstrated the role played by OH radicals. In this investigation, the soot was produced by burning a methane-oxygen mixture with a fuel equivalence ratio of 2.1. After partial cooling, the soot was transferred to a second chamber in the presence of oxygen and gases from the primary combustion. The gaseous non-radical constituents were sampled and subjected to chromatographic analysis ; the concentrations of hydrogen radicals were measured by the Li/LiOH method. The concentrations of OH and O radicals were computed by using the H, H_2O and H_2 equilibra in rich flames and the H, H_2O and O_2 equilibra in poor flames.

The rate of soot combustion was followed by measuring the particle size and number by means of an optical method, similar to that which we used to investigate the mechanism of soot formation.

Basically, the method used to determine the nature of the main oxidizing agent is very simple. For each species the coefficient of collision γ_i was computed from the values of the combustion rates, using the probability of removing a carbon atom by collision between a soot particle and an oxidizing species.

For a species to be favored, the variations of the efficiency coefficient in the flames must be unimportant (except in regions with a strong thermal gradient), and the values recorded reasonable, so that species with γ_i values higher than 1 are precluded.

Among the many curves recorded by Neoh et al, we selected those corresponding to the O_2 and OH species (Figure 11). γO_2 varies of two orders of magnitude and, in the experimental conditions, O_2 was not favored as an oxidizing agent of soots. γ_{OH}, (Figure 12), exhibits a comparatively constant value, between 0.1 and 0.3.

It is apparent from the data shown in the figures 11 and 12, that the OH radical is the main oxidizing agent of carbon in flames. However, when the conditions are such that the OH concentration is very low in comparison with that of molecular oxygen, the latter species may become an important oxidizing agent.

It should be noted, that the preceding results do not provide any information on the effect of the crystalline structure and the porous structure of the carbonaceous material on its oxidation rate and its properties as a final material on partial oxidation.

For commercial carbon blacks prepared according to a flame method (furnace type blacks), the coherence distance of X rays in the direction of the crystallographic axis parallel to the graphite planes, is (27) between 12 and 20 Å. A rough calculation shows that the ratio of the number of boundary atoms over the number of basalplane atoms is comprised between 0.33 and 0.20.

Since the value of γ_{OH} and the relative proportion of boundary atoms are very comparable, it may be asked whether, for a given soot, the value of γ_{OH} is not related to the crystal structure of the solid, which would be in keeping with data obtained at lower temperature.

To sum up, it seems well established that the OH radical is the main oxidizing agent of soots in flames. The oxidation mechanisms and the influence of the properties of the carbonaceous solid on the combustion kinetics have still not been elaborated.

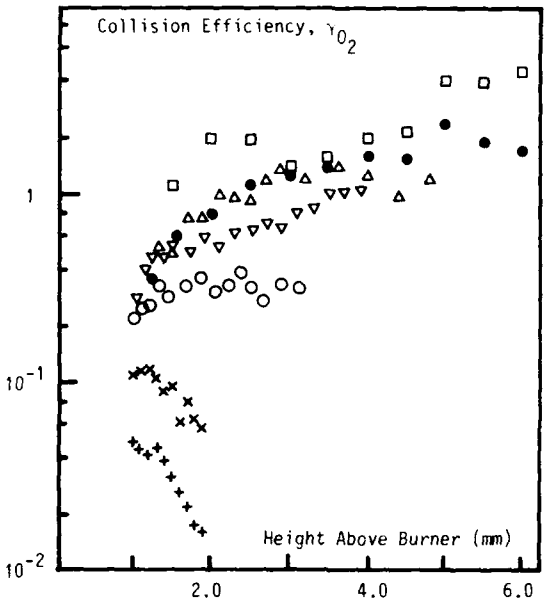


Fig. 11 - Collision efficiency γ_{O_2} versus height above burner h for different fuel equivalence ratios : +0.85, x0.95, o1.05, ●1.10, □1.15, △1.15 (+ CH_4), ▽1.15 (+ CH_4 + CO_2) (Ref.26)

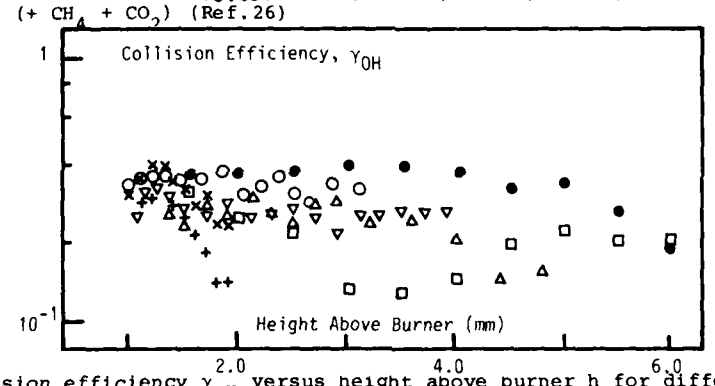


Fig. 12 - Collision efficiency γ_{OH} versus height above burner h for different fuel equivalence ratios : +0.85, x0.95, o1.05, ●1.10, □1.15, △1.15 (+ CH_4), ▽1.15 (+ CH_4 + CO_2) (Ref. 26)

V. Soot in gas turbine combustor

A best understanding of soot formation in gas turbine combustors is becoming increasingly important for civil and military utilizations.

A side from the environmental impact, and possible identification of military aircraft, a great problem about soot in gas turbine engines is the effect it has on combustor performances and liner durability.

1) Generalities

In a gas turbine combustor (28), a spray of fuel burns in the air with a turbulent diffusion flame. Experimental results (29) suggest that fuel droplets, Sauter mean diameter of which ranged between 40-120 µm, have little effect on the combustion efficiency ; in the present brief survey, the diameter of the droplets will not be considered as an important parameter of the system during soot formation. In a gas turbine, as the combustion gas leaves the primary zone, the secondary air cools down the combustion gases to the required turbine inlet temperature. In the early stages of combustion the major species are carbon monoxide, hydrogen and water. Soot forms as a nonequilibrium product. The complete burning of soot requires a high degree of homogeneity of mixing with oxygen, and a temperature above 1300 K to give rapid reaction. In the intermediate and dilution zones the temperature will generally range from 2000 K to 1000 K. At a combustion temperature within this range, the residence time in the combustor is sufficient to consume carbon particles in the flame (29). Thus, a large proportion of carbon produced in the primary zone will be removed in the secondary and even in the dilution zone.

2) Parameters affecting soot formation

Five main parameters are usually mentioned in the literature ; namely fuel equivalence ratio, pressure, temperature, turbulence and fuel type.

It is quite difficult, however, to precise the influence of a given parameter because it cannot be modified independently. The following observations have been made by Najjar et al (28).

- Equivalence ratio (Ø)

With rich mixtures there are considerable differences among the various fuels with respect to the critical temperature at which the rate of the cracking reaction exceeds that of oxidation. This temperature is considerably lower for heavy fuels than for lighter ones. Poor mixing and excessive fuel-rich pockets within the primary zone of the combustor result in soot formation. Hence, it is the local equivalence ratio due to the heterogeneous combustion rather than the average equivalence ratio that is the significant factor in the soot formation process.

- Pressure

The increase in soot formation with pressure results from several effects :

. the penetration distance is inversely proportional to the cube root of the gas pressure.
. the extension of the rich limit of flammability, with combustion possibility at very rich equivalence ratios.
. the increase of the fuel evaporation temperature, the pressure effect on the rate of cracking being proportional to $P^{1-1.6}$ whereas on the rate of vaporization to $p^{-0.2-0.6}$.
. at high pressure the combustion process is normally more rapid, thus the time allowed for the fuel to seek air for combustion is reduced.
. the reduction of the spray angle with an increase of the diameter of the droplets. However, higher gas pressures are associated with higher injection pressures which reduce the Sauter mean diameter.

- Temperature

The flame is determined mainly by the inlet temperature, the equivalence ratio and the combustion efficiency. Figure 13 (31) shows the relation between the flame temperature (soot temperature measured by the Kurlbaum technique) and the relative soot concentration (measured by flame opacity technique), in the primary zone of the combustor.

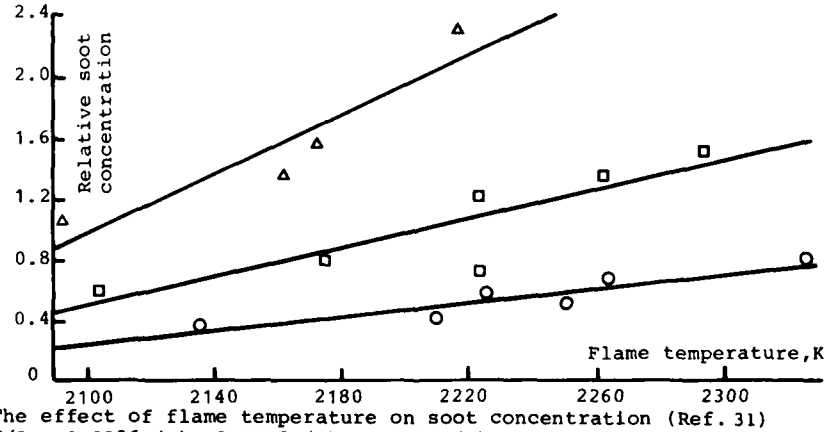


Fig. 13 - The effect of flame temperature on soot concentration (Ref. 31)
F/A : 0.0096 (o), 0.0108 (□), 0.0136 (△).

Clearly, the soot concentration increases with both flame temperature and fuel/air ratio. The same authors verify the influence of burner inlet temperature on flame temperature.

- Turbulence

Becker (32) demonstrated that the soot concentration field is mixing controlled, and no pronounced effect of Reynolds number on soot formation in the turbulent flames could be observed. However, soot increases with a change from a turbulent to a laminar condition.

- Fuel type

The formation of soot is influenced by the following effects of fuel properties : viscosity on atomization ; volatility, on evaporation ; and thermal stability on the tendency to crack.

Chemically, the fuel soot-forming propensity increases with aromatic content, carbon/hydrogen ratio and the free energy of formation which is correlated to the structure of fuel.

Future fuel may content less hydrogen, more polycyclic aromatics, nitrogen (33) and sulphur and have a higher final boiling point. These evolutions will increase soot formation.

. Correlation parameter.

For a given type of turbine, there is a correlation parameter between the H/C composition of fuel and the radiation of the reacting mixture.

As an example, Naegeli (31) shows correlation of flame radiation with H/C ratio for different fuels derived from oil shale, coal, tar sands, emulsions containing both water and alcohols, and solutions of alcohols and jet fuel (Figure 14).

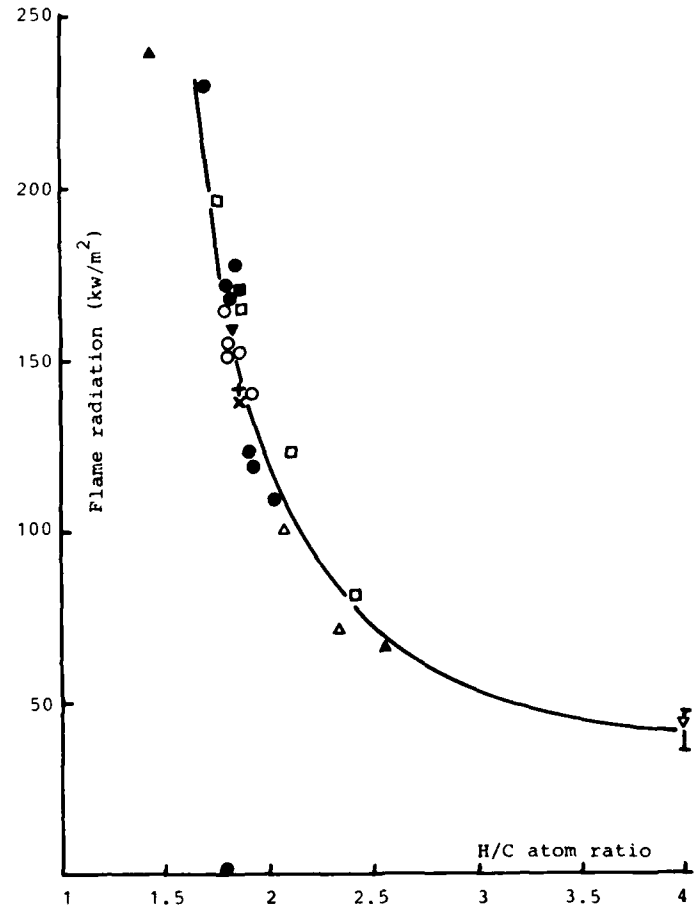


Fig. 14 - Effect of hydrogen to carbon ratio on flame radiation (Ref. 31)
Fuel identification :

- ● Jet fuel/aromatic blends
- + JP-5 (Shale oil)
- ■ JP-5 (Coal)
- × JP-5 (Tar sands)
- ○ JP-5DFM/Gasoline Blends
- ▾ JP-5 + Decaline
- □ Petroleum emulsions
- △ Syncrude emulsions
- ▲ Aromatics/Methanol blends
- ▽ Methanol

This correlation, e.g. radiation vs H/C ratio, is generally assumed to be a linear function of the H/C ratio if the range of fuel hydrogen contents is not too large (34). The slope (figure 15) dR/d(H/C) of the line is usually defined as the sensitivity to hydrogen content. However, it is often more useful to compare the relative, or percentage, change in radiation with the H/C ratio by using a normalized sensitivity given by $S = \frac{(1/R)dR}{d(H/C)}$ (slope of the line Ln(R) versus (H/C) ratio).

This factor, which is analogous to Jackson and Blazowski's normalized liner temperature parameter, can be used to compare the relative sensitivities of different engines or the same engine at different operating conditions.

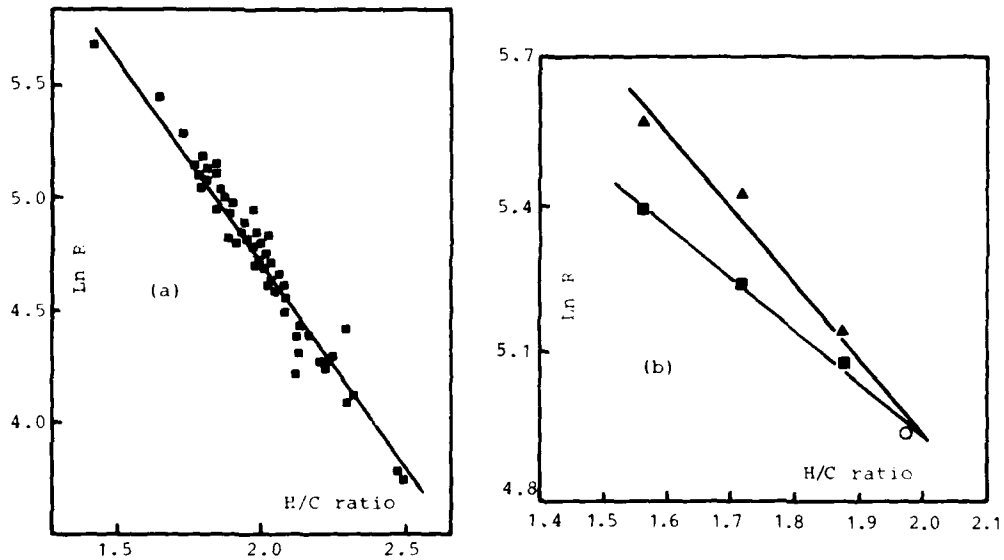


Fig. 15 - Correlations of flame radiation with H/C ratio (Ref. 33)
(Different varieties of fuels)
a) T-63 Turbine Combustion b) Phillips Research Combustion

The effects of operating parameters (inlet temperature T, gas density ρ, fuel/air ratio, and gas velocity V) on the plot of sensitivity (S_1) of the sooting tendency versus H/C ratio for fuels containing monocyclic aromatics are shown on figure 16a. The same diagram is plotted figure 16b for fuels containing polycyclic aromatics (S_3).

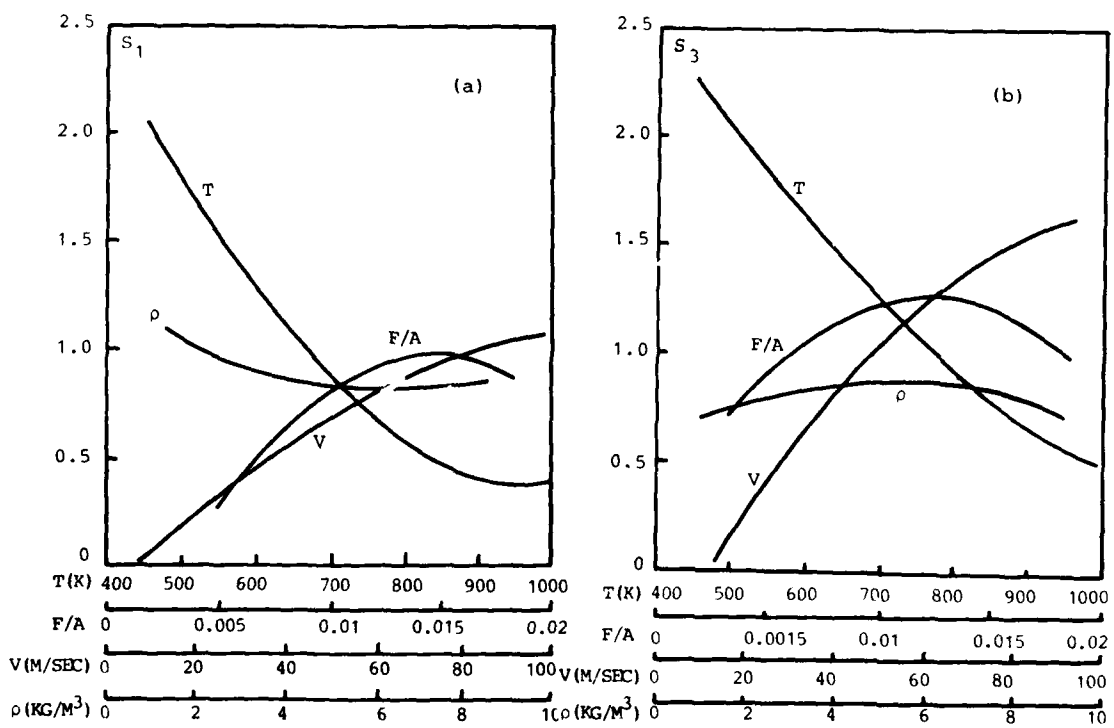


Fig. 16 - Effects of operating parameters on the sensitivity of the sooting tendency to the H/C ratio for fuel containing monocyclic (a) and polycyclic (b) aromatics.

The correlations show that the sensitivities of flame radiation to H/C ratio decrease rapidly with increased burner inlet temperatures, S_1 decreases faster than S_3. The sensitivities increase rapidly with velocity V, S_3 increased faster than S_1. The F/A ratio had a greater effect on S_1 than S_3 ; changes in burner inlet gas density had very little effect on the sensitivities.

. The increase in soot formation caused by polycyclic aromatics was directly proportional to the aromatic carbon in the fuel.

CONCLUSIONS

. Soot formation, in gas turbine combustors are dependent on operating conditions. The relative importance of soot formation and oxidation steps varies with inlet air temperature, gas velocity and fuel/air ratio.
. The characteristic times for fuel pyrolysis and mixing seem to be comparable. The pyrolysis reactions are rate controlling in the formation of soot precursors while the oxidation is limited by the mixing rate. THe importance of the H/C ratio as a parameter in the oxidation process is linked to the oxidizer character of OH radical on soot particles as previously seen.

Table I : Radical mechanism of P.A.H. formation

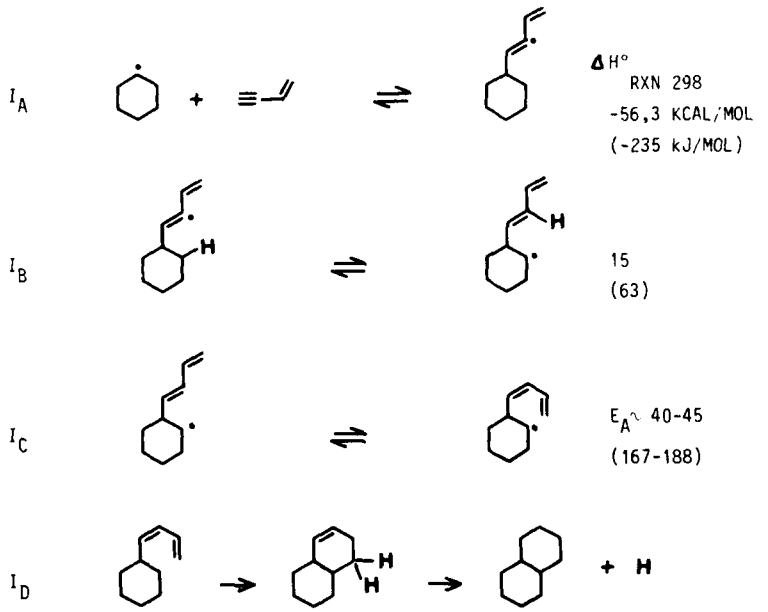
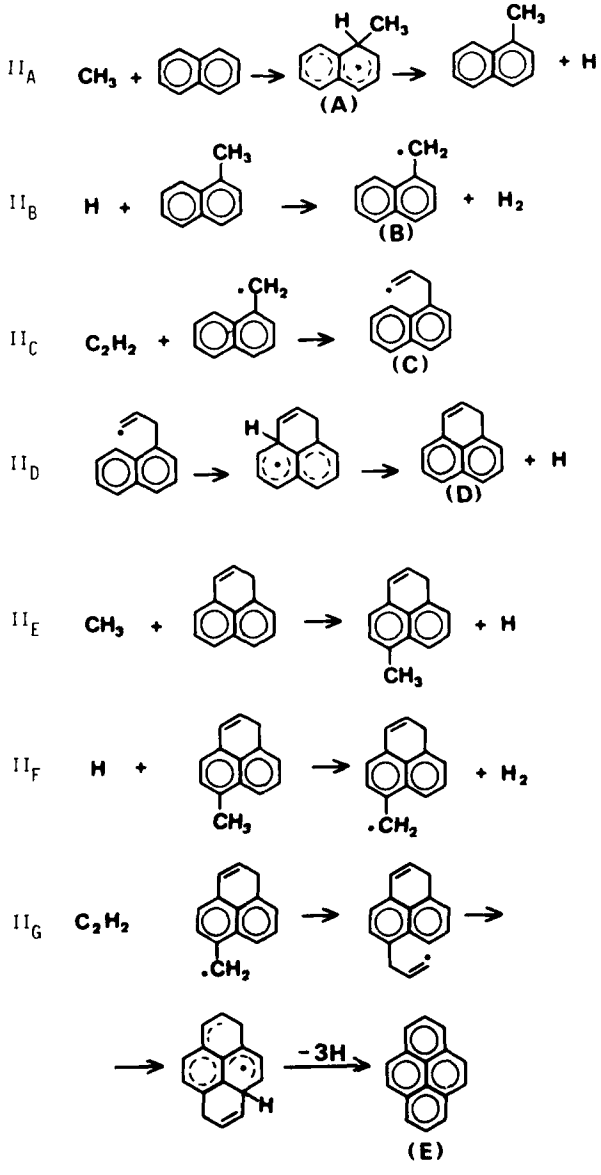


Table II : Radical mechanism of P.A.H. formation



REFERENCES

1) G. PRADO
"Mécanisme de formation des particules de noir de carbone lors de la décomposition thermique de benzène"
Doctorate of Science Thesis, Strasbourg, France, (1972)

2) Center for Health Effects of Fossil Fuel Utilization.
2nd Annual Progress Report, Massachusetts Institute of Technology, (1980)

3) B.D. CRITTENDEN and R. LONG
Combustion and Flame, 20, 359, (1973)

4) H. WENZ
Bestimmung der Konzentrationsprofile. Polyzyklischer Aromatischer Kohlenwasserstoffe an einer Russendent Propan-Sauerstoff-Flamme.
Diplomarbeit - Technischer Hochschule Darmstadt, (1978)

5) B.S. HAYNES, H. JANDER and H. Gg. WAGNER
Ber. Bunsenges. Phys. Chem., vol. 84, p. 585 (1980)

6) G. PRADO, A. GARO, J. LAHAYE and A. SAROFIM
(to be published)

7) A. D'ALESSIO
personal communication

8) G. PRADO, M.L. LEE, R.A. HITES, D.P. HOULT and J.B. HOWARD
Sixteenth Symposium (International) on Combustion,
The Combustion Institute, Pittsburg, p. 649, (1977)

9) J.D. BITTNER and J.B. HOWARD
. 18th Symposium (International) on Combustion
(The Combustion Institute, Pittsburgh Pa), p. 1105 (1981)

. Particulate Carbon - Formation during Combustion.
D.C. Siegla and G.W. Smith editors
Plenum Press, New-York - London, (1981)

. Soot in Combustion Systems and its Toxic Properties.
J. Lahaye and G. Prado editors
Plenum Press, New-York - London, (1983)

10) J.C. STREET and S. THOMAS
Fuel 34, 4, (1955)

11) R.L. SCHALLA and G.E. Mc DONALD
Ind. and Eng. Chem. 45, 1497 (1953)

12) R.A. HUNT
Ind. and Eng. Chem. 45, 602 (1953)

13) J.D. FRAZEE and R.C. ANDERSON
Proc. Third Conf. on Carbon, Pergamon, p. 405, (1959)

14) W.S. BLAZOWSKI, R.B. EDELMAN and P.T. HARSHA
"Fundamental Characterization of Alternate Fuel Effects in Continuous Combustion Systems"
Technical Progress Report for Department of Energy
Contract EC-77-C-03-1543, September 1978

15) G. PRADO, J. LAHAYE and B.S. HAYNES
"Soot Particle Nucleation and Agglomeration" in "Soot in Combustion Systems and its Toxic Properties",
J. Lahaye and G. Prado editors
N.A.T.O. Conference Series, Series VI : Materials Science, Plenum Press, p. 145, (1983)

16) A. D'ALESSIO, A. DI LORENZO, A. BORGHESE, F. BERETTA and S. MASI
Sixteenth Symposium (Intern.) on Combustion, the Combustion Institute, Pittsburg, p. 695, (1977)

17) B.S. HAYNES, H. JANDER and H. Gg. WAGNER
Seventeenth Symposium (Intern.) on Combustion
The Combustion Institute, Pittsburg, p. 1365, (1979)

18) G. PRADO, I.J. JAGODA, K. NEOH and J. LAHAYE
Eighteenth Symposium (Intern.) on Combustion,
The Combustion Institute, Pittsburg, p. 1127, (1981)

19) H. Gg. WAGNER
"Mass Growth of Soot" in "Soot in Combustion Systems and its Toxic Properties"
J. Lahaye and G. Prado editors
N.A.T.O. Conference Series, Series VI, Materials Science, Plenum Press, p. 171, (1983)

20) J.B. DONNET and J. LAHAYE
"Burnout of Soot Particles" in "Soot in Combustion Systems and its Toxic Properties"
J. Lahaye and G. Prado editors
N.A.T.O. Conference Series, Series VI, Materials Science, Plenum Press, P. 259, (1983)

21) N.R. LAINE, F.J. VASTOLA and P.L. WALKER Jr
J. Phys. Chem. 67, 2030, (1963)

22) M. LETORT, L. BONNETAIN, G. HOYNANT and H. GUERIN
"Les Carbones", A. Pacault Ed., Masson et Cie, 234, (1965)

23) J. NAGLE and R.F. STRICKLAND-CONSTABLE,
Ext. Abst. 5th Conf. on Carbon, 1, 154, (1963)

24) C.P. FENIMORE and G.W. JONES,
J. Phys. Chem. 71, 593 (1967)

25) K.G. NEOH
"Soot Burnout in Flames", Sc. D. Thesis, Department of Chemical Engineering,
Massachusetts Institute of Technology (October 1980)

26) K.G. NEOH, J.B. HOWARD and A.F. SAROFIM,
Soot Oxidation in Flames, in "Particulate Carbon : Formation During Combustion",
D.C. Siegla and G.W. Smith, Editors, Plenum Press, New York, (1981)

27) M.L. STUDEBAKER,
Rubber Chem. And Technol. 30, 1400,(1957)

28) Y.S. NAJJAR, E.M. GOODGER
Fuel, 60, 980, (1981)

29) D. KRETSCHMER, J. ODGERS
J. Trans. ASME, 94 A, 173, (1972)

30) T. DURRANT
9th International Aeronautical Congress Paris, A 69-33350, June 1969

31) D.W. NAEGELI, L.G. DODGE, C.A. MOSES
"Effect of Flame Temperature and Fuel Composition on Soot Formation in Gas Turbine
Engines" (to be published)

32) H.A. BECKER, S. YAMAZAKI
Sixteenth Symposium (Intern.) on Combustion, The Combustion Institute
Pittsburg, p. 681, (1977)

33) D.W. NAEGELI, L.G. DODGE, C.A. MOSES
J. Energy 7, 2, p. 168, (1983)

34) W.S. BLAZOWSKI, A.F. SAROFIM, J.C. KECK
Transactions of the ASME
J. of Engineering for Power 103, 43, (1981)

DISCUSSION

C.Moses, US

What were the flame temperatures in the diffusion flame experiments discussed early in the paper? You talked about small molecules building into aromatic ring structures. In his work Graham concluded that above 1800°K aromatic rings broke down into C and C_2 radicals before going to soot. These seem contradictory. Perhaps the mechanisms are dependent on the experiment and hence one must be careful about generalizing theories of soot forming mechanisms.

Author's Reply

It is usually considered that soot formation involves C_n species (C_1, C_2, . . .) above c.a. 2300°K. The stability of the aromatic ring, however, is dependent upon temperature, residence time and ambient environment so that it is difficult to indicate with accuracy the temperature where disruption becomes more important than ring formation. In the diffusion flames we have used, P.A.H. and soot are produced at temperatures below 1800°K.
We have not indicated that rings are built up from small species. Referring to T.Bittner and J.B.Howard's work on the combustion of benzene, aromatic rings grow by reaction between existing rings and unsaturated hydrocarbon species resulting from the disruption of a part of the initial aromatic rings.

J.Tilston, UK

The observations of carbon particle charge shown in Paper 19 lead us to think that collision efficiencies in agglomeration should be less than 100 percent. For example, collisions between similarly charged particles may very well not lead to agglomeration. Figure 7 in Paper 20 shows measured and calculated agglomeration rates. Was 100 percent efficiency assumed in the calculation? If it was and if the statistics from your own charge measurements were used to modify this efficiency, would the agreement between theory and measurement be improved significantly?

Author's Reply

The rate constants in the model for soot particle coagulation, which is based on the collision theory, have to be modified to include the dependence of charge equal or opposite and polarization in the collisional cross section. It is well known that the coagulation can be strongly impeded by increasing the degree of soot particle ionization through seeding the flame with metal salts of low ionization potential. In unseeded flames the effect of ionization on the total collision frequency factor is not so relevant in the stage of coagulation. A small degree of ionization could even lead to a larger overall collision frequency due to ion-induced dipole-interaction of the colliding particles. Moreover, when the number density of soot particles and accordingly the rate of their coagulation is still high the relative number of charged soot particles is small. This increases when the particles grow larger. Therefore, it is more probable that in unseeded flames the later stages of agglomeration into grape- and chain-like clusters is influenced appreciably by charge than the early stage of coagulation. Whether or not this modification would lead to a better agreement between the experimental and calculated number densities in Figure 7 of Paper No.20 is difficult to judge without knowing the number densities of positively and negatively charged particles in that flame.

AD-P003 146

OPTICAL MEASUREMENTS OF SOOT SIZE AND NUMBER DENSITY IN A COMPLEX FLOW, SWIRL-STABILIZED COMBUSTOR

G.S. Samuelsen
Professor of Mechanical Engineering
C.P. Wood
Staff Research Associate
T.A. Jackson
Research Assistant

UCI Combustion Laboratory
Mechanical Engineering
University of California
Irvine, California 92717

Summary

In-flame optical measurements of soot particulates in a turbulent, recirculating (i.e., complex flow) model laboratory combustor are described. A nonintrusive optical probe based on large angle (60°, 20°) intensity ratio scattering was used to yield a point measurement of particulate in the size range of 0.08 to 0.38 μm. The performance of the optical technique was evaluated, and an exploratory assessment of the spatial distribution of soot was conducted with attention to fuel molecular structure, fuel loading, and a smoke-suppressant additive (ferrocene). Isooctane and mixtures of isooctane with various ring and aromatic compounds blended to yield the smoke point of a JP-8 stock were prevaporized and introduced through a hollow cone nozzle. The addition of ring compounds to the base isooctane substantially changed the distribution of soot and increased the overall emission by 300%. The production of soot was substantially reduced by a decrease in fuel loading, and marginally reduced or not affected by the additive depending on fuel structure. The optical technique is a potentially powerful tool for providing the experimental evidence necessary to understand the processes of soot formation and burnout in complex flows typical of gas turbine combustors. However, scanning electron micrographs of extracted samples established that the technique is limited to the large particle wing of the soot size distribution, and optical and electronic processing can induce biasing and uncertainties which must be understood and controlled before the potential of the technique can be fulfilled.

Introduction

Fuel flexibility is a viable and realistic approach to assure adequate availability of aviation fuel through this century. To achieve this position, the relationship of fuel properties and composition to combustion hardware performance and durability must be identified more precisely. Such information is necessary if fuel specifications are to be successfully relaxed to a level that both maintains the required performance of the combustion system (and other subsystems) and permits the desired latitude in the portion of hydrocarbon resources (petroleum, oil shale, coal, tar sands, etc.) that can be utilized to produce aviation fuel. These potential changes in fuel processing and fuel source make future fuel composition effects on gas turbines a primary consideration and concern.

Currently, the specification limit on aromatics for aviation fuel is a maximum of 20% (Jet A) or 25% (JP4, JP5, JP8) by volume. The limit is set to preclude a series of combustion related problems associated with the production of soot, examples of which include increased flame iation, deposit of carbonaceous material, and emission of particulates. The first two examples influence hardware durability and performance; the latter results in aesthetic and tactical problems. The aromatic content is of special interest because a relaxed specification for aromatics could ease the demand for hydrogen addition in the refining of low hydrogen resources. An upper limit of 35% aromatics has been discussed [1].

To accomodate an increased fuel aromaticity, the production of soot from combustors operating on relaxed-specification fuels must be reduced. The principal approaches being considered are smoke-suppressant fuel additives and combustor modifications. Smoke-suppressant fuel additives avert the economic penalties associated with retrofit by providing an alternative for existing gas turbine engines. Combustion modification is important for the next generation of gas turbine engines which will eventually replace the current inventory. To implement either of these approaches, an understanding of the mechanisms responsible for soot formation and burnout in complex (i.e., turbulent and recirculating) flows is required. Toward this end, experimental evidence is needed with respect to the effects that fuel properties, fuel-additive properties, and combustor operating conditions have on soot formation and burnout. Of particular interest are the mass emission, size distribution, and composition of the soot particulate. Extractive probe measurements have been used in the past to derive this set of information (e.g., [2,3, and 4]) but, in complex flows where backmixing can exacerbate and widely distribute perturbations introduced by the presence of a physical probe, caution must be exercised in the use of such methods [5]. This may include limiting the measurements to the combustor exit-plane, far downstream of the recirculation zone. Such a limit substantially restricts the information available. Excluded is the spatial distribution of local soot size and soot number density in the near wake of the recirculation zone and within the recirculation zone itself. Such measurements must be nonintrusive and therefore rely on optical techniques. Although optical techniques have been successfully employed to measure soot in relatively simple flows (flat flame and diffusion flames), a limited application to a complex flow has only recently been demonstrated [5].

The present study addressed the application of a nonintrusive, optical probe to a complex flow with the following objectives:

- To evaluate the performance of large angle intensity ratioing for the purpose of measuring optically the local soot size and soot number density in the reaction zones of a complex flow.
- To conduct an exploratory assessment of the spatial distribution of soot within a complex flow with attention to the effect of fuel molecular structure, fuel loading, and the smoke-suppressant fuel additive ferrocene on the local soot size and soot number density.

Such information is necessary to establish where the soot is formed and burned out in a flow dominated by complex aerodynamics. Such insight could then (1) provide the basis to assess the effect of fuel properties, fuel/air distribution, fuel additives, and other operational parameters on the soot production, and (2) thereby guide nozzle design, combustor design, and fuel property specifications.

Background

A. Soot Formation

Although the evidence has yet to be documented, the formation of soot in gas turbine combustors is envisioned to occur in locally fuel-rich, high-temperature regions of the primary zone. Detailed measurements of soot within the combustor will be required to uncover the governing mechanism. Nevertheless, the global data collected to date (e.g., gross soot emissions, liner temperature) identify a strong coupling between the soot produced and those parameters that govern mixing, local temperature, and local species composition; namely, combustor operating pressure, fuel properties, and fuel injection. The swing of combustor pressure over the range of operating conditions from idle to full load affects spray penetration, fuel evaporation rate, peak temperature, and reaction rates. Soot production rates have been found to be directly proportional to pressure [6], although a plateau at a critical Reynolds number has been asserted [7]. Elevated pressure is an unavoidable consequence of gas turbine combustion, however, and thus represents a relatively inflexible parameter. In contrast, fuel properties and fuel injection represent two parameters over which more control is available.

Fuel Properties. The use of relaxed-specification fuels will impact soot formation in current gas turbine engines in two main respects. First, physical properties such as viscosity and volatility can affect the atomization and evaporation of the fuel, impeding the fuel/air mixing process and promoting the formation of soot. Second, future fuel composition will be relatively high in aromaticity due to the higher aromatic content of future resources.

Tests in an Allison T-63 engine found the viscosity and distillation end point (a measure of volatility) to have little effect on the measured smoke and radiation [8]. Other evaluations support this, showing little or no sensitivity of soot formation to fuel physical properties [9,10].

In contrast, changes in smoke emission and flame radiation are closely aligned with changes in fuel composition. The specification on fuel aromatic content has been a means of controlling these changes. An alternate means of such control is to specify limits on fuel hydrogen content which has been correlated to the production of soot measured by either liner temperature or flame radiation [8,11,12,13].

If the chemical composition of the fuel is substantially perturbed, the correlation on fuel hydrogen may change appreciably. Hence, fuel molecular structure likely plays a principal role in soot production as well. Extensive studies in a well-stirred reactor, which allows for the study of the chemical process in the absence of heat and mass transfer limitations, demonstrate that nonaromatic hydrocarbons are capable of being burned at substantially higher equivalence ratios than aromatics without forming soot [14,15]. Hydrocarbons tested in one study [15] were grouped into three categories (Table 1). The first group, composed of aliphatic hydrocarbons, produced large amounts of exhaust hydrocarbons without sooting. The second group, consisting primarily of single ring aromatics, produced significant amounts of soot as the fuel/air mixture was increased. Finally, the third group, consisting only of 1-methylnaphthalene, produced substantially higher quantities of soot at equivalent mixture ratios.

Table 1 Categorization of Hydrocarbons with Similar Sooting Characteristics in a Well-Stirred Reactor

Group 1	Group 2	Group 3
Ethylene	Toluene	1-Methylnaphthalene
Hexane	o-Xylene	
Cyclohexane	m-Xylene	
n-Octane	p-Xylene	
Isooctane	Cumene	
1-Octane	Tetralin	
Cyclooctane	Dicyclopentadiene	
Decalin		

Source: Reference 15

Fuel mixtures formed from elements of any two groups sooted in a manner corresponding to the more aromatic component. Thus, unsaturated ring compounds dominate the soot production. Tests run on a JT9D combustor appear to support this assertion [16]. A linear trend of increasing smoke number was found with increasing aromatic content except for a 16.2 volume percent naphthalene blend which produced more than twice the smoke number expected from the correlation found with the other fuels. Also, combustor tests using fuels blended to achieve an equivalent hydrogen content with varying molecular structure, resulted in a range of measured flame radiation with the naphthalene containing fuels deviating significantly from any hydrogen correlation [17]. The critical difference appears to be the amount of dicyclic aromatics in the fuels. It should be noted, however, that the naphthalene present in these fuels substantially exceed current or proposed jet fuel specification levels.

Fuel Injection. Dual-orifice pressure atomization provides a wide range of stable operating conditions and, as a result, is commonly used for fuel injection in gas turbine operation. A central pilot orifice supplies the fuel required at low fuel flow conditions and a surrounding annular main orifice supplies the remaining fuel required under load. The atomizer, by concentrating the fuel in an oxygen-deficient core of the primary zone, promotes the formation of soot and relies upon the dilution zone to oxidize the soot generated. The relatively low sooting propensity of current specification fuels has resulted in acceptable emission levels under most conditions. The increased soot loading associated with future fuels, however, may result in unacceptable soot production with this injection method.

Improvements can be gained by increasing the air flow into the primary zone, but only at the expense of stability and ignition performance. A piloted airblast atomizer mitigates this problem [18]. The pilot nozzle supplies the fuel at low fuel flows, and the airblast atomizer supplies the remaining fuel at load. The airblast atomization process promotes mixing of fuel and air prior to combustion which significantly reduces the soot formation. Comparative measurements of the atomization characteristics of airblast and pressure atomizing injectors have shown that airblast injectors are capable of providing a finer spray (30 percent lower Sauter Mean Diameter) than the spray produced by a pressure atomizing injector [19]. Combustor liner temperature data from the CF6-50 engine with airblast fuel injection and a leaner primary combustion zone [20] demonstrated far less sensitivity to fuel hydrogen content than conventional systems equipped with pressure atomizing fuel nozzles [11]. Atomization has even been found to improve with increasing chamber pressure, thereby promoting more rapid fuel vaporation, mixing and combustion [21]. These merits have prompted the installation of airblast atomizers in a wide range of industrial and aircraft engines in recent years.

B. Optical Measurements

Prior to the introduction of the laser to reacting flows, optical measurements were limited to photography (e.g., direct, Schlieren, shadowgraph), and temperature measurements of gases (e.g., sodium D-line) and particles (e.g., two-color pyrometry, Kurlbaum). Now, nonintrusive laser anemometry measurements are regularly made of local flow velocity, and laser-induced measurements of local temperature and composition are reported for limited conditions. Laser-based optical measurements of soot size, on the other hand, are in their infancy and have to date been limited principally to simple flames.

When a particle is illuminated by an incident laser beam, light is diffracted out of the direction of the beam. The portion of the light which is diffracted, referred to as scattered light, is distributed in all directions. The distribution is a function of the incident wavelength, refractive index, particle size, scattering angle, and for polarized light, the polarization angle (the angle between the polarization vector and the scattering plane). By measuring the scattered intensity at an angle, particle size can be determined from Mie theory if the incident intensity, wavelength, refractive index, and the scattering and polarization angles are known.

For absorbing particles such as soot, an alternative optical method is available: extinction. Extinction is an integrated measurement of scattering and absorption along the trajectory of the incident beam. While scattering affects the angular distribution of intensity, absorption represents an attenuation of the incident radiation in the forward direction. As a result, scattering measurements other than in the forward direction offer better spatial resolution than extinction. However, the measured scattered intensity may be much less than that from extinction measurements.

Both extinction and scattering have been applied to simple flame systems, including premixed flat flames (e.g., [22,23]) and diffusion flames (e.g., [24,25]). The techniques employed, while useful in providing soot size information, require assumptions (e.g., size distribution, local temperature) and/or optical conditions (e.g., light-of-sight measurement, low number density) that preclude application to a complex flow where local point measurements must be resolved.

In an earlier study, an optical method was first applied to a complex flow [5]. Scattering intensity ratioing was used to gain a first insight into the perturbation of an extractive physical probe on the local soot size and soot data rate. The angles used for ratioing were 10° and 5° which yielded a size range of 0.3 to 1.8 μm. This size range is not optimal for in-situ soot measurement where the soot size is expected to be generally less than 0.5 μm. For the present study, the scattering intensity ratio technique was (1) expanded to larger angles in order to reduce the lower limit of size resolved to 0.08 μm, and (2) employed to obtain spatially resolved distributions of soot size and number density in a complex flow combustor.

Experiment

A. Approach

The present study was undertaken to evaluate the performance of a nonintrusive optical technique for the point measurement of soot size and number density within the flowfield of a complex flow

combustor, and to conduct an exploratory assessment of key fuel and combustor parameters -- fuel molecular structure, fuel loading, and a soot suppressant additive -- on the spatial distribution of soot size and number density. Laboratory combustion tests were performed in a model combustor with isooctane and three fuel blends injected in a prevaporized state. Prevaporization removed from consideration the mechanics of evaporation and the associated ambiguity in spatial variation of the fuel distribution that would thereby result. The optical technique employed was scattering intensity ratioing at two angles, 60° and 20°.

B. Combustor

The combustor employed was a model laboratory combustor developed in a series of tests [26,27]. The configuration is presented in Figure 1. The Dilute Swirl Combustor (DSC) features an aerodynamically controlled, swirl-stabilized recirculation zone to simulate important features of practical combustors (e.g., swirl and highly-turbulent recirculation).

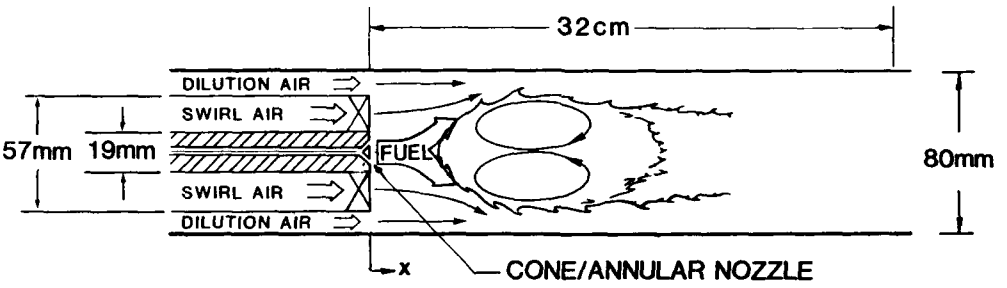


Figure 1 Dilute Swirl Combustor

For the present work, the housing consisted of an 80 mm I.D. cylindrical stainless steel tube that extended 32 cm from the plane of the nozzle. Rectangular, flat windows (25 x 306 mm) were mounted perpendicular to the horizontal plane on both sides of the combustor tube to provide a clear, optical access for the laser measurements.

A set of swirl vanes (57 mm O.D.) were concentrically located within the tube around a 19 mm O.D. centrally positioned fuel delivery tube. Dilution and swirl air were metered separately. The dilution air was introduced through flow straighteners in the outer annulus. The swirl air passed through swirl vanes with seventy percent (70%) blockage which imparted an angle of turn to the flow of 60°. For the swirl-to-dilution air flow ratio of unity used in the present study, the swirl number obtained by integrating across the swirl vanes is 0.8; that obtained by integrating the total inlet mass flux is 0.3. The combustor was operated at atmospheric pressure.

Prevaporized fuel was introduced through a cone/annular gas injector (Figure 1), sized to emulate the directional momentum flux of a hollow-cone liquid spray nozzle at the end of the fuel delivery tube. The included spray angle of the nozzle was 30°. The exit plane of the fuel nozzle was set at the same axial location as the exit plane of the swirl air to provide a clean, well-defined boundary condition.

C. Fuels

The present study employed four liquid fuels of varying molecular structure representative of compounds found in petroleum, shale, and coal derived fuels. Isooctane (2,2,4-trimethylpentane) was selected as the base fuel as it represents a major component of JP-8 and serves as the reference fuel in the ASTM smoke point test. The three remaining fuels consisted of mixtures of isooctane with one of three compounds with varying degrees of saturation and ring number (Figure 2) -- toluene, tetralin (1,2,3,4-tetrahydronaphthalene), or 1-methylnaphthalene. Hence, hydrocarbons in each of three groups listed in Table 1 are included.

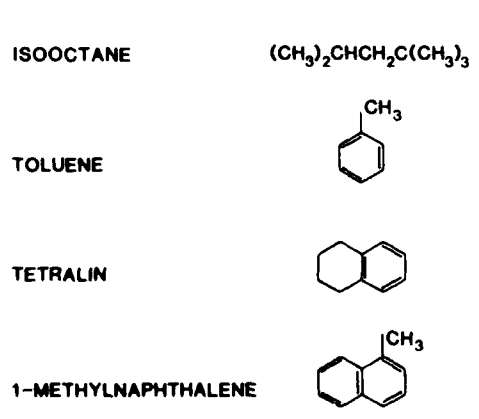


Figure 2 Test Fuel Molecular Structure

The amount of hydrocarbon blended with the isooctane was selected to yield the same ASTM smoke point typical for a JP-8 stock. The amount of each compound blended with isooctane was determined by first preparing a curve of smoke point vs. volume percent isooctane (Figure 3). Table 2 summarizes the composition and the actual smoke point found for each blend. The smoke points, while not identical, are equivalent within the achievable accuracy of the smoke point test (± 1mm) shown by the error bands in Figure 3. A single ferrocene additive concentration of 0.05% by weight was selected based on data in Naval Air Propulsion Test Center reports [28].

Table 2 Fuel Summary

Fuel	Smoke Point[a] Without Additive mm	With Additive mm	H wt. %
Isooctane	43.0	>50.0	15.79
JP-8	23.0	24.7	13.89[b]
Blend 1 21% Toluene 79% Isooctane	24.0	26.3	14.02
Blend 2 8% Tetralin 92% Isooctane	25.3	30.0	15.06
Blend 3 5% 1-Methylnaphthalene 95% Isooctane	22.2	35.0	15.16

[a] Distance above base of burner at which sooting first occurs
[b] Wright Patterson AFB
Source: Reference 4

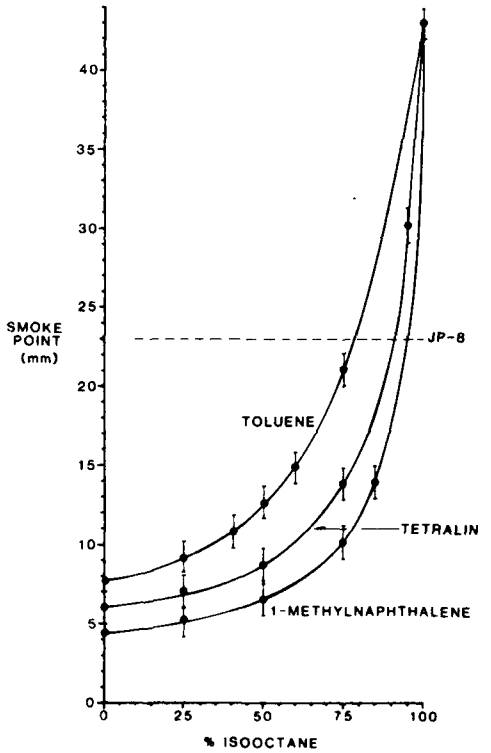


Figure 3 ASTM Smoke Point

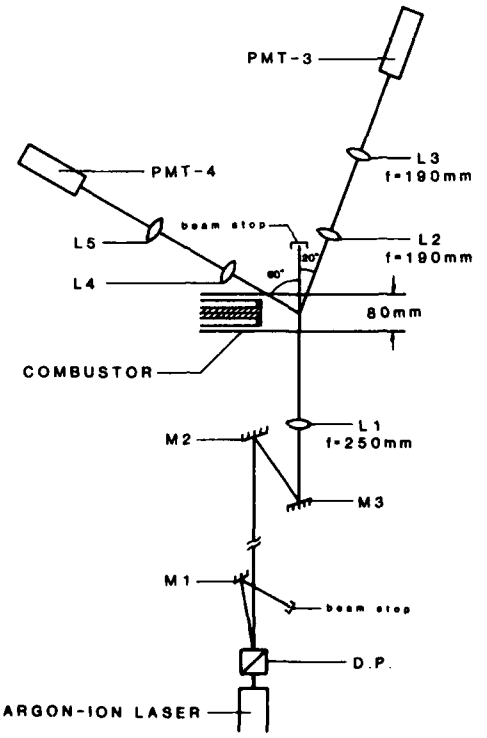


Figure 4 Optical Configuration

D. Optical System

The method adopted for the point-measurement of particle size and number density of soot particulate was scattering intensity ratioing. Figure 4 illustrates the optical configuration, a modification of that used previously [5]. This earlier work utilized collection optics at 10° and 5° off the optical axis. The current work employed collection optics at 60° and 20° to reduce the smallest size of particles that can be resolved from 0.3 to 0.08 μm.

A 5-watt Model 165 Spectra-Physics argon-ion laser operating in the multiline mode was used as the source of light. The laser lines were separated by a dispersion prism to resolve the green line (514.5 nm) and blue line (488.0 nm). The green line was directed to a beam stop. The active beam, the blue laser line, was focused to a 110 μm waist diameter using a 50 mm diameter F/5 focusing lens. The

scattered intensity was detected at 60° and 20° which provides a particle size detection band of 0.08 μm < d_p < 0.38 μm. Other angles are available but 60°/20° provides the smallest resolvable size (0.08 μm) of those pairs available.

The scattered light was focused to two photomultiplier tubes (RCA Model 8575) having quantum efficiencies of approximately 15% at the 488.0 nm wavelength. The supply voltage to the tubes was approximately 1100 volts.

The output signal from the photomultiplier tubes was passed into a Spectron Development Laboratories (SDL) Model LA-1000 logarithmic amplifier which converted the negative current to a positive voltage and was scaled for +10 volts peak output when the input current was -1 mA. The amplified signals were then fed to a SDL Model RP-1001 Intensity Ratio Processor (RP). The RP registered and processed the peaks of the two signals provided certain criteria were met. The DC levels input from the two channels were processed by an analog subtractor circuit which amplified the signal with a gain of five (5) and converted the signal to an 8-bit binary number. The RP had a variable lower threshold voltage, allowing a measure of control over the rejection of background noise.

The binary output was fed to an Apple II microcomputer, which resolved this output into 62 bins. The size distribution was determined by the number of counts in each bin, where each bin encompassed a discrete size range. The counts in each bin were then divided by the time required to collect them, resulting in a count rate (counts/sec). A histogram was then generated of normalized data rate versus size (in microns). The normalization of this histogram was under the operator's control through the system software. The histogram could be normalized to itself (giving the bin with the highest sooting rate an intensity of 1.0); it could be normalized to the highest sooting rate among all the histograms generated for a particular fuel; or it could be normalized to the highest sooting rate among any number of fuels or operating conditions. The results of this normalization procedure are evident in Figures 6,8,9, and 10.

The interpretation of the measured intensity ratio is based on the analysis of the Mie scattering properties of a homogeneous, isotropic spherical particle. The effects caused by nonspherical scatterers with an uncertain index of refraction, however, requiries special consideration. An evaluation of such effects, considered in an earlier study, concluded that the combined error was 20-30 percent with some broadening of the distribution [5].

Calibration of the optical system was performed using polystyrene particles of a known size (mean diameter = 0.255 μm, standard deviation = 0.9%). The calibration was then routinely followed by a system performance check, performed using propylene (Matheson C.P. grade, 99.0% minimum). After attaining thermal equilibrium, six points in the flow field were monitored for soot data rate and size distribution. This check was instituted to track the day-to-day variation in combustor performance. Thus, it served as a means of checking the continuity between the tests of different fuels and of different operating conditions performed over a span of two months. At any given station, the variation in the peak of the size distribution of the soot generated from propylene never exceeded 10% of the nominal value of 0.27 μm. The data rate was more variable. At the three axial stations, variation in the data rate along the centerline over the two-month period was approximately 30%. Away from the centerline (e.g., r/R = 0.50), the variability in data rate reached 40 to 50%. However, the variability was generally excessive only at positions where sample collection rates were relatively low. The variability of the data rates is not unreasonable at this juncture of the system development. Several parameters of the measurement system can influence the rate including the alignment and focusing of two optical detectors at a coincident point, and the signal processor thresholds.

E. Test Matrix

The test matrix for the present study is presented in Table 3. The nominal overall equivalence ratio for the isooctane and three blends was 0.5. For the dilution-to-swirl air ratio of unity, the primary zone loading approximated the value in a practical combustor of near-stoichiometric. The effects of fuel loading and ferrocene additive were demonstrated for two of the blends. The combustor was operated at a reference velocity of 7.5 m/s.

Table 3 Test Matrix

Fuel	Overall Equivalence Ratio ϕ	Figure
Isooctane	0.5	5,6
Blend 1 - 21% Toluene 79% Isooctane	0.5 0.3 0.5*	7,8,9,10 9 10
Blend 2 - 8% Tetralin 92% Isooctane	0.5	8
Blend 3 - 5% 1-Methylnaphthalene 95% Isooctane	0.5 0.3 0.5*	8,9,10 9 10

*ferrocene additive

Results

The results are presented in two groups. The performance and utility of the optical system for in-situ, nonintrusive measurements of soot size and number density is first evaluated. Second, the effects of fuel molecular structure, fuel loading, and ferrocene additive on the spatial variation of soot size and number density within the combustor are assessed.

A. Evaluation

Performance. An example of the data provided by the optical system is shown in Figure 5. The histogram represents the distribution of intensity ratio for 16094 validated samples. The data rate is derived as the division of the number of validated samples (16094) by the total sample time (8.6 seconds) to yield a value of 1871 Hz. The data rate for each sampling location is listed in Table 4.

DATE: 31MAY83
SERIES: ISOOCT RUN: 1603 31MAY83
COMMENT: D=DATA HV=1180/1220 LASER=1W
R/R=0.50 X/R=2.3 EQ/R=0.5 V=7.5M/S

MAX RAW COUNT = 764
TOTAL RAW COUNT = 16094
SAMPLE TIME: 8.6 SECONDS

LISTING OF RAW COUNTS

RATIO	BIN COUNT	RATIO	BIN COUNT
.946	31	.321	598
.913	58	.31	658
.881	46	.299	471
.85	62	.289	441
.82	50	.278	470
.791	81	.268	397
.763	104	.259	274
.736	108	.25	262
.71	127	.241	213
.685	145	.232	195
.661	181	.224	167
.637	202	.216	136
.615	183	.209	109
.593	294	.201	89
.572	318	.194	60
.552	365	.187	53
.532	413	.181	40
.513	449	.174	44
.495	555	.168	42
.478	589	.162	27
.461	545	.156	28
.444	644	.151	15
.429	632	.145	14
.414	719	.14	15
.399	663	.135	12
.385	759	.13	10
.371	764	.126	9
.358	748	.121	10
.345	673	.113	7
.333	714		

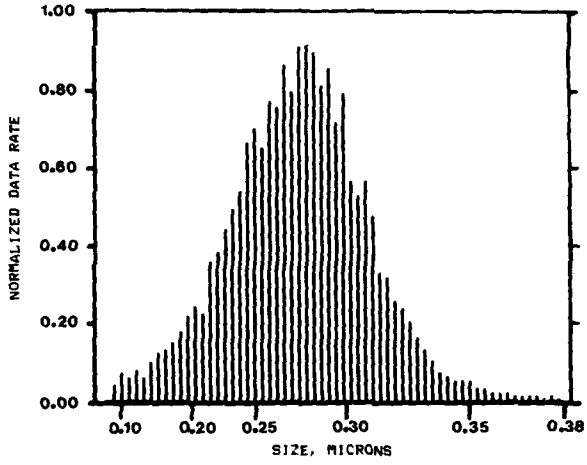


Figure 5 Representative Optical Data
(Isooctane, ϕ = 0.5, x/R = 2.3, r/R = 0.50)

The utility of a point measurement is the ability to map the combustor for soot size and number density. An example of such a mapping is presented in Figure 6. Radial profiles of optically-measured soot size and number density are presented at three axial locations within the combustor. In this figure, and in Figures 8,9, and 10, radial and axial locations are non-dimensionalized to the combustor radius, R = 40 mm. For purposes of scaling the histograms in these three-dimensional plots, the histogram that exhibits the peak data rate in the field is presented in the upper left corner of each plot. The histograms of Figure 6 are normalized to the peak sooting rate of the isooctane/tetralin blend in Figure 8. As a result, the peak data rate in Figure 6 (as shown in the histogram in the upper left corner) is less than unity. (Note also that this histogram corresponds identically to the histogram of Figure 5). The areas of peak soot concentration for isooctane can be identified (x/R = 2.3; r/R = 0.50, 0.67), and the reduction of soot at progressive stations downstream is clearly evident. No substantial change in particle size distribution is evident.



Figure 6 Spatial Map
(Isooctane, ϕ = 0.5)

Table 4 Data Rate (Hz)

Fuel	Equivalence Ratio Ø	Location							Figure
		Axial x/R	Radial r/R						
			0	0.17	0.33	0.50	0.67	0.83	
Isooctane	0.5	2.3	710	894	1450	1871	1675	647	5,6
		3.7	889	580	617	884	1147	1295	
		5.0	601	389	216	248	365	561	
Blend 1	0.5	2.3	1055	1304	875	647	1468	2563	8,9,10
21% Toluene		3.7	1178	1422	1637	1750	2037	1755	
79% Isooctane		5.0	1321	1441	1801	2104	2193	2076	
	0.3	2.3	1432	1108	871	1187	1208	732	9
		3.7	1328	925	528	416	505	619	
		5.0	1187	753	374	221	216	304	
w/ferrocene	0.5	2.3	1628	1478	1339	1025	1443	1548	10
		3.7	1364	1258	1458	1760	2081	2388	
		5.0	1268	1190	1460	1844	2094	2373	
Blend 2	0.5	2.3	1200	1590	1347	1175	1631	2236	8
8% Tetralin		3.7	1269	1293	1717	2104	2361	2708	
92% Isooctane		5.0	1164	1081	1291	1686	2032	2405	
Blend 3	0.5	2.3	1178	1578	1549	1077	1010	826	8,9,10
5% 1-Methyl-naphthalene		3.7	1375	1353	1697	2192	2135	1526	
95% Isooctane		5.0	1223	1073	1191	1612	2090	2411	
	0.3	2.3	643	408	284	742	1464	1796	9
		3.7	507	234	116	213	566	1131	
		5.0	407	215	87	65	136	281	
w/ferrocene	0.5	2.3	1235	1485	1643	1434	1492	1558	10
		3.7	1246	1186	1438	1939	2339	1984	
		5.0	982	855	909	1311	1764	2293	

Validation. To validate the optical system, the optical probe was positioned at the entrance of an extractive probe used previously [5]. The extractive probe was located at an axial plane ($x/R = 5.0$) and radial location ($r/R = 0.83$) well displaced from the centerline where flow perturbation was expected to be minimized. Two analyses of the extracted sample -- scanning electron microscopy and gravimetric -- were conducted and compared to the optical results.

The morphology of the soot is agglomerates of smaller (~0.05 μm) spherical particles which is consistent with the morphology and size observed in other combustor studies (e.g., [4,5,29,30]). An example of the size distribution derived from a scanning electron micrograph (SEM) of the extracted sample is compared to the optical measurement for an isooctane/toluene blend in Figure 7a. Particle sizes observed optically are also revealed by the SEM data. However, it is evident that the range of particle sizes resolved by the 60°/20° intensity ratioing (1) is at the large particle end of the SEM distribution, (2) encompasses only a small portion of the total number of particles, (3) includes the agglomerates, and (4) excludes the primary particles.

Although the optical data do not include the peak size of the actual distribution (~0.05 μm, the size of the primary particles), the optical data appear to accurately reflect a secondary peak located in the large particle wing of the SEM data. To more effectively compare the two sets of data, the SEM data are renormalized in Figure 7b to the secondary peak in data rate that occurs in the large particle wing of the SEM distribution ($d_p \sim 0.22$ μm). The optically-measured peak in data rate appears to be real and reflect a discontinuity in particle size associated with agglomerate growth. However, the extent to which the optically-measured data rate is reduced on the small particle side of the peak may be exaggerated. This is attributed to an inaccuracy in the optical technique associated with the Gaussian intensity profile of the incident laser beam. A relatively small particle passing though the laser beam at the wing of the Gaussian intensity profile may not scatter enough light to the detectors to meet established threshold levels on the RP, whereas a larger particle, passing through the same region of the beam, will scatter enough light to be recorded. This acts to artificially suppress the low end of the distribution. This inaccuracy is amenable to an analytically derived "probe volume" correction which could be implemented through the reduction software, in essense giving the system a flat response throughout the range of sizes it is theoretically capable of measuring.

The present application of this optical technique uncovered other factors that also can influence the measured size distribution. The event threshold setting is a Schmidt-trigger based control used to prevent the RP from triggering more than once per particle count due to a noisy signal. Upon the initial detection of a rising signal, the RP drops its reset level immediately to a lower voltage, insuring that noise superimposed on the true signal does not reset the RP and produce multiple-count responses as one particle passes through the laser beam. As the event threshold setting is manually lowered, an increasing number of small particles are able to meet the threshold voltage. The small particle end of the distribution can thus be boosted relative to the large particle end. In addition to

the threshold setting, the dynamic range of the system is maximized by setting the high voltage on each photo-multiplier tube (PMT). The procedure is to set the PMT gains such that the maximum-size particle capable of being measured gives a 10V output to the RP. This maximum-size particle (0.38 μm for 60°/20° IR), however, scatters light to the PMTs with an intensity dependent upon where it traverses the Gaussian intensity profile of the laser beam. If the PMT gains are set too low, small particles may not reach the lower threshold value. If set too high, some larger particles (but still below 0.38 μm in size) may cause an output of >10V to the RP and be invalidated. Thus, the resulting size distribution can be altered and/or truncated at the low or high end, depending on the PMT gains. Finally, alignment to insure that the two detectors are viewing identical areas at the waist of the laser beam is necessary. If the viewing area of one detector is moved relative to the viewing area of the other, the area of coincidence may be narrowed and reside on the wing of the Gaussian intensity profile of the laser beam, thereby suppressing the low end of the distribution. A calibration of the optical technique using either monodispersed latex seeds of at least three sizes, or a carefully prepared and introduced polydispersed mixture of known distribution may be effective in setting the threshold, PMT gains, and alignment to the optimum values and thereby minimize the uncertainty associated with the measured size distribution.

In Figure 7c, both the optical and SEM distributions are presented in terms of mass density. Although the difference in relative peak levels is not as pronounced, it is nonetheless still striking. The gravimetric sample extracted yielded a mass concentration of ~2000 μg/m^3 whereas a mass concentration, calculated by combining the optical data (size distribution, data rate) with the size of the optical probe cross-sectional area relative to that of the extractive probe, indicated a level of ~250 μg/m^3. Because the size range resolved by the optical technique represents approximately one-half the total mass of the particulate (Figure 7c), the optically-deduced mass concentration must be doubled to ~500 μg/m^3 for direct comparison to the gravimetric value. The resultant factor of four difference between the optical and gravimetric values is attributed to both the rejection by the RP of a portion of the particle scores due to validity checks and approximations (e.g., effective optical sampling volume) associated with the calculation of the mass concentration from the optical data.

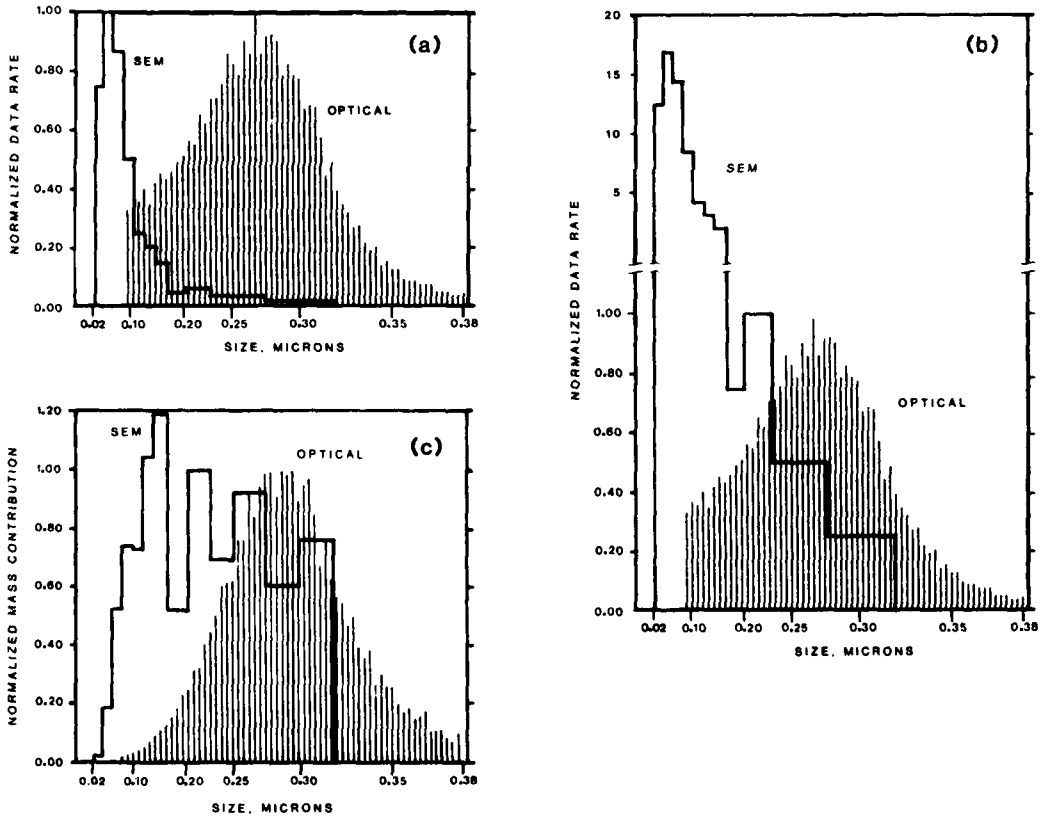


Figure 7 Validation
(Isooctane/Toluene, ϕ = 0.5, x/R = 5.0, r/R = 0.83)
(a) Number Density
(b) Number Density Renormalized
(c) Mass Density

B. Parametric Assessment

Fuel Molecular Structure. The results for the effect of fuel molecular structure on soot size and

number density are presented in Figure 8 for the three blends (79% isooctane/21% toluene; 92% isooctane/8% tetralin; 95% isooctane/5% 1-methylnaphthalene) prepared to yield the same smoke point as a JP-8 stock. The data are normalized to the peak data rate observed with the three fuels, namely that of the tetralin blend. The data rates are tabulated in Table 4.

It is first noteworthy to compare the results for the isooctane blends with the results for the pure isooctane (Figure 6), which is also normalized to the tetralin blend. The data rate for the blends are generally a factor of 3 higher than the data rates observed for the pure isooctane. Hence, the addition of ring compounds (as small as 5% by volume in the case of 1-methylnaphthalene) has a substantial impact on the soot produced. Secondly, a significant increase on the small particle side of the distribution occurs in the case of the blends, especially for isooctane/toluene and isooctane/tetralin, indicating that a peak in the number density of the agglomerates, if real, is not as sharp as that observed for isooctane. Thirdly, the position in the flowfield where the data rate peaks is clearly different for the blends. For isooctane, the data rate peak occurs at a radial position midway between the centerline and the wall, approximately coincident with the radial boundary (i.e., shear layer) of the recirculation zone. For the blends, the peak occurs at the wall, varying only in

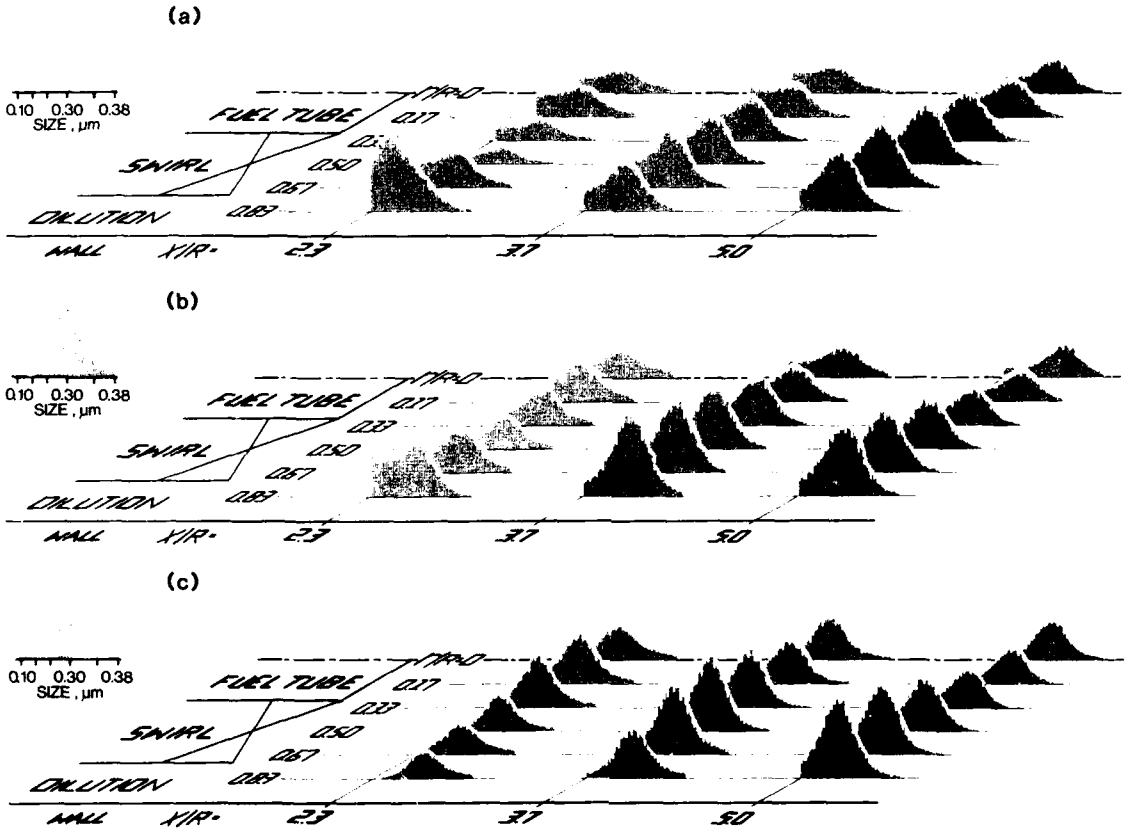


Figure 8 Fuel Molecular Structure
(ϕ = 0.5)
(a) Isooctane/Toluene
(b) Isooctane/Tetralin
(c) Isooctane/1-Methylnaphthalene

axial location among the blends. This suggests that the slower rate of pyrolysis associated with the ring compounds extends the time over which soot is formed (as well as increasing the amount) leading to a different spatial distribution of soot than that found for pure isooctane. The implication is that, to accommodate a fuel of significantly different fuel molecular structure in a given combustor, the fuel spray pattern and/or the primary zone aerodynamics must be modified to suppress an attendent increase in the production of soot.

Finally, the production of soot is remarkedly similar for the three blends mixed to yield the same ASTM smoke point. In this regard it should be noted that the three fuel blends of the same smoke point are of different hydrogen contents (Table 2). The tetralin blend and the 1-methylnaphthalene blend are essentially of the same hydrogen content as well as smoke point. Their similar sooting properties in the complex flow are not surprising. The hydrogen content of the toluene blend is one weight percent lower. A soot-hydrogen content correlation would predict its sooting tendency to be higher than that of the two other blends. The fact that the blends containing multiring elements soot in a manner similar to the lower hydrogen content, single ring aromatic blend is consistent with the results in a stirred reactor [15] and practical combustors [16,17].

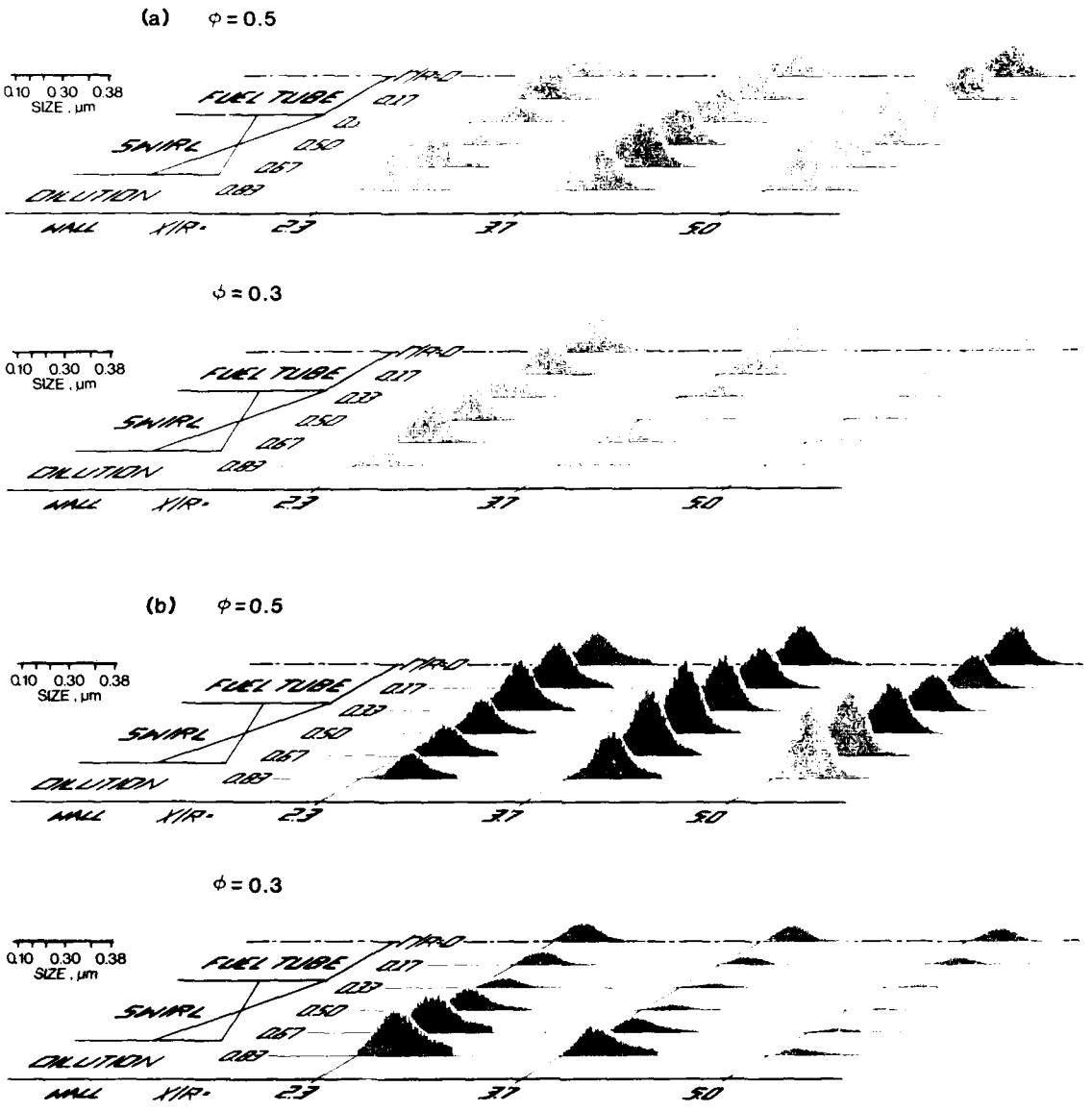
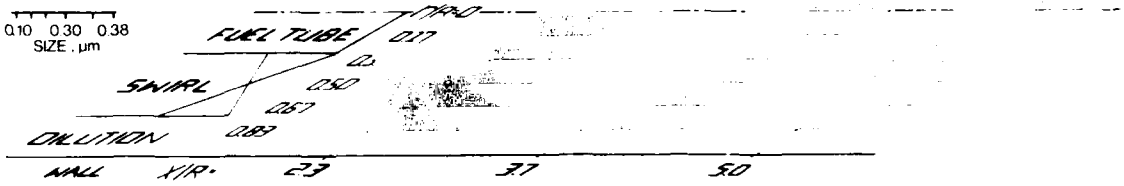


Figure 9 Fuel Loading
(a) Isooctane/Toluene
(b) Isooctane/1-Methlynaphthalene

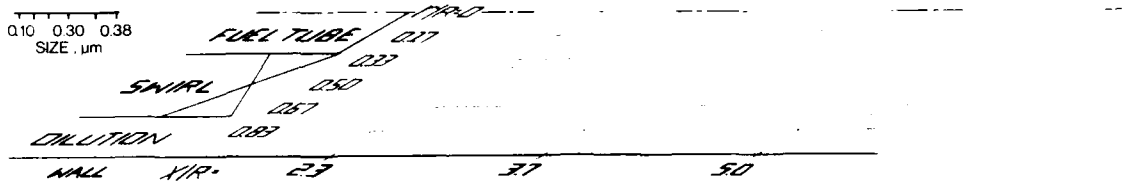
Fuel Loading. Optical measurements were taken at a reduced overall equivalence ratio (ϕ = 0.3) to test the effect of fuel loading. For brevity, results are presented for two blends (79% isooctane/21% toluene; 95% isooctane/5% 1-methylnaphthalene) in Figure 9. The data rate histograms are normalized to the peak data rate for the parent fuel at the elevated fuel loading (ϕ = 0.5). The reduction in fuel loading has a substantial impact on the soot produced. Such a change affects not only the total fuel introduced, but also the spatial distribution of the fuel introduced, the local mixture ratio, and the local temperature.

Ferrocene. The ferrocene additive was added to the same two fuel blends evaluated under fuel loading (Figure 10). The effect of the ferrocene addition on the ASTM smoke number is presented in Table 2. The additive was effective in raising the smoke point in both cases (indicating that the sooting propensity was reduced) although the relative effectiveness depended on the fuel type. In the aerodynamically controlled flow of the DSC, the effect of the ferrocene depended on fuel structure. A calculation of the total soot passing the x/R = 5.0 axial plane (obtained by combining the data rates of Table 4 with the annular cross sectional area represented by each of the six radial sampling locations -- note that the x/R = 0.83 radial sampling point represents 50% of the total cross-sectional area) yielded a reduction in soot emitted in the presence of ferrocene of 20% for the 1-methylnaphthalene blend and no change for the toluene blend. The toluene results are consistent with an earlier study [4], but the 1-methylnaphthalene results are opposite from those observed earlier where an increase in

(a) nominal



ferrocene



(b) nominal



ferrocene



Figure 10 Ferrocene
(a) Isooctane/Toluene
(b) Isooctane/1-Methylnaphthalene

sooting for the double ring aromatic blend (95% isooctane/5% 1-methylnaphthalene) was observed. This difference is attributed to the relatively high fuel loading in the primary zone of the combustor configuration and nozzle employed in the earlier study as compared to the present study, and indicates the role of the fuel/air mixing and fuel molecular structure in determining the additive impact.

Conclusions

An optical system for the local, in-situ measurement of soot size and number density has been demonstrated in an aerodynamically controlled flowfield representative of a practical turbine combustor. The utility of such a diagnostic tool is the provision of detailed mapping to identify the regions of soot formation and burnout in a complex flow. In the present case, this capability was applied to changes in fuel molecular structure, fuel loading, and the addition of a fuel additive.

Regions of particulate formation and reduction are indicated by spatial maps of soot size and number density. The addition of ring compounds to the base isooctane substantially changed the

distribution of soot and increased the overall emissions by 300%. The production of soot was substantially reduced by a decrease in fuel loading, and marginally reduced or not affected by the addition of ferrocene depending on fuel structure. Not only was the number density of soot affected, but the point in the flow where the soot number density peaked changed significantly with changes in fuel molecular structure, and additive introduction. These spatial variations in the amount of soot produced point to the importance of spatially-resolved, nonintrusive optical measurements in order to guide combustor design, nozzle design, and fuel property specifications for future fuels.

Although the demonstration itself was successful, and the parametric variation was valuable in providing the first insights into the sooting behavior resident in these types of flows, questions raised during the conduct of this study must be resolved if (1) the optical technique is to reach its full potential, and (2) the data derived from such systems is to be of quantitative value as well as qualitative value.

A probe volume correction is necessary to supppress the biasing of the size distribution at the small particle end of the distribution, and a refined calibration method is necessary to reduce the uncertainty in the distribution associated with alignment of the two detectors, setting various threshold levels, and establishing the PMT gains. In addition, complementary or alternative optical techniques must be pursued to extend the resolvable size to encompass sizes below 0.05 μm if the entire size distribution is to be represented.

Acknowledgements

The results presented were obtained in a soot formation/alternative fuels study in progress at the UCI Combustion Laboratory and supported by the Air Force Engineering and Service Center, Research and Development Directorate, Environics Division (Air Force Contract FU-8635-83-C-0052) with Lt. Jeffery Jenkins as the project monitor. The authors gratefully acknowledge the assistance of Thad Bond, Robyn Maupin, and Mark Sollberger in the collection, reduction, and presentation of the data. The optical system was developed under subcontract to Spectron Development Laboratories with Dr. Chie Poon serving as the principal in the design.

References

1. Churchill, A.V., DeLaney, C.L. and Lander, H.R. (1978). "Future Aviation Turbine Fuels," J. Aircraft, Vol. 15, No. 11, pp. 731-734.

2. Prado, G.P., Lee, M.L., Hites, R.A., Hoult, D.P., and Howard, J.B. (1976). "Soot and Hydrocarbon Formation in a Turbulent Diffusion Flame," Sixteenth Symposium (International) on Combustion, The Combustion Institute, pp. 649-661.

3. Wyatt, W.R., Clark, J.A., Peters, J.E., and Mellor, A.M. (1979). "Size Distribution and Surface Area Measurements of Gas Turbine Combustor Smoke," Journal of Energy, Vol. 3, No. 5, pp. 285-290.

4. Himes, R.M., Samuelsen, G.S., and Hack, R.L. (1982). "Chemical and Physical Properties of Soot as a Function of Fuel Molecular Structure in a Swirl-Stablized Combustor," ASME Paper 82-GT-109.

5. Hack, R.L., Samuelsen, G.S., Poon, C.C., and Bachalo, W.D. (1981). "An Exploratory Study of Soot Sample Integrity and Probe Perturbation in a Swirl-Stabilized Combustor," Journal of Engineering for Power, Vol. 103, No. 10, pp. 759-771.

6. Schirmer, R.M. (1972). "Effect of Fuel Composition on Particulate Emissions from Gas Turbine Engines," Emissions from Continuous Combustion Systems, edited by W. Cornelius and W.G. Agnew, Plenum Publishing Corp., pp. 189-210.

7. Hoult, D.P. and Ekchian, A. (1980). "Soot Formation in a Turbulent Swirl Stabilized Laboratory Combustor," ASME Paper 80-GT-77.

8. Naegeli, D.W. and Moses, C.A. (1978). "Effects of Fuel Properties on Soot Formation in Turbine Combustion," SAE Paper No. 781026.

9. Gleason, C.C., Oller, G.L., Shayeson, M.W., and Bahr, D.W. (1979a). "Evaluation of Fuel Character Effects on J79 Engine Combustion System," AFAPL-TR-79-2015.

10. Gleason, C.C., Oller, G.L., Shayeson, M.W., and Bahr, D.W. (1979b). "Evaluation of Fuel Character Effects on F101 Engine Combustion System," AFAPL-TR-79-2018.

11. Blazowski, W.S. (1977). "Combustion Considerations for Future Jet Fuel," Sixteenth Symposium (International) on Combustion, The Combustion Institute, pp. 1631-1639.

12. Friswell, N.J. (1979). "The Influence of Fuel Composition on Smoke Emission from Gas-Turbine-Type Combustors: Effect of Combustor Design and Operating Conditions," Combustion Sci. Tech., Vol. 19, pp. 119-127.

13. Gleason, C.C. and Martone, J.A. (1980). "Fuel Character Effects on J79 and F101 Engine Combustor Emissions," ASME Paper 80-GT-70.

14. Wright, F.J. (1969). "The Formatin of Carbon Under Well-Stirred Conditions," Twelfth Symposium (International) on Combustion, The Combustion Institute, pp. 867-875.

15. Blazowski, W.S. (1979). "Dependence of Soot Production on Fuel Blend Characteristics and Combustion Conditions," ASME Paper 79-GT-155.

16. Szetela, E.J., Lohman, P., and Smith, A.L. (1979). "Analysis of the Impact of the Use of Broad Specification Fuels on Combustors for Commercial Aircraft Gas Turbine Combustors," AIAA Paper 79-1195.

17. Naegeli, D.W. and Moses, C.A. (1980). "Effect of Fuel Molecular Structure on Soot Formation in Gas Turbine Engines," ASME Paper 80-GT-62.

18. Norster, E.R. and Lefebvre, A.H. (1972). "Effects of Fuel Injection Method on Gas Turbine Combustor Emissions," Emissions from Continuous Combustion Systems, edited by W. Cornelius and W.G. Agnew, Plenum Publishing Corp., pp. 255-278.

19. Lefebvre, A.H., Mellor, A.M., Peters, J.E. (1978). "Ignition/Stabilization/Atomization - Alternative Fuels in Gas Turbine Engines," in Bowman, C.T. and Birkeland, J. (Eds.), Alternative Hydrocarbon Fuels: Combustion and Chemical Kinetics, Progress in Astronautics and Aeronautics, Vol. 62, AIAA, pp. 137-159.

20. Gleason, C.C. and Bahr, D.W. (1980) "Fuel Property Effects on Life Characteristics of Aircraft Turbine Engine Combustors," ASME Paper 80-GT-55.

21. Bryan, R. Godbole, P.S. and Norster, E.R. (1971). "Some Observations of the Atomizing Characteristics of Air Blast Atomizers," Cranfield International Symposium Series, Vol. 11, Edited by E.R. Norster, Pergammon Press.

22. D'Alessio, A., Di Lorenzo, A., Beretta, F., and Venitozzi, C. (1973). "Optical and Chemical Investigations on Fuel-Rich Methane-Oxygen Premixed Flames at Atmospheric Pressure," Fourteenth Symposium (International) on Combustion, The Combustion Institute, pp. 941-953.

23. D'Alessio, A., Di Lorenzo, A., Sarofim, A.F., Beretta, F., Masi, S., and Venitozzi, C. (1975). "Soot Formation in Methane-Oxygen Falmes," Fifteenth Symposium (International) on Combustion, The Combustion Institute, pp. 1427-1438.

24. Kunugi, M. and Jinno, H. (1967). "Determination of Size and Concentration of Soot Particles in Diffusion Flames by a Light-Scattering Technique," Eleventh Symposium (International) on Combustion, The Combustion Institute, pp. 257-266.

25. Dalzell, W.H., Williams, G.C., and Hottel, H.C. (1970). "A Light-Scattering Method for Soot Concentration Measurements," Combustion and Flame, Vol. 14, pp. 161-170.

26. Brum, R.D. and Samuelsen, G.S. (1982a). "Assessment of a Dilute Swirl Combustor as a Bench Scale, Complex Flow Test Bed for Modeling, Diagnostics, and Fuels Effects Studies," AIAA Paper 82-1263.

27. Brum, R.D. and Samuelsen, G.S. (1982b). "Two-Component Laser Anemometry Measurements in a Non-Reacting and Reacting Complex Flow Model Combustor," WSS/CI Paper 82-53.

28. Klarman, A.F. (1977). "Evaluation of the Extended Use of Ferrocene for Test Cell Smoke Abatement; Engine and Environmental Test Results," Navy Report No. NAPTC-PE-110.

29. Sawyer, R.F., (1972). "Experimental Studies of Chemical Processes in a Model Gas Turbine Combustor," Emissions From Continuous Combustion Systems, edited by W. Cornelius and W.G. Agnew, Plenum Publishing Co., New York, pp. 243-254.

30. Fenton, D.L., Luebcke, E.H., and Norstrom, E. (1979). "Physical Characterization of Particulate Material From a Turbine Engine," ASME Paper 79-GT-179.

DISCUSSION

S.Wittig, Ge

Your results are quite encouraging especially in their extension to smaller particles. However, when we at Purdue and later in Karlsruhe continued to develop the RSPC (Ratio-Single-Particle-Counter) based on Gravatt's ideas and extended it to multiple scattering (MRSPC), we tried to stay close to the forward scattering lobe for reasons which have been explained by us in detail and are well known (refractive index, distance of the probe volume from the wall etc.). How sensitive are your measurements using relatively large angles (60°) to changes in the refractive index? Do you feel your arrangement can be applied to practical combustors with large diameters? How did you achieve the high sensitivity? Finally a brief comment: the biasing problem has been solved by us in Karlsruhe. The computer program in combination with optical modifications is routinely used practically on-line. Excellent results even in narrow bimodal distributions are obtained.

Author's Reply

The effect due to an uncertain index of refraction was inspected by both Chu and Robinson (1977) and Hirleman (1977). Their findings show that, for absorbing particles (as in the case with soot particles), the error due to an uncertainty in the index of refraction is very small (typically several percent). However, for nonabsorbing particles (as is the case in the cold flow calibration described here), an error as much as 25 percent can occur depending on the size of the particles. For the present study at 60° 20°, the scattering calculations using indices of refraction for soot and polystyrene latex particles of $n = 1.57 - 0.56i$ and $n = 1.60 - 0i$, respectively, yielded identical results for scattering intensity ratio vs. size except for a band of particle sizes $0.25 < d < 0.35\ \mu m$ where the deviation in size approached 7 percent. The 60° scattering angle requires a wide window of optical access that will restrict application to laboratory combustors rather than practical combustors (where optical access will likely be limited).

The intensity of light scattered from particles in the size range $0.08\ \mu m$ to $0.38\ \mu m$ varies by d^6 or a factor greater than 10^4. To obtain adequate sensitivity over this large dynamic range, a logarithmic amplifier was designed to yield a 2 volt output for every decade change in input from the photomultiplier. This output provides a high signal-to-noise ratio and, in combination with noise discrimination logic in the Ratio Processor, yields a high valid to invalid data rate.

References

Chu, W.P. and Robinson, D.M. (1977). Scattering from a Moving Spherical Particle by Two Crossed Coherent Plane Waves, *Applied Optics*, March, p.619.

Hirleman, E.D. (1977). Optical Technique for Particulate Characterization in Combustion Environments: The Multiple Ratio Single Particle Computer, Ph.D. Thesis, Purdue University, August.

ETUDE EXPERIMENTALE ET MODELISATION DE LA CINETIQUE DE COMBUSTION DES HYDROCARBURES

M. CATHONNET, F. GAILLARD, J.C. BOETTNER, H. JAMES

Centre de Recherches sur la Chimie de la Combustion
et des Hautes Températures, C.N.R.S., 45045 Orléans-Cedex, France

Les toutes premières étapes de la combustion des hydrocarbures sont caractérisées par une dégradation de l'hydrocarbure initial en fragments hydrocarbonés à petit nombre d'atomes de carbone. La modélisation de la combustion dans les turbomachines nécessite donc la connaissance de la cinétique d'oxydation de ces fragments.

On présente les résultats d'études effectuées sur l'oxydation du propène et de l'éthylène dans des réacteurs à écoulement, pour des pressions comprises entre 1 et 10 bars.

On propose un mécanisme détaillé pour rendre compte, par simulation, de nos résultats expérimentaux ainsi que de ceux obtenus par d'autres auteurs selon des techniques différentes et couvrant un champ expérimental étendu.

POSITION DU PROBLEME

La chimie de la combustion tient une place importante dans la modélisation des foyers de turboréacteurs et les progrès réalisés dans les méthodes d'analyse numérique permettent de décrire de manière de plus en plus précise les mécanismes réactionnels susceptibles d'intervenir dans les chambres de combustion. La complexité croissante des cinétiques proposées va de pair avec le développement des méthodes de calcul.

A l'heure actuelle, les modèles cinétiques auxquels on fait appel sont nécessairement simplifiés, car les connaissances concernant les étapes élémentaires de la combustion d'hydrocarbures lourds sont encore très limitées; il est en effet impossible de décrire de manière détaillée la combustion d'un mélange aussi complexe que le kérosène.

La mise au point d'un mécanisme simplifié nécessite l'obtention de données cinétiques à l'aide d'expériences suffisamment représentatives des conditions régnant dans un foyer, mais permettant une interprétation plus aisée des résultats. Ainsi, un certain nombre de travaux (1) ont permis de montrer que les premières étapes de la combustion des hydrocarbures supérieurs sont caractérisées par une pyrolyse de la molécule initiale en fragments hydrocarbonés de plus faible poids moléculaire. Les expériences réalisées dans un réacteur à écoulement turbulent sur des alcanes de C_2 à C_8 révèlent la présence de propène et d'éthylène comme intermédiaires prépondérants (2). Quant à l'étude de la distribution des produits de dégradation primaire du kérosène, elle reste encore à faire, mais il a été montré (3) qu'à partir de 800°C environ, les produits légers ($C < 5$) deviennent prépondérants. Si l'on excepte les zones situées immédiatement à la sortie des injecteurs et les zones où se forment les suies, la combustion du kérosène est en grande partie une combustion d'hydrocarbures de C_2 à C_4.

Intérêt des mécanismes détaillés:

Les modèles cinétiques à une seule réaction globale ont été longtemps les seuls utilisés pour décrire la combustion dans un foyer de turbomachine ou un foyer homogène. Une étude de Westbrook et Dryer (4) rend compte des résultats obtenus avec une telle cinétique pour calculer des vitesses de flammes d'hydrocarbures. La même étude indique les limites d'application d'une cinétique globale à une réaction et présente les améliorations apportées par les schémas cinétiques à deux étapes, ainsi que par un modèle quasi-global du type de celui proposé par Edelman et Fortune (5). Ces deux schémas permettent de reproduire correctement les vitesses de flammes d'un grand nombre d'hydrocarbures; cependant, il est montré que le modèle quasi-global ne donne pas une bonne représentation des profils de concentration de l'oxyde de carbone et des atomes ou radicaux dans une flamme laminaire. Ceci provient de la représentation trop simplifiée en une seule étape de l'oxydation de l'hydrocarbure initial en oxyde de carbone et hydrogène.

A cet égard, une amélioration a été apportée par Duterque et al. (6) au schéma quasi-global de Edelman. En effet, la première étape globale de leur schéma forme intermédiairement un ou plusieurs composés hydrocarbonés, ce qui rend mieux compte de la nature séquentielle (2) de l'oxydation des hydrocarbures. Cette évolution séquentielle est représentée, dans le schéma de Hautman et al. (7), par quatre étapes faisant intervenir l'éthylène comme intermédiaire. Cependant, les coefficients numériques intervenant dans les expressions cinétiques semi-globales proposées par ces auteurs doivent être évaluées empiriquement et demandent à être ajustées cas par cas pour pouvoir représenter correctement une combustion dans des conditions expérimentales données.

La supériorité des mécanismes détaillés est de permettre de représenter, à l'aide d'un mécanisme unique, la combustion d'un hydrocarbure dans des conditions opératoires très différentes. Dans le cas d'un écoulement simple, la résolution d'un tel système ne pose pas de difficulté, mais il n'en est pas de même dans un écoulement complexe. Toutefois, à partir du mécanisme détaillé, il est possible d'écrire des expressions simplifiées qui reflètent les étapes prépondérantes dans des conditions expérimentales données. Un tel exemple d'expression cinétique simplifiée obtenue à partir d'un mécanisme détaillé nous est donné par Abdalla et al. (8) pour la modélisation d'une flamme turbulente de méthane en mélange pauvre.

Mais, si le mécanisme détaillé de la combustion du méthane en mélange pauvre est maintenant bien connu, il n'en est pas de même pour celui de la combustion en mélange riche ou en présence d'hydrocarbures supérieurs. Dans ce cas, en effet, il est nécessaire de faire intervenir les réactions de combustion de l'éthylène et de son principal produit d'oxydation: l'acétylène; or, les mécanismes proposés pour l'oxydation de es deux intermédiaires de la combustion des hydrocarbures supérieurs diffèrent d'un auteur à l'autre. C'est pourquoi de nombreuses confrontations expérience-simulation sont encore nécessaires pour préciser les différents points encore obscurs de ces mécanismes et pour établir des expressions cinétiques de la combustion des hydrocarbures supérieurs sur des bases moins empiriques.

C'est dans ce but qu'ont été entreprises, depuis quelques années, des recherches sur l'oxydation de haute température des hydrocarbures dans notre Laboratoire.

ETUDE EN REACTEUR TUBULAIRE

A. Description de l'appareillage.

La technique du réacteur à écoulement turbulent développée aux U.S.A. dans le laboratoire du Professeur Glassman (2) a permis de faire progresser les connaissances concernant les processus réactionnels qui interviennent dans l'oxydation des hydrocarbures.

Dans le but d'étendre le domaine d'étude aux pressions supérieures à la pression atmosphérique, nous avons mis en oeuvre un réacteur tubulaire en quartz pouvant opérer jusqu'à 10 atmosphères (9). Dans ce réacteur, qui est de conception analogue à celui de Princeton, le combustible est introduit fortement dilué (concentration de l'ordre de 1%) dans un courant d'azote et d'oxygène préchauffé à la température de l'étude, par quatre orifices perpendiculaires au courant gazeux principal. Ses dimensions sont cependant beaucoup plus réduites: sa longueur est de 60 cm, son diamètre intérieur de 8 mm (diamètre extérieur: 13 mm), le diamètre de l'injecteur est de 4 mm et celui des trous d'injection de 0,1 mm.

Les expériences ont été réalisées en régime d'écoulement laminaire, pour des vitesses d'écoulement suffisamment importantes pour qu'il soit possible de négliger la diffusion longitudinale; en outre, le faible diamètre du réacteur, favorisant la diffusion radiale des espèces gazeuses, permet de faire l'hypothèse de l'écoulement piston. Mais cette approximation n'est plus vérifiée en présence d'une importante élévation de température due à la réaction, car on observe alors un gradient de température entre l'axe et la paroi du réacteur (réacteur non adiabatique). Ceci nous a contraints à limiter pratiquement nos études aux premières étapes de l'oxydation des hydrocarbures (conversion en oléfine et oxydation en oxyde de carbone), étapes qui sont thermoneutres ou faiblement exothermiques.

Le réacteur est placé dans un four comprenant plusieurs zones de chauffage, dans lequel ont été insérés quatre caloducs, ceci permettant d'obtenir, en l'absence de réaction, une température uniforme jusqu'à 50 cm de l'injecteur. Le chauffage du gaz vecteur et le chauffage du four entourant le réacteur sont assurés par des résistances électriques dont la tension est stabilisée par un régulateur électronique. La température du milieu gazeux est mesurée en déplaçant un thermocouple en chromel-alumel le long de l'axe du réacteur. Le prélèvement des espèces gazeuses dans le réacteur est effectué en remplaçant le thermocouple par une sonde en quartz effilée à son extrémité. Les gaz sont prélevés dans la sonde sous faible pression (< 15 torrs), à travers un orifice de très petit diamètre; ils sont ensuite stockés dans des ballons en pyrex, avant d'être analysés par chromatographie en phase gazeuse ou spectrométrie de masse.

B. Résultats expérimentaux.

Les premiers résultats expérimentaux obtenus selon cette technique, concernant l'oxydation du propane (1 à 6 bars) et du butane (1 bar) vers 1000 K, ont été publiés antérieurement (9).

De nouveaux résultats sur l'oxydation du propane ont été obtenus depuis, dans un domaine plus étendu de pressions (jusqu'à 10 bars) et de températures (jusqu'à 1170 K). D'autre part, afin de mieux appréhender la phase réactionnelle immédiatement préalable à la consommation de l'oxyde de carbone, il nous est apparu nécessaire d'entreprendre l'étude de l'oxydation de l'éthylène, susceptible d'apporter des données nouvelles sur la cinétique d'oxydation de cet important intermédiaire de la combustion des hydrocarbures. Cette étude a été effectuée dans un domaine de pressions compris entre 1 et 10 bars, entre 990 et 1100 K et pour des richesses comprises entre 0,25 et 4 .

Les figures 1, 2, 3 et 4 représentent quelques exemples de résultats expérimentaux. Bien que nous ayons pu doser également le méthane, l'éthane, l'hydrogène et l'acétylène (détecté à l'état de traces), nous n'avons reporté sur ces figures que les concentrations des composés majoritaires. Les profils de concentration des espèces en fonction de la distance à l'injecteur ont été convertis, à partir des valeurs des débits volumiques des gaz, en profils de concentration au cours du temps.

ETUDES EN REACTEUR HOMOGENE

Les limitations du domaine de validité de l'écoulement piston à un avancement réactionnel limité nous ont conduits à envisager une autre technique plus adaptée à l'étude des réactions à grand avancement: le réacteur parfaitement agité.

Villermaux et ses collaborateurs (10, 11) ont mis au point un réacteur auto-agi-

té par jets par jets gazeux, pouvant fonctionner pour des temps de passage de l'ordre de la seconde. De tels réacteurs ont été utilisés, en particulier, pour l'étude de la pyrolyse des hydrocarbures (12, 13) avec des temps de passage compris entre 0,05 et 10 secondes.

Utilisant les règles de construction préconisées par David, nous avons réalisé au Laboratoire un réacteur sphérique en quartz de 4 cm de diamètre, muni d'un injecteur en croix comprenant quatre orifices de 1 mm de diamètre. Ce réacteur possède la particularité d'être situé dans une enceinte étanche, ce qui permet son utilisation sous pression. Un thermocouple en chromel-alumel peut être déplacé à l'intérieur pour vérifier l'homogénéité de la température du milieu gazeux et la mesurer. Une sonde en quartz permet de prélever les espèces gazeuses en différents points dans le réacteur. Le chauffage du réacteur et le préchauffage du gaz vecteur sont assurés par des résistances électriques dont la tension est régulée.

Une étude préalable de la distribution des temps de séjour dans le réacteur, au moyen de l'injection d'un traceur inerte, a montré que les qualités du mélange ne sont pas modifiées dans la gamme de temps de passage précitée si le réacteur est utilisé à 10 bars au lieu de la pression atmosphérique.

Nous avons étudié, dans ce réacteur, l'oxydation de l'éthylène et du propane dans le domaine de pression 1-10 bars et pour des températures voisines de 1000 K. Un exemple des résultats expérimentaux est donné sur la figure 5.

INTERPRETATION

A. Modélisation en cinétique chimique.

Nous avons, depuis quelques années, abordé au Laboratoire, et en partie résolu, les problèmes concrets rencontrés en modélisation cinétique en faisant les hypothèses suivantes:

- la réaction chimique étudiée est représentable par un ensemble de réactions supposées élémentaires, constituant un mécanisme en chaînes. La vitesse de formation de l'espèce i est une combinaison linéaire des vitesses élémentaires directes et inverses des réactions mises en oeuvre dans le mécanisme. Le déroulement de la réaction peut être représenté par le système différentiel suivant:

$$dx_i/dt = f_i\ (t, x) \qquad (i = 1, N)$$

(t = temps,
x = tableau de dimension N, contenant les concentrations des N différentes espèces)

et:

$$dT/dt = -\frac{\Sigma h_j\, r_j}{\Sigma c_i\, x_i} - B\frac{(T - T_o)}{\Sigma c_i\, x_i}$$

représentant, selon le modèle thermique de Semenov, la vitesse d'évolution de la température au cours du temps, dans laquelle:

T est la température des gaz à l'instant t,
T_o, la température initiale des gaz,
h_j, le changement d'enthalpie produit par la réaction j, calculé à la température T à partir des enthalpies de formation de chaque espèce (h_i),
r_j, la vitesse de la réaction élémentaire j,
et c_i, la chaleur spécifique de l'espèce i à la température T.

Les valeurs des h_i et c_i, utilisés pour calculer la température et les constantes de vitesse des réactions inverses sont tirées des tables de Bahn (14).

B est un coefficient d'échange de chaleur (pris égal à $5.\ 10^{-2} cal.s^{-1}.cm^{-3}.K^{-1}$).

- il n'est pas nécessaire d'adjoindre au système ci-dessus d'équations décrivant les phénomènes de transport.

Le programme d'intégration utilise la méthode de Gear (15) dans la version E.P.I.S.O.D.E. (16), parfaitement adaptée aux problèmes rencontrés en cinétique. Il nous est ainsi possible d'être informé sur l'allure de la variation de concentration des composés au cours du temps, sur l'ordre de grandeur de leurs concentrations et sur l'importance relative des réactions en présence.

B. Recherche d'un mécanisme détaillé.

Nous avions proposé antérieurement un mécanisme détaillé, fondé sur les données cinétiques de la littérature, pour l'oxydation du propane et du butane. Ce mécanisme permettait de simuler correctement les résultats expérimentaux obtenus en réacteur tubulaire aux environs de 1000 K et jusqu'à un avancement limité à 50% de consommation du réactif initial. Toutefois, le schéma proposé ne prenait pas en compte l'intégralité des étapes élémentaires assurant la transformation de l'éthylène en oxyde de carbone, la vitesse de consommation de l'oléfine étant très faible dans ces conditions d'avancement limité. Ainsi, il n'était pas possible de vérifier la validité du mécanisme spécifique de l'oxydation de l'éthylène, tel que nous l'avions inclus dans le mécanisme global. Il est de fait que cette partie de notre ancien mécanisme ne nous a pas permis de simuler correctement les expériences réalisées sur l'éthylène pur en réacteur tubulaire.

Nous appuyant sur les mises au point les plus récentes de la littérature, nous avons considéré les mécanismes de Warnatz (17) et de Westbrook et al. (18) pour l'oxydation de l'éthylène. Le travail a consisté à tenter d'établir un mécanisme qui permette de simuler les expériences effectuées sur le propane et l'éthylène dans le domaine de températures compris entre 900 et 1200 K et de pressions compris entre 1 et 10 bars. Nous avons en outre testé la validité des différents mécanismes, quant à la simulation d'expériences

réalisées par Bellet et coll. (19) sur la combustion du propane et de l'éthylène dans un foyer turbulent tubulaire entre 1200 et 1600 K. Nous avons enfin comparé les délais d'inflammation expérimentaux obtenus par Burcat et al. (20) au cours d'une étude de la combustion du propane en tube à choc avec les délais calculés dans les mêmes conditions de température et de pression.

Cet ensemble de confrontations nous a amenés à retenir les propositions suivantes:

B.1 Oxydation de l'éthylène:

- le mécanisme proposé par Westbrook (18) doit être pris en compte. Il fait intervenir la formation d'acétylène par l'intermédiaire de radicaux CH_3 issus de l'interaction entre l'éthylène et les radicaux OH ou les atomes H, à savoir une séquence pouvant être schématisée sous la forme:

$$C_2H_4 + OH \rightleftharpoons \begin{cases} CH_3 + CH_2O \\ C_2H_3 + H_2O \end{cases}$$ } importance relative variable selon la richesse

$$C_2H_4 + H \longrightarrow C_2H_3 + H_2$$

$$C_2H_3 + M \longrightarrow C_2H_2 + H + M$$

La consommation ultérieure de l'acétylène s'effectue par l'intermédiaire des radicaux OH:

$$C_2H_2 + OH \longrightarrow C_2H + H_2O$$

$$C_2H_2 + OH \longrightarrow CH_3 + CO$$

avec formation préférentielle de C_2H et CH_3;

- les étapes suggérées récemment par Miller et al. (21) pour les radicaux CH_2, tels qu'ils les fait intervenir au cours de l'oxydation de l'acétylène:

$$CH_2 + O_2 \longrightarrow CO_2 + H_2$$

$$CH_2 + O_2 \longrightarrow CO_2 + H + H$$

$$CH_2 + O_2 \longrightarrow CO + H_2O$$

$$CH_2 + O_2 \longrightarrow CO + OH + H$$

doivent être considérées.

En ce qui concerne nos expériences, on observe un décalage entre les profils expérimentaux de concentration des espèces et les profils calculés, indiquant que la réaction démarre plus rapidement que ne le prévoit la simulation. L'étude de sensibilité montre que ce décalage varie de façon significative avec les valeurs attribuées aux constantes de vitesse des réactions:

$$C_2H_4 + OH \xrightarrow{18} C_2H_3 + H_2O$$

et $$C_2H_3 + O_2 \xrightarrow{31} C_2H_2 + HO_2$$

Pour réduire ce décalage, nous avons été amenés à attribuer à ces constantes les valeurs indiquées dans le tableau 1, au lieu de celles proposées par Westbrook , qui étaient les suivantes:

$$k_{18} = 4{,}8.\ 10^{12} \exp(-1{,}2/RT)\ cm^3.mol^{-1}.\ s^{-1}$$

$$k_{31} = 10^{12} \exp(-10/RT)\ cm^3.mol^{-1}.\ s^{-1}$$

Cet ajustement permet de réduire le décalage et non de l'annuler, ce qui nous conduit, ainsi que l'ont fait préalablement Westbrook et al., à incriminer le dispositif d'injection dans lequel l'éthylène commence de réagir avant de parvenir au réacteur. Ce démarrage précoce de la réaction d'oxydation de l'éthylène est pris en compte dans la simulation par la suppression de la période de délai.

La simulation de l'expérience de Bellet et coll. à partir des hypothèses précédentes montre toutefois que le mécanisme indiqué conduit à des délais d'inflammation beaucoup plus courts que ceux mesurés par ces auteurs. L'étude de sensibilité indique que ces délais sont très sensibles à la valeur de la constante de vitesse de la réaction 57, réaction rarement invoquée dans la littérature:

$$CH_3 + HO_2 \longrightarrow CH_3O + OH$$

Pour que les délais calculés soient du même ordre de grandeur que les délais expérimentaux, nous avons dû attribuer à cette constante de vitesse une valeur différente de celle utilisée par Westbrook ($k_{57} = 3{,}2.\ 10^{13}\ cm^3.mol^{-1}.\ s^{-1}$).

Compte tenu de cet ensemble de modifications, la comparaison entre les profils calculés et les profils expérimentaux est illustrée par les figures 1, 2 et 6.

B.2 Oxydation du propane:

Le mécanisme proposé antérieurement pour les réactions du propane et des radicaux C_3H_7 est resté inchangé (réactions 84 à 104). Mais le mécanisme d'oxydation du propène utilisé est celui proposé par Warnatz (17). Sur les figures 3 et 4, on peut comparer les profils de concentration calculés à partir du mécanisme du tableau 1 et les profils expérimen-

taux obtenus dans notre réacteur.

Sur la figure 7, nous avons confronté les résultats expérimentaux obtenus par Bellet et coll. au cours de l'étude de la combustion d'un mélange propane-éthylène 10% avec les résultats delasimulation.

Enfin, le tableau 2 permet la comparaison entre les délais d'inflammation obtenus en tube à choc par Burcat et al. (20) pour des mélanges propane-oxygène de richesses différentes et les délais calculés. Le délai d'inflammation calculé est ici défini comme le temps d'atteinte du maximum de concentration de OH. A quelques exceptions près, les délais calculés sont très voisins des délais expérimentaux, quelle que soit la richesse du mélange.

CONCLUSION

Les résultats qui viennent d'être présentés ont permis de progresser dans la connaissance de la cinétique détaillée d'oxydation du propane et de l'éthylène et le mécanisme proposé reflète correctement les observations effectuées dans des conditions expérimentales variées.

Il ne faut toutefois pas méconnaître qu'un tel mécanisme ne peut être utilisé sous sa forme intégrale pour modéliser les chambres de combustion. Une chambre peut être en effet considérée comme un assemblage de foyers homogènes, au sein desquels il est nécessaire d'envisager un couplage entre les phénomènes chimiques et les phénomènes de transport. A cet effet, la simplification du mécanisme s'avère indispensable.

Les études de sensibilité que nous avons entreprises ont déjà permis d'apprécier l'importance du rôle joué par certaines réactions élémentaires vis-à-vis de la morphologie des phénomènes observés. En outre, la possibilité que nous avons de comparer entre elles les vitesses des différentes étapes participant au mécanisme,à chaque instant de l'évolution réactionnelle,est un moyen de sélection des étapes à retenir pour la représentation d'un phénomène expérimental donné.

C'est dans ce sens que nous orientons actuellement notre démarche. Notre objectif de simplification devrait être atteint à court terme et fournir ainsi aux motoristes une base de travail mieux adaptée à la modélisation de la combustion dans les foyers de turboréacteurs.

REFERENCES

(1) W.C. GARDINER et D.B. OLSON: Ann. Rev. Phys. Chem. (B.S. RABINOVITCH, J.M. SCHURR et H.L. STRAUSS, Editors),Annual Reviews, Inc., Palo Alto, 1980, vol. 31, p. 377.
(2) I. GLASSMAN, F.L. DRYER et R. COHEN: "Second International Symposium onChemical Reaction Dynamics", Padova, 1975, p.138.
(3) G. LENGELLE et J.DUTERQUE: La Recherche Aerospatiale, n° 5, 1972, p. 249.
(4) C.K. WESTBROOK et F.L. DRYER: Comb. Sci. and Techno., vol. 27, 1981, p. 31.
(5) R.B. EDELMAN et O.F. FORTUNE: A.I.A.A. Paper n° 69-86, présenté au "A.I.A.A. 7th Aerospace Sciences Meeting",1969.
(6) J. DUTERQUE, R. BORGHI etH.TICHTINSKY: Comb. Sci.and Techno., vol. 26, 1981, p. 1.
(7) D.J. HAUTMAN, F.L. DRYER, K.P. SCHUG et I. GLASSMAN: Comb. Sci. and Techno.,vol. 25, 1981, p. 219.
(8) A.Y. ABDALLA, D. BRADLEY et S.B. CHIN: Comb. and Flame, vol. 43, 1981, p. 131.
(9) M. CATHONNET, J.C. BOETTNER et H.JAMES: 18th Symp. (Inetrnational) on Combustion, The Combustion Institute,1981,p. 903.
(10) R. DAVID et D. MATRAS: Can. J. Chem. Eng. Science, vol. 53, 1975, p. 297.
(11) M. FERRER, R. DAVID et J. VILLERMAUX: Second Specialists Meeting (International) of theCombustion Institute, Budapesy, 1982.
(12) P.M. MARQUAIRE et G.M. COME: React. Kin. Cat. Letters,vol. 9, n° 165, 1978,p. 171.
(13) C. JUSTE: Thèse D.I., Nancy, 1980.
(14) G.S. BAHN: Rep. N.A.S.A., CR 2178 , n° 73 20 932 , 1973.
(15) C.W. GEAR: Comm. Ass. Comp. Mach., vol. 14, 1971 p. 185.
(16) A.C. HINDMARSH et G.D. BYRNE: Comp. and Chem. Eng., vol. 1, 1977, p. 133.
(17) J. WARNATZ: 18th Symp. (International) on Combustion, The Combustion Institute, 1981 p. 369.
(18) C.K. WESTBROOK, F.L. DRYER et K.P. SCHUG: 19th Symp. (International) on Combustion, 1982 (à paraître).
(19) J.C. BELLET et coll.: Rapport de synthèse du contrat D.R.E.T. n° 82/071, 1983; Communication privée.
(20) A. BURCAT, A. LIFSHITZ, K. SCHELLER et G.B. SKINNER: 13th Symp. (International) on Combustion, 1971, p. 745.
(21) A. MILLER, R.E. MITCHELL, M.D. SMOOKE et R.J. KEE: 19th Symp. (International) on Combustion, 1982 (à paraître).
(22) D.L. ALLARA et D. EDELSON: Int. J. Chem. Kin., vol. 7 (1975), p. 479.
(23) R.W. WALKER: "Reaction Kinetics", vol. 1, S.P.R. Chemical Society, 1975,p. 161.
(24) R.W. WALKER: "Reaction Kinetics and Energy Transfer", vol. 2, S.P.R. ChemicalSociety, 1977, p. 296.
(25) A.G. MACLAIN, C.J. JACHIMOWSKI: "Chemical Kinetic Modeling of Propane Oxidation behind Shock Waves", N.A.S.A. TN D-8501, 1977.
(26) K.M. SUNDARAM et G.F. FROMENT: I. and E.C. Fundamentals, vol. 17, 1978, p.174.
(27) J.A. KERR et E. RATAJCKZACK: "Third Supplementary Tables of Bimolecular Gas Reactions", Department of Chemistry, The University of Birmingham, 1977.
(28) R.E. HUIEet J.T. HERRON: "Progrss in Reaction Kinetics" (K.R. JENNINGS et R.B. CUNDALL, Ed.), vol.8, Pergamon Press,1978, p. 1.

REMERCIEMENTS

Ce travail a été effectué avec le soutien de la Direction des Recherches, Etudes et Techniques, dans le cadre du contrat n° 81/140.

Nous adressons nos remerciements à Monsieur J.P. ROUAN, Ingénieur au C.N.R.S., pour l'aide qu'il nous a apportée dans la conception et la réalisation du réacteur parfaitement agité.

Tableau 1: Mécanisme d'oxydation du propane

Constantes de vitesse sous la forme: $k = A.T^{n}.\exp(-E/RT)$

Unités: cm^3, mole, s, kcal

n°	Réaction							A	n	E	Ref
1	CO2	O		=>	CO	O2		2.7E+12	0.0	43.8	18
2	CO	HO2		=>	CO2	OH		1.5E+14	0.0	23.6	18
3	CO	O	INER	=>	CO2	INER		2.4E+15	0.0	4.3	18
4	CO	OH		=>	CO2	H		1.5E+07	1.3	-.8	18
5	H2	INER		=>	H	H	INER	2.2E+14	0.0	96.0	18
6	H	HO2		=>	H2	O2		2.5E+13	0.0	.7	18
7	H	HO2		=>	OH	OH		2.5E+14	0.0	1.9	18
8	H	OH	INER	=>	H2O	INER		1.4E+23	-2.0	0.0	18
9	O	H2		=>	OH	H		1.8E+10	1.0	8.9	18
10	HO2	HO2		=>H2O2		O2		1.0E+13	0.0	1.0	18
11	OH	OH	INER	=>H2O2		INER		9.1E+14	0.0	-5.1	18
12	H	O2	INER	=>	HO2	INER		1.5E+15	0.0	-1.0	18
13	H	O2		=>	OH	O		2.2E+14	0.0	16.8	18
14	C2H4	O2		=>C2H3		HO2		4.0E+13	0.0	61.5	18
15	C2H4	INER		=>C2H2		H2	INER	9.3E+16	0.0	77.2	18
16	C2H4	INER		=>C2H3		H	INER	6.3E+18	0.0	108.7	18
17	C2H4	C2H4		=>C2H5		C2H3		5.0E+14	0.0	64.7	18
18	C2H4	OH		=>C2H3		H2O		4.8E+11	0.0	1.2	*
19	C2H4	OH		=>	CH3	CH2O		2.0E+12	0.0	1.0	18
20	C2H4	O		=>CH2O		CH2		2.5E+13	0.0	5.0	18
21	C2H4	O		=>	CH3	HCO		3.3E+12	0.0	1.1	18
22	C2H4	H		=>C2H3		H2		1.5E+07	2.0	6.0	18
23	C2H6	OH		=>C2H5		H2O		1.1E+13	0.0	2.4	18
24	C2H6	O		=>C2H5		OH		2.5E+13	0.0	6.4	18
25	C2H6	H		=>C2H5		H2		5.3E+02	3.5	5.2	18
26	C2H6	CH3		=>C2H5		CH4		5.5E-01	4.0	8.3	18
27	C2H6			=>	CH3	CH3		2.2E+19	-1.0	88.4	18
28	C2H5	INER		=>C2H4		H	INER	2.0E+15	0.0	30.0	18
29	C2H5	O2		=>C2H4		HO2		1.0E+12	0.0	5.0	18
30	C2H3	INER		=>C2H2		H	INER	7.9E+14	0.0	31.5	18
31	C2H3	O2		=>C2H2		HO2		1.0E+11	0.0	10.0	*
32	C2H2	O2		=>	HCO	HCO		4.0E+12	0.0	28.0	18
33	C2H2	INER		=>	C2H	H	INER	1.0E+14	0.0	114.0	18
34	C2H2	OH		=>	C2H	H2O		6.3E+12	0.0	7.0	18
35	C2H2	OH		=>	CH3	CO		1.2E+12	0.0	.5	18
36	C2H2	H		=>	C2H	H2		2.0E+14	0.0	19.0	18
37	C2H2	O		=>	CH2	CO		2.2E+10	1.0	2.6	21
38	C2H2	O		=>	C2H	OH		3.0E+15	-.6	17.0	18
39	C2H	O2		=>	HCO	CO		1.0E+13	0.0	7.0	18
40	CH2	O2		=>	HCO	OH		1.0E+14	0.0	3.7	21
41	CH2	O2		=>	CO2	H2		6.9E+11	0.0	.5	21
42	CH2	O2		=>	CO2	H	H	1.6E+12	0.0	1.0	21
43	CH2	O2		=>	CO	H2O		1.9E+10	0.0	-1.0	21
44	CH2	O2		=>	CO	OH	H	8.7E+10	0.0	-.5	21
45	C2H	O		=>	CO	CH		5.0E+13	0.0	0.0	18
46	CH2	O		=>	CH	OH		1.9E+11	.7	25.0	18
47	CH2	H		=>	CH	H2		2.7E+11	.7	25.7	18
48	CH2	OH		=>	CH	H2O		2.7E+11	.7	25.7	18
49	CH	O2		=>	CO	OH		1.3E+11	.7	25.7	18
50	CH	O2		=>	HCO	O		1.0E+13	0.0	0.0	18
51	CH4	INER		=>	CH3	H	INER	1.4E+17	0.0	88.4	18
52	CH4	OH		=>	CH3	H2O		3.5E+03	3.1	2.0	18
53	CH4	H		=>	CH3	H2		1.3E+14	0.0	11.9	18
54	CH4	O		=>	CH3	OH		1.6E+13	0.0	9.2	18
55	CH4	HO2		=>	CH3	H2O2		2.0E+13	0.0	18.0	18

Tableau 1 (suite)

n°	Réaction						A	n	E	Ref
56	CH3	O2		=>CH3O	O		4.8E+13	0.0	29.0	18
57	CH3	HO2		=>CH3O	OH		1.6E+12	0.0	0.0	*
58	CH3	HO2		=> CH4	O2		1.0E+12	0.0	.4	18
59	CH3	OH		=>CH2O	H2		4.0E+12	0.0	0.0	18
60	CH3	O		=>CH2O	H		1.3E+14	0.0	2.0	18
61	CH3	HCO		=> CH4	CO		3.0E+11	.5	0.0	18
62	CH2O	INER		=> HCO	H	INER	3.3E+16	0.0	81.0	18
63	CH2O	OH		=> HCO	H2O		7.6E+12	0.0	.2	18
64	CH2O	H		=> HCO	H2		3.3E+14	0.0	10.5	18
65	CH2O	HO2		=> HCO	H2O2		1.0E+12	0.0	8.0	18
66	CH2O	O		=> HCO	OH		5.0E+13	0.0	4.6	18
67	CH2O	CH3		=> HCO	CH4		1.0E+10	.5	6.0	18
68	CH3O	INER		=>CH2O	H	INER	5.0E+13	0.0	21.0	18
69	CH3O	O2		=>CH2O	HO2		1.0E+12	0.0	6.0	18
70	HCO	O2		=> CO	HO2		3.2E+12	0.0	7.0	18
71	HCO	INER		=> H	CO	INER	1.4E+14	0.0	19.0	18
72	HCO	OH		=> CO	H2O		1.0E+14	0.0	0.0	18
73	HCO	H		=> CO	H2		2.0E+14	0.0	0.0	18
74	HCO	O		=> CO	OH		1.0E+14	0.0	0.0	18
75	HCO	HO2		=>CH2O	O2		1.0E+14	0.0	3.0	18
76	H2O2	OH		=> H2O	HO2		1.0E+13	0.0	1.8	18
77	H2O2	H		=> H2	HO2		1.7E+12	0.0	3.8	18
78	H2	OH		=> H2O	H		2.2E+13	0.0	5.1	18
79	H2O	O		=> OH	OH		6.8E+13	0.0	18.4	18
80	HO2	OH		=> H2O	O2		5.0E+13	0.0	1.0	18
81	HO2	O		=> OH	O2		5.0E+13	0.0	1.0	18
82	O2	INER		=> O	O	INER	5.1E+15	0.0	115.0	18
83	O	H	INER	=> OH	INER		1.0E+16	0.0	0.0	18
84	C3H8			=>C2H5	CH3		4.0E+16	0.0	84.5	22
85	C3H8	O2		=>N3H7	HO2		4.0E+13	0.0	47.5	23
86	C3H8	O2		=>I3H7	HO2		4.0E+13	0.0	47.5	23
87	C3H8	C2H5		=>N3H7	C2H6		1.0E+11	0.0	13.4	22
88	C3H8	C2H5		=>I3H7	C2H6		5.0E+10	0.0	10.4	22
89	C3H8	CH3		=>N3H7	CH4		2.9E+12	0.0	11.7	23
90	C3H8	CH3		=>I3H7	CH4		6.6E+11	0.0	10.1	23
91	C3H8	H		=>N3H7	H2		1.3E+14	0.0	9.7	22
92	C3H8	H		=>I3H7	H2		1.0E+14	0.0	8.3	22
93	C3H8	OH		=>N3H7	H2O		3.7E+12	0.0	1.6	23
94	C3H8	OH		=>I3H7	H2O		2.8E+12	0.0	.9	23
95	C3H8	O		=>N3H7	OH		3.0E+13	0.0	5.8	23
96	C3H8	O		=>I3H7	OH		2.6E+13	0.0	4.5	23
97	C3H8	HO2		=>N3H7	H2O2		2.9E+11	0.0	14.9	24
98	C3H8	HO2		=>I3H7	H2O2		9.8E+10	0.0	12.6	24
99	N3H7			=>C2H4	CH3		1.6E+13	0.0	32.0	22
100	I3H7			=>C2H4	CH3		1.0E+12	0.0	34.5	25
101	N3H7			=>C3H6	H		2.0E+13	0.0	38.4	26
102	I3H7			=>C3H6	H		4.0E+13	0.0	40.3	22
103	N3H7	O2		=>C3H6	HO2		1.0E+12	0.0	5.8	9
104	I3H7	O2		=>C3H6	HO2		7.3E+12	0.0	5.8	9
105	C3H6	C2H5		=>C3H5	C2H6		1.0E+11	0.0	9.2	26
106	C3H6	OH		=>MCHO	CH3		7.0E+12	0.0	0.0	17
107	C3H6	OH		=>C3H5	H2O		8.0E+12	0.0	0.0	27
108	C3H6	H		=>C3H5	H2		1.0E+14	0.0	3.8	22
109	C3H6	O		=>C2H5	HCO		1.5E+12	0.0	0.0	28
110	C2H3	H		=>C2H2	H2		2.0E+13	0.0	2.5	18
111	MCHO	H		=> MCO	H2		4.0E+13	0.0	4.2	17
112	MCHO	O		=> MCO	OH		5.0E+12	0.0	1.8	17
113	MCHO	OH		=> MCO	H2O		1.0E+13	0.0	0.0	17
114	MCO	INER		=> CH3	CO	INER	1.0E+15	0.0	9.4	17

N_3H_7 = n C_3H_7 $\quad$ I_3H_7 = i C_3H_7 $\quad$ * voir texte

MCHO = CH_3CHO $\quad$ MCO = CH_3CO

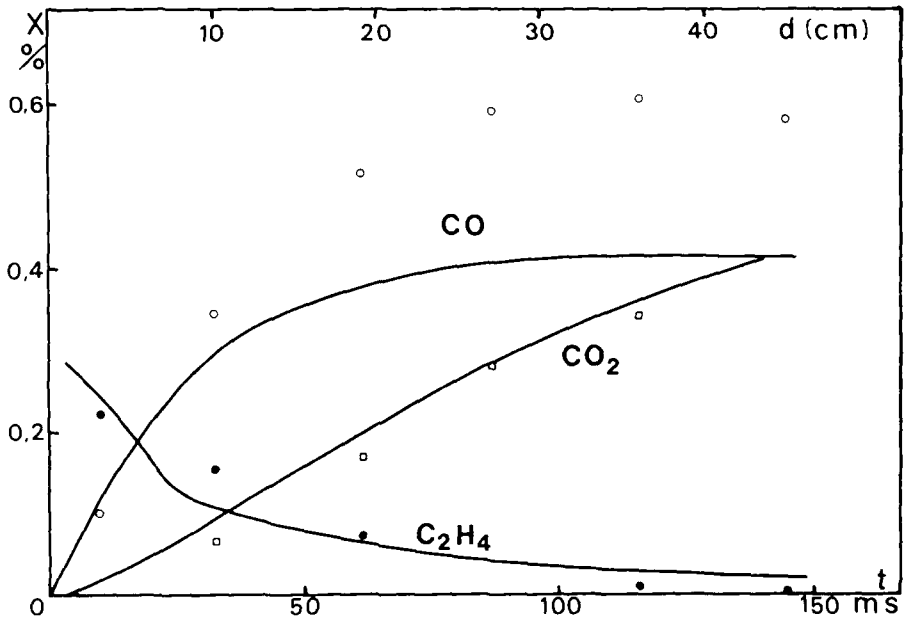


Figure 1 : Oxydation en réacteur tubulaire
Mélange C_2H_4-O_2-N_2 ϕ = 1 P = 5 bars T_o = 1048 K
Comparaison entre les profils calculés et les points expérimentaux

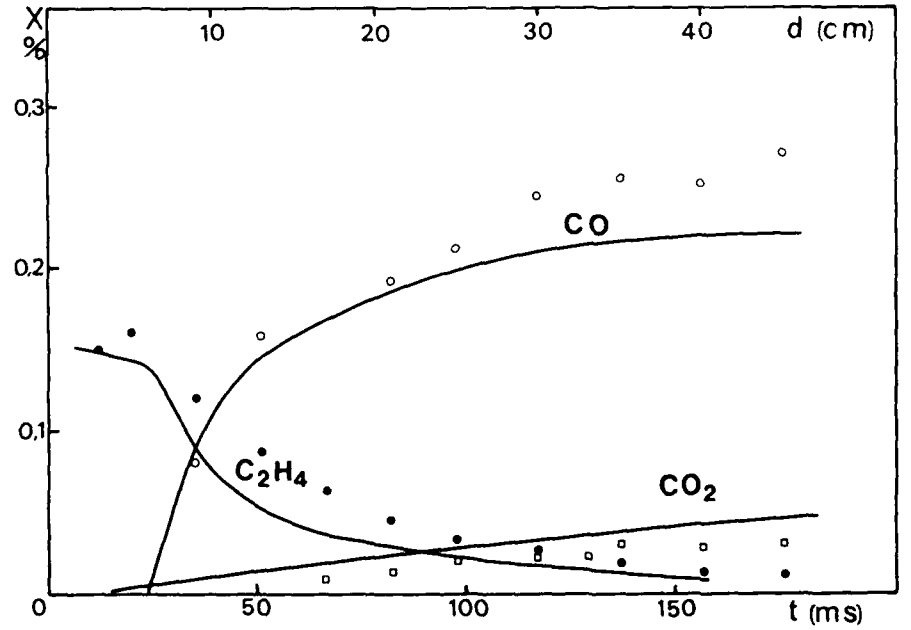


Figure 2 : Oxydation en réacteur tubulaire
Mélange C_2H_4-O_2-N_2 ϕ=0,75 P=10 bars T_o = 1047 K
Comparaison entre les profils calculés et les points expérimentaux

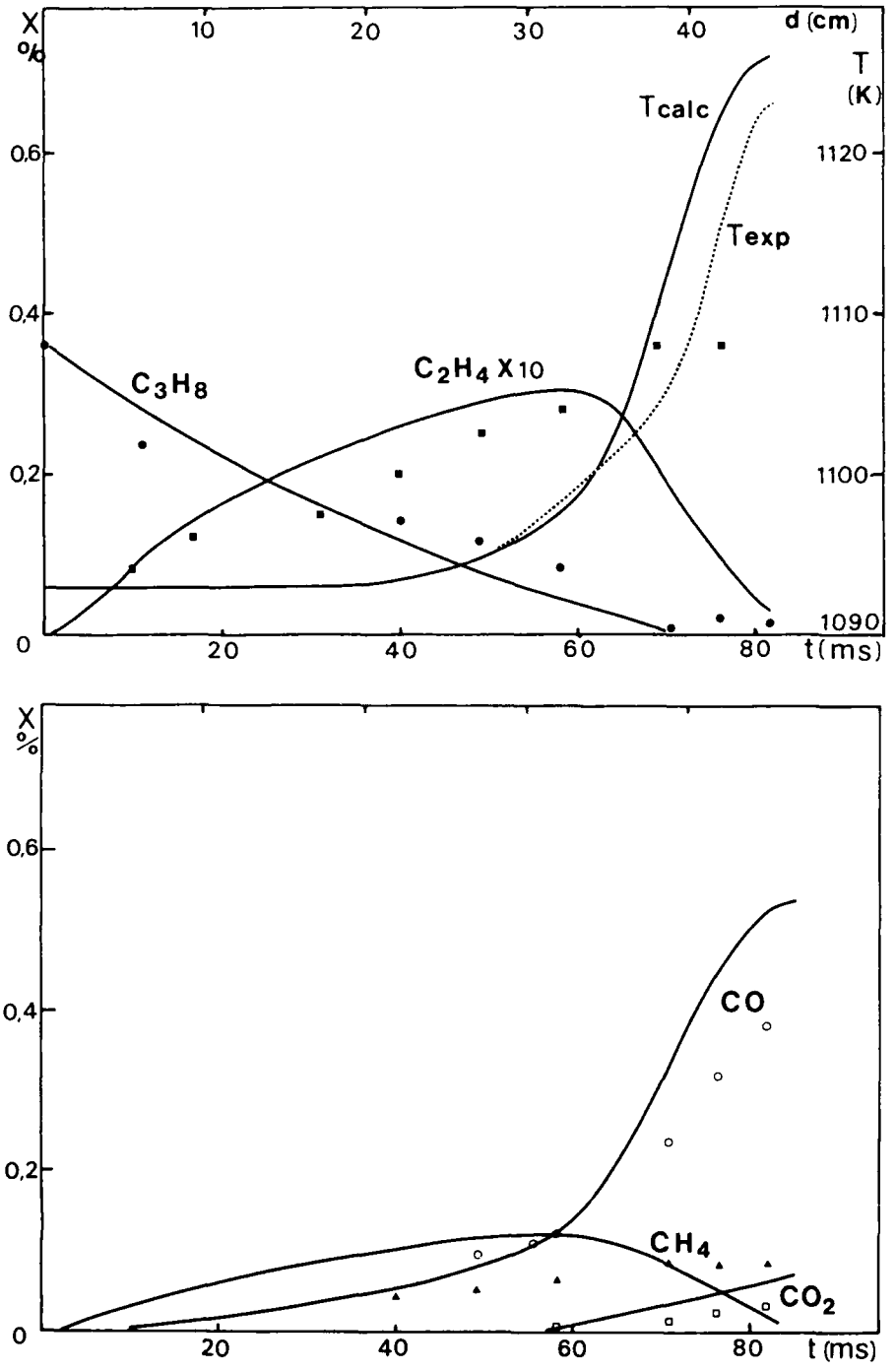


Figure 3 : Oxydation en réacteur tubulaire
Mélange C_3H_8-O_2-N_2 $\Phi = 0,75$ P = 5 bars T_o = 1093 K
Comparaison entre les profils calculés et les points expérimentaux

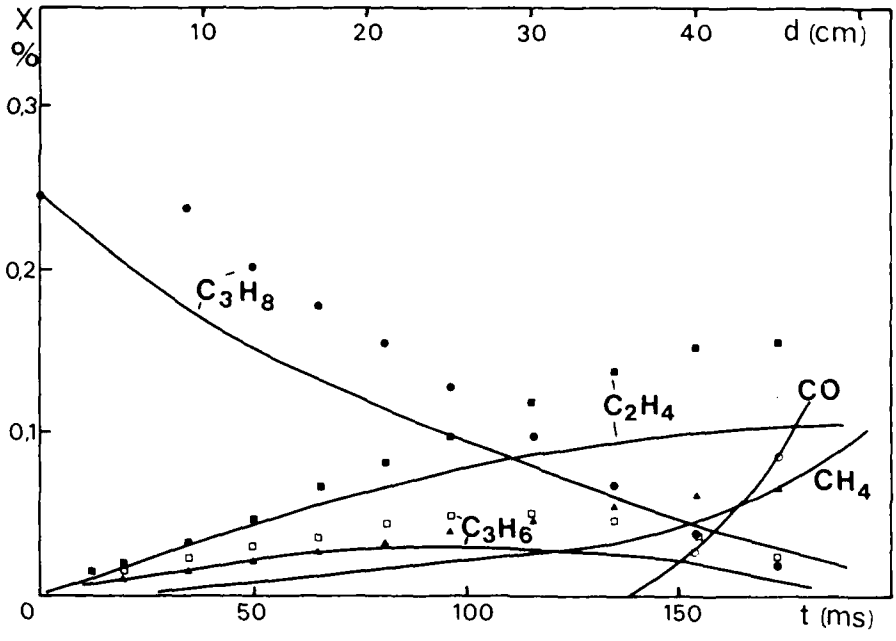


Figure 4 : Oxydation en réacteur tubulaire
Mélange C_3H_8-O_2-N_2 Φ = 1 P = 10 bars T_o = 1050 K
Comparaison entre les profils calculés et les points expérimentaux

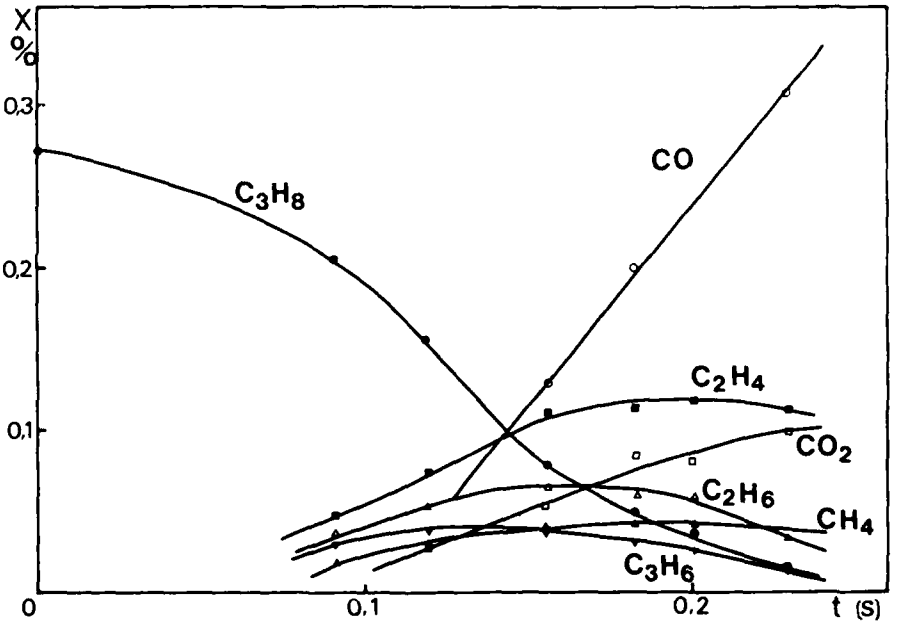


Figure 5 : Oxydation en réacteur agité
Mélange C_3H_8-O_2-N_2 Φ = 0,5 P = 5 bars T_o = 973 K
Distribution des produits en fonction du temps de séjour

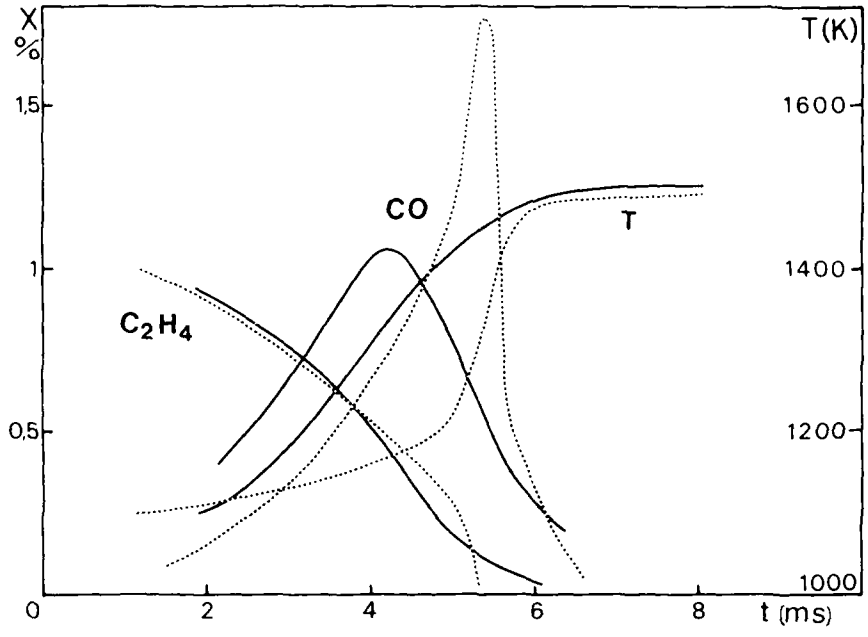


Figure 6 : Combustion de l'éthylène

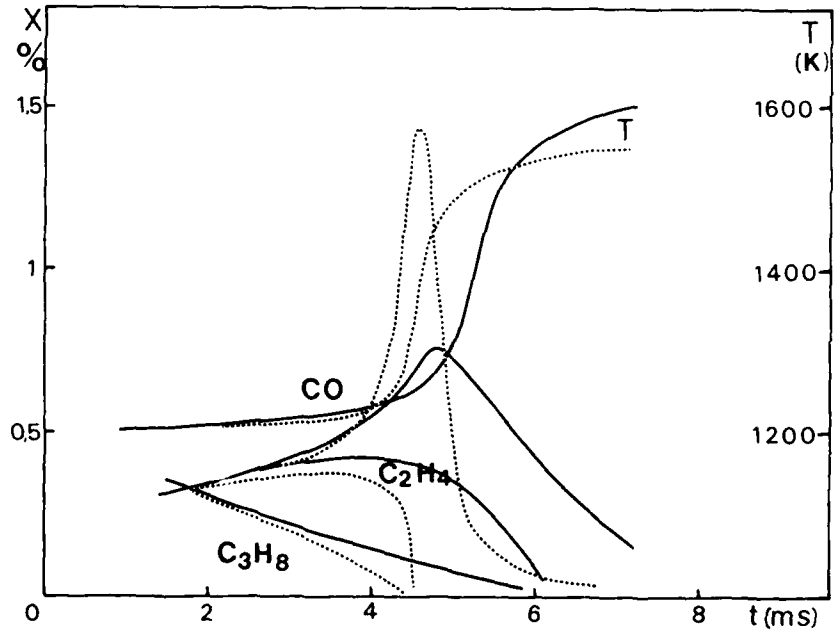


Figure 7 : Combustion d'un mélange propane-éthylène

Combustion en présence de gaz brulés dans un écoulement turbulent monodimensionnel (Bellet et coll., ref. 19)
Comparaison entre les profils expérimentaux —— et calculés ----

Tableau 2

Comparaison entre les délais d'inflammation mesurés en tube à choc (ref. 20) et calculés

n°	Composition		Rapport	T	P	Délai (µs)	
	% C_3H_8	% O_2	d'équivalence	(°K)	(atm)	expérimental	calculé
130	0,41	16,4	0,125	1425	8,08	40	40
142	0,41	16,4	0,125	1262	7,17	340	440
144	0,8	16	0,25	1367	8,19	90	90
156	0,8	16	0,25	1340	8,30	140	130
59	0,8	8	0,5	1423	7,66	70	70
75	0,8	8	0,5	1292	6,63	425	510
95	0,41	4,1	0,5	1393	6,77	205	160
112	0,41	4,1	0,5	1492	7,67	77	40
1	1,6	8	1	1495	2,62	68	84
3	1,6	8	1	1440	2,45	195	155
29	1,6	8	1	1302	8,29	390	525
30	1,6	8	1	1352	8,45	185	245
26	0,48	2,4	1	1495	8,66	85	65
28	0,48	2,4	1	1374	7,55	415	380
45	3,85	19,23	1	1587	14,07	12	8
78	0,84	2,1	2	1439	7,6	545	585
79	0,84	2,1	2	1539	8,32	230	60
114	1,6	4	2	1447	8,10	225	165
116	1,6	4	2	1354	7,24	580	680

AD-P003 147

THE DESIGN AND DEVELOPMENT OF A LOW EMISSION TRANSPLY COMBUSTOR FOR THE CIVIL RB211 ENGINE

BY

Dr. C.K. Bhargava and Mr. D.M. Snape,*
Combustion Technology,
Rolls-Royce Limited,
Moor Lane,
P.O. Box 31,
DERBY,
DE2 8BJ,
U.K.

Mr. S.R. Bentley,
Spey Engine Development,
Rolls-Royce Limited,
East Fields,
DERBY,
DE2 8BJ,
U.K.

SUMMARY

This paper describes the design and development of a low emissions 'can-annular' combustor for service in the Spey aero gas turbine engine. The combustors, two of which form the annular combustion system, are constructed from an advanced cooling material known as Transply. The use of this pseudo transpiration cooling material enables a significant saving to be made in the utilisation of the wall cooling air. This air is used in optimising the primary zone and intermediate zone stoichiometry which, combined with the use of an aerodynamic curved vane swirler, results in substantial reductions in the emission levels.

A number of significant durability problems have been overcome to meet the rigours of aero-engine operation. The paper outlines the development process, starting with the constraints imposed by an existing engine design and describing the rig and engine test programme leading to full definition of the aero-thermodynamics of the developed combustor.

RESUME

Les auteurs décrivent l'étude et le développement d'un système de combustion tubo-annulaire, à faible niveau d'émission, actuellement mis en service sur le moteur d'avion à turbine à gaz 'Spey'. Le système est composé de dix chambres de combustion constituées d'un matériau de refroidissement de technologie avancée, connu sous le nom de 'Transply'. Ce matériau de refroidissement, qui agit par transpiration, permet d'économiser de façon significative l'air de refroidissement des parois. Cet air est utilisé pour optimiser la stoechiométrie de la zone primaire et de la zone intermédiaire; ce principe, associé à l'utilisation d'aubes de turbulence aérodynamiques incurvées, permet de réduire les niveaux d'émission de façon substantielle.

Pour répondre aux strictes exigences de fonctionnement d'un moteur d'avion, il a fallu résoudre un certain nombre de problèmes importants de longévité. Les auteurs exposent dans ses grandes lignes le processus de développement, depuis les contraintes imposées par la configuration d'un moteur existant, et décrivent le programme d'essais sur banc et sur moteur qui a permis de définir en détail l'aéro-thermodynamique du foyer mis au point.

NOMENCLATURE

FAR	Fuel Air Ratio
UHC	Unburnt Hydrocarbons
CO	Carbon Monoxide
CO_2	Carbon Dioxide
NOx	Oxides of Nitrogen
SAE	Smoke Number
EI	Emission Index
DP/Foo	Landing Take-off (LTO) cycle integrated pollution parameter (g/kN)
ϕ	Equivalence Ratio
CAA	U.K. Civil Aviation Authority
EPA	U.S. Environmental Protection Agency
ICAO	International Civil Aviation Organisation

* All communications should be addressed to D.M. Snape

INTRODUCTION

The process to control exhaust emissions from aircraft gas turbines started in the late [illegible]. By the late 1970's ICAO and EPA had iterated towards internationally agreed standards and [illegible] procedures. In ref. 1 ICAO published standards that countries states are expected to [illegible] legislation to control smoke only from 1 January 1981 and then, CHC, CO and NO_x from 1 January 1983. It was in anticipation of this proposed legislation that work was started in 1977 on a low emissions combustor for the Civil Spey Mk555 engine, with a view to developing a low [illegible] for 1983 and a fully compliant combustor for 1986. In December 1981 EPA published their final [illegible] rules promulgating UHC and smoke standards only from 1 January 1984.

The Rolls-Royce Spey engine family was conceived in the late fifties, with Mark [illegible] first [illegible] in the Trident I. The design of the combustor for this engine was derived by [illegible] then existing in the Rolls-Royce Medway engine. At this time, no special consideration was given to minimising the emissions from the engine. Regrettably (with hindsight) a low [illegible] drawn was carried out rather than one on the basis of the combustor volume resulting in:-

(a) a highly loaded combustor i.e. shorter residence time, Figure 1

(b) a large surface to volume ratio i.e. disproportionately large quantities of wall [illegible] flows, Figure 2

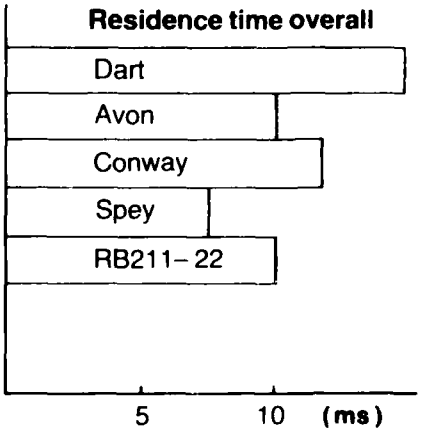
Neither of these factors are conducive to low emissions, particularly [illegible] prevented the primary zone being weakened to air/fuel ratio levels necessary for a [illegible] invisible smoke trail. The fuel injection and control systems were also based on proven, earlier technology. A duplex fuel schedule was selected so that the pilot atomiser could be [illegible] entirely for the flight restarting role, which is particularly difficult in non-annular [illegible]. Fuel atomisation depended on a high fuel supply pressure as airspray atomisation technology was [illegible] then sufficiently advanced. This approach did however, permit a very small injector [illegible] and advantage was taken of this to reduce the access apertures in the highly-stressed combustor outer casing.

Combustor wall cooling was achieved by film devices, the body being cooled by a [illegible] which was chosen for its durability and cheapness in comparison to contemporary fabricated [illegible] rings.

The film cooled Spey Mk 555 combustion and fuel/injector system is illustrated in Figure 3. The emissions performance of this engine is compared to the regulatory limits in the table below:

TABLE 1	DP/Foo (g/kN)			MAX SMOKE (SAE)
	UHC	CO	NO_x	
Mk 555-15 W/S combustor	487	685	60	37
ICAO Regulatory Limits	19.6	118	70.2	25.7

This paper describes the work carried out to develop a low emissions combustor to comply with the ICAO requirements.



SMC 1477

Fig. 1 Comparison of combustor residence times

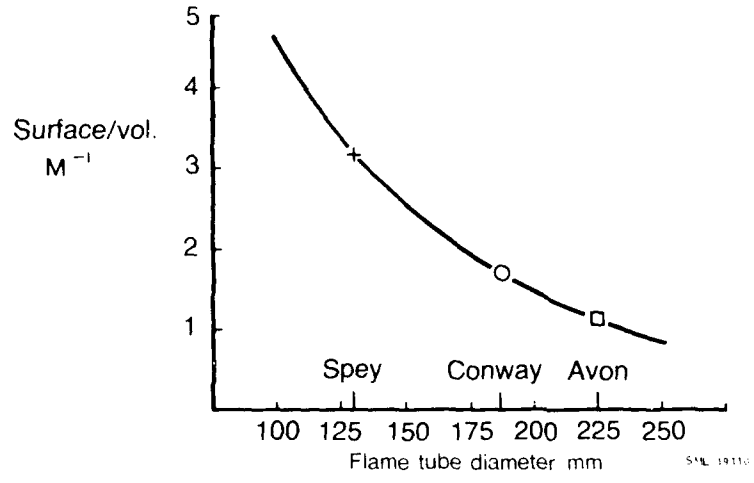


Fig.2 Cooled - surface/burning - volume ratio comparison - tubo-annular combustors

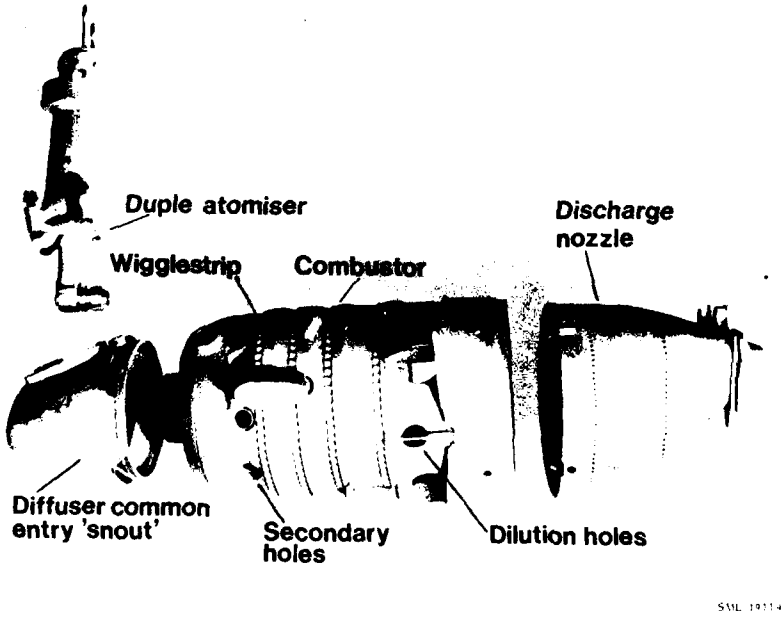


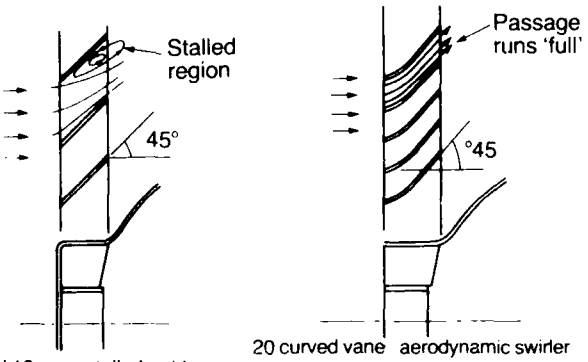
Fig.3 Spey Mk.555 film - fed combustion system

In the primary zone the hydrocarbons are converted into CO and carbon particles in fuel rich regions. In addition, the hot reverse flow in the primary zone is deficient in oxygen preventing any subsequent oxidation of particles. This problem can be alleviated either by entraining more of the secondary air or by increasing the recirculation ratio of the swirler flow. The latter course was chosen because it has the additional benefit, at ground idle, of the hot re-circulating products mixing with the incoming fuel and air mixture and thus increasing the reaction temperature of the fuel rich zone. This objective was attained by employing an aerodynamic curved vane swirler, as shown in Figure 4. In principle, the curved vane swirler should increase ground idle combustion efficiency and decrease peak smoke simultaneously. This was demonstrated practically during the development of the low smoke combustion system for the Spey Mk 511-5, the powerplant for the Trident Air Space 3211 aircraft.

In the intermediate zone, where the temperature is sensibly constant, CO and carbon particles are oxidised to CO$_2$ by the fresh oxygen made available by the secondary air, provided the residence time is long enough. Since the conditions necessary for NO$_x$ reductions are not fully compatible with UHC and CO reductions at lower power, no attempt was made to minimise NOx levels. Thus the new intermediate design was based on minimising the CO level at ground idle. To this end, the CO concentration at a given elapsed time was determined by reference to a chemical kinetic scheme of the reactions occurring at ground idle (Ref. 8). The emission index EI_{CO} is plotted against elapsed time for a fully mixed system for various equivalence ratios in Figure 5.

For the Spey to comply with the proposed ICAO/EPA emission level for CO, the ground idle EI_{CO} needs to be less than 15. Figure 5 shows that an intermediate zone equivalence ratio of around 0.7 is required to attain the emission target. It is possible from these curves to derive an optimum rate of dilution of the primary zone gases to produce minimum CO levels. This is obtained by plotting d(EI)/dt against t for each equivalence ratio, and taking the maximum consumption rate at each condition. The result is shown in Figure 6 where the equivalence ratio is plotted against elapsed time. This shows that the equivalence ratio of 0.7 should be achieved in 0.7 milli-seconds, a design objective which was attained by incorporating two axially spaced rows of secondary holes and assuming a fully pre-mixed system. The position and size i.e. the penetration, of each hole was determined to yield good mixing at each station. In practice, the quality of mixing will determine departures from the optimum CO levels. Past experience has shown that the resulting equivalence ratio at peak power is also near optimum for consumption of soot particles. The level of UHC was reduced by minimising wall cooling flows.

The method used to reduce the cooling air flows was to employ the Rolls-Royce psuedo transpiration material called Transply.



Standard 10 vane stalled swirler
Creates a rich region along burner axis in PZ
→ excess free carbon → high black smoke.

20 curved vane aerodynamic swirler
This device generates more efficient swirl → higher swirl number → higher mass flow recirculation back along burner axis → lower smoke and improved combustion efficiency. SML 19111

Fig.4 Differences between standard 10 vane stalled swirler and 20 curved vane aerodynamic swirler

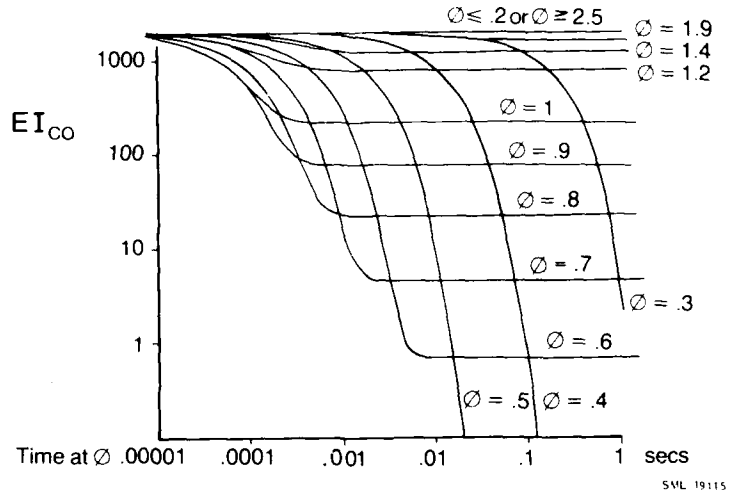


Fig.5 EI_{CO} burn up for Spey idle conditions

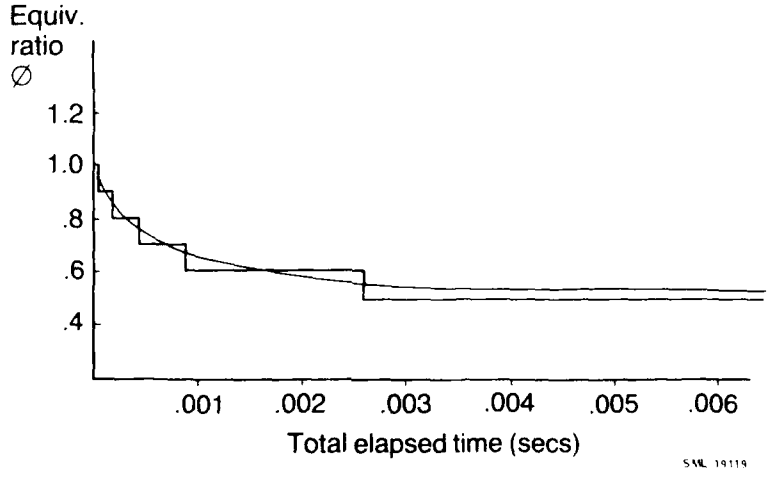


Fig.6 Optimum rate of dilution for CO burn up (fully mixed)

TRANSPLY

Transply is produced by brazing together two or more laminates of a high temperature alloy containing an interrelated pattern of holes and channels, produced by electro-chemical machining. This provides an advanced cooling configuration in sheet form with an overall thickness typical of current combustor materials. Figure 7 shows how two laminate transply is assembled. The development of this material has been described in detail in Ref.4. Various standards of two laminate Transply have been produced with different orientations of holes in the feedside and hot gas side laminate. The metering of the flow through Transply is carried out by the feedside holes.

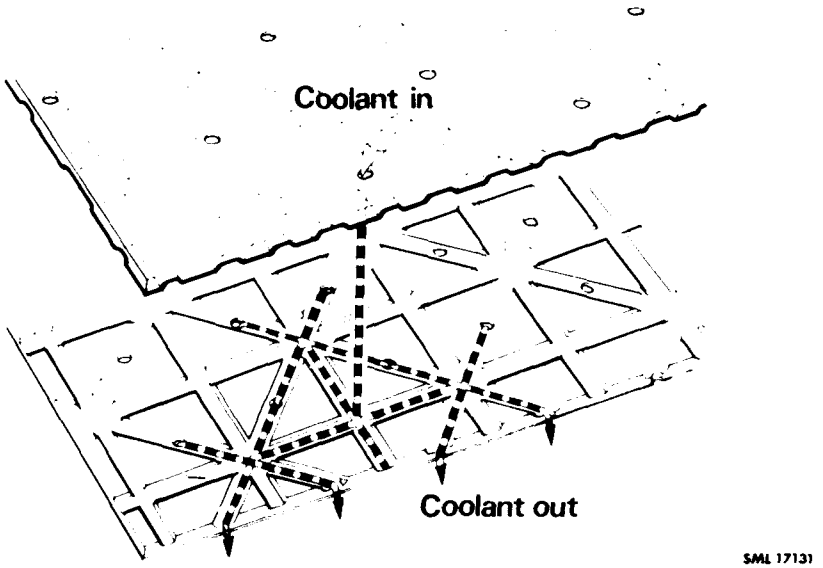


Fig.7 Two-laminate Transply

4. RIG AND ENGINE DEVELOPMENT

The definition of the combustor now in airline service is the result of an extensive rig and engine test programme lasting a number of years. Rig testing has taken various forms viz:

(i) Water analogy tests - These have been used to visualise flow patterns within full size transparent (Perspex) model combustors. This technique was particularly useful in the early development of the curved vane swirler.

(ii) Airflow tests - Full scale single sector tests, used to confirm calculated predictions of combustor pressure loss and to determine aerodynamic effects in the annuli, have been supplemented by smaller scale airflow testing on all of the major individual combustor components including the Transply.

(iii) Atmospheric pressure tests - Single sector testing at atmospheric pressure has been used for flame observation in screening various modifications. This qualitative approach has proved useful and is now being supplemented by a quantitative method. Here gas sampling traverses are carried out at various planes within the combustor leading to contour plots of fuel air ratio, unburnt hydrocarbons and carbon monoxide. It is expected that this technique will lead to further improvements to future standards of the combustor. Tests to determine the basic ignition performance of the combustor are also carried out at atmospheric pressure.

(iv) High pressure single sector tests - facilities for this type of testing (see Figure 8) extend across the whole range of engine operating conditions enabling the following combustor parameters to be determined:-

- Emissions measurement - Combustion efficiency is normally measured at 7% thrust conditions for comparison with the lowest of the EPA/ICAO mode points. Gas samples are transported via heated lines to a mobile laboratory where concentrations of carbon monoxide, unburnt hydrocarbons and carbon dioxide are measured. The heated line sample transport system and the laboratory conform to the requirements of Ref.1. Good agreement has been obtained between rig measured results and measurements taken on engine tests. Measurements of smoke and oxides of nitrogen are made using the same basic set-up at maximum take-off conditions. Gas samples for rig smoke measurement are taken directly from the hot gas stream, i.e. without dilution by the bypass stream. A good correlation between rig and engine test results has been established once an allowance is made for the bypass ratio.

- Pattern factor - the combustor outlet temperature pattern factor is normally measured at maximum take-off conditions using a single thermocouple probe to produce a 72 point measurement array.

- Metal temperature - thermal paints are used to assess the effect on wall temperatures of all modifications to combustors. Direct measurement of metal wall temperature using embedded thermocouples has also been carried out. This technique enables measurements to be taken over a range of conditions both inside and outside the engine operating envelope.

(v) Sub Atmospheric Tests - altitude ignition and light-round performance has been assessed using a triple sector (i.e. 3 interconnected combustors) rig which runs at simulated altitude windmilling conditions.

The engine test programme has run in parallel with the rig programme, the value of all of the parameters monitored at exit. Particular emphasis has been placed on the durability aspects of the combustor in engine testing. Since this book is [illegible] rig assessment, no attempt is made here to report more than a small portion of the test results obtained.

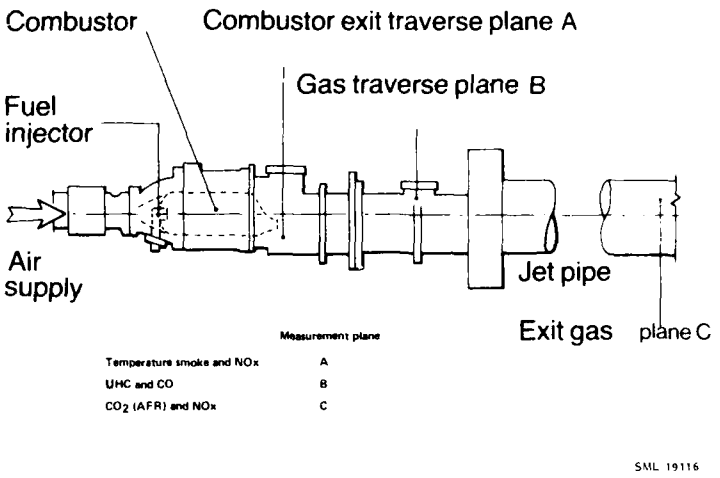


Fig.8 Spey single-sector high pressure high temperature rig

5. TRANSPLY I COMBUSTOR

The first fully viable Spey all Transply combustor, Transply I, is illustrated diagramatically in Figure 9. The design had its origins both in research work carried out on earlier Spey sized Transply combustors and in the theoretical studies described in Section 2. The requirement that the new combustor should be a direct replacement for the existing standard determined the design of features such as method of location. The standard discharge nozzle, cooled by splash strips and the existing duple fuel spray nozzles were retained. Novel features of Transply I were:

(a) A 20 vane aerodynamic curved vane swirler with 45° vane angle. The number of vanes and the vane angle were based on an empirical study into the effect of these parameters on pollutant formation.

(b) Z Cooling rings at the point where the Transply barrel was joined to the head and to the downstream sheet metal section. The filming characteristics of Transply, Ref.4, showed the need for a starter film device and for a means of cooling sheet metal components immediately downstream of the Transply barrel.

(c) Transply for the hemispherical head and cylindrical barrel, chosen to minimise air requirements whilst maintaining adequate cooling performance. The configuration and porosity of the Transply required was determined from data obtained as part of the Transply material evaluation programme.

(d) Plunged secondary and dilution holes and plain intermediate zone holes sized to obtain the optimum zonal fuel air ratio distribution discussed in Section 2. A new technique of hole plunging was developed specifically for use with Transply.

The design was further finessed during a development programme using the single sector HP test rig. The main achievements of the programme being in emissions improvements brought about by 'fine-tuning' of the zonal fuel air ratios.

Full HP rig evaluation of the combustor performance showed substantial improvements in both gaseous emissions and smoke, compared to the conventional combustor. The outlet temperature pattern factor and sea level ignition characteristics were also superior to those of the standard combustor. Results from a rig thermal-paint test at maximum take-off condition (Figure 10) show the Transply head to be at an acceptable temperature except where the Transply is welded to the first section of the Z cooling ring. The barrel showed substantial areas of over-heat, most severe downstream of plunged secondary and dilution holes, along the axial weld and around the downstream Z cooling ring.

Engine test results largely confirmed the rig results, the emissions performance (Figure 11) meeting the proposed smoke limit and making substantial progress towards meeting proposed limits on carbon monoxide and unburnt hydrocarbons. A 50 hour cyclic endurance test produced the result illustrated in Figure 12. The thermal fatigue cracks on the combustor could be correlated with hot areas shown up by thermal paint.

It was concluded from the results obtained with the Transply I Combustor that the basic philosophy used to gain an emissions reduction was sound but that a redesign was required to produce improvements in durability.

The development time foreseen to be required led to a decision at that point to aim to comply initially with the smoke limit proposed for 1983, and to develop the combustor later to meet the proposed ICAO 1986 CO, UHC and NOx limits.

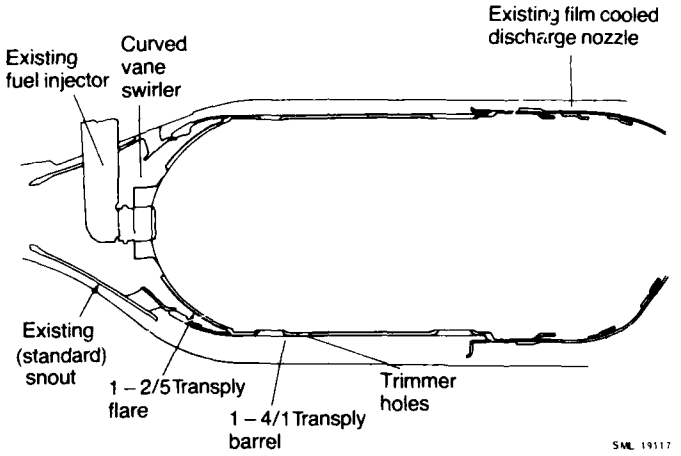


Fig.9 Transply I combustor

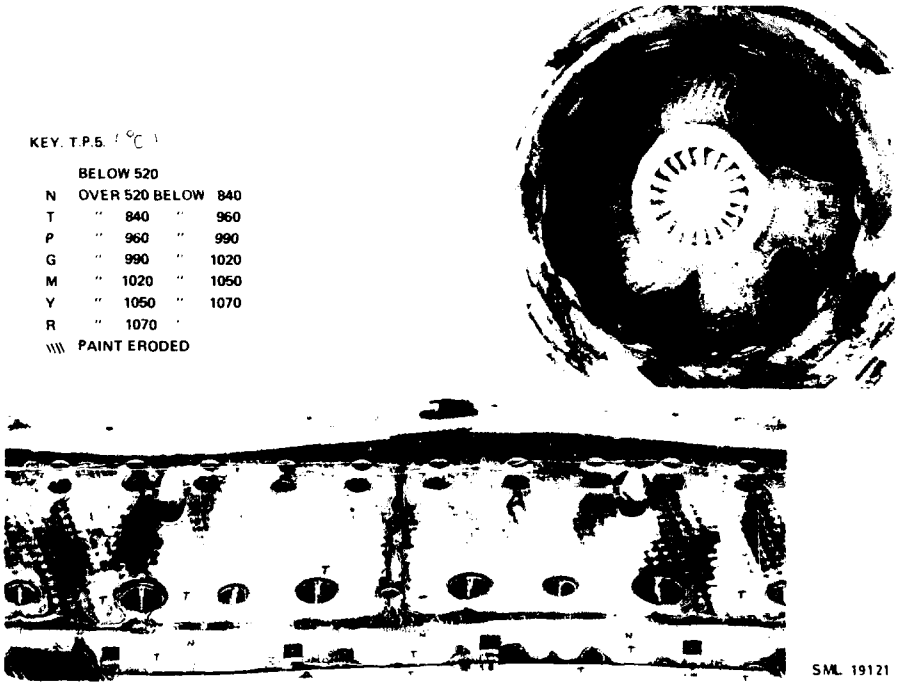


Fig.10 Transply I thermal paint results

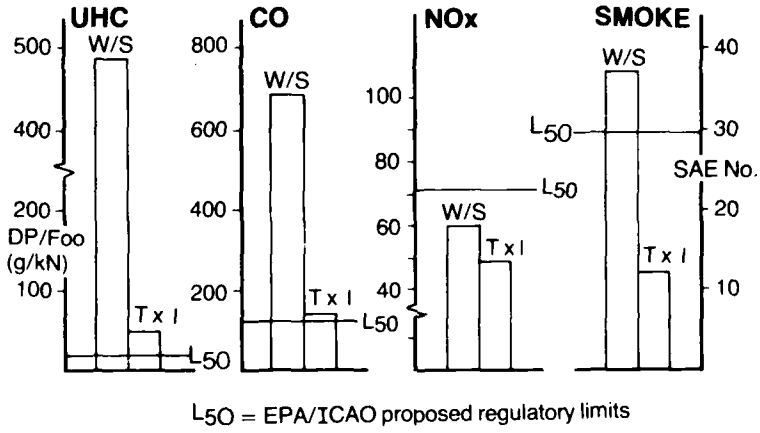


Fig.11 Engine measured emissions results for Transply I (Tx I) and conventional wigglestrip (W/S) combustors

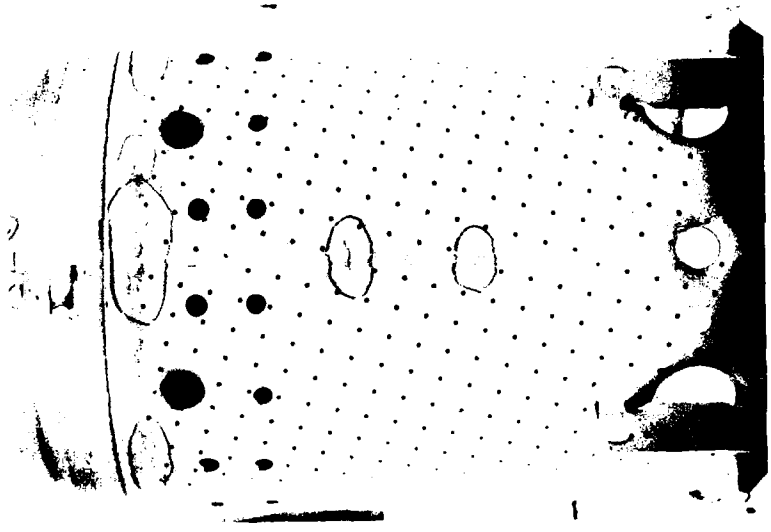


Fig.12 Transply I combustor cracks after 50 Hr cyclic endurance test

6. TRANSPLY II COMBUSTOR

The redesigned all Transply combustor, designated Transply II, is shown in Figure 13. The aim was to maintain the zonal stoichiometry of Transply I, so the secondary and dilution hole patterns were retained. However, the following design changes were made:

- The 20 vane 45° curved vane swirler was retained but redesigned to be more suitable for production, based on experience gained in putting a combustor fitted with a curved vane swirler into production in 1979 in the Spey Mk 511-8 engine.
- The Transply used for the combustor head was changed to a later standard having the same porosity and filming characteristics but improved internal heat transfer properties.
- The barrel Transply was changed to a grade with 50% increased porosity and improved internal heat transfer. The porosity increase was considered to be the only means of achieving the desired metal temperatures in the combustor barrel. The required increase in porosity was determined from the experimentally measured cooling effectiveness - versus mass flow characteristic of Transply.

- The dilution hole plunging was deleted and the Transply section extended downstream for the full barrel length. The upstream Z cooling ring was replaced by one of improved design.

The Transply II combustor underwent an intensive rig and engine development programme which led to the following modifications:

(i) Optimisation of swirler and upstream cooling ring flows to improve ground idle combustion efficiency. The effective area of these devices was found to be very important in its effect on emissions production and conventional inspection techniques were found to be inadequate to achieve the desired control. This led to the design of test rigs to measure airflows in both development and subsequently, production combustors. The porosity of the Transply material is also checked, both in sheet form and once formed into finished combustors.

(ii) Modifications to the dilution system to achieve the required level of pressure loss.

The combustor resulting from the development excercise has been designated Transply IIB. Thermal paint results for Transply IIB are presented in Figure 14 which shows the significant improvements gained over the Transply I results. Figure 15 compares the Transply IIB metal temperatures with those of the conventional combustor.

Rig and engine measured performance parameters for the IIB combustor are tatulated below and illustrated in Figure 16.

TABLE II

TRANSPLY IIB PERFORMANCE

		7% idle Combustion Efficiency (%)	Smoke SAE	Pattern Factor %	Radial Temperature Profile % @ % Turbine Blade Height
ENGINE	(5 tests)				
Mean		97.79	18.6	36.6	13.2 @ 50
Range		97.61-97.96	12.1-24.1	-	-
RIG	(7 tests)				
Mean		98.00	23.0	28.8	9.8 @ 52
Range		97.6-98.45	18.0-25.0	23.5-32.8	8.5-11.0 @ 50

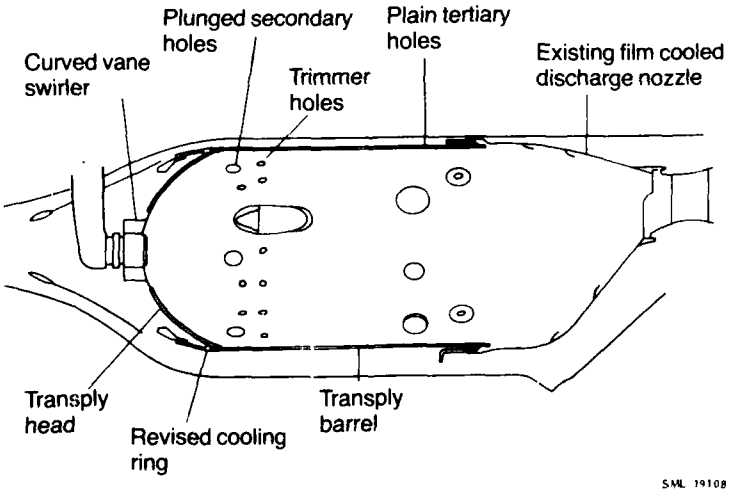


Fig.13 Transply II combustor

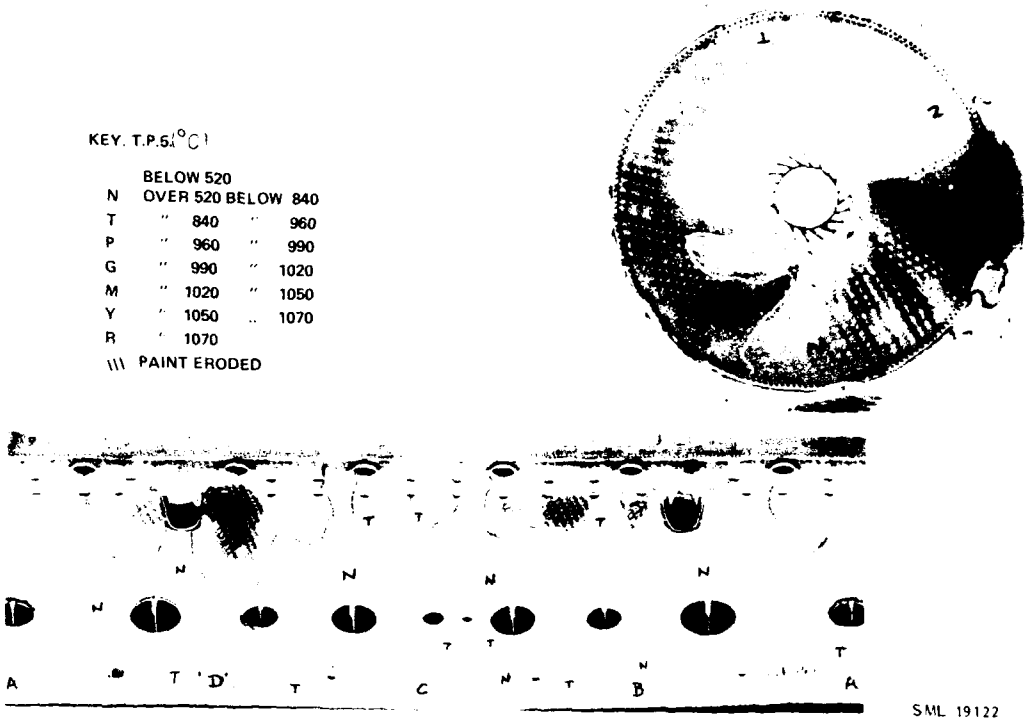


Fig.14 Transply IIB thermal paint results

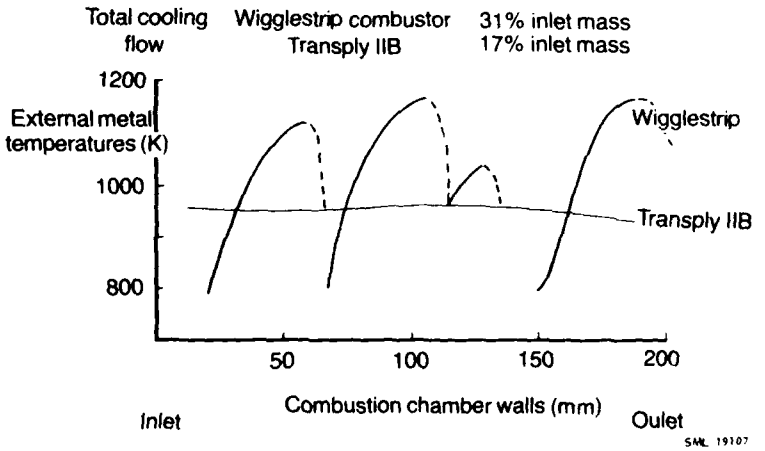


Fig.15 Transply IIB and wigglestrip metal temperatures

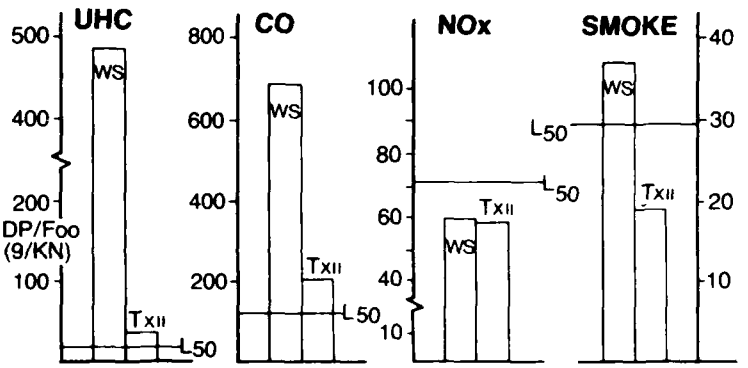


Fig.16 Engine measured emission results for Transply IIB (Tx II) and conventional (W/S) combustors

7. DURABILITY

Bench Engine Tests

A set of Transply IIB combustors, reworked from an earlier standard, has completed two successive 150 hours modification approval tests and a 100 hours (1000 cycles) cyclic endurance test These tests were carried out at a turbine entry temperature of 1440K compared to a normal in-service maximum of 1395K. The combustors had some thermal fatigue cracking in the barrel and head, the cracks in the barrel being in an area possibly distressed during re-work. Part of this set is being subjected to further engine running to determine the crack propagation characteristics of the combustor. Evidence so far indicates that cracks propagate steadily with no sudden failure. The downstream turbine components of the engine were in better condition following the above tests than would be the case with conventional combustors.

In order to fully assess the rigour of the types of endurance testing to which the combustor has been subjected, since the rich primary zone might be expected to reach its maximum temperature below take-off conditions, a parametric metal temperature study was carried out. This consisted of embedding 24 thermocouples into the Transply hot-side laminate and continuously monitoring temperatures over a range of rig operating conditions extending from ground idle to beyond maximum take-off. Conditions, particularly fuel air ratio, extending outside the normal engine running range were also included. The results showed a monotonic relationship between engine power setting and metal temperatures, thus indicating that the engine bench development experience will highlight the likely service problems.

Service Evaluation

The durability of Transply in an airline service environment has been assessed making use of the Transply Intermediate Zone (TIZ) combustor. This combustor, Figure 17, consists of a Spey Mk 512 flametube head as far as the rear of the second wiggle strip where a Transply barrel is attached with a seam weld. The barrel which also incorporates an axial weld is butt welded to the discharge nozzle mounting ring.

The tertiary dilution hole pattern is scaled to the Spey Mk 512 standard to maintain the same overall pressure loss and outlet temperature profile.

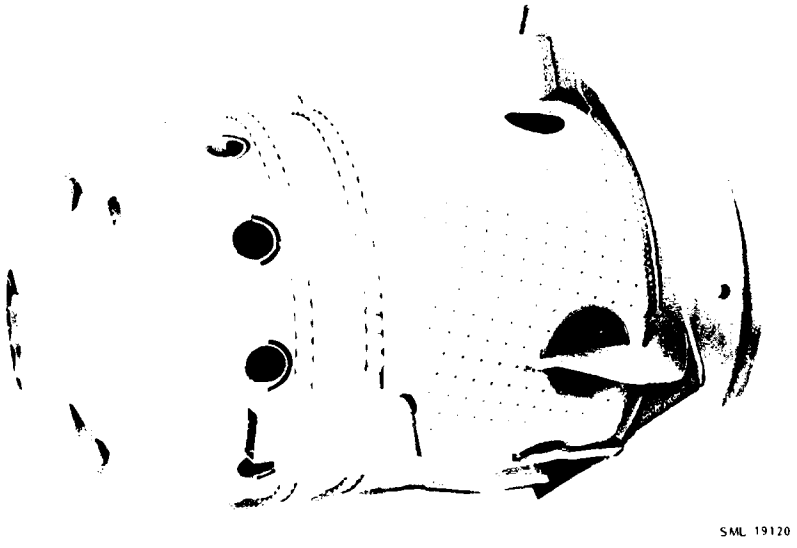
Four TIZ combustors combined with six standard Spey Mk 512 combustors were fitted to each of 6 engines and introduced into service as below:

Operator	Engine No.	Total Hours
British Caledonian	Spey 7701	3071
British Caledonian	Spey 7795	3001
Monarch	Spey 7728	2450
Dan Air	Spey 7730	3093
British Airways	Spey 4754	3400
British Airways	Spey 7518	4000

The first four sets of TIZ combustors which had been removed were in good condition, with only minor cracking of the inward venting holes, the worst crack propagating to the next venting hole but not through to the outer skin. Metallurgical examination of the cracked holes showed that the initial failure mechanism was thermal fatigue. This problem has been avoided on the full Transply combustor by using slot venting dilution holes and the endurance testing confirms this. Post test airflow checks showed a three percent increase in flow through the Transply section of approximately 5%. This is due to rounding of the sharp edged inlet material lost in the Transply material, once this process is complete the airflow remains constant.

Sand Ingestion Tests

It has been suggested that if Transply combustors were operating in a sandy environment the internal passages might become blocked. To check if this could occur, a sand ingestion test was carried out. The all Transply combustors used for the test were similar in design to the Transply IIB standard, except for the swirler. The test consisted of running the engine in cycles comprising three minutes at ground idle and two minutes at maximum take-off, injecting sand every alternate cycle. The engine completed a total of 150 cycles including wet starts. Examination of the combustors revealed only minor evidence of sand adhesion. Airflow checks revealed that no blockage of the internal passageways had occurred.



SML 19120

Fig.17 Transply intermediate zone (TIZ) combustor

8. ENGINE PERFORMANCE

The improvement in combustion efficiency produced by use of the Transply IIB combustor (Figure 19) has resulted in an overall improvement to engine fuel efficiency. This is illustrated in Figure 19 which shows how a 1.1% reduction in fuel burn is achieved over a typical Spey Mk 555 operating cycle.

The flight relight capability of the engine, fitted with the new combustor standard has been assessed by equipping one engine of a Fokker F28 flight development aircraft with Transply IIB combustors. The engine relit at all conditions guaranteed in the Flight Manual, as shown in Figure 20 (ref.5). The only unsuccessful starts during the test were at positions 2, 3 and 8 (Figure 20). However, at these conditions the combustors relit satisfactorily. No attempt was made to check the full boundaries of the relight envelope. Simulated altitude relight tests on a low pressure rig indicate that the Transply IIB relight capability is superior to that of the conventional combustor. Engine handling during the flight relight tests revealed no problems.

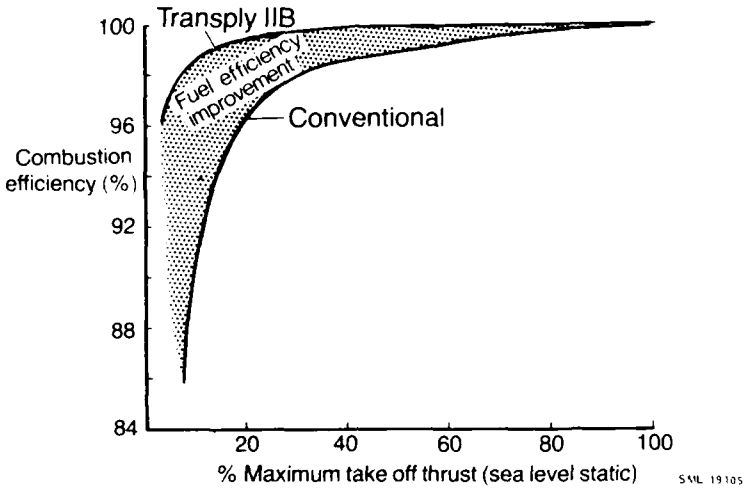


Fig.18 Comparison of combustion efficiencies - conventional and Transply IIB combusters

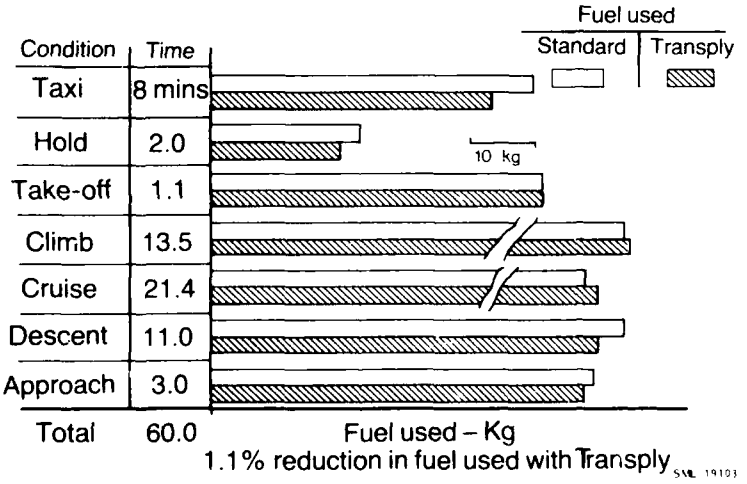


Fig.19 Typical Spey engine flight cycle fuel burn - Comparison of Transply Vs standard combustor

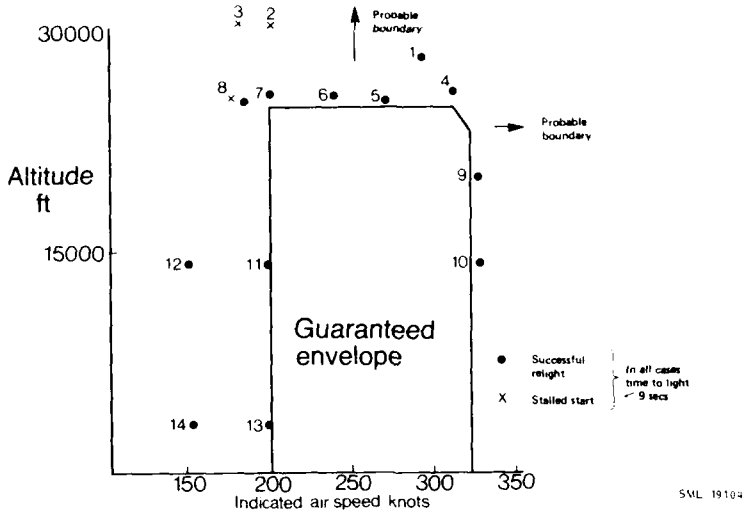


Fig.20 Transply IIB relight envelope (source Ref.5)

7. ENTRY INTO SERVICE

As a result of the extensive test programme outlined previously, the Transply IIB combustor has been certified for full airline service and has been fitted to all new production Spey Mk 555-15 engines since January, 1989. The combustor is illustrated in Figure 21 alongside the conventional one which it replaces.

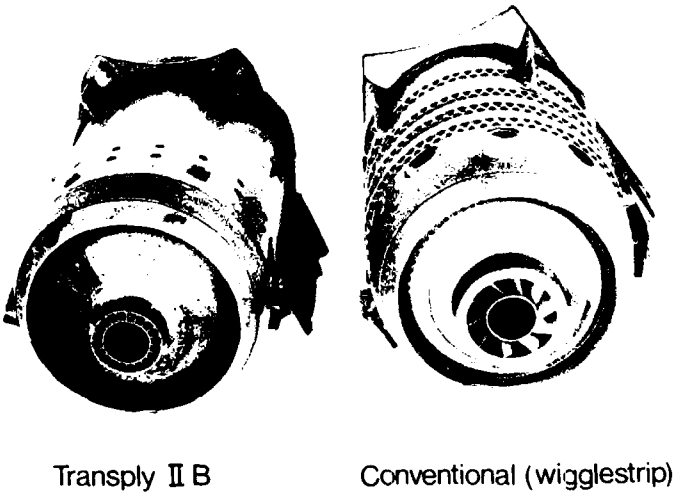


Fig.21 Comparison of Spey Mk.555 combustors

[illegible]

The all Triumph combustor now in service forms the basis [illegible] head tests, aimed at full emissions compliance in the Spey Mk [illegible] have [illegible] which are presently being explored.

a Multi-Hole Triumph

The pattern of perforated holes in the two [illegible] of Triumph [illegible] the photographic mask used in the early stages of the [illegible] production. It is possible to produce [illegible] of Triumph which [illegible] of swirl. This enables combustors to be fabricated with [illegible] to the differing demands of the various combustor zones. A typical [illegible] has been developed which has concentric rings [illegible] holes. These [illegible] tests on this have shown a completely [illegible] level temperature.

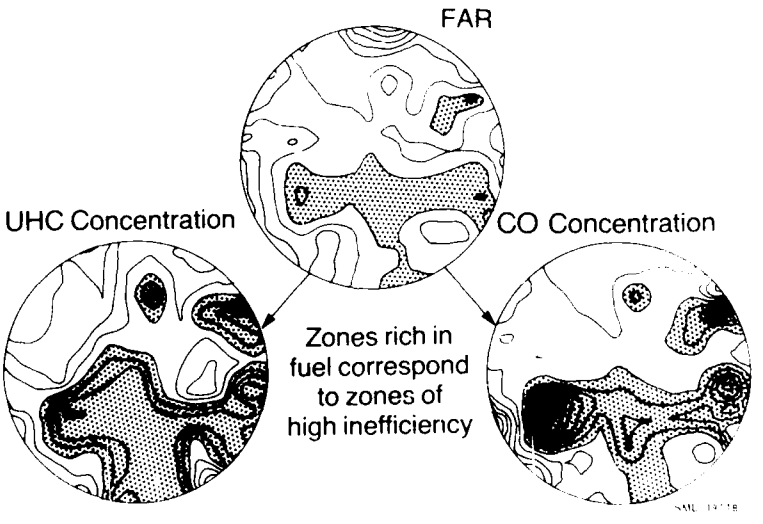
b Thermal Barrier Coatings

The unique internal heat transfer characteristics of Triumph make it particularly [illegible] the use of low conductivity thermal barrier coatings in reducing metal temperatures [illegible] and consequent thermal fatigue life improvements. Work on this started in [illegible]. Initial results on a four Spey all Triumph combustor rig have indicated that a 15 mil [illegible] stabilised zirconia texture can successfully be applied with a significant [illegible] by [illegible].

c Primary Intermediate Zone Modifications

Minor modifications to the Triumph 11B primary zone, have produced further substantial reductions in emissions of unburnt hydrocarbons and carbon monoxide. Engine testing has confirmed that this standard of combustor has a [illegible] stability [illegible] with the rig measured value of 23.5 and fully meets the requirements of all projected [illegible] on emissions in the Spey Mk 555 engine. The durability of this standard of combustor is yet to be fully assessed.

A fundamental understanding of the mechanisms within the combustor intermediate zone is being approached by gas sampling at various planes within the combustor during [illegible] atmospheric pressure. Figure 12 illustrates typical results of this work showing the relationship between a fuel rich zone, where the intermediates interrupt the pattern of the primary holes, and high CO and UHC concentrations. It is anticipated that detailed attention to such effects will lead to further significant improvements in all aspects of combustor performance.



shaded areas denote high concentration

Fig. 12 Results of gas [illegible] of Triumph holes.

CONCLUSIONS

- The difficult task of reducing emission levels from the highly loaded Spey combustor, whilst maintaining acceptable performance in other combustor parameters, has been achieved by using Transply. In fact, the ignition performance of the combustor has been enhanced relative to the wigglestrip standard.

- The Transply IIB combustor, currently in service in the F28 aircraft, complies with the ICAO/EPA smoke limits and procedures. The UHC emissions have been reduced by a factor of 20 relative to the datum wigglestrip combustor.

- An engine test on a modified version of Transply IIB combustor has demonstrated full UHC, CO, NOx and Smoke compliance with the 1986 ICAO limits. It is currently being developed for full engineering clearance

- As a result of the above achievements the Transply combustor, which will comply fully with the emission targets, has been chosen for the recently announced Rolls-Royce Tay engine.

REFERENCES

1. ICAO - Aircraft Engine Emissions, Volume II, Part III of Annex 16, June, 1981.

2. EPA - Federal Register, Volume 47, No. 251, December, 1982.

3. Baulch DL, Drysdale DD, Dudbury J and Grant S.J.

   "Evaluated Kinetic Data for High Temperature Reactions"

   Volume 3, (Butterworth, London/Boston) 1976.

4. Wassell A.B. and Bhangu J.K.

   "The Development and Application of Improved Combustor Wall Cooling Techniques"

   ASME 80-GT-66, March, 1980.

5. Meuzelaar J. (Fokker BV Amsterdam.)

   "F28/RB183 Mark 555, Relight Tests with Transply Combustors to Mod 5964", July, 1982, Report No. UM-28-84.

ACKNOWLEDGEMENTS

The authors wish to thank the Directors of Rolls-Royce Limited for permission to produce this paper and to acknowledge the contribution made by many colleagues. The support of the Procurement Executive, Ministry of Defence is also acknowledged.

© Rolls-Royce Limited 1983

DISCUSSION

D.Hennecke

(1) In Figure 15 you show a remarkably uniform wall temperature of the Transply combustor. Was this achieved by metering the local cooling flow through the Transply according to the local heat load from the flame?

(2) In your introduction you mentioned that you also considered the economics of the new combustor. How does the cost of the Transply combustor compare to the cost of the wigglestrip combustor?

Author's Reply

(1) The current standard of combustor uses two grades of Transply, one in the head and one in the barrel. Each of these grades is homogeneous. Some development work has been done using graded (i.e. non-homogeneous) flow Transply in both head and barrel. The results of this were very good but the technique increases the manufacturing complexity since specific areas from a graded Transply sheet have to be selected for a particular component.

(2) The Transply combustor is simpler to fabricate than the wigglestrip design. This leads to a reduction in fabrication costs, but this is offset both by the high cost of producing Transply and by the costs of stringent and novel methods of quality control. The overall effect is to make the Transply combustor more expensive by some 10–15 percent.

J.Monlibert, Fr

Est-ce que cette chambre de combustion est plus légère que la précédente? Quelles sont les possibilités de réparation?

Author's Reply

Yes, it is a little lighter. There are some possibilities of repairing this type of combustor. I have mentioned a development combustor for which we changed the combustor head. We are now looking into repair in some detail.

AD-P003 148

ADVANCED COMBUSTOR LINER COOLING CONCEPTS

B. Simon, D. Schubert, U. Basler
MTU MOTOREN- UND TURBINEN-UNION MÜNCHEN GMBH
P.O.B. 50 06 40
8000 München 50, Germany

SUMMARY

Small gas turbine liner cooling is especially difficult due to the low combustor air flow and relatively large flame tube areas. Therefore, it is desirable to increase the cooling potential of the cooling air by application of combined convective-film cooling. Its advantage must be balanced carefully against the disadvantage of increased weight and production cost.

The large number of variable parameters of a combined cooling configuration requires a computer model which allows the simulation of different cooling approaches. For the verification of this, model tests with various configurations were conducted in a 2D-cooling rig.

Good agreement between measured and calculated liner temperatures could be achieved. Thus, the model is suitable to show under which conditions a marked decrease of wall temperature can be reached compared with the case of straight film cooling under the same conditions.

SYMBOLS

C/H	-	carbon/hydrogen ratio by weight
L	-	Luminosity factor
P	bar	pressure
T	K	temperature
W	m/s	velocity
x	mm	distance

Indices

an	annulus
C	cooling air
F	film
FT	flame tube
G	hot gas
Su	not film cooled surface
Sad	adiabatic surface
2D	test model conditions
4	combustor outlet

1. INTRODUCTION

The quest for gas turbine engines with higher thrust-to-weight ratio and lower specific fuel consumption entails increasing turbine entry temperatures and pressure ratios. In accordance with Ref. 1 the pressure ratios in the 1000 kW engine bracket are expected to grow from a present 12 to 20, and the turbine entry temperatures from 1400 K to 1600 K and over. For combustion chamber applications, this means that the temperature of the hot gases, as well as that of the compressor air used for cooling purposes, is bound to grow. Accordingly, wall temperatures will rise unless inhibited by a higher allotment of cooling air or by an improved cooling method doing a more effective job. The relationship will become apparent from Fig. 1, where the effects of pressure ratio and turbine entry temperature have been combined in accordance with Ref. 2 into a parameter plotted on the abscissa, while the ordinate represents the cooling air requirement for the respective flame tube surface area. The shape of the curve qualitatively reflects the relationship between these two quantities for straight film cooling. Below the shaded area is the region in which the flame tube walls are undercooled, and above it they are overheated.

The engine points on the graph were determined on the assumption that 60 % of the combustion chamber air is allotted to wall cooling and that 1270 K is the maximum allowable wall temperature. At these conditions the combustion chambers of large engines like the CF6-50 and PWA 2037 are just about undercooled, so that the cooling air flow could safely be reduced or the cooling method be less effective.

Not so with small engines, where at a pressure ratio of 13 and a turbine entry temperature of 1550 K, a fully 60 % share of the cooling air supply is not enough to cool the flame tube. The patently different cooling requirements of small versus large engines is explained by differences in construction. With small engines, coming with a centrifugal-flow final compressor stage as they generally do, the preference is for reverse-flow annular combustion chambers, which mate up well with the centrifugal-flow compressor. While this gives an advantageously short, compact construction to the engine, for which see Fig. 2, it makes the surface of the combustion chamber unproportionately large, because of its location above the turbine. Add to this the deflector elbow, which deviates the combustion gases to the turbine through an angle of 180° and equally requires cooling. All of which puts much more emphasis on combustor cooling problems than is standard in big-engine work.

For the small engines, therefore, more effective cooling methods to give more cooling power for the same if not reduced cooling air input is called for. This greater cooling effectiveness can be achieved by preceding film cooling with convective outer surface cooling for improved utilisation of the cooling capacity of the air. Fig. 3 illustrates various approaches to convective outer surface cooling, which may be of the impingement or the convection duct type.

For both cooling methods, there exists a large number of parameters with which to affect cooling. In impingement cooling this would be, mainly, the pattern and size of impingement holes, the depth of duct, and selective allocation of the impingement and film cooling shares of the total pressure loss of the cooling figuration. With the convection duct, the depth of duct and the type and effective roughness of fitted items, such as spoilers, fins, pimples and pins all play a part as well.

The cooling effect can in either case be controlled additionally by the manner in which the flow is routed in convection and film cooling. As shown in Fig. 3 the flow can be parallel, counterflow or parallel and counterflow combined.

As it will already have become apparent from the schematic arrangements of Fig. 3, design feasibility is an important aspect to consider in the selection of a cooling method. While this aspect is set aside in the present paper, it is nevertheless admitted that added complexity of design will as an immediate drawback entail cost and weight penalties. Before contemplating the embodiment of cooling methods in hardware designs, therefore, one should have proper proof that the total effectiveness of the combined convection and film cooling methods will be clearly superior to that of straight film cooling; otherwise, the effort would not be warranted.

Investigations into cooling configurations in a realistic combustion chamber environment are rather impracticable, owing to the high pressures and temperatures involved. More moderate temperatures and ambient pressures substantially facilitate testing, but are suspected to compromise results. For truly representative evidence, not only the geometric similarity but also the pressure loss across the cooling configuration, the Reynold's numbers inside and outside of the hot gas wall and finally the mass flow and temperature ratios of hot gas to cooling film entry air would have to be kept constant. This being an onerous job, an alternative approach is here attempted, where the results obtained under test rig conditions are reproduced by means of a newly evolved computational procedure. The rig tests, accordingly, merely serve to verify the general validity of the computational procedure, and no attempt is made to assess the cooling method on the strength of rig test evidence. Actual comparison of the relative merits of the various cooling methods is then made by computation at small gas turbine level.

2. TESTS

2.1 Test Setup and Conditions

Fig. 4 is a schematic arrangement of the rig setup used in testing cooling effectiveness. The respective test specimen separates the cooling air duct from the hot air duct in the test section.

Having passed through an air heater, the heated air reaches the test section through an insulated rectangular-section duct. A spoiler grid produces the intended degree of turbulence in the hot air duct. In plane 1 on the sketch a probe can be traversed in three directions.

The cooling air enters the secondary air duct from above. The respective setting for the cooling air to hot air duct pressure ratio allows cooling air to flow through the test specimen and into the hot air duct. The air bypassing the test specimen issues from the rig through a pipe line.

In the experiments designed to test the effectiveness of the cooling film the secondary air duct was sealed off in the test specimen area by an insulation layer.

The tests were run at the following standard conditions:

T_G = 873 K
T_C/T_G = 0.4
W_G = 50 m/s
T = 3 %
W_{an} = 18 m/s (at tests without insulation)

2.2 Description of Test Specimens

Three different cooling methods were investigated:

- straight film cooling
- combined impingement / film cooling
- convection duct cooling

For each cooling method, two specimens were available (cf. Fig. 5). The film cooling specimens F1 and F2 are identical in construction except for the free flow area. The test specimen F1, which was designed to represent a configuration for a large-size combustion chamber, has 3.8 times the flow area of test specimen F2. The unconventional form of the test specimens comes as a result of two considerations: One, the lip was to be as short as possible, for which the additional length of passage that was needed to

blend the discrete incoming jets into a film was obtained by deflection. Two, a configuration of this type is suitable for producing combined impingement/film cooling, which operates on the counterflow principle. As it will become apparent from Fig. 5 the test specimens PF1 and PF2 were produced simply by tack-welding perforated plates to the film cooling specimens F1 and F2. The perforation of the plates is indicated in Tab. 1.

The convection duct specimens KF1 and KF2 are made of two cover plates separated by a corrugated metal sheet forming cooling passages. For improved heat transfer, the metal sheets either form off-set fins as with test specimen KF1, or are slotted as with test specimen KF2.

2.3 Test Results

First, the flow characteristics of all test specimens were charted. Plotted in Fig. 6 is the reduced mass flow versus pressure loss. As it will readily become apparent the test specimens F1 and PF1 exhibit a considerably larger flow than F2 and PF2 . The cover plates of the combined impingement/film cooling configuration were designed to have about 25 % of the pressure loss caused by the impingement holes. Another 35 % of the pressure loss was caused by the air dedicated to film cooling. The duct flow causes the greatest pressure loss. The effective area of the film cooling holes varied with the presence or absence of the cover plate, the C_D value improving when a cover plate was tacked in place. Flow differences of similar magnitudes were noted also for test specimens KF1 and KF2. The test specimens with the large flows simulated combustion chamber environments in large engines, while those with the small flows were typical of conditions in the reverse-flow annular combustion chambers used in small gas turbine engines.

Fig. 7 shows the cooling film effectiveness of cooling film configurations F1 and F2 versus the Odger Winter parameter, which in accordance with Ref. 3 represents a correlation quantity permitting effectiveness to be evaluated at randomly selected conditions. The cooling film effectiveness was evaluated in accordance with the following equation:

$$\eta_F = \frac{T_{Su} - T_{Sad}}{T_{Su} - T_C}$$

where T_{Su} is the temperature of the insulated specimen wall in the absence of film cooling, and T_{Sad} is the temperature of the insulated wall with film cooling applied.

Obviously the results obtained with cooling film F1 can readily be correlated, while for cooling film F2, the pressure loss makes itself clearly felt. It is suspected that the air flow diverted for cooling film F2 does not fully fill the film gap and that the thickness of film varies with the pressure loss. This property remaining intact at elevated pressures and temperatures, however, the results will also in that form be acceptable for subsequent extrapolation to engine applications.

The Nusselt numbers in the duct of test specimens KF1 and KF2 were first determined separately in a special rig, with the results shown in Fig. 8. They are needed for computational verification of the evidence obtained on the cooling test rig. The Nusselt number of test specimen KF1 is greater than that of KF2 at the same Reynolds number over a wide range.

Fig. 9 shows typical readings taken on the test specimens PF1 and KF1. In both cases, thermal conduction effects were apparent. On test specimen KF1 the cooling air forms a film at the end of the duct and operates in the manner of film cooling. Combination of film with convection cooling was deliberately omitted, because it was intended to first isolate the detail effects. It is envisioned to couple the two effects together by computation at a later date.

Comparison of the two cooling methods was not attempted. Conditions underlying the respective measurements were too different for true comparison - the flow being much higher for KF1 but in the absence of the film cooling enjoyed by PF1. Yet the measurements were not intended to support an assessment of the cooling methods. The intention rather was to obtain readings suitable for comparison with computed values. The computational procedure used for the purpose is described below.

3. COMPUTATIONAL PROCEDURE

The computational procedure bases on a one-dimensional heat flow model as it is illustrated in Fig. 10 by way of a control volume of the cooling configuration. On the hot gas side, heat transfer is by radiation and convection, after which the heat is conducted through the hot gas wall, with a thermally insulating layer being optionally considered. In the convection duct the heat picked up by the air axially must be allowed for, apart from the heat transfer between the gas and the wall. The heat transfer to the secondary duct again is by conduction, convection and radiation.

The metal plate used in the construction of combustion chambers being rather thin, axial thermal conduction was ignored.

3.1 Heat Transfer on the Hot Gas Side

Heat transfer on the hot gas side is by radiation and convection. To determine the convection term, resort was made to the cooling film effectiveness measurements.

Turbulence in the combustion chamber flow can be considered in accordance with Ref. 4 by the following statement:

$$\frac{\eta_{FT}}{\eta_{2D}} = \frac{1 + \frac{\tau_{2D}\ x}{100\ M\ s}}{1 + \frac{\tau_{FT}\ x}{100\ M\ s}}$$

where M is the mass flow density ratio of cooling air to hot gas at the film entry, and s is the depth of slot. On the 2-D-rig, a spoiler grid was used to maintain a turbulence intensity of a constant 3 %. LDA measurements taken at the exit of a Larzac combustion chamber (Ref. 5) indicate a turbulence intensity of 15 %. In accordance with Ref. 6, however, the turbulence is assumed to be less in a reverse-flow annular combustion chamber, owing to the lower reference speed. The value assumed for the reverse-flow annular combustion chamber, therefore, was 9 %.

In hot gas radiation, a great amount of uncertainty exists regarding the luminosity factor, which allows for augmentation of gas radiation by smoke particles. In accordance with Ref. 3 the luminosity factor is formed as a function of fuel composition in accordance with the following equation:

$$L = 0.0691\ (C/H - 1.82)^{2.71}$$

This equation was used in the computation of hot gas radiation. The formulation for the exchange of radiation between the gas and the wall was made in accordance with Ref. 7.

3.2 Heat Transfer in the Convection Duct

Heat transfer in the convection duct was determined for impingement cooling using Nusselt numbers stated in Ref. 8. They base on measurements taken over a wide range of jet Reynolds numbers. This effective range also covers the constellation encountered with the combustion chamber.

If the convection duct would be finned, use could either be made of measured Nusselt numbers, or the Nusselt numbers could be computed via the fin efficiency. Various fin geometries, such as rectangular or triangular, could be selected.

Exchange of radiation in the convection duct is limited to that between the walls. The cooling air can be routed in the convection duct in either parallel or counterflow.

3.3 Heat Transfer to the Combustion Chamber Annulus

On the outside of the flame tube wall, heat transfer occurs by convection to the combustion chamber secondary air and by radiation to the combustion chamber casing.

Use was made of a duct relation to determine the heat transfer coefficient.

4. COMPARISON BETWEEN MEASUREMENT AND COMPUTATION AT MODEL TEST RIG CONDITIONS

Fig. 11 compares the wall temperatures in the presence of cooling films F1 and F2. In both cases the test rig conditions described in Chapter 2 were maintained. Unlike in earlier presentations of cooling film effectiveness the outer wall of the test specimens was not insulated; the flow velocity in the secondary duct was 18 m/s.

Agreement of the test points with the computed curves is excellent over the entire flow path tested.

Fig. 12 is a comparison between measurement and computation for the combined impingement/film cooling and the convective duct cooling methods.

In impingement/film cooling the deviation of the computed axial temperature variation over the entire test section does not exceed 2.5 %. It is solely the last test point, lying as it does in the impingement cooled section of the test specimen, which exhibits a greater amount of deviation. This is attributable to axial heat conduction effects ignored in the computation model.

In the case of convection cooling the measurement was made in the absence of film cooling. The outside of the test specimen was insulated for maximum freedom from interference with the measurements. In this case, again, the only major deviation of the computed from the measured results was at the edge of the test specimen, which is again attributable to axial conduction effects. On balance the computational model makes sufficiently accurate predictions of the temperature profile of the test specimen wall.

5. ASSESSMENT OF THE VARIOUS COOLING METHODS

5.1 Comparison at Test Rig Conditions

From the cooling aspect, comparison of the three cooling methods one with the other is of special interest. This comparison is shown in Fig. 13, which illustrates the cooling configurations F2, PF2 and KF2, with the amount of cooling air being the same for all three. The test specimen KF2 had film cooling applied additionally, when it was assumed that film cooling was caused by a preceding configuration identical to KF2. In contrast with the previously shown configurations the cooling air flow is substantially

less and approximately corresponds to conditions encountered in the reverse-flow annular combustion chamber of a small gas turbine.

At these conditions, impingement film cooling makes for no lower wall temperatures than straight film cooling, for the reason that the film cooling effect, which is compromised by the heat imparted to the cooling air, cannot be overcompensated by the improved external heat transfer. Conceivably, optimisation of the local pattern and size of impingement holes and the depth of duct might lead to somewhat lower the temperature and alleviate especially the axial temperature gradient; in the final analysis, however, impingement cooling will - at 2D rig conditions simulating a small engine combustion chamber - afford the advantage of a more homogeneous temperature distribution.

The highest wall temperatures were found for the convective duct/film cooling which results from low heat transfer in the convection duct in combination with poor effectiveness of the cooling film under test model conditions.

5.2 Comparison at Combustion Chamber Conditions

For definition of combustion chamber flow conditions, the type of combustion chamber and the size of engine should be specified, considering that the amount of cooling air available varies importantly with these boundary conditions. The present paper takes a look at typical conditions in the combustion chamber area of a small engine. Fig. 14 shows the combustion chamber of this engine. The thermodynamic cycle conditions of this combustion chamber are:

$$P_{an} = 13 \text{ bar}$$
$$T_C = 667 \text{ K}$$
$$M_4 = 3.2 \text{ kg/s}$$
$$T_4 = 1550 \text{ K}$$

Further important data entering into the wall temperature calculation are the local flow and hot gas temperature conditions. These obviously vary with the axial position along the combustion chamber. With reverse-flow combustion chambers, changes are especially drastic. Flow conditions may be prevailing on the outer liner, e.g., at which the secondary flow moves in a direction counter that of the hot gas or film flow. For straight film cooling, this may have notable impact on wall temperatures.

For the wall temperature calculation, the following significant quantities were selected:

$$W_G = 10 \text{ m/s}$$
$$Ma_{an} = 0.038 \quad W_{an} = 20 \text{ m/s}$$
$$T = 9 \text{ \%}$$

For these conditions the computer model was used to determine the wall temperature profile for the three different cooling methods, when a 3 % pressure loss was maintained in all cases and the air flow through the configuration was a constant 4 %. In the case of configuration KF2 these conditions can be established by using suitable perforations at the inlet.

The result is shown in Fig. 15.

Straight film cooling makes for the highest wall temperatures and the steepest wall temperature gradients when film and secondary air flows run in the same direction. This cooling method would appear much more promising - in regard to both peak temperature and temperature distribution - if the secondary flow is made to run counter the film, as it is the case on the outer liner of the flame tube.

Compared with this constellation the combined impingement/film cooling method affords no essential advantage, although admittedly the configuration used was, again, no optimised solution, but rather the standard configuration of Tab. 1.

The combined convection duct/film cooling method is the most effective of the lot. Compared with impingement cooling the maximum wall temperature was lowered by 100 K, and compared with film cooling in counterflow, by 150 K. The effectiveness can still be improved when use is made of the counterflow principle. This very much levels the temperature distribution and the temperature peak is again reduced.

The question surfaced whether or not the superiority of the convection/film cooling method might be due to the failure to optimize the impingement/film configuration. It was therefore attempted to improve the cooling effectiveness by varying the depth of duct, the diameters, the number of impingement holes or the stagger of the rows of holes (see Tab. 1). The results are shown in Fig. 16. While starting from the basic configuration the above changes indeed improves the effectiveness, this amounted to relatively modest reduction of some 30 K in the maximum temperature.

Conceivably the temperature could be made more uniform if impingement holes of various diameters axially were used. Calculation was prevented, however, for the lack of Nusselt relations for this case.

5.3 Potential Cooling Air Savings

From the practical combustion chamber development aspect the objective is not to use improved cooling methods to lower wall temperatures below the level achieved with present methods. Rather, it is attempted to achieve the same wall temperatures despite reductions

in the amount of cooling air expended. Fig. 17, therefore, shows how much cooling air can be economised if combined convection/film cooling is used in comparison to straight film cooling.

The comparison was made for the standard combustion chamber conditions previously defined. The cooling air flow at film cooling was 4 % of the entire combustion chamber air. At these conditions the combined convection/film cooling method required only nearly one-half of the air being used in straight film cooling at parallel flow conditions.

6. CONCLUSIONS

The use of combined cooling methods has its merits only where it clearly raises the cooling effectiveness over straight film cooling. This effectiveness, therefore, first needs analysing. Test rig measurements will provide no conclusive evidence, because it is limited to a few configurations. Also, the rig testing effort becomes prohibitive when it is attempted to test at actual combustion chamber conditions. Measurements taken on the model test rig nevertheless show that as an immediate gain, no convincing advantages over straight film cooling can be achieved using combined cooling methods at reduced conditions.

The test results, therefore, were essentially used to verify a computer procedure developed to test the effectiveness of diverse cooling configurations and subsequently extrapolate them to the conditions prevailing in a small reverse-flow annular combustion chamber.

It was then seen that the convection duct/film cooling method gave the best effectiveness by far.

A very important consideration in the assessment of the impingement/film cooling method is what the local combustion chamber flow conditions are. If there exists a strong flame tube outside flow in a direction counter the flame tube flow, as it is often the case with reverse-flow annular combustion chambers, this combined method provides little if any advantage over straight film cooling. But if the outside flow is moderate, as in the rear region of the inner liner, considerable advantages may result over the straight film cooling method, because impingement cooling will provide the convective outer flow that otherwise would be missing.

The use of combined convection/film cooling configurations is made difficult by the high stresses set up between the two duct walls. The design effort required to take care of these is considerable and involves cost and weight penalties. Ultimately, then, use will be made of the cooling method that gives adequate cooling for the least investment. Judgement in the matter will rest on the existence of safe methods of forecasting the wall temperatures.

Acknowledgment

Part of the work reported was financed by the German Ministry of Defence. This support is gratefully acknowledged.

8. REFERENCES

1 Demetri, E.P. et al., "Study of Research and Development Requirements of Small Gas Turbine Combustors", NASA CR-159796 (1980)

2 Henderson, R.E., "Turbopropulsion Combustion Technology Assessment", AFAPL-TR-2115 (1980)

3 Kretschmer, D., Odgers, J., "A Simple Method for the Prediction of Wall Temperatures in Gas Turbines", ASME No. 78-GT 90 (1978)

4 Marek, C.J., Tacina, R.R., "Effect of Free Stream Turbulence on Film Cooling", NASA TN D 7958 (1975)

5 Schäfer, H.G., Koch, B., Horny, G., Masure, B., "Laseranemometrische Messungen der mittleren Geschwindigkeit und des Turbulenzgrades in der Austrittsebene einer Brennkammer des Typs Larzac", Techn. Bericht RT 513/77 (1977)

6 Norgren, C.T., Riddlbaugh, S.M., "Small Gas Turbine Combustor Study - Combustor Liner Evaluation", AIAA No. 83-0337 (1983)

7 Lefevbre, A.H., Herberts, M.V., "Heat Transfer Processes in Gas Turbine Combustion Chambers", Proceedings of the Institution of Mechanical Engineers, Vol. 174,12, (1960)

8 Florschuetz, L.W., Truman, C.R., Metzger, D.E., "Streamwise Flow and Heat Transfer Distributions for Jet Array Impingement with Crossflow", ASME No. 81-GT-77, (1981)



Reverse flow combustor
Conditions for PF2
$\frac{\Delta p}{p}$ = 3 % $\frac{M_C}{M_4}$ = 4 %

		d_{HC} mm	$\frac{s_C}{d_{HC}}$ –	N_x –	$\frac{X_R}{d_{HC}}$	$\frac{Y_R}{d_{HC}}$	N_y –
PF1	Testmodel configuration	1.8	1.94	5	5.55		15
PF2 (see Fig. 16)	1 Basic configuration	0.85	2	4	7.35		179
	2 Reduction of channel height		1				
	3 Decrease number of holes in x- and y-direction	1.13	2	3			134
	4 Decrease number of holes in x-direction Increase number of holes in y-direction	0.88			9.46	5.68	224

Tab. 1: Hole Configurations of the Impingement Plates

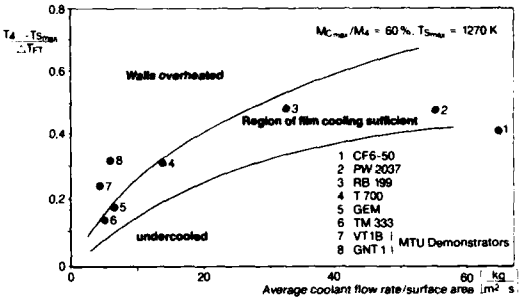


Fig. 1: Coolant Demand for Film Cooling

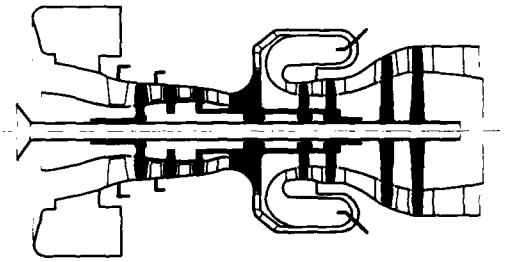


Fig. 2: Scheme of a Small Gas Turbine with Reverse Flow Combustor

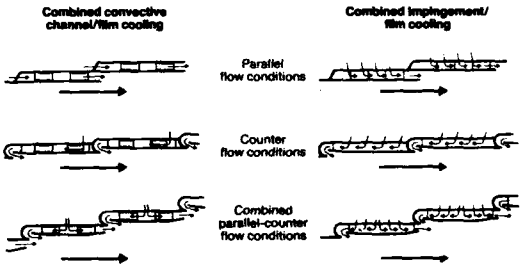


Fig. 3: Combined Cooling Methods

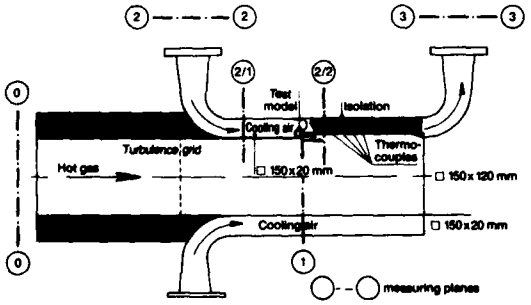


Fig. 4: Film Cooling Test Section

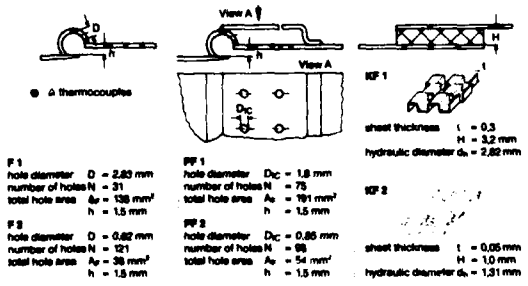


Fig. 5: Film Cooling Test Specimens

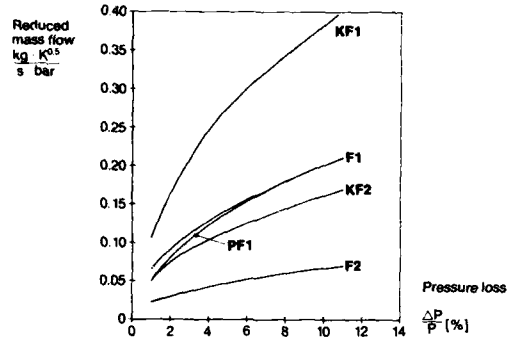


Fig. 6: Mass Flow Characteristics for Test Specimens F1, F2, PF1, KF1, KF2

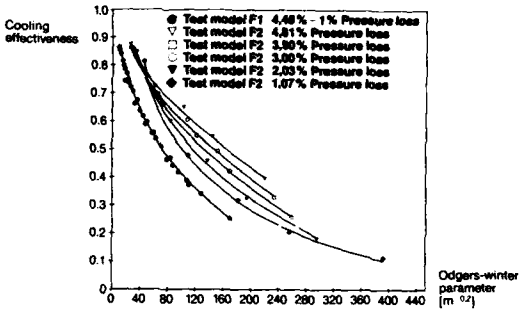


Fig. 7: Film Cooling Effectiveness of Configuration F1, F2

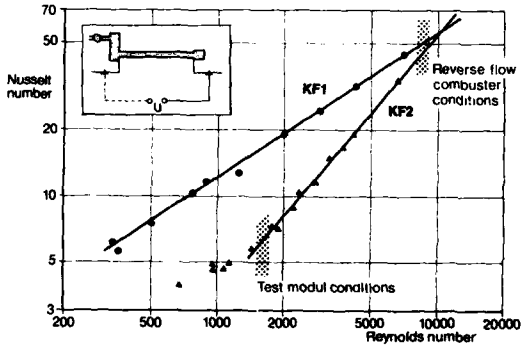


Fig. 8: Nusselt Number for KF1 and KF2

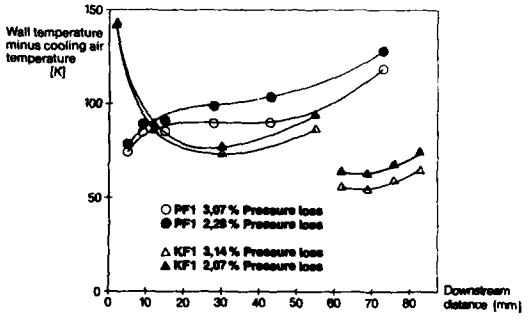


Fig. 9: Wall Temperature Distribution for PF1 and KF1

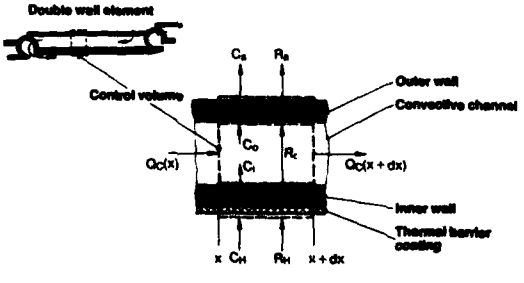


Fig. 10: Analytical Model

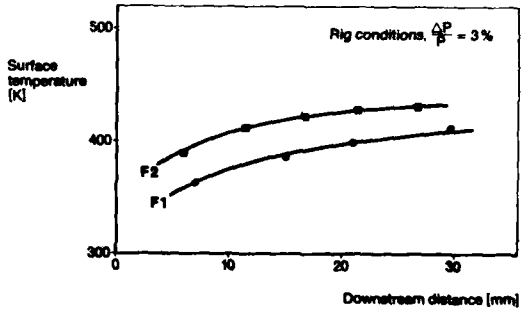


Fig. 11: Comparison of Measured and Calculated Surface Temperatures for Pure Film Cooling

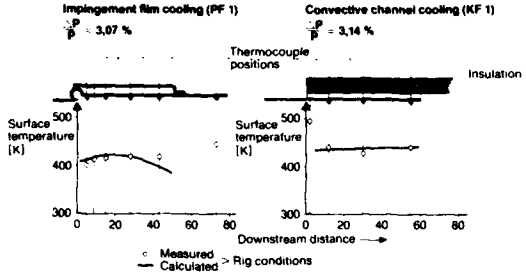


Fig. 12: Comparison of Measured and Calculated Surface Temperatures

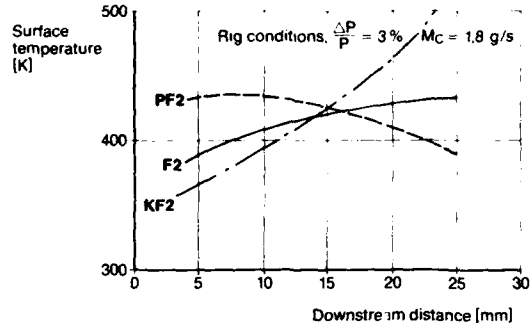


Fig. 13: Comparison of Different Cooling Methods under Rig Conditions

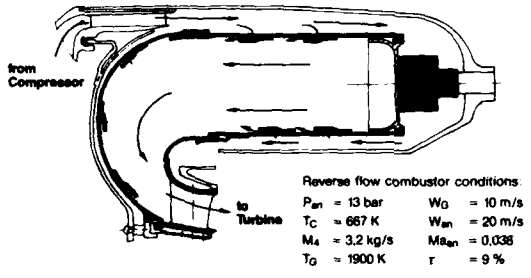


Fig. 14: Reverse Flow Combustor

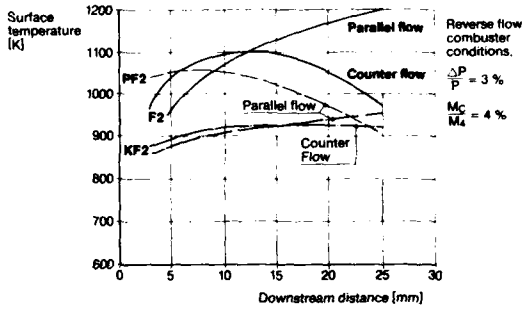


Fig. 15: Surface Temperatures for Different Cooling Methods

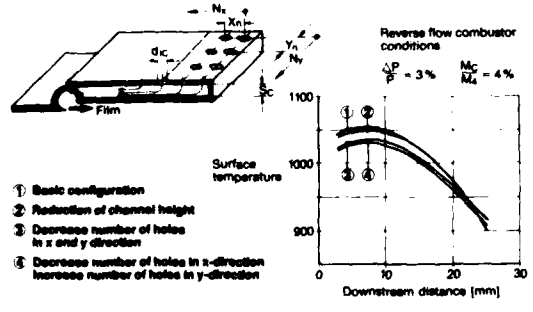


Fig. 16: Variation of Multi Hole Impingement Configuration

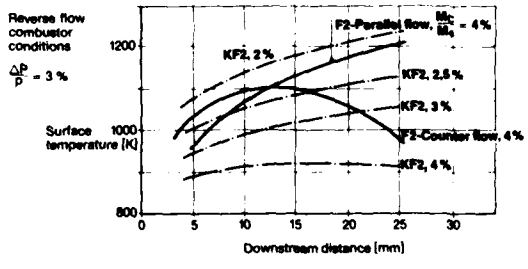


Fig. 17: Reduction of Cooling Air Demand by Combined Convective-Film Cooling

DISCUSSION

K.Collin

(1) What is the length of the film cooling specimens?

(2) Do you optimize this length for pressure drop?

(3) Have you a feeling about the cost penalties of the three film cooling schemes?

Author's Reply

(1) The length of the film cooling specimens was about 70 mm.

(2) In the case of the combined convective channel-film cooling configuration only a very low dependence of the pressure drop on the length of the specimen was observed. The greatest contribution to pressure loss resulted from a row of metering holes in the front of the configuration.

(3) Estimation of cost penalties of the combined methods is only possible if the difference of the cooling effectiveness of all three methods is well known. To investigate the latter was the task of this paper. Cost problems should be considered in connection with a practical application.

D.Snape, UK

Have you made any attempts to understand the fundamental processes of impingement type cooling, e.g. by maintaining the effects of hole diameter pitch ratio? If so, do you have any indications of how impingement effectiveness can be optimized?

Author's Reply

We tested some variations in hole diameters, pitch ratio and channel height. These investigations are given in the paper but they are very limited. Optimal configurations should include the variation of the hole diameter in the axial direction. Those configurations could not be calculated because of the lack of suitable heat transfer numbers.

P.Ramette, Fr

Avez vous fait une comparaison des contraintes thermiques dans les matériaux pour les trois types de refroidissement que vous avez étudiés?

Author's Reply

Not yet. We first wanted to know which cooling type gives the best effectiveness. This will be studied later.

AD-P003 149

DEVELOPMENT OF TEMPERATURE-, VELOCITY- AND CONCENTRATION-PROFILES IN A CURVED COMBUSTOR

by

S. Wittig, R. Kutz, B.E. Noll and K.-H. Platzer
Lehrstuhl und Institut für Thermische Strömungsmaschinen
Universität Karlsruhe (TH)
Kaiserstr. 12, D-7500 Karlsruhe 1, West-Germany

SUMMARY

The influence of bends, as found in reverse-flow combustors or in various stationary gas turbines, on the flow exiting the mixing zone is studied experimentally.

In a first approach, a duct with circular cross-section was chosen with a predetermined temperature-, velocity- and concentration-profile exiting the primary zone of an atmospheric burner. The velocity profiles were measured in three planes (0°, 45°, 90°) and downstream of the bend using a five-hole spherical probe. Also, the temperature and pressure distribution as well as the concentration profiles, particularly of CO_2, were measured in the respective planes. It was found, that energy as well as species-transport arises primarily from secondary flow phenomena combined with strong pressure gradients. In a first attempt to clarify the various phenomena, the development of the static pressure and the temperature is calculated for two-dimensional flow using a finite difference scheme utilizing the well-known k-ε-turbulence model. It is shown that similar pressure characteristics are obtained. Corresponding temperature profiles, however, result from different sources.

LIST OF SYMBOLS

H_{inlet}	duct height at inlet
k	kinetic energy of turbulence
p	static pressure
p_∞	ambient static pressure
R	radius
T_{tot}	total temperature
X	coordinate
Y	coordinate
Z	coordinate
ϵ	dissipation rate of turbulence

INTRODUCTION

In a variety of gas turbine combustor designs it is found that the hot gases exiting the combustor have to be ducted through bends towards the first stage of the turbine. This applies for silo-combustors of stationary gas turbines as well as to reverse-flow combustors of small compact engines as found in helicopter application, for example. Due to the increasing operating values of engine pressure and temperature, it is extremly important in designing the turbine to clarify the effect of bends on the temperature and velocity profile of the flow exiting the combustor.

Up to now, the majority of studies concerned with similar problems were conducted under incompressible, isothermal flow using primarily water. In a recent investigation, Taylor et al. [9] report on velocity measurements in a 90 degree bended square-sectioned duct with strong secondary motion and Reynolds numbers of 790 and 40.000 in water. They indicate that partially parabolic techniques seem to be applicable in describing the flow. In an associated earlier study, Humphrey et al. [3] analyze the turbulent flow in the same duct and attempt a comparison with an elliptic finite difference scheme. Patankar et al. [8] compare predicted total velocity contours in a 180 degree bend with experimental measurements. They find a reduced accuracy in comparison with laminar flow predictions. Moore and Moore [5] calculate the stagnation pressure losses in a rectangular elbow for viscous compressible flow. The comparison with Stanitz' measurements shows relatively good agreement. For turbomachinery applications, Fister et al. [2] report on theoretical and experimental studies in reverse-bend channels of hydraulic turbomachines. Here, the flow is assumed to be parabolic. It is obvious that under these conditions the complexity of the measurements and calculations is drastically reduced in comparison to combustor flow analysis. The information required from the designer, therefore, remains incomplete. The present investigation is concerned with the flow characteristics in a 90 degree bend under non-isothermal conditions. Primary emphasis was directed towards the influence of a non-uniform temperature profile. Under considerations of immediate application, 90 degree bends with circular cross section were used in the experimental study. In order to check the influence of secondary flows, initial calculations were directed towards the numerical analysis of two-dimensional 90 degree bends.

EXPERIMENTAL

The hot gas tunnel and the test section are shown in Figure 1. Hot flame gases from an oil burner mixed with cold ambient air are used in generating a velocity- and temperature-profile entering cross-section I. The velocity profile, the temperature distribution and the concentration of selected species are monitored in planes I, II, III and IV as indicated. The mass-flow rate is determined by a throttling valve in front of an exhaust fan of high capacity. It should be noted that any initial angular momentum of the flow is suppressed by the inlet guide nozzle equipped with additional guide vanes. The main flow velocity was approximately 20 m/sec in the duct of 200 mm ID and a bend radius of 290 mm. As shown, the measurement planes I, II and III were at 0°, 45° and 90° respectively, whereas plane IV was located almost 1000 mm downstream from plane III. Average flow Reynolds numbers were of the order of $2 \cdot 10^5$. As indicated earlier, the following parameters were recorded:

1. static pressure
2. velocity vectors
3. temperature and
4. concentration (primarily CO_2).

Due to the relatively low temperatures, any secondary reactions can be excluded. It, therefore, is possible to utilize the CO_2-concentration generated by the burner as an additional indicator for the transport phenomena.

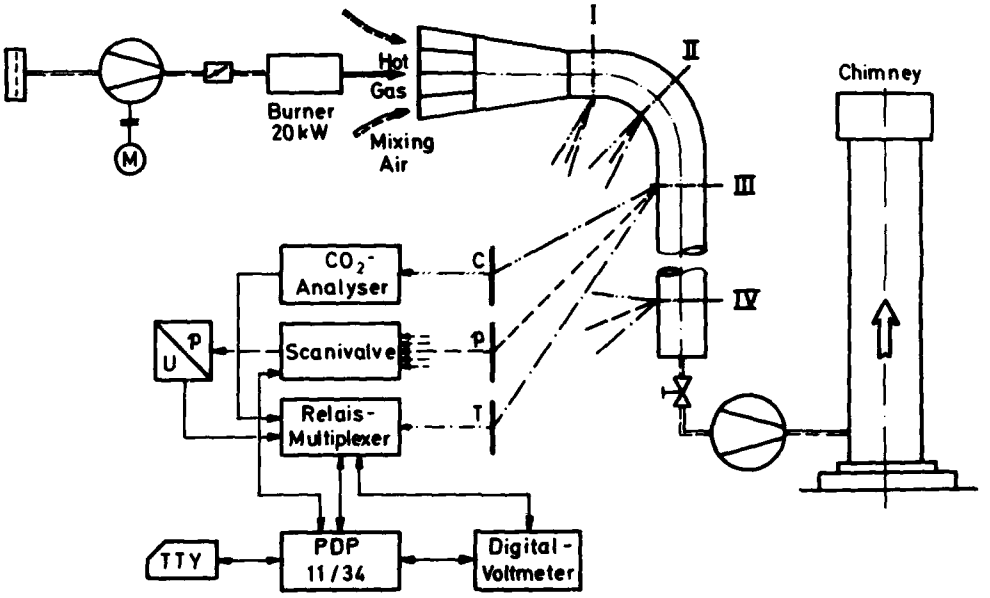


Fig. 1: Experimental facility

Specifically, as the flow in certain sections of the duct is of three-dimensional character, a five-hole spherical miniature-probe was used. The probe has a diameter of 2.9 mm with pressure taps of 0.3 mm and was calibrated in a special calibration tunnel for three-dimensional velocity and pressure analysis. All pressures are recorded via a scanivalve equipped with a high accuracy pressure transducer and a data-acquisition system as shown in Figure 1. The main components of the system are the relay-multiplexer and the digital-voltmeter which are controlled by a PDP 11/34 computer, providing an almost online data reduction.

The temperature is recorded as usual using NiCr-Ni thermocouples. The data acquisition chain is also shown in Figure 1. The concentration of CO_2 - as well as of O_2, CO, NO_x and unburned hydrocarbons - was recorded in planes I, II, III and IV using an automated system. A simple suction probe, 1.5 mm OD, was applied. For CO_2, an NDIR-type gas analyzer was used.

EXPERIMENTAL RESULTS

Table 1 summarizes the experiments. Four primary studies were of dominant interest:

1. As a first step, cold flow without mixing with hot gases was analyzed for reference purposes.
2. A flow with an initially symmetrical temperature profile was generated and its variations in the bend were recorded.
3. In contrast, an initial temperature profile with its maximum shifted towards the outer radius of the bend and its development was observed.
4. A temperature profile with its maximum at an inner radius was used for comparison.

It should be noted, however, that the velocity profiles were not identical under all four conditions.

Table 1: Experimental Program

No.	Quantity Measured: Total Temp.	Quantity Measured: Velocity Field	Quantity Measured: Tracer Gas	Comments
1	-	yes	-	Reference
2	yes	yes	-	Symmetrical temperature profile
3	yes	yes	yes	Temperature profile shifted towards the outer radius
4	yes	-	-	Temperature profile shifted towards the inner radius

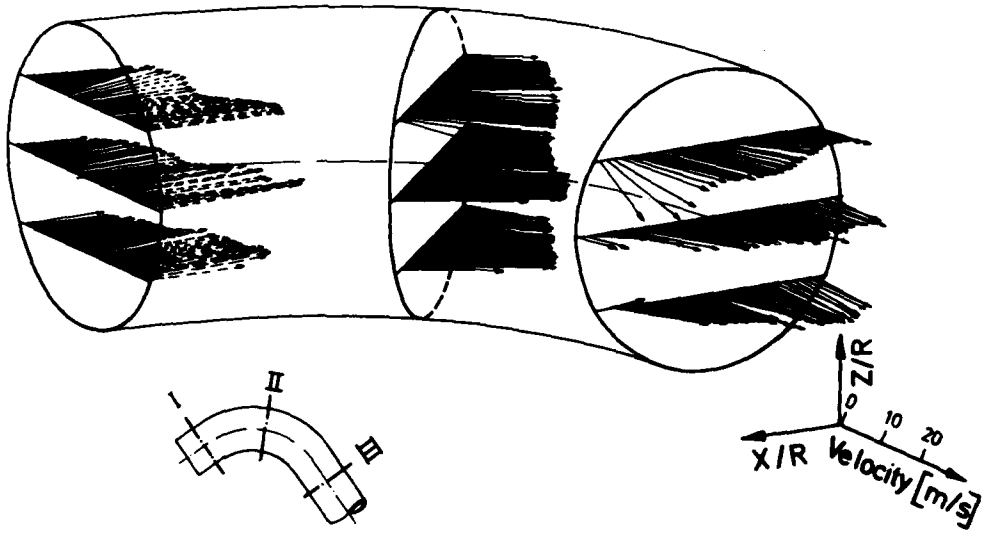


Fig. 2: Measured velocity distribution

Typical profile developments are shown in Figure 2 where the velocity vectors in planes I, II and III are presented for test No. 3, Table 1. The developing three-dimensional character of the flow is obvious. In consulting Figure 3, the developing secondary flow is evident [9], starting with plane I where the X- and Z-components are still relatively weak with increasing tendency up to plane III. It is shown that strong secondary flows exist in the bend whereas in the straight exit duct a dampening effect is observed. This seems to be in good agreement with expectations.

Fairly strong influence of the bend on the temperature profile development is observed as shown in Figure 4. It can be seen that an equilibrization of the temperature occurs. Similar behaviour is found for the CO_2 concentration as shown in comparing Figures 4 and 5. A summary of the results provide Figures 6 through 8. It is interesting to note that for all properties a shift and even a reversal of the original profile develops. For example, the maximum temperature at plane I is found at X/R of approximately 0.4. In passing through the bend, this maximum is reduced considerably and finally the coldest part is at larger radii with a drastic temperature increase at lower inner diameters. The concentra-

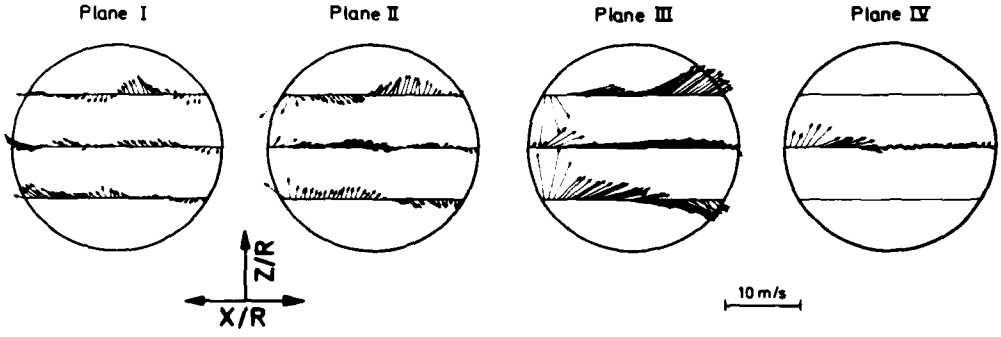


Fig. 3: Development of secondary flow in a 90-degree curved duct

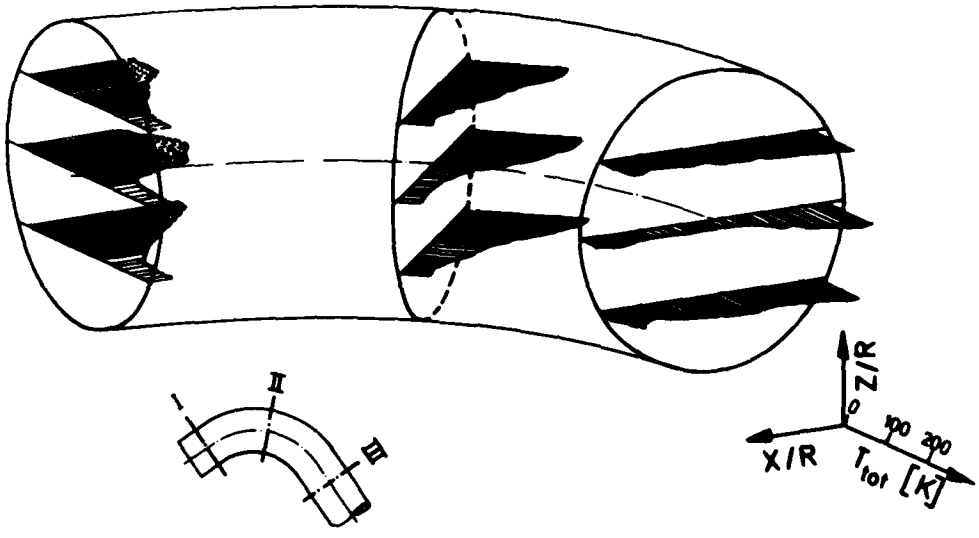


Fig. 4: Measured total temperature distribution

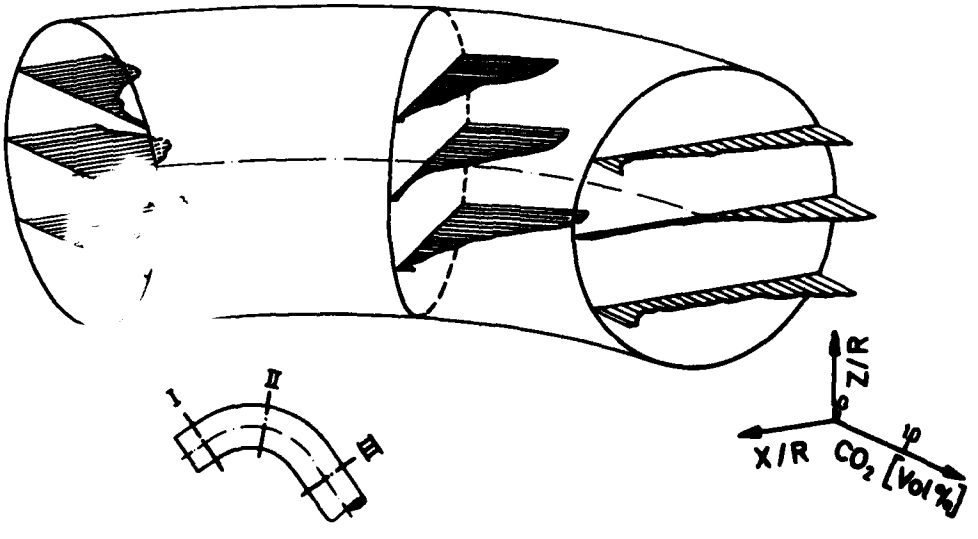


Fig. 5: Measured tracergas distribution

tion profiles behave analogous. It should be emphasized, however, that the data shown are at the midspan.

Obviously, various effects are responsible for the energy and mass transport. First, the developing strong pressure gradients have to be mentioned with the associated velocities [5]. A major source are the secondary flows which serve to transport the heat and species from the outer zones into the inner and central regions. The figures indicate that strong mixing effects are connected. The higher density of the cold zones supports a stabilization of the colder flow at the outer wall. It should be noted that the flow observed is not of the potential vortex type. The relative importance of the temperature, concentration and pressure gradient shift, therefore, is dependent on the initial conditions. Qualitatively, similar characteristics are observed under all conditions studied.

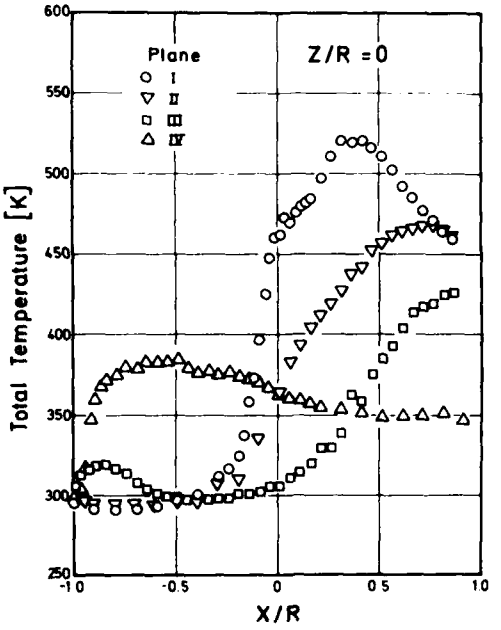


Fig. 6: Measured total temperatures at planes I, II, III and IV

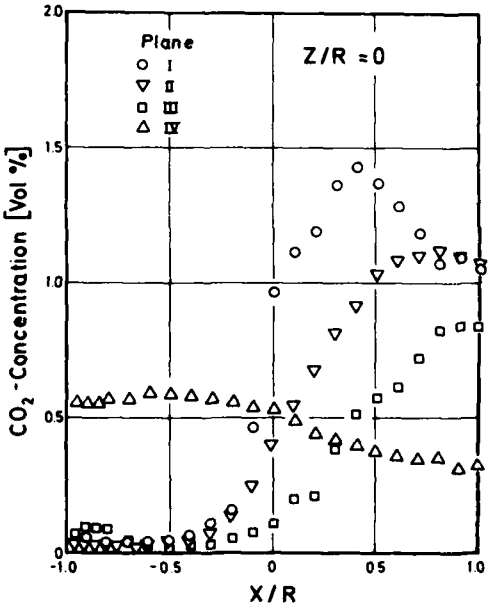


Fig. 7: Measured CO_2-concentrations at planes I, II, III and IV

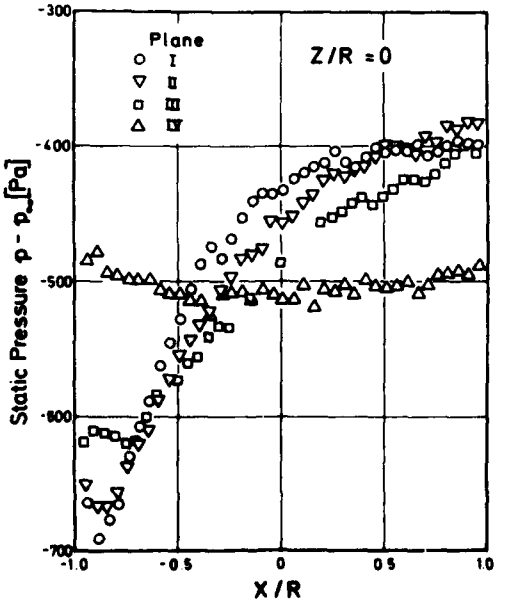


Fig. 8: Measured static pressures at planes I, II, III and IV

THEORETICAL ANALYSIS

In a first attempt to clarify the importance of the secondary flows on the heat and mass transport, numerical calculations were performed for a purely two-dimensional channel. In addition, these calculational procedures can be used in analyzing reverse-flow annular combustors. Due to its two-dimensional character, secondary flow phenomena are avoided. In using a rectangular bend, however, recirculating flows are introduced.

The numerical procedure chosen for the description of the time-averaged equations has been described by us at various occasions [1]. The equations for momentum and energy as well as for the turbulence parameters k and ε can be solved as shown by numerous other groups [4, 7]. In general, the grid size chosen was 28 x 28 points with a small grid spacing close to the inner and outer corners. As an outflow boundary condition, parabolic flow was assumed. Due to separation and recirculation relatively small relaxation factors had to be chosen. Still, neglecting relatively long computation times the equations can be solved on a conventional mini-computer. Typically, 1500 iterations were necessary to arrive at a solution.

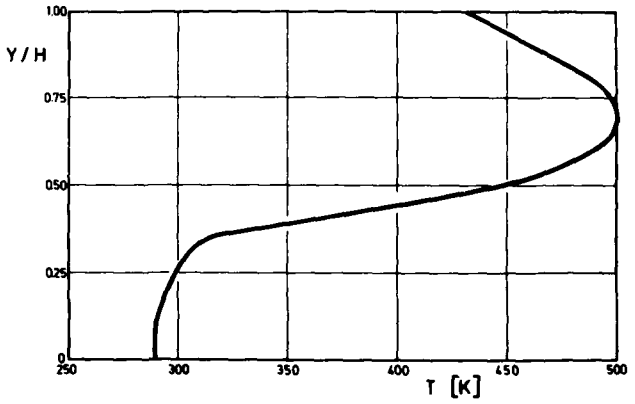


Fig. 9: Inlet temperature profile

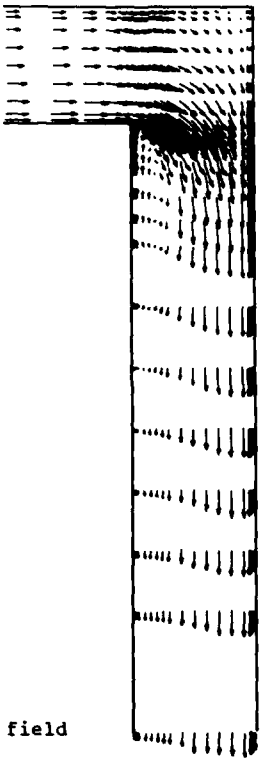


Fig. 10: Calculated velocity field

NUMERICAL RESULTS

A typical initial temperature profile employed is shown in Figure 9 and a characteristic velocity distribution calculated for the channel is shown in Figure 10. In agreement with earlier studies [6] it can be seen that two recirculation zones downstream of the inner corner and in the outer corner region develop. This leads to a shift of the flow towards the outer wall. The resulting temperatures are illustrated in Figure 11.

In comparing the various cross-sectional areas, it is interesting to note that the temperature maximum is reduced by a considerable amount (see planes I and IV in Figure 12). In plane II, the profile is only shown up to the channel width, i.e. the outer corner region has been omitted. Although the reduction of the temperature is similar to that in the flow of the circular duct, an inversion is not observed (compare Figures 6 and 12). This is quite understandable as predominantly recirculation is responsible for the temperature distribution at the inner wall which is in contrast to the secondary flow phenomena in the circular duct. On the other hand, the pressure distributions for both flows is qualitatively of good agreement as illustrated by Figures 8 and 14. Despite pressure gradients of similar magnitude and density gradients due to differences in temperatures and pressures, the heat and mass transport in the purely two-dimensional case is not enhanced as with secondary flows. This is clearly shown in the present comparison.

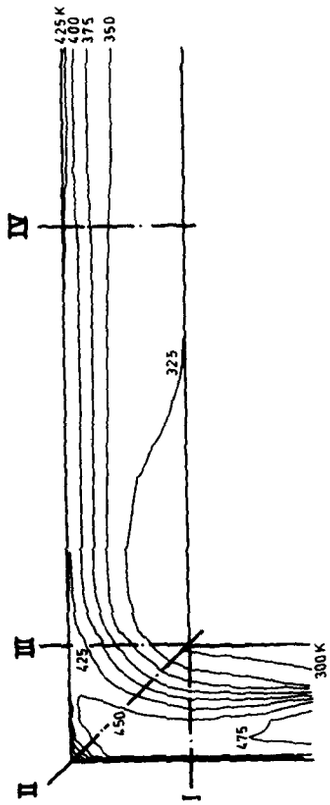


Fig. 11: Calculated isotherms

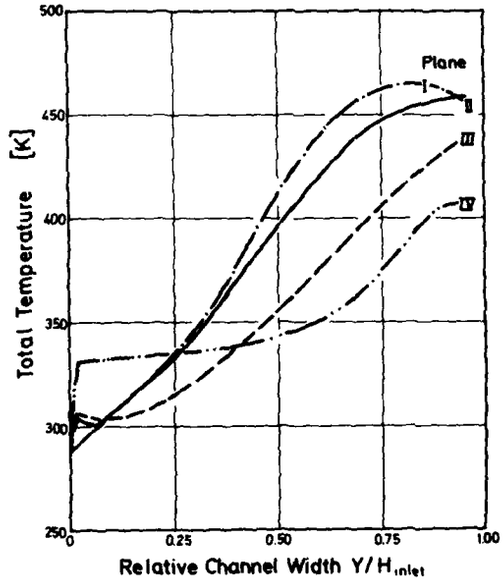


Fig. 12: Calculated total temperature at planes I, II, III and IV

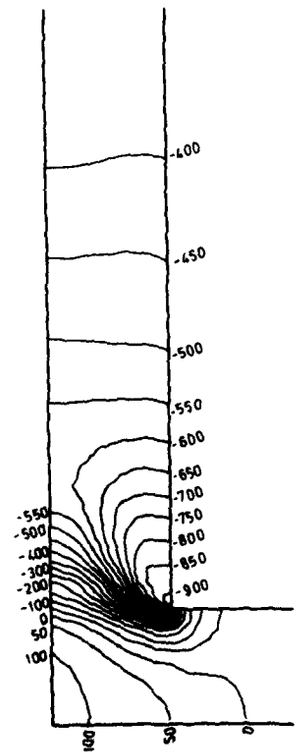


Fig. 13: Calculated isobars

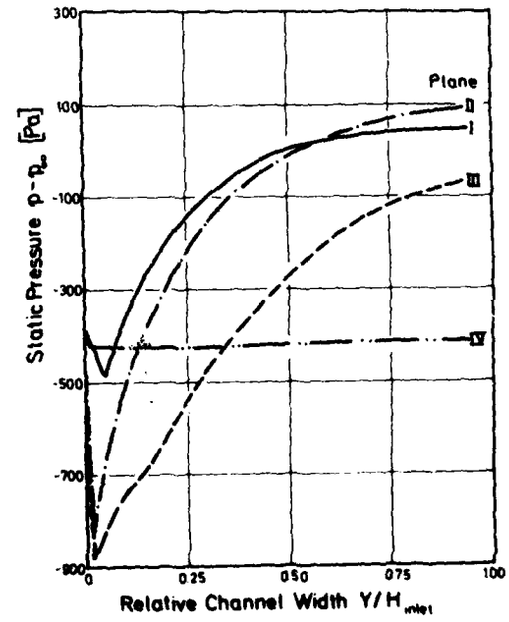


Fig. 14: Calculated static pressure at planes I, II, III and IV

CONCLUSIONS

In comparing compressible, non-isothermal flows through a bend of circular cross-section monitored experimentally with the flow through a two-dimensional bend it is shown that secondary flow phenomena are of primary importance in the heat and mass transport - it is temperature distribution and concentration profile - under circular pipe flow conditions. It is observed that under both conditions the mixing of hot and cold flow is enhanced. Under two-dimensional conditions the inner recirculation zone is of primary importance. A non-uniform exit velocity profile is induced whereas the vortices in a circular duct lead fairly soon to more uniform conditions. In both cases, however, a strong influence of the bend on the property distribution is observed. Three-dimensional, elliptic calculations are required for the complete description of the temperature and velocity profiles in circular ducts, whereas two-dimensional elliptic codes seem to be helpful in analyzing annular combustor-type flows.

REFERENCES

[1] Elbahar, O.M.F. and S.L.K. Wittig: On the Prediction of Temperature Profiles at the Exit of Annular Combustors. AGARD PEP Specialist's Meeting, Köln, Oct. 1979, pp 7-1

[2] Fister, W., G. Zahn and F.-W. Adrian: Theoretische und experimentelle Untersuchungen an Rückführkanälen hydraulischer Strömungsmaschinen. VDI-Berichte Nr. 424, 1981, p 173-192

[3] Humphrey, J.A.C., J.H. Whitelaw and A. Yee: Turbulent Flow in a Square Duct with Strong Curvature. J. of Fluid Mech., Vol. 103, 1981, pp 443

[4] Launder, B.E. and D.B. Spalding: The Numerical Computation of Turbulent Flows. Computermethods in Applied Mechanics and Engineering, Vol. 3, 1974, pp 269

[5] Moore, J., J.G. Moore: A Calculation Procedure for Three-Dimensional, Viscous, Compressible Duct Flow. Part II - Stagnation Pressure Losses in a Rectangular Elbow. J. of Fluid Eng., Vol. 101, Dec. 1979, p 423-428

[6] Neunaß, E.: Praktische Strömungslehre. VEB-Verlag Technik, Berlin, 1967

[7] Patankar, S.V.: Numerical Heat Transfer and Fluid Flow. Hemisphere Publishing Corporation, 1980

[8] Patankar, S.V., V.S. Pratap and D.B. Spalding: Prediction of Turbulent Flow in Curved Pipes. J. Fluid Mech., Vol. 67, 1975, pp 583

[9] Taylor, A.M.K.P., J.H. Whitelaw and M. Yianneskis: Curved Ducts with Strong Secondary Motion: Velocity Measurements of Developing Laminar and Turbulent Flow. J. of Fluid Eng., Vol. 104, Sept. 1982, p 350-359

ACKNOWLEDGEMENT

Thanks are due to the Deutsche Forschungsgemeinschaft (DFG, German Science Foundation) for its financial support of the ongoing project.

DISCUSSION

F.Dupoirieux, Fr

Concernant le code de calcul numérique, avez-vous évalué la viscosité numérique due à la discrétisation spatiale, et ne pensez-vous pas que les profils de pression statique obtenus sont affectés par la viscosité numérique?

Author's Reply

We made some experiments with different spacing; it did not seem to affect the results.

J.L.Monlibert, Fr

Vous avez fait une présentation très détaillée des écoulements à l'intérieur de tubes courbes. J'aimerais savoir comment vous passez des tubes courbes aux chambres de combustion annulaires à flux inversé?

Author's Reply

In a reverse flow combustor you have strong three-dimensional effects with secondary flows. Our intention was to find out what are the consequences of three-dimensional effects on the temperature profile. We made the application for a bend with a circular cross-section, but we had not the time to do it for a reverse flow combustor.

AD-P003 150

An Investigation of the Interaction between Multiple Dilution Jets and Combustion Products

by
P.V.Chleboun*, S.H. Nasser#, F.B. Sebbowa# and C.G.W. Sheppard#

#Department of Mechanical Engineering, Leeds University, Leeds LS2 9JT, U.K.
*Combustion Department, Rolls Royce Ltd., P.O.Box 3, Filton, Bristol BS12 7QE, U.K.

SUMMARY

An investigation ~~has been~~ made of the interaction between multiple dilution jets discharging from a common annulus into hot combustion products. Gas concentrations, mean and fluctuating gas temperatures (using compensated fine wire thermocouples) have been measured throughout the mixing region for three dilution jet flow rates. A parallel theoretical study of the same flows has been conducted using the Rolls-Royce PACE computer code; this is a finite difference program employing a k-ε turbulence sub-model. The output from this program has proved useful in visualizing the flow and interpreting the experimental data. Attention is drawn to the care needed when comparing various types of experimental information and apparently similar parameters output from computer codes on a mass flow weighted basis.

INTRODUCTION

In order to achieve satisfactory exhaust temperature traverse quality, and to avoid premature quenching of flame reaction, it is necessary to understand the interaction between multiple dilution jets and combustion products. Reported in the literature are a number of experimental techniques that have been employed to visualise and interpret the complex nature of such flows (1-7). Often such studies have with good reason been concerned with simplified geometries, e.g. single jets supplied with air via stub pipes to ensure developed flow. The present study has employed a layout more representative of that encountered in gas turbine practice, with multiple jets fed from a common annulus. Detailed gas analysis and thermocouple surveys have been undertaken for a range of three dilution flows. In addition, for one dilution flow rate, very fine wire thermocouples have been used in an attempt to gain information about the turbulence structure generated between the two streams.

In recent years an alternative approach to the visualisation and understanding of complex reacting flows has been made possible by major improvements in computer modelling(8). The work currently reported is in fact part of a long term collaborative programme between Rolls-Royce and Leeds University directed towards the step by step validation and improvement of a computer model suitable for gas turbine combustors. A preliminary stage, reported elsewhere (9,10), demonstrated the need for adequate definition of boundary conditions for the model and established an encouraging degree of confidence in the model's ability to generate a realistic flowfield under isothermal conditions. The present study concerns an intermediate stage where for a similar geometry the jets impinge into a flow of hot combustion products. This particular experiment was designed to avoid chemical reaction between the combustion products and the incoming jets.

EXPERIMENTAL APPARATUS

(a) Combustor and Mixing Section

The apparatus used in the experiments, shown diagrammatically in Fig. 1, comprised three main elements: primary zone, plain ducting and mixing section. The primary zone was of conventional design, similar to that used by Noyce (11). It consisted of combustor head of conical internal geometry, incorporating a nine vane swirler to promote stability, and a 162.5mm length of 175mm internal diameter flametube. Punched into the flametube were sixteen equi-spaced primary ports of 15.9mm diameter. In this zone combustion products were generated by the lean burning of propane vapour and air. Throughout the work reported, air was supplied to the primary zone at atmospheric pressure and a temperature of 325K by a centrifugal blower at a mass rate of flow of 0.35kg/s. A propane vapour flowrate of 4.25g/s was adopted in all tests; the resultant primary zone equivalence ratio was 0.19. The fuel was injected via a nozzle with eight equi-spaced holes of 2mm diameter on a cone of 100° included angle, at a pressure of 345kN/m².

The 330mm length of 175mm diameter plain ducting which followed the primary zone was designed to allow thorough mixing of the products in order to achieve a uniform stream prior to the dilution air addition in the mixing section.

The mixing section was of similar design to that used in an earlier isothermal flow study (10). It consisted of a further 162.5mm length of 175mm diameter flametube in the circumference of which were punched eight equi-spaced dilution ports of 25.4mm diameter. The dilution hole pitch to diameter ratio was 2.7. Air was supplied to the dilution jets, as shown in Fig. 1, via an annulus formed by a concentric outer tube - the annular gap being 12.5mm. The mixing section was connected to a water cooled exhaust system by a further length of plain 175mm diameter tubing. Three dilution air flow rates were adopted: 0.15, 0.25 and 0.30 kg/s. These corresponded exactly to the mass flowrates used in the earlier isothermal work and will henceforth be referred to as the low, medium and high dilution flowrates.

(b) Gas Analysis

Gas samples were withdrawn through a cranked water cooled sampling probe, constructed of four concentric stainless steel tubes. The innermost tube, of 1mm diameter, carried the gas sample. This was surrounded by a loose fitting "insulation" tube over all but the first 10mm of its length. This tube was in turn encased within two outer concentric tubes; these carried flow and return cooling water. The purpose of the insulating tube was, following a short "rapid quench" length, to avoid excessive sample cooling which might lead to condensation within the sample tube. To the same end the extracted sample was led to the gas analysis equipment via an electrically heated line which maintained the sample at a temperature of about 120°C. The outermost tube had an external diameter of 25.4mm over much of its length, to lend rigidity and provide accurate probe location. However to minimize flow interference its outer diameter was 12.7mm at the cranked head section; tapering to just over 2mm at the sampling tip. This probe could be located at any position within the mixing section.

The gases were analysed for total unburned hydrocarbons, CO, CO_2 and O_2 using conventional gas analysis equipment; viz. Analysis Automation Series 523 Flame Ionization Detector, Grubb Parsons Series 20 infra-red CO and CO_2 gas analysers and Beckman paramagnetic oxygen monitor respectively. The instruments could be read manually or have their output fed via a DEC LSI 11-23 mini-computer to a VAX computer for storage and further analysis. In generating the axial plots shown later a basic sampling grid of seven radial and eighteen axial positions was employed, and for radial plots a basic grid of seven radii at 7.5° circumferential spacing over a 90° sector was used. In both cases intermediate points were placed in areas of high gradient of the measured parameter (12).

(c) Mean Temperature Measurement

Mean gas temperatures were measured using bare platinum-20% rhodium versus platinum-40% rhodium thermocouples. The sensing element wires were of 0.127mm diameter, fused at the junction to a sphere of approximately 0.25mm diameter. The wires were strung across prongs formed by two 0.5mm diameter support wires of identical materials. These in turn were built into a twin bore alumina tube which fitted into a cranked traversing probe of similar basic design to the gas sampling probe. The support wires were soldered to standard insulated copper compensating leads. Bare thermocouple wires were used because catalytic effects were considered insignificant at the temperatures encountered in the present work (less than 720K). Similarly radiation losses at these temperatures were estimated to be negligible, on the basis of the calculation procedure outlined by Hankinson (13).

(d) Fluctuating Temperature Measurements

Fluctuating temperatures were measured using uncoated platinum versus platinum-10% rhodium thermocouples formed from 50μm diameter wires, welded to form a bead of 1.25 to 1.5 times wire diameter. The element was suspended between the prongs of matching 0.5mm diameter support wires. These wires were 15mm long and 12mm apart at the sensing element end. As with the mean temperature thermocouple, the support wires were fixed into a twin bore alumina tube housed in the earthed traversing stainless steel probe. Compensating leads were again employed within the probe.

The principle of electrical compensation of thermocouples pioneered by Shepard and Warshawsky (14) has been applied in an attempt to overcome thermal inertia effects. The local time constant necessary to perform the compensation has been derived on the basis of the d.c. pulsing technique developed by Yule et al (15). The use of high grade electronic equipment in conjunction with an on-line VAX 11/780 computer resulted in a noise limited cut-off frequency (16) of 5kHz. Full details of the techniques and equipment used are to be found in the work of Lam (17).

The thermocouple signals could alternatively be transferred to an integrator and associated amplifiers in order to generate a mean temperature signal. This provided a useful check against the temperatures measured with the thicker and more robust thermocouple described previously.

EXPERIMENTAL RESULTS

Preliminary experiments established that uniform conditions had in fact been achieved at entry to the mixing section. At a position 100mm ahead of the dilution jet plane concentrations of the gases measured were all within ±5% of their respective means over a 90° sector. Indeed the conditions remained constant up to a plane only 40mm ahead of the dilution jet centreline. The uniformity of the mixture as expressed by the

parameter s, where s is the standard deviation in concentration (σ) divided by the mean concentration ($\bar{x}$), was at the very low value of 0.032. The equivalent variation in mean gas temperature from the overall average of 715K was even lower. These preliminary experiments also established that no further chemical reaction proceeded within the mixing section. Average temperature and gas concentrations well downstream of the dilution plane, where near uniformity was again achieved, were in accord with what one would expect on the basis of pure dilution for the given mass flow rates. No further conversion of unburned hydrocarbon to CO or CO_2 occurred in the mixing section, the combustion efficiency remained constant. Thus the concentrations of the various gases measured were not independent variables, although they did provide a useful check on the behaviour of the gas analysis instruments. An excellent degree of unanimity was obtained between these various "trace gases"; to reduce the required number of diagrams only data for CO_2 are presented in this paper.

Shown in Fig.2 are CO_2 concentration contours plotted for a plane through a dilution jet and midway between two adjacent jets, for each dilution flow rate. The diagrams extend from 40mm ahead to 100mm behind the centre of the dilution jet, and the CO_2 concentrations are expressed in the form of percentage of mean upstream CO_2 level. An expected increase in jet penetration with greater dilution jet flowrate is evident. It is also clear that the mixing of the two streams towards the expected downstream concentrations, of 0.70%, 0.58% and 0.54% respectively, occurs within a shorter length of duct with the higher jet velocities. This is in accord with the findings for the earlier isothermal study (10), although for given mass flow rates the jet penetrations are lower in the present work. However, there is no evidence of the toroidal recirculation set up ahead of the jets (for the higher dilution flowrates) which were encountered previously. This is because the reduced density of the axial stream has led to higher axial velocities and thus lower ratios of dilution jet to mainstream velocities (1.29, 2.04 and 2.39 c.f. 2.6, 4.34 and 5.21 in the earlier work). On the basis of this velocity ratio the high dilution flowrate of the present work is roughly comparable with the low flowrate for the isothermal case. Shown in Fig. 3 are equivalent concentrations of trace gas obtaind in the isothermal study for the velocity ratio of 2.6.

Comparison with Fig. 2(c) demonstrates considerable similarity, although the jet penetration is more marked for the case of the hot axial stream. The jet also stayed coherent longer, requiring a greater axial length of duct for dissipation.

Shown in Fig. 4 are mean gas temperature contours for the same two axial planes used in Fig. 2 for the three dilution flowrates. While there is a large degree of agreement between the concentration and mean temperature patterns, it is clear that in each case jet penetration (as indicated by the dashed trajectory lines) seems to be greater for the concentration measurements. This effect, which has been noted previously elsewhere (5), is demonstrated more graphically in Fig. 5 where the increase in temperature and trace gas concentration for the incoming jet as it mixes with the axial stream is expressed in non-dimensional form by:

$$T_n = \frac{T - T_J}{T_F - T_J} \times 100\% \quad , \quad C_n = \frac{C - C_J}{C_F - C_J} \times 100\%$$

where C_n, T_n are the normalised versions of the local concentration (C) and temperature (T). Suffices J and F refer to incoming jet and final (well downstream) average values of these parameters. The differences between the two sets of contours could possibly be ascribed to different thermal and mass diffusion rates. This would have important consequences for computer modelling. However in interpreting the data of Fig. 5 it should be remembered that they have been derived on the basis of rather different experimental techniques. In withdrawing a sample in a fluctuating turbulent flow the gas analysis technique will determine a mass weighted average quantity, whereas the fine wire thermocouple will be less sensitive to the mass flow per unit volume (18). It should also be remembered that the gas sampling probe will extract gas from some finite volume within the mixing tube, and present an average for this volume. The position of the centroid of this volume will equally vary according to the direction of the flow; isokinetic sampling was not feasible for the adopted geometry. The thermocouple will not experience this effect in the same way. Finally it should be borne in mind that the flametube walls are not truly adiabatic; this will affect temperature readings close to the wall.

Corresponding radial mean temperature contours at the dilution plane and at planes 10, 25 and 60mm downstream of this are shown in Fig. 6 for the highest dilution flowrate. The 180° sectors have been generated by mirror imaging the 90° measured sector data. The movement of the jet trajectory away from the wall and the diffusion of the jet into the main stream can clearly be seen in these sequences. It is also possible to detect, for the high flowrate, the development of the classical kidney shaped vortices formed by the interaction of the flows (19). In the high flowrate case this has led to the area of lowest concentration at the 60mm plane lying between the jets rather than in line with them. The effect was less marked at the lower dilution flow rates. It is also possible to detect areas of high temperature at the wall immediately behind each jet hole. This is a characteristic of some gas turbine primary and dilution jets. It is a consequence of the expansion behind the jets of those hot axial gases flowing between the blockage caused by the incoming jet flows and into the low pressure region just downstream of the jet.

The "relative efficiencies" of mixing for the the three dilution flowrates are shown in Fig. 7(b), where the parameter $s(=\sigma/\bar{T})$ is plotted as a function of distance. The stronger disruption and faster mixing to a low value of s for the highest flowrate is very evident. It is also of interest to note the almost exponential decay in mixing rate. These data were evaluated from the radial plane temperatures.

Shown in Fig.8 are mean and compensated r.m.s. fluctuating temperatures derived from compensated fine wire thermocouple measurements for an axial plane through a jet hole centre for the middle dilution flowrate. The mean temperature contours are in accord with those measured by the thicker thermocouple. However, it is interesting to note that the influence of the jet is detected by turbulent fluctuations penetrating deeper into the flow than indicated by mean temperatures and gas concentrations. It is particularly interesting to note the high r.m.s. temperature values associated with the severe shearing action at the leading edge of the jet, this is noticeably greater than at the trailing edge of the jet. This is in part due to the high radial jet velocity and in part due to the high axial velocity of the axial stream as the blockage generated by the jets causes it to accelerate in the central area of the tube.

THEORETICAL MODEL

Calculations of the flows described were carried out using a variant of the PACE computer code (8). This program uses the finite difference technique to solve the equations of motion for fully three dimensional turbulent flow. A k-ε turbulence sub-model is used to describe the turbulent velocity fluctuations.

For this work the equations solved were the finite difference representations of continuity, momentum, scalar conservation, scalar mean variance, turbulence energy (k) and turbulence dissipation. A more detailed description of the program and the constants used can be found in references (8) and (10). For the computations reported in this work a grid of 30 nodes in the axial direction, 15 in the radial direction and 10 in the circumferential direction was used. Previous work indicated that grid independent solutions could be obtained provided the grid was concentrated in regions of high angled velocity (10). As a consequence selective grid refinement was carried out in the region of the dilution hole.

The temperature used for the axial flow was the mean value measured on the rig; similarly the temperature adopted for the dilution air flow was that measured at delivery to the outer annulus. A flat velocity profile was assumed for the axial stream at entry to the mixing section. The angle of inclination of the jet through the dilution port was taken as 68^{o}, in accord with the mean of that measured for the earlier isothermal work (10). A flat jet entry velocity profile was assumed, as was the absence of swirl in both streams. For the calculation of temperature the mixing chamber walls were considered adiabatic, so that temperature could be treated as a conserved scalar - i.e. the gradient of temperature was taken to be zero at the walls.

In addition to calculating Favre averaged temperatures at each point in the flow, the program is capable of deriving a value of variance in the fluctuating temperature. In the computer code the variance has been calculated as a conserved scalar, with a source proportional to the variance multiplied by $\rho\varepsilon/k$ plus a term proportional to $\rho k^2(\nabla\tilde{T}).(\nabla\tilde{T})/\varepsilon$. The constants of proportionality adopted were -2 and 2 x 0.9/Pr respectively, where Pr is the turbulent Prandtl number (taken as 0.7).

THEORETICAL RESULTS AND DISCUSSION

Shown in Fig.9 are the computed contours of Favre averaged temperatures, together with streak line plots for the intermediate dilution flowrate. The streak line diagrams are particularly valuable for vizualizing the flow, clarifying the general picture drawn from the experimental data. Comparison of Fig. 4(b) with Fig. 9(b) reveals a fair measure of agreement between experimental and computed data. However, the computed trajectory of jet penetration is greater, and the rate of jet dissipation less, than that observed experimentally. The same effects were noted at the two other dilution flowrates.

The computed jet trajectory is more closely in agreement with that found experimentally by the gas analysis technique, Fig. 2(b). In the earlier discussion of the differences between the two sets of experimental data it was noted that the gas analysis results were subject to a mass flow weighted averaging effect, whereas the temperature measurements were not. In this respect the concentration data might be thought to provide a better basis for comparison with the computed results (18), since the latter are Favre averaged at each point. However computed time-mean averaged temperatures, calculated using the computed fluctuating temperatures together with the Favre averaged temperatures, proved little different to the latter in the present study. Since the degree of agreement between theory and experiment was better in the isothermal study it is possible that the neglect of the jet entry velocity profile in the present work might be significant.

Other reasons for the observed slower diffusion indicated by the computed results might be associated with the neglect of swirl in the jet flows or with the assumption of too low a turbulence intensity for the incoming jet. However a parametric study of the effect of the jet inlet turbulence intensity showed this to be relatively unimportant - the turbulence generated by the shearing action of the jet renders that initially within the jet relatively insignificant. Perhaps a more serious error is the neglect of an

axial flow velocity profile. In practice the maximum velocity will occur in the central core of the flow - this would tend to reduce jet penetration. Finally, it should be noted that the assumption of identical thermal and mass diffusion in the model may be questionable. By using different values of turbulent Prandtl number for mass concentration and temperature calculations, it has indeed been possible to reproduce the experimentally observed differences in concentration and temperature profiles.

The square root of the calculated Favre averaged variance in temperature is shown in Fig.9(c) - again for the intermediate dilution jet flow rate. It can clearly be seen that the variance is greatest in the shear layers at the leading and trailing edges of the jet. This is in accord with the picture implied by the experimental root mean square of fluctuating temperature data derived from the compensated thermocouple, Fig. 8(b). Care should be exercised when viewing Figs. 9(c) and 8(b) together, as the two parameters plotted are not identical. Nevertheless, as an order of magnitude measure and indicator of areas of mixing activity, the observed degree of similarity is considered gratifying.

CONCLUSIONS

1. The experimental data generated by gas analysis and thermocouple techniques have confirmed the basic features of cross flow jet mixing expected, although the observed jet trajectories were often at variance with those noted with more idealized geometries (20).

2. Although doubts have been quite widely expressed about the validity of compensated fine wire thermocouple data, in the present work fluctuating temperature measurements proved useful for indicating areas of intense mixing activity.

3. Great care is needed when comparing averaged data derived using alternative experimental techniques and, likewise, apparently similar parameters output from computer codes. Different physical and numerical averaging effects can result in significant variations in observed phenomena.

4. Within the above limitations good agreement between experimental and theoretical data was obtained in the current work. Computer programs of the PACE type are, in their present state of development, considered to be valid development tools in combustor design. At the very least they are capable of providing (more quickly and flexibly) a degree of understanding of a flowfield comparable with that generated by physical water flow modelling.

5. Using computed data it is possible to pinpoint areas within a flow where energy dissipation is unaccompanied by useful mixing of fluid; i.e. unnecessary pressure loss. There is some evidence in the present study that cross flow jet mixing may be inefficient in this respect, lending support to the development of alternative combustor design concepts that eliminate conventional dilution zones (21).

REFERENCES

1. Fearn, R. and Weston, R. "Velocity field of a round jet in a cross flow for various jet injection angles and velocity ratios". NASA TP 1506 (1979).

2. Patrick, M.A. "Experimental investigation of mixing and flow in a round turbulent jet injected perpendicularly into a main stream". J.Inst.Fuel 40 312 (1967).

3. Gollahalli, S.R., Brzustowski, T.A. and Sullivan, H.F. "Characteristics of a turbulent diffusion flame in a cross-wind". Trans. Canadian Soc. for Mech. Eng., 3 No.4 (1975).

4. Raghunathan, S. and Reid, M., "A study of multiple jets". AIAA J. 19, 124 (1980).

5. Kamotani, Y. and Grebor, I. "Experiments on a turbulent jet in a cross flow". AIAA J. 10 1425 (1972).

6. Rao, K.V. and Brzustowski, T.A. "Tracer studies of jets and diffusion flames in cross flow". Comb.Sci. and Tech. 27, 229 (1982).

7. Krothapalli, A., Baganoff, D. and Karamcheti, K. "Development and structure of a rectangular jet in a multiple jet configuration". AIAA J. 18, 945 (1980).

8. Jones, W.P. and Priddin, C.H. "Prediction of the flow field and local gas composition in gas turbine combustors". 17th Symp.(Int) on Comb., pp.399-409, The Combustion Institute, 1978.

9. Chleboun, P.V., Craig, P.J., Sebbowa, F.B. and Sheppard, C.G.W. "A study of transverse turbulent jets in a cross flow", Comb. Sci. and Tech., 29, 107 (1982).

10. Chleboun, P.V., Craig, P.J., Sebbowa, F.B. and Sheppard, C.G.W. "Transverse jet flow relevant to gas turbine combustors". Int. Symp. on Refined Modelling of Flows, I.A.H.R., Paris, 7-10 Sept. (1982).

11. Noyce, J.R. and Sheppard, C.G.W., "The influence of equivalence ratio variation on pollutant formation in a gas turbine type combustor", Comb. Sci. and Tech., 29, 37 (1982).

12. Sebbowa, F.B., "Transverse jet mixing relevant to gas turbine combustors: non-isothermal flow". Dept.Mech.Eng. Tech. Report T33, Leeds University (1982).

13. Hankinson, G., "Combustion in recirculating flows". Ph.D. Thesis, Leeds University (1975).

14. Shepard, C.E. and Warshawsky, I., "Electrical techniques for compensation of thermal time lag of thermocouple and resistance thermometer elements", N.A.C.A., TN 2703 (1952).

15. Yule, A.J., Taylor, D.S. and Chigier, N.A., "On line digital compensation and processing of thermocouple signals for temperature measurement in turbulent flames". AIAA. Paper No. 78-30 (1978).

16. Ballantyne, A. and Moss, J.B., "Fine wire thermocouple measurements of fluctuating temperature", Comb.Sci. and Tech., 17, 63 (1977).

17. Lam, C. "The effects of turbulence upon combustion reactions". Ph.D. Thesis, Leeds University, (1982).

18. Toral, H. and Whitelaw, "Velocity and scalar characteristics of the isothermal and combusting flows in a combustor sector rig". Comb. and Flame, 45, 251 (1982).

19. Abramovich, G.N. "The Theory of Turbulent Jets", M.I.T. Press (1963).

20. Sebbowa, F.B., "Cross flow jet mixing relevant to gas turbine combustors". Ph.D. Thesis, Leeds University (1982).

21. Hakluytt, J.P.D. and Tilston, J.R., "On the prospects for close control of combustion by shear layer mechanics". Paper C87/83, p.95, Proc. Int.Conf. "Combustion in Engineering". publ. I.Mech.E. (1983).

ACKNOWLEDGEMENTS

The help of Derek Bradley and co-workers in the use of compensated fine wire thermocouples is gratefully acknowledged, as is the encouragement lent by Arthur Sotheran and the financial assistance given by Rolls-Royce Ltd. Thanks are also extended to all those who have helped in the production of this paper.

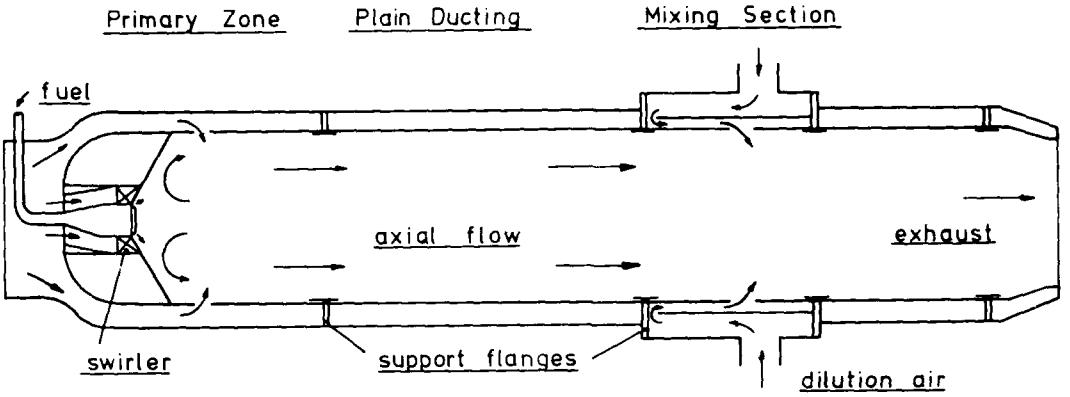
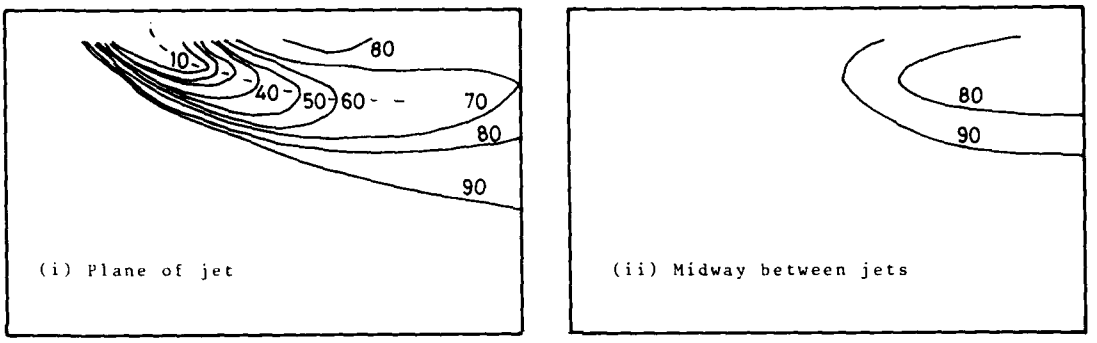
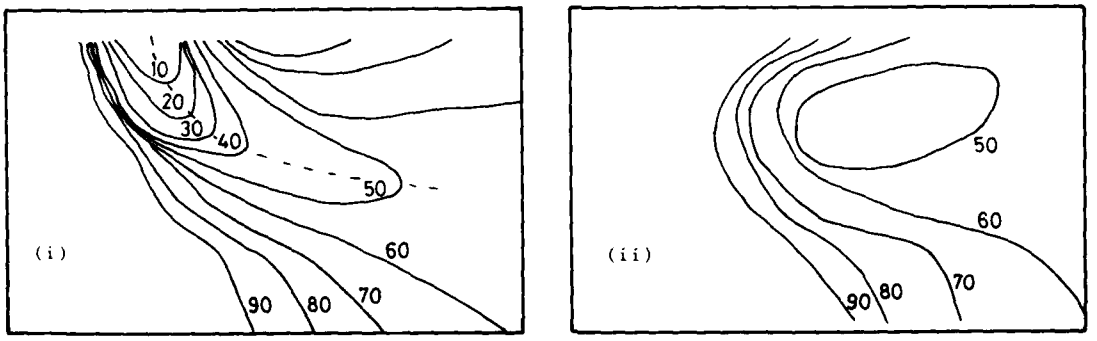


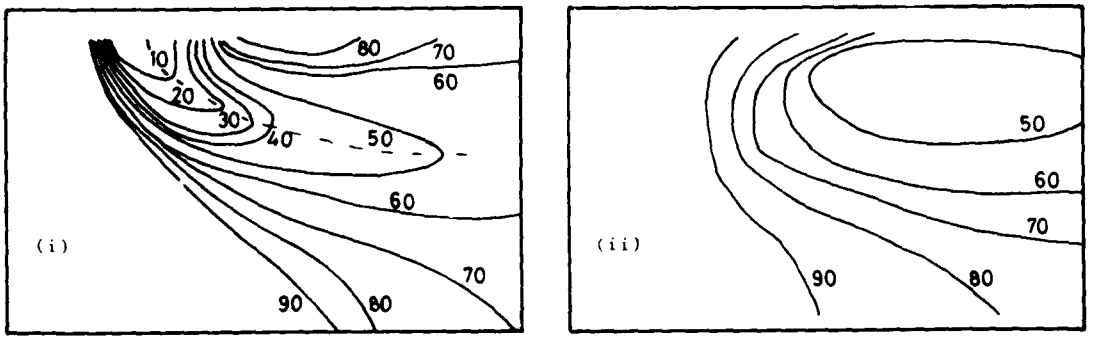
Figure 1. Diagrammatic Representation of Combustor



(a) dilution flowrate 0.15 kg/s



(b) dilution flowrate 0.25 kg/s



(c) dilution flowrate 0.30 kg/s

Figure 2. Contours of CO_2 Concentration (% of mean upstream value)

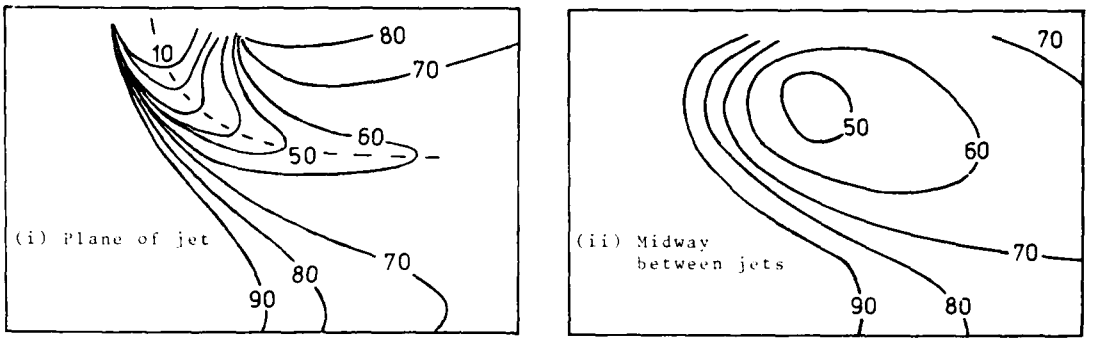
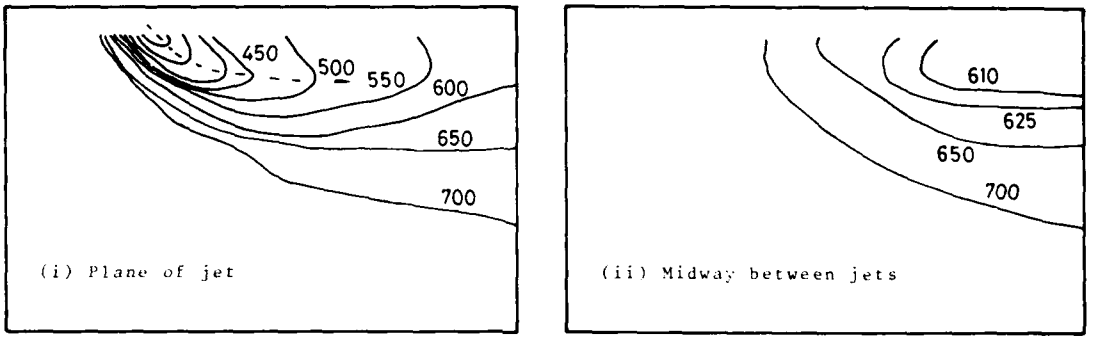
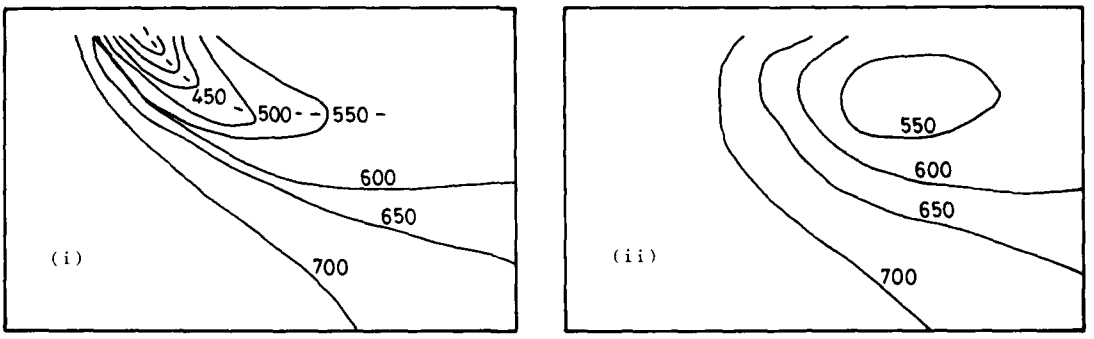


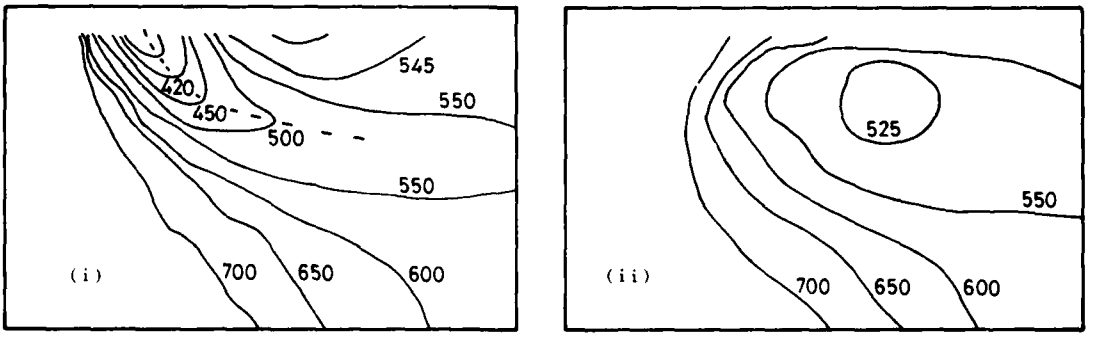
Figure 3. Trace Gas Concentrations (% mean upstream value) - Isothermal Case



(a) dilution flowrate 0.15 kg/s

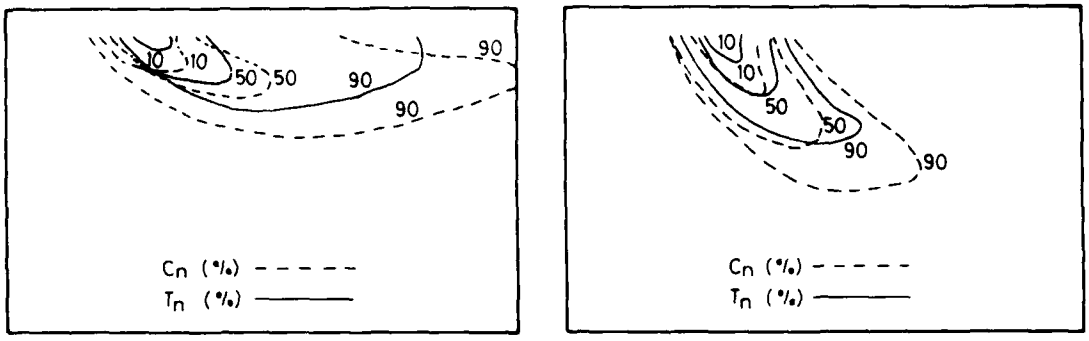


(b) dilution flowrate 0.25 kg/s



(c) dilution flowrate 0.3 kg/s

Figure 4. Contours of Mean Gas Temperature (K)



(a) dilution flowrate 0.15 kg/s (b) dilution flowrate 0.30 kg/s

Figure 5. Non-dimensionalized Temperatures and Concentrations

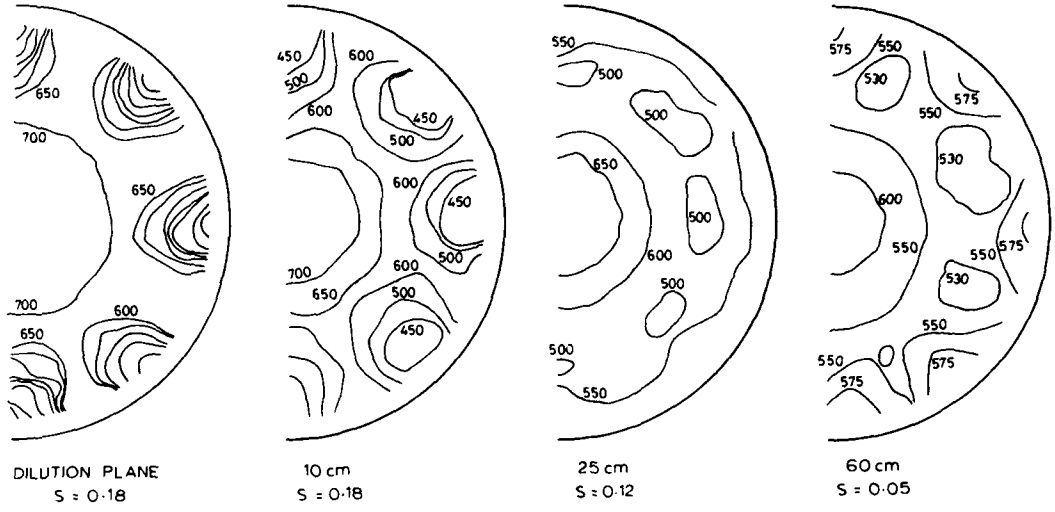


Figure 6. Radial Mean Temperature Contours (K), high dilution flowrate

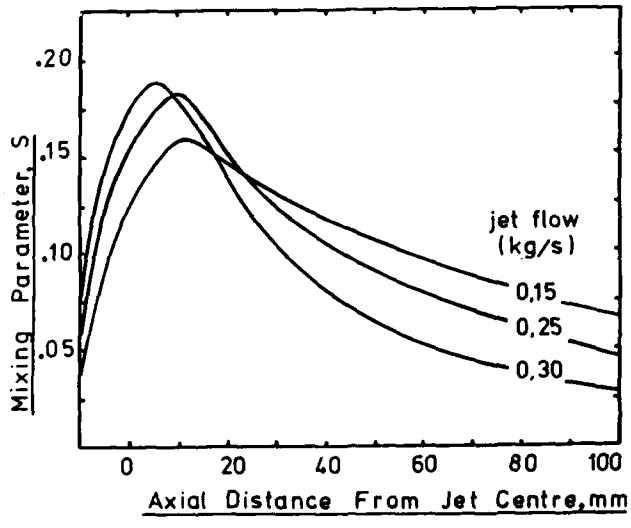


Figure 7. Variation of Mixing Parameter (s) with Axial Distance and Dilution Flowrate

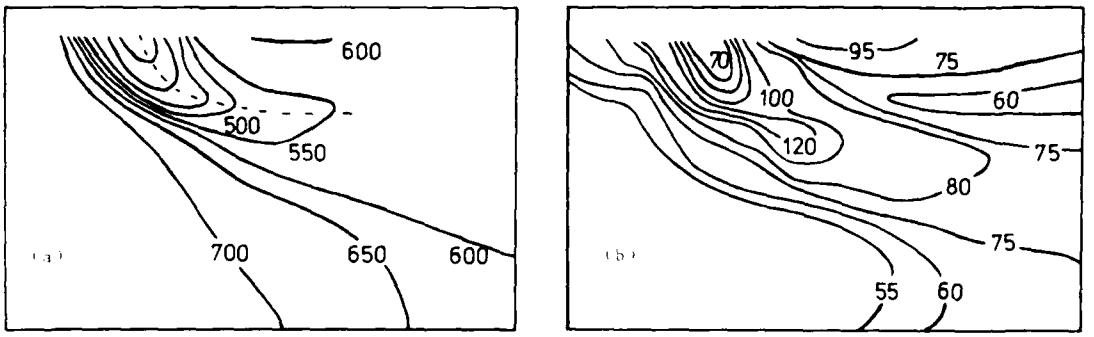
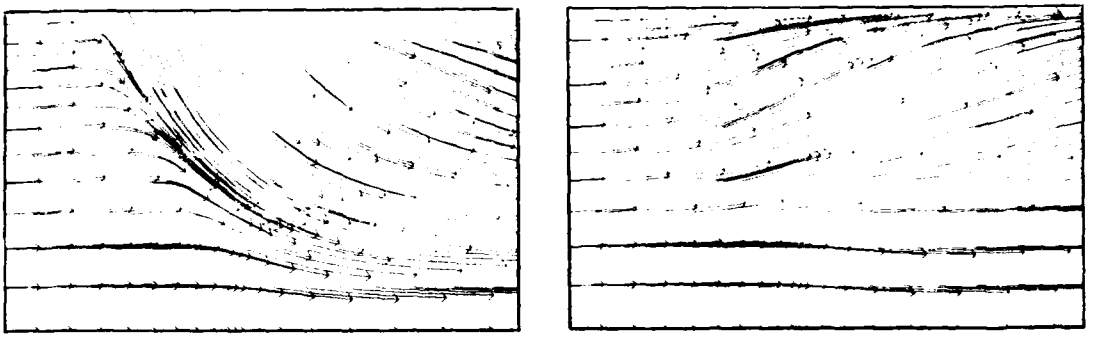
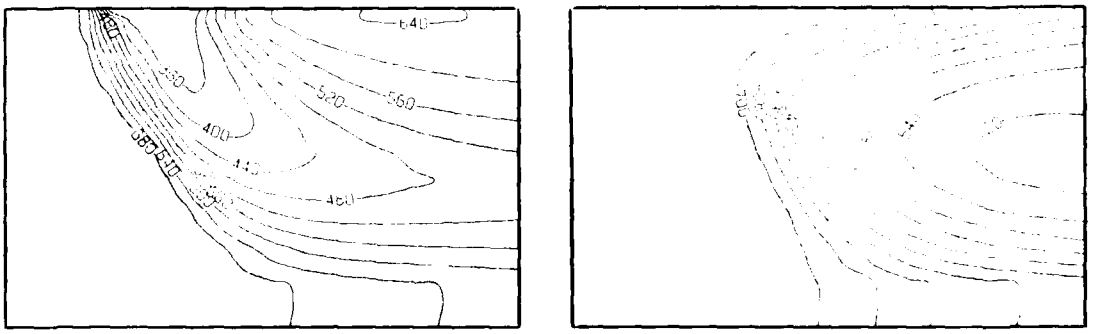


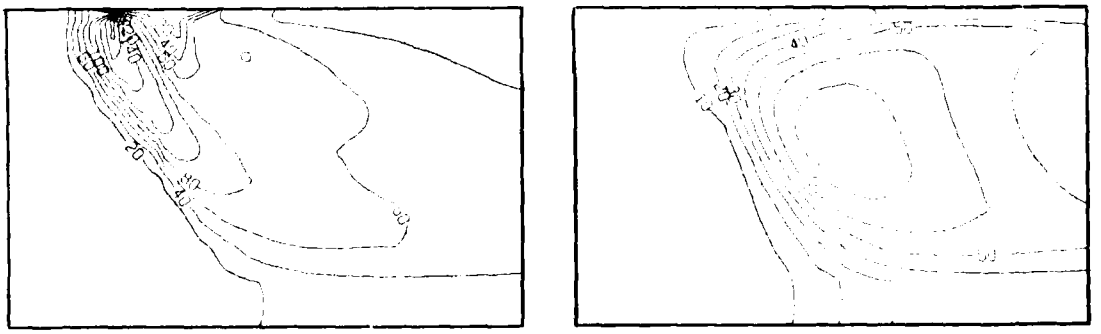
Figure 8. (a) Mean and (b) r.m.s. Fluctuating Temperature (0.25 kg/s dilution flowrate)



(a) Streakline Diagram



(b) Contours of Favre Averaged Temperatures (K)



(c) Contours of Square Root of Favre Averaged Variance in Temperature

Figure 9. Computed Data for Medium Dilution Flowrate (0.25 kg/s)

DISCUSSION

H.Eickhoff, Ge

To attribute the differences in the mixing pattern of temperature and concentration to difference exchange coefficients for heat and mass is contradictive with many other experimental results. Did you study the influence of different initial and boundary conditions on the predicted mixing patterns?

Author's Reply

The experimentally observed differences in temperature and concentration mixing contours are not attributed to different exchange coefficients for heat and mass transfer; this is only one of a number of possible explanations considered in the paper. We are not alone in observing this type of behaviour, which has also been reported by Kamotani and Greber – reference [5] in the text.

We have computationally assessed, in the purely parametric manner, the influence of varying turbulence intensity at the boundaries. However, as stated in the paper, it was found that the jet inlet turbulence intensity is relatively unimportant – the turbulence subsequently generated at the interface of the two streams overwhelms that initially within them.

P.Hebrard, Fr

Est ce que vous avez vérifié que l'écoulement était effectivement uniforme en amont des trous de dilution? Une distance d'environ 2 diamètres entre les orifices primaires et les orifices de dilution me paraît faible pour avoir un écoulement uniforme.

Le modèle de calcul est-il parabolique ou elliptique? Je suis étonné qu'il n'y ait aucune zone de recirculation.

Author's Reply

Yes, we have checked that temperature, concentration and velocity were uniform upstream of the dilution holes. The model is elliptic. We did not notice any recirculation. In our earlier work, with a larger flow ratio and a greater penetration we had recirculation ahead of the jet and we found the calculated recirculation was overestimated.

P.Ramette, Fr

Avez-vous visualisé ou calculé le champ de vitesse dans un plan perpendiculaire à l'écoulement principal de la chambre? En particulier, les tourbillons contrarotatifs provoqués par l'interaction d'un jet avec l'écoulement principal ne sont-ils pas positionnés à l'intérieur du jet plutôt qu'à l'extérieur? Ne pensez-vous pas que ces tourbillons peuvent être une zone de dissipation d'énergie accompagnée de peu de dilution ce que pourrait éventuellement expliquer la différence que vous avez observée entre les courbes de température et les courbes de concentration?

Author's Reply

Yes the calculation has been done in planes perpendicular to the main flow. There were vortices outside of the jet. I agree that the effect of those vortices could change the dissipation rate and could explain the results which were obtained.

ETUDE DE PROBLEMES FONDAMENTAUX DE LA COMBUSTION DANS LES FOYERS DE TURBOREACTEURS AU MOYEN D'UN REACTEUR TUBULAIRE

J.C. BELLET, P. CAMBRAY, M. CHAMPION, D. KARMED
Laboratoire d'Energétique et de Détonique
(Laboratoire Associé au C.N.R.S. n° 193)
E.N.S.M.A., rue Guillaume VII, 86034 POITIERS Cédex (France)

RESUME -

Un foyer tubulaire, à l'entrée duquel des gaz frais (hydrocarbure-air) et des gaz brûlés sont mélangés rapidement de façon à simuler une combustion stabilisée par recirculation de gaz brûlés, est utilisé pour :
- valider, dans des conditions représentatives des foyers, des schémas cinétiques de la combustion des hydrocarbures proposés par d'autres auteurs,
- étudier les interactions entre turbulence thermique et taux de production chimique.

Les résultats obtenus précédemment ayant montré :
- que l'influence de la turbulence sur les taux de production chimique peut être négligée en première approximation,
- que l'écoulement peut être considéré comme quasi-monodimensionnel au voisinage de l'axe,

les profils des fractions molaires mesurées sont utilisés pour tester les modèles cinétiques proposés pour la combustion du propane. Il apparaît principalement que, si les modèles les plus récents prédisent correctement la première phase de la combustion, ils surestiment les vitesses de réaction en fin de combustion, tout au moins dans le cas d'un mélange propane-air-gaz brûlés.

Par ailleurs, on a constaté que, comme le prévoit la théorie, la combustion augmente l'amplitude des fluctuations de température présentes dans le mélange initial.

1. INTRODUCTION -

Dans la zone primaire des foyers de turboréacteurs, la combustion est stabilisée par recirculation de gaz brûlés dans les gaz frais. Les phénomènes élémentaires qui contrôlent ce processus, et par conséquent la modélisation qui doit en être faite, dépendent fondamentalement des valeurs relatives du temps caractéristique des réactions de combustion d'une part, et du temps caractéristique du mélange entre gaz frais et gaz brûlés d'autre part. Si le mélange est très rapide par rapport à la combustion, le processus est contrôlé par la cinétique chimique, les réactions s'effectuant au sein d'une "zone de combustion distribuée" (suivant la terminologie proposée par LIBBY et WILLIAMS /1/). Dans le cas contraire, le processus est contrôlé par la dynamique de l'écoulement et ses interactions avec des fronts de flamme minces. Dans la pratique il est probable que les deux cas existent suivant les différentes parties de la zone primaire et suivant les régimes de fonctionnement du moteur, et qu'il existe aussi des situations intermédiaires.

Au Laboratoire d'Energétique et de Détonique de l'E.N.S.M.A., ces deux cas limites sont étudiés, respectivement :

a) dans un foyer tubulaire à l'entrée duquel gaz frais et gaz brûlés sont mélangés de façon intense : les principaux résultats obtenus à ce jour dans le cadre de cette première étude sont résumés ici ;

b) dans une expérience de combustion en couche limite avec injection pariétale de gaz frais dans un écoulement de gaz brûlés : les premiers résultats de cette seconde étude ont été présentés par ailleurs, en particulier dans la référence 2.

Le foyer tubulaire est donc principalement destiné à fournir des données expérimentales sur la cinétique de la combustion d'un mélange hydrocarbure-air-gaz brûlés, afin de permettre de tester divers modèles cinétiques dans des conditions de composition plus représentatives des foyers de turboréacteur que lorsque les réactifs sont dilués dans un gaz inerte. Par ailleurs, le mélange entre gaz frais et gaz brûlés étant turbulent, ce foyer tubulaire permet aussi d'étudier certains aspects des interactions entre turbulence et réactions chimiques.

2. DISPOSITIF EXPERIMENTAL -

Le foyer tubulaire a été conçu en collaboration avec la SNECMA, de façon que deux flux de gaz frais et de gaz brûlés soient mélangés en un temps court par rapport au temps de réaction du mélange résultant, qui est en conditions d'auto-inflammation. Il est constitué (fig. 1) :
- d'une chambre de précombustion où les gaz brûlés sont produits à partir d'un mélange propane-air de richesse ϕ_0,
- d'un mélangeur qui est traversé par les gaz chauds grâce à 100 orifices disposés suivant une grille de maille carrée de côté 1 cm, et qui injecte les gaz frais de richesse ϕ_2 par 81 injecteurs intercalés entre les trous précédents,
- d'une veine d'expérience de section carrée 10 cm x 10 cm et de longueur 1 m.

Les parois de la chambre de précombustion et le mélange sont refroidies par circulation d'eau, mais les parois de la veine d'expérience sont constituées de panneaux en fibres réfractaires non refroidis, maintenus par un fourreau en acier inoxydable.

Pour un débit total donné $\dot{m}$, il est possible de stabiliser une zone de combustion à une distance donnée en aval du mélangeur, en ajustant la température de mélange T_3 par l'intermédiaire de la

richesse ϕ_o et du rapport $R = \mathring{m}_o/\mathring{m}_2$ des débits chaud et froid : la position de cette zone de combustion est très sensible aux variations de ces deux paramètres, qui doivent être contrôlés avec une précision de l'ordre de 1%.

Des conditions d'expérience typiques pour la combustion de propane sont :

p = 1 atm	ϕ_o = 1	R = 1.56
$\mathring{m}$ = 300 g/s	$\phi_2 \leq 0.7$	

Dans ces conditions la température de mélange T_3 est d'environ 1200 K, et le début des réactions exothermiques se situe à environ 20 cm en aval du mélangeur, le délai d'inflammation augmentant sensiblement avec la richesse ϕ_2. Cette dernière caractéristique entraine la limitation de ϕ_2 à environ 0,7 : au-delà de cette valeur il faudrait augmenter T_3 plus que ne le permet la technologie du mélangeur.

3. METHODES DE DIAGNOSTIC -

Les fractions molaires des principales espèces stables sont mesurées par prélèvement, à l'aide de sondes en acier inoxydable refroidies par circulation d'eau, d'échantillons qui sont ensuite analysés à l'aide de chromatographes.

La vitesse d'écoulement est mesurée à l'aide d'une chaîne de vélocimétrie laser reliée à un système de traitement de données, l'écoulement étant ensemencé en particules de zircone de diamètre moyen 2 µm.

La température moyenne de l'écoulement est mesurée à l'aide de thermocouples chromel-alumel ou platine-platine rhodié (protégés des effets catalytiques) réalisés en fils de diamètre 0,2 mm. On procède à la correction de l'effet du rayonnement.

Les fluctuations de température sont mesurées de deux façons :

- soit à l'aide de thermocouples chromel-alumel ou platine-platine rhodié réalisés en fils de diamètre 25 µm soudés bout à bout, avec compensation numérique de la constante de temps mesurée par surchauffage électrique /3/ ou déterminée par calcul direct, ou avec détermination de la moyenne quadratique par intégration du spectre énergétique /4/ ;
- soit par la méthode de pyrométrie infrarouge d'émission-absorption, développée à l'ONERA par CHARPENEL /5/, et qui permet de déterminer la moyenne quadratique des fluctuations de température dans le cas d'un milieu statistiquement homogène le long du chemin optique de mesure.

Les deux méthodes sont complémentaires :

- la première fournit une mesure ponctuelle mais avec une réponse en fréquence,
- la seconde a une bande passante étendue mais ne fournit qu'une mesure intégrée : elle permet cependant de connaître la moyenne quadratique des fluctuations locales si l'on détermine en même temps l'échelle intégrale de turbulence /5/.

4. PROPRIETES CARACTERISTIQUES DE LA COMBUSTION DANS LE FOYER TUBULAIRE -

4.1 - Etat d'avancement du mélange avant combustion -

Afin de vérifier que le foyer tubulaire fonctionne bien conformément à l'objectif fixé, c'est-à-dire avec une combustion contrôlée par la cinétique chimique, nous avons mesuré les fluctuations de température à x = 15 cm en aval du mélangeur, dans les conditions de fonctionnement précédemment citées (§ 2). La question était de savoir si à cette distance le mélange est devenu quasi-homogène (fonction densité de probabilité de la température quasi-gaussienne) ou s'il est constitué de paquets accolés de gaz frais et de gaz brûlés (fonction densité de probabilité bimodale).

Par analyse spectrale des signaux délivrés par les thermocouples fins, sans et avec compensation, on a déterminé dans quelles limites la méthode permet de détecter une succession de paquets de gaz frais et de gaz brûlés, en fonction de la taille moyenne de ces paquets, de la dispersion de cette taille, et de l'écart de température entre les paquets /3/. C'est ainsi, par exemple, que pour un écoulement à 130 m/s, des paquets de taille caractéristique moyenne de 8 mm, avec une différence de température de 1200 K sont détectés même avec une dispersion en taille de l'ordre de 100%. On a aussi vérifié que les spectres d'énergie des signaux obtenus par les deux méthodes sont compatibles, ce qui permet d'extrapoler la décroissance du spectre du signal délivré par les thermocouples au-delà de la limitation due au bruit et d'en déduire par intégration l'énergie totale contenue en dehors du bruit /4/.

Les deux méthodes ont conduit, avec un accord à 20% près, à un écart quadratique moyen de 40 K pour T_3 = 1200 K, qui caractérise un mélange quasi-homogène. Dans ces conditions, le modèle monodimensionnel de combustion turbulente développé par CHAMPION /6, 7, 8/ montre que l'influence des fluctuations de température sur les taux de production chimique peut être négligé en première approximation, et que, pour la confrontation avec les modèles cinétiques, l'écoulement peut être considéré comme laminaire.

4.2 - Influence éventuelle des effets bidimensionnels -

Pour utiliser la propriété précédente, il importait de plus de s'assurer que l'écoulement peut être considéré comme monodimensionnel, au moins sur l'axe de la veine d'expérience. En effet le caractère adiabatique des parois de cette dernière provoque une inflammation plus précoce dans les couches limites que sur l'axe, et il peut en résulter des effets bidimensionnels importants.

On a donc procédé à une étude expérimentale détaillée de l'écoulement, et confronté les résultats obtenus avec les prédictions fournies par un modèle bidimensionnel de type k-ε-g où la combustion est représentée par une seule réaction globale /4/. Il est d'abord apparu que, pour obtenir une représentation satisfaisante, il fallait faire précéder cette réaction globale par un délai quasi-isotherme, qui a été déduit de l'expérience. La comparaison de la représentation fournie par ce modèle bidimensionnel, avec celle fournie par un modèle monodimensionnel comportant le même schéma cinétique, a montré que les profils de température moyenne ainsi déterminés coïncident sauf au voisinage de la sortie du foyer ($x \geq 90$ cm).

4.3 - Conclusions pour l'interprétation des résultats expérimentaux -

L'ensemble de ces travaux préliminaires a donc prouvé que le foyer tubulaire peut être utilisé pour tester des modèles cinétiques en considérant, en première approximation au moins, que l'écoulement est monodimensionnel et laminaire sur l'axe. Il convient toutefois de noter que la confrontation ne permet pas de valider avec exactitude la représentation de la phase d'inflammation dans la mesure où, dans l'expérience, une partie de cette phase s'effectue pendant le mélange entre gaz brûlés et gaz frais.

Par ailleurs l'étude de l'évolution des fluctuations de température doit permettre de vérifier les effets des interactions avec la combustion prédites par le modèle de combustion turbulente.

5. TRAVAUX SUR LA CINETIQUE DES REACTIONS DE COMBUSTION EN MELANGE HYDROCARBURE-AIR-GAZ BRULES -

Les expériences ont pour l'instant été limitées aux hydrocarbures gazeux (propane, éthylène) dont les schémas réactionnels détaillés sont encore loin d'être bien connus malgré les progrès en cours /9, 10, 11, 12/. Compte tenu du fait que la phase d'oxydation de l'éthylène (espèce intermédiaire hydrocarbonée la plus importante dans la combustion des hydrocarbures plus lourds) paraît la phase la moins bien connue, nous avons aussi procédé à des expériences de combustion de propane additionné d'éthylène, de façon à permettre de tester la prise en compte de la concentration en éthylène dans les schémas proposés.

5.1 - Résultats expérimentaux -

Sur les figures 2 à 6 sont représentés des exemples de profils de la température et des fractions molaires mesurées sur l'axe dans le cas de la combustion respectivement :

- du propane pur (fig. 2)
- de l'éthylène pur (fig. 3)
- des mélanges : 95% C_3H_8 + 5 % C_2H_4 (fig. 4)
  90% C_3H_8 + 10% C_2H_4 (fig. 5)
  80% C_3H_8 + 20% C_2H_4 (fig. 6).

On remarque en particulier que dans le cas du propane le profil de la concentration en CO est assez aplati, alors que dans le cas de l'éthylène il présente un maximum plus accentué, correspondant à une formation et une consommation retardées mais plus rapides.

Par ailleurs on constate que l'addition d'éthylène au propane accélère la formation d'éthylène et de méthane, et donne au profil de concentration de CO une allure plus proche du cas de l'éthylène pur que du cas du propane pur.

5.2 - Comparaison avec les schémas cinétiques -

5.2.1 - On trouvera dans la communication de CATHONNET et al. à ce même Symposium /13/ un exemple d'utilisation de nos résultats pour la mise au point d'un schéma cinétique détaillé de la combustion du propane. L'intérêt de la mise au point de tels mécanismes est fondamental et peut conduire à l'élaboration de schémas simplifiés à partir de la définition des principales étapes réactionnelles. Mais leur application directe paraît limitée aux modèles de chambre de combustion constitués par l'assemblage de foyers homogènes /14/. Si l'on souhaite mettre au point des modèles bi- ou tri-dimensionnels, il faudra bien recourir à des schémas simplifiés, et, si l'on souhaite prévoir par exemple l'émission de CO ou les limites de stabilité en fonction de la richesse, on ne pourra se limiter à l'utilisation d'une seule réaction globale.

Les travaux de CATHONNET et al. /13/ montrent qu'il est déjà possible de représenter correctement le début de la combustion mais que les calculs ont tendance à surestimer les vitesses de réaction en fin de combustion.

5.2.2 - Nous avons par ailleurs entrepris de confronter nos résultats avec des schémas simplifiés proposés par d'autres auteurs. Nous avons déjà montré /3/ que les schémas "quasi-globaux" (qui comporte une seule réaction globale pour la formation de CO et H_2, à laquelle sont associées les réactions élémentaires intervenant dans l'oxydation de CO et H_2 en CO_2 et H_2O /15, 16, 17/) ne permettent pas de représenter une phase de délai quasi-isotherme dont la longueur croît avec la richesse. Par contre le modèle à 4 réactions de HAUTMAN et al. /18/ nous a paru particulièrement intéressant, dans la mesure où il comporte 2 réactions pour la formation de CO et H_2. Rappelons que ce schéma (valable pour d'autres hydrocarbures aliphatiques) s'écrit :

$$C_3H_8 \rightarrow 3/2\ C_2H_4 + H_2 \qquad (R_1)$$

$$C_2H_4 + O_2 \rightarrow 2\ CO + 2\ H_2 \qquad (R_2)$$

$$CO + 1/2\ O_2 \rightarrow CO_2 \qquad (R_3)$$

$$H_2 + 1/2\ O_2 \rightarrow H_2O \qquad (R_4)$$

où l'éthylène représente en réalité des oléfines intermédiaires (principalement éthylène et propène).

Selon les auteurs, les taux de production chimique respectifs de chacune de ces réactions s'écrivent :

$$\left(\frac{d(C_3H_8)}{dt}\right)_1 = -\,10^{x_1}\, e^{-E_1/RT}\, (C_3H_8)^{a_1}\, (O_2)^{b_1}\, (C_2H_4)^{c_1}$$

$$\left(\frac{d(C_2H_4)}{dt}\right)_2 = -\,10^{x_2}\, e^{-E_2/RT}\, (C_2H_4)^{a_2}\, (O_2)^{b_2}\, (C_3H_8)^{c_2}$$

$$\left(\frac{d(CO)}{dt}\right)_3 = -10^{x_3} e^{-E_3/RT} (CO)^{a_3} (O_2)^{b_3} (H_2O)^{c_3} \times S$$

$$\left(\frac{d(H_2)}{dt}\right)_4 = -10^{x_4} e^{-E_4/RT} (H_2)^{a_4} (O_2)^{b_4} (C_2H_4)^{c_4}$$

avec les paramètres ci-dessous :

	x	E	a	b	c
R_1	17.32 ± 0.88	49600± 2400	0.5 ± 0.02	1.07 ± 0.05	0.4 ± 0.03
R_2	14.70 ± 2.00	50000± 5000	0.9 ± 0.08	1.18 ± 0.1	-0.37± 0.04
R_3	14.60 ± 2.50	40000± 1200	1.0	0.25	0.50
R_4	13.52 ± 2.2	41000± 6400	0.85± 0.16	1.42 ± 0.11	-0.56± 0.2

et : $S = 7.93 \exp(-2.48\,\phi_o)$ (ϕ_o : richesse initiale)
et la condition $S \leq 1$.

On remarque que, dans l'élaboration de ce schéma, les auteurs ont été conduits à adopter des exposants c_2 et c_4 négatifs, et qu'en conséquence les vitesses des réactions R_2 et R_4 vont croître très rapidement lorsque les concentrations en C_3H_8 et C_2H_4 vont respectivement tendre vers zéro.

Ceci permet une représentation satisfaisante de la phase initiale de la combustion (au besoin en ajustant les valeurs des divers paramètres) mais pas de la phase finale. A titre d'exemples, nous donnons les résultats des confrontations entre nos expériences et les calculs effectués pour le propane pur (fig. 7) et les mélanges à 5 % (fig. 8) et 20 % (fig. 9) d'éthylène, avec les valeurs suivantes des paramètres du schéma (en regroupant les alcanes avec le propane et les autres hydrocarbures avec l'éthylène) :

	x	E	a	b	c
R_1	16.40	47200	0.5	1.07	0.4
R_2	14.80	55000	0.82	1.18	-0.41
R_3	14.00	41200	1.0	0.25	0.5
R_4	14.60	46000	0.93	1.42	-0.56

La fin des réactions apparaît trop rapide et cette même tendance se manifeste dans certains résultats présentés par les auteurs eux-mêmes.

Par ailleurs, le caractère "raide" de ce système d'équations peut entraîner des difficultés d'intégration numérique lors de son utilisation pour la modélisation d'écoulements réactifs.

C'est pourquoi nous avons cherché s'il était possible d'apporter des aménagements à ce schéma afin d'éviter les inconvénients ci-dessus. De manière générale les taux de production chimique proposés par les auteurs sont exprimés en fonction des concentrations des réactifs, avec un facteur correctif introduit pour tenir compte du fait qu'il ne s'agit pas de réactions élémentaires, et pour représenter certaines tendances du mécanisme réel : ils ont été conduits à exprimer ce facteur correctif en fonction de la concentration d'une troisième espèce intervenant dans le schéma. Compte tenu des espèces choisies, un exposant négatif est apparu pour 2 des 4 réactions.

Nous avons pensé qu'une autre voie de recherche possible consiste à exprimer ce facteur correctif en fonction d'une grandeur caractérisant la "réactivité" du mélange à chaque instant. A défaut de prendre en compte les espèces radicalaires, qui n'apparaissent pas dans le schéma, une solution pourrait être de choisir la concentration en CO formé depuis l'instant initial, noté CO^x, afin de le distinguer du CO présent initialement dans le cas d'un mélange comportant des gaz brûlés.

Une tentative pour représenter nos propres résultats expérimentaux (limités, rappelons-le, à des mélanges pauvres) a conduit aux résultats qui apparaissent sur les figures 10 et 11, et qui ont été obtenus avec le schéma suivant :

$$C_3H_8 \rightarrow 3/2\ C_2H_4 + H_2 \qquad (R_1)$$
$$C_2H_4 + O_2 \rightarrow 2\ CO^x + 2\ H_2 \qquad (R_2')$$
$$CO + 1/2\ O_2 \rightarrow CO_2 \qquad (R_3)$$
$$CO^x + 1/2\ O_2 \rightarrow CO_2 \qquad (R_3')$$
$$H_2 + 1/2\ O_2 \rightarrow H_2O \qquad (R_4)$$

$$\frac{d(C_3H_8)}{dt}_1 = -10^{-x_1} e^{-E_1/RT} (C_3H_8)^{a_1} (O_2)^{b_1}$$

$$\frac{d(C_2H_4)}{dt}_{2'} = -10^{-x_2'} e^{-E_2'/RT} (C_2H_4)^{a_2'} (O_2)^{b_2'} (CO^x)^{c_2'}$$

$$\frac{d(CO)}{dt}_3 = -10^{-x_3} e^{-E_3/RT} (CO)^{a_3} (O_2)^{b_3} (CO^x)^{c_3}$$

$$\frac{d(CO^x)}{dt}_{3'} = -10^{-x_3} e^{-E_3/RT} (CO^x)^{a_3} (O_2)^{b_3} (CO^x)^{c_3}$$

$$\frac{d(H_2)}{dt}_4 = -10^{-x_4} e^{-E_4/RT} (H_2)^{a_4} (O_2)^{b_4} (CO^x)^{c_4}$$

où les paramètres ont les valeurs ci-dessous :

	x	E	a	b	c
R_1	19.80	40000	1.5	1.07	0
R_2'	31.65	60000	2	1.18	1
R_3 et R_3'	14.45	39000	1	0.25	0.5
R_4	20.80	40000	1	1.42	0.3

On constate que la représentation est relativement satisfaisante, et les inconvénients liés aux exposants négatifs ont évidemment disparu. Cette approche paraît donc possible, mais il reste encore à la confronter aux résultats expérimentaux obtenus dans des conditions différentes, notamment en mélange riche et à pression supérieure à la pression atmosphérique.

6. TRAVAUX CONCERNANT LES INTERACTIONS TURBULENCE-COMBUSTION -

Le modèle de combustion turbulente en écoulement monodimensionnel développé par CHAMPION /6, 7, 8/ montre que les fluctuations de température présentes dans le mélange initial sont amplifiées par les réactions. Nous avons procédé à des mesures de fluctuations de température à l'aide de thermocouples fins à constante de temps compensée. Les résultats obtenus à diverses abscisses x en aval du mélangeur pour $\phi_2 = 0{,}6$ sont résumées dans le tableau ci-dessous :

x (cm)	15	45	75	90
σ_T (K)	45	96	73	59

On constate bien l'augmentation de l'écart quadratique moyen des fluctuations dans la région des réactions exothermiques, suivie de l'amortissement de ces fluctuations. Ces résultats ne peuvent pour l'instant constituer qu'une vérification qualitative des prédictions du modèle de combustion turbulente, qui a été développé avec un schéma de type quasi-global pour représenter la cinétique chimique, et donc mal adapté au cas considéré.

7. CONCLUSIONS -

Les résultats obtenus avec le foyer tubulaire, dans des conditions cinétiques qui simulent la stabilisation de la combustion par recirculation de gaz brûlés, constituent principalement une contribution à la validation expérimentale des schémas réactionnels de la combustion des hydrocarbures

gazeux. Ils complètent les résultats obtenus par d'autres auteurs et permettent de voir si les schémas cinétiques proposés peuvent correctement prendre en compte la présence de gaz brûlés en proportion importante dans le mélange avant réaction. Ces gaz brûlés ne peuvent en effet être assimilés à un gaz inerte :

- ni pour déterminer les vitesses des réactions globales des schémas simplifiés, car leur présence favorise dans la réalité les réactions inverses (à la différence d'un gaz inerte qui ne fait que diluer les réactifs),
- ni dans la mise au point de schémas détaillés, où les vitesses de réactions de recombinaison en présence d'un troisième corps ne sont pas les mêmes selon que ce dernier est de l'azote ou un constituant des gaz brûlés.

En ce qui concerne les schémas simplifiés, celui à 4 réactions proposé par HAUTMAN et al. /18/ paraît, sous réserve de certains aménagements comme celui que nous proposons ici, permettre une représentation satisfaisante de l'évolution de 7 espèces et de la température, et peut être très utile pour le développement de modèles de foyers.

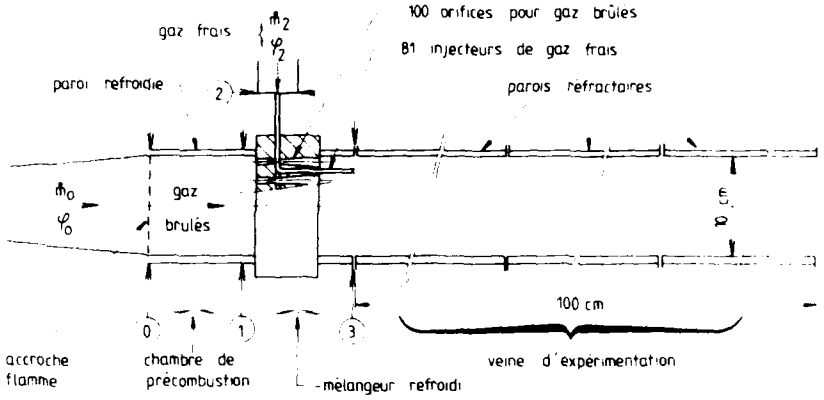
Par ailleurs le foyer tubulaire permet de tester des modèles de combustion turbulente dans le cas d'un écoulement de configuration simple, où la cinétique chimique doit être représentée de façon réaliste. Nous avons ainsi pu vérifier qu'au sein d'une zone de combustion distribuée les fluctuations initiales de température sont amplifiées par les réactions chimiques.

REFERENCES -

1. LIBBY P.A. and WILLIAMS F.A., Turbulent flows involving chemical reactions, Annual Review of Fluid Mechanics, 6, 1976, p. 351.
2. MEUNIER S., CHAMPION M. and BELLET J.C., Premixed combustion in a turbulent boundary layer with injection, Combust. Flame, 50, 1983, p. 231.
3. CHAUVEAU Y., CAMBRAY P., GENGEMBRE E., CHAMPION M. and BELLET J.C., Characterization of a turbulent combustion zone in a tubular reactor, 8th Int. Coll. on Gasdynamics of Explosions and Reactive Systems, Minsk, 1981 (to appear in Progress in Astronautics and Aeronautics, A.I.A.A.).
4. CHAUVEAU Y., CAMBRAY P., CHAMPION M. and BELLET J.C., Experimental study and modelling of the reactive flow in a constant section reactor, Physico-chemical Hydrodynamics, vol. 4, n°3, 1983, p. 231.
5. CHARPENEL M., Mesures instantanées par pyrométrie infrarouge de température de gaz de combustion : application à la turbulence thermique, Revue de Physique Appliquée, 14, 1979, p. 491.
6. CHAMPION M., BRAY K.N.C. and MOSS J.B., The turbulent combustion of a propane-air mixture, Acta Astronautica, 5, 1978, p. 1063.
7. CHAMPION M. et BELLET J.C., Influence des fluctuations de température initiale sur le développement des réactions dans une zone de combustion distribuée, Comptes Rendus Acad. Sciences, Paris, 287, série B, 1978, p. 159.
8. CHAMPION M., Premixed turbulent combustion controlled by complex chemical kinetics, Combust. Sci. Technol., 24, 1980, p. 23.
9. WESTBROOK C.K. and DRYER F.L., Chemical kinetics and modelling of combustion processes, 18th Symp. (Int.) on Combustion, the Combustion Institute, 1981, p. 749.
10. WARNATZ J., The structure of laminar alkane-, alkene-, and acetylene flames, 18th Symposium (Int.) on Combustion, The Combustion Institute, 1981, p. 369.
11. CATHONNET M., BOETTNER J.C. and JAMES H., Experimental study and numerical modelling of high temperature oxidation of propane and n-butane, 18th Symposium (Int.) on Combustion, the Combustion Institute, 1981, p. 903.
12. WESTBROOK C.K., DRYER F.L. and SCHUG K.P., A comprehensive mechanism for the pyrolisis and oxidation of ethylene, 19th Symposium (Int.) on Combustion, TheCombustion Institute, 1983, p. 153.
13. CATHONNET M., GAILLARD F., BOETTNER J.C. et JAMES H., Etude expérimentale et modélisation de la cinétique de combustion des hydrocarbures, 62nd AGARD P.E.P. Symposium, Paper 62-22, Cesme, 1983.
14. CHAUVEAU Y., DESAULTY M. et BAYLE-LABOURE G., Modélisation des chambres de combustion par assemblage de foyers homogènes, 62nd AGARD P.E.P. Symposium, Paper 62-34, Cesme, 1983.
15. EDELMAN R.B. and FORTUNE O.F., A quasi-global chemical kinetic model for finite rate combustion of hydrocarbon fuels with application to turbulent burning and mixing in hypersonic engines and nozzles, A.I.A.A. Paper 69-86, 1969.
16. EDELMAN R.B. and HARSHA P.T., Some observations on turbulent mixing with chemical reactions, Progress in Astronautics and Aeronautics, A.I.A.A., vol. 58, 1978, p. 55.
17. DUTERQUE J., BORGHI R. and TICHTINSKY H., Study of quasi-global schemes for hydrocarbon combustion, Combust. Sci. Technol., 26, 1981, p. 1.
18. HAUTMAN D.J., DRYER F.L., SCHUG K.P. and GLASSMAN I., A multi-step overal kinetic mechanism for the oxidation of hydrocarbons, Combust. Sci. Technol., 25, 1981, p. 219.

REMERCIEMENTS -

Ces travaux ont été effectués avec l'aide de la Direction des Recherches, Etudes et Techniques (Contrat N° 82/071).



_ Fig 1 _ Schéma du foyer tubulaire

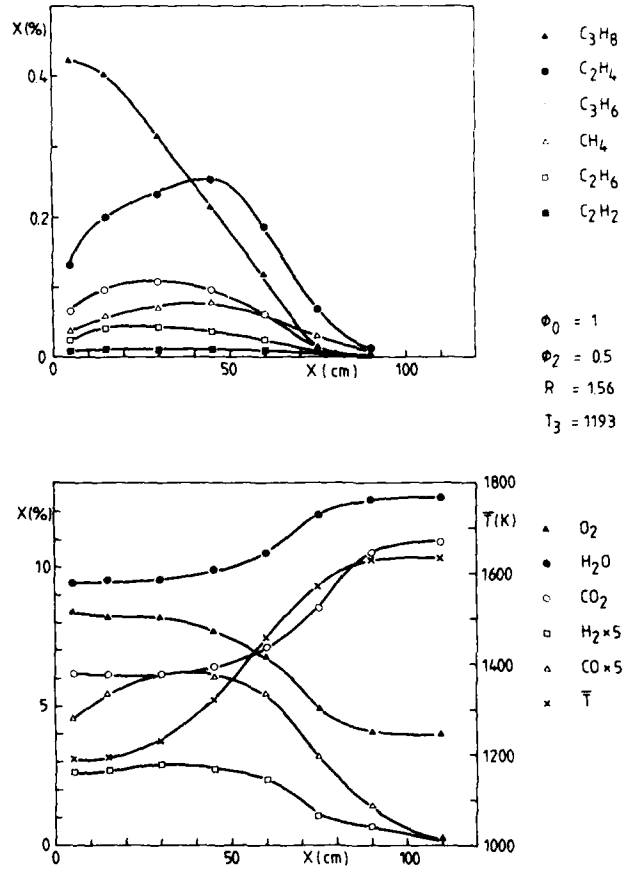


Fig. 2 - Combustion de propane pur

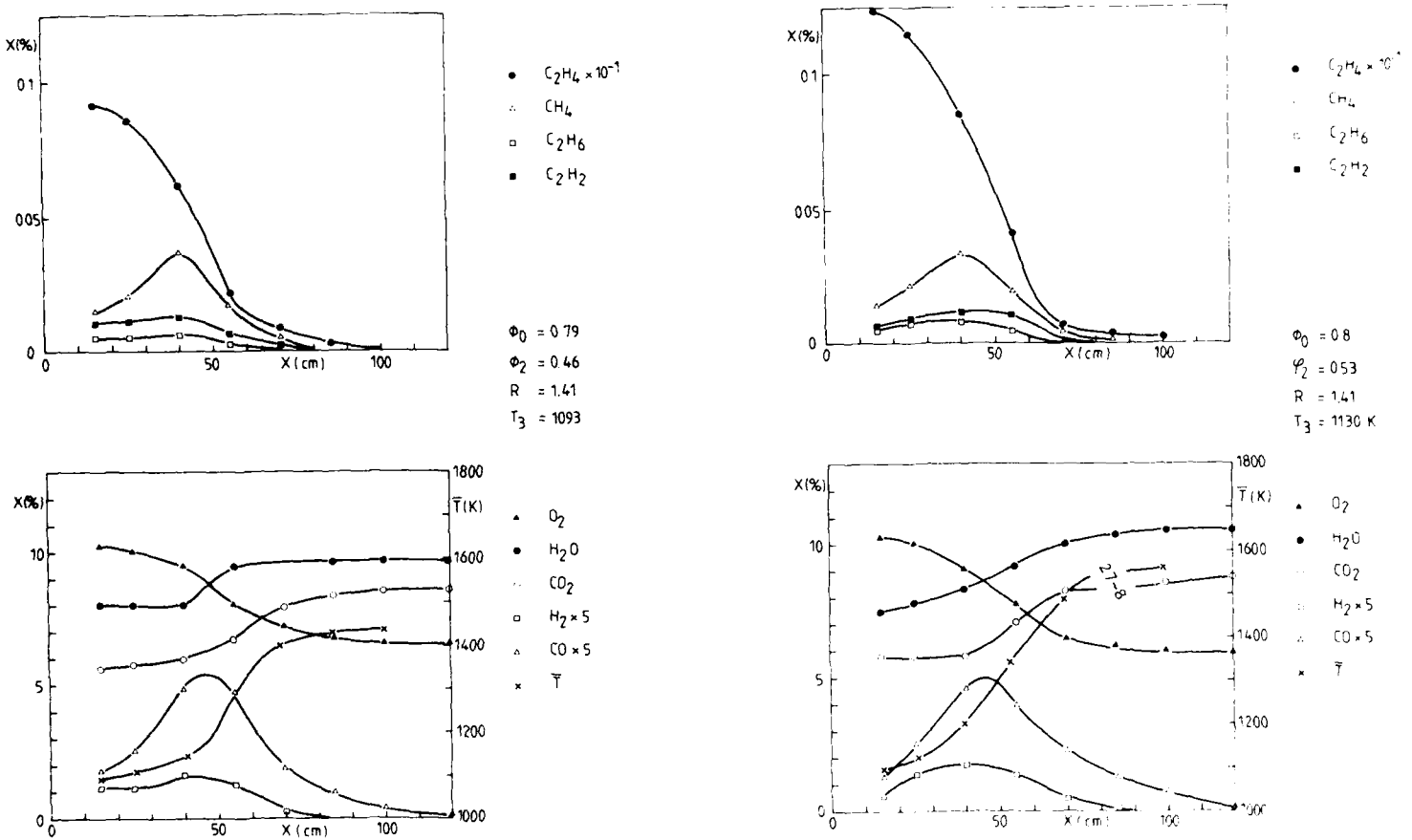


Fig. 3 - Combustion d'éthylène

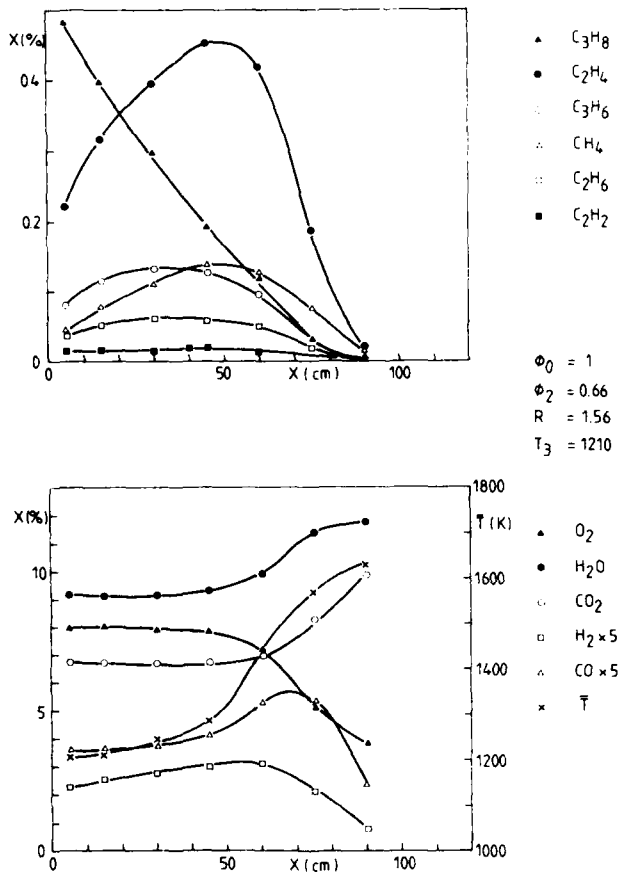


Fig. 4 - Combustion d'un mélange
95 % C_3H_8 + 5 % C_2H_4

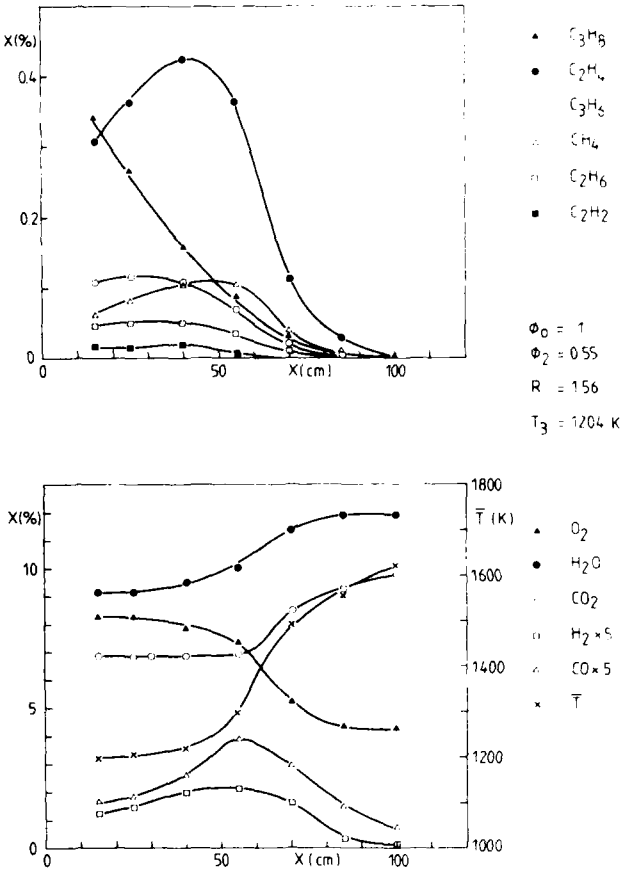


Fig. 5 - Combustion d'un mélange
90 % C_3H_8 + 10 % C_2H_4

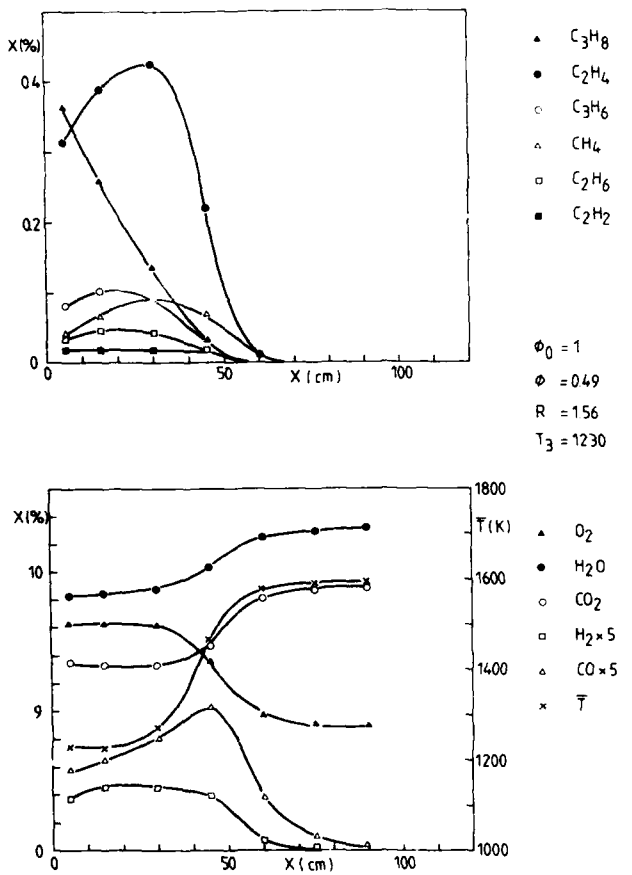


Fig. 6 - Combustion d'un mélange
80 % C_3H_8 + 20 % C_2H_4

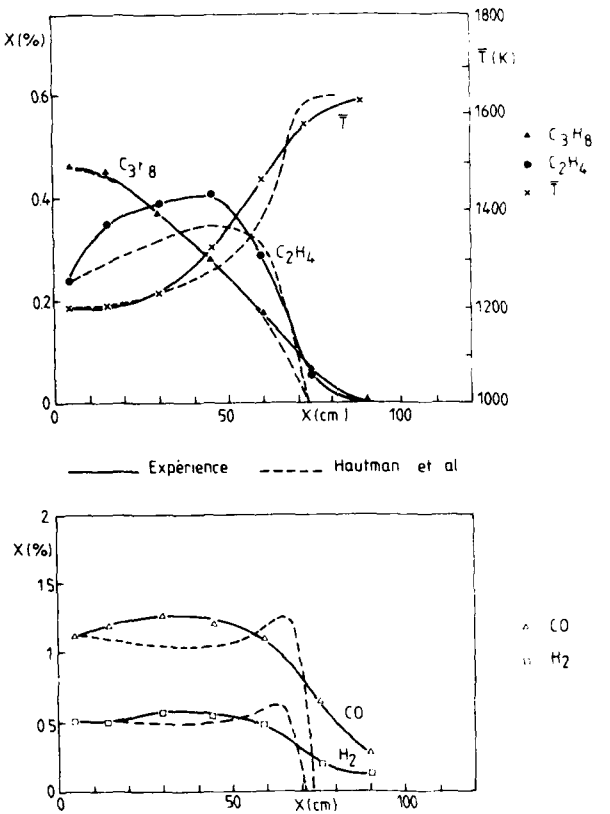


Fig. 7 - Comparaison avec une simulation par le schéma d'HAUTMAN et al.
Cas du propane pur.

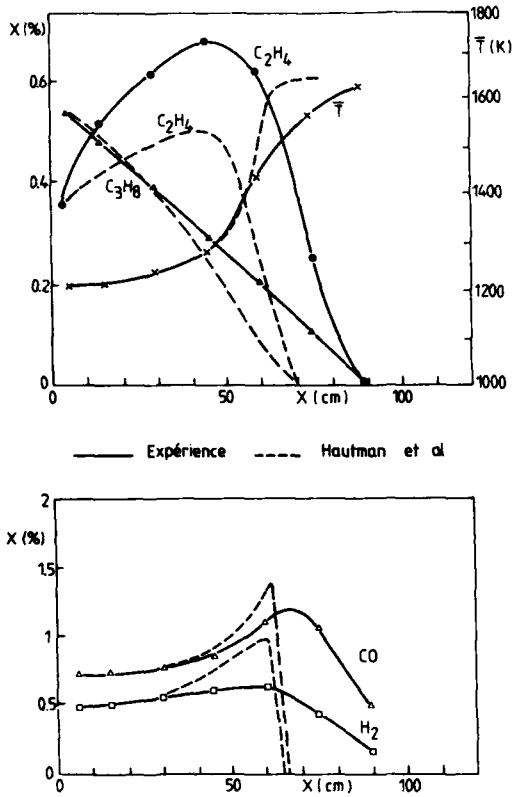


Fig. 8 - Comparaison avec une simulation par le schéma d'HAUTMAN et al.
cas d'un mélange 95 % C_3H_8 + 5 % C_2H_4

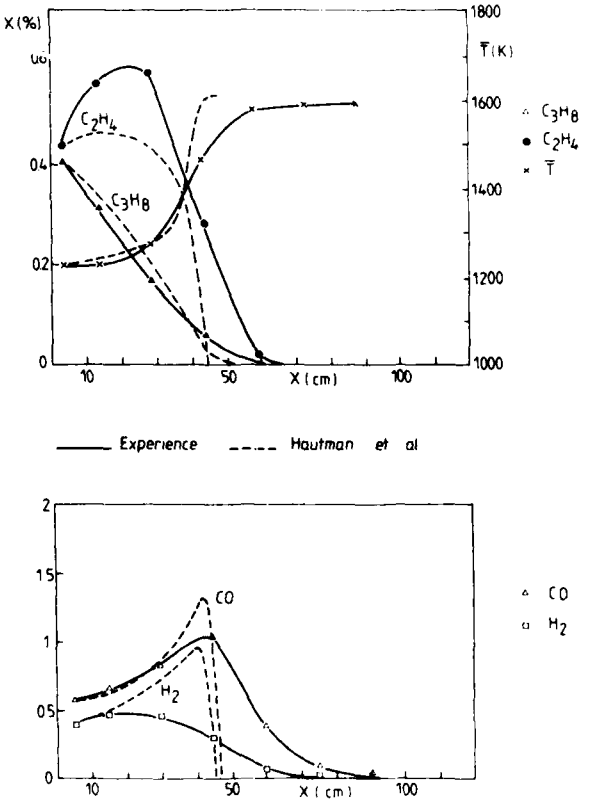


Fig. 9 - Comparaison avec une simulation par le schéma d'HAUTMAN et al.
cas d'un mélange 80 % C_3H_8 + 20 % C_2H_4

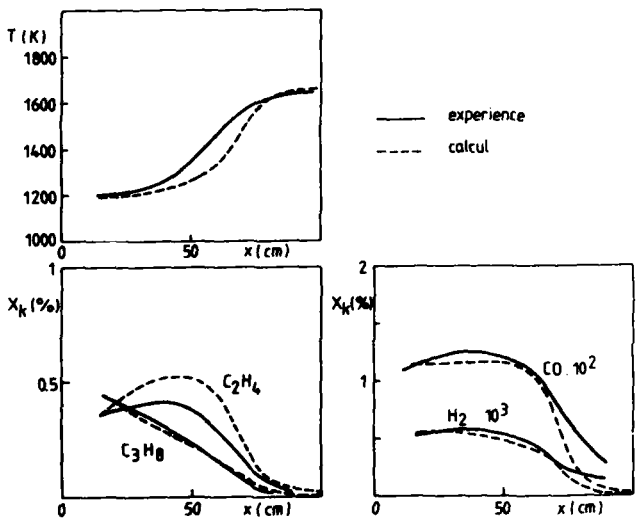


Fig. 10 - Comparaison avec une simulation par le schéma d'HAUTMAN et al. modifié : cas du propane pur.

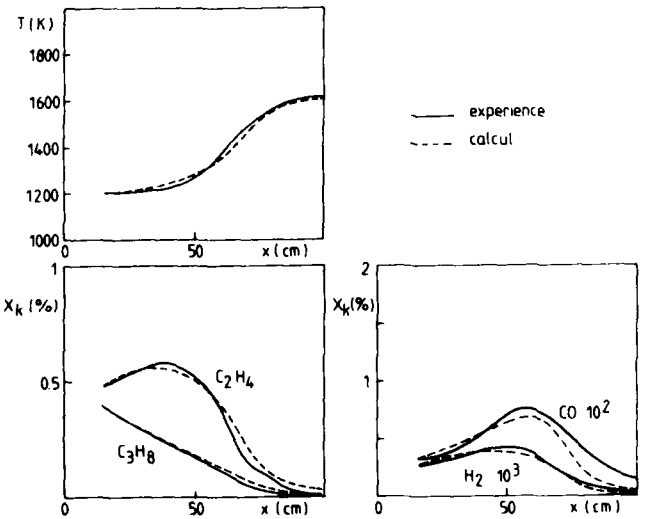


Fig. 11 - Comparaison avec une simulation par le schéma d'HAUTMAN et al. modifié : cas d'un mélange 90 % C_3H_8 + 10 % C_2H_4

DISCUSSION

R.Monti, It

How are your conclusions affected by the initial temperature distribution due to the cooled walls of the pre-combustor chamber?

Réponse d'Auteur

Nous avons faits des mesures transversales de température. La principale difficulté vient d'une inflammation plus rapide dans les couches limites, ce qui donne très rapidement un profil de température avec des températures plus élevées près des parois, à tel point que les corrections de rayonnement sur les thermocouples sont faites en sens inverse de ce qui est habituel, car ce sont les parois qui rayonnent vers les thermocouples.

EVALUATION OF MULTI-DIMENSIONAL FLUX MODELS FOR RADIATIVE TRANSFER IN COMBUSTION CHAMBERS: A REVIEW

Assoc.Prof.Dr. Nevin Selçuk
Department of Chemical Engineering
Middle East Technical University
Ankara/Turkey

AD-P003 151

In recent years, flux methods have been widely employed as alternative, albeit intrinsically less accurate, procedures to the zone or Monte-Carlo methods in complete prediction procedures. Flux models of radiation fields take the form of partial differential equations, which can conveniently and economically be solved simultaneously with the equations representing flow and reaction. The flux models are usually tested and evaluated from the point of view of predictive accuracy by comparing their predictions with 'exact' values produced using the zone or Monte-Carlo models. In the present paper, evaluations of various multi-dimensional flux-type models, such as De Marco and Lockwood, Discrete-Ordinate, Schuster-Schwarzschild and moment, are reviewed from the points of view of both accuracy and computational economy. A six-flux model of Schuster-Schwarzschild type with angular subdivisions related to the enclosure geometry is recommended for incorporation into existing procedures for complete mathematical modelling of rectangular combustion chambers.

1. NOMENCLATURE

A,B,C	dimensionless multiplying coefficients in the equations for the six-flux model
D1 to D10	dimensionless multiplying coefficients in the generalised flux-type model equations
e_b	black-body emissive power at a point on a bounding solid surface (W m^{-2})
E_b	black-body emissive power at a point within the enclosed emitting-absorbing medium (W m^{-2})
G	total intensity of incident radiation (W m^{-2})
I	intensity of radiation in a specified direction at the general point (W m^{-2} sr^{-1})
K	volumetric absorption coefficient of the enclosed medium (m^{-1})
L	sum of intensities in vertically opposite solid angles (W m^{-2} sr^{-1})
$\bar{n}$	unit vector normal to a surface (m)
N	number of smaller solid angles into which the total solid angle of 4π sr is subdivided
q_ξ^+	half-range radiative flux density in positive ξ direction (W m^{-2})
q_ξ^-	half-range radiative flux density in negative ξ direction (W m^{-2})
q_ξ	net radiative flux density in ξ direction (W m^{-2})
$\bar{q}$	radiative flux vector (W m^{-2})
Q	source term for radiative energy (W m^{-3})
$\bar{r}$	position vector of a point (m)
S	quantity occurring in equation of radiative energy transfer (W m^{-3})
T	absolute temperature at a point in the enclosed medium (K)
x,y,z	rectangular cartesian coordinates (m)

Greek symbols

ε	total hemispherical emissivity of a surface point
σ	Stefan-Boltzmann constant
ω	magnitude of a solid angle (sr)
$\bar{\Omega}$	unit vector denoting direction in which intensity is considered (m)

Subscripts

i	denotes the ith smaller solid angle
n	in the direction of the normal to a surface
w	on the surface of a bounding wall
x,y,z	in the directions of the rectangular coordinate axes
ξ	in direction ξ = x,y or z.

Superscripts

+	in the positive direction
-	in the negative direction

2. INTRODUCTION

Rapid increases in fuel costs over the past decade had led to intensive investigations of possible methods of increasing the overall thermal efficiency of combustion chambers by modification in design and/or mode of operation. Such modifications can cause considerable changes in the temperature and heat flux distributions within the combustor. Although the new distributions can obviously be determined by extensive and expensive experimental investigation programmes, it is more economical and desirable to be able to predict the effects of modifications in design, mode of operation or method of firing by using mathematical models of the combustion chamber behaviour. Accurate temperature predictions are especially important for the prediction of pollutant emission levels since the chemical kinetics involved are extremely temperature dependent.

At the high temperatures encountered in most furnaces and combustors, thermal radiation is the predominant mechanism of heat transfer. Any procedure for the complete prediction of furnace or combustor behaviour must, therefore, utilise a realistic approximate mathematical model of the radiation field.

From the point of view of mathematical modelling, any furnace or combustor may be visualised as an enclosure containing a radiatively emitting-absorbing-and possibly scattering medium which is in motion, within which heat is being released as a result of chemical reaction, and which is exchanging thermal energy with all solid surfaces with which it is in contact.

The most accurate procedures available for mathematical modelling of radiation fields within enclosures are the zone [1,2,3] and Monte-Carlo [4,5] methods, both of which have been extensively developed and tested [3,6,7] for enclosures for which complete knowledge of the flow and concentration fields was available. Utilising this information, the radiation model was used to predict temperature and radiative flux density distributions, which were then compared with measured values.

However, these radiation models have not been used as part of a complete prediction procedure. One reason for this is that, in the complete prediction procedure, the flow, concentration and reaction fields are mathematically modelled by simultaneous partial differential equations. The equations modelling the radiation field are not differential in form, and, hence, their numerical solution in conjunction with the differential equations is neither convenient nor simple. In addition, the arithmetical labour and machine storage capacity required by these radiation models puts the complete modelling procedure utilising them beyond the capacity of many computers.

In order to overcome these disadvantages, flux methods [8,9] have been widely employed as alternative, albeit intrinsically less accurate, procedures to the zone or Monte-Carlo methods in complete prediction procedures. Flux models of radiation fields take the form of partial differential equations, which can conveniently and economically be solved simultaneously with the equations representing flow, reaction etc.

Previous multi-dimensional evaluations of the accuracy of flux models of radiation fields have taken the following form:

The flux model has been employed as part of a complete prediction procedure [8,9], and predicted temperature and radiative heat flux distributions have been compared with experimentally determined values [8,9,10,11,12]. This procedure suffers from two disadvantages: discrepancies between predicted and measured values may be partly due to errors in the experimentally determined data; even if the experimentally determined data is correct, it is impossible to decide whether discrepancies in the predicted temperature and radiative flux distributions are attributable directly to the flux model employed or to inaccuracies in the models used for the prediction of flow, reaction etc.

More recently, the above disadvantages of previous testings of flux models have been overcome by testing the flux model in isolation from the modelling of other physical processes. The tests have been carried out by using a prescribed radiative energy source term distribution, and comparing predicted temperature and radiative heat flux distributions with values predicted utilising the zone or Monte-Carlo methods [13,14,15]. However, a second factor of considerable importance which should also be taken into account in the assessment of a model is its economy of prediction in terms of computer time. A new model which produces a small percentage improvement in accuracy at the expense of a doubling of computer time may well prove to be unacceptable.

In this paper, a brief review of the flux-type models is presented and evaluations of previously proposed and tested flux models [13,15,16,17] for radiative transfer in box-shaped enclosures are reviewed from the points of view of both accuracy and computational economy.

3. EXACT EQUATIONS FOR THE RADIATION FIELD WITHIN AN ENCLOSURE

Equations for the Enclosed Medium

The basis of all flux methods for the solution of radiation problems is the equation of radiant energy transfer. For an emitting-absorbing grey medium in local thermodynamic equilibrium, and for which quasi-stationary conditions exist, this takes the form

$$\nabla.\{\bar{\Omega}I(\bar{r},\bar{\Omega})\} = -K(\bar{r})I(\bar{r},\bar{\Omega}) + \frac{K(\bar{r})}{4\pi}G(\bar{r}) + \frac{1}{4\pi}S(\bar{r}) \qquad (1)$$

where $I(\bar{r},\bar{\Omega})$ is the intensity of radiation at point $P(\bar{r})$ and in a direction defined by unit vector $\bar{\Omega}$, and $K(\bar{r})$ is the volumetric absorption coefficient of the medium. $S(\bar{r})$ is defined by the relationship

$$S(\bar{r}) = K(\bar{r})\{4E_b(\bar{r}) - G(\bar{r})\} \qquad (2)$$

where $E_b(\bar{r})$ is the black-body emissive power of the medium, which is related to its absolute temperature $T(\bar{r})$ by the expression

$$E_b(\bar{r}) = \sigma\{T(\bar{r})\}^4 \qquad (3)$$

where σ is the Stefan-Botlzmann constant. $G(\bar{r})$ is the total intensity of incident radiation at point P, which is obtained by angular integration of intensity over the total solid angle of 4π steradians surrounding the point

$$G(\bar{r}) = \int_{4\pi} I(\bar{r},\bar{\Omega})d\omega \qquad (4)$$

where $d\omega$ is a small element of solid angle.

Integration of equation (1) over 4π steradians produces an equation representing a balance on the radiant energy travelling in all directions through the point

$$\nabla.\bar{q}(\bar{r}) = S(\bar{r}) \tag{5}$$

in which $\bar{q}(\bar{r})$ is the radiative flux vector, which is defined by the integral

$$\bar{q}(\bar{r}) = \int_{4\pi} \bar{\Omega} I(\bar{r},\bar{\Omega}) d\omega \tag{6}$$

Coupling of radiative energy transfer to the transfers by other mechanisms occurs in the enthalpy balance, which can be expressed in the form

$$\nabla.\bar{q}(\bar{r}) = Q(\bar{r}) \tag{7}$$

where $Q(\bar{r})$ is the source term for radiative energy, which accounts for the transfers of energy by conduction, convection and turbulent diffusion, and the liberation of energy by chemical reaction.

Elimination of $\nabla.\bar{q}$ between Eqs. (5) and (7) establishes the identity of S and Q.

$$S(\bar{r}) = Q(\bar{r}) \tag{8}$$

The form of $S(\bar{r})$ to be used for calculation purposes depends upon the initial information available for a particular enclosure problem; if the distribution of $E_b(\bar{r})$ is specified in advance, then $S(\bar{r})$ is expressed in terms of $E_b(\bar{r})$ as in Eq. (2); alternatively, Eq. (8) is used if the distribution of $Q(\bar{r})$ is prespecified.

The relationship between the radiative energy source term and the black-body emissive power can be found by equating the right-hand sides of Eqs. (2) and (8)

$$Q(\bar{r}) = K(\bar{r})\{4E_b(\bar{r}) - G(\bar{r})\} \tag{9}$$

Further exact equations for the radiation field may be derived by subdividing the total solid angle surrounding the general point into N smaller solid angles Ω_i. If equation (1) is integrated over each smaller solid angle in turn, the following N additional exact equations for the radiation field are obtained.

$$\int_{\Omega_i} \{\nabla.(\bar{\Omega} I)\} d\omega = -K \int_{\Omega_i} I d\omega + \frac{\omega_i}{4\pi}(KG + S), \quad i = 1 \text{ to } N \tag{10}$$

where ω_i is the magnitude of solid angle Ω_i.

Radiation Balances at Bounding Solid Surfaces

Complete modelling of the radiant energy exchanges within an enclosure requires the use of radiant energy balances at all interior bounding surfaces in addition to the balances within the enclosed medium. If the surfaces are assumed to be grey diffuse emitters and reflectors of radiation for which the absorptivity equals the emissivity, the radiant energy balance for surface point $U(r_w)$ may be written in the form

$$q_n^+(\bar{r}_w) = \varepsilon(\bar{r}_w) e_b(\bar{r}_w) + \{1-\varepsilon(\bar{r}_w)\} q_n^-(\bar{r}_w) \tag{11}$$

where ε is the emissivity and e_b the black-body emissive power of the wall point, and q_n^+ and q_n^- are the forward and backward half-range radiative flux densities in the direction of the unit normal vector $\bar{n}$ from the surface point into the enclosure. q_n^+ and q_n^- are defined by the angular integrals

$$q_n^+(\bar{r}_w) = \int_{\bar{n}.\Omega>0} \bar{n}.\bar{\Omega} I(\bar{r}_w,\bar{\Omega}) d\omega \tag{12}$$

$$q_n^-(\bar{r}_w) = -\int_{\bar{n}.\Omega<0} \bar{n}.\bar{\Omega} I(\bar{r}_w,\bar{\Omega}) d\omega \tag{13}$$

The net flux density of radiation in the direction of $\bar{n}|q_n(\bar{r}_w)|$ is given by the difference of the half-range values

$$q_n(\bar{r}_w) = q_n^+(\bar{r}_w) - q_n^-(\bar{r}_w) \tag{14}$$

4. FLUX MODELS FOR THE RADIATION FIELD WITHIN A COMBUSTION CHAMBER

Exact modelling of a radiation field would involve prediction of numerical values of the intensity of radiation in every direction at each point within the medium and on the interior bounding walls, from which exact values of radiation variables could be calculated.

The aim of all flux-type models of radiation fields is to reduce the arithmetical effort involved in producing a solution by predicting only a finite number of the potentially infinite set of unknown intensity and radiative flux density values. The smaller the number of values in the finite set, the more approximate is the mathematical model of the actual radiation field. The final choice of the number of values in the finite set is usually a compromise between accuracy and computing effort.

Flux models are based on the use of some simplifying assumption for the angular variation of intensity at any point. The mathematical model of the radiation field at the point then takes the form of a set of simultaneous partial differential equations with respect to position in terms of the unknown parameters in the approximate angular representation of intensity variation.

A number of different flux-type models have been developed for approximate mathematical modelling of radiation fields in enclosures. These can be broadly classified as shown in Figure 1.

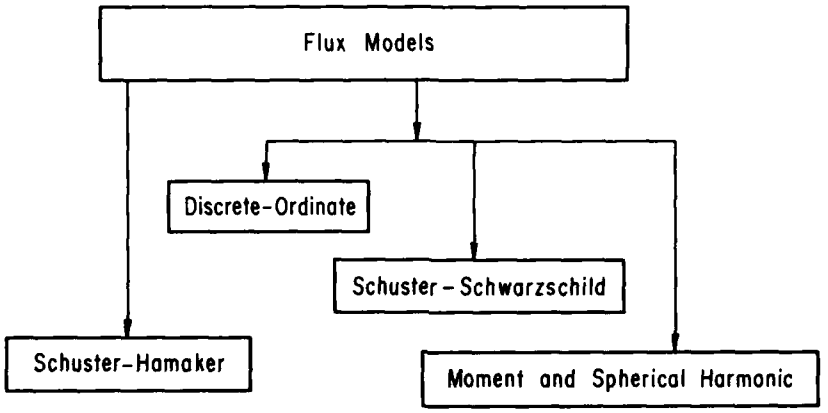


Figure 1. Classification of flux models.

Schuster-Hamaker Type Models

Models of this type utilise the simplest and least accurate representation of the intensity variation; plane parallel radiation is assumed in each dimension in which variation of the radiation parameters occurs. Two differential equations are produced from first principles for each dimension by carrying out radiative energy balances for the forward and backward directions.

A four-flux model of Schuster-Hamaker type for axi-symmetrical radiation field has been proposed and employed by Gosman and Lockwood [10] to determine the radiative behaviour of a large-scale experimental furnace. More recently, Patankar and Spalding [11] have used a six-flux model of the same type as a sub-model for radiation field in the complete mathematical modelling of a gas turbine combustion chamber. Later on the results of the complete prediction procedure have been tested by comparison with experimental data taken on Ijmuiden furnace [12].

Schuster-Schwarzschild Type Models

The basis of these models is to subdivide the total solid angle surrounding a point into smaller solid angles in each of which intensity is assumed to be uniform. Discontinuous changes in intensity, therefore, occur in passing from one smaller solid angle to any adjacent smaller solid angle. Integration of the equation of radiant energy transfer for each smaller solid angle, in turn, produces a group of partial differential equations in the unknown intensities.

Alternative four-flux models of Schuster-Schwarzschild type for axi-symmetrical radiation fields have been proposed and tested by various research workers [8,9,18]. A six-flux model of the same type for three-dimensional radiation field has been derived and tested by Siddall and Selçuk [15].

Discrete-Ordinate Models

Discrete-Ordinate model utilises the assumption that intensity varies in a continuous but unspecified

manner with angular direction at any point. The total solid angle surrounding the point is then subdivided into smaller solid angles in each of which a direction for the intensity is specified. Application of equation of radiant energy transfer into each direction produces differential equations in terms of the unknown intensities in the specified directions. Any angular integral of the intensity at a point may be found by treating the subdivision scheme described as a quadrature scheme.

A six-term Discrete-Ordinate model for three-dimensional radiation field has been derived and tested by Selçuk and Siddall [17].

Moment and Spherical Harmonic Models

With these models the intensity is assumed to vary in a specified continuous manner with angular direction. In the moment model the intensity in any direction is expressed as a polynomial series in the direction cosines of the same direction with respect to the coordinate axes. The spherical harmonic model, which is a particular form of the more general polynomial moment model, is based on expanding the intensity in a series of spherical harmonics of the polar and azimuthal angular coordinates of the direction. In both models, first order differential equations-equal in number to the number of terms in the series-in the unknown multiplying coefficients of the terms in series are produced by multiplying the equation of radiative transfer by each term in the expression of intensity in turn and integrating over 4π steradians.

A moment model for radiative transfer in box-shaped furnaces has been derived [16] and tested against Monte-Carlo predictions [15]. Chou and Tien [19] have applied the moment model to concentric spheres and cylinders and evaluated its accuracy by comparing its predictions with the results of the Monte-Carlo method.

The accuracy of spherical harmonic model for axi-symmetrical radiation fields have been tested by various researchers [19,20,21] and found to produce more satisfactory results in comparison with Schuster-Hamaker type models [21].

4. FLUX-TYPE MODELS TESTED

The six-flux models which have been compared are:

a. A six-term model derived by De Marco and Lockwood [13], using a combination of the Schuster-Schwarzschild and Discrete Ordinate methods-Model 1.
b. A six-term moment model derived by Selçuk and Siddall [16]-Model 2.
c. A six-term Discrete-Ordinate model derived by Selçuk and Siddall [17]-Model 3.
d. A six-flux model of Schuster-Schwarzschild type derived by Siddall and Selçuk [15], utilising six equal subdivisions of the total solid angle surrounding any point within the enclosures-Model 4.
e. A six-flux model of Schuster-Schwarzschild type derived by Siddall and Selçuk [15], utilising subdivisions of the total solid angle based upon the geometry of the enclosure under consideration-Model 5.

The equations representing the above-mentioned flux-type models can be expressed in the following common forms [15,17]:

The Flux Equations

$$(\partial^2 L_\xi/\partial\xi^2) = K^2(D1)_\xi \left\{(D2)_\xi L_\xi - (D3)_\xi L_{next\,\xi} - (D4)_\xi L_{remaining\,\xi} - \frac{S}{2K\pi}\right\} \qquad \xi = x,y,z \qquad (15)$$

The Boundary Equations

$$(\partial L_\xi/\partial\xi) = \pm \frac{K\epsilon}{(2-\epsilon)} (D5)_\xi \left\{(D6)_\xi L_\xi + (D7)_\xi L_{next\,\xi} + (D8)_\xi L_{remaining\,\xi} - \frac{2e_b}{\pi}\right\} \qquad \xi = x,y,z \qquad (16)$$

where

$$L_\xi = I_\xi^+ + I_\xi^- \qquad \xi = x,y,z \qquad (17)$$

In Eqs. (15) and (16), the sequence to be followed in determining "next ξ" and "remaining ξ" is $x \to y$, $y \to z$, $z \to x$, so that, for example, in the flux equation for the y direction, $\xi = y$, "next ξ" = z, and "remaining ξ" = x. L denotes the sum of intensities in vertically opposite solid angles.

Components of the Radiative Flux Density Vector

$$q_\xi = -\frac{\pi}{K} (D9)_\xi \frac{\partial L_\xi}{\partial\xi} \qquad \xi = x,y,z \qquad (18)$$

where q_ξ is the net radiative flux density in ξ direction.

The Total Incident Flux Density

$$G = \sum_{\xi=x,y,z} (D10)_\xi L_\xi \qquad (19)$$

The values of the coefficients $(D1)_\xi$, $(D2)_\xi$, ... , $(D10)_\xi$ for the models considered are given in Table 1.

Table 1. Values of coefficients for the flux-type models tested.

Coefficient	Model 1 (De Marco and Lockwood)	Model 2 (Moment)	Model 3 (Discrete-Ordinate)	Model 4 and 5 15 (Schuster-Schwarzschild)
$(D1)_\xi$	1	1	1	$(\ldots_\xi/A_\xi)^2$
$(D2)_\xi$	8/3	5/3	1-1/2π	$1-\omega_\xi/2\pi$
$(D3)_\xi$	2/3	1/6	1/2π	$\omega_{next\,\xi}/2\pi$
$(D4)_\xi$	2/3	1/6	1/2π	$\omega_{remaining\,\xi}/2\pi$
$(D5)_\xi$	3/2	3/2	3/2	$\pi\omega_\xi/A_\xi^2$
$(D6)_\xi$	1	3/4	2/3	A_ξ/π
$(D7)_\xi$	0	1/8	1/6	$2\,B_\xi/\pi$
$(D8)_\xi$	0	1/8	1/6	$2\,C_\xi/\pi$
$(D9)_\xi$	2/3	2/3	2/3	$A_\xi^2/\pi\omega_\xi$
$(D10)_\xi$	2/3	2/3	2/3	ω_ξ/π

5. TEST PROBLEMS

The flux-type models considered have previously been tested by making predictions for two idealised enclosure problems for which accurate results have been produced previously by Jenner, and reported by De Marco and Lockwood [13]. Both enclosure problems are based on an assumed uniform distribution of the radiative energy source term (Q) throughout the enclosed gaseous medium. This use of a pre-specified distribution of Q (although far removed from the highly non-uniform distribution which would be expected to occur in a furnace or heater) effectively de-couples the modelling of radiative energy transfer from other physical phenomena and, thereby, removes the necessity for simultaneous modelling of flow, reaction and other mechanisms of heat transfer, which is involved in any complete prediction of operating enclosure behaviour.

Enclosure A is cubic in shape, of side length 10 m, and filled with a grey gas of uniform absorption coefficient 0.2 m^{-1}, within which the radiative energy source term is uniform (i.e. Q=20kW m^{-3} at each point within the gas). Two of the walls are radiatively adiabatic, and the other four have specified uniform temperatures and emissivities, as shown in Figure 2. Jenner's results for the average radiative flux densities from the enclosed medium to each of the sixteen smaller squares on the shaded face have been used as the basis of comparison for the flux-type model predictions for the cube.

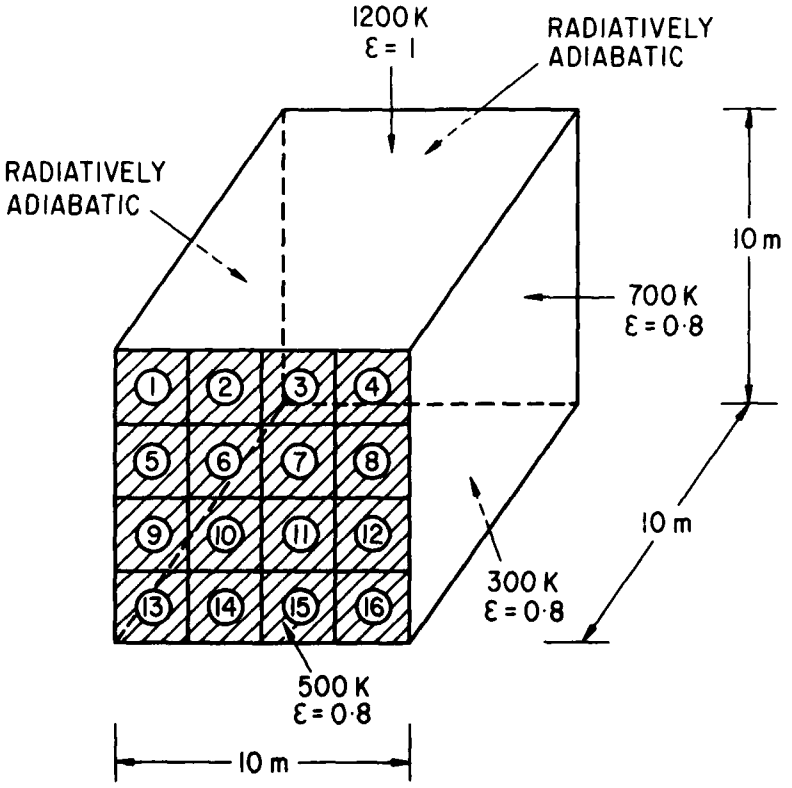


Figure 2. Cubic enclosure A.

Enclosure B is a box of size 1m x 1m x 4m, containing grey gas of uniform absorption coefficient $2m^{-1}$ within which the radiative energy source term is zero at all points ($Q = 0$). All six bounding walls are radiatively black and have specified uniform temperatures, as illustrated in Figure 3. As with enclosure A, Jenner's results for the sixteen average flux densities to the smaller squares on the shaded face provide the basis for testing the flux-type model predictions.

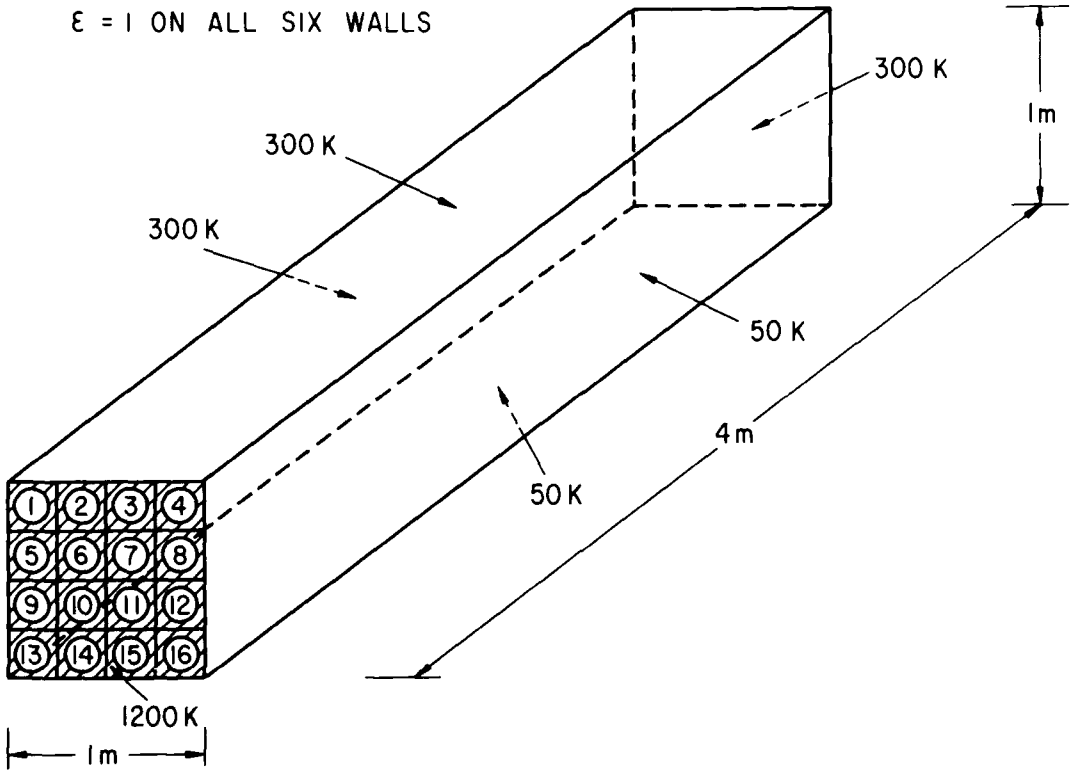


Figure 3. Rectangular parallelepiped shaped enclosure B.

7. NUMERICAL SOLUTION OF THE FLUX-TYPE MODEL EQUATIONS

The common equations for the flux-type models (Eqs. (15) and (16)) have been solved for both enclosure problems by using the finite-difference technique for replacement of the differential terms occurring on the left-hand side [15,17]. A grid of 5 x 5 x 5 points has been employed for enclosure A, and a grid of 5 x 5 x 17 points for enclosure B. The resulting sets of 3 x 5 x 5 x 5 and 3 x 5 x 5 x 17 simultaneous algebraic equations in the unknown values of $L_\xi(\xi = x,y \text{ and } z)$ at the grid points have then been solved by making initial guesses for the unknown values, and iterating to produce new values. The iterative procedure employed was one developed by Peaceman and Rachford [22] for numerical solution of the algebraic equations resulting from finite difference representation of the differential equation for steady-state conduction in a solid. With this procedure, convergence of iteration has been assumed to be complete when each of the values of L_ξ at every grid point differs by less than a prespecified percentage from its value in the previous step of iteration.

8. EVALUATION OF THE FLUX-TYPE MODEL PREDICTIONS

Average radiative flux densities to the sixteen small squares on the shaded face of enclosure A have been produced using Models 1, 2, 3 and 4 [15,17]. The percentage errors in the predicted average flux densities are shown in Table 2.

Predictions for enclosure B have also been produced using Models 1, 2, 3, 4 and 5 [15,17]. The percentage errors in the average flux densities predicted using the five models are shown in Table 3.

A condensed comparison of the flux-type model predictions is contained in Table 5. Four values are given for each model; the maximum point percentage error and the average absolute percentage error both of which give measures of the accuracy of prediction of point flux densities; the average percentage accuracy, which reflects the accuracy of prediction of the total net radiative flux to the surface; the number of iterations necessary to produce convergence of the iterated solution to within 0.01% of the values in the previous iteration at all grid points, which measures computing time.

Table 2. Monte-Carlo based flux density predictions for enclosure A, and errors in flux-type predictions.

Square		1	2	3	4	5	6	7	8
$qx10^{-4}$ W/m^2		8.68	9.51	8.77	6.72	7.98	8.06	7.70	6.15
% errors	Model 1	+ 8.93	- 3.12	- 1.19	+14.18	+10.04	+ 5.67	+ 3.04	+12.33
	Model 2	+10.15	- 1.92	+ 0.43	+17.37	+10.78	+ 6.59	+ 4.48	+15.45
	Model 3	-25.33	-23.54	- 5.71	-14.36	-24.07	-22.98	-15.24	-17.49
	Model 4	+ 8.26	- 3.58	- 1.14	+16.06	+ 9.14	+ 5.06	+ 3.16	+14.49

Square		9	10	11	12	13	14	15	16
$qx10^{-4}$ W/m^2		7.29	7.52	6.99	5.56	5.14	5.38	5.08	4.55
errors	Model 1	+ 6.79	+ 0.25	+ 0.16	+ 9.10	+23.09	+13.98	+12.30	+ 9.12
	Model 2	+ 7.61	+ 1.25	+ 1.73	+12.37	+25.25	+16.25	+15.26	+13.60
	Model 3	+ 0.26	-14.11	- 3.02	+12.37	+16.58	+ 6.38	+15.82	+24.74
	Model 4	+ 6.01	- 0.17	+ 0.54	+11.64	+22.74	+14.14	+13.68	+13.14

q= Average flux density to the square from the medium, predicted using the Monte-Carlo method.

Percentage error= (1-flux model value/Monte-Carlo value)x100

Table 3. Monte-Carlo based flux density predictions for enclosure B, and errors in flux-type model predictions.

Square		1	2	3	4	5	6	7	8
$-qx10^{-4}$ W/m^2		10.0	9.39	9.50	10.0	9.47	8.81	8.67	9.57
% errors	Model 1	+ 4.85	+ 7.35	+ 6.15	+ 4.99	+ 6.44	+ 9.00	+10.82	+ 5.50
	Model 2	+10.11	+13.00	+11.74	+10.25	+12.05	+15.13	+17.05	+11.03
	Model 3	+ 2.20	+ 6.56	+ 5.37	+ 2.31	+ 5.66	+10.85	+12.68	+ 4.68
	Model 4	+ 5.63	+ 8.42	+ 7.21	+ 5.76	+ 7.51	+10.45	+12.30	+ 6.53
	Model 5	- 1.61	- 0.46	- 1.57	- 1.49	- 1.30	- 0.68	+ 0.97	- 2.18

Square		9	10	11	12	13	14	15	16
$-qx10^{-4}$ W/m^2		9.51	8.65	8.72	9.27	10.1	9.52	9.51	10.0
% errors	Model 1	+ 6.04	+11.08	+10.24	+ 8.95	+ 3.95	+ 6.05	+ 6.20	+ 5.13
	Model 2	+11.62	+17.32	+16.43	+14.67	+ 9.16	+11.62	+11.78	+10.39
	Model 3	+ 5.26	+12.94	+12.08	+ 8.11	+ 1.30	+ 5.23	+ 5.38	+ 2.42
	Model 4	+ 7.10	+12.55	+11.70	+10.02	+ 4.71	+ 7.09	+ 7.25	+ 5.88
	Model 5	- 1.67	+ 1.20	+ 0.44	+ 1.02	- 2.47	- 1.67	- 1.52	- 1.36

q= Average flux density to the square from the medium, predicted using the Monte-Carlo method.

Percentage error= (1-flux model value/Monte-Carlo value)x100

Table 4. Comparison of flux-type model prediction of surface fluxes.

Problem	Model	Maximum % error	Average absolute % error	Average % error	Number of iterations
Enclosure A: Cube	1	+ 23.09	8.33	+ 6.83	28
	2	+ 25.25	10.03	+ 8.65	19
	3	- 25.33	15.12	- 5.61	10
	4	+ 22.74	8.93	+ 7.17	11
Enclosure B: Cube	1	+ 11.08	+ 6.94	+ 6.94	26
	2	+ 17.32	+12.59	+12.59	17
	3	+ 12.94	+ 6.25	+ 6.25	9
	4	+ 12.55	+ 8.01	+ 8.01	14
	5	- 2.47	+ 1.35	- 0.94	8

As can be seen from Table 4, the six-term Discrete-Ordinate model (Model 3) and the six-flux model with equal subdivisions (Model 4) economically produce good results for both enclosures, and is, overall, better than Models 1 and 2. The additional advantage of using a subdivision based on the geometry of the enclosure is demonstrated by comparison of the results obtained for the box-shaped enclosure. Model 5 produces a substantial improvement in both accuracy and economy.

8. CONCLUSIONS

For the prediction of three-dimensional radiative energy transfer in rectangular furnaces, the six-flux model of Schuster-Schwarzschild type utilising subdivisions of the total solid angle based upon the geometry of the enclosure has been shown, by comparison with other flux-type models and Monte-Carlo results, to produce acceptably accurate predictions and savings in computational expense. It should, therefore, prove to be a useful component for incorporation into existing procedures for complete mathematical modelling of combustion chambers.

9. REFERENCES

1. Hottel,H.C. and Cohen,E.S., "Radiant heat exchange in a gas filled enclosure : allowance for non-uniformity of gas temperature", A.I.Ch.E. Journal, 4, 1, 1958, 3-14.

2. Hottel,H.C. and Sarofim,A.F., "The effects of gas flow patterns on radiative transfer in cylindrical furnaces", Int.J. Heat and Mass Transfer, 8 , 1965, 1153-1169.

3. Johnson,T.R. and Beer,J.M., "Radiative heat transfer in furnaces: further development of the zone method of analysis", 14th Symposium (Int.) on Combustion, The Combustion Institute, Pittsburgh, Pa., 1973, 639-649.

4. Steward,F.R. and Cannon,P., "The calculation of radiative heat flux in a cylindrical furnace using the Monte-Carlo methods", Int.J. Heat and Mass Transfer, 14 , 1971, 245-262.

5. Steward,F.R., Osuwan,S. and Picot,J.J.C., "Heat transfer measurements in a cylindrical test furnace", 14th Symposium (Int.) on Combustion, 1973 , 651-660.

6. Steward,F.R. and Osuwan,S., "A mathematical simulation of radiative heat transfer in a cylindrical test furnace", Can.J.Chem.Eng., 50, 1972, 450-455.

7. Arscott,J.A., Gibb,J. and Jenner,R., "The application of N-E diffusion theory and Monte-Carlo methods to predict the heat transfer performance of a 500 MW power station boiler from isothermal flow data", 1st European Combustion Symposium, 1973 , 674-679.

8. Lowes,T.M., Bartelds,H., Heap M.P., Michelfelder, S. and Pai,B.R , "Prediction of radiant heat flux distribution", I.F.R.F., Doc.No. G 02/a/26, 1973.

9. Richter,W. and Quack,R., "A mathematical model of a low volatile pulverised fuel flame", Heat Transfer in Flames (editors: Afgan,N.H. and Beer,J.M.) Scripta Book Comp., Washington D.C., 1974, 95-110.

10. Gosman,A.D. and Lockwood,F.C., "Incorporation of a flux model for radiation into a finite difference procedure for furnace calculations", 14th Symposium (Int.) on Combustion, 1973 , 661-671.

11. Patankar,S.V. and Spalding,D.B., "Simultaneous predictions of flow pattern and radiation for three-dimensional flames", Heat Transfer in Flames (editors: Afgan, N.H. and Beer,J.M.), Scripta Book Comp., Washington D.C., 1974, 73-94.

12. Pai,B.R., Michelfelder,S. and Spalding,D.B., "Prediction of furnace heat transfer with a three-dimensional mathematical model", Int.J.Heat and Mass Transfer, 21 , 1978, 571-580.

13. De Marco, A.G. and Lockwood, F.C., "A new flux model for the calculation of radiation in furnaces", Italian Flame Day, La Rivista dei Combustibili, 29 , 5-6, 1975, 184-196.

14. Lockwood,F.C., and Shah,N.G., "An improved flux model for the calculation of radiation heat transfer in combustion chambers", ASME Paper No. 76-HT-55, 1976.

15. Siddall,R.G. and Selçuk,N., "Evaluation of a new six-flux model for radiative transfer in rectangular enclosures", Trans.I.Chem.E., 57 , 1979, 163-169.

16. Selçuk,N. and Siddall R.G., "A new moment model for radiatively emitting-absorbing-scattering media in rectangular furnaces and combustors", V.Int. Symposium on Combustion processes, Krakow, Poland, 1977.

17. Selçuk,N. and Siddall,R.G., "Prediction of multi-dimensional radiative heat transfer by a new six-flux model in industrial furnaces", Proceedings of 2.National Heat Science and Technology Conference, 1980, 456-469.

18. Siddall,R.G. and Selçuk,N., "Two-flux modelling of two-dimensional radiative transfer in axi-symmetrical furnaces", J.Inst. Fuel, 49 , 1976, 10-20.

19. Selçuk,N. and Siddall,R.G., "Two-flux spherical harmonic modelling of two-dimensional radiative transfer in furnaces", Int.J. Heat and Mass Transfer, 19, 1976, 313-321.

20. Higenyi,J. and Bayazıtoğlu,Y., "Differential approximation of radiative heat transfer in a gray medium" J.Heat Transfer, 102, 1980, 719-723.

21. Whitacre,G.R. and McCann,R.A., "Comparison of methods for the prediction of radiant heat flux distribution and temperature", ASME Paper No. 75-HT-9, 1975.

22. Peaceman,D.W. and Rachford,H.H., "The numerical solution of parabolic and elliptic differential equations", J.Soc.Indust Appl.Math., 3, 1955, 1-28.

DISCUSSION

P.Ramette, Fr

Pour le modème de flux de Schuster-Schwarzschild avec des divisions d'angle solide inégales, quelle est la méthode pour déterminer la dimension des différents angles solides?

Author's Reply

Subdivision of the total solid angle surrounding a point depends on the position of the point within the enclosure. For a particular point under consideration, the subdivision is achieved by connecting the point to the corners of the enclosure.

D.Grouset, Fr

Le modèle n° 1 est celui de Lockwood et Marco.

Il considère une distribution polynominale du flux en chaque point et découpe l'espace en six angles égaux.

Avez vous essayé la formulation de Lockwood et Shah qui utilise la même distribution polynominale mais découpe l'espace en six angles solides inégaux. Lockwood et Shah annoncent de meilleurs résultats dans le cas de distributions anisotropes.

Author's Reply

No, I have not tested the accuracy of the flux-type model proposed by Lockwood and Shah.

A Droplet Evaporation Rate Controlled Combustion Model

A.D. Bayka, B.Sc., M.Sc., Ph.D.
Assistant Professor
Mechanical Engineering Department
Middle East Technical University
Ankara - Turkey

AD-P003 152

SUMMARY

A computational model for predicting the rate of heat released during combustion of a fuel injected into a combustion chamber is proposed. In the mathematical model the burning rate was based on the ignition of combustible mixture elements formed, each having different ignition delays, depending on the state parameters they were subjected to in the combustion chamber. The rate of heat release was related to the rate of evaporation of the injected fuel. The rate of evaporation of the fuel was related to the size distribution of the fuel droplets which was divided into several groups with different diameters. The diameter and temperature histories of the droplets in each group were simultaneously obtained depending on the instantaneous droplet velocity, the rate of injection, type of nozzle, fuel and heat transferred to the evaporating droplets. The total evaporation rate of the fuel at any instant was the summation of the evaporation rates of all the droplets present in the cylinder at any time.

LIST OF SYMBOLS

A_p	Projected area of droplet (m^2)
a	Radius of droplet (m)
C_D	Drag coefficient
c_p	Specific heat at constant pressure ($kJ.kg^{-1}.K^{-1}$)
D	Diameter (m)
D_s	Sauter mean diameter (m)
D_f	Diffusion coefficient
E_v	Total rate of evaporation ($kg.s^{-1}$)
F	Drag force (N)
h_{fg}	Latent heat of vaporization ($kJ.kg^{-1}$)
k	Thermal conductivity ($kW.m^{-1}.K^{-1}$)
M	Mass (kg)
m	Mass of a single droplet (kg)
N	Number of droplets
Nu	Nusselt number
Q	Heat transferred (kJ)
Q_v	Amount of fuel delivery (mm^3)
q	Heat flux ($kW.m^{-2}$)
P	Pressure (kPa)
Pr	Prandtl number
Re	Reynolds number
r	Radial distance (m)
Sc	Schmidt number
Sh	Sherwood number
T	Temperature (K)
t	Time (s)
V	Velocity ($m.s^{-1}$)
v	Volume of single droplet (m^3)
W	Weber number
X	Mole fraction
y	Weight fraction
α	Thermal diffusivity ($m^2.s^{-1}$)
γ	Stefan-Boltzmann constant ($kW.m^{-2}.K^{-4}$)
δ_f	Boundary layer thickness (m)
δ_h	Thermal boundary layer thickness (m)
ϵ	Emissivity
λ	Surface Tension ($N.m^{-1}$)

μ Dynamic viscosity ($kg.m^{-1}.s^{-1}$)

ρ Density ($kg.m^{-3}$)

σ,τ Ignition lag (ms)

ϕ Equivalence ratio

Subscripts

i i th specie
g Gas
f Droplet
inj Injection
m Mean
n Nozzle
T Total
o Initial
c Cylinder
cr Critical
s Droplet surface
h Convective
r Radiative
ref Reference
mix Mixture

INTRODUCTION

A variety of combustion engines operate on the principle of mixing the fuel and oxygen in the combustion chamber. The fuel admitted in as a liquid has to vaporize and form a combustible mixture. The proposed combustion model is for fuel injected into high pressure hot air.

The rate of formation of the combustible mixture will affect the rate of heat release during combustion. In the case of intermittent operation the combustion during fuel injection may be examined in two parts. Initially some of the fuel injected into high pressure hot air will evaporate and form a combustible mixture during the initial ignition delay period. Therefore the combustion at the end of the delay period will be for a premixed fuel/air mixture. At this instant the yet unevaporated fuel at the core of the spray and the further injected fuel will form a highly rich mixture. A diffusive combustion will continue as more air is entrained into this mixture.

The ignition delay may be divided into physical and chemical ignition delays. After the start of injection, pockets of combustible mixture having approximately stoichiometric air/fuel ratios will be formed around the boundaries of the spray depending on the evaporation of fuel droplets and mixing with air. An element of combustible mixture formed at any instant at a sufficiently high temperature and pressure will be submitted to pre-flame reactions. The rate of these reactions will depend on the chemical composition, temperature, pressure and air/fuel ratio of the mixture. It has been experimentally observed that the rate of these reactions increase to very high values after a certain time interval which is termed as the chemical ignition delay period. It is assumed that the concentration of some of the partial products of the pre-flame reactions which act as chain carriers build up to a critical value after which the rate of the reaction suddenly increases.

After ignition as the temperature and pressure of the mixture increases the rate of preflame reactions will increase and thus the time required for the chain carriers to build up to a critical value will progressively decrease and this will lead to an explosive type of combustion.

OUTLINE OF THE MODEL

In this model it was assumed that the liquid fuel was discharged at a high velocity into the combustion chamber in the form of ligaments which broke up and contracted into droplets. The time required for the formation of the droplets was neglected. Therefore, it was assumed that the fuel was introduced in the form of a group of droplets of variable size.

The relative velocities of the droplets with respect to the gas in the chamber varied depending on their size, the injection rate of fuel and the density of the surrounding gas.

It was assumed that the droplets did not interact physically or thermally with each other during their travel. The droplets evaporated at varying rates of evaporation depending on their size, relative velocity and the thermodynamic state of the gaseous medium.

Droplets within predefined size ranges were assumed to be all at the mean diameter of the specified size range. Therefore the rate of evaporation of all the droplets was calculated by considering only the droplets having the mean diameters at the specified size ranges.

The evaporation process had an important effect on spray combustion and in the simulation model the knowledge of evaporation rate was used in predicting the burning rate. The rate at which a combustible mixture was formed was assumed to be determined by the rate of evaporation.

The chemical ignition delay of an element of combustible mixture was defined as the time from its formation until its ignition. Its magnitude depended on the temperature, pressure, chemical composition and the air/fuel ratio of the combustible mixture. Therefore the ignition delays of the combustible mixture elements formed at different instants would be different since they would all have different histories of temperature, pressure and oxygen concentration. Following the initial ignition of the combustible mixture

μ Dynamic viscosity ($kg.m^{-1}.s^{-1}$)

ρ Density ($kg.m^{-3}$)

σ,τ Ignition lag (ms)

ϕ Equivalence ratio

Subscripts

i i th specie
g Gas
f Droplet
inj Injection
m Mean
n Nozzle
T Total
o Initial
c Cylinder
cr Critical
s Droplet surface
h Convective
r Radiative
ref Reference
mix Mixture

INTRODUCTION

A variety of combustion engines operate on the principle of mixing the fuel and oxygen in the combustion chamber. The fuel admitted in as a liquid has to vaporize and form a combustible mixture. The proposed combustion model is for fuel injected into high pressure hot air.

The rate of formation of the combustible mixture will affect the rate of heat release during combustion. In the case of intermittent operation the combustion during fuel injection may be examined in two parts. Initially some of the fuel injected into high pressure hot air will evaporate and form a combustible mixture during the initial ignition delay period. Therefore the combustion at the end of the delay period will be for a premixed fuel/air mixture. At this instant the yet unevaporated fuel at the core of the spray and the further injected fuel will form a highly rich mixture. A diffusive combustion will continue as more air is entrained into this mixture.

The ignition delay may be divided into physical and chemical ignition delays. After the start of injection, pockets of combustible mixture having approximately stoichiometric air/fuel ratios will be formed around the boundaries of the spray depending on the evaporation of fuel droplets and mixing with air. An element of combustible mixture formed at any instant at a sufficiently high temperature and pressure will be submitted to pre-flame reactions. The rate of these reactions will depend on the chemical composition, temperature, pressure and air/fuel ratio of the mixture. It has been experimentally observed that the rate of these reactions increase to very high values after a certain time interval which is termed as the chemical ignition delay period. It is assumed that the concentration of some of the partial products of the pre-flame reactions which act as chain carriers build up to a critical value after which the rate of the reaction suddenly increases.

After ignition as the temperature and pressure of the mixture increases the rate of preflame reactions will increase and thus the time required for the chain carriers to build up to a critical value will progressively decrease and this will lead to an explosive type of combustion.

OUTLINE OF THE MODEL

In this model it was assumed that the liquid fuel was discharged at a high velocity into the combustion chamber in the form of ligaments which broke up and contracted into droplets. The time required for the formation of the droplets was neglected. Therefore, it was assumed that the fuel was introduced in the form of a group of droplets of variable size.

The relative velocities of the droplets with respect to the gas in the chamber varied depending on their size, the injection rate of fuel and the density of the surrounding gas.

It was assumed that the droplets did not interact physically or thermally with each other during their travel. The droplets evaporated at varying rates of evaporation depending on their size, relative velocity and the thermodynamic state of the gaseous medium.

Droplets within predefined size ranges were assumed to be all at the mean diameter of the specified size range. Therefore the rate of evaporation of all the droplets was calculated by considering only the droplets having the mean diameters at the specified size ranges.

The evaporation process had an important effect on spray combustion and in the simulation model the knowledge of evaporation rate was used in predicting the burning rate. The rate at which a combustible mixture was formed was assumed to be determined by the rate of evaporation.

The chemical ignition delay of an element of combustible mixture was defined as the time from its formation until its ignition. Its magnitude depended on the temperature, pressure, chemical composition and the air/fuel ratio of the combustible mixture. Therefore the ignition delays of the combustible mixture elements formed at different instants would be different since they would all have different histories of temperature, pressure and oxygen concentration. Following the initial ignition of the combustible mixture

elements as the temperature and pressure increased the ignition delays of successively formed combustible mixture elements would progressively decrease resulting in a high rate of heat release imposing an explosive nature on the early stages of combustion. Therefore the rate of heat release during this stage would depend on the rate of change of the time difference between the formation and ignition of the successively formed combustible elements. This difference would decrease to a negligible value as the premixed air/fuel mixture burned such that the rate of heat release during the later stages of combustion, of the yet unevaporated fuel at the core of the spray and the further injected fuel, would depend on the rate of formation of the combustible mixture elements.

FORMULATION OF THE MODEL

The formulation of the model has been based on previous theoretical and experimental work done by various investigators on droplet evaporation, spray formation and simulation of the thermodynamic cycle of compression ignition engines. Therefore this study may be viewed as an analysis and synthesis of various independant work leading to a droplet evaporation rate controlled combustion model.

GROUPING OF THE DROPLETS IN SIZE RANGES

The rate of evaporation of the fuel was derived from the rate of evaporation of single droplets. The spray of injected fuel is a grouping of droplets having very many different diameters. In order to simplify the analysis of such a spray the droplets were classified into several size ranges. The analysis was then carried on for only a number of droplets equal to the number of size ranges. The sauter mean diameter was selected as a reference since the surface area and volume of a droplet affected its evaporation.

The sauter mean diameter is defined as the diameter of a droplet that has the same surface to volume ratio as that of the total spray.

$$D_s = \frac{\sum_{i=1}^{N_T} N_i D_i^3}{\sum_{i=1}^{N_T} N_i D_i^2} \tag{1}$$

The empirical relation used for finding D_s depending on the effective injection pressure, gas density and quantity of fuel delivery was [1]:

$$D_s = A(\Delta P)^{-0.135} (\rho_c)^{0.121} (Q_v)^{0.131} \tag{2}$$

where A was a constant depending on the type of nozzle. The mean effective pressure drop, P, was determined from the equation of incompressible flow through an orifice;

$$\Delta P = \frac{\rho_f V_{inj}^2}{2C} \tag{3}$$

The nozzle flow coefficient, C, has been determined [2] from an analysis of a set of experimental data, which included a number of different nozzles. The results indicated a constant coefficient of 0.78, independent of the pressure or Reynolds number. A value of 0.8 was used in this study. The mean injection velocity was determined from;

$$V_{inj} = \frac{4}{\pi \cdot \rho_f \cdot D_n^2} \cdot \frac{dM_m}{dt} \tag{4}$$

and the mean injection rate was:

$$\frac{dM_m}{dt} = \frac{M_T}{t_{inj}} \tag{5}$$

The size distribution, with respect to the sauter mean diameter, of the droplets in a spray was experimentally investigated [1]. The droplet size data were obtained for various types of nozzles, various back pressures, different sampling positions, various pump speeds and various rack positions of the injection pump. The following non-dimensional expression, independent of the operating conditions and the nozzle type was used in this study for the size distribution of the droplets sprayed into a high pressure gaseous environment:

$$\frac{dM}{M_T} = 13.5 \left(\frac{D}{D_s}\right)^3 \text{Exp}\left[-3\left(\frac{D}{D_s}\right)\right] d\left(\frac{D}{D_s}\right) \tag{6}$$

The fuel injection rate was expressed in a polynomial form. The amount of fuel injected was determined by integrating this injection rate curve.

As a result of assuming that the droplets were grouped into several size ranges equation (6) was expressed for discrete size ranges Fig.(1).

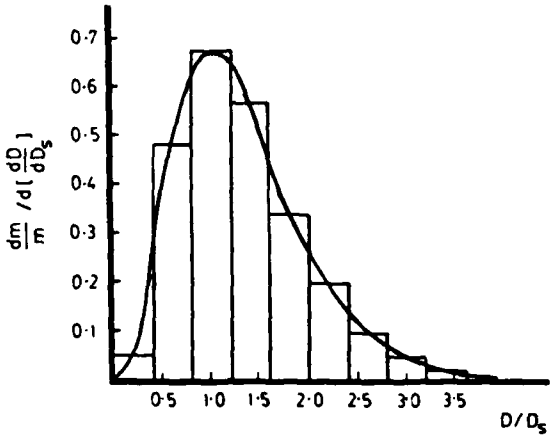


FIGURE 1. SIZE DISTRIBUTION OF DROPLETS

Therefore the mass fractions of the droplets in discrete size ranges for a mass of fuel element, ΔM_{inj}, injected in an incremental time is:

$$\frac{M_i}{\Delta M_{inj}} = 13.5\left(\frac{D_i}{D_s}\right)^3 \text{Exp}\left[-3\left(\frac{D_i}{D_s}\right)\right] \Delta\left(\frac{D_i}{D_s}\right) \tag{7}$$

and the number of droplets in a specific size range was:

$$N_i = \frac{6M_i}{\pi . \rho_f . D_i^3} \tag{8}$$

RELATIVE VELOCITIES OF THE DROPLETS

It was assumed that the relative velocity between a droplet and gas did not exceed a certain critical velocity determined by the droplet diameter, gas density, surface tension of the fuel and the critical Weber number. Therefore the initial relative velocities of the droplets without considering the different directions in which they traveled was:

$$V_o = \frac{4}{\pi \rho_f D_n^2} \frac{dM_i}{dt} \tag{9}$$

and for $V_o > V_{cr}$;

$$V_o = V_{cr} \tag{10}$$

where

$$V_{cr} = \left(\frac{2 \lambda W_{cr}}{\rho_g D_i}\right)^{1/2} \tag{11}$$

A critical Weber number of 10 was used as suggested in reference [3].

The equation of motion of a single droplet, neglecting gravitational force is:

$$m_i \frac{dV_i}{dt} + F_i = 0 \tag{12}$$

where

$$F_i = C_D \left(\frac{\rho_f V_i^2}{2}\right) A_{pi} \tag{13}$$

where the drag coefficient C_D was given as;

$$C_D = \frac{24}{Re} \qquad (Re < 0.48)$$

$$C_D = \frac{27}{Re^{0.84}} \qquad (0.48 < Re < 78)$$

$$C_D = \frac{0.271}{Re^{0.217}} \qquad (Re > 78)$$

and substituting in equation (12)

$$\frac{dV_i}{dt} = -\frac{3}{4}\frac{C_D \rho_g}{D_i \rho_f} V_i^2 \tag{14}$$

Equation (14) was solved by using the initial condition V_o at t=0.

EVAPORATION OF A SINGLE DROPLET

As the droplets traveled through high temperature and pressure gas they were subjected to heat and mass transfer. It was assumed that the droplets were spherical and that they did not interact with each other. The temperature of the droplets, which were assumed to be radially uniform, increased during their travel depending on the enthalpy carried out by mass transfer and the convective and radiative heat transferred from the surrounding gas. The diameter of the droplets decreased depending on mainly the rate of mass transfer and the effect of the change of the specific volume of the liquid with temperature was neglected.

A spherical boundary layer of vaporized fuel was formed around each droplet. The thickness of this boundary layer depended on the size and velocity of the droplet as well as the mass diffusion coefficient and density and viscosity of the gaseous phase. Diffusion of fuel was assumed to be due to the driving force of the concentration gradient in the boundary layer. The boundary layer was assumed to by spherically symmetrical with only radial heat and mass transfer.

A spherical fuel droplet of uniform temperature T_f and radius a in the surrounding gas of bulk mean cylinder temperature T_c (Fig.2) received heat from the ambient gas as vapor flowed out from the droplet. The rate of mass transfer at an arbitrary radius from the droplet centre could be expressed in the following form of Fick's first law with respect to stationary coordinates:

$$\dot{m}_f = y_f (\dot{m}_f + \dot{m}_g) - 4 \pi r^2 \rho_g D_f \frac{dy_f}{dr} \tag{15}$$

Assuming that the flow of cylinder gas into the droplet was negligible, that is $\dot{m}_g = 0$, equation (15) became:

$$\dot{m}_f = -\frac{4 \pi r^2 \rho_g D_f}{1 - y_f} \frac{dy_f}{dr} \tag{16}$$

The fuel vapor weight fraction profile was obtained by a mass balance;

$$\frac{d}{dr}(\dot{m}_f) = 0 \tag{17}$$

Substituting $\dot{m}_f$ from equation (16) gave the following nondimensional relation;

$$\frac{d}{dx}\left(x^2 \frac{dy_f}{dx}\right) = \frac{\dot{m}_f}{4 \pi a \rho_g D_f} \frac{dy_f}{dx} \tag{18}$$

where $x = \frac{r}{a}$ and $\frac{d}{dr}(\rho_g D_f) \simeq 0$.

The boundary conditions for equation (18) were

$$x_1 = 1 \qquad y_f = y_s$$

$$x_2 = \frac{a+\delta_f}{a} \qquad y_f = 0$$

Solving equation (18);

$$y(x) = y_s \left[\frac{Exp(-\theta/x_2) - Exp(-\theta/x)}{Exp(-\theta/x_2) - Exp(-\theta)}\right] \tag{19}$$

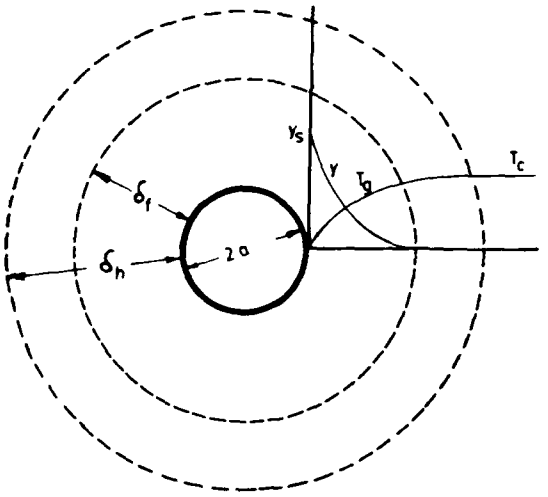


FIGURE 2. CONCENTRATION AND THERMAL BOUNDARY LAYERS AROUND AN EVAPORATING DROPLET

where

$$\theta = \frac{\dot{m}_f}{4 \pi a \rho_g D_f}$$

Expressing equation (16) at the surface of the droplet with diameter D;

$$\dot{m}_f = - \frac{2 \pi D \rho_g D_f}{1 - y_s} \left. \frac{dy}{dx} \right|_{x=x_1} \tag{20}$$

Differentiating equation (19) and substituting into equation (20);

$$\dot{m}_f = 2 \pi \rho_g D_f (D + 2\delta_f) \ln (1 - y_s) \tag{21}$$

where

$$\delta_f = \frac{D}{Sh-2} \tag{22}$$

and the Sherwood number, Sh, was calculated from the following empirical relation [5];

$$Sh = 2 + 0.6 \, Re^{1/2} \, Sc^{1/3} \tag{23}$$

where the Reynolds and Schmidt numbers were respectively defined as;

$$Re = \frac{D \rho_g V}{\mu_g} \tag{24}$$

$$Sc = \frac{\mu_g}{\rho_g D_f} \tag{25}$$

The relative velocity, V, between droplet and gas was calculated through equation (14). The mass diffusion coefficient, D_f, was calculated by the following equation given by Hirschfelder [6];

$$D_f = 2.628 \times 10^{-19} \frac{\sqrt{T^3 \left(\frac{1}{M_a} + \frac{1}{M_b}\right)}}{P \cdot r_{ab} \cdot I_D} \tag{26}$$

where M_a, M_b = Molecular weights of species a and b (kg/kgmol)

r_{ab}, I_d = Lennard-Jones constants

P = Total pressure (atm)

r_{ab} could be evaluated from $r_{ab} = \frac{1}{2}(r_a + r_b)$ where r_a and r_b were the collision diameters for each molecular species. If they were not known Hirschfelder [6] recommended the following relation:

$$r = 2.44 \left(\frac{T_{cr}}{P_{cr}}\right)^{1/3} \tag{27}$$

where T_{cr} and P_{cr} were the critical temperature and pressure of the species. I_d was given in reference [6] if the parameter kT/E_{ab} was known where the intermolecular potential parameter E_{ab}/k was given as:

$$\frac{E_{ab}}{k} = \frac{E_a}{k} \cdot \frac{E_b}{k} \tag{28}$$

if $\frac{E}{k}$ was not known Hirschfelder recommended the following relation:

$$\frac{E}{k} = 0.77\ T_{cr} \tag{29}$$

Since equation (26) gave better predictions at lower temperatures, the diffusion coefficient at higher temperatures was obtained from the following relation [7];

$$\frac{D_f}{D_{f_{ref}}} = \frac{c+T_{ref}}{c+T} \left(\frac{T}{T_{ref}}\right)^{5/2} \tag{30}$$

where c was the Sutherland constant of the mixture. It was taken as the geometric mean of the values for the species. In case it was not known it could be estimated from;

$$c = 1.47\ T_{bp} \tag{31}$$

where T_{bp} was the boiling point in degree Kelvin.

Fuel vapor weight fraction at the droplet surface, y_s, was evaluated by assuming that the fuel vapor was saturated at the droplet surface. The vapor pressure, P_v, of the fuel was obtained from the Antonie equation;

$$\log P_v = A - \frac{B}{T_f + C} \tag{32}$$

where A, B and C were constants obtained from reference [8]. The mole fraction of the fuel vapor at the droplet surface was;

$$X_s = \frac{P_v}{P} \tag{33}$$

and the weight fraction of the fuel vapor at the droplet surface was

$$y_s = \frac{X_s M_f}{X_s M_f + (1-X_s) M_{mix}} \tag{34}$$

The physical properties in the boundary layer were evaluated closer to the wall than the mean film value as recommended by Hubbard [9]

$$T = T_f + \frac{1}{3}(T_c - T_f) \tag{35}$$

where T_f and T_c were temperatures at the surface and far away from the evaporating droplet respectively.

In order to find the instantaneous droplet temperature an energy balance was applied;

$$\frac{dQ}{dt} = -\frac{dm_f}{dt} h_{fg} + m c_p \frac{dT_f}{dt} \tag{36}$$

$$\frac{dQ}{dt} = 4\pi a^2 (q_h + q_r) \tag{37}$$

$$q_r = \gamma \varepsilon (T_c^4 - T_f^4) \tag{38}$$

and $\varepsilon = 0.49$ from reference [10]. Assuming a quasi-steady process the convective heat flux from the mixture of fuel vapor and gas in the boundary layer to the droplet could be expressed in terms of the temperature in the thermal boundary layer at the surface of the droplet;

$$q_h = -k_{mix} \left.\frac{dT_{mix}}{dr}\right|_{r=a} \tag{39}$$

The temperature profile could be found by applying an energy balance to a spherical shell in the thermal boundary layer;

$$\frac{d}{dr}\left[4\pi r^2 k_{mix} \frac{dT_{mix}}{dr} + c_{p_{mix}} \dot{m}_f T_{mix}\right] = 0 \tag{40}$$

The boundary conditions were;

$$T_{mix} = T_f \quad \text{at} \quad x = 1$$

$$T_{mix} = T_c \quad \text{at} \quad x = \frac{a+\delta_h}{a}$$

where $x = \frac{r}{a}$.

The solution of equation (40) was

$$T(x) = T_c \frac{Exp(-\psi/x) - Exp(-\psi)}{Exp(-\psi/x_2) - Exp(-\psi)} + T_f \frac{Exp(-\psi/x_2) - Exp(-\psi/x)}{Exp(-\psi/x_2) - Exp(-\psi)} \tag{41}$$

where $$\psi = \frac{\dot{m}_f}{4\pi a \rho_{mix} \alpha_{mix}} \tag{42}$$

and $$x_2 = \frac{a+\delta_h}{a} \tag{43}$$

The temperature profile at the droplet surface was;

$$\left.\frac{dT_{mix}}{dx}\right|_{x=1} = \frac{\psi(T_f - T_c)}{1-Exp[\psi(x_2-1)/x_2]} \tag{44}$$

The thickness of the thermal boundary layer, δ_h, was given by [11],

$$\delta_h = \frac{D}{Nu-2} \tag{45}$$

and from [5];

$$Nu = 2 + 0.6\, Re^{1/2}\, Pr^{1/3} \tag{46}$$

where a constant value of 0.7 was taken for the Prandtl number.

Having calculated, q_h, from equation (39) by substituting equations (44) and (45) the rate of change of the droplet temperature was expressed from equation (36) as;

$$\frac{dT_f}{dt} = \frac{1}{m\, c_{pf}} [h_{fg} \dot{m}_f + \pi D^2 (q_h + q_r)] \tag{47}$$

The rate of change of the droplet diameter in terms of the rate of evaporation was;

$$\dot{m}_f = \rho_f \frac{dv_f}{dt} \tag{48}$$

Therefore

$$\frac{dD}{dt} = \frac{2}{\pi \rho_f D^2} \dot{m}_f \tag{49}$$

Equations (47) and (49) were solved simultaneously.

HEAT RELEASE RATE

The chemical ignition delay of various homogeneous fuel/air mixtures at constant temperature, pressure and oxygen concentration were experimentally correlated as [12,13,14];

$$\tau = A\, P^{B}\, \phi^{C}\, EXP\,(D/T) \tag{50}$$

In the case of varying temperature, pressure and equivalence ratio, Livengood and Wu [12] proposed the following relation for the ignition delay;

$$\int_{0}^{} \frac{dt}{\tau} = 1 \tag{51}$$

The above integral could be solved with a state, time history of the process. It was assumed that an element of combustible mixture did not release any heat during its delay period and was converted into final products releasing its total energy when it ignited.

Depending on the rate of evaporation of the fuel and mixing with air, an element of combustible mixture was formed at each incremental time. For an element of combustible mixture formed at time t equation (51) was expressed as;

$$\int_{t}^{t+\tau} \frac{dt}{\tau(t)} = 1 \tag{52}$$

Instead of calculating equation (52) separately for each element of combustible mixture formed, Nagao et.al. [5] proposed to introduce the time variable z for scaling the formation of combustible mixture to distinguish it from the time variable t for measuring the heat release rate. The origin of both variables were taken as the formation of the first element of combustible mixture. A mixture element formed at time z ignited at time t after a delay period of τ such that;

$$\tau = t - z \tag{53}$$

The relationship between z and t was given as;

$$\frac{dz}{dt} = \frac{\sigma(z)}{\sigma(t)} \tag{54}$$

with the initial condition $z(\tau_0) = 0$ where τ_0 was calculated from equation (51).

In order to obtain the rate of heat release the amount of available energy at any instant was defined as;

$$c(z) = E_v(z)\, Q_L \tag{55}$$

where $E_v(z)$ was the total evaporation rate of the fuel which was found by summation of the evaporation rates of all the droplets present in the combustion chamber at any instant. Referring to Fig.(3) an element of combustible mixture formed at time z, and having an available energy of $c(z).\Delta z$, ignited after a delay period at time t, releasing its energy in the form of heat;

$$c(z).\Delta z = \dot{Q}_h(t).\Delta t \tag{56}$$

Expressing in differential form;

$$\dot{Q}_h(t) = c(z).\frac{dz}{dt} \tag{57}$$

and substituting equation (54), for $t > \tau_0$;

$$\dot{Q}_h(t) = c(z).\frac{\sigma(z)}{\sigma(t)} \tag{58}$$

where $\sigma(z)$ was interpolated from the stored history of $\sigma(t)$.

CRITICAL REVIEW OF THE MODEL

The model based the rate of combustible mixture formation on the rate of evaporation of the fuel. The accuracy of the empirical expressions relating the sauter mean diameter and the size distribution of the droplets were directly reflected on the calculated rate of evaporation which was dependant on the diameter of a droplet. The accuracy in the prediction of the diffusion coefficient for the fuel vapor-air binary system by equation (26) was within 7 to 8 percent [7] which had a proportional effect on the accuracy in determining the rate of evaporation of droplets.

In the model a phase of rapid combustion was followed by a phase of diffusive combustion. In the latter stage all mixture elements once formed were assumed to burn almost without delay. In reality the evaporated fuel mixed with the fresh air and formed a combustible mixture. The air movement and the spray form thus have an important effect on the formation of combustible mixture during this period. However, in the model it was assumed that the evaporated fuel immediately found enough air to form a combustible mixture, thus the rate of mixture formation was assumed to be the rate of evaporation. This would probably cause

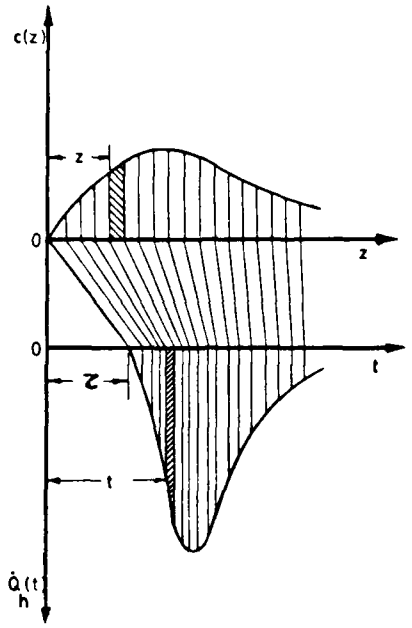


FIGURE 3. SCHEMATIC REPRESENTATION OF THE RELATION BETWEEN THE RATE OF HEAT RELEASE AND THE AVAILABLE ENERGY

the prediction of a higher rate of burning during the diffusive combustion stage.

The motion of the air into which the fuel was injected was not included into the model. However, air motion will definitely affect the rate of evaporation of the fuel droplets and the availability of oxygen.

Therefore the model may be improved by considering the geometry of the fuel spray, the motion of the gas in the cylinder and the variation of the concentration profiles within the spray cone.

REFERENCES

[1] Hiroyasu, H. and Kadota, T., "Fuel Droplet Size Distribution in Diesel Combustion Chamber", SAE Trans., Vol. 83, pp. 2615-2624, 1974.

[2] Scullen, R.S. and Hames, R.J., "Computer Simulation of the GM Unit Injector", SAE Trans., Vol. 87, pp. 618-633, 1978.

[3] Kamimoto, T. and Matsuoka, S., "Prediction of Spray Evaporation in Reciprocating Engines", SAE Trans., Vol. 87, pp. 1792-1802, 1978.

[4] Ingebo, R.D., "Atomization, Acceleration and Vaporization of Liquid Fuels", Sixth Symp. (Int.) on Comb., p. 684, 1957.

[5] Ranz, W.E. and Marshall, W.R., "Evaporation From Drops", Parts 1 and 2, Chem. Eng. Prog., Vol. 48, pp. 141-146 and 173-180, 1952.

[6] Hirschfelder, J.O., Curtiss, C.F. and Bird, R.B., "Molecular Theory of Gases and Liquids", Wiley, New York, p. 539, 1954.

[7] Perry, R.H., "Chem. Engrs. Handbook", McGraw Book Company, p. 539, 1950.

[8] Dreisbach, R.R., "Physical Properties of Chemical Compounds", American Chemical Society, Vol. 2, 1959.

[9] Hobbard, G.L., Denny, V.E. and Mills, A.F., "Droplet Evaporation: Effects of Transients and Variable Properties", Int. J. Heat and Mass Transfer, Vol. 18, pp. 1003-1008, 1975.

[10] Hottel, H.C., "Combustion of Droplets of Heavy Liquid Fuels", Fifth Symp. (Int.) on Comb., p. 101, 1955.

[11] Sanqiovanni, I.J. and Kesten, A.S., "A Theoretical and Experimental Investigation of the Ignition of Fuel Droplets", Comb. Sci. and Tech., Vol. 16, pp. 59-70, 1977.

12 Livengood, J.C. and Wu, P.C., "Correlation of Autoignition Phenomena in Internal Combustion Engines and Rapid Compression Machines", Fifth Symp. (Int.) on Comb., pp. 347-356, 1955.

13 Hurn, R.W. and Smith, H.M., "Hydrocarbons in the Diesel Boiling Range", Ind. Engng. Chem., Vol. 43, No. 12, pp. 2788-2793, 1951.

14 Mullaney, G., "Autoignition of Liquid Fuel Sprays", Ind. Engng. Chem., Vol. 51, No. 6, pp. 779-782, 1959.

15 Nagao, F., Ikegami, M. and Oshima, K., "An Analysis of Combustion Knock in a Diesel Engine", Bull. JSME, Vol. 18, No. 39, pp. 532-542, 1967.

DISCUSSION

K.Collin,
Have you compared your modelling with any real combustor or combustor measurements?

Author's Reply
Yes, the results were compared with the experimental results obtained from a Petter single cylinder, naturally aspirated, air cooled, four stroke direct injection diesel engine. Results were very satisfactory for the initial pressure rise and maximum pressures.

P.Sampath, Ca
Have you studied the interaction of one burning droplet with the evaporation of adjacent droplets?

Author's Reply
No, we did not. It was assumed that there was no interaction among droplets.

N.Selçuk, Tu
Your model is for fuel injected into stationary air. Have you tested the accuracy of your model by comparing its predictions with measured data?

Author's Reply
Yes, with successful results.

P.Ramette, Fr
Ne pensez-vous pas que l'introduction de la vitesse de l'air dans votre modélisation modifiera considérablement les résultats, en particulier pour le taux d'évaporation des gouttelettes?

Author's Reply
Not necessarily. The heat transfer and mass transfer characteristics will change due to Reynolds number. However the model is not restricted to stationary air. If air movement is introduced, it will affect the relative velocities of the droplets.

PREDICTION D'ECOULEMENTS TURBULENTS REACTIFS

par

Francis DUPOIRIEUX

OFFICE NATIONAL D'ETUDES ET DE RECHERCHES AEROSPATIALES
B.P. n° 72 - 92322 CHATILLON Cedex (FRANCE)

SOMMAIRE

La prédiction d'écoulements turbulents réactifs est effectuée à l'aide d'une méthode du type volumes finis implicite en temps. Le modèle de combustion turbulente permet de traiter les écoulements réactifs pour lesquels la richesse n'est pas homogène à l'entrée. Le maillage utilisé pour la discrétisation spatiale peut être adapté à n'importe quel conduit plan ou axisymétrique. Les résultats numériques sont du point de vue qualitatif en accord avec les résultats expérimentaux. Par ailleurs, la méthode implicite est nettement moins coûteuse en temps de calcul que la méthode explicite comportant les mêmes modèles.

PREDICTION OF TURBULENT REACTIVE FLOW

SUMMARY

Turbulent reactive flows are predicted by a numerical finite-volume method which is implicit with regard to the time. A model of turbulent combustion enables to deal with reactive flows for which the mixture ratio is heterogeneous. The grid proceeding from the spatial discretization can be applied to any shape of plane or axisymmetrical duct. Numerical results are qualitatively in agreement with experiments. Moreover, this implicit method is less expensive than the equivalent explicit one concerning the time needed to reach the asymptotical regime.

NOTATIONS

- c : constante du modèle de turbulence de sous-grille
- C_p : chaleur spécifique à pression constante
- $\mathcal{D}$: coefficient de diffusion de masse
- H : enthalpie totale
- ℓ : "longueur de mélange"
- p : pression
- q_x : composante longitudinale de la quantité de mouvement
- q_r : composante transversale de la quantité de mouvement
- r : coordonnée spatiale transversale
- R : constante de l'équation d'état
- Sc : nombre de Schmidt
- t : temps
- T : température
- u : composante longitudinale de la vitesse
- v : composante transversale de la vitesse
- x : coordonnée spatiale longitudinale

Travaux effectués sous contrats DRET et SNECMA

Y : fraction massique (Y_K , Y_O , Y_I respectivement pour les espèces K, O, I)

$\dot{w}$: taux de réaction

Symboles grecs

α : paramètre de la géométrie (Cf. texte)

β : coefficient de frottement de paroi

δ_o : aire du pic de Dirac en $Y_K = 0$

ΔQ : chaleur de réaction

ρ : masse volumique

τ_y : constante de temps du modèle de combustion turbulente

Φ : fraction massique d'une espèce inerte

Autres symboles

$\overline{\cdot}$: moyenne classique

$\widetilde{\cdot}$: moyenne de Favre

$\cdot'$: écart entre valeur instantanée et moyenne

1 - INTRODUCTION

Pour minimiser les dimensions des chambres de combustion, en particulier dans les moteurs d'avion, les transferts de masse, d'énergie et de quantité de mouvement dans les écoulements qui y circulent doivent être les plus élevés possibles. Aussi, les écoulements réactifs sont fortement turbulents et ont souvent une géométrie complexe avec recirculation. C'est pourquoi la prédiction numérique des écoulements dans les chambres de combustion n'est pas simple et est fonction des modèles de flux et taux de réaction turbulents. Néanmoins, celle-ci est d'un grand intérêt pour diminuer les coûts de conception des moteurs.

Le présent travail consiste en une méthode numérique de prédiction d'écoulements réactifs se développant dans des géométries planes ou axisymétriques quelconques. Cette méthode est adaptée pour calculer les flammes prémélangées, avec hétérogénéités de richesse, stabilisées par flamme pilote ou par recirculation. Les calculs peuvent être effectués pour un large domaine de vitesses d'entrée, de 5 m/s (valeur correspondant aux expériences de GANJI et SAWYER [1], PITZ et DAILY [2]) à 200 m/s, valeur à partir de laquelle on risque d'obtenir un blocage thermique.

La méthode numérique, qui est implicite en temps donne l'évolution transitoire de l'écoulement mais la taille du pas en temps et les modèles de turbulence sont compatibles seulement avec le régime asymptotique. La discrétisation spatiale est faite grâce à une méthode de volumes finis dans un maillage adaptable à n'importe quel conduit plan ou axisymétrique.

2 - EQUATIONS DU PROBLEME

Des équations de bilan sont résolues simultanément pour la masse totale, la quantité de mouvement (dans chaque direction de l'espace), l'enthalpie et la fraction massique de chaque espèce. La moyenne de Favre est utilisée à cause du fait que la combustion rend les écoulements très fortement compressibles. Les équations sont les suivantes :

(1) masse totale $$\frac{\partial}{\partial t}\left(\bar{\rho}\, r^\alpha\right) + \frac{\partial}{\partial x}\left(\bar{q}_x\, r^\alpha\right) + \frac{\partial}{\partial r}\left(q_r\, r^\alpha\right) = 0$$

(2) quantité de mouvement dans la direction longitudinale

$$\frac{\partial}{\partial t}\left(\bar{q}_x r^\alpha\right) + \frac{\partial}{\partial x}\left[\left(\frac{\bar{q}_x^2}{\bar{\rho}} + \bar{p} + \rho\,\widetilde{u'^2}\right) r^\alpha\right] + \frac{\partial}{\partial r}\left[\left(\frac{\bar{q}_x \bar{q}_r}{\bar{\rho}} + \bar{\rho}\,\widetilde{u'v'}\right) r^\alpha\right] = 0$$

(3) quantité de mouvement dans la direction transversale

$$\frac{\partial}{\partial t}\left(\bar{q}_x r^\alpha\right) + \frac{\partial}{\partial x}\left[\left(\frac{\bar{q}_x \bar{q}_r}{\bar{\rho}} + \bar{\rho}\,\widetilde{u'v'}\right) r^\alpha\right] + \frac{\partial}{\partial r}\left[\left(\frac{\bar{q}_r^2}{\bar{\rho}} + \bar{\rho}\,\widetilde{v'^2}\right) r^\alpha\right] + r^\alpha \frac{\partial \bar{p}}{\partial r} = 0$$

(4) enthalpie

$$\frac{\partial}{\partial t}\left(\bar{\rho}\widetilde{H}r^{\alpha}\right)+\frac{\partial}{\partial x}\left[\left(\bar{q}_x\widetilde{H}+\bar{\rho}\widetilde{u''H''}\right)r^{\alpha}\right]+\frac{\partial}{\partial r}\left[\left(\bar{q}_r\widetilde{H}+\bar{\rho}\widetilde{v''H''}\right)r^{\alpha}\right]=\frac{\partial\bar{p}}{\partial t}$$

(5) fraction massique du combustible

$$\frac{\partial}{\partial t}\left(\bar{\rho}\widetilde{Y}_K r^{\alpha}\right)+\frac{\partial}{\partial x}\left[\left(\bar{q}_x\widetilde{Y}_K+\bar{\rho}\widetilde{u''Y''_K}\right)r^{\alpha}\right]+\frac{\partial}{\partial r}\left[\left(\bar{q}_r\widetilde{Y}_K+\bar{\rho}\widetilde{v''Y''_K}\right)r^{\alpha}\right]=\bar{\rho}\,\widetilde{\dot{\omega}}\;r^{\alpha}$$

(6) fraction massique d'une espèce inerte

$$\frac{\partial}{\partial t}\left(\bar{\rho}\widetilde{\Phi}_i r^{\alpha}\right)+\frac{\partial}{\partial x}\left[\left(\bar{q}_x\widetilde{\Phi}_i+\bar{\rho}\widetilde{u''\Phi''_i}\right)r^{\alpha}\right]+\frac{\partial}{\partial r}\left[\left(\bar{q}_r\widetilde{\Phi}_i+\bar{\rho}\widetilde{v''\Phi''_i}\right)r^{\alpha}\right]=0$$

L'équation d'état s'écrit :

(7) $$\bar{p}=\bar{\rho}R\widetilde{T}=\bar{\rho}R\,\frac{\widetilde{H}-\widetilde{Y}\Delta Q-\frac{u^2+v^2}{2}}{C_p}$$

De façon classique, on utilise un paramètre pour fixer la géométrie : $\alpha = 0 \longrightarrow$ conduit plan ; $\alpha = 1 \longrightarrow$ conduit axisymétrique. Les flux de diffusion moléculaire sont négligés devant les flux de diffusion turbulente. Dans la quantité H sont inclues l'enthalpie physicochimique et l'énergie cinétique :

$$dH = C_p\,dT + \Delta Q\,dY_K + d\frac{(u^2+v^2)}{2}$$

ΔQ, la chaleur dégagée dans la réaction chimique, et C_p, la chaleur spécifique, sont dans un souci de simplification supposées constant. Cela permet, entre autres, que soient vérifiées les relations $\widetilde{C_p dT} = \widetilde{C_p}\,d\widetilde{T}$ et $\widetilde{Y_K\Delta Q} = \widetilde{Y_K}\,\Delta Q$. $\widetilde{T}$, la température moyenne, peut alors aisément être déduite à partir des valeurs de $\widetilde{H}$ et $\widetilde{Y}_K$. Dans l'équation de l'enthalpie (4), certaines corrélations de vitesses provenant du terme d'énergie cinétique ($\widetilde{u''v''}$, $\widetilde{u''u''v''}$, ...) sont négligées du fait que : $(u^2+v^2)/2 \ll C_pT + Y_K\Delta Q$. Avec ces hypothèses, l'équation d'enthalpie ne contient pas de terme source exceptê $\partial\bar{p}/\partial t$. Il apparaît que, pour des conditions aux limites convenables (conduit adiabatique), lorsque la pression varie lentement dans le temps, la solution est : H = Cte. Ainsi, l'équation (4) (comme l'équation 6) n'apparaît pas comme une équation primordiale du système. Par contre, l'équation (5) qui contient le terme $\widetilde{\dot{\omega}}$ provenant de la réaction est fortement couplée avec les équations (1), (2) et (3) par l'intermédiaire de l'équation d'état (7).

La fraction massique d'oxydant est déduite de l'équation (6) dans laquelle la quantité Φ_i représente la variable de Shvab-Zeldovich $\nu Y_K - Y_O$. L'utilisation de cette variable suppose que les coefficients de diffusion des espèces O et K sont identiques et que la réaction chimique se résume à :

$$K + \nu O \longrightarrow \text{Produits}$$

Cette hypothèse est compatible avec le modèle de combustion turbulente pour lequel il est supposé que le mélange turbulent est l'effet prépondérant dans le pilotage de la réaction. Plusieurs équations comme (6) sont résolues simultanément. Leur solution dépend seulement des conditions aux limites qui sont spécifiques à chacune d'elles.

3 - MODELES DE TURBULENCE

Les corrélations qui apparaissent dans les équations de bilan doivent être modélisées. Les flux de diffusion turbulente sont de façon classique exprimés en fonction des gradients des valeurs moyennes :

(8) $$\bar{\rho}\widetilde{u''_\alpha u''_\beta} = -\mu_{turb}\left(\frac{\partial\widetilde{u}_\alpha}{\partial x_\beta}+\frac{\partial\widetilde{u}_\beta}{\partial x_\alpha}\right)$$

(9) $$\overline{\rho u''_\alpha H''} = -\left(\frac{\lambda}{C_p}\right)_{turb} \frac{\partial \tilde{H}}{\partial x_\alpha}$$

(10) $$\overline{\rho u''_\alpha Y''_K} = -(\rho \mathcal{D})_{turb} \frac{\partial \tilde{Y}_K}{\partial x_\alpha}$$

(11) $$\overline{\rho u''_\alpha \Phi''_i} = -(\rho \mathcal{D})_{turb} \frac{\partial \tilde{\Phi}_i}{\partial x_\alpha}$$

$(\alpha = 1,2 \quad \beta = 1,2 \quad x_1 = x \quad x_2 = r \quad u''_1 = u'' \quad u''_2 = v'')$

Comme la quantité H contient le terme $Y_K \Delta \mathcal{D}$, le nombre de Lewis turbulent doit être supposé égal à 1 pour que l'égalité (9) soit vérifiée.

Selon les cas, différentes hypothèses de fermeture sont considérées ; ces hypothèses tiennent dans les modèles algébriques simples suivants :

- $\mu_{turb} = cte$ et $$(Sc)_{turb} = \frac{\mu_{turb}}{(\rho \mathcal{D})_{turb}} = 0.83$$

- modèle de longueur de mélange : $\mu_{turb} = \rho l^2 \left|\frac{\partial \tilde{u}}{\partial r}\right|$ et $(Sc)_{turb} = 0.83$

Ce modèle est appliqué aux écoulements pour lesquels la vitesse transversale est en tout point négligeable par rapport à la vitesse longitudinale (donc sans recirculation)

- modèle de sous-grille : $\mu_{turb} = k_0 \left(2\left(\frac{\partial \tilde{u}}{\partial x}\right)^2 + 2\left(\frac{\partial \tilde{v}}{\partial y}\right)^2 + \left(\frac{\partial \tilde{u}}{\partial y} + \frac{\partial \tilde{v}}{\partial x}\right)^2\right)^{\frac{1}{2}}$ avec $k_0 = \rho c \Delta x \Delta y$ et $(Sc)_{turb} = 0.83$.

On a posé $y = r$ pour tenir compte du fait que cette formule a été établie seulement pour une géométrie bidimensionnelle plane. Seule la turbulence dont l'échelle est inférieure à la taille de la maille de calcul est prise en compte par ce modèle. L'autre partie de la turbulence est censée apparaître sous la forme d'instabilités, le régime asymptotique étant alors instationnaire.

4 - MODELE DE COMBUSTION TURBULENTE

Un modèle de combustion turbulente a été établi avec ces hypothèses :

- la richesse est partout inférieure à 1,
- le temps caractéristique de la chimie est beaucoup plus petit que le temps caractéristique de la turbulence.

Ce modèle a été établi à partir du modèle lagrangien d'interaction par échange avec la moyenne dit IEM [3] qui suppose que Y_K satisfait l'équation suivante :

$$\frac{dY_K}{dt} = \frac{\tilde{Y}_K - Y_K}{\tau_Y} - \dot{w}$$

Cette équation n'est autre que l'équation de bilan :

$$\frac{dY_K}{dt} = \frac{1}{\rho} \operatorname{div}\left[\rho \mathcal{D} \overrightarrow{\operatorname{grad}} Y_K\right] - \dot{w}$$

dans laquelle le terme de diffusion a été modélisé par $\frac{\tilde{Y}_K - Y_K}{\tau_Y}$.

La seconde hypothèse impose pour $\dot{w}$ la forme représentée sur la figure 1.

Conformément à la première hypothèse, l'oxydant est supposé en excès de sorte que le minimum de Y_K est zéro. La valeur maximale de $\dot{w}$ est supposée grande de sorte que l'aire contenue sous la courbe $\dot{w}(Y_K)$ a une valeur finie.

Etant donné la forme de $\dot{w}(Y_K)$, on peut considérer que, pour $Y_K > 0$, on a $\dot{w} = 0$. Par contre lorsque $\dot{w}$ devient positif, Y_K devient égal à zéro ; dans ce dernier cas, $-\dot{w}$ et $(\tilde{Y}_K - Y_K)/\tau_Y$ prennent des valeurs grandes et opposées de sorte que : $dY_K/dt \ll -\dot{w}$ et $dY_K/dt \ll (\tilde{Y}_K - Y_K)/\tau_Y$; d'après le modèle IEM, $\dot{w}$ devient alors égal à $\tilde{Y}_K/\tau_Y$. Finalement :

- lorsque $Y_K \neq 0$: $\dot{w} = 0$
- lorsque $Y_K = 0$: $\dot{w} = \frac{\tilde{Y}_K}{\tau_Y}$

On en déduit que : $\widetilde{\dot{\omega}} = \dfrac{\widetilde{Y}_K}{\tau_Y}\,\delta_o$

τ_Y est une échelle de temps qui est supposée reliée au temps caractéristique de la turbulence. δ_o est l'aire du pic de la fonction densité de probabilité de Y_K (notée $Y_K - Fdp$) en $Y_K = 0$. La connaissance de $\widetilde{\dot{\omega}}$ est subordonnée à celle de δ_o. Pour la détermination de δ_o, on introduit une espèce fictive <u>inerte</u> I qui est injectée exactement dans les mêmes conditions que l'espèce combustible K.

Supposons que les espèces K et I soient injectées avec une fraction massique allant de Y_1 à Y_2. Dans le plan Y_K, Y_I, les particules gazeuses constituant l'écoulement sont réparties sur deux segments [AB] et [CD] (cf. fig. 2).

Etant donné que la chimie est très rapide et que l'oxydant est en excès, les particules qui brûlent arrivent immédiatement sur le segment [AB] où Y_K est nul ; d'un autre côté, les particules qui se mélangent sans brûler se déplacent sur le segment [CD] où on a : $Y_I = Y_K$. La fraction de particules qui sont sur [AB] est naturellement δ_o. Soit P_{Y_K} la fonction densité de probabilité de Y_K ; on a :

$$\widetilde{Y}_K = \int_{Y_1}^{Y_2} Y_K\, P_{Y_K}(Y_K)\, dY_K$$

Si les formes de la distribution des particules sur chacun des segments [AB] et [CD] sont les mêmes, on a aussi :

$$\widetilde{Y}_I = \int_{Y_1}^{Y_2} Y_I\, P_{Y_K}(Y_K) \left[\frac{dY_K}{dY_I}\right]_{[CD]} dY_I + \delta_o\, \widetilde{Y}_I$$

Comme, sur le segment [CD], Y_K est égal à Y_I, $\left[\dfrac{dY_K}{dY_I}\right]_{[CD]}$ vaut 1 et finalement :

$$\widetilde{Y}_I = \widetilde{Y}_K + \delta_o \widetilde{Y}_I \quad \text{ou} \quad \delta_o = 1 - \frac{\widetilde{Y}_K}{\widetilde{Y}_I}$$

Le taux de réaction moyen peut alors être exprimé :

$$\widetilde{\dot{\omega}} = \frac{\widetilde{Y}_K}{\tau_Y}\left(1 - \frac{\widetilde{Y}_K}{\widetilde{Y}_I}\right)$$

$\widetilde{Y}_I$ est calculé à partir d'une équation de bilan identique à l'équation (6) et ayant mêmes conditions aux limites que l'équation (5). On peut noter que lorsque le combustible est injecté avec une fraction massique unique et constante Y_m, ce modèle simple de combustion turbulente se réduit au modèle bien connu dénommé "Eddy break up" :

$$\widetilde{\dot{\omega}} = K \widetilde{Y}_K \left(Y_m - \widetilde{Y}_K\right)$$

En effet, dans ce cas, la solution de l'équation de bilan pour $\widetilde{Y}_I$ est $\widetilde{Y}_I = Y_m$ en tout point.

A défaut d'information sur τ_Y, ce temps caractéristique est posé proportionnel à $\overline{\rho} / (\mu_{comb}\, \Delta x\, \Delta y)$.

5 - CONDITIONS INITIALES ET AUX LIMITES

- Les conditions initiales sont l'état du gaz au repos. La mise en mouvement est obtenue par une augmentation progressive de la pression d'arrêt amont.

- Dans la section d'entrée, on impose les quantités suivantes :
  - l'enthalpie,
  - la fraction massique de chaque espèce chimique,
  - la pression d'arrêt ou le flux de masse.

Avant l'allumage, c'est la pression d'arrêt qui est imposée. Durant l'allumage, il est nécessaire d'imposer le flux de masse dans chaque cellule de la section d'entrée pour y éviter des courants de retour.

. A la sortie, on impose :
- la pression statique,
- les gradients de chaque quantité scalaire ($\widetilde{H}$, $\widetilde{Y}_K$, $\widetilde{\Phi}_\lambda$, ...) qui sont maintenus nuls.

. A la paroi, on impose un transfert de chaleur soit nul (conduit adiabatique) soit proportionnel à une certaine différence de température. La contrainte visqueuse à la paroi est exprimée de la façon suivante :

$$\widetilde{\sigma} = \mu_{turb} \frac{\widetilde{u}_p}{\Delta e} \beta$$

$\widetilde{u}_p$: vitesse dans une cellule limitée par la paroi,

Δe : longueur entre le centre de la cellule et la paroi,

β est un coefficient inférieur à 1 qui est fonction du nombre de Reynolds basé sur la taille de la cellule. Ce coefficient est nécessaire pour prendre en compte le fait que la sous-couche visqueuse a une épaisseur bien inférieure à

6 - RESULTATS

La figure 3 présente les résultats obtenus avec des données correspondant aux expériences de PITZ et DAILY [1]. Sur la partie supérieure, on a le champ de vitesse correspondant à l'écoulement non réactif, sur la partie inférieure, le champ de vitesse correspondant à l'écoulement stabilisé en combustion. La vitesse moyenne amont est 5 m/s. La richesse est supposée constante à l'entrée et la température de fin de combustion est 1600 K. Le modèle de turbulence est le plus simple : μ_{turb} = cte = 2.10^{-3} kg/ms. Cette valeur de 2 x 10^{-3} kg/ms est celle qui donne la même longueur de recirculation pour l'écoulement non réactif que dans l'expérience. Par ailleurs, le frottement à la paroi est supposé élevé. Comme on l'observe dans l'expérience, la zone de recirculation est plus petite dans le cas de la combustion. On peut penser que cela est dû à l'expansion des gaz chauds. Néanmoins, la recirculation calculée est, pour l'écoulement en combustion, de taille inférieure à celle qui est observée dans l'expérience. Cela peut s'expliquer par le fait que le calcul de l'écoulement réactif a été réalisé avec la même valeur de la viscosité turbulente que pour l'écoulement non réactif. Or, PITZ et DAILY ont mis en évidence le fait que la répartition de la turbulence est fortement modifiée par la combustion.

La figure 4 présente les lignes isothermes obtenues avec des données correspondant à un foyer de réchauffe à deux accroche-flammes toriques (géométrie axisymétrique), les niveaux de vitesse et de température d'écoulement étant réalistes. La richesse à l'entrée est supposée constante et la température de fin de combustion correspond à un mélange global stoechiométrique. Le modèle de turbulence est le modèle de longueur de mélange sauf au voisinage des accroche-flammes. Le frottement à la paroi est supposé faible. Le rendement de combustion en fonction de la distance derrière les accroche-flammes, qu'il est possible de déduire de ces courbes, semble correspondre à la réalité.

La figure 5 présente les courbes isothermes dans un écoulement réactif stabilisé par flamme pilote (géométrie plane). L'adaptation du modèle de combustion présenté ci-dessus à ce type de stabilisation est aisée. Les conditions d'entrée sont les suivantes :

- pour le mélange air-combustible frais :

$\widetilde{Y}_K$ = 0,05 (combustible)

$\widetilde{Y}_I = \widetilde{Y}_K$ = 0,05 (espèce inerte fictive),

- pour les gaz chauds de la flamme pilote :

$\widetilde{Y}_K$ = 0 (combustible),

$\widetilde{Y}_I$ = 0,05 (espèce inerte fictive).

Les gaz chauds de la flamme pilote sont considérés comme une partie de l'écoulement principal qui a été prélevée puis brûlée complètement avant d'être injectée dans la section d'entrée.

Les figures 6 et 7 présentent respectivement le champ de vitesse et les lignes isothermes pour un écoulement réactif stabilisé par recirculation dans une cavité. Dans ce cas, μ_{turb} a été pris constant. La vitesse moyenne et la température amont sont respectivement 170 m/s et 525 K. A la sortie, ces grandeurs passent respectivement à 340 m/s et 1150 K.

Par ailleurs, des essais numériques ont été tentés avec le modèle de turbulence de sous-grille. Des mouvements du gaz sont observés ; cependant, on ne peut pas encore être sûr que ces mouvements sont dûs aux grandes échelles de la turbulence car, avec une viscosité turbulente faible, l'évolution transitoire peut être tellement longue que le régime asymptotique peut ne pas avoir été atteint au cours de ces essais numériques.

7 - CONCLUSION

La méthode numérique implicite permet dans le cas général d'atteindre le régime asymptotique des écoulements réactifs avec un temps de calcul relativement court. Par ailleurs, la stabilisation est obtenue avec plus de précision que par les méthodes explicites (pas de fluctuation numérique).

Le modèle de combustion turbulente est simple mais plus général que le modèle "Eddy break up" souvent utilisé. Il ne nécessite qu'une équation de bilan supplémentaire pour une espèce inerte.

Les résultats numériques sont du point de vue qualitatif en accord avec les expériences. Cependant, pour les écoulements présentant des recirculations, il semble nécessaire d'introduire un modèle de turbulence $k-\epsilon$, ce qui comporte certaines difficultés, les équations pour k et ϵ étant très fortement couplées.

Par ailleurs, l'un des avantages du code de calcul est que chaque cellule du domaine de calcul peut à volonté jouer le rôle d'un obstacle solide ou laisser le passage à l'écoulement. Cela permet l'adaptation facile à diverses géométries.

REFERENCES

[1] - GANJI R., SAWYER R.F.
An experimental study of the flow field and pollutant formation in a two-dimensional premixed turbulent flame. 17th Aerospace Science Meeting, 15-17 janvier 1979, New Orleans.

[2] - PITZ W., DAILY J.W.
Experimental study of combustion in a turbulent free shear layer formed at a rearward facing step. 19th Aerospace Science Meeting, 12-15 janvier 1981, St Louis (Missouri).

[3] - AUBRY C., VILLERMAUX J.
Chemical Engineering Science, vol 30, p. 457 (1975).

[4] - BORGHI R., POURBAIX E.
AIAA 19th Aerospace Science Meeting, 12-15 janvier 1981, St Louis (Missouri).

[5] - DUTOYA D., MICHARD P.
Une méthode de volumes finis de type implicite pour le calcul des écoulements elliptiques. La Recherche Aérospatiale 1980-2.

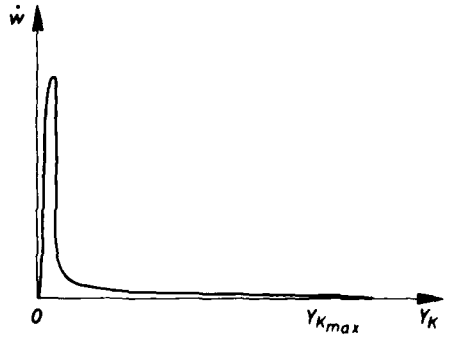


Fig. 1 – Allure de courbe $\dot{w}$ (Y_K.)

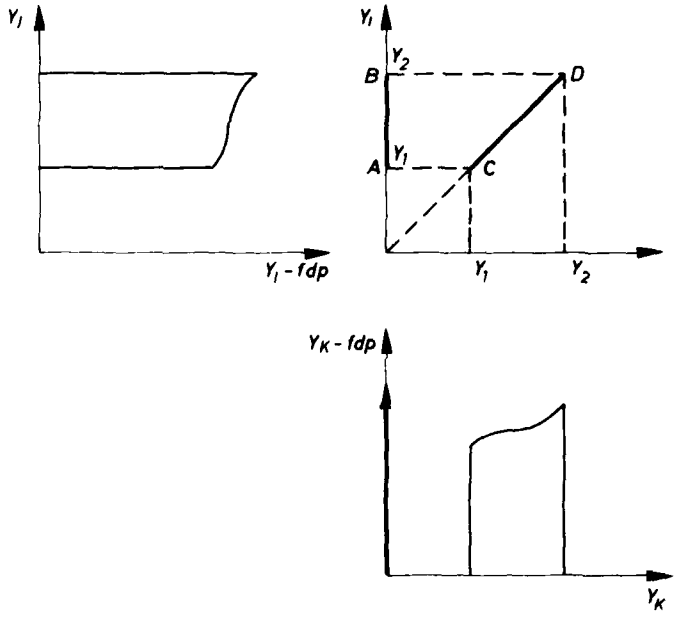
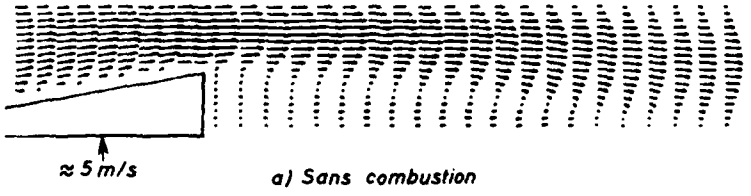


Fig. 2 – Allure des Fdp des espèces I et K



a) Sans combustion



b) Avec combustion

Fig. 3 – Champs de vitesse derrière une marche.

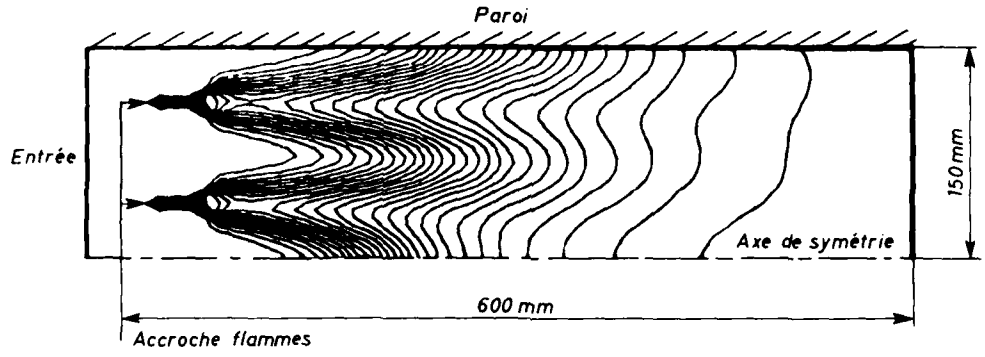


Fig. 4 – Courbes isothermes dans un foyer de réchauffe.

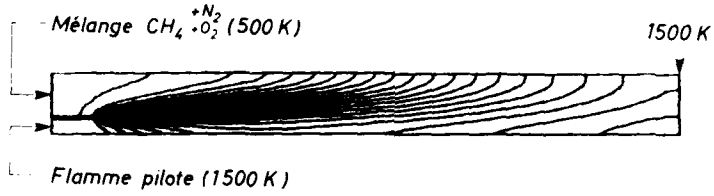


Fig. 5 – Courbes isothermes pour un écoulement réactif stabilisé par flamme pilote.

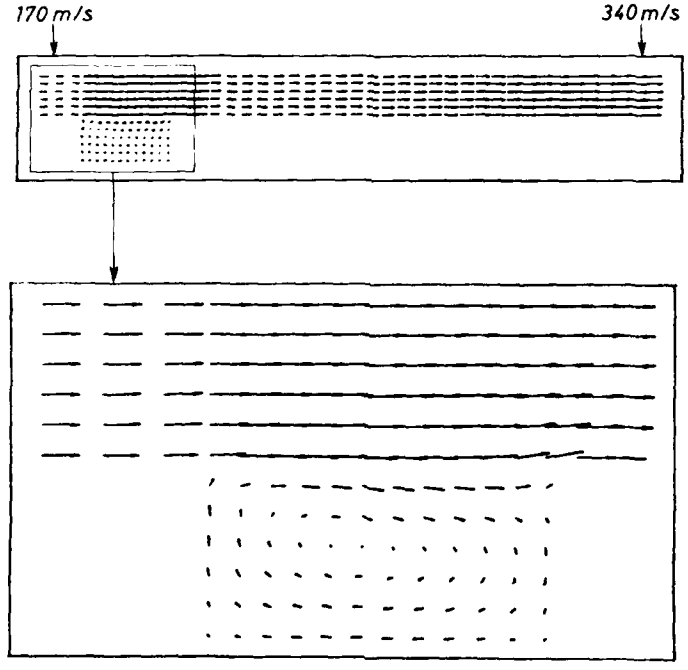


Fig.6 – Champ de vitesse pour un écoulement réactif stabilisé par recirculation dans une cavité.

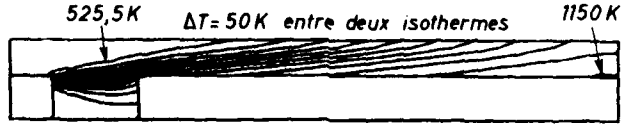


Fig. 7 – Courbes isothermes pour un écoulement réactif stabilisé par recirculation dans dans une cavité.

DISCUSSION

N.Selçuk, Tu

Have you done a quantitative comparison between the results of your model and experimental data?
Have you neglected the radiative energy in your enthalpy balance, and do you have comparisons for temperature?

Réponse d'Auteur

Nous avons déterminé des rendements de combustion qui se recoupent à 5% près avec des mesures faites sur un canal de réchauffe. D'autre part des mesures de vélocimétrie laser effectuées dans une flamme derrière une marche sont en accord avec les calculs, en particulier pour la longueur de la zone de recirculation.
Nous avons négligé les transferts radiatifs. En effet les flux de diffusion turbulente sont prépondérants par rapport aux flux radiatifs. Nous n'avons pas effectué de mesures de température.

P.Ramette, Fr

Avez-vous essayé votre programme de calcul avec un maillage non rectangulaire, pour mieux prendre en compte des obstacles à l'intérieur de l'écoulement, par exemple dans le cas d'un accroche-flamme?

Réponse d'Auteur

Malheureusement non. Une des limitations de ce code de calcul est qu'il utilise nécessairement un maillage rectangulaire.

J.Fabri

En augmentant le nombre de mailles on peut pratiquement décrire n'importe quel type d'obstacle.

P.Hebrard, Fr

Est-ce que vous utilisez la même viscosité turbulente dans le cas avec combustion et sans combustion?
Pensez-vous étendre ce modèle au cas d'écoulements diphasiques?

Réponse d'Auteur

Oui, et c'est la raison pour laquelle, si on n'utilise pas le modèle de longueur de mélange, la recirculation avec combustion n'a pas la bonne longueur. Effectivement, plus que les transferts radiatifs, c'est surtout le modèle de viscosité turbulente qui doit être amélioré.
Il est sans doute nécessaire d'étendre le modèle au cas des écoulements diphasiques. Par exemple, dans le cas des canaux de réchauffe, il est probable que le combustible n'est pas complètement évaporé dans la zone des accroche-flammes.

R.Monti, It

Can you explain why an implicit method is faster than an explicit method?

Réponse d'Auteur

Dans une méthode implicite, le pas en temps peut être 40 fois plus grand que le pas en temps CFL. Comme la résolution d'un pas en temps en implicite est plus grande, on ne gagne pas un facteur 40, mais une méthode implicite peut être 5 à 15 fois plus rapide qu'une méthode explicite.

PREDICTED TF41 PERFORMANCE WITH THE AGARD RESEARCH FUEL

by
J. E. Peters
Department of Mechanical and Industrial Engineering
University of Illinois at Urbana-Champaign
Urbana, IL 61801

Sixty-second Symposium of the
AGARD Propulsion and Energetics Panel on
Combustion Problems in Turbine Engines
Cesme, Turkey

AD-P003 153

ABSTRACT

Calculations are presented to predict the performance of an alternative fuel in a conventional gas turbine combustor. Existing data for fuel effects on the Detroit Diesel Allison TF41 combustor, a can-annular burner, are correlated with the semi-empirical characteristic time model. The correlations are used to predict the ignition, stability and combustion efficiency performance of a proposed alternative fuel, the AGARD Research Fuel, in the TF41 combustor. Compared to standard NATO F-40 and F-35 fuels the alternative fuel will provide similar combustion efficiency levels, reduced flame stability and significantly degraded ignition performance.

NOMENCLATURE

a	Empirically selected weighting factor
b	Pre-exponential factor
d_{comb}	Combustor diameter
d_o	Sauter mean diameter
d_q	Spark kernel diameter
E	Activation energy
ℓ_{co}	Mixing length for CO
ℓ_q	Quenching length
R	Universal gas constant
T_{exh}	Combustor exhaust temperature
T_{in}	Combustor inlet temperature
T_η	Temperature for combustion efficiency kinetics
$T_{\phi=1}$	Stoichiometric adiabatic flame temperature
V_{ref}	Combustor reference velocity
β	Evaporation coefficient
η_c	Combustion efficiency
ρ_g	Gas phase density
τ_{eb}	Droplet evaporation time
τ_{hc}	Kinetic time for ignition and lean blowoff
$\tau_{s\ell}$	Mixing time
τ_η	Kinetic time for combustion efficiency
ϕ	Equivalence ratio

INTRODUCTION

The introduction of alternative fuels and the relaxation of fuel property specifications of current fuels are areas of concern for the gas turbine community because changes in fuels or fuel properties raise questions regarding engine performance. Although the importance of specific fuel properties on the performance of an engine may be known qualitatively (front end boiling points on ignition and carbon to hydrogen ratio (and/or aromatics) on soot, for example)[1-3], quantitative understanding for determining the effects of new and previously untested fuels is often lacking. In this paper, calculations are presented for gas turbine engine performance predictions in the areas of ignition, lean blowoff and combustion efficiency for an alternative fuel. Calculations are also made for standard fuels for which performance data are available to establish the validity of the predictions.

The combustion system for which the predictions will be made is the Detroit Diesel Allison TF41. The TF41 is a turbofan engine which features a ten can can-annular combustion chamber. Fuel is introduced with ten dual-orifice pressure atomizing nozzles and ignition is achieved with surface discharge plugs located in two cans. Further details of the engine can be found elsewhere[4]. The TF41 experimental data used in this paper were obtained from single can rig tests by Vogel et al[4,5]. In their study, two fuels, JP-4 (F-40) and JP-8 (F-35), were used and blends of each of these fuels with different components were also tested to provide a total of twelve test fuels.

Characteristic Time Model

The characteristic time model will be used to predict the performance of the TF41. This model was selected for two primary reasons. The model is relatively simple to employ; the important physical processes are determined and computed through times (evaporation, kinetic and mixing, for example) which are representative of the processes. Also this approach has previously been shown to work well for correlating emissions data, ignition and lean blowoff limits, and combustion efficiency data from both fundamental experiments and actual gas turbine hardware[6-9].

The times of importance for this work are listed in Table 1. The turbulent mixing time is estimated by a length scale divided by the combustor reference velocity. The evaporation time is given by the square of the Sauter mean diameter (estimated from empirical relations) divided by the evaporation coefficient. Finally, kinetics are taken into account by Arrhenius expressions. The similarities and differences of these times for ignition, lean blowoff, and combustion efficiency will be described, along with the model formulations for each case, in the following sections.

Ignition

For ignition to occur in a gas turbine engine, the rate of heat release (which is controlled first by the evaporation of the fuel and then by chemical kinetics) must exceed the heat loss rate (controlled by turbulent mixing) from the spark kernel. Therefore, in terms of the characteristic time model, the ignition limit is given by

$$\tau_{s\ell} \sim \tau_{hc} + a\,\tau_{eb}/\phi \qquad (1)$$

where the proportionality and the constant weighting factor, a, are necessary because the times are simply estimates of the processes involved and are not expected to be quantitatively exact.

As noted in Table 1, the length scale for ignition is the spark kernel diameter, defined as the diameter of a sphere which would be heated to the stoichiometric adiabatic flame temperature by the spark energy. Also from Table 1, the droplet evaporation time is computed from the "d^2-law"[10] and the drop size is calculated from an empirical equation[11]. Dividing the evaporation time by the equivalence ratio takes into account the fact that adding more fuel (more drops) decreases the time it takes for a given amount of fuel to reach the vapor phase. Finally, for the kinetic time, $b = 10^{-5}$, $E = 26{,}100$ cal/mole and ρ_g is the gas phase density in kg/m^3. For details on the derivations of these terms, see Peters[12].

The TF41 ignition data include sea level start and altitude relight data at a flight Mach number of 0.6. These data are used to calculate the terms in Eq. (1) and the results are shown in Fig. 1 where a least squares fit line and one standard deviation about that line are included. (The weighting factor of 0.021 was selected from previous work[12].) The fit is statistically good ($r > 0.9$) although the correlation does not pass through the origin as the model suggests it should. The large intercept on the ordinate has been observed by others[13] and is believed to be caused by significant amounts of energy not participating in the ignition process due to losses in the ignition circuit. One other point of interest is that the equivalence ratio (at the spark gap) that appears in Eq. (1) and in the kinetic time was previously found to be constant for can type combustors (and assumed equal to one). This approach is verified here because no correlation could be found by letting ϕ vary with the primary zone equivalence ratio; Fig. 1 is a result of setting the equivalence ratio at the spark gap equal to one.

The best fit line separates the figure into two regions, ignition and no ignition. If an engine is operating in the upper left-hand portion of the figure, ignition is possible. The ignition limit is approached by moving horizontally (increasing the evaporation time by increasing drop size or decreasing volatility, for example) or vertically (decreasing the mixing time by increasing the reference velocity or decreasing the ignition energy).

Table 1 Characteristic Times

		Definitions		
Time	Meaning	Ignition	Lean Blowoff	Efficiency
$\tau_{s\ell}$	Mixing	d_q/V_{ref}	ℓ_{co}/V_{ref}	ℓ_{co}/V_{ref}
τ_{eb}	Evaporation	d_o^2/β	d_o^2/β	d_o^2/β
τ_{hc}	Kinetics	$\dfrac{b\,\exp(E/RT_{\phi=1})}{\rho_g\,\phi}$	$\dfrac{b\,\exp(E/RT_{\phi=1})}{\phi}$	---
τ_n	Kinetics	---	---	$\dfrac{b\,\exp(E/RT_n)}{\phi}$

Based on the ignition correlation in Fig. 1, ignition limit calculations can now be made. This paper will focus on the three fuels listed in Table 2. The JP-4 (F-40) and JP-8 (F-35) fuels will be included in the calculations to act as a comparison of the model with available data and as a comparison to the predicted performance of an alternative fuel, the AGARD Research Fuel (ARF). Generally speaking, JP-4 (F-40) is the "lightest" fuel as indicated by the lower boiling points and viscosity. ARF is a representative of possible future alternative fuels with higher boiling points, higher viscosity and lower hydrogen content. ARF properties were defined by the Propulsion and Energetics Panel Working Group 13 as a proposed test fuel.

The fuel properties in Table 2 were used in conjunction with the correlation of Fig. 1 to determine the percent decrease in drop size required to achieve ignition for JP-8 (F-35) and ARF compared to the JP-4 (F-40) baseline fuel; the results are shown in Fig. 2. As in all the predictions for this paper, the sea level calculations were performed for idle inlet conditions and the altitude calculations for a Mach number of 0.6. The graph clearly indicates that the atomization quality has to improve for the "heavier" fuels to ignite. In other words, to obtain the evaporation rate required for ignition, the drop sizes of JP-8 (F-35) and ARF must decrease to compensate for their lower volatilities. The improvements required in atomization quality is largest at the idle condition and nearly constant at the various altitudes.

Table 2 Fuel Properties

Property	JP-4 (F-40)*	JP-8 (F-35)*	ARF**
Density at 21°C, g/cm^3	0.760	0.807	0.800
Viscosity at 25°C, cs	0.98	1.94	3.75
Surface Tension at 21°C, dynes/cm	23.7	26.9	26.3
Hydrogen weight %	14.4	13.9	13.2
Lower Heating Value, MJ/kg	43.5	43.1	43
10% boiling point, K	360	451	478
50% boiling point, K	438	499	525

* Fuel properties listed are for the ignition and lean blowoff tests. The fuels for the combustion efficiency tests had slightly different properties. See Ref. 4 for details.

* Properties not included in the ARF specification were estimated.

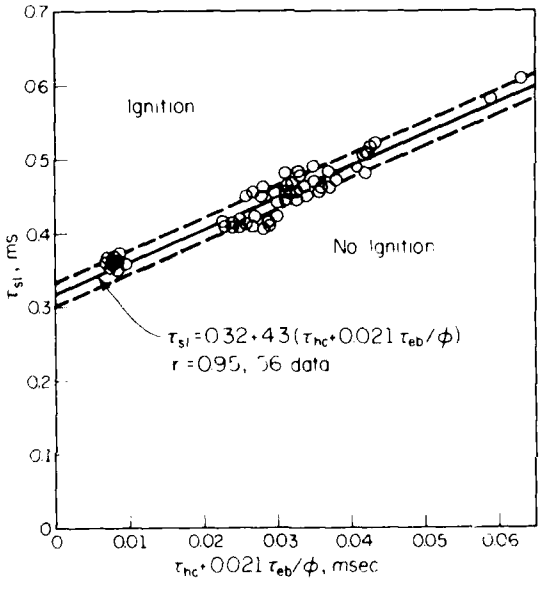


Figure 1 TF41 ignition correlation (data from reference 4)

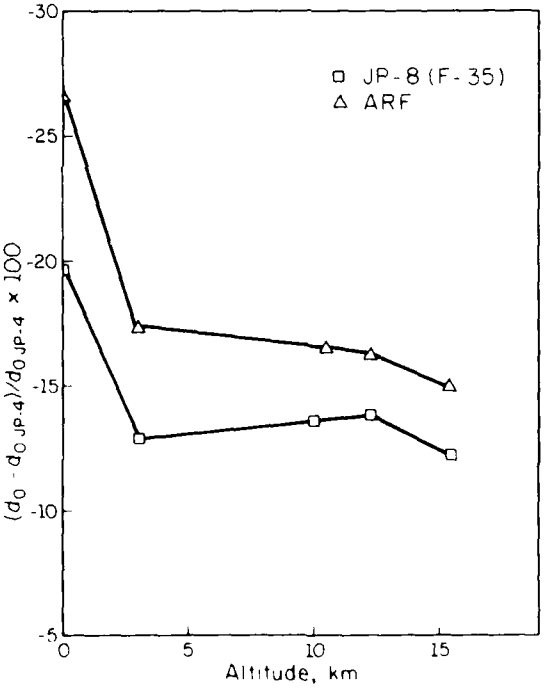


Figure 2 Predictions of the decrease in drop size required for ignition capabilities equivalent to JP-4 (F-40)

The improvement in atomization indicated in Fig. 2 is substantial. This is illustrated in Fig. 3 where the predicted primary zone equivalence ratio required for ignition (assuming all the fuel flows through the pilot nozzle which would give the best atomization) is plotted against altitude. The standard deviation of the correlation in Fig. 1 was used to determine the "error bars" on the JP-4 (F-40) calculations. This provides an indication of the accuracy of the model. Since the TF41 employs a pressure atomizing nozzle, to decrease drop size fuel flow must increase. In addition, JP-8 (F-35) and ARF are more viscous than JP-4 (F-40) and this requires a further increase in fuel flow to reduce the drop size. The net result is that the fuel flow rate required for ignition with an alternative fuel such as ARF is significantly higher than the flowrate required for a standard fuel such as JP-4 (F-40). In fact, the fuel flow rate required to achieve the drop sizes and primary zone equivalence ratios required for ARF is so high that it cannot be reached due to fuel pressure limitations. This indicates that for the TF41 to accommodate ARF and retain the same ignition capabilities, changes in the fuel injection system would be required.

Lean Blowoff

Flame stabilization (or lean blowoff) and ignition are similar phenomena. In both cases, a fuel and air mixture must be heated so that the fuel evaporates, mixes with the air, and chemical reactions begin at a rate sufficient for establishing a flame. The difference between ignition and flame stabilization is the energy source which initiates combustion, hot recirculating gases for flame stabilization and a spark for ignition. Consequently, it is not surprising that the formulation of the characteristic time model for lean blowoff is very similar to the ignition model. The lean blowoff model is

$$\tau_{s\ell} \sim \tau'_{hc} + a\,\tau'_{eb} \qquad (2)$$

where the definitions of the terms can be found in Table 1.

The length scale for the mixing time is selected as the length scale for CO emissions, ℓ_{co}, defined by

$$\ell_{co} = [d_{comb}^{-1} + \ell_{q}^{-1}]^{-1} \qquad (3)$$

where the quench length is chosen as the axial distance from the fuel injector to the primary air addition jets. The droplet lifetime is defined as before and for the kinetic time the pre-exponential factor is 10^{-4}, the activation energy is 21,000 cal/mole and the equivalence ratio is evaluated as the primary zone equivalence ratio. The "prime" denotes that the times are multiplied by the temperature ratio, T_{pzl}/T_{in}. This accounts for the acceleration of the flow due to the heat release in the primary zone and is included on the right-hand side of the equation to remove chemistry effects from the mixing time. For further details see Ref. 8.

The TF41 lean blowoff data were obtained at the same inlet conditions as the ignition data. The terms in Eq. (2) were calculated from the blowoff data and are shown in Fig. 4. Also included in this figure are data from two single-can combustors, the Detroit Diesel Allison T63 and the Avco-Lycoming AGT 1500. The additional data were included because of the rather narrow range of the TF41 data. With the weighting factor of 0.033 chosen to give the best fit, the correlation is not as good as the ignition correlation, but certainly statistically significant. The weighting factor and slope shown in Fig. 4 are different then those found elsewhere[8], but this is to be expected because the evaluation of fuel properties in this paper was based on the 10 percent boiling point rather than the 50 percent point used by Leonard and Mellor[8]. The 10 percent point was selected to make the calculations consistent with the ignition work where the lighter fractions of the fuel are known to be more important in the ignition process. While Fig. 4 indicates that the 10 percent point can also be used for lean blowoff, the previous correlation[8], based on the 50 percent point, may be somewhat better (lower intercept on the ordinate, but still not zero).

Figure 4 is interpreted in a manner similar to Fig. 1. The regions of stable and unstable operation of the combustor are separated by the best fit line which represents the lean limit. From a stable operating point, one moves towards the limit by decreasing the primary zon equivalence ratio (increasing τ'_{hc}) or decreasing the fuel volatility (increasing τ'_{eb}), for example. Increasing the reference velocity would result in a decrease in $\tau_{s\ell}$ and again the lean limit would be approached.

Based on the correlation in Fig. 4 the primary zone equivalence ratios at blowoff were predicted for the TF41 and the three fuels listed in Table 2; the results are presented in Fig. 5. Included in the figure are the actual data from the TF41 for JP-4 (F-40) and JP-8 (F-35). The trends of the model are validated by the data although in some cases there is disagreement between the measured and calculated values. Based on the scatter of the correlation in Fig. 4, this is to be expected.

One can see that the heavier fuels are less stable (require a higher primary zone equivalence ratio) than the lighter fuels. This difference is most pronounced at the higher altitudes with little difference occurring at the sea level condition. Based on these results, an alternative fuel with properties similar to ARF will be significantly less stable at high altitude although the effect of fuel type on lean blowoff is not as large as it is for ignition. This is partially due to the fact that droplet evaporation is not as critical a factor for lean blowoff, as discussed below.

For the ignition results, a plot comparing the change in drop size required for equivalent ignition performance of the fuels was presented. This indicated the dominance of evaporation as the controlling step in ignition. However, a plot of the drop size at the lean blowoff limit for ARF and JP-4 (F-40) in Fig. 6 shows that at the lower altitudes ARF has the larger drops. At the lower altitudes where the flame is more stable, relatively small fuel flows are required for both fuels and since the viscosity is larger for ARF the drop sizes for ARF are found to be larger. For the higher altitude cases which are

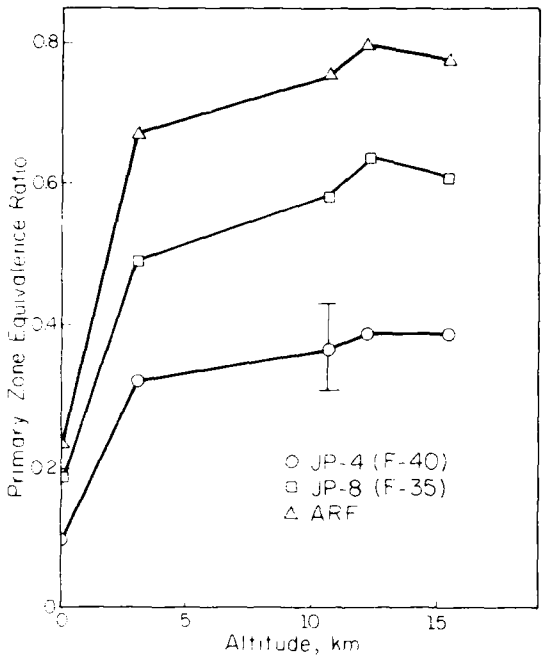


Figure 3 Predictions of primary zone equivalence ratio required for ignition

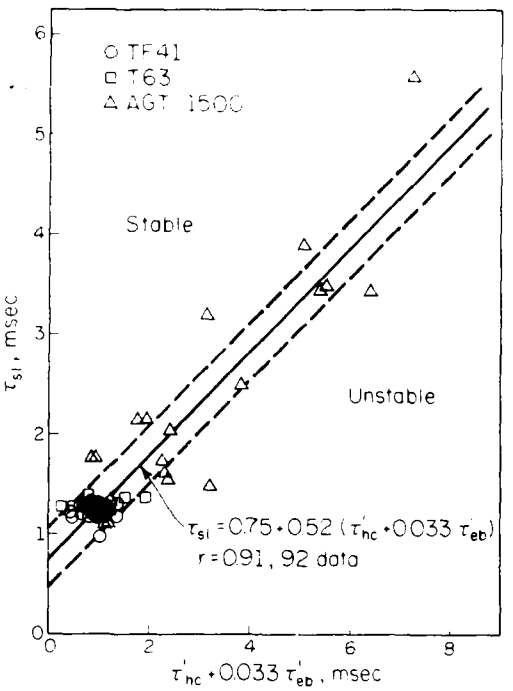


Figure 4 Lean blowoff correlation for three combustors (data from references 4, 8, 13 and 14)

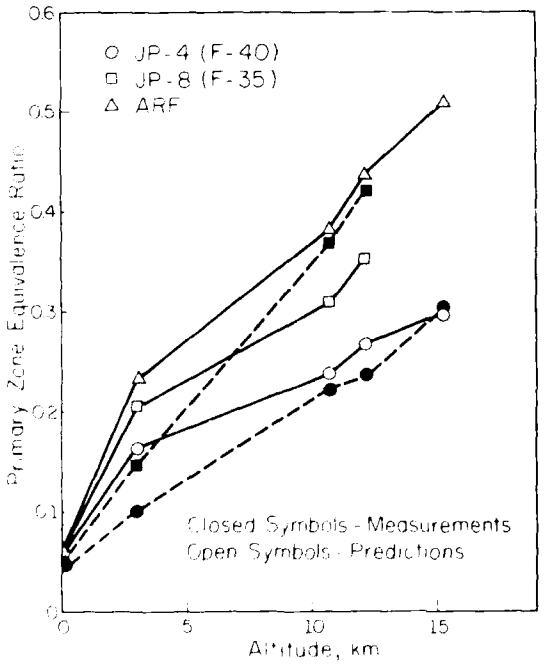


Figure 5 Predicted and measured lean limit primary zone equivalence ratios (measurements from reference 4)

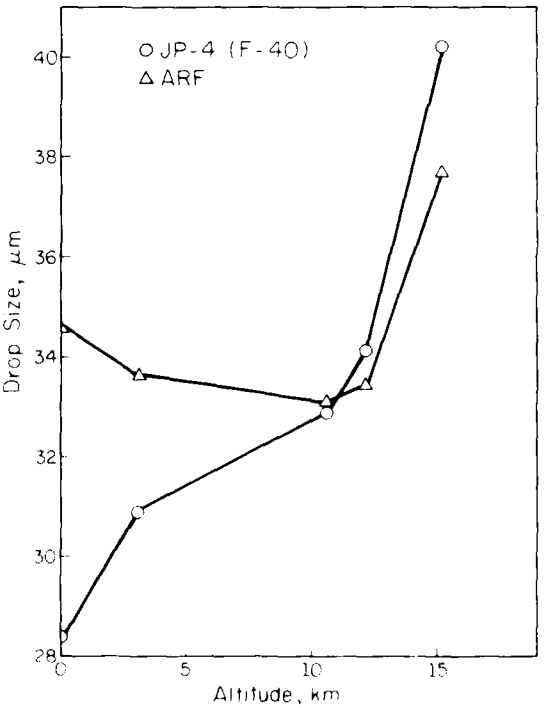


Figure 6 Predicted variation of drop size at lean blowoff

less stable, more fuel is required for ARF than for JP-4 (F-40) and consequently, the drop size for ARF is smaller than the drop size for JP-4 (F-40). Therefore, drop size changes (or evaporation rates) alone do not characterize the lean limit performance but both kinetics and evaporation are important. The important point is that the characteristic time model includes both kinetics and evaporation and by using the model the important parameters for the problem of interest can be determined.

COMBUSTION EFFICIENCY

When evaporation effects are negligible, the process which controls gas turbine combustion efficiency is the mixing of CO and hydrocarbons out of the hot shear layers before complete combustion occurs and into cooler regions of the combustor where they are quenched. In terms of the characteristic time model this means that combustion inefficiency should be proportional to the ratio of the kinetic and mixing times,

$$(1 - \eta_c) \sim \tau_\eta/\tau_{s\ell}. \qquad (4)$$

When evaporation is slow Leonard argued that the longer life (and trajectory) of the drops can cause the addition of more CO and hydrocarbons into the cooler, quenching regions[9]. With this additional contribution to combustion inefficiency the model becomes

$$(1 - \eta_c) \sim (\tau_\eta/\tau_{s\ell})/(1 + a\,\tau_{eb}/\tau_{s\ell}). \qquad (5)$$

The mixing and evaporation times are shown in Table 1 to be the same as those used for lean blowoff although for combustion efficiency the fuel properties are evaluated at the 50 percent boiling point. For the kinetic time the pre-exponential factor is 10^{-2}, the activation energy is 4500 cal/mole and the temperature is a weighted average between the inlet and exhaust,

$$T_\eta = 0.9\,T_{in} + 0.1\,T_{exh}. \qquad (6)$$

Details on the derivations of these terms can be found elsewhere[9].

With combustion efficiency data from Vogel et al.[4] at four run conditions (idle, cruise, dash and takeoff) and Eq. 5, the correlation shown in Fig. 7 was generated for the TF41. The weighting factor of 0.05 was obtained from Leonard[9] and the slope of the correlation, 3.4, compares favorably with the slope of 3.2 found by Leonard[9] for three other engines. Again, scatter is evident about the best fit line but the correlation coefficient indicates a statistically significant fit.

Based on the correlation in Fig. 7, combustion efficiency predictions were made for ARF and are presented in Fig. 8 with calculations for JP-4 (F-40) and JP-8 (F-35). As before the "error bar" indicates the range of predicted efficiency based on one standard deviation about the correlation. Above idle conditions the efficiencies are quite high and little difference is exhibited with fuel type although ARF is predicted to have the lowest efficiency. At idle conditions the separation of fuels is more pronounced indicating the increased influence of slower evaporation at the low power point of the "heavier" ARF. In general the effect of an alternative fuel with properties similar to ARF on combustion efficiency in the TF41 is small, especially at high power conditions.

CONCLUSIONS

Illustrated in this paper were the predictions of the performance of an alternative fuel in a conventional gas turbine combustor. These predictions were obtained from a relatively simple model and the predictions were supported by the favorable comparison of performance calculations for existing fuels for which data were available.

The results indicate that, for this particular engine and alternative fuel, ignition is most sensitive to fuel changes, lean limit stability performance is degraded to a lesser degree and combustion efficiency is only modestly influenced, in agreement with the conclusions of Vogel et al.[4] In particular, it was shown that fuel injection modifications would be required to retain good ignition characteristics with the alternative fuel.

The quantitative changes in performance as a function of fuel type presented in this paper can also be predicted in other engines for other alternative fuels to provide input into future combustor and fuel type considerations.

REFERENCES

1. Lefebvre, A. H., A. M. Mellor, and J. E. Peters, "Ignition/Stabilization/Atomization: Alternative Fuels in Gas Turbine Combustors," Progress in Astronautics and Aeronautics, Vol. 62, 1978, pp. 137-159.
2. Bahr, D. W., "Impacts of Broadened-Specification Fuels on Aircraft Turbine Engine Combustors," AIAA J. Energy, Vol. 6, November 1982, pp. 392-398.
3. Naegeli, D. W., L. G. Dodge, and C. A. Moses, "Sooting Tendency of Fuels Containing Polycyclic Aromatics in a Research Combustor,"AIAA J. Energy, Vol. 7, March 1983, pp. 168-175.
4. Vogel, R. E., D. L. Troth, and A. J. Verdouw, "Fuel Character Effects on Current, High Pressure Ratio, Can-Type Turbine Combustion Systems," Technical Report AFAPL-TR-79-2072, 1980.
5. Vogel, R. E., and D. L. Troth, "Fuel Character Effects on the TF41 Engine Combustion System," AIAA J. Energy, Vol. 7, May 1983, pp. 218-225.
6. Mellor, A. M., and R. M. Washam, "Characteristic Time Correlations of Pollutant Emissions from an Annular Gas Turbine Combustor," AIAA J. Energy, Vol. 3, July 1979, pp. 250-253.

7. Peters, J. E. and A. M. Mellor, "A Spark Ignition Model for Liquid Fuel Sprays Applied to Gas Turbine Engines," AIAA J. Energy, Vol. 6, July 1982, pp. 272-274.
8. Leonard, P. A. and A. M. Mellor, "Correlation of Lean Blowoff of Gas Turbine Combustors Using Alternative Fuels," to be published in the AIAA J. Energy.
9. Leonard, P. A., "Correlation of the Effects of Fuel Type on Gas Turbine Combustor Efficiency," Ph.D. Thesis, Purdue University 1981.
10. Godsave, G. A. E., "Studies on the Combustion of Drops in a Fuel Spray-the Burning of Single Drops of Fuel," Fourth Symposium (International) on Combustion, Williams and Wilkins, Baltimore, 1953, pp. 818-830.
11. Jasuja, A. K., "Atomization of Crude and Residual Fuel Oils," ASME Paper No. 48-GT-83.
12. Peters, J. E., "An Ignition Model for Gas Turbine Engines," Ph.D. Thesis, Purdue University, 1981.
13. Moses, C. A., and D. W. Naegeli, "Fuel Property Effects on Combustor Performance," Gas Turbine Combustor Design Problems, Lefebvre, A. H., ed., Hemisphere Publishing, New York, 1978, pp. 39-69.
14. Schmidt, D. A., Personal communication from Avco-Lycoming, 1979.

ACKNOWLEDGEMENTS

The author wishes to thank R. Enlow and J. Kirwan for their help with the calculations required for this paper.

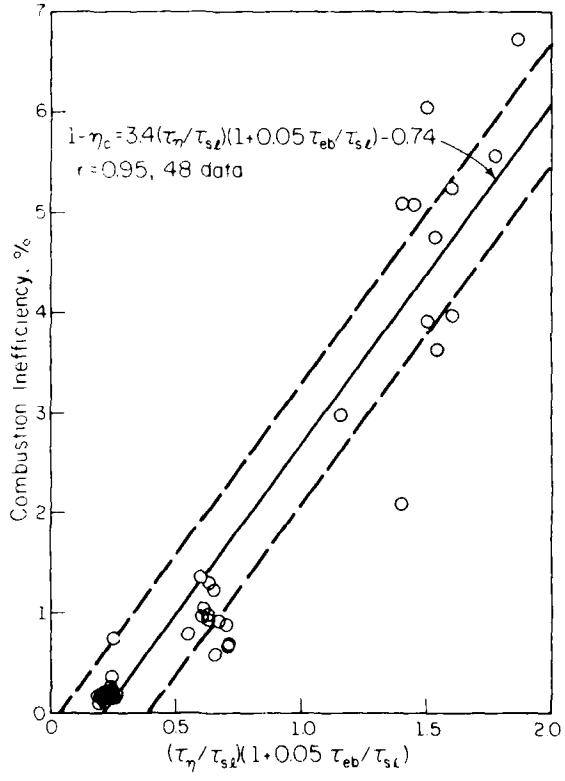


Figure 7 TF41 combustion efficiency correlation (data from reference 4)

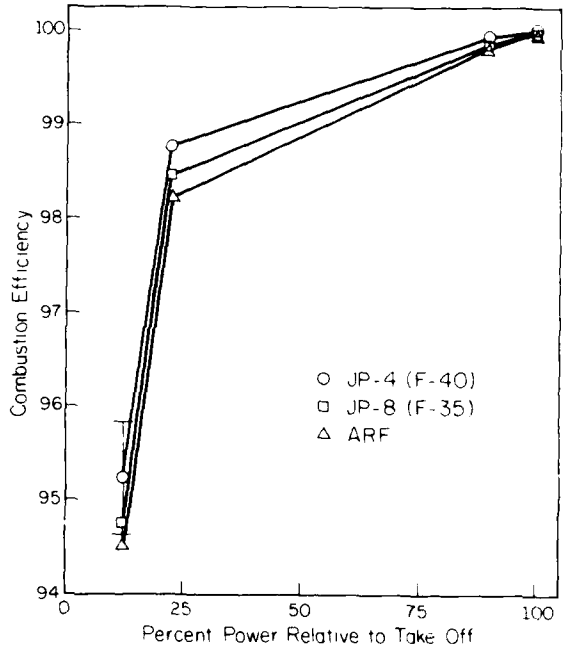


Figure 8 Predictions of combustion efficiency

DISCUSSION

D.Snape, UK

(1) Your correlations lead to results for ignition only. Have you considered the effects on the whole primary and post primary zones leading to any conclusions about the inter-combustor light-round phase of start-up, which is particularly difficult in tubo-annular systems?

(2) You conclude that combustion efficiency is only moderately influenced by fuel type. Would you expect this to hold good for combustors, such as the Transply combustor in Paper 23, which have much higher combustion efficiencies throughout the engine operating range?

Author's Reply

(1) The ignition model currently considers only the growth of the spark kernel and not the question of flame spread from can to can. This would be an interesting and important problem to address.

(2) Based on the analysis of other engines which do have high efficiencies throughout their operating range (see Leonard and Mellor, Journal of Energy), I expect the conclusion that combustion efficiency will be only slightly influenced by fuel type to hold for engines which are efficient at low power.

J.Tilston, UK

In Figure 7 the correlation, which you said contained data scatter, is made on the basis of a linear relationship of efficiency with characteristic times. The relationship should correlate on the basis of the conventional loading equations which, from first principles, would contain exponential and power law terms. The data certainly look as though they would be much better fitted by a fairly simple curve.

Author's Reply

In the development of the carbon monoxide correlation parameter (see Tuttle et al., *16th Symposium (International) on Combustion*) an exponential does occur but it is expanded and all higher order terms are dropped for simplicity. Retaining the more complete exponential term might be useful but as yet has not been necessary.

P.Ramette, Fr

L'efficacité de combustion est exprimée en fonction d'un temps cinétique, fonction exponentielle d'une température cinétique qui est une pondération entre les températures d'entrée et de sortie. Comment est déterminée cette pondération? Est-ce que la pression ne devrait pas intervenir?

Author's Reply

The temperature that appears in the kinetic time was empirically selected to provide the best correlation of efficiency data obtained from earlier experimental work. Certainly a kinetic time can be derived which includes pressure, but the model has been successfully applied to data with pressure variations between 200 and 800 kPa and therefore a pressure term is not necessarily required.

ETUDE AERODYNAMIQUE DE LA COMBUSTION DANS LES FOYERS DE TURBOMACHINES : APPROCHES EXPERIMENTALES ET THEORIQUES

par Guy FRAGER, Patrick HEBRARD, Gérard LAVERGNE, Ahmed MIR

OFFICE NATIONAL D'ETUDES ET DE RECHERCHES AEROSPATIALES
CENTRE D'ETUDES ET DE RECHERCHES DE TOULOUSE
Département de Mécanique et Energétique des Systèmes (DERMES)
2, Avenue Edouard Belin. 31055 TOULOUSE CEDEX
FRANCE

RESUME :

Au lieu des méthodes locales de résolution souvent trop coûteuses au stade de l'avant-projet de foyers, on a souvent avantage à utiliser une des deux approches suivantes:méthode modulaire, méthode mixte.

- Méthode modulaire:De nombreuses expériences menées sur maquettes hydrauliques et faisant appel à diverses techniques de traitement d'image vidéo fournissent les données de base utilisées dans la schématisation de divers foyers sous forme d'une combinaison de réacteurs élémentaires. L'adjonction de cinétiques chimiques plus ou moins détaillées (modèle global, semi global, avec vaporisation) permet de prédire avec une bonne précision les performances globales de ces divers foyers.

- Méthode mixte : Dans cette seconde méthode, plus précise, seules les zones de recirculation sont modélisées par assemblage de réacteurs élémentaires. Les régions d'écoulement direct (jet, swirlers...) font l'objet d'un calcul local (K, ε) dans lequel le comportement des gouttes (taille, trajectoire, vaporisation) est pris en compte à partir d'un ensemble de mesures géométriques effectuées au DERMES.

NOTATIONS :

B	Blocage géométrique
C	Concentration
C_{vap}	Chaleur spécifique du gaz
d, $\bar{d}$, DM	Diamètre des gouttes (valeur individuelle ou moyenne)
f (t)	Distribution de temps de séjour
f (d)	Histogramme de tailles de gouttes
f_J	Concentration en moles/kg de gouttes de la classe J
J	Classe de gouttes
L	Chaleur latente de vaporisation
Pp et PL	Grandeurs intervenant pour la mesure de tailles de gouttes
q	Débit de traceur
Q	Débit de gaz
Q_1	Débit des jets primaires
Q_2	Débit des jets de dilution
Qsw	Débit des injecteurs à swirler
Q_c	Débit des cannes de prévaporisation
$QF_{C\ 1,\ 2..}$	Débit de refroidissement
QR_1	Débit recirculé en fond de chambre
QR_2	Débit recirculé latéralement
$Re = \frac{Vrel \times d}{\nu}$	Nombre de Reynolds
$S = r^2 = d^2/4$	
T	Température
V, Va,	Vitesse de l'air
Vrel	Vitesse relative goutte air
W°	Vitesse de réaction
n, a, E	Constantes de la vitesse de réaction
α_m	Angle des jets (par rapport à la normale)
ΔP_J	Pression d'injection
τ	Temps de séjour moyen
φ	Richesse
$\Omega = \frac{Q}{\sqrt{p^{T/E}}}$	Facteur de charge
λ	Longueur d'onde, conduction phase vapeur
σ	Tension superficielle
ρ	Masse volumique

I - INTRODUCTION

Les processus rencontrés dans les chambres de combustion sont particulièrement complexes et fortement couplés entre eux (écoulement turbulent 3.D en régime stationnaire ou non avec mélange diphasique, cinétique chimique, radiation...) De ce fait, le calcul des performances de foyers (stabilité, rendement, pollution) exige la mise en oeuvre de techniques de modèlisation qui peuvent se classer selon les trois groupes suivants correspondant à une description plus ou moins fine de l'aérodynamique du foyer :

L'approche locale (par exemple 16) consiste à résoudre un ensemble d'équations aux dérivées partielles régissant les différents phénomènes évoqués plus haut. (Combustion turbulente dans un écoulement tridimensionnel éventuellement diphasique). Utile pour accèder à la description fine de l'écoulement, cette méthode conduit souvent à de réelles difficultés dans sa mise en oeuvre : adaptation du modèle numérique à chaque cas étudié, difficulté de convergence avec des géométries complexes, cinétique chimique limitée. De ce fait, au moins au stade initial de développement d'un foyer, on lui préfère souvent une approche de type modulaire.

Dans cette approche modulaire (1 à 12) permettant d'apprécier les mêmes phénomènes à une échelle plus grossière, l'écoulement est discrétisé en plusieurs modules (réacteurs élémentaires) vérifiant certaines hypothèses (nature, volume, débit). Souvent utilisée en particulier pour des études paramètriques ou d'optimisation, cette méthode présente fréquemment un certain empirisme dans la définition de modèles souvent choisis a priori.

Enfin une troisième approche dite mixte (13 à 15) tente de réaliser un compromis entre les deux précédentes en ce sens qu'elle combine un calcul local pour les zones d'écoulement direct (jets, swirlers..) et un calcul modulaire dans les zones où cette dernière devient délicate (zones de recirculation). Outre l'avantage que certaines valeurs de variables (par exemple les répartitions de débit) sont un résultat de calcul et non pas une donnée expérimentale, cette méthode permet aussi, sans entraîner des coûts excessifs, de rendre compte de façon assez fine du comportement des gouttes de carburant (pulvérisation, vaporisation, trajectoires).

Etant plus spécialement intéressés aux deux dernières approches, que nous présentons dans cet article, nous nous sommes appuyés sur des résultats expérimentaux obtenus au C.E.R.T., concernant soit la description aérodynamique de l'écoulement, soit les caractéristiques granulométriques des injecteurs.

Pour la description aérodynamique de l'écoulement, les caractéristiques (nature, volume, distribution de temps de séjour) des réacteurs élémentaires utilisés dans le modèle modulaire sont déduites d'expériences menées sur maquettes hydrauliques. Une analyse automatique d'images vidéo obtenues sur l'écoulement donne diverses informations, telles que : concentration, débits, temps de séjour. Ces informations, associées à diverses techniques d'identification permettent de définir pour chaque chambre essayée une représentation adéquate sous forme de combinaison de réacteurs élémentaires. L'utilisation de ces méthodes pour des géométries de chambres très variées nous a conduit à dégager diverses corrélations tant sur la représentation modulaire de ces foyers que sur certaines répartitions de débits en fonction de paramètres caractéristiques.

Afin de pouvoir mieux caractériser l'influence de la pulvérisation de carburants liquides sur la cinétique chimique, une simulation a été réalisée au moyen de mélange eau alcool injecté sous pression dans un écoulement à grande vitesse. Une technique originale de granulométrie appliquée à diverses conditions d'écoulement nous a conduit à déterminer des lois d'évolution du diamètre moyen de Sauter et de la forme de panaches en fonction des paramètres principaux (pression d'injection, vitesse moyenne et taux de turbulence de l'écoulement, liquide injecté...).

Enfin, la prise en compte d'une cinétique chimique sous la forme de modèles "global" à une seule réaction ou "semi global" à deux étapes et tenant compte de la vaporisation des gouttes permet de calculer les performances globales des foyers. Ces résultats de calcul, comparés aux mesures en combustion effectuées à l'O.N.E.R.A., permettent par leur précision de justifier a posteriori le bien fondé d'une telle démarche, au moins au stade de l'avant-projet.

II - ETUDE EXPERIMENTALE

Comme permet de le montrer un survol rapide de la littérature sur ce sujet (1 à 12), un des principaux problèmes dans la représentation modulaire de foyer est de caractériser ces différents réacteurs élémentaires en termes de volume, position, interconnection. De la même façon, l'existence de deux phases dans l'écoulement nécessite de pouvoir définir correctement les caractéristiques de pulvérisation relatives à chaque type d'injection.

Pour ces deux approches, nous avons choisi des conditions expérimentales en écoulement isotherme : maquettes hydrauliques pour étudier l'aérodynamique interne, banc aérodynamique aux conditions atmosphériques pour étudier la pulvérisation. Bien que sujet à controverses, ce choix a été fait avant tout afin de permettre un nombre important de mesures dans des conditions expérimentales plus simples, le but étant principalement de donner une description grossière mais réaliste de l'écoulement plutôt que de préciser de façon ponctuelle ses conditions exactes avec et sans combustion. Il semble suffisant d'assurer une similitude géométrique ainsi qu'un nombre de Reynolds supérieur à une valeur critique (17) le passage aux conditions avec combustion se faisant soit sans correction, soit à partir de corrélations, soit au moyen de certaines règles, telles que celles suggérées par Spalding (17).

2.1. Moyens d'essai

2.1.1. Tunnel hydrodynamique

Comme le montre la photo 1 un tunnel hydrodynamqiue à veine horizontale fonctionnant en circuit ouvert (10 l/s) ou fermé (20 l/s) permet d'étudier différents modèles de maquettes réalisées en plexiglass. Ces maquettes transparentes sont de trois types :

- maquettes à échelle réduite de foyers réels (en général foyers de statoréacteurs)
- représentation bidimensionnelle de secteur de foyers annulaires
- modèles simplifiés de zones primaires.

De nombreux résultats concernant plusieurs de ces maquettes ont déjà été présentés (12,18, 19), les résultats contenus dans cet article sont relatifs à deux maquettes de secteur de foyer annulaire comportant des injecteurs à simple et double swirlers.

2.1.2. Banc granulomètrique

Ce banc (Fig. 2) est constitué par une veine d'essais 150 x 150 réalisée en plexiglass dans laquelle on peut générer un écoulement à vitesse (0 à 150 m/s) et taux de turbulence (2% à 10%) variables. Afin de simuler au mieux les conditions d'injection réelles, on peut y introduire diverses singularités telles que accroche flamme, générateur de swirl... L'injecteur à caractériser, peut se translater dans trois directions ; un système d'injection comportant un réservoir pressurisé (0 à 20 bar), un capteur de pression, une électrovanne permet d'injecter le liquide à étudier (par exemple un mélange eau alcool assurant une tension superficielle σ_J variant de 23 à 72 dynes/cm) sous une pression Δp_J variable.

2.2. Moyens de visualisation et de mesure

En plus des techniques classiques de visualisation (bulles d'air ou d'hydrogène, particules de polystyrène, fluorescéine) utilisées sur le banc hydraulique nous avons développé un certain nombre de moyens associant : caméra vidéo ou C.C.D, microcalculateur et interfaces afin de compléter ces visualisations par différentes mesures. Ces méthodes sont largement décrites par ailleurs (20 à 23), nous les résumons succintement.

2.2.1. Mesure de concentration

Dans cette application la concentration instantanée d'un traceur coloré (fluorescéine), moyennée à l'intérieur d'une surface élémentaire définie par le plan d'éclairage (fente lumineuse, "tranche" laser) et une fenêtre d'analyse générée sur le moniteur associé à la caméra observant l'écoulement est mesurée. De nombreux étalonnages effectués "in situ" (20, 23) nous ont permis de relier, pour des conditions d'éclairage données, la concentration du traceur à la brillance locale de l'image vidéo. Cette brillance, convertie en une tension analogique qui peut être numérisée sur 12 bits et mise en mémoire du calculateur en synchronisme avec chaque trame, permet donc pour diverses conditions d'injection pilotées par le calculateur (continue, Dirac, échelon) de mesurer les grandeurs suivantes : débit, temps de séjour, concentration.... Moyennant certaines précautions (23), cette méthode permet de mesurer en continu (une information par trame soit tous les 50ème ou 60 ème de seconde) une concentration locale ou moyenne avec une précision de 1% à 2%. (Figure 5).

2.2.2. Mesure de taille de gouttes

Comme le montre la figure 2 , la mesure granulomètrique est obtenue dans un plan (parallèle ou perpendiculaire à l'écoulement) défini par un laser He/Ne de 15 mW auquel est éventuellement associé un miroir vibrant ou une lentille plan convexe (22). Le système de mesure comporte : un dispositif optique, une caméra CCD Hitachi, un microcalculateur et ses périphériques, plusieurs interfaces. (Figure 3).

Dispositif optique : compte tenu du faible diamètre des gouttelettes (10 µm à 100 µm) un dispositif optique est nécessaire pour produire sur la matrice de la caméra une image de taille suffisante. Ce dispositif comporte un télescope Newton (focale 600 mm, diamètre 150 mm) et un microscope (grossisement G = 8) monté sur la caméra avec une bague rallonge.

Module d'acquisition : Ce module, réalisé au C.E.R.T./D.E.R.M.E.S., comporte trois cartes à fonctions distinctes (22) :

① Elle synchronise la caméra au balayage moniteur du microcalculateur et numérise sur 1 bit l'image des gouttelettes (240 lignes x 320 pixels par ligne) vues sur le moniteur.

② Cette seconde carte mémorise l'image (200 lignes x 320 pixels) en une trame en synchronisme avec le microcalculateur.

③ La troisième carte permet l'analyse de cette image en 6 s au moyen d'un curseur vertical comptant le nombre de points Pp situés à l'intérieur des images de gouttes et le nombre d'intersections PL avec le maillage. Comme le montre la figure 2 , pour chaque image, le diamètre moyen est donné (24) par :

$$DM = 3\ Pp\ /PL$$

Compte tenu du principe, un étalonnage du système est nécessaire (22-25) afin de déterminer le coefficient d'étalonnage en fonction des divers paramètres (angle de prise de vue β, grossissement G, indice de réfraction n, longueur d'onde λ, seuil de détection S). Ceci est effectué avec des microbilles de verre calibrées présentant le même indice ; on obtient ainsi une précision voisine de 5 µm avec un seuil de détection de 5 µm.

2.3. Techniques d'identification

A partir des mesures de concentration effectuées suivant le principe décrit en 2.2.1., plusieurs méthodes ont été définies de façon à donner diverses informations quantitatives suivant les modes d'injection de traceur (23).

2.3.1. Injection continue

Dans le cas où le traceur coloré est injecté de façon continue avec un débit q, la mesure de la concentration $\bar{C}$ moyennée sur un volume (réacteur) élémentaire permet de mesurer :

- soit le débit Q le traversant si le traceur est injecté dans ce volume,

$$Q = q/\bar{C}$$

Cette mesure de débit par dilution est très utile pour déterminer les divers débits alimentant le foyer (débit primaire, dilution...) ainsi que certains débits caractéristiques (QR_1 : débit recirculant en fond de chambre)

- soit la concentration (richesse) locale en fonction de la concentration (richesse) à laquelle est injecté, à l'intérieur ou à l'extérieur du volume, un traceur simulant le carburant.

2.3.2. Injection suivant un échelon

Dans ce cas, la variation de concentration Cs (t) est proportionnelle à la fonction

de répartition de temps de séjour

$$Cs(t) \sim F(t) = \int_0^t f(t)\,dt \qquad (26)$$

On peut ainsi obtenir les premières informations sur la nature du macromélange (foyer homogène, réacteur piston...) ainsi que sur le volume du réacteur élémentaire considéré à partir de la mesure du temps de séjour moyen τ.

$$V = Q.\tau \qquad (26\ )$$

2.3.3. Injection suivant un Dirac

Les mesures obtenues à partir d'une injection sous forme d'un "créneau" de durée Δt négligeable par rapport aux temps caractéristiques ($\Delta t / \tau \ll 10^{-1}$) permettent d'obtenir plus d'informations puisque dans ce cas Cs (t) varie comme la distribution de temps de séjour (26)

$$Cs(t) \sim f(t)$$

Les courbes obtenues présentent l'allure caractéristique montrée à la figure 4 à partir de laquelle on peut identifier l'écoulement à un ensemble de réacteurs avec retour tel que représenté sur Fig. 4 . Afin d'effectuer ceci, nous avons développé un ensemble de méthodes simples d'identification (23) permettant de déterminer les caractéristiques principales de l'assemblage de foyers (nombre de foyers homogènes dans la chaîne directe : N et retour : M, taux de débit entraîné R, temps de séjour moyen...) en fonction de caractéristiques simples de la courbe f (t) (temps du premier pic θmax, et entre pics tc, écart type $\Delta\theta$).

Ces méthodes, particulièrement simples à utiliser permettent dans la majeure partie des cas d'aboutir à une représentation modulaire détaillée de l'écoulement à partir des mesures de concentration et des visualisations qualitatives.

2.4. Résultats sur l'aérodynamique des chambres

2.4.1. Description de l'écoulement (Figures 5, 6).

La chambre étudiée comporte d'amont en aval :

- un ensemble d'injecteurs à swirler situés sur le fond (simple ou double vrilles) traversés par un débit Qsw et recevant le carburant liquide,
- sur chaque côté une rangée d'orifices primaires circulaires recevant un débit Q_1
- en aval deux rangées d'orifices de dilution traversés par Q_2
- enfin d'amont en aval, un ensemble de films de refroidissement de débits notés QFC_1, QFC_2 - -

Comme le montrent les figures 5 et 6 , on peut distinguer les deux zones suivantes :

amont des orifices primaires : ce fond de chambre est alimenté par les trois débits suivants : Qsw (débit swirler) QR_1 (fraction du jet primaire recirculant en fond de chambre) QFC_1 dont une partie, proportionnelle au blocage des jets primaires alimente le fond de chambre.

Comme on peut le voir, le débit Qsw génère deux zones tourbillonnaires : 1 à l'intérieur du cône, 2 entre le cône et la chambre.

Cette description aérodynamique, voisine de celle décrite dans (1) correspond bien aux trois types de recirculation distincts dus à l'écoulement principal :

- A l'intérieur du cône, la recirculation centrale notée 1 est due au gradient de pression causé par le swirl (1 à 12), sa présence explique la stabilité de la flamme dans la zone primaire grâce au courant de retour central qui permet de recirculer en entrée une partie des gaz chauds.

- Entre les swirlers et le tube à flamme, la recirculation notée 2 est due avant tout à l'effet d'élargissement brusque entre le diamètre des swirlers et le tube à flamme. Elle est souvent ignorée par de nombreux auteurs (1,4...)

- Contrairement aux deux précédentes associées à une recirculation de gaz chauds et réactifs en fond de chambre, la troisième zone notée 1' correspond à une recirculation d'une partie des gaz frais issus des jets primaires (QR_1). Ce phénomène, dû avant tout à l'impact des jets est cité en particulier dans (3 à 7) et dans une certaine mesure (8,9).

Remarque 1 : Comme on peut le voir à la figure 6 , chaque zone de recirculation 1 2 , 1' est représentée par un foyer homogène 1, 2, 1'dans le cas du double swirler. Pour un swirler unique et dans la majorité des cas, on regroupe les deux réacteurs 1 et 1' en un réacteur unique (12, 18, 19). (Figure 5).

Remarque 2 : Comme permet de le montrer la figure 7 , la modélisation des volumes 1 ou 2 suivant un seul foyer homogène constitue une schematisation par rapport à la realité. En effet chaque volume comporte un écoulement principal I et un courant de retour II entre lesquels circule un débit entraîné qui souvent confondu dans la littérature avec le débit recirculé QR_1

Entre les orifices : Cette zone est le siège de tourbillons longitudinaux importants (12) alimentés par une partie QR_2 du débit des jets primaires, le débit venant du fond de chambre ainsi qu'une partie du débit de refroidissement.(Figures 5 et 6).

Remarque : Il est intéressant de rapprocher cette description succinte de l'écoulement donnée plus en détail dans (27) ainsi que la modélisation qui lui est associée de celle obtenue pour d'autres géométries de chambre (12, 18, 19) afin d'en dégager certaines règles.

- Dans tous les cas la zone entre orifices primaires et dilution comporte une zone de réacteur piston (partie Qp du jet primaire, et film de refroidissement) une recirculation importante (foyer homogène et réacteur piston en série) alimentée par QR_2 et le débit de fond de chambre.

- Le fond de chambre est alimenté par une partie QR_1 du débit primaire fonction de divers

paramètres (voir 2.4...) et éventuellement des débits annexes Qsw (swirlers), Qc (cannes à prévaporisation), QFC (refroidissement). Par contre, la représentation modulaire dépend du mode d'injection en se simplifiant lorsque l'on passe de la configuration avec double puis simple swirler, cannes de prévaporisation, à celle sans rien.

- De façon générale, on peut considérer que le débit des films de refroidissement se répartit dans la chambre au pro rata du blocage des jets rencontrés.

2.4.2. Corrélations pour le débit QR_1

La valeur du débit QR_1 venant recirculer en fond de chambre est un paramètre capital puisque ce débit participe directement à la combustion, or de nombreux auteurs (1, 11) la fixent de façon empirique ou sujette à caution.

Une partie importante du travail effectué au C.E.R.T. étant une étude paramétrique particulièrement utile aux premiers stades de développement d'un foyer, il nous semblait important de connaître l'influence de paramètres géométriques sur les différents débits Q_1, Q_2... ainsi que sur la décomposition de Q_1 entre les débits QR_1, QR_2 et QP. Ce travail a été effectué d'une part expérimentalement à partir de chambres (turboréacteurs, statoréacteurs, géométries simplifiées) de géométries diverses (12, 18, 19) d'autre part analytiquement à partir de considérations simples sur les équations de bilan (continuité, quantité de mouvement...) (27 à 29).

Ces deux approches conduisent à des résultats semblables qui mettent en évidence l'influence des paramètres principaux suivants :

α_m angle des jets primaires

B blocage des jets primaires

débit des cannes ou du swirler Qc/Q_1 ou Qsw/Q_1

(éventuellement) volume du dôme.

Nota : Ces résultats ont été confrontés avec succès pour des géométries de chambres très diverses et les résultats de calcul comparés aux essais combustion (12, 19) confirmant bien le fait que, au moins à faibles valeurs de blocage et d'angle, la combustion n'a qu'un effet secondaire sur le taux QR_1/Q_1 (29). Ceci n'est évidemment pas le cas sur le débit entraîné Qe dont le taux Qe/Q_1 varie sensiblement comme suit :

$$Qe/Q_1 \sim (TJ/Tc)^{1/2} \qquad (29)$$

TJ : température moyenne du jet
Tc : température moyenne de la recirculation.

2.5. Résultats sur la pulvérisation

Comme nous l'avons noté plus haut, la méthode de mesure peut s'appliquer à divers cas d'écoulements. Cependant jusqu'à présent cette méthode, développée récemment, n'a été appliquée qu'au cas d'un injecteur aérodynamique à swirler placé dans un écoulement uniforme. Bien que les résultats obtenus ne soient pas directement applicables aux chambres de turboréacteur sans vérification supplémentaire, il nous a semblé utile de les présenter puisque nous les utilisons dans les modèlisations présentées ci-dessous.

Comme le montrent les diverses courbes (Fig. 9) présentées, le diamètre moyen de Sauter peut s'exprimer de la façon suivante :

$$\frac{DMS}{(DMS)_0} = \left(\frac{Va}{(Va)_0}\right)^{0,38} \cdot \left(\frac{\Delta P_j}{\Delta P_{j0}}\right)^{-0,22} \cdot (1+\tau_u) \cdot \left(\frac{\sigma}{\sigma_0}\right)^{0,42}$$

Ces résultats, donnés en détail dans (22, 25) sont voisins de ceux trouvés dans la littérature (voir dans 22). Notons cependant qu'ils correspondent à une moyenne ; de nombreuses mesures ayant été effectuées à diverses positions axiales et radiales par rapport à l'injecteur. Ces mesures ont aussi été complétées par des histogrammes tels que celui présenté à la figure 10.

III - MODELISATION

Dans l'introduction, nous avons succintement présenté les caractéristiques principales de deux méthodes de calcul que nous avons développé : méthode modulaire et méthode mixte. Avant de décrire chacune d'elle, il nous a semblé utile de donner quelques détails sur les équations utilisées, en particulier pour ce qui concerne le caractère diphasique de l'écoulement.

3.1. Mise en équations

Les équations de base pour étudier les différents phénomènes ne sont autres que les équations de transport pour diverses quantités : espèces (Y_i), énergie (h), gouttes liquides de taille (fJ)...
Toutes ces équations se présentent sous la forme classique suivante :

$$\frac{\partial \varphi}{\partial t} = \frac{\partial}{\partial x_i}\left(\Gamma_\varphi \frac{\partial \varphi}{\partial x_i}\right) + S_\varphi$$

Convection Diffusion source

avec φ : u, v, h, k, ε, Y_i

Le terme source S_φ qui dépend de la quantité φ transportée est relativement bien connu pour les variables classiques (30); nous allons établir la forme particulière de l'équation pour les différentes classes de gouttes J = 1, ..., K.

3.1.1. Modèle d'évaporation

En plus de la phase vapeur (J = 0) le fuel peut être représenté par k classes (J = 1....K) de gouttes de largeur constante et notée chacune par son diamètre moyen de J = 1 (petite classe) à J = K (taille maximale). En réalité, au lieu du diamètre on utilise en général $s = r^3$; la classe J est alors représentée par la concentration fJ (moles/Kg) de gouttes ayant une valeur de s entre s_{J-1} et s_J.

Afin d'évaluer le terme source de chaque classe J , nous avons utilisé le modèle d'évaporation de Wise et Agoston (31) modifié de façon à tenir compte de la convection forcée en cas de vitesse relative Vrel goutte-gaz :

$$m^\circ = 4\pi . r \frac{\lambda}{Cvap} \text{Log}\ (1 + B)\ (1 + 0{,}244\ Re^{0,5})$$

avec $B = CV \dfrac{T\infty - Tl}{L}$ et $Re = \dfrac{Vrel \times d}{\nu}$

Pour chaque classe J, le terme source peut se mettre sous la forme suivante (32)

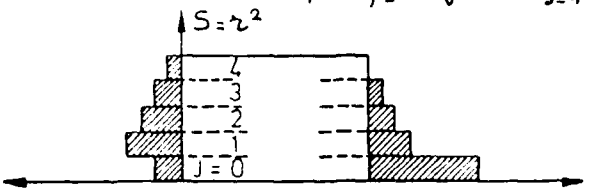
$$(S\psi)_J = \frac{2\pi r \rho}{\rho l} d\log(1+B)\left\{\frac{f_{J+1}}{S_{J+1} - S_J} - \frac{f_J}{S_J - S_{J-1}} - \frac{3}{2}\frac{f_J}{S_J}\right\}$$

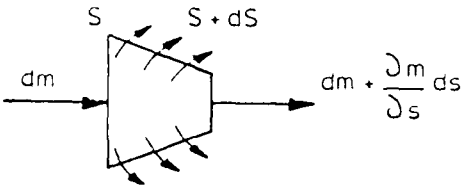
où les trois termes de la parenthèse désignent respectivement :

- le transfert de gouttes de la classe J + 1 à J
- le transfert de gouttes de la classe J à J - 1
- le taux d'évaporation de la classe J.

Le taux d'évaporation total est donc fourni par :

$$S_{vap} = \frac{2\pi r \rho}{\rho L} \log(1+B) \sum_{J=1}^{K} \frac{3}{2} \frac{f_J}{S_J}$$





3.1.2. Mise en vitesse des gouttes

Les gouttes étant généralement injectées avec une vitesse relative initiale par rapport à l'écoulement, cette dernière diminue avec le temps suivant la relation :

$$\frac{dVrel}{dt} = -\frac{3}{8} \frac{Cx\ \rho a}{r\ .\ \rho L} V\ rel^2$$

où le coefficient de trainée Cx est exprimé par la loi de Vincent (33) :

$Cx = 0{,}48 + 28/Re^{0,85}$

3.1.3. Cinétique chimique

Compte tenu de la complexité d'un modèle complet de cinétique chimique pour l'hydrocarbure, deux types de modèles simplifiés ont été utilisés. Il faut noter que bien que ceci ne représente pas la réalité, les phénomènes d'évaporation et de combustion sont considérés comme étant successifs, seule la phase gazeuse du fuel participant à la combustion.

Modèle global : Dans ce modèle (12, 19, 32, 34) spécialement adapté pour estimer les limites d'extinction pauvre, une seule réaction d'oxydation du combustible est envisagée

$$K + \nu O_2 \longrightarrow P$$

La vitesse de combustion est donnée par :

$$W^\circ = kT^{\alpha}\ (\rho\, yO_2)^a\ (\rho\, yK)^{n-a} e^{-E/T}$$

Modèle quasi global : Dans ce schéma proposé par Edelman et Fortune (35) on représente une première étape quasi globale donnant CO et H_2 suivi par plusieurs réactions d'oxydation usuelles pour CO et H_2.

Réaction		A	α	T
$C_{10}H_{20} + 5O_2 \rightarrow 10CO + 10\ H_2$		$8\ 10^{11}$	0	7500
$CO + OH \rightleftharpoons CO_2 + H$		$1.5\ 10^{11}$	0	500
$O + H_2O \rightleftharpoons 2OH$		$..7610^{13}$	-0.02	8370
$H + H + M \rightleftharpoons H_2 + M$		10^{12}	- 1	0
$O + O + M \rightleftharpoons O_2 + M$		$2\ 10^{9}$	-0.4	0
$OH + H + M \rightarrow H_2O + M$		$1.5\ 10^{11}$	-0.5	0
$H + O_2 \rightleftharpoons OH + O$		$2\ 10^{14}$	0	8330
$O + H_2 \rightleftharpoons OH + H$		$6\ 10^{13}$	0	5000
$H + H_2O \rightleftharpoons OH + H_2$		$5.5\ 10^{13}$	-0.01	9890
$OH + M \rightleftharpoons O + H + M$		$6.\ 961C^{13}$	0.21	50450
$N_2 + O \rightleftharpoons NO + N$		$0.8\ 10^{13}$	0	37500
$N + O_2 \rightleftharpoons NO + O$		2.6710^{10}	0.5	3521
$N + OH \rightleftharpoons NO + H$		$2.8\ 10^{13}$	0	0

3.2. Modèle modulaire

Après un bref rappel sur ce modèle déjà décrit par ailleurs (12, 18, 19, 27) on montre comment adapter l'aspect diphasique et quelques exemples sont présentés.

3.2.1. Modèle

Le concept de base de cette représentation est le "réacteur parfaitement mélangé" (R.P.M.) puisque le degré de mélange macroscopique, lié à la distribution de temps de séjour f (t), permet de représenter un réacteur quelconque par un assemblage : série, parallèle, retour de foyers homogènes (2.4.4. et 2.5).

Dans un tel réacteur, la dynamique du mélange est infiniment rapide constituant ainsi un microfluide idéal dans lequel la combustion est contrôlée par la cinétique chimique.

En réalité, des réacteurs élémentaires peuvent, tout comme le R.P.M. avoir un mélange macroscopique parfait avec :

$$f(t) = \frac{1}{\tau} e^{-t/\tau}$$

mais un degré de mélange microscopique partiel.

Dans ce cas deux approches sont envisageables :

- soit on utilise un modèle de combustion turbulente fondé sur la notion de densité de probabilité conjointe (30) tel le modèle "eddy break up",

- soit de manière simplifiée (15) on calcule la fraction de fluide mélangé de façon microscopique (fonction de la perte de charge).

Remarque 1 : Dans les différentes applications envisagées, on a essayé de tenir compte de l'existence d'une vitesse relative sous la forme suivante : à partir d'une vitesse relative initiale estimée par les conditions d'injection (pression) et la vitesse moyenne du gaz dans le réacteur (Vé = l/τ) on calcule la vitesse relative instantanée jusqu'à un temps égal à τ, la valeur moyenne entre 0 et τ est prise comme vitesse moyenne relative.

Remarque 2 : N'ayant pas forcément de résultats expérimentaux applicables aux cas étudiés, nous avons choisi a priori une distribution type Rosin Rambler

$$f(d) = \frac{1}{\bar{d}} \left(\frac{d}{\bar{d}}\right)^{n-1} e^{-(d/\bar{d})^n}$$

dans laquelle $\bar{d}$ est le diamètre moyen dont on estime la variation à partir des corrélations présentées ci-dessus (3.5) et n inversement proportionnel à la variance.

3.2.2. Application au R.P.M.

Le concept de R.P.M. permettant de rendre compte de certaines caractéristiques rencontrées dans les foyers réels mais en général de façon plus complexe (par exemple la stabilité); il peut être utile pour comprendre les bases de ces mécanismes et en dégager les tendances. Nous nous sommes donc intéressés à l'influence de la pulvérisation sur la stabilité d'un tel foyer.

A la figure 11 est représentée la limite pauvre d'extinction pour un R.P.M. de 1l de volume en fonction d'un diamètre caractéristique do.

Remarque : La valeur de do notée ici correspond à une référence fixée arbitrairement à φ = 0,2 et Ω = 13; comme le montrent les figures 11, 12 le calcul de $\bar{d}$ est effectué à chaque point de fonctionnement en fonction de φ, Ω à partir des corrélations (2 - 5).

On remarquera que mis à part aux faibles Ω, l'influence de la distribution est minime (do = 100 µm), ce phénomène étant à peine perceptible à do = 60 µm justifiant dans ce cas une classe unique de gouttes. Comme on peut le prévoir, ce phénomène est d'autant plus marqué que le volume du réacteur augmente (Fig. 12).

3.2.3. Application au réacteur avec double swirler

Un exemple de calcul appliqué au foyer de turboréacteur avec injection double swirler est présenté aux figures 13 et 14. Le modèle aérodynamique est celui présenté à la figure 6, dans laquelle les valeurs de débit et volume sont obtenues par mesure de temps de séjour et identification.

Extinction pauvre : aucune donnée n'étant disponible sur la taille des gouttes, nous avons essayé plusieurs tailles do (φ = 0,2) ; Ω = 13). La comparaison avec les essais combustion effectués à l'ONERA (36) semble correcte avec un diamètre de base voisin de 70 µm.

Mesures en sortie foyer : A la figure 14 sont présentées les comparaisons entre les profils moyens de température et d'inefficacité de combustion mesurés et calculés. Mis à part aux faibles richesses (pour θ) la comparaison nous semble intéressante.

Remarque : Comme nous l'avons noté plus haut, le calcul de stabilité est fait avec la cinétique globale alors que le rendement utilise le modèle quasi global.

3.3. Modèle mixte

Dans cette approche initialement proposée en écoulement monophasique par Harsha et Edelman (37) on utilise le couplage entre des zones de recirculation (elliptiques) représentées sous forme modulaire et des zones d'écoulement direct (paraboliques) calculées par résolution numérique des équations différentielles. Le couplage entre ces deux régions est assuré par une zone intermédiaire de type zone de mélange.

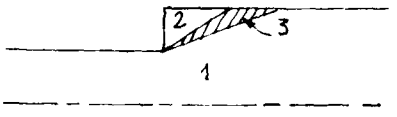
Ce modèle étant actuellement en cours de développement dans notre département, nous ne l'avons pas encore appliqué à des géométries de turboréacteurs (par exemple avec swirler). Le calcul présenté est donc relatif à une géométrie simplifiée type "élargissement brusque" avec un combustible liquide prémélangé.

3.3.1. Modèle

La géométrie étudiée est celle de la figure 15. L'écoulement est divisé en trois parties :

- un écoulement parabolique (EP) dans la partie directe

- une zone de recirculation qui sera assimilée à un R.P.M. et enfin une zone [illegible] (E.P.)



1 : E.P.
2 : R.P.M.
3 : E.P.

Dans la région directe les équations sont de forme parabolique et s'écrivent :

$$\frac{1}{\pi}\left(\frac{\partial}{\partial x}\left(\rho U r \varphi\right)+\frac{\partial}{\partial r}\left(\rho V r \varphi\right)-\frac{\partial}{\partial r}\left(\pi r \varphi \frac{\partial \varphi}{\partial r}\right)\right)= S\varphi$$

où φ représente une des quantités transportée (32).

- La zone de mélange joue un rôle important car c'est elle qui détermine les conditions aux limites pour l'écoulement parabolique et les conditions "d'entrée sortie" du R.P.M. Cette zone intervient par sa forme $r(x)$ et sa largeur $l(x) = ax + b$. On a pris une forme parabolique de cette zone de séparation. La longueur de cette zone est estimée de la manière suivante : à froid cette longueur est de l'ordre de 7 fois la marche, à chaud cette longueur est réduite selon $\left(\frac{T}{To}\right)^{1/2}$ ($T = 2000°$, $To = 300°$) ce qui fait que la longueur est divisée par 2.

On suppose également qu'à travers cette zone les variables varient linéairement de sorte que le gradient s'écrit :

$$\frac{\partial \varphi}{\partial r} = \left(\varphi_p - \varphi_r\right) / \rho(x)$$

φ_p : valeur de φ à la frontière de E.P.
φ_r : valeur de φ dans R.P.M.

- La zone de recirculation est représentée dans ce cas par un seul R.P.M.

L'ensemble des conditions aux limites ainsi que la méthode de résolution numérique sont donnés en détail dans (32).

3.3.2. Exemple d'application

Afin de tester cette méthode mixte utilisée en écoulement diphasique, nous avons calculé le cas correspondant à la géométrie décrite par Craig (37). Bien que ce dernier ne donne pas de détail sur la façon selon laquelle est injectée le carburant, la comparaison nous semble intéressante.

A la figure 15 on peut suivre l'évolution radiale des phases liquides et vapeur (avant et après combustion) à plusieurs sections ainsi que la déformation de l'histogramme de taille de gouttes qui se déforme vers un diamètre moyen inférieur vers les sections aval (du fait de la vaporisation).

Une comparaison intéressante est aussi donnée à la figure 16, elle porte sur l'inefficacité de combustion moyennée selon un rayon pour plusieurs sections.

IV - CONCLUSION

Ainsi que nous le notons en introduction, le but de ce travail était de présenter un ensemble de techniques expérimentales capables de fournir des données qualitatives et quantitatives suffisamment générales sur l'aérodynamique interne de foyers de turboréacteurs ; ceci afin de servir de base à deux types de modèles servant à calculer les performances de tels foyers. En effet, bien qu'elles soient obtenues dans des conditions d'écoulement isothermes, ces expériences se sont montrées capables de fournir des données aérodynamiques correctes pour une plage importante de conditions expérimentales. En particulier les diverses corrélations obtenues sur le débit recirculé QR_1 ainsi que sur la granulométrie se révèlent un outil précieux au stade de l'avant projet.

La méthode de calcul de type modulaire, dont les résultats dépendent fortement de cette description aérodynamique de l'écoulement, a été améliorée en tenant compte des phénomènes d'évaporation et de mélange des gouttes permettant ainsi d'expliquer la forme prise par certaines courbes de stabilité.

Enfin un développement intéressant réside dans l'utilisation du modèle mixte qui devrait pouvoir prochainement s'appliquer à des géométries plus complexes d'écoulement (impact de jets, injecteurs à swirler, échange entre film de refroidissement et recirculation...). Les premiers résultats obtenus sur une géométrie simplifiée paraissent en effet encourageants.

Il nous semble donc que cet ensemble de techniques expérimentales ainsi que de moyens de calcul permet, sans entraîner de coûts trop élevés, non seulement d'explorer différentes possibilités, idées ou sensibilité à des modifications géométriques mais aussi d'optimiser le dessin d'une chambre afin de lui permettre de répondre à divers critères de fonctionnement.

REFERENCES

1 - D.C.HAMMOND,A.M. MELLOR - Analytical calculation for the performance and pollutant emissions of gas turbine combustor. AIAA/SAE 71° propulsion joint conference. Salt lake city. 06/71.

2 - G.F. HIETT, G.E. POWELL - Three dimensional probe for investigation of flow patterns. The engineer 01/62.

3 - L. VERDE'ZIO, P. CAMPANARO - The air recirculation ratio in can type gas turbine combustion chambers. 10° symposium combustion - Cranfield 67.

4 - V.G. CHUMACHENKO et al - Study of mass exchange between primary zone and secondary air jets in gas turbine engine combustion chambers. Izvestiya VUZ Vol. 22 n° 1, 1979.

5 - R. ROBERTS et al - An analytical model for Nitric Oxyde formation in gas turbine combustor. AIAA Journal 06/72. P. 820.

6 - I. POLL - The application of partially stirred reactor modelling to pollutant minimisation in gas turbine combustors. Rept HIC 193. Univ. Sheffield. 1973.

7 - T.C. CLAYPOLE, N. SYRED - The combustion modelling of swirling flows in gas turbine combusters. 5° international symposium on airbreathing engines. 02.81. Bangalore (India).

[illegible] - [illegible] modelling [illegible] - [illegible] combustors. 17th Symposium on combustion. [illegible] and mathematics.

[illegible] - Combustion design [illegible]. 14th symposium [illegible].

[illegible] - Computer program for the analysis of annular combustors. [illegible] Rpt [illegible] - [illegible]. Naval Research and Engineering [illegible] edition, Mass.

[illegible] - Détermination de l'écoulement dans une chambre de combustion pour turbine à gaz par voie de calcul. Revue Brown Boveri [illegible].

[illegible] - Etude de l'aérodynamique d'une chambre de combustion en vue d'une modélisation semi empirique. 54e AGARD/PEP Cologne. Oct. 79.

[illegible] - Application of modular modelling to ramjet performance prediction. AIAA/SAE 14th conf. Las Vegas 78/78.

[illegible] - Combustor modeling for ramjet development programs. 58e AGARD/PEP - Londres. Oct. 81.

[illegible] - Fundamental modelling of mixing evaporation and kinetics in gas turbine combustors. 54e AGARD/PEP Cologne. Oct. 79.

[illegible] - Divers articles dans 54e AGARD/PEP. Cologne. Oct. 79.

[illegible] - The art of partial modeling. 9e Symposium on combustion 1982.

[illegible] - Modular modeling of combustion chambers. 4e int. Conf. for Mechanical power engineering. Le Caire - Oct. 82.

[illegible] - Etude théorique et expérimentale de chambres de combusiton avec recirculation. A.T.M.A. Session 1981. Paris.

[illegible] - Quantitative interpretation of flow visualizations coupling video technics and microcomputer. I.C.I.A.S.F. 81 Dayton. Sept. 81.

[illegible] - Quantitative flow visualizations with video methods and microcomputer. 3e Int. Symp. on flow visualization. Ann Arbor U.S.A. Sept. 83.

[illegible] - Television methods for in situ determination of particle size distribution in flows. 3e Symp. on flow visualization. Ann Arbor U.S.A. Sept. 83.

[illegible] - Mesure de concentration et de temps de séjour par technique vidéo. Thèse de spécialité. [illegible]louse. 1981.

[illegible] - Technique de mesure des aires interfaciales dans les écoulements à bulles. Rpt C.E.A. Grenoble 2/81.

[illegible] - Etude théorique et expérimentale des phénomènes de pulvérisation et de vaporisation. Etude approfondie n° 5 - ENSICA - 1983.

[illegible] - Chemical reaction engineering - John Willey and sons - 1972.

[illegible] - Etude aérodynamique de la combustion dans les foyers de turbomachines . Rapport CERT-DERMES 1/2127. Mars 82.

[illegible] - Etude hydrodynamique dans une chambre de combustion. Thèse de spécialité. Toulouse 1981.

[illegible] - Etude de l'écoulement recirculé dans une chambre de bombustion. Thèse de spécialité Toulouse. 1981.

[illegible] - Reactions chimiques en milieu turbulent - Thèse d'état - Paris. 1978.

[illegible] - Sixth symposium on combustion. P.708. Reinhold 1977.

[illegible] - Ecoulements turbulents réactifs ou de convection naturelle. Différentes approches theoriques Thèse d'Etat Toulouse. 1983.

[illegible] - Fuel spray evaporation in gas turbine combustors - I.H.D. Thesis Sheffield University. 78.

[illegible] - Etude théorique de l'optimisation de la combustion dans les foyers de turbomachines. Acta Astraunautica Vol. 1 (1974).

[illegible] - A quasi global chemical kinetic model for the finite rate combustion of hydrocarbon fuel with application to turbulent burning and mixing in hypersonic engines. AIAA Paper 8086. New York.

[illegible] - Rapport interne 1984

[illegible] - Coaxial dump combustor investigation. AIAA Paper 78 - 1107 AIAA/SAE.

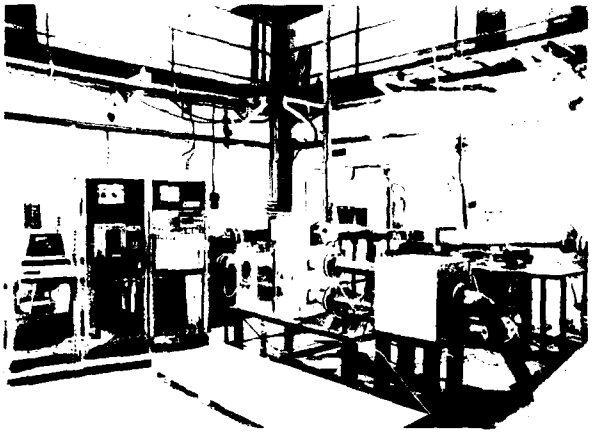


FIGURE 1 : BANC D'ESSAIS HYDRAULIQUE

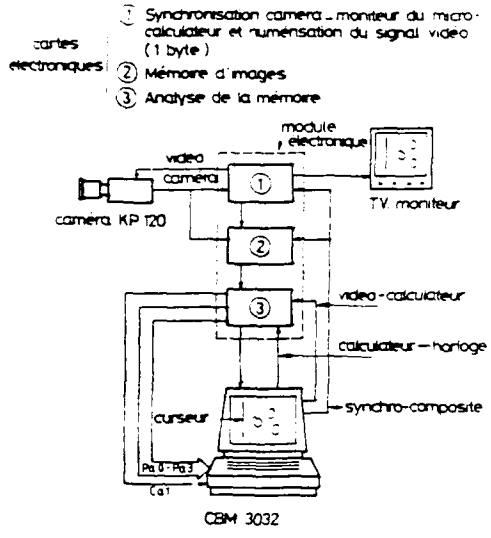
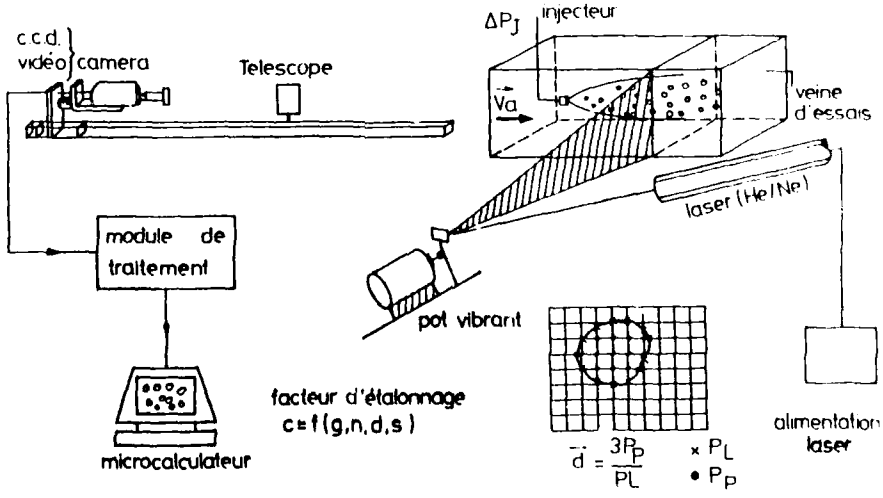


FIGURE 3 : MODULE D'ACQUISITION DE GRANULOMETRIE



PRINCIPE DE MESURE DU DIAMETRE MOYEN DES GOUTTELETTES

FIGURE 2 : BANC DE GRANULOMETRIE

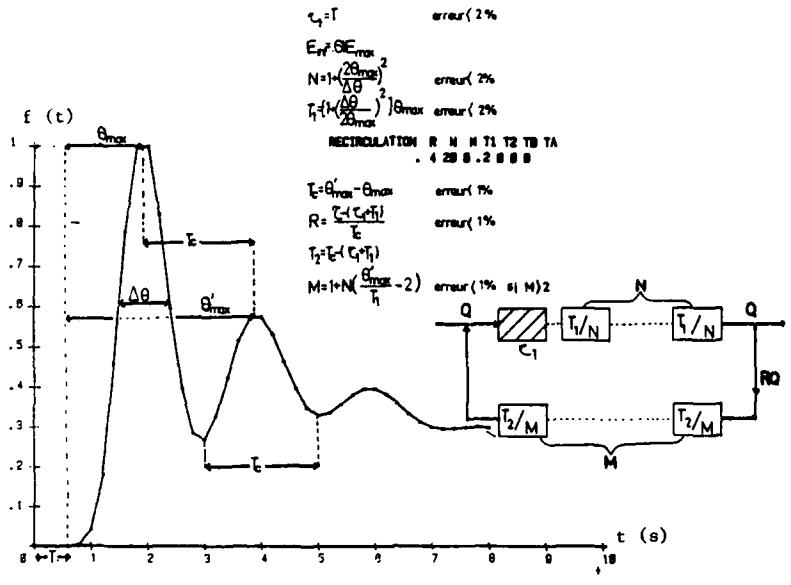
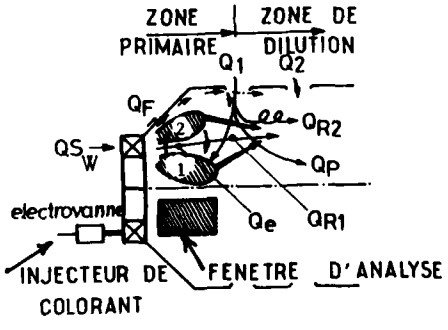
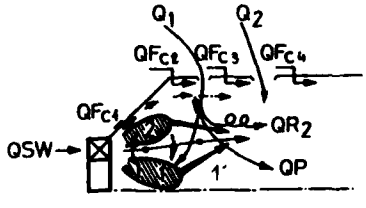
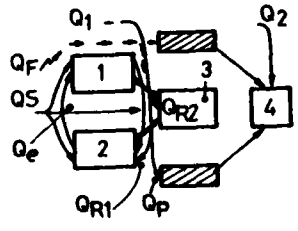


FIGURE 4 : DISTRIBUTION DE TEMPS DE SEJOUR - EXEMPLE D'IDENTIFICATION AVEC UN ASSEMBLAGE DE REACTEURS ELEMENTAIRES.







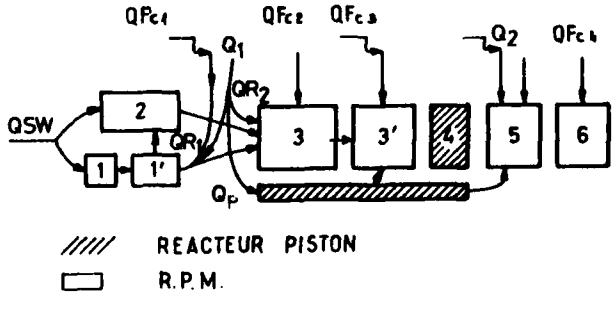


FIGURE 5 : SIMPLE SWIRLER

FIGURE 6 : DOUBLE SWIRLER

REPRESENTATION SCHEMATIQUE DE L'ECOULEMENT DANS UN FOYER DE TURBOMACHINE
MODELISATION PAR ASSEMBLAGE DE REACTEURS ELEMENTAIRES.

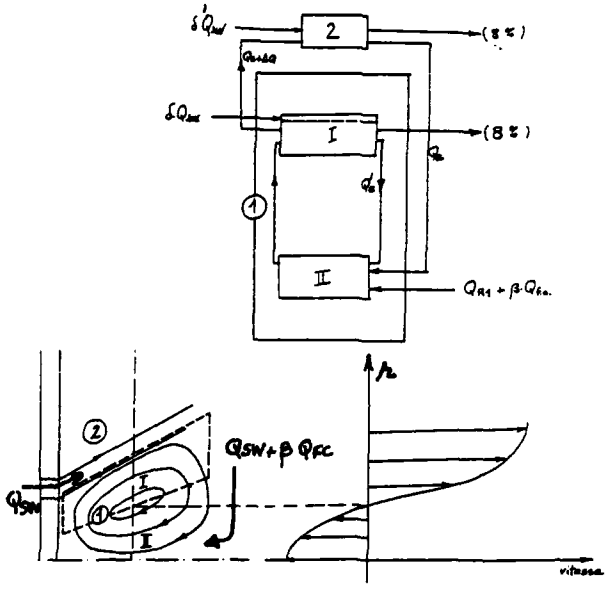


FIGURE 7 : EXEMPLE DE MODELISATION DETAILLEE

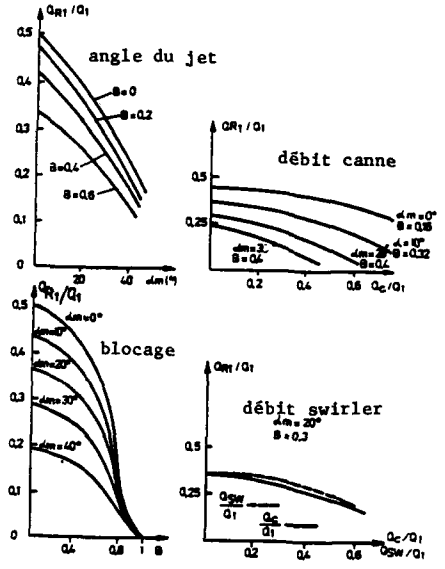


FIGURE 8 : ETUDE PARAMETRIQUE DU DEBIT RECIRCULE EN FOND DE CHAMBRE

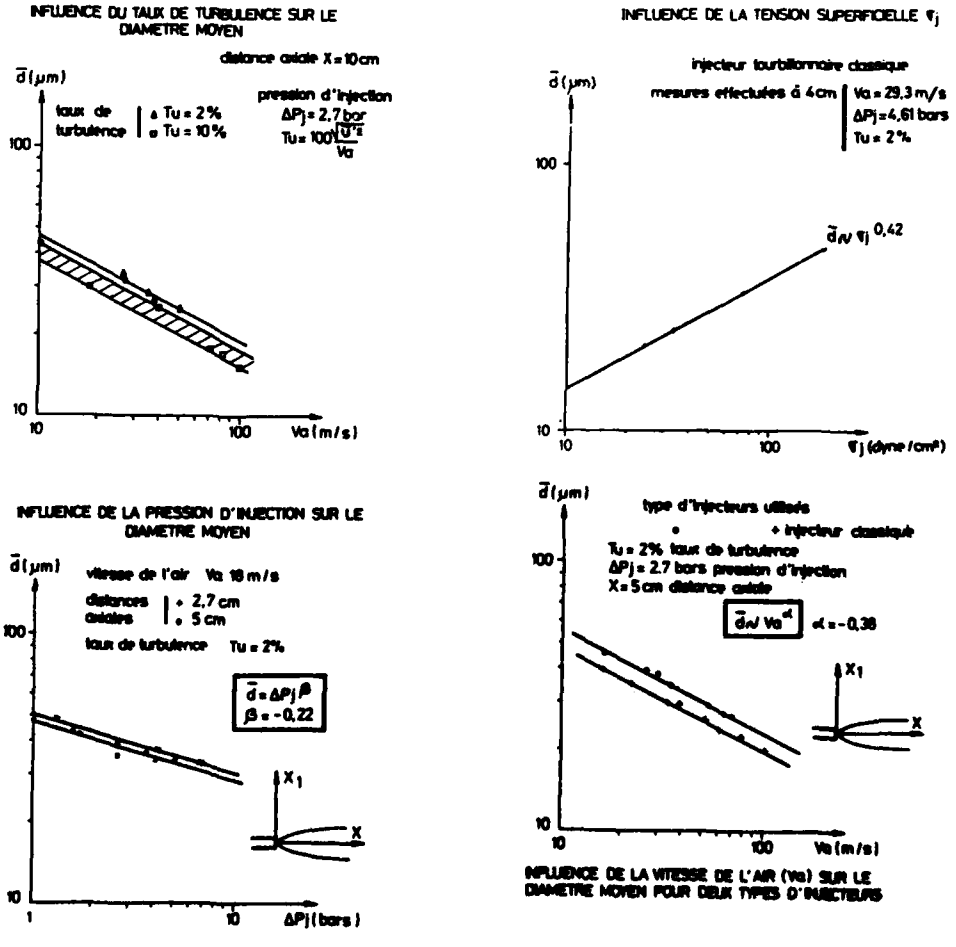


FIGURE 9 : MESURES DU DIAMETRE MOYEN DES GOUTTELETTES

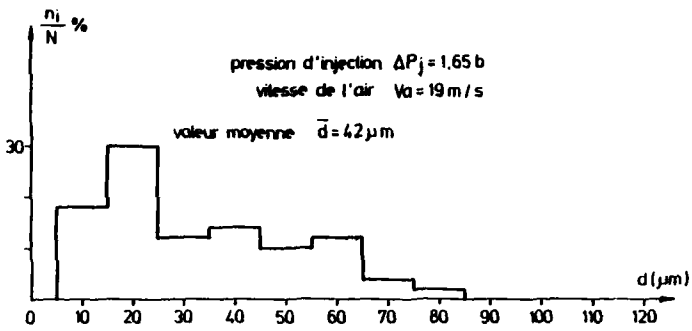




FIGURE 10 : EXEMPLE DE DISTRIBUTION DE TAILLES DE GOUTTELETTES

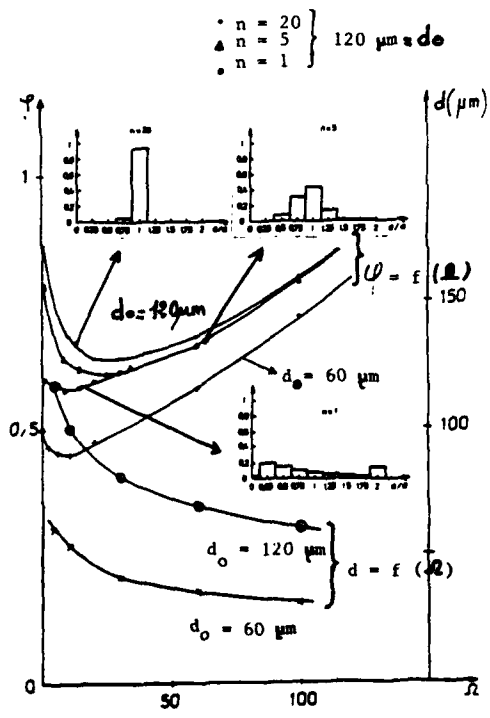


FIGURE 11 : EFFET DE LA PULVERISATION SUR LA LIMITE D'EXTINCTION PAUVRE D'UN R.P.M. V = 1 ℓ, d_o ET DISTRIBUTION VARIABLES

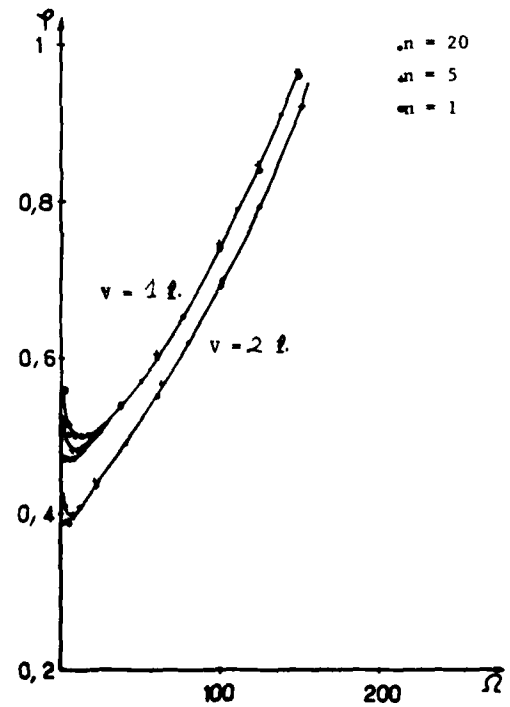


FIGURE 12 : EFFET DE LA PULVERISATION SUR LA LIMITE D'EXTINCTION PAUVRE D'UN R.P.M. VOLUME ET DISTRIBUTION VARIABLES d_o = 120 µm

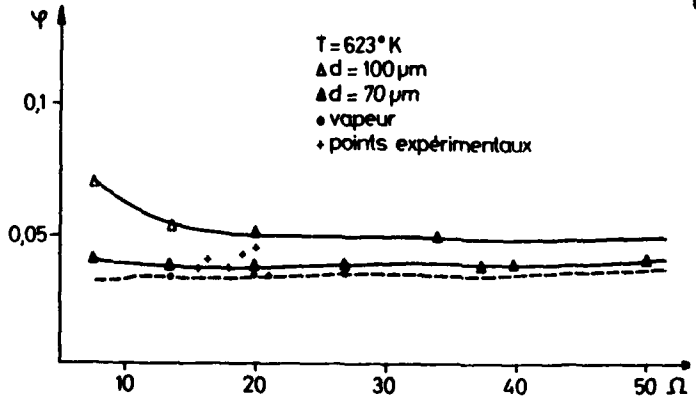


FIGURE 13 : LIMITE D'EXTINCTION PAUVRE SUR UN FOYER DE TURBOREACTEUR A DOUBLE SWIRLER COMPARAISON ENTRE ESSAIS COMBUSTION ET RESULTATS DU MODÈLE MODULAIRE. INFLUENCE DE LA PULVERISATION.

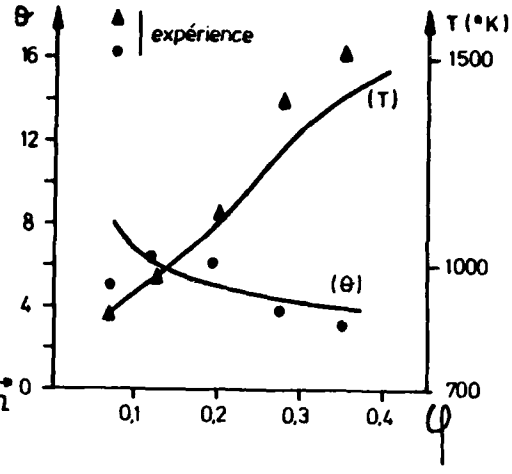


FIGURE 14 : INEFFICACITE DE COMBUSTION ET TEMPERATURE EN SORTIE DU TURBOREACTEUR A DOUBLE SWIRLER. COMPARAISON ENTRE ESSAIS COMBUSTION ET RESULTATS DU MODELE MODULAIRE.

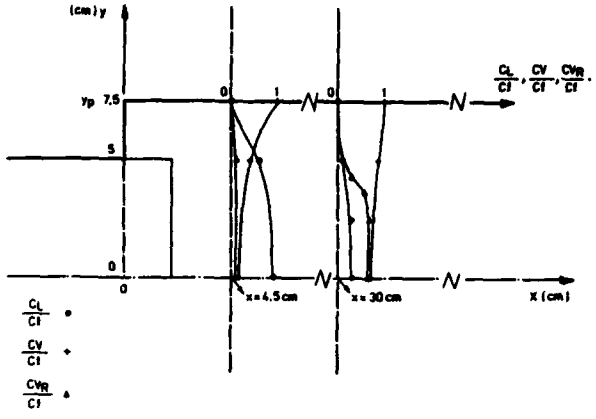


FIGURE 15 a

FIGURE 15 : CALCUL PAR METHODE MIXTE SUR UNE GEOMETRIE SIMPLIFIEE DE CHAMBRE

a) EVOLUTION DES CONCENTRATIONS FUEL LIQUIDE ET FUEL VAPEUR

b) EVOLUTION DE LA DISTRIBUTION DE LA TAILLE DES GOUTTES

C_f CONCENTRATION DE FUEL INJECTE

C_L CONCENTRATION DE FUEL SOUS FORME LIQUIDE

C_V CONCENTRATION DE FUEL SOUS FORME GAZEUSE

C_{VR} CONCENTRATION DE FUEL SOUS FORME GAZEUSE APRES COMBUSTION

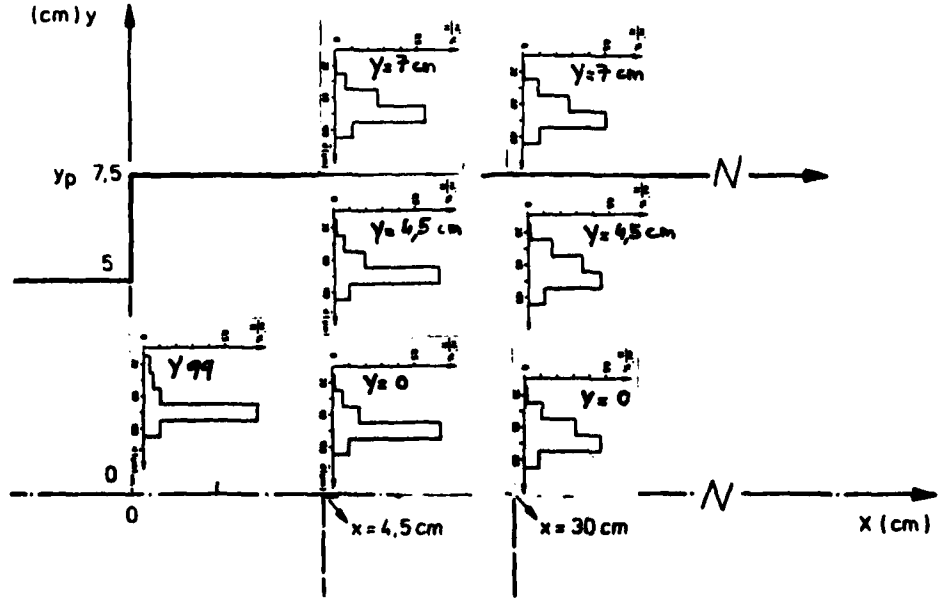


FIGURE 15 b

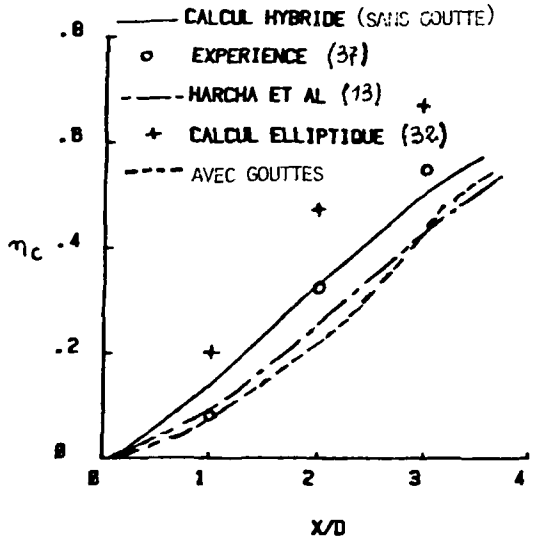


FIGURE 16 : CALCUL DE L'INEFFICACITE DE COMBUSTION
COMPARAISON AVEC LES RESULTATS EXPERIMENTAUX DE CRAIG

DISCUSSION

C.Sheppard, UK

The technique of breaking down a combustor into a series of well-stirred and plug flow reactors has the attraction of uncoupling mixing and chemistry, allowing the adoption of a realistic chemical kinetic scheme. However the method has a fundamental flaw in that it ignores the vital interaction between combustion and turbulence; a good representation of it is necessary to predict pollutant formation and stability. At Leeds, we have developed a mixing flow reactor which incorporates a series of coalescence and dispersion events, following the ideas of Pratt. Have you attempted to model your flows using such concepts? I would also appreciate your reaction to the above comments.

Réponse d'Auteur

Je connais effectivement les travaux de Pratt mais nous n'avons jamais essayé ce concept dans nos modèles de calcul modulaire.

Je suis d'accord avec vos commentaires, mais nous avons plutôt cherché à obtenir une représentation correcte de l'aérodynamique car sans cela tous les perfectionnements sur la cinétique chimique ou sur l'interaction entre combustion et turbulence n'ont que peu d'intérêt. Ensuite nous avons pris en compte le caractère diphasique de l'écoulement en considérant le mouvement, l'évaporation et la combustion des gouttes. Enfin le modèle peut aussi tenir compte des interactions entre turbulence et combustion au moyen d'un modèle simplifié de type "eddy break up"

G.Winterfeld, Ge

The correlations used in the model are developed for a SNECMA combustor. Can you comment on the use of the correlations for combustors of different geometries and hence different flow fields?

With respect to recirculation mass flows and residence times, work done at DFVLR shows that for recirculation zones behind bluff-bodies there are considerable differences between the isothermal case and the case with combustion. This is a point which should perhaps be looked at in more detail.

Réponse d'Auteur

Effectivement, je n'ai présenté que des comparaisons portant sur des maquettes SNECMA. Cependant, ces méthodes ont été appliquées à un nombre important de géométries de foyers de turbo ou de statoréacteurs. Les conclusions que nous tirons de ces études sont les suivantes:

Les différentes chambres de combustion rencontrées peuvent se modéliser à partie de 3 ou 4 modèles différents de foyers élémentaires;

certains paramètres tels que le débit recirculé peuvent s'exprimer simplement en fonction de paramètres géométriques ou cinématiques simples.

Je suis d'accord avec votre deuxième remarque, mais il me semble que l'influence de la combustion porte surtout sur les points suivants:

longueur de la zone de recirculation;

débit entraîné à l'intérieur de la recirculation;

échange massique entre la recirculation et l'extérieur.

PREDICTION DES PERFORMANCES DE RENDEMENT ET DE STABILITE D'UNE CHAMBRE DE COMBUSTION

Y. CHAUVEAU - M. DESAULTY - G. BAYLE-LABOURÉ

S.N.E.C.M.A
Centre de Villaroche
77550 MOISSY CRAMAYEL - FRANCE

RESUME

La recherche d'une compacité croissante des chambres de combustion modernes conduit à une optimisation de plus en plus poussée de ces dernières visant à assurer dans le volume le plus faible possible, les performances requises de rendement/pollution et de stabilité.

Cette optimisation ne peut être réalisée de manière économique qu'en développant des outils de calcul capables d'estimer les performances d'une chambre au stade de l'avant-projet.

Le modèle présenté dans cet article est basé sur le principe de la décomposition d'une chambre de combustion en foyers homogènes aérodynamiquement couplés entre eux et sièges de zones réactives où la combustion est pilotée par la cinétique chimique. Une comparaison portant sur les niveaux de pollution et les limites de stabilité calculés et expérimentaux a été effectuée pour un foyer bidimensionnel simulant une zone primaire de chambre de combustion d'une part, et pour une chambre complète d'autre part.

PREDICTING A COMBUSTOR EFFICIENCY AND STABILITY PERFORMANCES

ABSTRACT

The need for an increased compactness of modern combustors leads to an ever more developed optimization of these combustors, that aims at insuring the best efficiency/pollution and stability performances in the smallest possible volume.

One of the cheapest way to achieve such an optimization is to develop computer codes allowing to predict the performances of a combustor at the design stage.

The computer model presented in this paper is based on the principle of a description of the combustor as a series of well-stirred reactors, being aerodynamically coupled with each other, and acting as reactive zones where combustion is controlled by chemical kinetics. This paper also details the comparison between computed and measured emission indexes and stability limits for a two-dimensional reactor simulating a combustor primary zone, as well as for a complete combustor.

NOMENCLATURE

Cp	Chaleur spécifique du gaz au voisinage de la goutte
Cx	Coefficient de traînée
D	Débit d'air de la chambre de combustion
Dr	Débit réduit = $D\sqrt{Tte}/Pte$
L	Chaleur latente de vaporisation
$\dot{m}$	Débit masse évaporé par goutte
Pr	Nombre de Prandtl
Pte	Pression totale amont chambre
R	Rayon de goutte
Re	Nombre de Reynolds ramené au rayon de la goutte
SMD	Diamètre moyen de Sauter
T_L	Température de vaporisation du carburant
T_∞	Température de la chambre au voisinage de la goutte
Tte	Température amont chambre
V	Vitesse
ϕ^*	Rapport d'équivalence du fond de chambre
ΔP	Perte de charge
λ	Conductivité thermique du gaz
ρ	Masse volumique
Ω	Charge aérodynamique = $\dfrac{D}{\mathcal{V}.Pte^{1,8}\ e^{Tte/300}}$ ($\mathcal{V}$ volume de la chambre)
σ	Tension superficielle

INDICES

g	Gaz
G	Goutte
i	Etat initial
L	Liquide

1 - INTRODUCTION

L'augmentation du coût des essais partiels de combustion a conduit les motoristes et la SNECMA en particulier à se doter de méthodes de prévision permettant, au stade de l'avant-projet, d'aboutir à la conception d'un foyer dont les performances soient proches de l'objectif à atteindre.

Ce document présente une méthode de prédiction du rendement et de la stabilité et établit la synthèse des recoupements obtenus avec l'expérience concernant l'indice d'émission de CO et les limites de stabilité d'un foyer bidimensionnel simulant une zone primaire et d'une chambre de combustion complète.

2 - DESCRIPTION DU MODELE

2.1 - Principe de la méthode de calcul

Le principe de la modélisation adoptée pour le fonctionnement d'une chambre de combustion repose sur le concept de la décomposition de celle-ci en volumes élémentaires assimilables soit à des foyers homogènes, soit à des réacteurs pistons /1, 2, 3/. En dépit des difficultés de mise en oeuvre de la méthode sur le plan aérodynamique (identification des foyers élémentaires, couplages entre ceux-ci, distribution du carburant dans l'écoulement), ce type de modèle présente l'avantage par opposition aux modélisations bi et tri-dimensionnelles de permettre l'utilisation, pour des temps de calcul raisonnables, de descriptions détaillées des mécanismes de cinétique chimique.

2.2 - Description aérothermochimique de l'écoulement

2.2.1 - Caractérisation aérodynamique et représentation de la chambre

L'écoulement au sein de la chambre de combustion et notamment de la zone primaire a été caractérisé au moyen de mesures réalisées en analogie hydraulique sur une maquette en plexiglass simulant un secteur de chambre équipé de quatre injecteurs aérodynamiques à double vrille. Cette étude expérimentale a été effectuée par le CERT à TOULOUSE /4, 5/ et a nécessité la mise en ouvre de diverses techniques comme la visualisation à l'aide de traceurs afin de mettre en évidence les grosses structures de l'écoulement, la mesure de vitesses par fil chaud ou par ADL pour une analyse plus fine de l'écoulement, et la mesure de temps de séjour permettant d'identifier des volumes assimilables à des foyers élémentaires et d'établir les répartitions de débit et les échanges entre ces différents foyers.

La chambre de combustion est ainsi décomposée en volumes réactifs conformément aux résultats d'analogie hydraulique (figures 1 - 2 - 3). Les trois foyers représentant le fond de chambre sont alimentés en partie par le débit du système d'injection et sont couplés entre eux par des mouvements de recirculation, les deux foyers suivants complètent la zone primaire, et les autres foyers simulent la zone de dilution.

Des expressions analytiques traduisant l'influence des paramètres géométriques et aérodynamiques permettent de déterminer quantitativement les débits alimentant chacun de ces foyers.

2.2.2 - Modélisation de la chimie de la combustion

Les nombreuses études portant sur la cinétique chimique des réactions de combustion ont débouché sur la conception de mécanismes réactionnels de complexité croissante intervenant au cours de l'oxydation des hydrocarbures.

Il existe deux manières principales d'aborder la description de la chimie de la combustion : la première consiste à utiliser des schémas simplifiés tels que des schémas globaux qui ne comportent qu'une seule réaction, semi-globaux à plusieurs étapes /6, 7/, ou quasi-globaux avec une étape globale pour la décomposition de l'hydrocarbure et un modèle détaillé pour les phénomènes d'oxydation /8, 9/, la seconde réside dans l'utilisation de mécanismes détaillés pour décrire à la fois la phase de pyrolyse de l'hydrocarbure et la phase d'oxydation /10/.

Dans le cadre de cette étude des performances en stabilité des chambres, un schéma cinétique détaillé, dérivé du mécanisme établi par le CRCCHT d'ORLEANS /10/, a été introduit dans le modèle de calcul. Ce schéma est implanté dans une version qui comporte soixante réactions chimiques élémentaires et fait intervenir vingt cinq espèces.

Lors d'une récente étude des performances en pollution des chambres /11/, une comparaison a été effectuée entre un schéma quasi-global développé par la SNECMA et le schéma détaillé utilisé actuellement, et les résultats obtenus sur un foyer homogène unique ont montré l'intérêt du mécanisme détaillé par rapport au schéma quasi-global dont le comportement en régime surstoechiométrique est nettement erroné. En particulier, le domaine de stabilité du foyer homogène est très bien restitué par la cinétique détaillée.

2.3 - Répartition du carburant dans la chambre

Le carburant est introduit dans la chambre de combustion par un dispositif d'injection dite aérodynamique. Il est injecté sous forme de nappe liquide par une fente annulaire en présence d'écoulements d'air interne et externe au cylindre ainsi formé, animés de certaines vitesses initiales par rapport au carburant.

En vue d'aboutir à une modélisation par assemblage de foyers homogènes acceptable, plusieurs problèmes doivent être considérés : la caractérisation de la pulvérisation, la modélisation de la vitesse relative air - carburant et le modèle d'évaporation du carburant. En outre, la répartition initiale du carburant liquide entre les différents foyers suit une loi élémentaire faisant intervenir les débits d'air des différents orifices du système d'injection.

2.3.1 - Pulvérisation

La formation des gouttelettes résulte d'un processus de désintégration de la nappe liquide et leur taille revêt une importance capitale pour le fonctionnement de la chambre. Des études théoriques de l'injection aérodynamique basées sur des calculs de perturbations sont effectuées en laboratoire /12/ pour tenter d'expliquer les phénomènes de rupture de la nappe en ligaments et de formation de gouttes par rupture de ces ligaments.

Par ailleurs, la détermination expérimentale des tailles de gouttelettes par diffraction de lumière fait l'objet du développement de nouvelles techniques /13/ ; la SNECMA est pour sa part équipée d'un dispositif d'essais se composant d'un injecteur aérodynamique alimenté en air et en eau débouchant à l'air ambiant sous la forme d'un nuage de gouttes, et en aval duquel est disposé un granulomètre laser MALVERN /14/.

Le traitement différé du signal recueilli permet d'identifier une loi de distribution, par exemple de type Rosin-Rammler /15/, à la répartition en taille des gouttelettes, et de déterminer en particulier, pour différentes pertes de charge du système d'injection, le diamètre moyen de Sauter noté SMD /16, 17, 18, 19/ qu'il est possible de relier aux performances d'injection par une relation du type /20, 21/ :

SMD = f (débit carburant/débit d'air, caractéristiques physiques de l'air et du carburant, perte de charge et caractéristique géométrique de l'injecteur).

En l'absence de résultats expérimentaux pour un injecteur alimenté en kérosène, combustible dont la tension superficielle est nettement plus faible que celle de l'eau, les SMD équivalents pour le kérosène ont été déduits des SMD mesurés avec de l'eau d'après la formulation approchée suivante déterminée à partir de corrélations établies antérieurement /21/ :

$$\frac{SMD\ (kérosène,\ pression)}{SMD\ (eau,\ P_{atm})} \sim \left(\frac{\sigma\ kérosène}{\sigma\ eau} \cdot \frac{P_{atm}}{Pte}\right)^{0,6} \left(\frac{\rho kérosène}{\rho eau}\right)^{0,1}$$

La figure 4 présente l'évolution du rayon de goutte R_{Gi}, nécessaire à l'initialisation du calcul et déduit des mesures granulométriques, en fonction de la perte de charge de la chambre qui est liée au débit réduit $Dr = \frac{D\sqrt{Tte}}{Pte}$ caractérisant son fonctionnement.

La qualité de la pulvérisation est évidemment dégradée lorsque la pression décroît.

2.3.2 - Vitesse relative air - carburant

La modélisation par assemblage de foyers homogènes ne permet évidemment pas la description fine du champ aérodynamique de l'écoulement dans la chambre. Le mouvement des gouttes est donc supposé s'effectuer dans la même direction que l'écoulement principal, ce qui conduit à l'équation de mouvement suivante :

$$\frac{dV_G}{dt} = -\frac{3}{8}\ \frac{\rho g}{\rho G}\ \frac{Cx}{R_G}\ (V_G - V_g)\ \left\| V_G - V_g \right\|$$

où V_G désigne la vitesse des gouttes, de masse volumique ρG, et V_g la vitesse du gaz de masse volumique ρg, calculée dans un foyer à partir du débit masse, du volume et d'une dimension caractéristique.

Le rayon de goutte R_G est une fonction du temps /22/, la loi de décroissance utilisée est explicitée au paragraphe 2.3.3. La vitesse initiale des gouttes V_{Gi}, estimée à partir des conditions d'alimentation en carburant et de la géométrie du dispositif d'injection, est très faible par rapport à la vitesse du gaz au voisinage de l'extinction. Le coefficient de traînée des gouttes Cx est fonction du nombre de Reynolds /23/. L'erreur introduite par cette description schématique est négligeable car la vitesse relative gaz - liquide diminue rapidement après la phase de pulvérisation.

2.3.3 - Evaporation du carburant

Le carburant est injecté ponctuellement en fond de chambre, ce qui permet de supposer que la concentration locale en oxygène y est assez faible, et que le mouvement relatif gaz - gouttes est suffisant pour empêcher la combustion des gouttes en surface. Cette remarque conforte le choix de la loi d'évaporation simple /24/ qui a été introduite dans le modèle :

$$\dot{m} = \dot{m}s \ (1 + 0{,}276 \ Re^{1/2} \ Pr^{1/3})$$

avec : $\dot{m}s = \frac{4 \pi \lambda RG}{Cp} \ Log \ (1 + Cp \ (T_{\infty} - T_L) \ / \ L)$

3 - RESULTATS OBTENUS

3.1 - Dispositifs expérimentaux

En vue de procéder à des comparaisons entre les résultats du calcul et les résultats d'essais réalisés au banc, le modèle a été testé sur un foyer bidimensionnel comportant cinq injecteurs aérodynamiques et simulant la zone primaire d'une chambre de combustion d'une part et sur une chambre expérimentale complète d'autre part.

3.1.1 - Le foyer bidimensionnel - zone primaire

Le foyer bidimensionnel simulant une zone primaire est présenté sur la figure 1.

Celui-ci a été conçu de manière modulaire de façon à pouvoir étudier l'influence des paramètres suivants :

- le débit du système d'injection,
- le débit, le blocage, ou la position axiale des trous primaires.

Son fonctionnement a été étudié dans le domaine de pression et de température suivant :

$0{,}6 \text{ bar} < Pte < 4 \text{ bar}$

$300 \text{ K} < Tte < 625 \text{ K}.$

Ce domaine est celui où la modélisation chimique a le plus d'importance sur les résultats en sortie de zone primaire.

Des mesures par prélèvement au moyen d'une sonde d'analyse de gaz ont été effectuées dans le secteur des trois injecteurs centraux de manière à éviter les effets de bords. Les principales espèces, CO - CO_2 - CHx - NOx ont été mesurées.

3.1.2 - La chambre expérimentale complète

Il s'agit d'une chambre de combustion conique équipée d'un système d'injection aérodynamique à double vrille.

Une coupe schématique de la chambre est présentée sur la figure 2.

Son fonctionnement a été étudié dans le domaine de pression et de température suivant :

$0{,}3 \text{ bar} < Pte \leq 15 \text{ bar}$

$300 \text{ K} \leq Tte \leq 823 \text{ K}.$

3.2 - Etude de pollution

Une validation du code de calcul dans les conditions de fonctionnement présentées dans le paragraphe 3.1 et pour différentes configurations géométriques dans le cas du foyer modulaire a permis de vérifier la capacité du modèle à prédire les indices d'émission de polluants /11/. La figure 5 présentant la comparaison entre le calcul et les mesures d'indice d'émission de CO en fonction de la charge aérodynamique constitue une illustration du bon accord qui a pu être obtenu aussi bien sur le foyer bidimensionnel que sur la chambre complète.

3.3 - Etude de stabilité

3.3.1 - La zone primaire

Les limit s d'extinction pauvre du foyer ont été calculées pour des températures à l'entrée mprises entre 300 K et 623 K à la pression atmosphérique et en dépression à 0,6 bar e recoupement entre le calcul et l'expérience est satisfaisant compte-tenu inc titudes dues aux difficultés d'appréciation des limites expérimentales de ilité.

A titre d'exemple, la figure 6 établit la comparaison entre les relevés expérimentaux et les résultats de calcul à pression atmosphérique et pour une température amont de 300 K.

En ordonnée est porté le rapport d'équivalence Ø * du fond de chambre et en abscisse figure le rapport entre le débit réduit et le débit réduit nominal.

L'influence du rayon de gouttes initial est nettement mise en évidence aux faibles débits réduits pour lesquels la stabilité de la combustion est étroitement liée à la qualité de la pulvérisation. En revanche, pour des débits réduits plus élevés, la stabilité est essentiellement contrôlée par la cinétique, l'influence de la taille des gouttelettes n'étant plus sensible.

3.3.2 - La chambre complète

Des recoupements ont été réalisés à 300 K et pour un domaine de pression de 0,6 à 0,3 bar.

La figure 7 présente la comparaison entre le calcul et l'expérience pour une pression de fonctionnement de chambre de 0,3 bar. Les tendances enregistrées concernant les limites d'extinction pauvre ne font que confirmer les résultats obtenus avec le foyer bidimensionnel.

Les limites riches expérimentales ne sont pas des limites d'extinction proprement dites de la chambre, mais représentent en fait l'apparition du "torchage" sur banc d'essai résultant du déplacement vers l'aval de la chambre de la zone de combustion vive. Ce phénomène peut être interprêté par le calcul en considérant que le recul de la flamme entraîne une extinction du fond de chambre, d'où l'obtention d'une limite riche comparable à l'expérience. Les résultats du calcul sont en bon accord avec l'expérience sur une grande partie du domaine de fonctionnement.

4 - CONCLUSION

La modélisation des chambres de combustion par assemblage de foyers homogènes, associée à l'emploi d'un schéma cinétique détaillé permet de prévoir de manière satisfaisante et pour des coûts de calcul modérés, les performances de rendement/pollution et de stabilité des chambres.

Le choix d'une cinétique détaillée résulte de tests préliminaires qui ont montré l'intérêt de ce type de mécanisme. Le couplage aérodynamique entre les foyers élémentaires a été étudié expérimentalement par analogie hydraulique. Des essais spécifiques ont été effectués pour déterminer les caractéristiques de pulvérisation d'un injecteur de type aérodynamique.

Cette méthode de calcul constitue globalement un outil de prévision et d'extrapolation particulièrement utile pour le développement de chambres nouvelles.

BIBLIOGRAPHIE

1 - D.C. HAMMOND - A.M.MELLOR
Analytical calculation for the performance and pollutant emissions of a gas turbine combustion
AIAA Paper 71-711 (1971)

2 - J. SWITHENBANK - I. POLL - M.W. VINCENT
Combustion Design Fundamentals
14th Symposium on Combustion (1973)

3 - P. GASTEBOIS
Modélisation des foyers de turbomachines
AGARD CP 275 (1979)

4 - P. HEBRARD - P. MAGRE
Etude de l'aérodynamique d'une chambre de combustion en vue d'une modélisation semi-empirique
AGARD CP 275 (1979)

5 - P. HEBRARD - P. MAGRE
Etude théorique et expérimentale de chambres de combustion avec recirculation
81e session de l'ATMA (1981)

6 - D.J. HAUTMAN - F.L. DRYER - K.P. SCHUG - I. GLASSMAN
A multistep overall kinetic mechanism for the oxidation of hydrocarbons
Combustion Science and Technology Vol. 25 - 219 (1981)

7 - A.Y. ABDALLA - D. BRADLEY - S.B. CHIN
Combustion and Flame Vol. 43 - 131 (1981)

8 - R.B. EDELMAN - O.F. FORTUNE
A quasi global chemical kinetic model for the finite rate combustion of hydrocarbon fuels with application to turbulent burning and mixing in hypersonic engines and nozzles
AIAA Paper 69 - 86 (1969)

9 - J. DUTERQUE - R. BORGHI - M. TICHTINSKY
Study of quasi-global schemes for hydrocarbon combustion
Combustion Science and Technology Vol. 26 - 1 (1981)

10 - M. CATHONNET - J.C. BOETTNER - M. JAMES
Experimental study and numerical modelling of high temperature oxidation of propane and n-butane
18th Symposium on Combustion (1981)

11 - M. DESAULTY - Y. CHAUVEAU
Modélisation des chambres de combustion par assemblage de foyers homogènes
6th ISABE (1983)

12 - J. MARTINON
Instabilités d'une nappe liquide cylindrique en présence de deux écoulements gazeux
Rapport IDF/P/82-01 (1982)

13 - A. TARDIEU - S.M. CANDEL - E. ESPOSITO
Développement d'une nouvelle technique pour la détermination des tailles de gouttelettes par diffraction de lumière
9th International Colloquium on Dynamics of Explosion and reactive systems (1983)

14 - C. NEGUS - B.J. AZZOPARDI
The Malvern particle size distribution analyser : its accuracy and limitation
AERE R 9075 (1978)

15 - P. ROSIN - E. RAMMLER
Laws governing fineness of powdered coal
Journal of the Institute of Fuel 7 - 29 (1933)

16 - R.A. MUGELE - H.D. EVANS
Droplet size distribution in sprays
Industrial and Engineering Chemistry 43 - 1317 (1951)

17 - I.C. FINLAY - T. Mc MILLAN - J.L.K. BANNEL - C. NITHTINGALE
The measurement of droplet sizes leaving the throttle plate of an air valve carburettor
National Engineering Laboratory Report (1979)

18 - A.H. LEFEBVRE
Airblast atomization
Prog. Energy Combustion Science Vol. 6 (1980)

19 - N.K. RIZK - A.H. LEFEBVRE - PURDUE
Influence of airblast atomizer design features on mean drop size
AIAA/SAE/ASME 18th Joint Propulsion Conference (1982)

20 - D.C. HAMMOND - A.M. MELLOR
Combustion Science and Technology Vol. 2 (1970)

21 - M.S. EL. SHANAWANY - A.H. LEFEBVRE
Airblast Atomization : the effect of linear scale on mean drop size
ASME Gas Turbine Conference and Products Show (1980)

22 - C.K. LAW
Recent advances in droplet vaporization and combustion
Prog. Energy Combustion Science Vol. 8 - 171 (1982)

23 - R.A. DICKERSON - M.D. SCHUMAN
Journal of Spacecraft Vol. 2 - 99 (1956)

24 - A. WILLIAMS
Combustion of droplets of liquid fuels
Combustion and Flame Vol. 21 - 1 (1973)

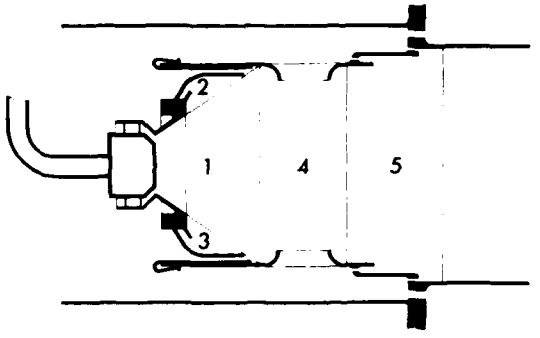


Figure 1 **ZONE PRIMAIRE**
PRIMARY ZONE

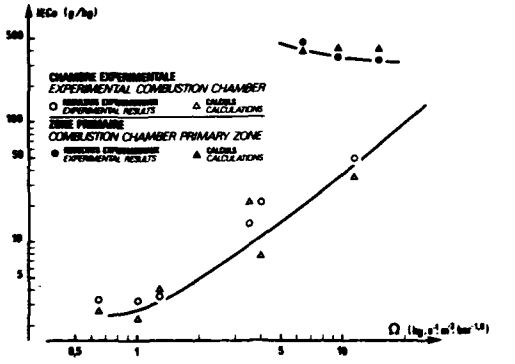


Figure 5 **COMPARAISON CALCUL/MESURES IECO EN FONCTION DE LA CHARGE AERODYNAMIQUE**
CORRELATION BETWEEN MEASURED AND COMPUTED EICO VERSUS AIR LOADING

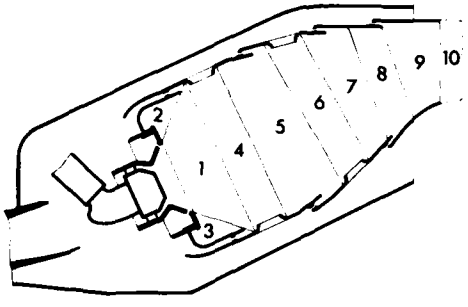


Figure 2 **CHAMBRE EXPERIMENTALE**
EXPERIMENTAL COMBUSTION CHAMBER

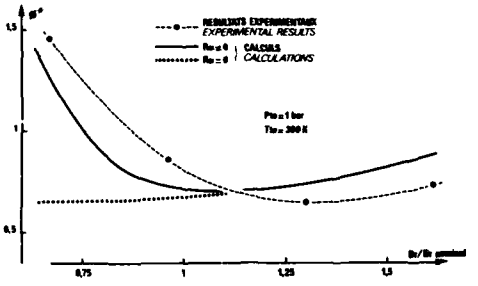


Figure 6 **ZONE PRIMAIRE - Comparaison des courbes de stabilité théoriques et expérimentales**
PRIMARY ZONE - Correlation between measured and computed stability characteristics

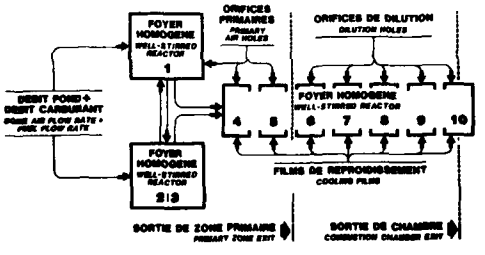


Figure 3 **DECOMPOSITION D'UNE CHAMBRE EN FOYERS HOMOGENES**
DESCRIPTION OF A COMBUSTION CHAMBER AS AN ASSEMBLY OF WELL STIRRED REACTORS

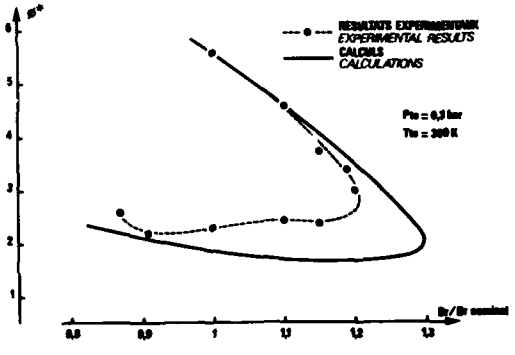


Figure 7 **CHAMBRE EXPERIMENTALE - Domaine de stabilité**
EXPERIMENTAL COMBUSTION CHAMBER - Stability characteristic

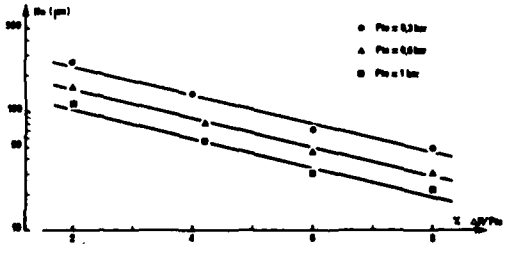


Figure 4 **EVOLUTION DU RAYON DE GOUTTE EN FONCTION DE LA PERTE DE CHARGE**
DROP SIZE VERSUS PRESSURE LOSS

CHARACTERIZATION OF HEAVY OIL SPRAYS IN ISOTHERMAL AND BURNING CONDITIONS WITH LASER LIGHT SCATTERING MEASUREMENTS IN THE SIDEWARD REGION

by
F. Beretta°, A. Cavaliere°, A. D'Alessio°°,
° Istituto di Ricerche sulla Combustione, C.N.R.
°° Istituto di Chimica Industriale e Impianti Chimici
Facoltà di Ingegneria dell'Università di Napoli
P.le V. Tecchio
80125 Napoli, ITALY

AD-P003 154

SUMMARY

A new drop-sizing technique for slightly absorbing liquid fuel is proposed. The technique relies on laser light scattering measurements at fixed scattering angle in the sideward region (ϑ=60°) and it exploits the effect of light absorption of the refracted rays that pass through the droplets. A theoretical calibration curve, computed on the ground of the geometrical optics theory, relates a measurable plane polarization state (the γ polarization ratio) with droplet dimensions for different levels of liquid fuel transparencies. The reasonably good approximation of the geometrical optics to the exact solution of Maxwell equation for a plane electromagnetic field incident on a sphere is also discussed. Furthermore the measure procedure and the sensitivity of the technique is illustrated through selected experimental examples. For this purpose heavy oil sprays have been generated by an air assisted nozzle on a vertical unconfined burner in isothermal and burning conditions. The radial distribution of droplet sizes and polarization ratios allow a characterization of spray evolution in the early regions of flame.

INTRODUCTION

Optical measurements methods are particularly suited to the study of the behaviour of sprays both in isothermal or evaporating regimes and a large body of literature has been generated on this subject /1,2,3/. A comparison between visualization methods and those based on laser light scattering effects indicates that the last ones offer the advantage of a better sensitivity toward the smaller droplets in the spray and allow more easily quantitative measurements.

So far the laser light scattering effects more largely exploited has been the measurement of the diffracted light in the forward region in the Fraunhofer lobe/4,5/. This method has the advantage of being independent from the optical properties of the droplets but suffers the inconvenience of a poor spatial resolution, which may be overcome only partially by complex tomographic procedures/6/. Therefore, in last few years, we started a program of researches in order to explore the potentialities of scattering measurements for spray diagnostics at different scattering angles with particular regard toward the side scattering region between ϑ=60° and ϑ=130°, where a better spatial resolution may be achieved. A further advantage of this approach is that the optical configuration is simpler than those employed in the forward scattering schemes and less subjected to ray distortions due to the temperature gradients in the medium,so that it may be used successfully also in the study of sprays in burning conditions.

A preliminary study was conducted on diesel oil sprays by measuring the complete angular pattern of the Stokes vectors of the scattered light and comparing the results with the geometrical optics computation for micronic non absorbing spheres /7/.The comparison showed that, while the forward scattering regions ($10°<\vartheta<70°$), dominated by the contribution of the refracted and reflected rays,was satisfactorily modelled by a geometrical optics approach, the analysis in the side scattering region around ϑ=90° has to be carried out in terms of the exact Lorenz Mie electromagnetic theory for polydisperse clouds of spheres. In a subsequent paper the polarization ratio of the scattered light at ϑ=105° was proposed as quantitative indicator of the modal size of droplets in light oil sprays and some examples of applications of the method to spray interacting with different air flow fields are also given /8/. More recently the study has been extended to the evaporation of sprays,generated by pressure driven and air assisted nozzles, in the combustion regime /9/. The straightforward extension of the method to sprays of different fuels requires the knowledge of its complex refractive index and a cumbersome integration of the Lorenz-Mie formulas over the polydispersion of sizes. However in the case of heavy oil fuels, which are absorbing in the visible, a simpler approach may be taken also using a geometrical optics analysis of scattering in the forward near ϑ=60°.

This paper has therefore the primary purpose of illustrating this new optical sizing method and presenting some results for both isothermal and burning heavy oil sprays .

1. THEORETICAL BACKGROUND

The quantity of relevance for LLS measurements is the angular scattering coefficient $Q_{ij}(\vartheta)$ defined as the intensity of light scattered in the unit volume, for unit intensity of the incident beam, under unit scattering solid angle; the i and j subscripts stand for horizontally (H) and vertically (V) polarized light in the incident and scattered beams respectively and ϑ is the scattering angle. In the regime of single scattering, the scattering coefficient for vertically polarized light is directly proportional to the total number concentration:

$$Q_{VV}(\vartheta) = N\, C_{VV}(\vartheta) \qquad (1)$$

where C_{VV} is the scattering cross section averaged over the size distribution of the scatterers; when the incident and scattered beams are both polarized in the horizontal planes, the scattering coefficient is

$$Q_{HH}(\vartheta) = N\, C_{HH}(\vartheta) \qquad (2)$$

The polarization ratio between the scattering coefficients $\gamma = Q_{HH}/Q_{VV}$ is independent on the density of scatterers and is determined only by the size, shape and optical properties of the particle.

Spray generated droplets are practically spherical and exhibit sizes ranging from 1 μm to 200 μm; the real part n of the complex refractive index m=n-ik in the visible varies between 1.45 and 1.55, depending on the paraffinic/aromatic ratio of the hydrocarbons mixture. The imaginary part of the refractive index k is directly related to the amount of polycyclic aromatic compounds in the fuel and changes appreciably with the scattering wavelengths, as it shall be discussed later.Therefore the dependence of the angular scattering cross sections in both polarization planes,upon the refractive index m and the size parameter

$\alpha = D/\lambda$ are exactly described by the Lorenz-Mie theory, in terms of infinite series. It may be shown that the series converges for a number of terms slightly higher than α and consequently a relevant number of terms has to be taken into account, because α inside a spray may vary between 5 and 1000; furthermore the solutions for a single sphere exhibit a strongly oscillatory behaviour in the angular and size domains. Consequently the Lorenz-Mie computations have to be averaged over a size distribution in order to make significative comparison with the experiments normally done on polydisperse droplets systems. Hansen and Hovenier/10/ executed such extensive computation of the angular scattering cross sections and of the polarization ratio for polydispersion of non absorbing spheres with n ranging from 1.33 to 1.5. For the size distribution they used a Γ function of the type:

$$f(\alpha) = C_1 \alpha^6 \exp(-6\alpha/\alpha_m) \qquad (3)$$

where α_m is the modal value of the distribution.

Fig. 1, adapted from Hansen and Hovenier paper, illustrates how the polarization ratio changes with the modal size for clouds of polydisperse transparent spheres with n=1.5 at selected scattering angles. The differences between the behaviour in the forward scattering at $\vartheta = 25°$ and $\vartheta = 60°$ and that in the side scattering at $\vartheta = 105°$ and in the backward at $\vartheta = 160°$ are quite evident.

At $\vartheta = 25°$ the γ ratio exhibits a relatively smooth transition from the Rayleigh values ($\alpha < 1$) to the constant geometrical optics limit ($\alpha >> 1$); the oscillations shown in the region between $\alpha = 3$ and 6 are due to anomalous diffraction generated by the interference between diffracted, reflected and transmitted light in the near forward/11/. The same behaviour is shown at $\vartheta = 60°$ also if the oscillation due to anomalous diffraction is more attenuated.

On the contrary in the side and backward regions γ rises from the Rayleigh values to a very marked maximum, which reaches values as high as seven for $\vartheta = 160°$, and then decreases, reaching the asymptotic geometrical optics limits at much larger α values respect to the forward scattering case. This high sensitivity of the polarization ratio may be understood in physical terms by considering that beyond $\vartheta = 97°$ the scattered light is the sum of surface waves and external reflected rays. While this last contribution can be treated on a geometrical optics basis, surface waves are described only by the elctromagnetic theory . Surface waves, which are generated by grazing rays and spray off their energy travelling around the periphery of the sphere, are preferentially polarized in the horizontal plane ($\gamma > 1$), as it has been pointed out by van de Hulst /11/. When the size parameter is increased the energy must be distributed over a larger surface, the external reflection contribution becames progressively more relevant and because the Fresnel equations predict a preferential polarization on the vertical plane the overall ratio declines.

Therefore the polarization effect discussed before may be used for determining the modal size of droplets inside a spray; a more detailed illustration of the method and some examples of applications to diesel oil sprays, atomized by pressure and air assisted nozzles, have been presented elsewhere/8,12/.

Fig.2 evidences that for fuel droplets which are transparent to the incident laser radiation only the side scattering or backward regions are usable for diagnostics based on polarization measurements at fixed angles. However when the droplets are able to absorb the incident radiation also the scattering in the forward direction may be used for sizing measurements. In fact in this region where the ray optics approximation is adequate, the scattered rays are due to the sum of refraction and external reflection, with a negligible contribution of surface waves effects.

The presence of a non zero absorption coefficient produces an attenuation of the refracted ray which travels inside the droplet, but has a minor importance on the intensity and the polarization properties of the reflected rays. Obviously the net effect on the polarization ratio depends also on the size of the particle and on the scattering angle. In fact the polarization ratio is expressed by the following expression:

$$\gamma = \frac{Q_{HH}^{refl} + Q_{HH}^{refr}}{Q_{VV}^{refl} + Q_{VV}^{refr}} = \frac{C_{HH}^{refl} + C_{HH}^{*refr} \exp(-K_{abs} D \sin\phi)}{C_{VV}^{refl} + C_{VV}^{*refr} \exp(-K_{abs} D \sin\phi)} \qquad (4)$$

where the superscripts refl and refr stand for external refraction and refraction, C^{*refr} are the cross-sections for the refractive contribution computed for a purely transparent sphere of diameter D. K_{abs} is the absorption coefficient of the liquid which is related to the imaginary part of the refractive index with the formula:

$$K_{abs} = 4\pi k/\lambda \qquad (5)$$

ϕ is the angle between the tangent at the impact point of the incident ray and the chord described by the refracted beam and is a function of the scattering angle ϑ /13/.

Fig.2 reports the angular profiles of the polarization ratio, computed through eq.4, for a 50μm particle with n=1.5 for the transparent case (k=0) for relatively high absorption ($k > 10^{-2}$) and for a slightly absorbing condition ($k = 10^{-3}$).

When k is equal or larger than 10^{-2} the refractive contribution is practically negligible and the polarization is determined by the external reflection and therefore is computed through the Fresnel equations. Consequentely the γ ratio is equal to one in the near forward, goes to zero in correspondence of the Brewster angle at $\theta = \text{arctg}(n) = 67°$ and then increases again in the side region.

The contribution of the refracted rays are fully manifested in the transparent case: in tha forward region ($5° < \vartheta < 70°$) the cross sections for refraction are almost one order of magnitude larger than those due to reflection and the γ ratio behaviour is almost completely determined by them.

The refracted beams are preferentially polarized on the horizontal plane and γ goes from one to a maximum of 1.4 in corrispondence of the Brewster angle.

For scattering angles larger than $\vartheta = 70°$ both C^{refl} and C^{refl} decline very rapidly and their contribution goes to zero beyond $\vartheta > 90°$, at the limit angle; therefore the γ ratio in this region falls down from values larger than one to the pure reflective regime discussed before.

The two minima at $\vartheta = 93°$ and $\vartheta = 157°$ are due to the rainbows generated by two and one internal reflection respectively /14/. However it is worthwhile to underline that this geometrical optics approach does not have a great relevance for the side and back scattering regions because it does not take into account surface wave effects and poorly describe s the rainbow and glory regions.

A partially absorbing particle has polarization ratios in the forward region intermediate between the two cases discussed above. The larger variations occur between $\vartheta = 60°$ and 90° because in this region the polarization ratio due to external reflection is particularly lower than that due to pure refraction. However the γ fall off in the region between the Brewster angle and the limit angle is very steep and is

influenced by the exact value of the real part of the refractive index, whereas at ϑ =60° the sensitivity of the γ ratio toward the optical depth $K_{abs}D$ is still high, but the choice of m and ϑ is not so critical.

The computed fall off of γ (60°) with kD is reported in fig.3 where the separated influences of the size and the optical absorption are also shown.The polarization ratio tends to its reflective limit for kD larger than 0.3 μm; it means that γ (60°) may be used for determining the sizes of droplets with an upper limit of 300 μm when the absorption index is equal to 10^{-3} but obviously it has sensitivity only for particles up to 3μm when k=10^{-1}

Hencefore a previous measurement of the absorption index of the liquid is critical for the application of the method and the spectrophotometric measurements of k from 200 to 800nm of the heavy oil used in this experiment are shown in fig.4, together with the corresponding curves for heavy and light crudes adapted from the fluorescence measurements by Hoge /15/.

The k profile has a peak at 220 nm with a value around 10^{-1} and then decrease in the visible; at 514.5 nm (at the laser wavelength), k is equal to 5.5×10^{-3} and at λ =800 nm it goes down to 1.2×10^{-3}.

The curve relative to the heavy crude is quite near to heavy oil distillate whereas that obtained for light crude exhibits a much lower absorption. These differences are indicative of different concentrations of the polycyclic aromatic compounds in the fuel mixtures.

2. EXPERIMENTAL

A schematic description of the apparatus for light scattering measurements is reported in Fig. 5. The light source used in our experiments was an Argon-Ion Laser tuned on the wavelength λ =514.5 nm with 1.4 W power. A finite segment of the laser ($\sim$ 300 μm) is focused through a condensing lens on the aperture of the detection system constituted by a monochromator, selecting only the laser wavelength, and a photomultiplier transducing the scattered radiation in a d.c. signal. The angle between the axes of the laser and of the collecting optics is defined as the scattering angle ϑ and both axes lie on the scattering plane which is the reference for the definition of the plane polarized light. In fact the vertical and horizontal polarization are respectively referred to the electrical field perpendicular or parallel to the scattering plane. The continuous rotation of the laser polarization plane was allowed in our experiment through a $\lambda/2$ retarder plate, placed in front of the laser, whereas the selection of the polarization plane of the scattered light was performed by means an analyser at the entrance of the detection system.

With this arrangement we can measure the two quantities of our interest Q_{VV} and Q_{HH}, i.e. the scattering coefficients measured at fixed scattering angle (ϑ=60°) when the incident and scattered light are the same: vertically polarized in the first case (Q_{VV}) and horizontally polarized in the latter one (Q_{HH}).

A more focused picture of the experimental set-up and of measuring methodology can be obtained by previous papers of the authors /16,17/.

Furthermore it is worthwhile to note that other polarization states /18/ or dissymmetry ratios between two scattering angles /17/ or dispersion ratios between two light wavelengths /19/ may also be explored with this kind of optical set-up for sizing or particle characterization techniques, but this paper will deal only with scattering measurements of fixed angle ϑ =60° in order to analyze the sensitivity of the polarization ratio to droplet size.

Vertical unconfined sprays in isothermal and burning regimes can be generated up to a fuel mass flow rate of 30 kg/h by a variable swirl burner described in previous papers for diesel oil flames / 17 , 20 /. The only relevant modification is constituted by the change of the pressure nozzle with an air assisted atomizer drawn in Fig. 6.

The heavy fuel oil is injected through four peripheral orifices into a pre-chamber where they meet the four air jets coaxial to the geometrical axis. Both the air and the liquid fuel are forced to pass through an orifice (ϕ=0.9 mm) at very high velocity. The atomization characteristics have been preliminary assessed using diesel fuel oil by analyzing drop sizes at different air-fuel mass ratios (R) /21/.

A spray with 20° aperture is generated when R>0.1 for diesel and heavy fuel oil and droplets diameter of the diesel oil on the axis is very low/12,21/; higher values of R do not affect sensitively the cone aperture but decrease the modal diameter up to R=0.05.

Two coaxial ducts (ϕ_I=28 mm, ϕ_{II}=74 mm) confine primary and secondary air, which are respectively axially and tangentially oriented. In this work the operative conditions are fixed as it follows

Fuel	Atomizing air	Primary air	Secondary air
v = 8 l/h T = 70°C	$\dot{v}$ = 500 Nl/h T = 70°C	$\dot{v}$ = 9000 Nl/h T = 170°C	$\dot{v}$ =150000 Nl/h T = 170°C n_{sw} = 0.48

The swirl number has been calculated following the formula by Beér and Chigier /22/ for a fixed position of radial swirl blades mounted at the entrance of the external duct.

3. EXPERIMENTAL RESULTS

The preliminary measurements of the γ polarization ratio have been performed on the isothermal spray, so that the measured ansorption index at λ=514.5 nm is surely constant everywhere in the spray (k=5.5×10^{-3}) and the γ variation can be attributed to different average sizes of the droplets.

The radial profiles of γ in the isothermal spray are reported in fig. 7 for five heights above the burner. A unit value on the centerline at all stations keeps constant whereas all the profiles evolve toward lower values outward. The most steep radial gradient is observed at z=20 mm, in fact at y=12 mm it attains a value of 0.43; relatively lower gradients are measured at z=30 mm and z=40 mm, eventhough the profiles are very similar to that one relatively to z=20 mm and the most peripheral position, where could be measured, is at all the three stations around 12 mm.

On the opposite side the other two stations show a more gradual decline and cover a larger area up to y=23 mm. The same curves, expressed in terms of diameters with assumption of monodisperse spray, have been deduced by the theoretical calibration of fig. 3 and they are reported in fig. 8. Analogous comments with inversion of trends can be repeated for these profiles: the first three curves evidence that the spray plume in the early region retains more a cylindrical shape tha a cone one and that higher is the height lower is the diameter of the droplets at the periphery of the spray. In fact the largest size of D=20 μm is observable at z=20 mm, y=10 mm, and this value declines to D=16 μm twenty millimeters downstream.

This radial size distribution is in reasonable agreement with the atomization mechanism proposed in a previous paper /21/ for the same nozzle spraying diesel oil: the high velocity slip between the two phases is responsible for the quite high level of atomization on the center whereas a little amount of liquid escapes the gas jet and it survives in form of relatively large droplets. In this early regions aerodynamic dispersion due to the central axial jet induce the small droplets to mask the larger ones. Only at the station z=50 mm the entrainment of the droplets due to the external swirled jet become evident and a more uniform profile is observable also at z=60 mm.

Finally it is interesting to follow the spatial distribution of the polarization ratio for a burning spray in fig. 9, where the iso-value contours of γ are reported for the same fluid-dynamic inlet conditions of the isothermal regime. Along the centerline the γ-ratio does not keep constant value, but it decreases quite rapidly in the first 50 mm and more gradually in the following part.

Much steeper gradient are observed moving outward from the axis and a relatively wide region, where γ ranges between 0.2 and 0.3, is detected at the periphery of the flame.

These low values are circumscribed within a dashed line in order to underline that they coincide with an area where a yellow luminosity is visually observed; so that it is not surprising that a γ value of 0.25 is also predicted by the theory for the submicronic soot particles /17/, which are, in fact, responsible for the light emission.

On the other side the axial and radial decrease of γ in the central part can be related to the increase of $K_{abs}D$; therefore it is open to speculation whether the γ variation has to be attributed to large dimensions on the border of the spray or to an increase of the absorption coefficient due to production of heavier polycyclic compounds through liquid phase pyrolysis near the flame fronts. It seems plausible that a selective vaporization favors the survival of large droplets near the nozzle and along the axis, whereas pyrolysis effects are more pronounced on the periphery where the temperature is relatively high to cause chemical alterations.

4. DISCUSSION OF THE OPTICAL TECHNIQUE

The main purpose of the paper was to explore the possibility of using the geometrical optics controlled features of the forward pattern of scattered light in order to determine the size of droplets; therefore a minor emphasis is given to the physical description of the spray.

This method offers the normal advantage of the LLS techniques over the visualization ones of being particularly sensitive towards the smaller droplets of the size distribution and it allows consequently a better physical understanding of the atomization process itself. Furthermore, being an ensemble LLS technique it offers the possibility of studying the dense regions of the spray where the single counting particle methods are not applicable /23/.

An obvious disadvantage of this method consists on the necessity of assuming a size distribution law. However the fact that the scattering cross sections are described by simple geometrical optics expressions instead of the complex Lorenz-Mie series allows to perform the integrations analitically.

The polarization ratio depends, as it was discussed before, also on the imaginary part of the refractive index of the medium. This effect may create some problems when the optical constants are varying for thermal or chemical processes, as it happens in the liquid pyrolysis phase inside burning sprays; however when the size of the droplets are known indipendently, e.g. from LLS measurements at other angles, the value of the γ polarization ratio might be used for inferring the absorption index itself.

Furthermore the strong dependence of the absorbing of hydrocarbons mixture on the wavelength enlarges the dynamic range of the technique when a tunable laser or polychromatic lamps are used as light sources. Also different scattering angles in the forward should be considered; for instance at the Brewster angle the horizontally polarized cross section due to refraction goes to zero and the overall ratio tends to particularly low values.

This circumstance has a relevance for burning sprays where also submicronic soot particles are present in the system because measurements of horizontally polarized scattered light at the Brewster angle furnish a direct signature for this last class of particles. A comparison between the polarization property of light scattered by ensemble of droplets in the forward and that scattered in the side scattering region is also interesting for physical and diagnostics aims. In fact side scattering polarization is determined by the sum of reflected light and surface waves as it was pointed out before; consequently independent evaluation of the particle size in the forward should permit to assess the importance of the surface scattering effects even in cases where the optical properties of the droplets are not precisely known.

A final comment must be addressed to a comparison between droplet diameters estimated in this paper for heavy oil spray with those obtained for light oil spray in a previous paper /21/. The radial size distribution show a quite similar behaviour for the two fuels at the same heights, eventhough droplet sizes of the heavy oil approximatively double those of the diesel oil. Therefore the same atomization mechanism can be inferred for both fuels, although some change in the physical properties make the droplet diameters higher. The viscosity, also taking into account the preheating of the heavy oil, is the only reasonable parameter, to which this effect can be attributed, since density and surface tension retain practically the same value. It has been documented /24/ that the shattering of the liquid due to velocity slip between the two phases is not affected by viscosity, so that the reasonable conclusion is that higher viscosity entails larger thickness of layers or filaments which are formed in the nozzle prechamber.

5. REFERENCES

1. Bayvel, L.P., Jones, A.R.:" Electromagnetic Scattering and Its Applications," Applied Science Publishers, London (1981)

2. Azzopardi, B.J.: "Measurement of Drop Sizes", J. Heat Mass Transfer, 22, 1245 (1979)

3. Chigier, N.: "Group Combustion Models and Laser Diagnostic Methods in Sprays: a Review", Comb. Flame, 51, 127 (1983)

4. Dobbins, R.A., Crocco, L., Glassman, I.: "Measurement of Mean Particle Sizes of Sprays from Diffractively Scattered Light", A.I.A.A.J., 1, 1882 (1963)

5. Swithenbank, J., Beér, J.M., Taylor, D.S., Abbott, D., McGreath, C.G.: "A Laser Diagnostic for the Measurement of Droplet and Particle Size Distributions", Progr. Astronaut. Aeronaut., 53, 421 (1976)

6. Yule, A.J., Ah Seng, C., Felton, P.G., Ungut, A., Chigier, N.A.: "A Laser Tomographic Investigation of Liquid Fuel Sprays", Proc. 18th Int. Symp. on Combustion, The Combustion Institute, Pittsburgh, p. 1501, 1981

7. Beretta, F., Cavaliere, A., D'Alessio, A.: "Experimental and Theoretical Analysis of the Angular Pattern Distribution and Polarization State of the Light Scattered by Isothermal Sprays and Oil Flames", Comb. Flame, 49, 183 (1983)

8. Beretta, F., Cavaliere, A., D'Alessio, A.: "Drop Size and Concentration in a Spray by Sideward Laser Light Scattering Measurements", Comb. Sci. Techn, in press

9. Nussenzveig, H.M.: "Complex Angular Momentum Theory of the Rainbow and the Glory", J. Opt. Soc. Am., 69, 1068 (1979)

10. Hansen, J.E., Hovenier, J.W.: "Interpretation of the Polarization of Venus", J. Atmos. Sci., 31, 1137 (1974)

11. van de Hulst, H.C.: "Light Scattering by Small Particles", J. Wiley, New York, 1957

12. Beretta, F., Cavaliere, A., D'Alessio, A.: "Laser Light Scattering Technique in the Diagnostics of Sprays in Isothermal and Burning Conditions", Proceeding of VI Int. Symp. on Air Breathing Engines, Paris, June 6-10, 1983

13. Hottel, H.C., Sarofim, A.F.: "Radiative Transfer", Mc Graw Hill, N.Y., 1967

14. D'Alessio, A., Cavaliere, A., Menna, P.: "Theoretical Models for the Interpretation of Light Scattering by Particles Present in Combustion Systems" in "Soot in Combustion Systems and its Toxic Properties", Edited by Lahaye J. and Prado G., Plenum Press, N.Y. and London, 1983, p. 327

15 Hoge, F.G.: Applied Optics, 21, 1725 (1982)

16. D'Alessio, A., Beretta, F., Cavaliere, A., Menna, P.: "Laser Light Scattering and Fluorescence in Fuel Rich Flames: Techniques and Selected Results" in "Soot in Combustion Systems and Its Toxic Properties", Edited by Lahaye J. and Prado G., Plenum Press, N.Y. and London, 1983, p. 355

17. D'Alessio, A.: "Laser Light Scattering and Fluorescence Diagnostics of Rich Flames Produced by Gaseous and Liquid Fuels" in "Particulate Carbon: Formation During Combustion", D.C. Siegla and G.W. Smith Eds., Plenum Publishing Corp., N.Y., 1982

18. Beretta, F., Cavaliere, A., D'Alessio, A.: "Experimental and Theoretical Analysis of the Angular Pattern Distribution and Polarization State of the Light Scattered by Isothermal Sprays and Oil Flames", Comb. Flame, 49, 183 (1983)

19. Menna, P., D'Alessio, A.: "Light Scattering and Extinction Coefficient for Soot Forming Flames in the Wavelength Range from 200 nm to 600 nm", XIX Symp. Int. on Combustion, The Combustion Institute, Pittsburgh, 1983, p. 1421

20. Beretta, F., Cavaliere, A., D'Alessio, A., Noviello, C.: "Visible and U.V. Spectral Emission and Extinction Measurements in Oil Spray Flame", Comb. Sci. Techn., 22, 1 (1980)

21. Beretta, F., Cavaliere, A., D'Alessio, A., Noviello, C.: "Analisi delle strutture di fiamme di miscele di carbone-olio combustibile con diagnostica di tipo ottico", Proceedings of XXXVIII Congresso dell'Associazione Termotecnica Italiana, Bari, September, 1983

22. Syred, N., Beér, J.M.: "Combustion in Swirling Flow a Review", Comb. Flame, 23, 143 (1974)

23. Holve, D.J.: "A Single Particle Counting Diagnostic System for Measuring Fine Particulates at High Number Densities in Research and Industrial Applications", SANDIA Report SAND 83-8246, Sandia National Laboratories, October, 1983

24. Yule, A.J., Eisenklam, P., Swithenbank, J.: Notes to "Short Course on Spray and atomization" UMIST, 26-28 September 1983, Thermodynamics and Fluid Mechanics Division, Department of Mechanical Engineering, UMIST, Manchester, U.K.

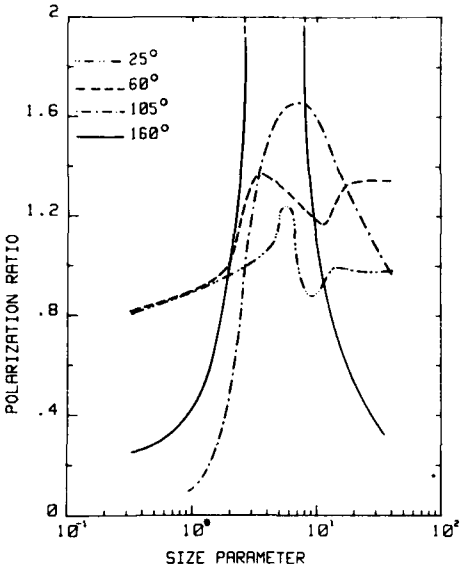


Fig. 1 - Polarization ratio ($\gamma = Q_{HH}/Q_{VV}$) as function of the modal size parameter ($\alpha = \pi D/\lambda$) for different scattering angles: ϑ=25°, 60°, 90°, 160°. Adapted by Hansen J.E. and Hovenier J.W., J. Atmos. Ser., 31, 1137 (1974)

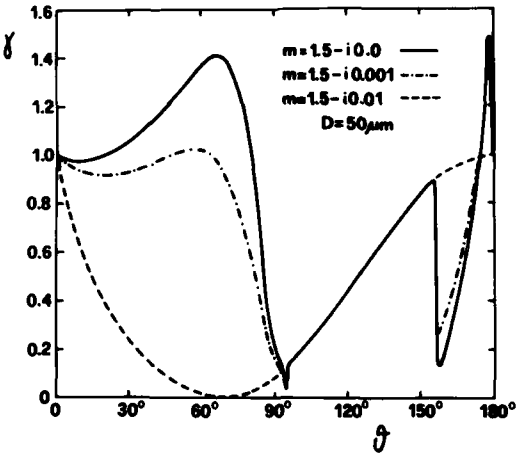


Fig. 2 - Angular patterns of the polarization ratio ($\gamma = Q_{HH}/Q_{VV}$) computed through the geometrical optics theory for three different imaginary parts of the refractive index and for a fixed droplet diameter.

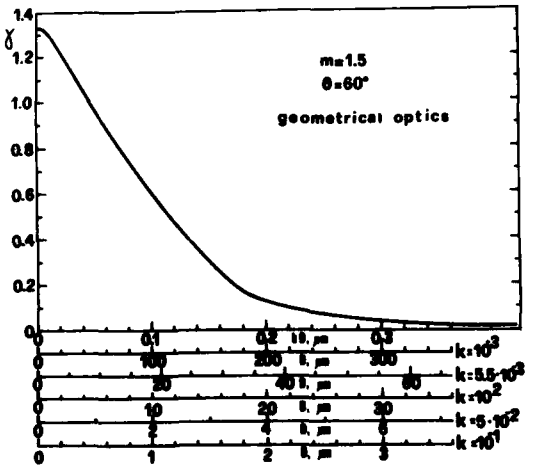


Fig. 3 - Polarization ratio ($\gamma = Q_{HH}/Q_{VV}$) as function of kD, computed through the geometrical optics theory for n=1.5 at the scattering angle ϑ=60°; k is the imaginary part of the refractive index and D is the droplet diameter. The lower abscissae report the droplets diameters calculated by kD at fixed value of k.

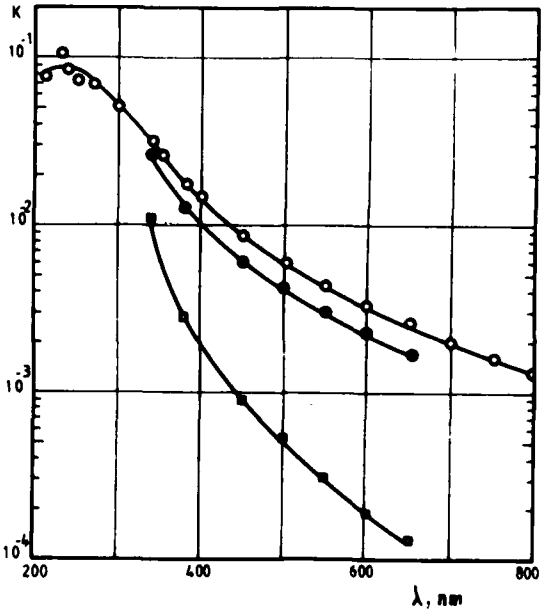


Fig. 4 - Spectral profile of the imaginary part of the refractive index between 200 and 800 nm. The curve with symbols (o) is relative to measured values for the heavy oil reported in this paper. The curve with symbols (o) and (□) are relative to values adapted by Hoge /15/ for heavy and light crude respectively.

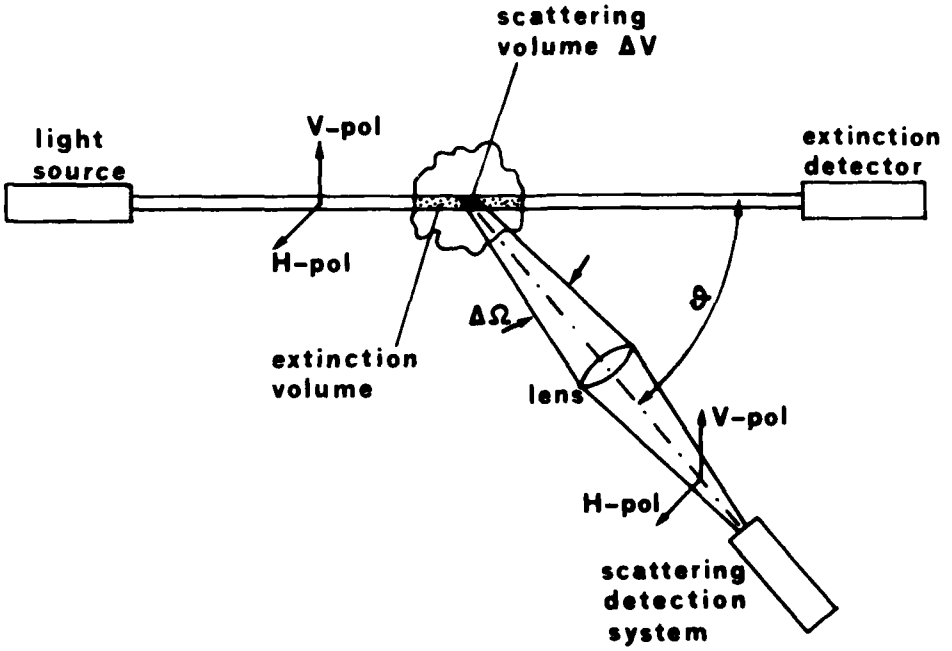


Fig. 5 - Sketch of the optical apparatus

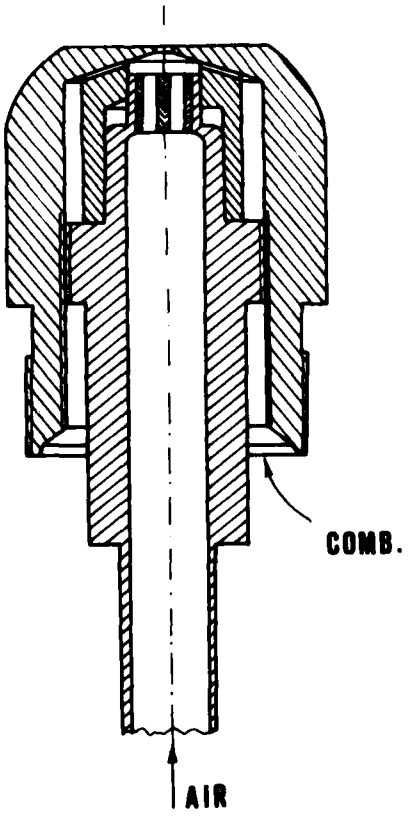


Fig. 6 - Vertical section of the air assisted nozzle.

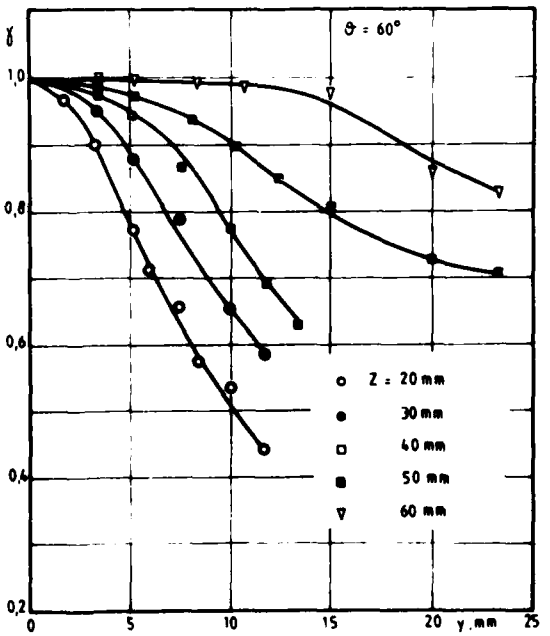


Fig. 7 - Radial profiles of the measured values of the polarization ratio ($\gamma = Q_{HH}/Q_{VV}$) for five different heights above the burner of a heavy oil isothermal spray at the scattering angle $\vartheta = 60°$.

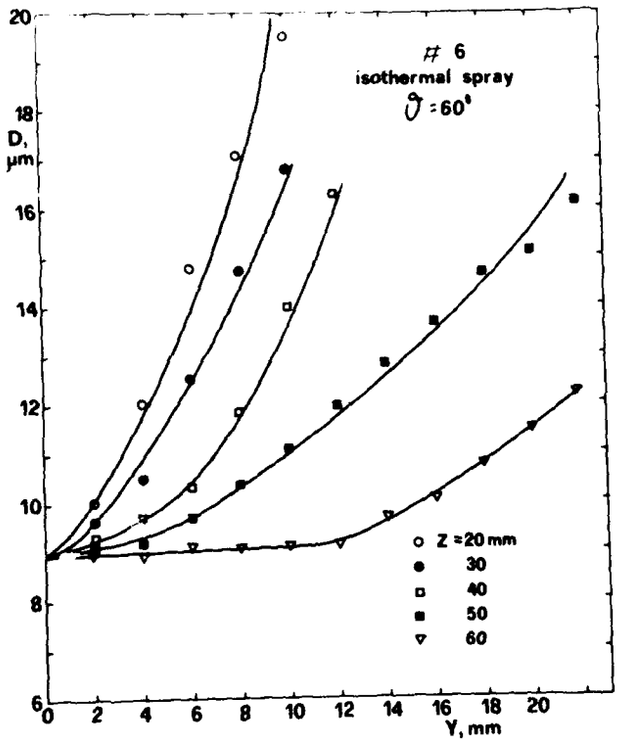


Fig. 8 - Radial profile of the droplet diameter obtained by Fig. 7 by means the calibration curve of Fig. 3.

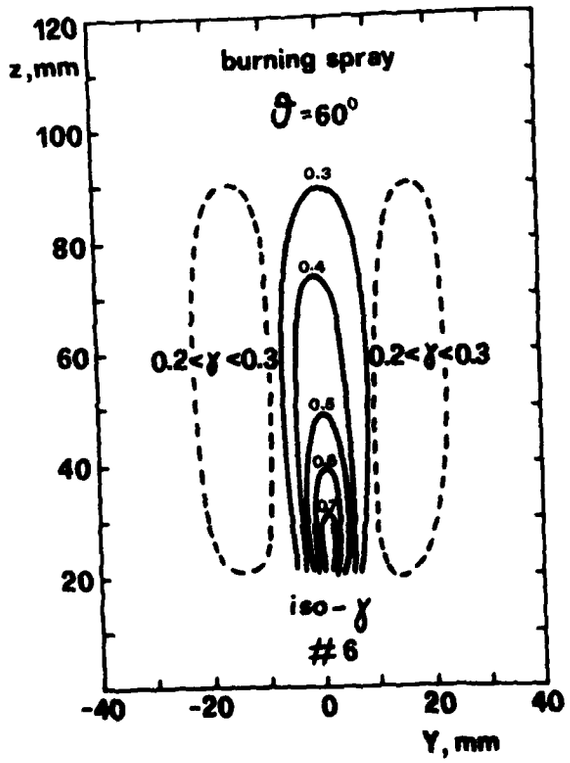


Fig. 9 - Iso-value contours of the measured polarization ratio ($\gamma = Q_{HH}/Q_{VV}$) relative to a heavy oil flame.

UTILIZATION OF LASER DIAGNOSTICS TO EVALUATE COMBUSTOR MODELS

W.M. Roquemore, R.P. Bradley, J.S. Stutrud, C.M. Reeves, C.A. Obringer
and R.L. Britton
Air Force Wright Aeronautical Laboratories
Aero Propulsion Laboratory
Wright-Patterson Air Force Base
Dayton, Ohio 45433, U.S.A.

AD-P003 155

1.0 SUMMARY

This paper presents an overview of results obtained in the Combustion Model Evaluation research program being sponsored by the Air Force Wright Aeronautical Laboratories. The characteristics of a bluff-body research combustor used in this program are described. Data obtained with a laser Doppler anemometer system and a coherent anti-Stokes Raman scattering system are presented. These results and those obtained with conventional probe devices and flow visualization techniques are compared to both time-averaged and time-dependent calculations of the near-wake region of the bluff-body flow field. The results of computer model experiments of the flow field for different diameter bluff bodies are also presented.

2.0 INTRODUCTION

Computer models are being developed and utilized in some combustor development programs in an attempt to reduce the development cycle and the associated development cost [1,2,3]. The combustor design models presently provide information about performance trends and give insights into the combustion processes instead of providing quantitative design information [4]. Consequently, considerable work is needed to thoroughly assess the performance of existing and future design models and to improve their predictive capabilities in practical combusting environments.

In 1977, the Air Force Wright Aeronautical Laboratories/Aero Propulsion Laboratory (AFWAL/APL) initiated a Combustor Model Evaluation (CME) research program. This was viewed as a long-term program with two primary objectives: to develop and evaluate the performance of probes and advanced laser measurement techniques in combustion environments and to use the proven techniques in experiments to evaluate and develop combustor models. To date, much of the work on the CME program has involved the development and study of a special research combustor at APL that is used to evaluate the performance of the measurement techniques and combustor models. Also, laser Doppler anemometry (LDA) and coherent anti-Stokes Raman spectroscopy (CARS) systems have been developed on Air Force contracts for utilization in the APL Combustion Research Facility.

This paper presents an overview of the results from the CME program. Results from high speed cine pictures, conventional probes and LDA studies of the turbulent processes in the APL research combustor are presented. CARS is just beginning to be used as a combustion research tool in the facility and some of the initial results are also presented. The data from these studies are used to evaluate both steady-state (time averaged) and unsteady (time-dependent) computer models. A good qualitative understanding of the rather complicated processes occurring in the research combustor has developed from several years of studying the combustor. This understanding has been enhanced by studying the results of computer model calculations. The experimental and theoretical results are presented in a way to illustrate the understanding gained from both a time-averaged and a dynamic view of the turbulent processes. Results which have been presented in other technical articles are referenced so that due credit is given to other participants in the CME program. Since results are stressed in this paper, detailed descriptions of the LDA and CARS systems and of the computer models are not presented. The interested reader can consult the referenced articles for these details.

3.0 APL COMBUSTION RESEARCH FACILITY

The APL combustor, shown in Figure 1, consists of a shrouded disk with fuel injected from a tube located in the center of the disk. This configuration was proposed by Dr S.N.B. Murthy and Dr J.A. Skifstad of Purdue University after reviewing Air Force combustion research needs, including those reported by Goulard, et al in Reference 5. The combustor has simple axisymmetric geometry for ease of modeling and the air velocity profile established at the combustor inlet plane is nearly flat. The configuration provides easy measurement access to the combustor inlet plane and the reaction zone. Also, the configuration permits complexities to be added to the combustion process such as changing from gaseous to liquid fuels, nonswirling to swirling air flows and unmixed to premixed fuel and air. However, the centerbody, with current dimensions, is not an ideal research combustor because the small diameter of the fuel jet and the large separation between the fuel jet and the annular jet cause problems in choosing a computational grid and in making measurements at the fuel exit plane. A large fuel jet has been investigated but the resulting flames were not symmetric. Even with these difficulties, we believe that the combustor offers an adequate simulation of practical, recirculating flow fields for evaluating combustor models and represents a good compromise between a simple, well controlled laboratory burner and a practical combustion device.

The centerbody is mounted in a specially designed duct as shown in Figure 2.* The duct, referred to as the combustion tunnel, has two viewing sections, one 106 cm long and the other 76 cm long. A total of nine access ports provide both optical and conventional probe access to important combustion regions. Each port is 30.5 cm long by 7.6 cm wide and can be filled with either an optical window or a

* The combustion tunnel was designed by Dr T.J. Rosjford of the United Technologies Research Laboratories and by Prof L.I. Boehman of the University of Dayton.

metal plate as required by the experiment. The access ports are arranged for probing various axial test regions from three ports located 90 degrees apart. Additional details about the combustion research facility are given in Reference 6.

Air supplied to the combustion tunnel can be preheated by passing it through an unvitiated air heater. This system is capable of supplying 3.4 kg/s of air at temperatures up to 900 K. The combustion tunnel was designed to operate at pressures up to 6.5 atms. To date, all experiments have been conducted at atmospheric pressure and room inlet temperatures.

4.0 INSTRUMENTATION DESCRIPTION

A 2-component LDA system was designed based on the experience obtained with a one-component system [7]. Polarization is used to separate the two velocity components and a Bragg cell is used to remove directional ambiguity. The scattered light is collected with off-axis optics and transmitted by optic fibers to two photomultipliers in the facility control room. The photomultiplier signals are amplified and processed by two modified TSI 1990A processor counters. A Norland Instruments Model 5400 multi-channel analyzer, connected to the processor counters, gives a preliminary on-line data viewing capability. The primary data are collected by interfacing the processor counters to the facility computer in a way that permits data collection rates up to 130K data points/s. A 10 MHz oscillator is used to clock events on each channel so that simultaneous two velocity component data can be obtained. Two fluidized-bed seeders are used to simultaneously seed both the fuel and air flows. Detailed descriptions of the LDA system are presented in References 8 and 9.

The CARS system is based upon a folded BOXCARS optical configuration which permits high spatial resolution [10,11]. The system design was based on the results of extensive laboratory tests [12,13] and the experiences gained by testing a hardened colinear CARS system in the APL Combustion Research Facility [14]. The system is capable of making simultaneous temperature, N_2 and O_2 concentration measurements at a point ($<1mm^3$) in a 10 ns time period. The CARS system is interfaced to the facility computer so that it can continuously collect and store the data from 14,000 laser shots at a rate of 10 Hz before filling a magnetic tape. Detailed descriptions of the optical configuration and the data-collection electronics are described in Reference 15.

Conventional probes are also used to make measurements in the combustor. The probe is mounted vertically through a special slide arrangement located on the top of the duct as illustrated in Figure 2. The slide permits access to axial regions covered by the window without removing the probe. In some experiments, CO_2 was injected from the central jet. CO_2 concentrations were measured with a 3.175 mm diameter probe and a gas sampling system. In combusting experiments, temperatures were measured with a Type-R shielded thermocouple probe. The radiation losses are assumed to be negligible and the indicated temperatures are presented. The probe housing is water cooled and has an outside diameter of 6.35 mm. Much of the understanding of the dynamic characteristics of the flame in the APL combustor has resulted from studying high speed cine pictures. A Photec IV high speed camera was used to make the pictures. The camera has an f stop of 2.8 with an 18 mm focal length lens. The framing rate could be varied from 500 to 8000 frames/s. Pictures were also made with a wide angle fish-eye lens with an f stop of 5.6.

5.0 THEORETICAL CONSIDERATIONS

Results of theoretical predictions from time-averaged and time-dependent fluid dynamic computer codes are presented in this paper. The time-averaged code was developed at Imperial College as a teaching aid and is called TEACH (Teaching Elliptic Axisymmetric Characteristics Heuristically) [16]. This code provides the framework for the codes that are presently used as design aids in gas turbine development programs [2,3]. The code uses a hybrid upwind/central finite differencing scheme to solve the elliptic form of the time-averaged Navier-Stokes equations as formulated from an Eulerian reference frame. Closure is obtained by using the k-ε turbulence model. A computational grid of 41 axial nodes and 34 radial nodes was used in the calculations. The axial grid extended 2.14D downstream which is well past the recirculation zone. The details of the calculations are given in Reference 17.

The TEACH Code predictions are given for nonreactive, imcompressible flow where CO_2 is injected from the central fuel jet with air injection from the annulus jet. The governing equations, as presented in Reference 17, are given in Table 1 where ϕ is a general dependent variable, S_ϕ is the source term for ϕ, Y_F is the mass fraction for the central jet, P_k is the rate of generation of turbulent energy. Γ_ϕ is the effective exchange coefficient for the transport of the variable ϕ and is given by μ_{eff}/σ_ϕ where μ_{eff} is the effective viscosity and σ_ϕ is the appropriate effective Prandtl/Schmidt number for ϕ. The effective viscosity is given by the sum of the laminar, μ, and turbulent eddy viscosity, μ_t where $\mu_t = C_\mu \rho k^2/\varepsilon_o$. C_μ is a constant equal to 0.09, ρ is the fluid density, k is the turbulent kinetic energy and ε is the turbulence energy dissipation which is equal to $k^{3/2}/\ell_1$ where ℓ_1 is the turbulent length scale. For the annulus jet the length scale ℓ_1 is given by λ (D´ - D)/2 where λ is a constant equal to 0.3333. For the central jet $\ell_1 = \lambda(d/2)$.

A summary of the boundary conditions used in the TEACH Code calculations is given in Table 2. The inlet velocities, W_{in} and turbulent kinetic energy, k, were specified in two different ways. In Case 1, flat velocity profiles were assumed for both the annulus jet and the central fuel jet. For this case, W_{in} is the average velocity calculated from the measured mass flow rate and k was set equal to (TURBIN)$(W_{in})^2$ where TURBIN has a constant value of 0.03. The Case 1 inlet profiles are given in Figures 3 and 4 along with the normalized experimental data. In Case 2, the best fit of the experimental velocity and rms data were used for the annulus jet. These profiles are given by the solid line curves in Figures 3 and 4. Flat profiles were used for the Case 2 fuel jet. The mass flow rate, obtained by integrating the measured velocity profiles for both the annular and central jets, agreed with the metered mass flow rates within 5% in both cases [9].

The time-dependent code was developed at the Air Force Wright Aeronautical Laboratories/Flight Dynamics Laboratory [18,19,20]. The time-dependent compressible Navier-Stokes equations are solved using MacCormack's explicit finite difference scheme [21]. Closure is automatically satisfied by the time-dependent Navier-Stokes equations provided that the computational grid has sufficient resolution. However, this is accomplished at the expense of large computing times with approximately 12½ hours being used on the CDC CYBER 750/175 computer to calculate 25,700 time steps that correspond to about 68 ms of real flow time. The turbulent frequencies resolved by the 60 axial and 46 radial grid points is about 3000 HZ which corresponds to large eddy simulation of the turbulence. The code is presently restricted to one species and was used to calculate the flow field for the centerbody with no flow from the central jet. Additional information about the time-dependent code, the computational grid and the boundary conditions used in the centerbody calculations are given in Reference 22.

6.0 TEST CONDITIONS

Experiments were conducted at various air and fuel flow rates. Isothermal experiments were conducted using CO_2 injection from the central jet. Combustion experiments used propane fuel. The experiments were conducted at a pressure of 0.98 bars. The air and fuel flow conditions are summarized in Tables 3 and 4.

7.0 TIME-AVERAGED RESULTS AND DISCUSSIONS

7.1 Annular Jet

Bluff bodies have been actively studied for the past 30 years. Much of the research is motivated by the need to understand their flame holding characteristics [23]. Although much has been learned, many of the details concerning the recirculation zone and, specifically, the role of the recirculation zone on flame stabilization are not understood. A major impediment has been the lack of suitable instrumentation for measuring velocities and turbulence intensities in combustion recirculation zones. For example, a probe technique has not been developed for measuring velocities in reacting, recirculating flows. Hotwire probes can provide useful information in nonreacting flows but they suffer from the inability to distinguish axial flow direction. Multipoint Pitot-static probes have been used with some success, but there is always the question about whether the probe has disturbed the flow and thus influenced the measurement [24]. LDA overcomes many of the problems associated with probes in that it can be used to make a point measurement of different velocity components and their associated turbulence intensities at high data rates in both nonreacting and reacting flows. Its development and application is a major step towards expanding the understanding of recirculating flows as illustrated in recent studies [25,26].

In this section, LDA will be used to examine the time-mean characteristics of the annular jet in the near-wake region of the bluff body without central fuel injection. Caution must be used in applying LDA because seeding can lead to significant bias errors that are difficult to assess [27]. The LDA data presented in this section were used to calculate the mass flux across the duct at different axial stations in the recirculation zone. The measured and integrated mass flux for air agreed within ±5% at all stations [9].

Figure 5a shows contour maps of the stream functions constructed from the LDA data and Figures 5b and 5c show TEACH Code calculations using measured (Case 2, see Section 6.0) and flat (Case 1) inlet profiles, respectively. There is very good agreement between the experimental and theoretical data for the region outside of the recirculation zone. In the recirculation zone, the experimental and theoretical contours show the same general trends and there appears to be reasonable quantitative agreement except for the location of the vortex center and the length of the recirculation zone. There is good agreement for the radial location of the vortex center; however, there is a large discrepancy in the axial location. The measured inlet conditions do improve the accuracy of the TEACH Code calculations of the vortex center but not for the length of the recirculation zone.

Figure 6 shows more comparisons of theoretical and experimental data. The predictions use the measured inlet profiles. In general, there is reasonable agreement between the measured and predicted values. Much of the disagreement that is present results from incorrect predictions of the vortex center and the end of the recirculation zone. The turbulence intensities along the centerline (Figure 6e) show the largest discrepancies. Near the end of the recirculation zone, the data shows a peaking in turbulence intensity, whereas, the TEACH Code shows a continuously decreasing trend. Large discrepancies in turbulence intensities have also been noted by other researchers and may be a result of the isotropic characteristics of the k-ε model [28].

The zero axial velocity surface (Figure 6a) is important in understanding the characteristics of the recirculation zone because it separates the forward and reverse flow regions. Also, the vortex center is located on this surface at the point where the radial velocity determined along the surface is zero as shown in Figure 6b. The vortex center occurs near the axial location where the axial velocity centerline profile has a maximum negative value (Figure 6c) and where the reverse mass flow rate peaks (Figure 6d). Although the experimentally determined vortex center is downstream from the theoretical value, the experimental data in Figures 6c and 6d also show this trend. Presenting the TEACH Code results in the way shown in Figure 6 makes it intuitively obvious that the vortex center should occur at the axial station where the reverse mass flow rate peaks and that this should be close to the axial location where a maximum negative velocity occurs on the centerline profile [17]. These simple results illustrated to us the potential of using the computer codes to gain new insights into complex turbulent flows.

Computer models offer a new tool to explore the characteristics of recirculating flows. It would take months, if not years, to accumulate the experimental data such as velocity, turbulence, kinetic

energy, species concentration, temperature, pressure, etc., in the detail that can be provided in a few minutes of computer time. The importance of these data can be significant because the trends, if not the accuracy, provided by the models are normally very good. This offers the opportunity to design computer experiments in which trends can be selectively explored as different parameters of the recirculating flow field are changed. The insights gained from such computer experiments can be of great aid in designing the actual experiments. An illustration of the insights provided by computer experiments is presented in the following paragraphs.

The computer experiments are patterned after recent experiments by Kundu and co-workers that demonstrated the importance of the recirculation strength on the flame stabilization characteristics of bluff bodies [29]. The recirculation strength is the maximum value of the normalized reverse mass flow rate (M_r/M_{in}). They reasoned that the process of heat exchange in a premixed, bluff-body stabilized flame is controlled by the fluid mechanics of the recirculation zone. Indeed, the recirculation strength, as determined from isothermal experiments, correlated well with the blow-off velocity and calculations of the heat exchanged between the mainstream and the recirculation zone. They also conducted experiments in isothermal flows in which the axial profiles of reverse mass flow rate were measured for different geometrics and widths of two-dimensional bluff bodies. We conducted a similar investigation using computer experiments to study the effects of various diameter centerbodies in the APL combustion tunnel on the recirculation zone. The same Case 1 (see Section 6.0) flat velocity and turbulent kinetic energy inlet profiles used in Reference 17 were also used in these computer experiments.

The first computer experiment was conducted to determine if the TEACH Code correctly predicts that the axial profile of reverse-mass flow rate is independent of air flow rate for a given bluff body geometry. The results in Figure 7 show that the TEACH Code does predict this. The next computer experiment was designed to determine the influence of centerbody diameter on reverse mass flow rate. It should be realized that in conducting computer experiments where the centerbody diameter is varied, that the turbulence length scale also varies because of the way the inlet conditions have been specified. The results given in Figure 8 show that the recirculation strength increases with increasing centerbody diameter. This trend, for two-dimensional bluff bodies, was measured by Kundu and co-workers [29]; however, there are also some differences. Their measurements show that the length of recirculation zone, normalized by the width of the bluff body, decreases with increasing bluff body width. This trend is just the opposite of that given in Figure 8. Also, they showed that the axial location of the peak reverse mass flow rate, which we know from the model results is the location of the vortex center, did not change with bluff body size for a given bluff body configuration; whereas, there is some dependence shown in Figure 8. The measured normalized lengths of the two-dimensional recirculation zones are about a factor of 3 longer than that for the centerbody.

Computer experiments were used to examine the relationship between the recirculation strength and the blockage ratio. Figure 9 shows the results of the TEACH Code calculations for the centerbody with and without curvature correction, the experimental results from Reference 29 for a two-dimensional plate, the results of Davis and Beer [30] for a disk without a duct and the APL centerbody experimental result. A description of the modified TEACH Code with streamline curvature is given in Reference 31. Kundu and co-workers' data show that the recirculation strength varies linearly with blockage ratio. The TEACH Code, without curvature effects, also predicts a near linear relationship for the blockage ratios used in Kundu's experiments, but over a wider range of blockage ratios a nonlinear relationship is predicted. The calculations with streamline curvature modifications of the k-ε turbulence model predicts a discontinuity at a blockage ratio of about 39%. The large differences between the Davis and Beer results and the APL results are suspected to be due to the fact that their flow was unconfined while ours was confined. It is now an experimental problem of determining if either the TEACH Code predictions with or without streamline curvature are correct for the higher blockage ratios. In any event, the calculations have provided a focus for an experimental study and has even indicated how the data can be efficiently collected. In concluding this section, we believe that the results demonstrate that computer experiments can provide fresh insights into turbulent recirculating flows in ways that can be efficiently examined in future experimental studies. This type of interaction between theory and experiment, which some might say is the essence of science, has been missing for too long in the area of recirculating flows.

7.2 Interaction of the Annular and Central Jets

The interaction of the annular and central jets of the centerbody were first investigated by visual observations of the flame as the fuel and air flow rates were varied [6]. The flame is believed to provide a visualization of the fuel and air mixing processes and thus, changes in the flame structure with changes in air and fuel flow rates are a representation of how the two jets interact. The structure of the flame changes dramatically as the air and fuel flow rates are varied. The flame structure is determined by whether the annular or central jet dominates the flow field. This is shown in Figure 10 where the flame is observed to change with increasing fuel flow rate from a cylindrical shape, when the annular jet dominates (Figure 10a) to a conical shape, when the central jet dominates (Figure 10c). Figure 10b shows the condition where neither jet dominates the flow. The flow fields inferred from observing the flame shape and TEACH Code calculations performed by Sturgess and Syed [28] for the different flow conditions are also given in Figure 10. We believe that for a research combustor designed to evaluate combustor models, such dramatic changes are an asset because of the challenge it offers to the models. In the following paragraphs, predictions and experimental results will be presented for various air and fuel flow rate conditions.

An examination of the inferred flow patterns and the calculated streamlines in Figure 10a shows that two stagnation points occur along the centerline when the annular jet dominates the flow field. The forward stagnation point is where the fuel jet is turned by the opposing flow of the recirculation zone and the rear stagnation point defines the axial extent of the recirculation zone. Figure 11 shows comparisons between measured and predicted locations of these stagnation points for an air flow rate of 2 kg/s and various CO_2 flow rates. The stagnation points were measured with a one-component LDA system [7,32]. The precision of the LDA measurements of stagnation point Z/D

locations and the repeatability of the combustor is estimated to be about 10%. Theory predicts a small change in the location of the rear stagnation point with an increase in CO_2 flow rate. Considering the uncertainties in the measurements, it would be difficult to experimentally detect such a small change. Both theory and measurements show a near linear dependence of the location of the forward stagnation point with CO_2 jet exit velocity but there is a difference in the slope of the two curves.

Figure 12 shows centerline plots of measured and theoretical axial velocities, CO_2 concentrations in mole fraction and axial velocity fluctuations for an air flow rate of 2 kg/s and various CO_2 flow rates. The velocities were measured with the two-component LDA system [9]. Case 2 inlet conditions (See Section 5.0) were used in the TEACH Code calculations. It is observed in Figure 12a that the location of the forward stagnation points are underpredicted and the location of the rear stagnation point is slightly over predicted as was the case in Figure 11. The forward stagnation point is important in predicting the characteristics of the flow field. The measured and predicted velocity profiles in Figure 12a, for a CO_2 flow rate of 6 kg/hr, show that the velocities just downstream of the forward stagnation point have the same profiles as the case when the CO_2 flow rate is zero (Figure 6c). That is, the flow field downstream of the forward stagnation is not affected by the central jet. This is also shown by the turbulence intensities in Figure 12b and the CO_2 concentrations in Figure 12c . At the forward stagnation points and beyond, the CO_2 concentrations have a near constant value and the turbulence intensities have the same values as for the annular jet flow in Figure 6e. In general, it appears that the TEACH Code correctly predicts the important qualitative trends associated with the forward stagnation point; however, the accuracy of the absolute values of the velocity, CO_2 concentrations and turbulence intensity centerline profiles could be significantly improved.

Figure 13 shows the measured and predicted centerline profiles of velocity, turbulence intensity and temperature for a combusting flow. The theoretical and experimental data have been normalized to the maximum experimental values. The velocity data were measured with a one-component LDA system [7,32] and the TEACH Code predictions were obtained from Reference 33. A point-by-point comparison of predictions with measurements shows that the TEACH Code does a very poor job of accurately predicting the centerline profiles of velocity, turbulence intensity, and temperature. The predictions are poor because the TEACH Code did not correctly predict that the central jet had penetrated the recirculation zone. The TEACH Code does however correctly predict other important trends. The experimental data in Figure 13a show a strong correlation between the normalized turbulence intensity and temperature with the peak value occurring at a location just upstream of where the velocity is a minimum. The TEACH Code also predicts the same strong correlation between temperature and turbulence intensity (Figure 13b) with the peak magnitude occurring at the axial location just upstream of the forward stagnation point. Although the data are too limited to draw conclusions, they do suggest that the accuracy of the TEACH Code predictions for combusting flows are not as good as they are for isothermal flows.

The inability of the TEACH Code to accurately predict a complex recirculating flow field, especially with combustion, while correctly predicting trends of the data, is expected based on the results of others [4]. There are several potential sources of error that could contribute to the inaccuracies in the TEACH Code precitions. The turbulence model is as one of these sources. To explore the nature of the processes responsible for the fuel and air mixing in the centerbody combustors, one must consider the dynamic characteristics of the flow. This means that a giant mental step must be taken in which the time-averaged view is replaced by a dynamic view. Such a mental transition is not easy. Since the time averaged descriptions are such an important part of most investigations of recirculating flows, it is easy to forget that the flow field viewed in time probably doesn't look anything like that represented by the time-averaged view. Indeed, the time-averaged view can be a mask that gives misleading or incorrect perceptions about the fundamental processes occurring in the flow. An attempt is made in the next section to shed this mask so that some of the fundamental dynamic characteristics of the flow that are responsible for the presented time-averaged results can be identified.

8.0 TIME-RESOLVED (DYNAMIC) RESULTS AND DISCUSSION

There are few measurement techniques that can be used to study the dynamic characteristics of recirculating flow fields. Normally, the processes to be studied involve dynamic structures of the size of the bluff body. The interpretation of single or even multipoint continuous time-resolved measurements in terms of the large scale structures is very difficult. This difficulty arises in part because of the problems of interpreting point measurements in terms of the large structures that are convected past a stationary measurement station. That is, the measurements are made from an Eulerian reference frame but the structures should be interpreted from a Lagranian frame. High speed cine pictures give a Lagrangian view of the dynamic structures but have the disadvantage that quantitative information is not normally recorded. However, cine pictures can greatly aid in the interpretation of point measurements. Measurement techniques that involve simultaneous high-speed cine pictures and time-resolved point measurements will be important in future studies of turbulent combusting flows. In this section, high speed cine pictures are used to gain a qualitative understanding of the flow field established by the centerbody. This understanding is used to interpret line-of-sight, continuous time measurements of flame luminosity and CARS time-resolved point measurements of temperature [13,34,35].

Vortex shedding plays an important and possibly dominant role in the mixing process of the centerbody flow field. However, it is not always easy to detect vortex shedding in combusting flows. The large diameter of the centerbody has proven advantageous because the shed vortices were large enough to observe with high-speed cine pictures. Unless one had the experience of knowing exactly what to look for, it is very likely that vortex shedding from a smaller bluff body would be completely overlooked. Even with the advantages of the large centerbody, the vortex shedding was not immediately recognized because the cine pictures of the flame can appear very different when taken from various reference frames, directions and at various framing speeds. Actually, the laboratory reference frame is not the most advantageous way of photographing a shed vortex because the circular motions of the vortex are masked by its large axial convection velocity. Recording the vortex from a reference frame that is moving with the convection velocity of the vortex would be more advantageous because the circular motion would be clearly shown. However, this is difficult to experimentally achieve in the APL

Combustion Research Facility. The cine pictures that are presented were taken from the laboratory reference frame but at various angles that tend to highlight different aspects of the vortex shedding process.

Figure 14 shows an end view of the centerbody and the side viewing windows. The centerbody diameter is larger than the height of the viewing window so that the top and bottom edges of the bluff body are not directly viewed when looking straight across the tunnel. The importance of seeing either the top or bottom edge of the bluff body can be understood by considering the structure of the shed vortex and the flame. As will be presently shown, the vortex is shed symmetrically from the centerbody. Considering the axisymmetric geometry of the combustor, the vortex should have a toroidal shape. The flame appears to be distributed around the toroidal vortex in discrete flame packets as illustrated in Figure 14. To an observer looking through the viewing windows straight across the central region of the combustion zone, the flame packets are semitransparent because of the space between them. The observer will probably overlook these flame packets and see only the flame occurring near the centerline of the combustor; whereas, an observer looking at the bottom edge of the bluff body would see the flame packets in the vortex. The observation of these flame packets makes the shed vortex visible.

Figure 15 shows one frame from a high-speed cine picture taken with the camera tilted as shown in Figure 14. The shed vortices identified by the black outline, are not as evident in the photograph as they are when viewing the film with a stop-action projector. The flow is from left to right. The flame between the two vortices is being rapidly stretched. This results in the flame burning out quickly in this region leaving a dark band separating the two vortices. These vortices can only be seen by observing the flame contained in them.

It is not readily evident from studying Figure 15, that the vortices are shed symmetrically. The symmetry of the shed vortices was examined using two photodetectors as arranged in Figure 14. The photodetectors were located 0.428D downstream and were tilted so that their fields-of-view were along the top and bottom edges of the centerbody. This viewing location was determined from studying high-speed cine pictures of the flame. As a shed vortex containing flame packets passes through the field-of-view of a photodetector, a voltage pulse is recorded by an oscilloscope. To easily compare the simultaneous time traces from the photodetectors, the voltage output from the bottom detector has been inverted and positioned on the oscilloscope so that the zero light intensity baseline is superimposed on that of the top detector. The symmetry of the shed vortices is apparent from the oscilloscope traces in Figure 16.

Figure 17 shows high speed cine pictures of the flame made with a camera with a wide angle (fish eye) lens. For reference, Figure 17a shows a metal rod placed in the fuel tube and a ruler placed along the bluff body face. The rod extends one centerbody diameter downstream. The flame packets, symmetrically distributed in a toroidal vortex, are clearly shown about one diameter downstream in Figure 17c. Also shown in this figure is the stretching action and burn out of the flame separating the shed vortex and another vortex that is forming near the face of the combustor. Normally, the flame packets contained in a shed vortex burn out before the vortex travels more than one centerbody diameter downstream. The shed vortex however is still present and only the means of visualizing it has vanished. Occasionally a flame packet in a shed vortex does not burn out quickly and can be used to track the vortex. For example, the flame packet at the top of the shed vortex in Figure 17c can be tracked downstream until it is just noticeable in Figure 17g. The end of the recirculation zone is about one and a half diameters downstream and the axial velocity of the shed vortex is small in this region. This is indicated by the lack of downstream movement of the flame packet in the shed vortex in Figures 17f and 17g. A second shed vortex is evident at the bottom of Figure 17f at about one diameter downstream. In Figure 17g, the second vortex has almost coalesced with the first vortex near the end of the recirculation zone. The formation of a large flame structure located at the centerline near the end of the recirculation zone, appears to occur at about the same time and at the same axial location that the two vortices coalesce. In subsequent frames, this large flame structure is observed to move downstream past the viewing window. The consequence of the formation of this flame structure, apparently by the shed vortices, is discussed in the next few paragraphs.

Figure 18 shows high speed cine pictures of the flame extending into two windows of the combustion tunnel [15]. The reader is reminded that the height of the viewing windows is less than the diameter of the centerbody so the top and bottom edges of the bluff body are not observed. The cine pictures were made at a rate of 500 frames/s but only every other frame is shown. The recirculation zone is confined to the region viewed through window W1. The bright band of flame at the Z/D=1 station in Figure 18a is a shed vortex. The fuel in the vortex shown in Figures 18c and 18d burns out just as it enters the second viewing window. However, a large flame structure, whose origin cannot be easily traced in the photographs, does appear in the second window at a slightly later time in Figure 18c. The structure is a discrete island of flame surrounded by nonluminous and supposedly nonreacting gases as clearly shown in Figure 18f. This large flame structure, referred to as a flame turbule, is believed to be formed by a shed vortex in much the same way as the large flame structure was noted to form near the end of the recirculation zone in Figure 17.

Time-averaged CARS and thermocouple measurements made downstream of the recirculation zone along the combustor centerline are shown in Figure 19. These measurements illustrate that the temperatures obtained by the two methods agree well within an anticipated 10% precision of the CARS measurements in the indicated temperature range [15]. The temperature profile appears to be similar to those measured in many nonrecirculating combusting flows. One would never suspect that the underlying dynamic process responsible for these time average measurements is the convection of the large flame turbules and the nonluminous regions (noted in Figure 18f) passed the measurement location. Indeed, such measurements do not provide any insight into the basic dynamic processes responsible for time-averaged results.

Figure 20 shows the temperature probability distribution functions (pdf's) constructed from the CARS measurements at three centerline axial locations [15]. The temperature interval or bin width corresponds to the uncertainty in the CARS measurements. The pdf's can be thought of as the fraction of time that the combusting flow exists in a given temperature state. The bimodal shape of the pdf's

suggests that at least two types of structures are occurring in the flow, one with temperatures less than 1000 K and the other above this temperature. From the cine pictures shown in Figure 18, one would suspect that the hot mode corresponds to the flame turbules and the cold mode corresponds to the nonluminous regions. These structures can be tracked over long distances in the flow and are clearly Lagrangian in nature. The Eulerian type measurements made with the CARS system should be interpreted in terms of the Lagrangian structures that are actually occurring in the flow. In developing a Langrangian interpretation it should be realized that properties of a fluid element, at one instance in time at a point, depend on the prior history or time evolution of the fluid element before it reaches the measurement station. The history of various fluid elements can be very different, thus, leading to a wide range of measured properties.

The centerline profile in Figure 19 shows that the average temperature decreases with increasing axial location. Inspection of the pdf in Figure 20 shows that the cold mode peaks at 300 K; whereas, the hot mode peak shifts to lower values at the downstream locations. Also, the fraction of time that the hot mode exists decreases with increasing axial location. Thus, the high temperature gas decays at an increasing rate due to mixing as the combusting gases move downstream. This implies that the cold inlet air is entrained and mixed with products within the flame turbules as they move downstream thus lowering the average temperature in the flame turbule. Heat production is declining due to reaction completion and quenching, thus, allowing inlet air entrainment to have a greater affect in reducing the average temperature. The 300 K temperature represents the fraction of time that the inlet air exists. The fluid elements at this temperature have not participated to a great degree in the combustion process; whereas, the other temperatures composing the cold mode do have combustion experiences obtained prior to reaching the measurement location. Examination of the 300 K temperature bin suggests that considerable entrainment of the inlet air is occurring as the flow moves downstream. Much of this entrained air is probably located between the flame turbules. However, some entrained air has obviously mixed with the hot gases from completed or quenched chemical reactions to give the other temperatures in the cold mode. It should also be noted that the average temperature occurs in the trough between the hot and cold modes. The flow field is actually at the average temperature less than 5% of the time.

Figure 21 depicts a Lagrangian view of the dynamic processes that are believed to be occurring in the centerbody combustor. This illustration can be considered in two different ways. It can be viewed as an instantaneous snapshot of the flow field or as the time evolution of the flow field where increasing time is represented by the distance traveled. In both cases the observer is moving with the vortices. It is convenient in discussing Figure 21 to track the fuel as it exits the central fuel jet. As the fuel exits, it decelerates by entraining hot gases and then breaks up into small packets as it moves downstream and becomes turbulent flow. The triangles represent the fuel break-up process and the shaded regions represent the burning fuel packets. These flame packets spend considerable time near the end of the recirculation zone since their average velocity is near zero in this region. Some of the flame packets are transported upstream. As they approach the combustor face, some of the flame packets are entrained into the central jet thus providing a source of heat and ignition for the incoming fuel in the central jet; however, most of the flame packets are turned radially outward along the combustor face until they encounter the high velocity air of the annular jet. The resulting discontinuity in the velocity field gives rise to a shed vortex. The vortex has a toroidal shape but, when viewed in the r,Z plane, it looks much like those observed in the two-dimensional shear layer experiments of Brown and Roshko [36]. The visibility of the shed vortex is soon lost as it moves downstream because the flame packets burn out. However, the shed vortex is still present. As the vortex continues to move downstream, it entrains the burning fuel mass that has collected near the end of the recirculation zone. The entrainment of the burning fuel is much more effective when two vortices coalesce near the end of the recirculation zone. The shed vortices carry the entrained fuel downstream and become the flame turbules.

Figure 22 shows the results of calculations of the dynamic flow field of the centerbody combustor for an air flow rate of 2 kg/s. Although the calculations are for a nonreacting flow without a central jet, one might expect that they would be qualitatively similar to a combusting flow condition where the annular jet dominates the flow field. Indeed, the similarities between the illustrated flow field in Figure 21, which was postulated before the calculations were performed, and those in Figure 22 are evident. It is easy to envision, based upon the calculations, that the vortices moving past the end of the recirculation zone entrain the fuel near the combustor centerline and become the flame turbules as the vortices move on downstream. Also, the coalescence of two shed vortices are shown in the 20700 and 21200 time iteration flow fields. Such calculation provide insights into the dynamic processes and stimulates new ideas to test the predictions.

Figure 23 shows the side view of a reacting shear layer experiment performed by Breidenthal [37]. The experiment was conducted in a two dimensional water tunnel with reactants A and B separated by a splitter plate. The reaction of A and B was mixing limited with negligible heat release. The product was colored and could be easily visualized by high speed cine pictures. The result of this experiment, as shown in Figure 22, was that the mixing, and thus the product formation, occurs inside the large scale structures generated by the shear layer. The product formed by the mixing of A and B downstream of the splitter plate was detected by optical absorption in an analogous way that flame luminosity was used to detect the shed vortices in the centerbody combustor. Figure 24a shows a time trace of the product as recorded at one location in the shear layer [37]. The peaks in the product concentration correspond to the large scale structures being convected passed the measurement station. Figure 24b shows a time record of a flame luminosity as recorded by a photodetector looking directly through the recirculation zone of the centerbody combustor [34]. Figure 24c is a time record of the temperature at the exit plane of a gas turbine combustor measured by Diis [38]. The temperature fluctations are several hundred degrees K and are far above the thermocouple noise level. The time records in Figures 24a and 24b are known to be the result of large scale structures. Their similarity to the temperature fluctuations in a gas turbine combustor is evident.

The similarities of the time records in Figure 24 raise the practical question of whether it is important to know if large scale structures play an significant role in the dynamic mixing processes in

gas turbine combustors. It is conceivable that fluid structures of a size comparable to the combustor width could be formed in a gas turbine combustor as a result of the free shear layer character of the primary, intermediate or dilution jets. On the other hand, swirl, intense mixing of the jets or combustion might wash out any large structures. It seems very likely that large scale structures would be shed from V-gutters and could be important to the stability characteristics of afterburners. It is known that large scale structures play an important role in two-dimensional, premixed dump combustors with high heat release rates [39,40]. Unfortunately, the dynamic mixing processes inside gas turbine combustors or afterburners cannot be determined from the available data.

We believe that it is important to know if large scale structures significantly contribute to the mixing processes in gas turbine combustors and afterburners. There are two reasons that are readily apparent. First, if large scale structures are present, a strong correlation between heat release rates and velocity fluctuations could exist. This could contribute significantly to the heat transfer to the turbine. Dils and Follansbee, using a LDA and a fast response thermocouple probe, determined that there is only a small correlation between the fluctuating velocities and temperatures [41]. We believe the measurements are of such importance that they should be repeated for a variety of different engines and run conditions. The second reason is of more direct importance to the combustor modeling community. Recent studies in shear layers and turbulent jets have shown that gradient transport and eddy diffusivity do not adequately describe flows where large scale structures have a dominate role in the mixing process [12,43,44,45]. Indeed, this could be a contributing factor to the inaccuracies of the TEACH Code predictions for the centerbody combustor. Combustor design models must use the correct physics if predictive accuracy is to be improved for a wide range of combustor designs. It seems that the physics is closely tied to the question of whether large scale structures significantly contribute to the mixing in gas turbine combustors, afterburners and other practical systems where the models are to be applied.

9.0 CONCLUDING REMARKS

The following comments, conclusions and recommendations are offered from several years of active combustion research and advanced combustion diagnostic development.

Combustor: The centerbody combustor is a useful test device for evaluating the performance of laser diagnostic techniques, time-averaged combustor models and unsteady fluid dynamic computer codes. This assessment is based on the challenge offered to computer codes in predicting the various flow fields that are easily established in the near-wake region of the centerbody combustor, the good measurement access to this region and the simple centerbody geometry. The large diameter of the centerbody has proven advantageous in studying, with high speed cine pictures, the effects of shed vortices on the flow field. The wide spacing between the annular jet and the central jet causes some problems in chosing a computational grid. In overall performance, we believe the centerbody represents a good compromise between simple laboratory burners and practical combusting devices such as gas turbine combustors or afterburners.

Diagnostics: The LDA system is a valuable tool for studying turbulent flow fields. Obtaining uniform seeding, at the high rates and for the long time periods (hours) needed to map a flow field, is considered to be a major problem. The CARS system has developed to the point where it can be actively used in the APL combustion tunnel to study combusting flow fields. It is essential that the laser techniques, used to collect data for combustor model evaluation and development, be interfaced to a computer. For those interested in developing and using laser techniques to study turbulent flows, it should be realized that the hardware and software development requires as much effort as the optical system development.

Computer Codes: The TEACH Code successfully predicted the dominant characteristics and trends of the recirculating flow field of the centerbody combustor when it was operated at various air and fuel flow rates with and without combustion. The accuracy of the TEACH Code predictions of velocities and CO_2 concentrations in isothermal flows is typically about 15%. The errors in predicting turbulence intensities are considerably larger. Also, the trends for the turbulence intensities are not always correctly predicted. Based on a very limited experimental and computational data base, the errors in the TEACH Code predictions of combusting flows are considerably larger than those for isothermal flows.

Many, if not most, computer model studies involve after-the-fact predictions of reported experimental results. We believe that the models are developed to the point where they can contribute to the understanding of flows that have only been partially studied. Since the TEACH Code and other similar codes can successfully predict trends, we recommend that they be exploited in computer experiments that will provide new insights into the complex flows which will both aid and challenge experimentalists so that theory and experiments can develop hand-in-hand in a truly scientific fashion.

The predictive accuracy of the unsteady code has not been evaluated for the centerbody flow field. Qualitatively, the predictions have the same general features that are observed experimentally. We believe that the unsteady code offers the promise of providing insights into the dynamic nature of complex flows that are almost impossible to gain experimentally.

Practical Combustors: Our studies of the centerbody combustor have shown that large scale structures are important in the fuel and air mixing process. It has not been fully established whether the dynamic characteristics of the centerbody flow field are similar to those of practical combusting devices. We believe it is important for future combusting and heat transfer model developments that a determination be made about the significance of large structures in gas turbine combustors and afterburners and to determine if there is a strong correlation between velocity and temperature fluctuations. Such determinations could force a reevaluation of models with gradient transport and eddy diffusivity in future combustor design codes.

REFERENCES

1. I.T. Osgerby, "Literature Review of Turbine Combustor Modeling," AIAA Jour., 12, 743-754 (1974).

2. T.W. Bruce, H.C. Mongia and R.S. Reynolds, "Combustor Design Criteria Validation Vol. 1, Element Tests and Model Validation," USAR TL-TR-78-55A (March 1979).

3. G.J. Sturgess and S.A. Syed, "Application of Numerical Modeling to Gas Turbine Combustor Development Problems," Symposium Fluid Mechanics of Combustion Systems, Joint ASME/ASCE Mechanics Conference, Boulder, Colorado, pp. 241-250 (June 1981).

4. Melvin Gerstein, ed., "Fundamentals of Gas Turbine Combustion," NASA Conference Publication 2087 (Feb. 1979).

5. R. Goulard, A.M. Mellor and R.W. Bilger, "Review and Suggested Experiments," Combustion Measurements, Academic Press, N.Y., pp 419-470 (1976).

6. W.M. Roquemore, et al., "Preliminary Evaluation of a Combustor for Use in Modeling and Diagnostic Development," ASME Publication 80-GT-43 (March 1980).

7. A.J. Lightman, et al., "Velocity Measurements in a Bluff-Body Diffusion Flame," AIAA-80-1544 (July 1980).

8. P.D. Magill, et al., "Simultaneous Velocity and Emission Measurements in a Bluff-Body Combustor," AIAA-82-0883 (June 1982).

9. A. Lightman, P.D. Magill and R.J. Andrews, "Laser Diagnostic Development and Modeling of Turbulent Flowfields of Jets and Wakes, Part I Two-Dimensional Laser Doppler Anemometer Measurements of Isothermal Flowfields in a Ducted Centerbody Combustor," AFWAL-TR-83-2044 Part I (June 1983).

10. Y. Prior, "Three-Dimensional Phase Matching in Four-Wave Mixing," Appl, Opt. 19, 1741 (1980).

11. J.A. Shirley, R.J. Hall and A.C. Eckbreth, "Folded BOXCARS for Rotational Raman Studies," Opt. Lett. 5, 380 (1980).

12. L.P. Goss, D.D. Trump, B.G. MacDonald and G. L. Switzer, "10-Hz Coherent Anti-Stokes Raman Spectroscopy Apparatus for Turbulent Combustion Studies," Rev. Sci. Instrum. 54, 5, 563 (May 1983).

13. G.L. Switzer and L.P. Goss, "A Hardened CARS System for Temperature and Species - Concentration Measurements in Practical Combustion Environments," Temperature Its Measurement and Control in Science and Industry, 5, pp 583-587 (1982).

14. G.L. Switzer, et al., "Application of CARS to Simulated Practical Combustion Systems," J. Energy 4, 209 (1980).

15. G.L. Switzer, et al., "Simultaneous CARS and Luminosity Measurements in a Bluff-Body Combustor," AIAA-83-1481 (June 1983).

16. A.D. Gosman, and W.M. Pun, "The Calculation of Recirculating Flows," Imperial College, London, England, Report HTS/74/2 (1974).

17. L. Krishnamurthy and S.O. Park, "Isothermal Predictions of Recirculating Turbulent Flowfields of Confined Dual Coaxial Jets Behind an Axisymmetric Bluff Body," ASME 83-FE-14 (June 1983).

18. J. S. Shang, "Oscillatory Compressible Flow Around a Cylinder," AIAA 82-0098 (Jan. 1982).

20. J.S. Shang, "Numerical Simulation of Wing-Fuselage Aerodynamic Interaction," AIAA 83-0225 (Jan. 1983).

21. R.W. MacCormack, "Numerical Solution of the Interactions of a Shock Wave with Laminar Boundary Layer," Lecture Notes in Physics, 59, pp 151-163 (1976).

22. J.N. Scott and W.L. Hankey, Jr., "Numerical Simulation of Cold Flow in an Axisymmetric Centerbody Combustor," AIAA-83-1741 (July 1983).

23. E.E. Zukoski and F.E. Marble, "Experiments Concerning the Mechanism of Flame Blow-Off from Bluff-Bodies," Proc. of the Gas-Dynamics Symp. on Thermochemistry, North Western University, Evanston, IL., p. 205 (1956).

24. N.A. Chigier and J.M. Beer, "The Flow Region Near the Nozzle in Concentric Jets," J. of Basic Engr., pp. 747-804 (Dec. 1964).

25. D.F. Durao and J.H., Whitelaw, "Velocity Characteristics of the Flow in the Near Wake of a Disk," J. Fluid Mech,. 85, Part 2, pp 369-385 (1978).

26. Fujii and K. Eguchi, "A Comparison of Cold and Reacting Flows Around a Bluff-Body Flame Stabilizer," J. Fluids Eng., 103, p 328 (June 1981).

27. Timothy C. Roesler, W.H. Stevenson and H. Doyle Thompson, "Investigation of Bias Errors in Laser Doppler Velocimeter Measurements," AFWAL-TR-2105 (Dec. 1980).

28. G.J. Sturgess and S.A. Syed, "Widely-Spaced Co-Axial Jet, Diffusion-Flame Combustor: Isothermal Flow Calculations Using the Two-Equation Turbulence Model," AIAA-82-0113 (Jan. 1982).

29. K.M. Kundu, D. Banerjee, D. Bhaduri, "On Flame Stabilization by Bluff Bodies," J. Eng. for Power, 102, p 209 (Jan. 1980).

30. T.W. Davis and J.M. Beer, Thirteenth Symp. (International) on Combustion, The Combustion Institute, Pittsburg, p 631 (1971).

31. L. Krishnamurthy and S.O. Park, "Streamline Curvature Effects in Confined Isothermal Recirculating Flowfields Behind an Axisymmetric Bluff Body; Numerical Calculations with the k-ε Turbulence Model," Fourth Symposium on Turbulent Shear Flows, Karlsruhe, F.R. Germany (Sept. 1983).

32. Allan J. Lightman and Peter D. Magill, "Velocity Measurements in Confined Dual Coaxial Jets Behind an Axisymmetric Bluff Body: Isothermal and Combusting Flows," AFWAL-TR-81-2018 (April 1981).

33. Private communication with G.J. Sturgess of United Technologies Corp., East Hartford CT.

34. W.M. Roquemore, et al., "Investigation of the Dynamic Behvainr of a Bluff-Body Diffusion Flame Using Flame Emission," AIAA-82-0178 (Jan. 1982).

35. W.M. Roquemore, et al., "Influence of the Vortex Shedding Process on a Bluff-Body Diffusion Flame," AIAA-83-0335 (Jan. 1983).

36. G.L. Brown and A. Roshko, J. Fluid Mech., Vol 64, p 775 (1974).

37. R. Breidenthal, "Structure in Turbulent Mixing Layers and Wakes Using a Chemical Reaction," J. Fluid Mech., Vol 107, pp 1-24 (1981).

38. R.R. Dils, "Dynamic Gas Temperature Measurements in a Gas Turbine Transition Duct Exit," J. Eng. Power, Trans. ASME, Series A. 95, No. 3, p 265 (1973).

39. A.R. Ganji and R.F. Sawyer, "Turbulence, Combustion, Pollutant, and Stability Characterization of a Premixed, Step Combustor," NASA Report No. 3230 (1980).

40. R.W. Pitz and J.W. Daily, "Experimental Study of Combustion in a Turbulent Free Shear Layer Formed at a Rearward Facing Step," AIAA-81-0106 (Jan. 1981).

41. R.R. Dils and P.S. Follanskee, "Wide Bandwidth Gas Temperature Measurements in Combustor and Combustor Exhaust Gases," 22nd International Instrumentation Symposium of the ISA (May 1976).

42. J.E. Broadwell and R.E. Breidenthal, "A Simple Model of Mixing and Chemical Reaction in a Turbulent Shear Layer," J. Fluid Mech., Vol 125, pp 397-410 (1982).

43. M.M. Koochesfahani, P.E. Dimotakis and J.E. Broadwell, "Chemically Reacting Turbulent Shear Layers," AIAA-83-0475 (1983).

44. P.E. Dimotakis, J.E. Broadwell and R.D. Howard, "Chemically Reacting Turbulent Jets," AIAA-83-0474 (1983).

45. B.J. Walker, "Turbulence Model Comparisons for Shear Layers and Axisymmetric Jets," U.S. Army Missile Command Tech. Rep. RD-8-1 (1979).

ACKNOWLEDGEMENTS

The authors wish to thank Mr Melvin Russell for operating the combustion tunnel and Mr Don Jacks for collecting the CO_2 concentration data. We also express appreciation to Mr Charles Martel, Mr Dale Hudson, Dr A. J. Lightman, Dr L. Krishnamurthy and Dr D. R. Ballal for their helpful suggestions in preparing the text. This work was funded in part by the Air Force Office of Scientific Research under Aero Propulsion Work Unit 2308S705.

TABLE 1: GOVERNING EQUATIONS

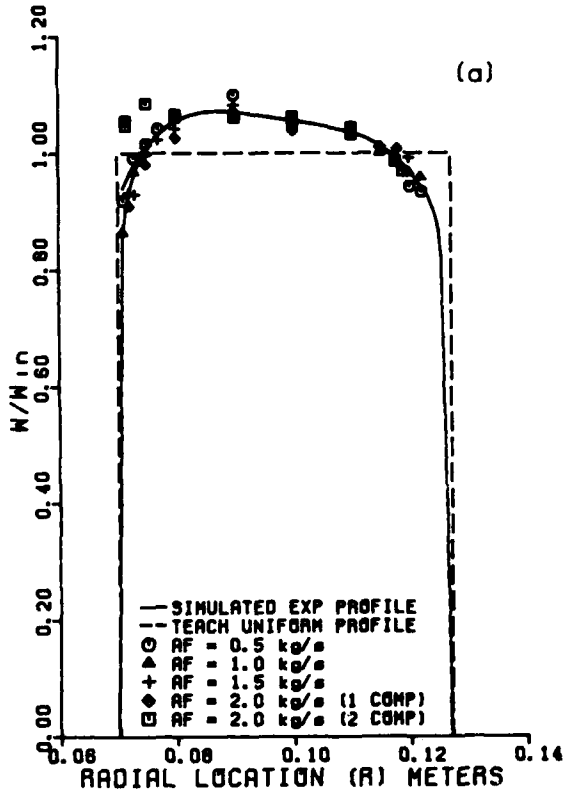
Equation	$\bar{\phi}$	Γ_ϕ	S_ϕ
Continuity	1	0	0
Axial (Mean) Momentum	$\bar{W}$	μ_{eff}	$-\frac{\partial \bar{P}}{\partial z} + \frac{\partial}{\partial z}\left(\mu_{eff}\frac{\partial \bar{W}}{\partial z}\right) + \frac{1}{r}\frac{\partial}{\partial r}\left(r\mu_{eff}\frac{\partial \bar{U}}{\partial z}\right)$
Radial (Mean) Momentum	$\bar{U}$	μ_{eff}	$-\frac{\partial \bar{P}}{\partial r} + \frac{\partial}{\partial z}\left(\mu_{eff}\frac{\partial \bar{W}}{\partial r}\right) + \frac{1}{r}\frac{\partial}{\partial r}\left(r\mu_{eff}\frac{\partial \bar{U}}{\partial r}\right) - \frac{2\mu_{eff}\bar{U}}{r^2}$
Species (Passive Scalar) Mass Fraction	$\bar{Y}_F$	μ_{eff}/σ_F	0
Turbulence Kinetic Energy	k	μ_{eff}/σ_k	$P_k - \bar{\rho}\varepsilon$
Turbulence Energy Dissipation	ε	$\mu_{eff}/\sigma_\varepsilon$	$C_1(\varepsilon/k)P_k - C_2\bar{\rho}\varepsilon^2/k$

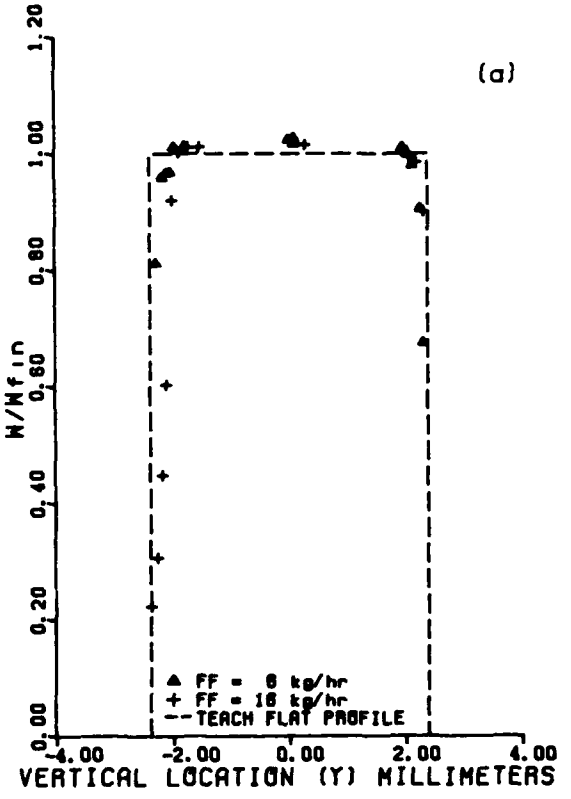
σ_F	σ_k	σ_ε	C_1	C_2
1	1	1.3	1.44	1.92

$$P_k = \mu_{eff}\left\{2\left[\left(\frac{\partial \bar{W}}{\partial z}\right)^2 + \left(\frac{\partial \bar{U}}{\partial r}\right)^2 + \left(\frac{\bar{U}}{r}\right)^2\right] + \left(\frac{\partial \bar{W}}{\partial r} + \frac{\partial \bar{U}}{\partial z}\right)^2\right\}$$

TABLE 2: BOUNDARY CONDITIONS

$\bar{\phi}$	Top Boundary (Duct Wall)	Bottom Boundary (Axis of Symmetry)	Left Boundary: Inlets	Left Boundary: Centerbody Face	Right Boundary (Outflow)
$\bar{W}$	Law of the Wall to Relate the Wall Shear Stress τ_w	$\frac{\partial \bar{W}}{\partial r} = 0$	$\bar{W}$ Specified $= W_{in}$	$\bar{W} = 0$	Overall Mass Conservation
$\bar{U}$	$\bar{U} = 0$	$\bar{U} = 0$	$\bar{U} = 0$	Law of the Wall to Relate the Wall Shear Stress τ_w	$\frac{\partial \bar{U}}{\partial z} = 0$
$\bar{Y}_F$	$\frac{\partial \bar{Y}_F}{\partial r} = 0$	$\frac{\partial \bar{Y}_F}{\partial r} = 0$	$\bar{Y}_F$ Specified (1^F for Central and 0 for Annular Inlets)	$\frac{\partial \bar{Y}_F}{\partial z} = 0$	$\frac{\partial \bar{Y}_F}{\partial z} = 0$
k	Given by Wall Functions	$\frac{\partial k}{\partial r} = 0$	k Specified $=(TURBIN)(Win)^2$	Given by Wall Functions	$\frac{\partial k}{\partial z} = 0$
ε		$\frac{\partial \varepsilon}{\partial r} = 0$	ε (see Table 3)		$\frac{\partial \varepsilon}{\partial z} = 0$





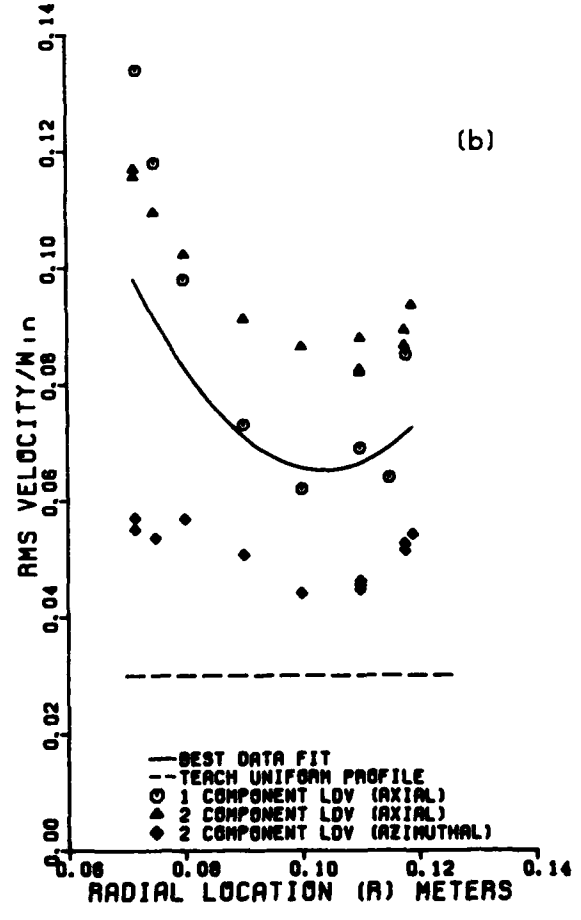


Figure 3. Inlet profiles of the annular jet at Z = 0.1 cm [9].

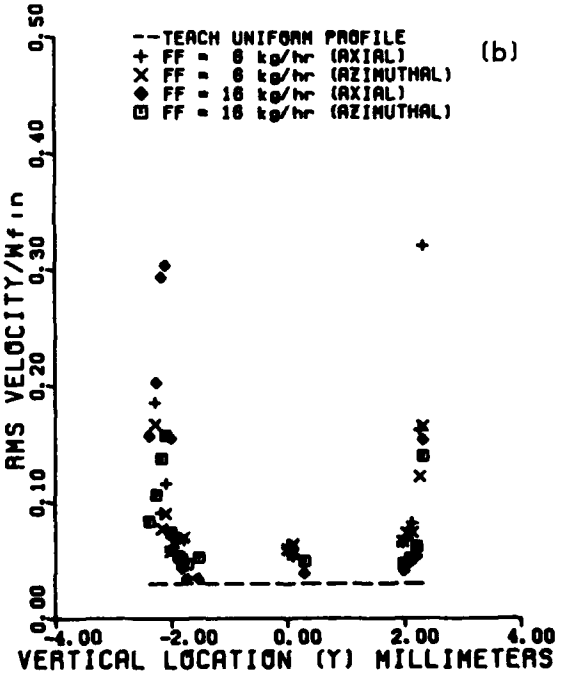


Figure 4. Inlet profiles of the central jet at Z = 0.4 cm [9].

TABLE 3: AIR FLOW CONDITIONS

FLOW RATE (k/s)	AVG INLET TEMP (K)	AVG ANNULUS VELOCITY (m/s)	AVG DUCT VELOCITY (m/s)	AIR RE NO ($X10^{-5}$)*
0.5	294	11.6	8.2	0.76
1.0	294	23.3	16.4	1.52
1.5	294	34.9	24.6	2.27
2.0	294	46.6	32.8	3.02

*Using duct velocity and centerbody diameter

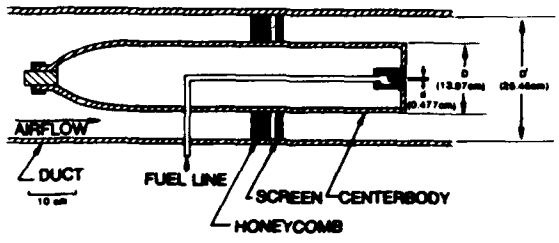


Figure 1. Illustration of centerbody combustor.

TABLE 4: FUEL FLOW CONDITIONS

FUEL TYPE	FLOW RATE (kg/hr.)	AVG INLET TEMP (K)	AVG INLET VELOCITY (m/s)	RE $(X10^{-4})$
CO_2	6.0	294	50.8	3.0
CO_2	16.0	294	135.0	8.0
C_3H_8	6.0	400	69.6	4.2
C_3H_8	8.0	391	91.0	5.7

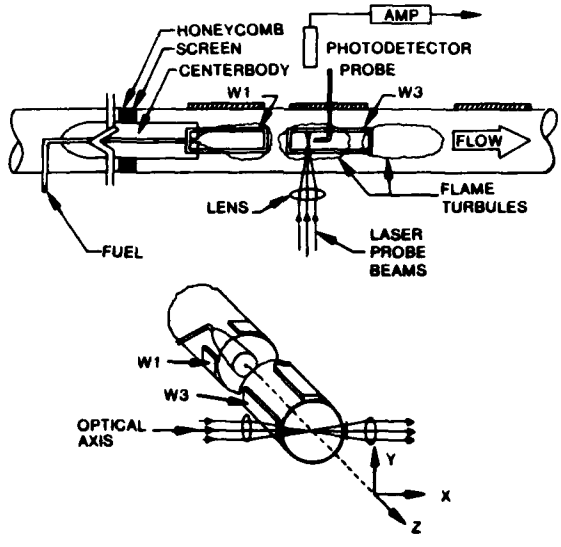
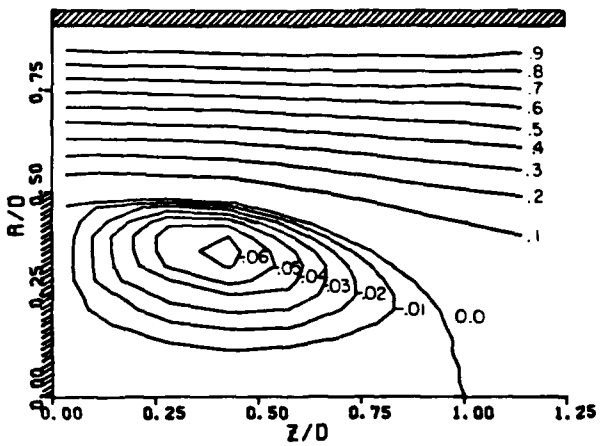
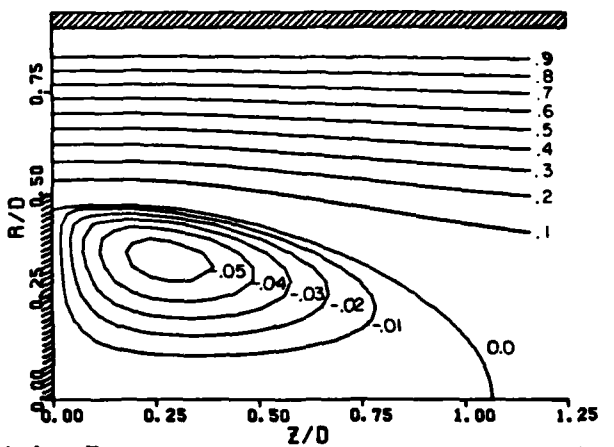


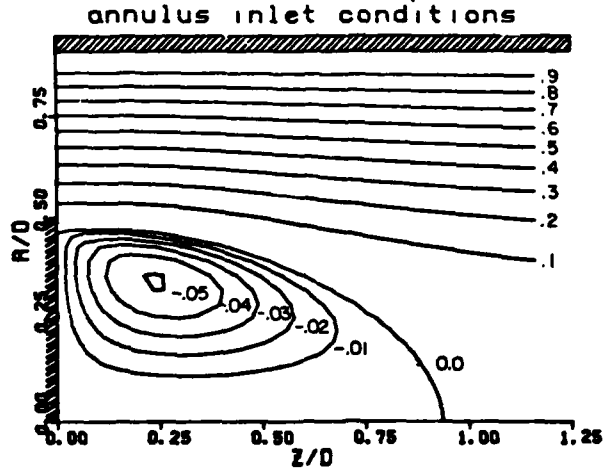
Figure 2. Illustration of the combustion tunnel.



(a) Experimental data from LDA

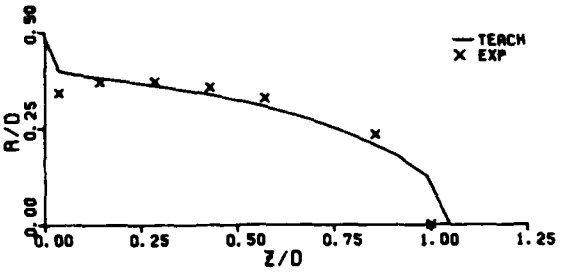


(b) Teach code with experimental annulus inlet conditions

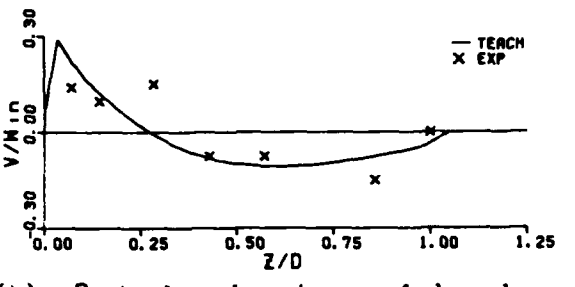


(c) Teach code with uniform inlet conditions

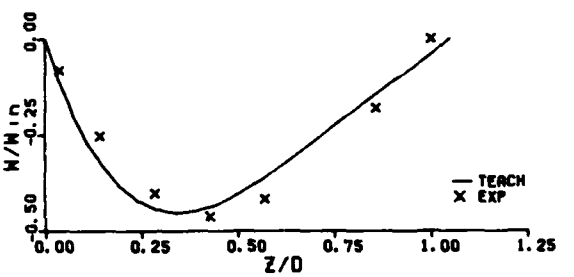
Figure 5. Measured and predicted stream functions for air flow of 2 kg/s.



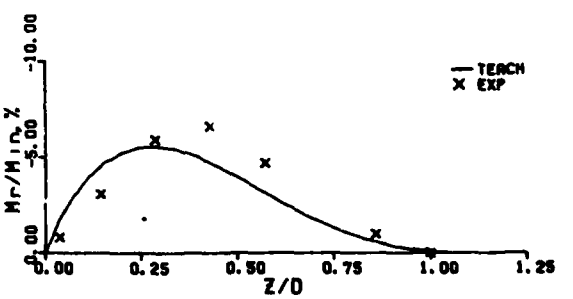
(a) Zero axial velocity contour



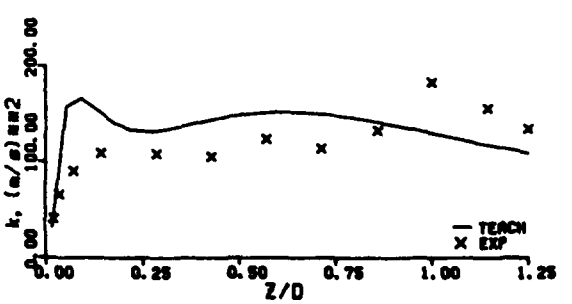
(b) Radial velocity profile along the zero axial contour



(c) Axial velocity profile at centerline



(d) Reverse mass flow rate profile



(e) Turbulence intensity profile at centerline

Figure 6. Measured and predicted recirculation zone characteristics.

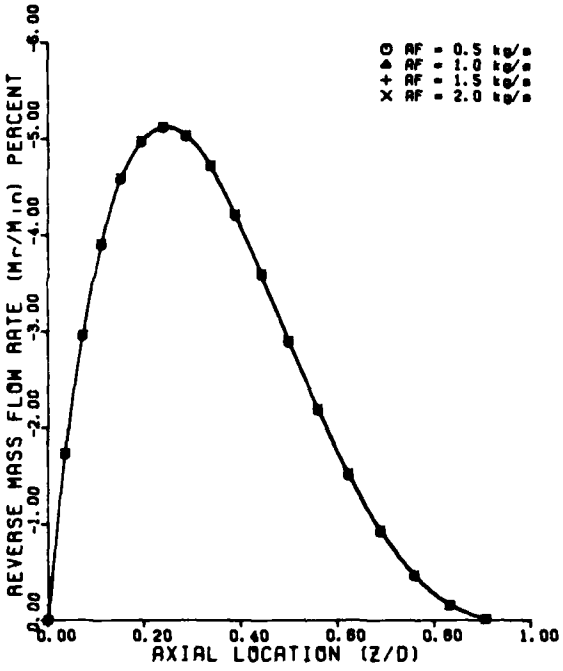


Figure 7. Predicted reverse mass flow rate for a 14 cm centerbody at various air flow rates.

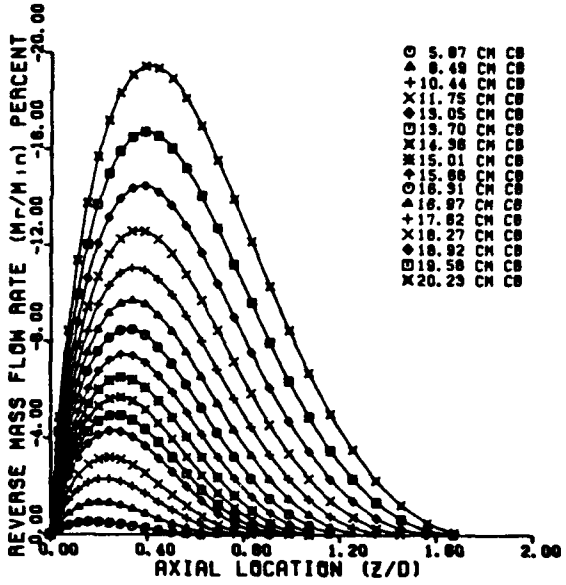


Figure 8. Predicted variation of reverse mass flow rate for different diameter centerbodies at an air flow rate of 2 kg/s.

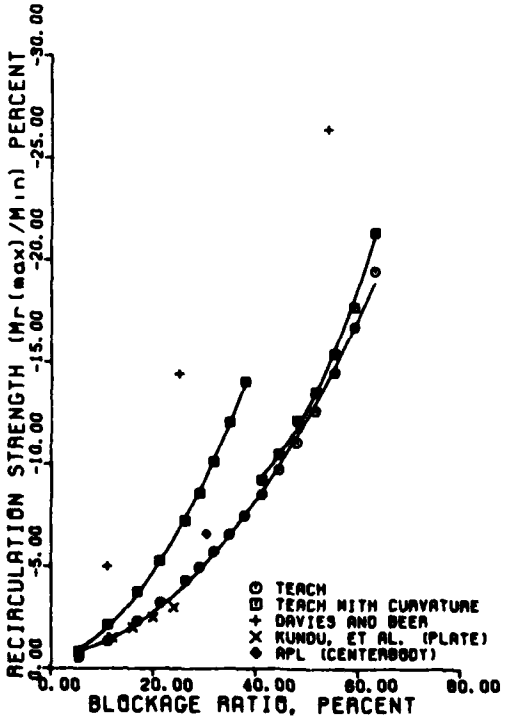


Figure 9. Variation of recirculation strength with blockage ratio.

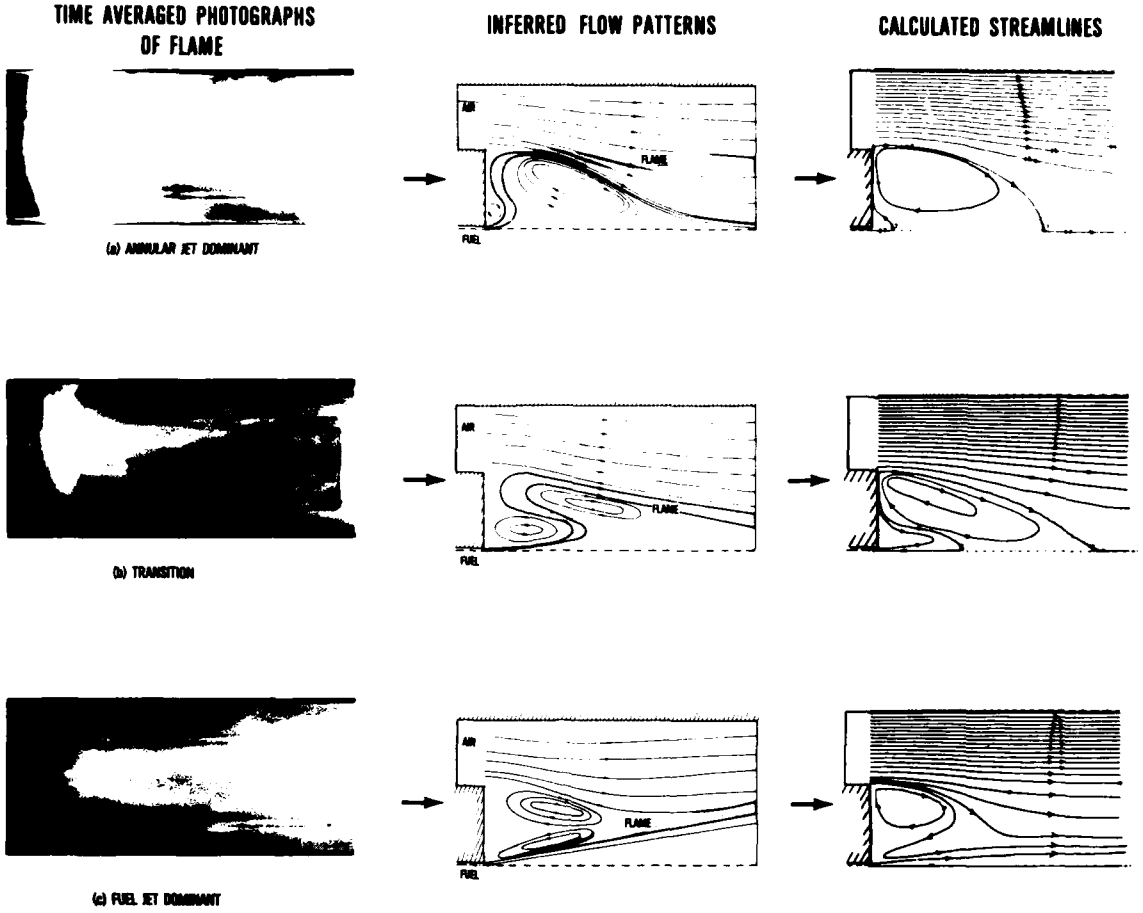


Figure 10. Flame photographs, flow field inferred from the flame photographs and calculated streamlines from Reference 28 for an air flow rate of 1 kg/s and fuel flow rates of (a) 8 kg/hr, (b) 10 kg/hr and (c) 13 kg/hr.

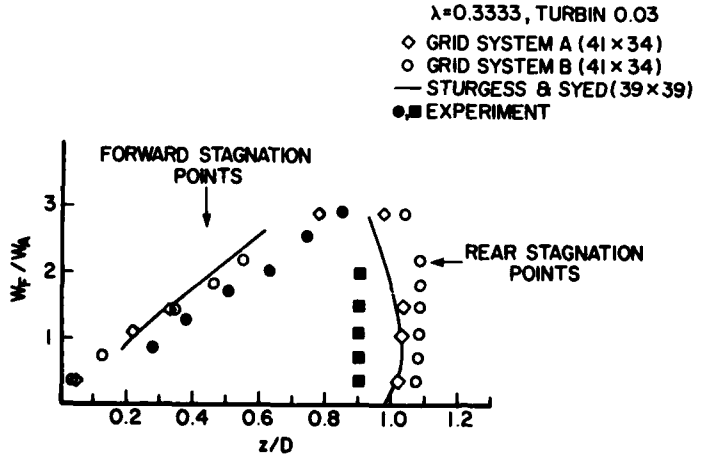


Figure 11. Comparison of measured and predicted centerline stagnation points for an air flow rate of 2 kg/s and different CO_2 flow rates [17].

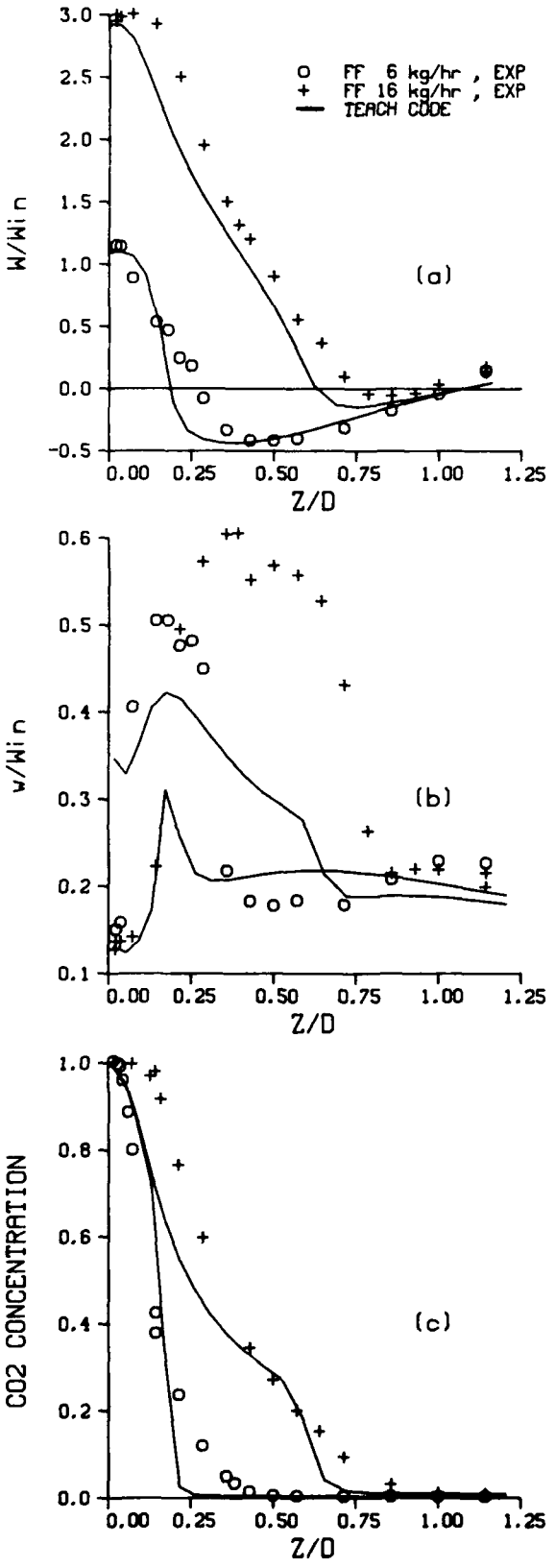


Figure 12. Measured and predicted isothermal centerline profiles for an air flow rate of 2 kg/s.

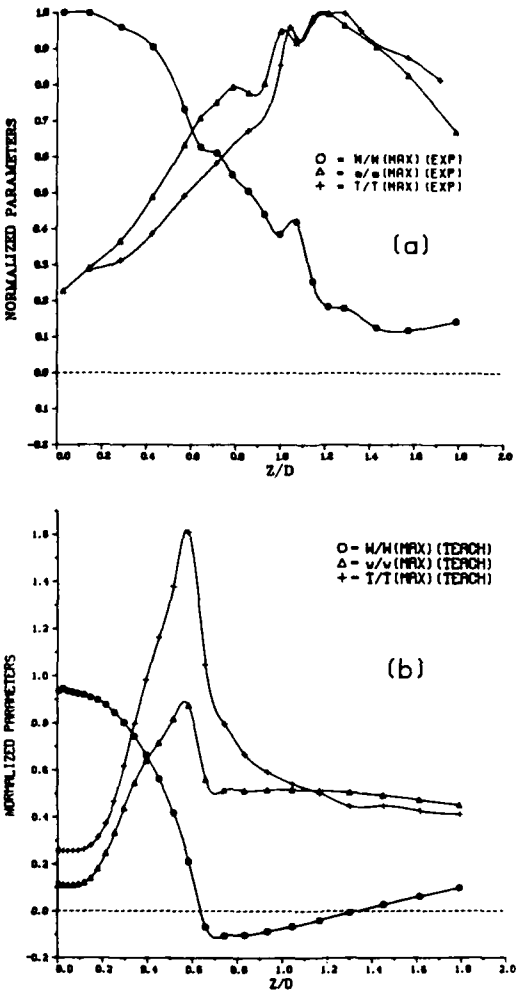


Figure 13. Measured and predicted centerline profiles for an air flow rate of 2 kg/s and a propane flow rate of 8 kg/hr.

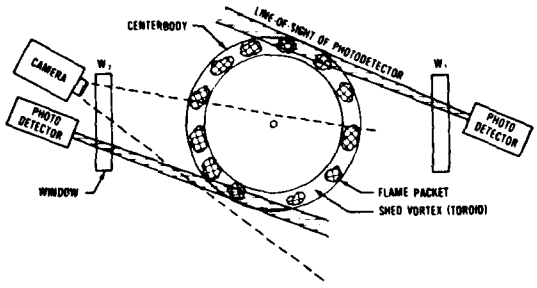


Figure 14. Downstream end view of the combustion tunnel illustrating the camera and photodetector views of toroidal vortex shedding from the centerbody face [35].



Figure 15. Snapshot of shed vortices for an air flow rate of 1 kg/s and fuel flow rate of 6 kg/hr.

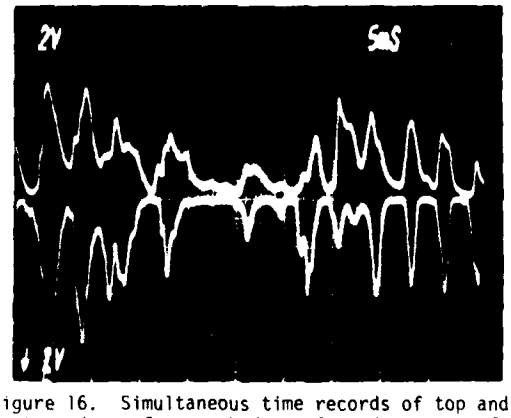


Figure 16. Simultaneous time records of top and bottom edges of centerbody at 6 cm downstream for an air flow rate of 2 kg/s and fuel flow rate of 6 kg/hr [35].

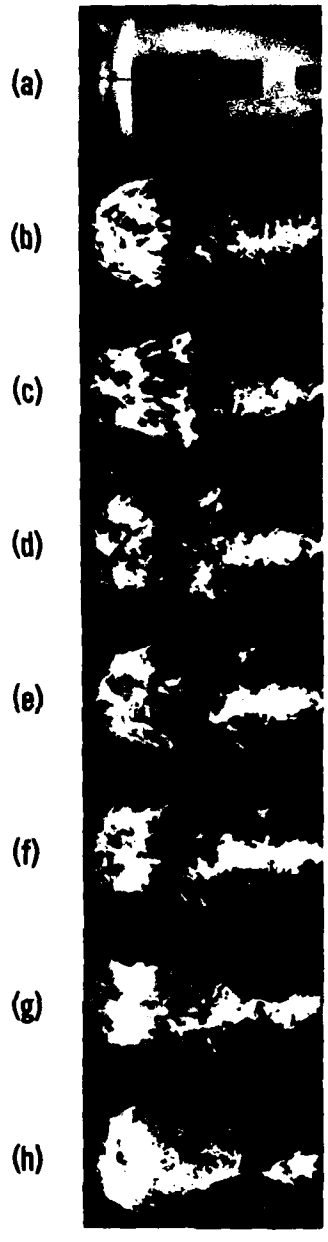


Figure 17. High speed cine pictures (3000 frames/s) of the flame for an air flow rate of 1 kg/s and a fuel flow rate of 6 kg/hr [35].

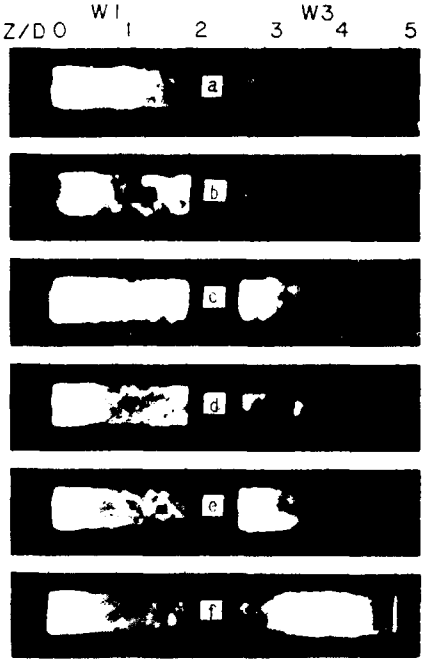


Figure 18. High speed cine pictures (500 frames/s) of the flame for an air flow rate of 1 kg/s and a fuel flow rate of 6 kg/hr [15]. Every other frame is shown.

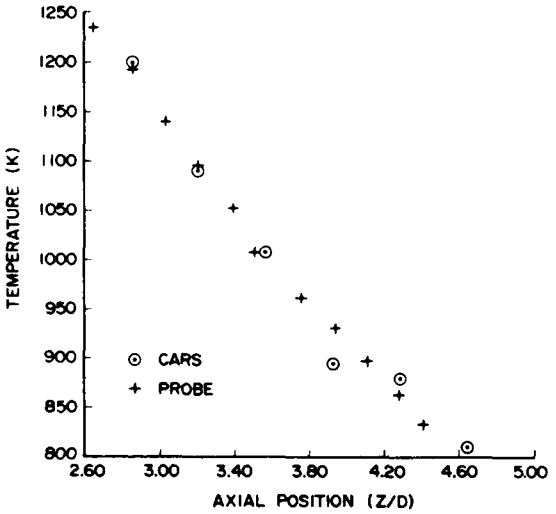


Figure 19. Comparison of time-averaged CARS and thermocouple measuremented temperatures along duct centerline for an air flow of 1 kg/s and fuel flow of 6 kg/hr [15].

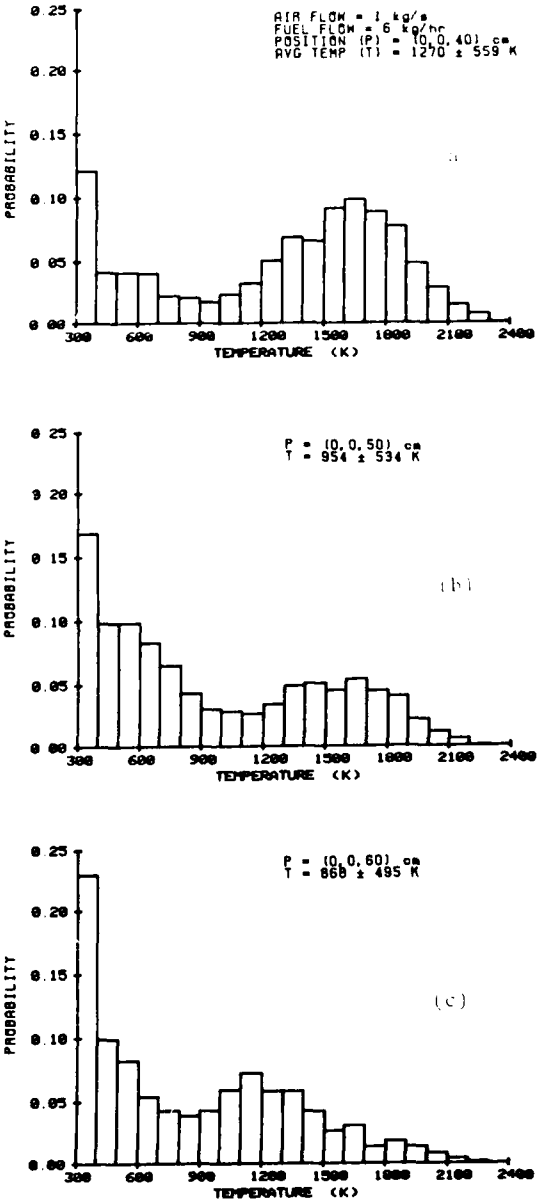


Figure 20. CARS measured temperature pdf's along the duct centerline at various axial locations for an air flow of 1 kg/s and a fuel flow of 6 kg/hr [15].

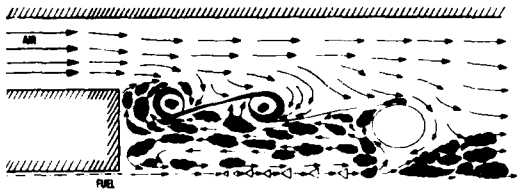


Figure 21. Illustration of the dynamic combustion processes in the centerbody combustor [35].

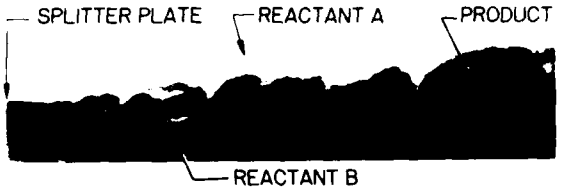


Figure 23. Side view of reacting shear layer [37].

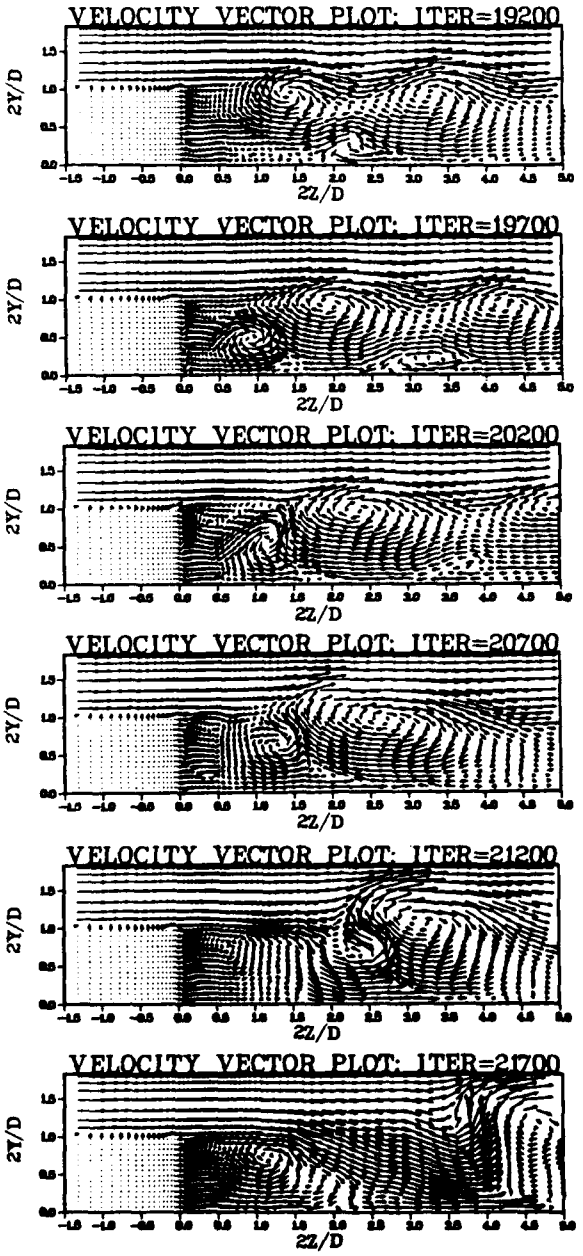


Figure 22. Predicted velocity vector fields at different time iterations (1 ITER = $3X10^{-6}$s) for the centerbody combustor operating at an air flow of 2 kg/s and zero fuel flow [22].

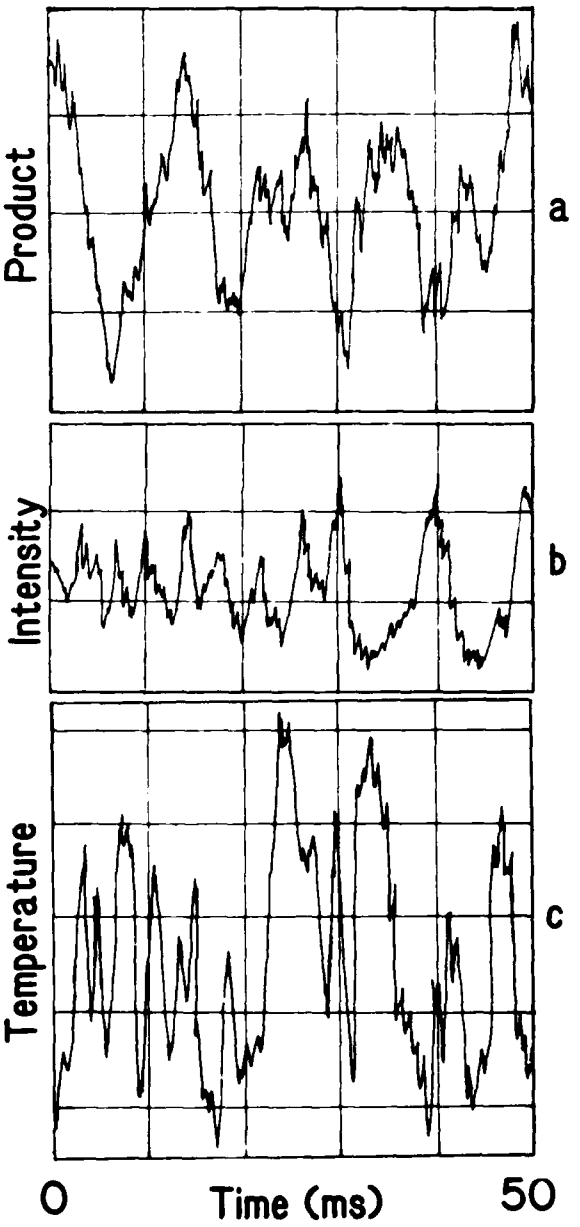


Figure 24. Time trace of (a) product concentration in a reacting shear layer [37], (b) flame luminosity in the near-wake region of the centerbody combustor [34] and (c) temperature at the exit plane of a gas turbine combustor [38].

DISCUSSION

J.Fabri, Fr

Vous avez présenté des résultats qui montrent une bonne comparaison entre les mesures effectuées par DRASC et par thermocouples pour une vitesse d'écoulement de l'ordre de 20 m/s. Dans une chambre de combustion réelle, les vitesses d'écoulement sont plutôt de l'ordre de 70 à 100 m/s. Avez-vous des résultats pour des vitesses de cet ordre de grandeur?

Author's Reply

A direct answer to your question is no, we have not. We have made comparisons between CARS and a shielded thermocouple at 46 m/s and the results showed good agreement. I do not see any reason why any problems would result at twice this velocity.

G.Winterfeld, Ge

You have presented information about the unsteady character of flames which is of great interest for all combustion modellers. It could be interesting to see whether the same observations can be made for a premixed combustible flow.

Author's Reply

Ganji and Sawyer (reference 39) and Pitz and Daily (reference 40) have observed shed vortices in a two-dimensional step combustor. We have not investigated a premixed combustor; however, a combustion tunnel that is much smaller than the APL combustion tunnel described in the paper is currently being fabricated. One of the first experiments in the smaller combustion tunnel will involve high speed ciné pictures of a premixed combusting flow.

J.Tilston, UK

I can confirm on Dr Roquemore's behalf that premixed combustion does give exactly the same effects – at least so far as high speed ciné and high speed ciné schlieren are concerned.

PROBLEM INDEPENDENT NUMERICAL SIMULATION OF TWO-PHASE FLOW IN COMBUSTORS

W.H. Ayers, F. Boysan, B.C.R. Ewan, J.Swithenbank

Department of Chemical Engineering and Fuel Technology,
University of Sheffield, Mappin Street, Sheffield, S1 3JD.

AD-P003 156

Introduction.

The process of applying 3-D computer codes to isothermal and combusting two-phase flows is a multi-faceted one, which can incorporate developments from many areas of study. In the combustion case, this can involve the refinement of models for fuel droplet trajectories, droplet evaporation and radiation heat transfer (1) - each sub-group being worthy of individual study in depth.

In the area of fluid dynamics, the subject of turbulence modelling is also of basic importance, and the realisation that many combustion flows do not satisfy the conditions of isotropy demanded by conventional models, has stimulated more fundamental approaches to the Reynolds stress description in other areas (2) and can be expected to do so in the combustion case in the near future.

Since the common objective of such applications is to provide a basis for design, there is also a need for codes which are versatile, and easy to operate, and which are interactive.

The present study reports some of the current progress in the areas mentioned and rests on many years of development work in combustion modelling. In particular, a number of aspects of the present code are presented including the coupling of flow and droplet motions and the interactive setting up procedure to define an arbitrary geometry. Calculated and measured velocity fields are shown for the isothermal flow in a coaxial dump combustor and in addition, results are presented for the combustion case using a baffle stabiliser.

Governing Equations.

Since the devices of interest display a degree of axial symmetry, it is convenient to present the conservation equations in cylindrical coordinates. For a 3-d flow these take the form

Mass conservation

$$\frac{1}{r}\frac{\partial}{\partial r}(\rho r v) + \frac{1}{r}\frac{\partial}{\partial \theta}(\rho w) + \frac{\partial}{\partial x}(\rho u) = \dot{m}'''$$

x-momentum.

$$\frac{1}{r}\left[\frac{\partial p}{\partial x}(r\rho u^2) + \frac{\partial}{\partial r}(r\rho vu) + \frac{\partial}{\partial \theta}(\rho wu)\right] = -\frac{\partial p}{\partial x}$$

$$+ \frac{1}{r}\frac{\partial}{\partial r}\left[r\mu\left[\frac{\partial u}{\partial r} + \frac{\partial v}{\partial x}\right]\right] + \frac{1}{r}\frac{\partial}{\partial \theta}\left[\mu\left[\frac{1}{r}\frac{\partial u}{\partial \theta} + \frac{\partial w}{\partial x}\right]\right]$$

$$+ \frac{\partial}{\partial x}\left[2\mu\frac{\partial u}{\partial x}\right] + F_x$$

r-momentum.

$$\frac{1}{r}\left[\frac{\partial}{\partial x}(r\rho uv) + \frac{\partial}{\partial r}(r\rho v^2) + \frac{\partial}{\partial \theta}(\rho wv) - \rho w^2\right] = -\frac{\partial p}{\partial r}$$

$$+ \frac{1}{r}\frac{\partial}{\partial r}\left[2r\mu\frac{\partial v}{\partial r}\right] + \frac{1}{r}\frac{\partial}{\partial \theta}\left[\mu\left[r\frac{\partial}{\partial r}(w/r) + \frac{1}{r}\frac{\partial v}{\partial \theta}\right]\right] -$$

$$2\frac{\mu}{r}\left[\frac{1}{r}\frac{\partial w}{\partial \theta} + \frac{v}{r}\right] + \frac{\partial}{\partial x}\left[\mu\left(\frac{\partial u}{\partial r} + \frac{\partial v}{\partial x}\right)\right] + F_r$$

θ-momentum.

$$\frac{1}{r}\left[\frac{\partial}{\partial x}(r\rho uw) + \frac{\partial}{\partial r}(r\rho vw) + \frac{\partial}{\partial \theta}(\rho w^2) + \rho vw\right] = -\frac{1}{r}\frac{\partial p}{\partial \theta}$$

$$+ \frac{1}{r}\frac{\partial}{\partial \theta}\left[r\mu\left[r\frac{\partial}{\partial r}(w/r) + \frac{1}{r}\frac{\partial v}{\partial \theta}\right]\right] + \frac{\mu}{r}\left[r\frac{\partial}{\partial r}(w/r) + \frac{1}{r}\frac{\partial v}{\partial \theta}\right]$$

$$+ \frac{1}{r}\frac{\partial}{\partial \theta}\left[\mu\left[\frac{2}{r}\frac{\partial w}{\partial \theta} + \frac{2v}{r}\right]\right] + \frac{\partial}{\partial x}\left[\mu\left[\frac{\partial w}{\partial x} + \frac{1}{r}\frac{\partial u}{\partial \theta}\right]\right] + F_\theta$$

It can be seen that the mass conservation equation contains the term $\dot{m}''$ due to the mass addition from the evaporating fuel spray for liquid fuelled combustors. In addition, the momentum interaction between the two phases is contained in the terms F_x, F_r and F_θ.

For stabiliser devices with some cyclic symmetry, e.g. multi-element baffles, the solution of these equations is restricted to the symmetry sector, thus improving the grid resolution. In some cases, for example with swirl stabilisers, full axial symmetry can be assumed.

Following the presentation of the fluid velocities in terms of a mean and fluctuating component, the way in which the effects of turbulence are included depends on the model used to represent the Reynolds stresses. One of the simpler possibilities involves the definition of an effective viscosity which may be related to the Reynolds stresses (Boussinesq hypothesis) and also the mean turbulence properties.

Alternatively, transport equations may be solved for the individual Reynolds stresses themselves, either numerically or algebraically, giving rise to a more fundamental description.

These two possibilities have been investigated in depth in the past, the latter giving rise to shear stress modelling, which has been found necessary for swirling flows.

The effective viscosity approach is simpler and has found widespread use and success by many groups. The distribution of viscosity is provided by the parameters of the turbulence model used. Those used most commonly are the kinetic energy of the fluctuating motion $\underline{k}$ and its dissipation rate $\underline{\varepsilon}$. These are obtained by the wolution of their respective transport equations given by -

for $\underline{k}$

$$\frac{1}{r}\left[\frac{\partial}{\partial x}(r\rho uk) + \frac{\partial}{\partial r}(r\rho vk) + \frac{\partial}{\partial \theta}(\rho wk)\right]$$

$$= \frac{1}{r}\frac{\partial}{\partial r}\left[r\,\frac{\mu}{\sigma_k}\frac{\partial k}{\partial r}\right] + \frac{1}{r}\frac{\partial}{\partial \theta}\left[\frac{\mu}{r_k}\frac{\partial k}{\partial \theta}\right]$$

$$+ \frac{\partial}{\partial x}\left[\frac{\mu}{\sigma_k}\frac{\partial k}{\partial x}\right] + G_k - \rho\varepsilon$$

and for $\underline{\varepsilon}$

$$\frac{1}{r}\left[\frac{\partial}{\partial x}(r\rho u\varepsilon) + \frac{\partial}{\partial r}(r\rho v\varepsilon) + \frac{\partial}{\partial \theta}(\rho w\varepsilon)\right] + \frac{1}{r}\frac{\partial}{\partial r}\left[r\,\frac{\mu}{\sigma_\varepsilon}\frac{\partial \varepsilon}{\partial r}\right]$$

$$+ \frac{1}{r}\frac{\partial}{\partial \theta}\left[\frac{\mu\partial\varepsilon}{\sigma_\varepsilon r\partial\theta}\right] + \frac{\partial}{\partial x}\left[\frac{\mu}{\sigma_\varepsilon}\frac{\partial \varepsilon}{\partial x}\right] + C_1\,\frac{\varepsilon}{k}\,G_k - C_2\,\rho\,\frac{\varepsilon^2}{k}$$

where G_k is the generation term of k and is given by

$$G_k = \mu\left[2\left[\left(\frac{\partial u}{\partial x}\right)^2 + \left(\frac{\partial v}{\partial r}\right)^2 + \left(\frac{1}{r}\frac{\partial w}{\partial \theta} + \frac{v}{r}\right)^2\right] + \left(\frac{\partial u}{\partial r} + \frac{\partial v}{\partial x}\right)^2\right.$$

$$\left. + \left(\frac{\partial w}{\partial x} + \frac{1}{r}\frac{\partial u}{\partial \theta}\right)^2 + \left(\frac{1}{r}\frac{\partial v}{\partial \theta} + \frac{\partial w}{\partial r} - \frac{w}{r}\right)^2\right]$$

The turbulent viscosity is related to k and ε by the expression

$$\mu_t = C_\mu\,\frac{k^2}{\varepsilon}$$

The coefficients C_1, C_2, C_μ, σ_k and σ_ε are constants which have the following values

$$C_1 = 1.44, \quad C_2 = 1.92, \quad C_\mu = 0.09, \quad \sigma_k = 1.0, \quad \sigma_\varepsilon = 1.3$$

This is the turbulence model which has been used in the present dump combustor study.

For reacting flows additional conservation equations for enthalpy and chemical species are required, these being

for enthalpy

$$\frac{1}{r}\left[\frac{\partial}{\partial x}(r\rho uh) + \frac{\partial}{\partial r}(r\rho vh) + \frac{\partial}{\partial \theta}(\rho wh)\right] = \frac{1}{r}\frac{\partial}{\partial r}\left[r\,\frac{\mu}{\sigma_h}\frac{\partial h}{\partial r}\right]$$

$$+ \frac{1}{r}\frac{\partial}{\partial \theta}\left[\frac{1}{r}\,\frac{\mu}{\sigma_h}\frac{\partial h}{\partial \theta}\right] + \frac{\partial}{\partial x}\left[\frac{\mu}{\sigma_h}\frac{\partial h}{\partial \theta}\right] + S_h$$

where S_h includes radiation sources, shear work and spray gas interaction terms and σ_h is the turbulent Prandtl number for enthalpy.

For chemical species j

$$\frac{1}{r}\left[\frac{\partial}{\partial x}(r\rho um_j) + \frac{\partial}{\partial r}(r\rho vm_j) + \frac{\partial}{\partial \theta}(\rho wm_j)\right] = \frac{1}{r}\frac{\partial}{\partial r}\left[r\,\frac{\mu_t}{\sigma_j}\frac{\partial m}{\partial r}\right]$$

$$+ \frac{1}{r}\frac{\partial}{\partial \theta}\left[\frac{1}{r}\,\frac{\mu}{\sigma_j}\frac{\partial m_j}{\partial \theta}\right] + \frac{\partial}{\partial x}\left[\frac{\mu}{\sigma_j}\frac{\partial m_j}{\partial x}\right] + R_j + S_j$$

where m_j is the mass fraction of species j, R_j is the mass rate of depletion or creation by reaction and S_j is the rate of creation by evaporation from the liquid phase.

The effect of turbulence on the reaction rate is taken into account by employing the eddy breakup model of Spalding (3). In this case the reaction rate for m_{fu} is taken to be the smaller of the two expressions given by the Arrhenius formulation and the eddy breakup model. The latter can be expressed as

$$R_{fu} = -4\rho\frac{\varepsilon}{k}\left[m_{fu}\,,\ m_{ox}/s\right]$$

where the term in brackets indicates the lesser of m_{fu} and m_{ox}

The radiation contribution to the enthalpy equation is evaluated by the solution of three differential equations for the radiant fluxes R_x, R_r and R_θ and is given by

$$S_{h,rad} = 2a\left[R_x + R_r + R_\theta - 3E\right]$$

where a is a flux absorption coefficient and $E = \sigma T^4$ is the black body emissive power.

The present combustion model employs a random droplet tracking procedure for fuel droplets, based on the known initial droplet conditions of size and velocity, combined with the influence of the flow field on the droplets based on a suitable drag law. The process can also embody the random effect of turbulence by employing a randomised turbulent velocity fluctuation in each finite difference cell of magnitude proportional to the local turbulence and duration based on the characteristic lifetime of the eddy.

Knowledge of the trajectories for a large number of droplets combined with the current temperature profile enables evaporation patterns to be evaluated for the next computation cycle. The droplet drag force is given by

$$F = \frac{18\mu_g}{\rho_p D_p^2}\cdot\frac{C_D Re}{24}$$

where μ_g is the molecular viscosity of the gas, ρ_p is the density of the droplet and D its diameter. Re is the relative Reynolds number.

$$Re = \frac{\rho_g D\left|\tilde{u}_p - \tilde{u}_\infty\right|}{\mu_g}$$

Suitable expressions for the drag coefficient are available (4) and depend upon Re

$$C_D = 27\,Re^{-0.84} \qquad 0 < Re < 80$$

$$C_D = 0.271Re^{0.217} \qquad 80 < Re < 10^4$$

For evaporating drops the rate of change of diameter is given by

$$\frac{dD}{dt} = \frac{C_b}{2D}\left[1 + 0.23\,Re^{0.5}\right]$$

where the bracketed term represents the forced convective contribution to evaporation and C_b is the vaporisation rate constant which depends on the medium and droplet. A widely used expression for C_b due to Wise and Agoston (5) is

$$C_b = \frac{8\lambda}{\rho_l C_p}\ln\left[1 + \frac{C_p}{L}(T_\infty - T_l)\right]$$

where λ is the thermal conductivity of the gas, L is the latent heat of evaporation and T_∞ and T_l are the gas and droplet temperatures respectively.

Solution Procedure.

The initial setting up procedure is carried out interactively and involves primarily the definition of the system geometry. This is achieved by calling up in sequence successive planes of grid points. These grid points each carry an associated label which can be defined by the operator. These labels include such specifications as W(wall), I(inlet), O(outlet) and S(symmetry plane) etc. and their allocation defines the device geometry. The 3-D grid used depends on the symmetry of the problem but typically consists of 27 x 18 x 7 for the axial, radial and tangential directions. The iteration procedure consists of the following steps -

i) The u,v,w momentum equations are each solved in turn using guessed pressures.

ii) Since the velocities do not satisfy the mass continuity equation locally, a "Poisson type" equation is derived from the continuity equation and the three linearised momentum equations. This pressure correction equation is then solved to obtain the necessary corrections to the pressure field and the corresponding adjustments to the velocity components are made.

iii) The k and ε equations are solved using the updated velocity field to obtain the distribution of effective viscosity.

iv) Any auxiliary equations (e.g. enthalpy, species, conservation, radiation or turbulence properties) are solved using the previously updated values of the other variables.

v) Where interphase coupling is to be included, a solution of the equations of motion of the droplets is obtained at intervals and used to augment the source terms of the appropriate gas flow equations.

These steps can be continued until the error mentioned in (ii) has decreased to a required value.

Calculations and Measurements.

The work to be described concerns measurements and calculations on a single dump combustor of dimensions shown in Figure 1.

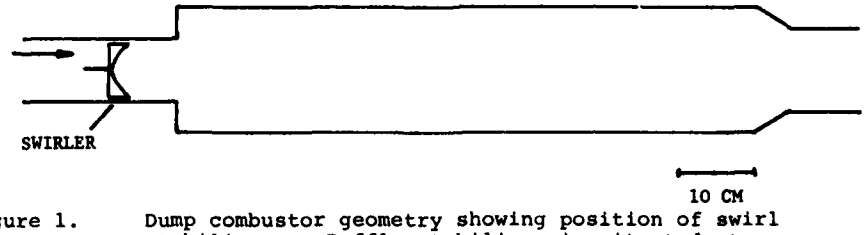


Figure 1. Dump combustor geometry showing position of swirl stabiliser. Baffle stabiliser is situated at dump plane.

The inlet conditions involved a) no stabiliser b) a three element baffle at the dump plane c) a swirl stabiliser at 8 cm upstream of the dump plane. In all cases k-ε turbulence modelling of the flow field has been applied and for the baffle case combustion calculations have also been performed. The baffle used consisted of thin plate with rectangular obstructions of 30% total blockage area. For the swirler, the design was based on that of Buckley et al. (6) and employed computed blade shapes which could produce different tangential profiles with a common swirl number. Three of these designs have been measured at swirl numbers of 0.4, as part of a larger study to investigage the influence of profile shape, although only results for approximately free vortex will be reported here.

The LDA system employed consisted of a backscatter arrangement with frequency shifting, and signal processing was by means of a burst correlator.

The light from a 488 nm argon laser was focused onto a rotating diffraction grating using a 200 mm focal length lens. This ensures a circular cross section of the diffracted beams thus maximising subsequent beam crossing and minimising uncorrelated noise.

Two further lenses collimate the ±1orders and also permit the choice of beam separation and hence fringe spacing in the manner described by Wigley (7). The beams are focused and crossed by an output lens at 1500 mm focal length thus providing some considerable distance between the test rig and the instrumentation. For single photon collection, as with this configuration, data processing is by autocorrelation and summation resulting in accumulated autocorrelation functions containing all velocity variations occurring during the sampling interval.

Each sampling operation is controlled by a PET microcomputer and data is analysed by a curve fitting procedure based on the analysis of Abbiss et al. (8).

The collection system, which was aligned at 15° to the output axis as a means of obtaining the desired longitudinal resolution, consisted of a 750 mm focal length collection lens of 112 mm aperture, focusing onto a collection pinhole which controlled the lateral resolution.

A Malvern Instruments RF313 photomultiplier which was capable of observing single photons, was focused on the collection pinhole and fed its output to the 50 nsec correlator.

In a typical experimental run the test rig, which is on a motor driven traverse, is scanned across the region of interest, with the fringe velocity being measured at each sample point simultaneously by feeding the counting pulses from a grating monitor to one of the correlator storage channels.

For the present work the fringe velocity employed was up to 130 M/s depending on turbulence level, and the fringe spacing was 88μ. The spatial resolution, which is determined largely by the angle of collection and waist diameter at the probe volume was around 1 mm both longitudinally and laterally, based on a 100 times drop in collected signal strength at these limits.

The accuracy with which the program calculated peak velocities was assessed using analytically generated correlation functions with different degrees of random noise superimposed. The error on peak velocities was thus estimated to be ± 0.25 M/s.

The air velocities used at the 80 mm diameter inlet were between 65 and 75 M/s being limited by the supply and seeding was by means of 0.5μ titanium dioxide particles generated by a fluidised bed. Background noise limited the closest approach to the inner walls to 9,24 mm.

Results.

Isothermal flows

The first results are shown in Figures 2, 3 and show a comparison of measured and calculated velocities at three axial stations. Each figure shows a radial profile in two cases - with the three element baffle and with no baffle. For the baffle case, the plane of measurement was on a reflection symmetry plane at 90° from the mid-line of one of the baffles. Figure 3 also has an example of the turbulence comparison at one of the stations.

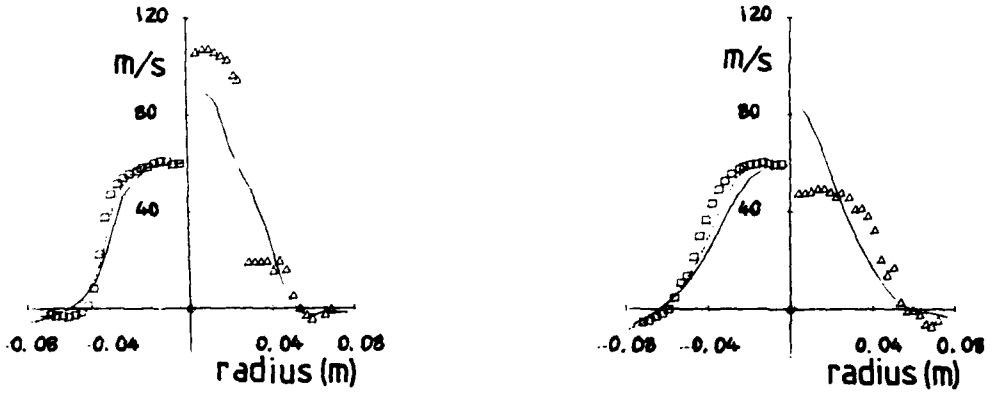


Figure 2. Radial variation of axial velocity with and without baffle stabiliser at A) 50 mm from dump and B) 150 mm from dump □ and △ are experimental points, _____ are calculated with coarse grid, ----- are calculated with fine grid.

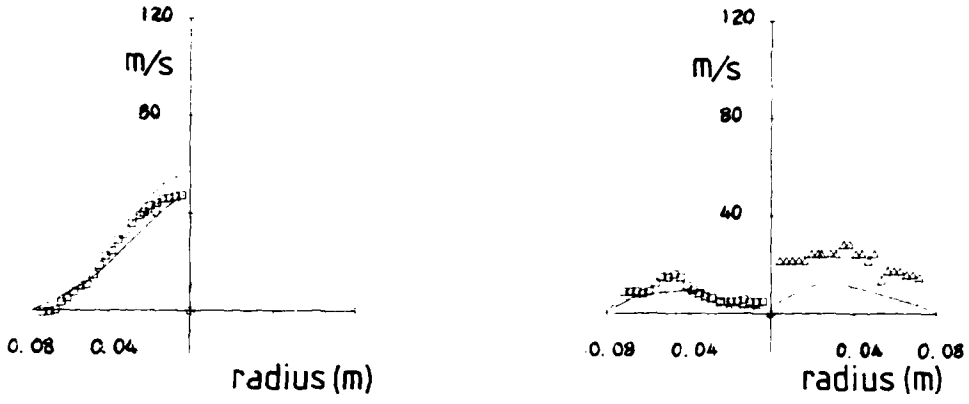


Figure 3. A) radial variation of axial velocity profile at 330 mm from dump plane. □ are experimental points, _____ are calculated with coarse grid, ------ are calculated with fine grid.
B) radial variation of rms turbulence at 150 mm from dump plane, with and without baffle, □ and △ are experimental points, _____ are calculated functions.

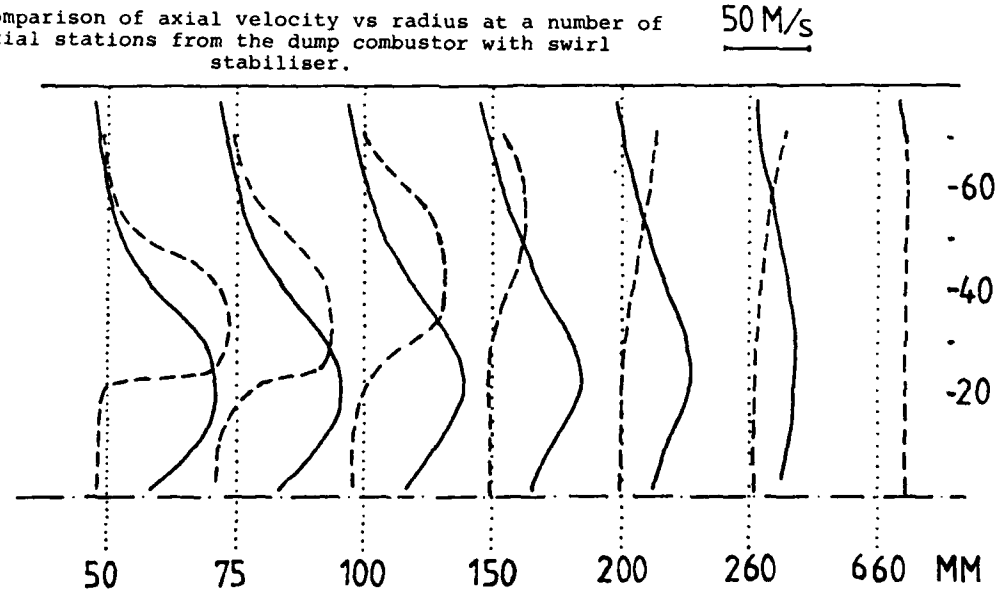
In all cases, the 'no baffle' condition shows good agreement between measured and calculated velocity and turbulence, showing that in this case, the k-ε model is satisfactory.

For the case with baffles, the agreement is moderately good at 50 mm from the dump plane but deteriorates as one goes down stream, with the measured values flattening out much more quickly. Examination of the turbulence values indicates that the model has greatly underestimated these, and most likely accounts for the much slower levelling out of the velocity.

Measurements have also been made with a swirl stabiliser situated at 8 cm upstream of the dump plane which produced approximately free vortex type swirl and an overall swirl number of 0.4. The comparison between calculated and measured fields is shown in Figure 4 at a number of axial stations. The measured values show a characteristic axial recirculation zone and a short reattachment distance to the dump wall. The k-ε model here however, is unable to reproduce even the main features of the flow, showing a strong axial forward flow. This confirms results obtained in other areas on swirling flows using this model and indicates, as with these, that a more fundamental turbulence algorithm is needed. This however, is a more complicated case than a 'tangentially driven' cyclone flow where the axial derivatives are much smaller, and most probably requires a more time consuming algebraic modelling approach than that case.

Figure 4.

Comparison of axial velocity vs radius at a number of axial stations from the dump combustor with swirl stabiliser.



Combustion case.

Figures 5, 6 and 7 show some typical results which can be obtained for fuel spray combustion. The three element baffle has been used here and a single spray is injected from upstream at right angles to the wall. A distribution of drop sizes is employed ranging from 5μ to 100 μ with a Rosin Rammler distribution of mean 50 μ and width parameter of 2.2.

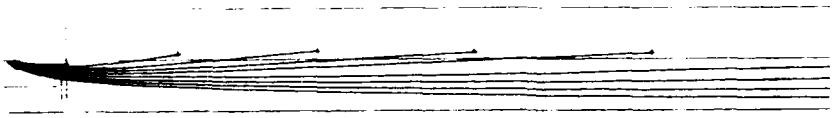


Figure 5. Trajectory patterns for a range of drop sizes from 5 to 100 microns. Crosses show points of evaporation.

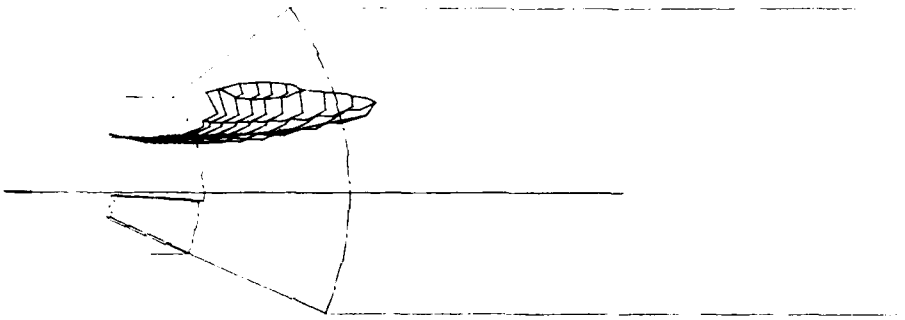


Figure 6. Three dimensional plot of constant mass fraction of evaporated fuel at mass fraction of 0.01.

Preheated air at 550^{o}K is used as input and a fuel/air ratio of 0.02 is used. Figure 5 shows the trajectory and evapo-ation history of ten drops of different sizes. The smallest penetrate least into the flow and are convected inside the dump. The crosses show the points at which they evaporate. It can also be seen that some of the larger droplets do not evaporate within the range considered, and it is clear that this kind of study is of some value in matching a particular atomiser to the flow field.

Figure 6 is derived from information of the kind seen in Figure 5 for each computational cell and shows a contour of constant evaporated fuel mass fraction. This is invaluable information in indicating where unburnt evaporated fuel originates and is convected. It can be seen from the figure that the pattern is following the general pattern and then becoming entrained in the strong recirculation zone behind the baffles.

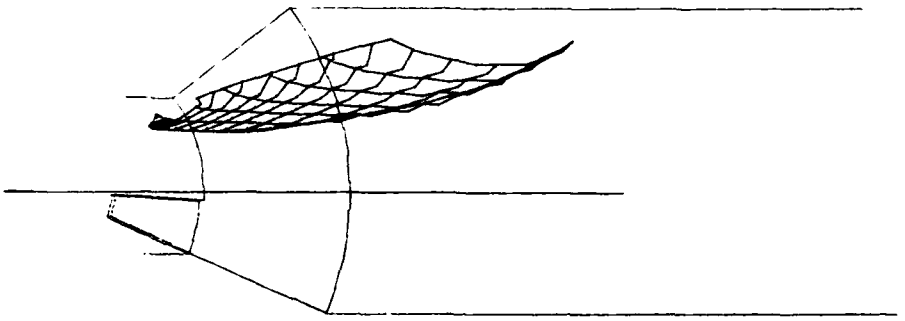


Figure 7. Three dimensional plot of constant temperature of 2000 K.

Figure 7 is a similar contour plot for temperature at 2000^{o}K and again shows the curvature associated with one of the recirculation bubbles. Such information is useful in association with evaporation patterns in correcting for hot wall regions.

Conclusions.

Some of the main features of the flow/combustion model have been described, and the ease of setting up a device geometry has been emphasised.

The dump combustor study has underlined some of the limits of applicability of the k-ε model and, in addition to the axially symmetric swirling flow these appear also to include flows with strong recirculation zones.

From previous work (2), it appears that a more fundamental approach to the shear stress modelling will correct most of the difficulty and the incorporation of these new developments for the strongly 3-D case is currently underway.

References.

1. F. Boysan, W.H. Ayers, J. Swithenbank, Z. Pan 'Three Dimensional Model of Spray Combustion in Gas Turbine Combustors', J.Energy 6(6), 368 (1982).

2. F. Boysan, B.C.R. Ewan, J. Swithenbank, W.H. Ayers 'Experimental and Theoretical Studies of Cyclone Separator Aerodynamics' I.Chem.E., POWTECH Conference, Birmingham, March 1983.

3. D.B. Spalding 'Mathematical Models of Turbulent Flames', Comb.Sci. and Tech., 13, 3 (1976).

4. S. Lambiris, L.P. Combs 'Steady State Combustion Measurements in LOX-RP-1 Rocket Chamber and Related Spray Burning Analysis' Detonation and Two Phase Flow, Academic Press, New York, Vol.6, 1962.

5. H. Wise, G.A. Agoston 'Literature on the Combustion of Petroleum', American Chem. Soc., Washington DC, 1958.

6. P.L. Buckley, R.R. Craig, D.L. Davis, K.G. Schwartzkopf 'The Design and Combustion Performance of Practical Swirlers for Integral Rocket Ramjets', AIAA/SAE/ASME 16th Joint Propulsion Conference Hartford, June 1980.

7. G. Wigley UKAEA Harwell Int.Rep.No. AERE R7886, 1974.

8. J.B. Abbiss, T.W. Chubb, E.R. Pike 'Laser Doppler Anemometry', Optics and Laser Technology 249 (1974).

Acknowledgements.

The authors would like to acknowledge support for this work by the USAF, Air Force Office of Scientific Research, under grant number AFOSR-82-0272.

DISCUSSION

C.Hirsch

Could you give some more details on the numerical techniques used and the type of scheme? In addition your results seem to draw a large grid dependence which is to be expected with the rather coarse grids you are using. How do you ensure therefore that the discrepancies between computation and date are solely due to the deficiencies of the k-e models?

Author's Reply

We have carried out extensive tests on different finite difference schemes including, for example; central difference, skew upwind difference, and the quadratic ("QUICK") scheme. In the study presented here the power law scheme was used which we have found to be the most suitable for general use, although others are more accurate. We have also studied the efficacy of different band matrix solution procedures. Whilst Stone's method yields more rapid solutions in many cases, the TDMA procedure used here has proved to be more robust in a wide variety of problems. Nevertheless, we expect further developments in the solution method in the future.
Grid independence of the solution has been verified provided the grid is fine enough to define the details of the flow field. Quantitative criteria can also be used to ensure that the grid is sufficiently fine and grid independence of the two-dimensional results presented here has been checked. Our lack of faith in the k-e model is largely based on earlier studies which we presented in References A and B. In that study we report our detailed L.D.A. experimental results for strongly sheared (swirling) flow and numerical results using both the k-e model and an algebraic stress turbulence model which we have developed. The inability of the k-e model to correctly predict such flows was demonstrated conclusively.

Reference A; Boysan, F. and Swithenbank, J., Numerical Prediction of Confined Vortex Flows, Second International Conference on Numerical Methods in Laminar and Turbulent Flow, Venice, 1981.
Reference B; Boysan, F., Ayers, W.H. and Swithenbank, J., Transactions of I. Chem. E., 601, 1982.

REPORT DOCUMENTATION PAGE

1. Recipient's Reference	2. Originator's Reference	3. Further Reference	4. Security Classification of Document
	AGARD-CP-353	ISBN 92-835-0346-5	UNCLASSIFIED

5. Originator Advisory Group for Aerospace Research and Development
North Atlantic Treaty Organization
7 rue Ancelle, 92200 Neuilly sur Seine, France

6. Title

COMBUSTION PROBLEMS IN TURBINE ENGINES

7. Presented at

the Propulsion and Energetics Panel 62nd Symposium, held in Çeşme, Turkey, 3–6 October 1983.

8. Author(s)/Editor(s)	9. Date
Various	January 1984
10. Author's/Editor's Address	**11. Pages**
Various	446

12. Distribution Statement This document is distributed in accordance with AGARD policies and regulations, which are outlined on the Outside Back Covers of all AGARD publications.

13. Keywords/Descriptors

Combustion	Fuel effects
Turbine engines	Fuel preparation
Combustors	Atomization of fuel
Burners	Soot formation
Liner cooling	Droplet size

14. Abstract

The Conference Proceedings contain 36 papers presented at the Propulsion and Energetics Panel 62nd Symposium on Combustion Problems in Turbine Engines which was held in Çeşme, Turkey, on 3–6 October 1983.

The Technical Evaluation Report is included at the beginning of the Proceedings. Questions and answers of the discussions follow each paper. The Symposium was arranged in seven sessions: Fuel Research (3); Fuel Effects in Main Burners (6); Fuel Preparation (8); Kinetics and Soot Formation (5); Liner Cooling and Traverse Quality (4); Combustion Model Elements (4); and Modelling for Main Burners (6).

The purpose of the Symposium was to review new results of modelling and experimental investigations in the combustion field performed in the last four years, and to provide a platform where research scientists from establishments and universities as well as development specialists from industry could discuss their problems.

AGARD Conference Proceedings No.533 Advisory Group for Aerospace Research and Development, NATO COMBUSTION PROBLEMS IN TURBINE ENGINES Published January 1984 446 pages The Conference Proceedings contain 36 papers presented at the Propulsion and Energetics Panel 62nd Symposium on Combustion Problems in Turbine Engines which was held in Çeşme, Turkey, on 3–6 October 1983. The Technical Evaluation Report is included at the beginning of the Proceedings. Questions and answers of the discussions follow each paper. The Symposium was arranged in seven sessions: Fuel Research (3); Fuel P.T.O.	AGARD-CP-353 Combustion Turbine engines Combustors Burners Liner cooling Fuel effects Fuel preparation Atomization of fuel Soot formation Droplet size	AGARD Conference Proceedings No.353 Advisory Group for Aerospace Research and Development, NATO COMBUSTION PROBLEMS IN TURBINE ENGINES Published January 1984 446 pages The Conference Proceedings contain 36 papers presented at the Propulsion and Energetics Panel 62nd Symposium on Combustion Problems in Turbine Engines which was held in Çeşme, Turkey, on 3–6 October 1983. The Technical Evaluation Report is included at the beginning of the Proceedings. Questions and answers of the discussions follow each paper. The Symposium was arranged in seven sessions: Fuel Research (3); Fuel P.T.O.	AGARD-CP-353 Combustion Turbine engines Combustors Burners Liner cooling Fuel effects Fuel preparation Atomization of fuel Soot formation Droplet size
AGARD Conference Proceedings No.353 Advisory Group for Aerospace Research and Development, NATO COMBUSTION PROBLEMS IN TURBINE ENGINES Published January 1984 446 pages The Conference Proceedings contain 36 papers presented at the Propulsion and Energetics Panel 62nd Symposium on Combustion Problems in Turbine Engines which was held in Çeşme, Turkey, on 3–6 October 1983. The Technical Evaluation Report is included at the beginning of the Proceedings. Questions and answers of the discussions follow each paper. The Symposium was arranged in seven sessions: Fuel Research (3); Fuel P.T.O.	AGARD-CP-353 Combustion Turbine engines Combustors Burners Liner cooling Fuel effects Fuel preparation Atomization of fuel Soot formation Droplet size	AGARD Conference Proceedings No.353 Advisory Group for Aerospace Research and Development, NATO COMBUSTION PROBLEMS IN TURBINE ENGINES Published January 1984 446 pages The Conference Proceedings contain 36 papers presented at the Propulsion and Energetics Panel 62nd Symposium on Combustion Problems in Turbine Engines which was held in Çeşme, Turkey, on 3–6 October 1983. The Technical Evaluation Report is included at the beginning of the Proceedings. Questions and answers of the discussions follow each paper. The Symposium was arranged in seven sessions: Fuel Research (3); Fuel P.T.O.	AGARD-CP-353 Combustion Turbine engines Combustors Burners Liner cooling Fuel effects Fuel preparation Atomization of fuel Soot formation Droplet size

Effects in Main Burners (6); Fuel Preparation (8); Kinetics and Soot Formation (5); Liner Cooling and Traverse Quality (4); Combustion Model Elements (4); and Modelling for Main Burners (6).

The purpose of the Symposium was to review new results of modelling and experimental investigations in the combustion field performed in the last four years, and to provide a platform where research scientists from establishments and universities as well as development specialists from industry could discuss their problems.

ISBN 92-835-0346-5

Effects in Main Burners (6); Fuel Preparation (8); Kinetics and Soot Formation (5); Liner Cooling and Traverse Quality (4); Combustion Model Elements (4); and Modelling for Main Burners (6).

The purpose of the Symposium was to review new results of modelling and experimental investigations in the combustion field performed in the last four years, and to provide a platform where research scientists from establishments and universities as well as development specialists from industry could discuss their problems.

ISBN 92-835-0346-5

Effects in Main Burners (6); Fuel Preparation (8); Kinetics and Soot Formation (5); Liner Cooling and Traverse Quality (4); Combustion Model Elements (4); and Modelling for Main Burners (6).

The purpose of the Symposium was to review new results of modelling and experimental investigations in the combustion field performed in the last four years, and to provide a platform where research scientists from establishments and universities as well as development specialists from industry could discuss their problems.

ISBN 92-835-0346-5

Effects in Main Burners (6); Fuel Preparation (8); Kinetics and Soot Formation (5); Liner Cooling and Traverse Quality (4); Combustion Model Elements (4); and Modelling for Main Burners (6).

The purpose of the Symposium was to review new results of modelling and experimental investigations in the combustion field performed in the last four years, and to provide a platform where research scientists from establishments and universities as well as development specialists from industry could discuss their problems.

ISBN 92-835-0346-5